

**Coupled poroelastic waves and electromagnetic fields in layered media
Theory, Modeling, and Interferometric Synthesis**

Grobbe, Niels

DOI

[10.4233/uuid:fe2c6d16-17cd-495a-99be-2f3ddefb06d2](https://doi.org/10.4233/uuid:fe2c6d16-17cd-495a-99be-2f3ddefb06d2)

Publication date

2016

Document Version

Final published version

Citation (APA)

Grobbe, N. (2016). *Coupled poroelastic waves and electromagnetic fields in layered media: Theory, Modeling, and Interferometric Synthesis*. [Dissertation (TU Delft), Delft University of Technology]. <https://doi.org/10.4233/uuid:fe2c6d16-17cd-495a-99be-2f3ddefb06d2>

Important note

To cite this publication, please use the final published version (if applicable).
Please check the document version above.

Copyright

Other than for strictly personal use, it is not permitted to download, forward or distribute the text or part of it, without the consent of the author(s) and/or copyright holder(s), unless the work is under an open content license such as Creative Commons.

Takedown policy

Please contact us and provide details if you believe this document breaches copyrights.
We will remove access to the work immediately and investigate your claim.

**Coupled Poroelastic Waves
and Electromagnetic Fields
in Layered Media**

Theory, Modeling, and Interferometric Synthesis

Coupled Poroelastic Waves and Electromagnetic Fields in Layered Media

Theory, Modeling, and Interferometric Synthesis

PROEFSCHRIFT

ter verkrijging van de graad van doctor
aan de Technische Universiteit Delft,
op gezag van de Rector Magnificus Prof.ir. K.Ch.A.M. Luyben,
voorzitter van het College voor Promoties,
in het openbaar te verdedigen op 7 juni, 2016 om 15.00 uur

door Niels GROBBE

Master of Science in Geophysics, Utrecht University
geboren te Ede.

Dit proefschrift is goedgekeurd door de promotoren:

Prof.dr.ir. E.C. Slob

Prof.dr.ir. C.P.A. Wapenaar

Samenstelling promotiecommissie:

Rector Magnificus, Technische Universiteit Delft, voorzitter

Prof.dr.ir. E.C. Slob, Technische Universiteit Delft, promotor

Prof.dr.ir. C.P.A. Wapenaar, Technische Universiteit Delft, promotor

Onafhankelijke leden:

Dr. B. Kuvshinov, Shell Global Solutions International B.V.

Dr. A. Revil, Université Savoie Mont Blanc, France

Dr. R. Sprik, Universiteit van Amsterdam

Prof.dr. W.A. Mulder, Technische Universiteit Delft

Prof.dr.ir. J.T. Fokkema, Technische Universiteit Delft

This work is part of the Industrial Partnership Programme (IPP) ‘Innovative Physics for Oil and Gas (iPOG)’ of the Foundation for Fundamental Research on Matter (FOM), which is part of the Netherlands Organisation for Scientific Research (NWO). The IPP iPOG is co-financed by Shell Global Solutions International B.V.

ISBN 978-9462-954-98-4

© 2016 by N. Grobde. All rights reserved. No part of this publication may be reproduced or distributed in any form or by any means, or stored in a database or retrieval system, without the prior written permission of the publisher.

Published by: Uitgeverij BOXPress, 's-Hertogenbosch, The Netherlands

Printed by: Proefschriftmaken.nl || Uitgeverij BOXPress

Cover design by: S. van den Herik || Proefschriftmaken.nl || Uitgeverij BOXPress

An electronic version of this dissertation is available at

<http://repository.tudelft.nl>

Dedicated to Frans W.J.J. Snel
Friend, Teacher, and an Inspiring Man

Contents

1	Introduction	1
1.1	Historical overview of coupled elastic waves and EM fields in porous media	1
1.2	What can the seismo-electromagnetic effect bring us?	4
1.3	Problem statement and thesis objectives	5
1.4	Thesis outline	7
2	Theory of the seismo-electromagnetic phenomenon	9
2.1	Overview seismo-electromagnetic governing equations	9
2.1.1	Pride's equations of motion	10
2.1.2	Rheology: Stress-strain relations	13
2.1.3	Maxwell's electromagnetic field equations with coupling to Biot's equations of motion	15
2.1.4	Seismo-Electromagnetic Theory based on Revil's Assumptions	16
2.2	Capturing the seismo-EM system in a general differential field equation	20
2.2.1	Separating horizontal from vertical derivatives	20
2.2.2	Taking horizontal derivatives and combining field quantities into mode quantities	25
2.3	Deriving the eigenvectors	32
2.3.1	Power flux-normalizing the Haartsen and Pride-based eigenvectors	34
2.3.2	Deriving alternative power-flux normalized eigenvector sets	38
2.3.A	Details of the Power-flux Normalization Procedure for the SH-TE HP Eigenvector Set	44
2.3.B	Details of the Alternatively Derived Power-Flux Normalized P-SV-TM GST Eigenvector Set	48
2.4	Explicit homogeneous space Green's function solutions	55
3	The model: Theory of seismo-EM layer-code modeling	59
3.1	Global reflection scheme for seismo-EM layer-code modeling	59
3.1.1	Two-way and one-way fields	59
3.1.2	Local and global reflection matrices	61

3.1.3	Calculating the global reflection matrices outside the source layer	63
3.1.4	Calculating the global reflection matrices in a homogeneous bounded subdomain with sources	66
3.1.5	Calculating the one-way fields outside the source layer	69
3.2	Including a pressure-free surface and fluid/porous medium/fluid boundaries	71
3.2.1	SH-TE scattering matrix at a free-surface	71
3.2.2	P-SV-TM scattering matrix at a free-surface	73
3.2.3	SH-TE local scattering matrix at a porous medium/fluid interface	76
3.2.4	SH-TE local scattering matrix at a fluid/porous medium interface	78
3.2.5	P-SV-TM scattering matrix at a porous medium/fluid interface	79
3.2.6	P-SV-TM scattering matrix at a fluid/porous medium interface	85
3.2.7	SH-TE global downgoing reflection matrix at a fluid/porous medium interface	86
3.2.8	SH-TE global upgoing reflection matrix at a porous medium/fluid interface	88
3.2.9	P-SV-TM global downgoing reflection matrix at a fluid/porous medium interface	90
3.2.10	P-SV-TM global upgoing reflection matrix at a porous medium/fluid interface	93
3.3	Field composition, combining modes and Fourier-Bessel transformations	97
3.3.1	Field decomposition and composition	97
3.3.2	Mode theory and combining the modes	100
3.3.3	Explicit Fourier-Bessel transformations	103
3.3.A	Explicit Fourier-Bessel transformations for all source-receiver combinations	109
3.4	2D and 3D numerical modeling with ESSEMOD	142
4	The model: Numerical results of seismo-EM layer-code modeling	143
4.1	Numerical tests with different eigenvector sets	143
4.1.1	Numerical Stability	144
4.1.2	Implications for the Seismo-Electromagnetic Modeling Results	148
4.1.3	Discussion	154
4.1.4	Conclusions	158
4.1.A	System Consistency Test using GST Eigenvectors	161
4.1.B	System Consistency Test using HP Eigenvectors	165
4.1.C	System Consistency Test using HPF Eigenvectors	169
4.1.D	Flux-Normalization Identity Test using GST eigenvectors	173
4.1.E	Flux-Normalization Identity Test using HPF Eigenvectors	177
4.2	Homogeneous Space Green's Function Validation	181

4.2.1	Introduction	181
4.2.2	Results	181
4.2.3	Conclusions	185
4.3	Numerical reciprocity checks	186
4.3.1	Homogeneous space reciprocity results	187
4.3.2	Models with interfaces	189
4.4	Numerical validation for fluid/porous medium/fluid configurations	192
4.4.1	Abstract	192
4.4.2	Introduction	192
4.4.3	Results	193
4.4.4	Discussion	196
4.4.5	Conclusions	197
4.5	Validation with seismo-EM modeling code of Garambois and Dietrich	197
4.5.1	Introduction	197
4.5.2	Results	198
4.5.3	Discussion and Conclusions	199
4.6	Seismo-electromagnetic feasibility study	200
4.6.1	Introduction	200
4.6.2	Results	200
4.6.3	Discussion	204
4.6.4	Conclusions	206
4.7	Seismo-electromagnetic thin-bed responses: natural signal enhancements?	207
4.7.1	Abstract	207
4.7.2	Introduction	208
4.7.3	Theory: Brief introduction to thin-beds and the relation with seismo-electromagnetics	209
4.7.4	Method: Numerical modeling	210
4.7.5	Results	211
4.7.6	Discussion	221
4.7.7	Conclusions	225
5	Theory and results Seismo-EM interferometry	227
5.1	Abstract	227
5.2	Introduction	228
5.3	Theory	229
5.3.1	Seismo-EM 2D SH-TE homogeneous space solutions	229
5.3.2	2D SH-TE interferometry	230
5.4	Numerical Results	232
5.4.1	2D SH-TE interferometry using homogeneous-space solutions	232
5.4.2	2D SH-TE interferometry using layer-code data	238
5.5	Discussion	242
5.6	Conclusions	242

6	Methods and applications of seismo-electromagnetic phenomena	243
6.1	Unified Multi-Depth-Level field decomposition	243
6.1.1	Abstract	243
6.1.2	Introduction	244
6.1.3	Unified theory of multi-depth-level field decomposition	246
6.1.4	Synthetic Elastodynamic Example 1: Configuration with Two Receiver Depth Levels	256
6.1.5	Synthetic Elastodynamic Example 2: Configuration with a Single Horizontal Sensor Array below a Free Surface	260
6.1.6	MC-MDL Acoustic Decomposition applied to a Field Land Data Set	266
6.1.7	Discussion	271
6.1.8	Conclusions	272
6.1.A	Acoustic Field Decomposition, Notches and Filters	275
6.1.B	Electromagnetic Field Decomposition	279
6.1.C	Elastodynamic Field Decomposition	282
6.1.D	Seismo-electromagnetic and Poroelastic Field Decomposition	283
6.2	Towards inversion: EM & Seismo-EM resolution function sensitivity analysis	288
6.2.1	Abstract	288
6.2.2	Introduction	288
6.2.3	Theory: seismo-electromagnetic resolution function for bulk density contrast	289
6.2.4	Numerical Results	294
6.2.5	Conclusions	298
6.3	Discussion on potential seismo-electromagnetic applications	298
7	Conclusions and Outlook	303
7.1	Conclusions	303
7.2	Outlook	307
	Bibliography	309
	Summary	324
	Samenvatting	327
	Acknowledgements	331

Chapter 1

Introduction

1.1 Historical overview of coupled elastic waves and electromagnetic fields in porous media

In the field of global geophysics, seismology is the most important tool for imaging the Earth, which makes use of the mechanical waves that are generated due to natural hazards like earthquakes. Also in the field of applied geophysics, which is concerned with shallower subsurface imaging and characterization using data measured at or below the Earth's surface, seismic imaging plays the key role in exploration. Increasing societal challenges such as environmental issues or the quest for natural resources have sparked the continuous search for improved imaging and characterization techniques. Besides seismic waves, other types of physical phenomena are therefore increasingly being exploited for geophysical purposes, both for global scale and exploration scale purposes. Examples are electromagnetic methods like Induced Polarization (IP) (e.g. [Marshall & Madden \(1959\)](#); [Oldenburg & Li \(1994\)](#); [Revil & Florsch \(2010\)](#)), MagnetoTelluric (MT) methods [Cagniard \(1953\)](#); [Vozoff \(1972\)](#); [Colombo & De Stefano \(2007\)](#); [Carbajal *et al.* \(2012\)](#)), Ground-Penetrating Radar (GPR) (e.g. [Sambuelli *et al.* \(1999\)](#); [Guha *et al.* \(2005\)](#); [Kruse *et al.* \(2006\)](#); [Feld & Slob \(2014\)](#)) and Controlled Source Electromagnetics (CSEM) (e.g. [Chave & Cox \(1982\)](#); [Eidesmo *et al.* \(2002\)](#); [Constable \(2010\)](#); [Hunziker *et al.* \(2011\)](#); [Colombo *et al.* \(2013\)](#); [Hunziker *et al.* \(2014\)](#)). Furthermore, even within seismic wave studies, different approaches exist as well. Classically, only acoustic waves were being used. In addition, elastodynamic systems are used to describe the pressure and shear wave propagation. More complex systems are being studied increasingly as well, like viscoelastic and poroelastic wave propagation (e.g. [Carcione *et al.* \(2010\)](#); [Rubino *et al.* \(2015\)](#)). There have also been studies focusing on interactions between mechanical wavefields and electromagnetic fields. Currently, we know two types of seismo-electromagnetic effects. In 1936, [Thompson \(1936\)](#) showed that an electric field change can occur associated to elastodynamic waves, since the mechanical disturbances change the local resistivity of the medium. He demonstrated this using a setup that actively generates a constant current between two electrodes and that measures

the potential difference. While measuring, an elastodynamic wave propagates in the medium, passing by the electrodes and creating a change in potential difference. [Thompson \(1936\)](#) suggested that these measurements could be used to distinguish the propagation direction of different arrivals (for example horizontal versus vertical propagation). The second type of seismo-electromagnetic effect was first described by [Ivanov \(1940\)](#), who discusses the coupling between mechanical waves and fully coupled electromagnetic fields, where the electric and magnetic fields are influencing each other. This is the type of seismo-electromagnetic (seismo-EM) phenomenon that we investigate in this thesis. A theory for wave propagation of electrokinetic phenomena in fluid-saturated porous media was developed by [Frenkel \(1944\)](#), in which he predicted the slow compressional wave and the seismo-electromagnetic effect. He made a marginal error in the development of the Biot-Gassmann constants and also only considered the electric effect and not the full Maxwell equations ([Pride & Garambois, 2005](#)). Martner and Sparks reported in 1959 that an electric potential difference generated by seismic wave propagation in the subsurface could be detected by electrode pairs ([Martner & Sparks, 1959](#)). A set of equations was presented by [Neev & Yeats \(1989\)](#), in an attempt to extend Biot's theory to include the electrokinetic effects associated with the flow of fluid in poroelastic media. The theory was restricted to the resistive (low-frequency) domain in both fluid flow and electrical conduction. The Onsager reciprocity conditions enabled thermodynamic consistency. They did not use the Maxwell equations and also did not include the frequency-dependence of the transport equations. Using the principle of volume-averaging, [Pride \(1994\)](#) derived a set of governing equations describing the seismo-electromagnetic system in fully-saturated porous media, by coupling Biot's poroelasticity equations to the full Maxwell electromagnetic equations. This boosted the geophysical research on seismo-electromagnetic phenomena. Several theoretical developments and numerical modeling experiments (e.g. [Haartsen & Pride \(1997\)](#); [Haines & Pride \(2006\)](#); [Garambois & Dietrich \(2002\)](#); [Haines \(2004\)](#); [Haines & Pride \(2006\)](#); [Revil *et al.* \(2007\)](#); [Zyserman *et al.* \(2010\)](#); [Sava & Revil \(2012\)](#); [Grobbe & Slob \(2013\)](#); [Kröger *et al.* \(2014\)](#); [Grobbe *et al.* \(2014, 2016a\)](#); [Revil *et al.* \(2015\)](#); [Grobbe & Slob \(2016\)](#)), as well as field tests (e.g. [Butler *et al.* \(1996\)](#); [Thompson *et al.* \(2007\)](#); [Dupuis *et al.* \(2007\)](#); [Dean & Dupuis \(2011a\)](#); [Dean *et al.* \(2012\)](#)) have been carried out in attempts to better understand this complex physical phenomenon and to develop applications for the geophysical community. Starting from the basic governing equations derived by [Pride \(1994\)](#), [Haartsen & Pride \(1997\)](#) derived a set of eigenvectors for modeling seismo-electromagnetic wavefields in horizontally layered, radially symmetric (1D), fluid-saturated porous media. To model 2D and 3D media, finite-difference (e.g. [Haines & Pride \(2006\)](#)) and finite-element schemes ([Zyserman *et al.*, 2010](#)) have been developed. Recently, [Warden *et al.* \(2013\)](#) have extended the theory to deal with partially-saturated media as well. Revil and coauthors have developed and tested an alternative formulation of the seismo-electromagnetic theory (e.g. [Revil *et al.* \(2003\)](#); [Jardani *et al.* \(2010\)](#); [Revil *et al.* \(2015\)](#)). In the seismo-electromagnetic theory of [Pride \(1994\)](#), full coupling between the electric and magnetic fields is considered, whereas Revil and coauthors make use of the well-known quasi-static approach for electromagnetic fields, which exploits the fact that

at low frequency (which seems to be applicable to the seismo-electromagnetic effect where seismic frequencies are considered), the electric and magnetic parts are not coupled. Hence, the curl-free electric field can be written as minus the gradient of an electrical potential. Since seismo-electromagnetic phenomena are sensitive to a large number of parameters, such a simpler representation of the system might be beneficial for both our understanding of the phenomenon as well as for further developing the technique towards imaging and inversion (e.g. [Jardani *et al.* \(2010\)](#); [Mahardika *et al.* \(2012\)](#); [Sava & Revil \(2012\)](#); [Revil *et al.* \(2015\)](#)). However, for this approximation, a frequency-limit holds that depends on the measurement configuration and the target depth. In seismo-electromagnetic phenomena, the actual coupling occurs in transport equations that are constituents of Biot's equations and Maxwell's equations. Different assumptions can be made regarding the physical mechanisms that underly the model. These assumptions have their effect on the actual model parameters. In the theory as presented by [Pride \(1994\)](#), and as adopted in our paper, he assumes that no wave induced diffusion effects occur, that there are no chemical gradients present (meaning that there are no free charges induced on the surfaces of the grains), that there is no wave scattering at the scale of the grains, that there are no piezoelectric or other anisotropic effects occurring and that the disturbances that happen in the medium only have linear effects. Furthermore, the pore fluids are assumed to be ideal electrolytes. It is important to realize that these postulates that [Pride \(1994\)](#) states, affecting the dynamic coupling coefficient and permeability as well as the electrical conductivity, are not per definition the correct ones. [Revil & Mahardika \(2013\)](#) present an elegant alternative using other assumptions. This results in theoretical complex conductivity expressions that agree with experimentally observed quadrature conductivities. Their formulation enables the investigation of seismo-electromagnetic effects (so in this case no quasi-static approach is used) in unsaturated porous media. Recently, [Jardani & Revil \(2015\)](#) extended the theory for full coupling in two-phase flow media. For the purpose of this thesis, we desire that all coupling effects (even very weak effects) are taken into account in our modeling. To this end, we do not want to make any approximations regarding the Maxwell equations, and prefer to model the fully-coupled Maxwell equations. In this thesis, we build upon the theory as developed by [Pride \(1994\)](#), but alternatively we could have followed the theory as formulated by [Revil & Mahardika \(2013\)](#).

Besides theoretical and numerical studies, laboratory studies have been carried out in attempts to better understand the electrokinetic foundations of coupled seismo-electromagnetics, the seismo-electromagnetic phenomenon itself and the responses that are to be expected (e.g. [Jouniaux & Pozzi \(1995\)](#); [Zhu *et al.* \(2000\)](#); [Zhu & Toksöz \(2005\)](#); [Revil *et al.* \(2007\)](#); [Allègre *et al.* \(2010\)](#); [Schakel *et al.* \(2011\)](#); [Haas *et al.* \(2013\)](#); [Smeulders *et al.* \(2014\)](#); [Bordes *et al.* \(2015\)](#)). By comparing laboratory experiments with theoretical models, several aspects of electrokinetic and seismo-electromagnetic theory have been validated (e.g. [Bordes *et al.* \(2008\)](#); [Schakel & Smeulders \(2010\)](#); [Schakel *et al.* \(2011\)](#); [Schoemaker *et al.* \(2012\)](#); [Smeulders *et al.* \(2014\)](#)). However, from all laboratory studies still no convincing match has been obtained between modeled and measured data on actual rock samples. This might imply that the theory still needs to be further developed. On the other hand, carry-

ing out seismo-electromagnetic experiments in a laboratory setting is quite difficult, and therefore easily prone to errors or deviations from theory. For single and multiple cylindrical pores in a sample, good results have been obtained validating the analytical models for the transport equations (Schoemaker *et al.*, 2012).

1.2 What can the seismo-electromagnetic effect bring us?

The seismo-electromagnetic method is complementary to conventional seismics or conventional controlled-source electromagnetics (CSEM). Conventional seismics can hardly distinguish between e.g. water- and oil-saturated rocks. Due to the subsurface coupling between the elastodynamic wavefields and the electromagnetic fields, the seismo-electromagnetic signals may provide both seismic resolution and electromagnetic fluid-sensitivity at the same time, potentially allowing to discriminate between these different types of rock saturation (Schoemaker *et al.*, 2012). Furthermore, several studies have already shown that the seismo-electromagnetic method can provide us with supplemental information on crucial reservoir parameters like porosity and permeability, as well as sensitivity to pore-fluid properties (e.g. Pride (1994); Haines & Pride (2006); Revil *et al.* (2007)). This can potentially be used for example to detect or monitor gas/oil/water or oil/water contacts (Revil & Mahardika, 2013; Smeulders *et al.*, 2014). Additionally, the seismo-electromagnetic method has been proven useful for imaging and monitoring of aquifers and aquifer contamination (Rosid & Kepic, 2005; Dupuis *et al.*, 2007; Revil & Mahardika, 2013), Vertical Seismic Profiling of glaciofluvial sediments (Dupuis & Butler, 2006), and for exploration of glaciers, e.g. for mapping thin water-bearing strata or for monitoring of ice fracturing (Kulesa *et al.*, 2006). For these reasons, the seismo-electromagnetic method is of interest to the oil and gas industry, as well as to e.g. hydrological institutes.

Recently, the seismo-electromagnetic effect is also studied for global scale applications, e.g. using seismo-electromagnetic phenomena for the detection of microcracks prior to ruptures generating earthquakes (e.g. Fujinawa *et al.* (2011); Ren *et al.* (2012b); Haas *et al.* (2013); Fujinawa & Noda (2016)).

We can distinguish two types of coupling in the seismo-electromagnetic phenomena (e.g. Garambois & Dietrich (2002); Revil *et al.* (2015)). The first is the coupling that occurs ‘inside’ the seismic wave or electromagnetic field, which is referred to as the coseismic electromagnetic field or the coelectromagnetic mechanical field, respectively. Since the coseismic field is generated locally, it can only provide us with localized information at the location where the wave passes and is recorded, i.e. at the receivers. This effect might therefore be useful for borehole applications, such as discussed by e.g. Zhu *et al.* (2000); Zhu & Toksöz (2005). Another borehole application might be to map the permeability close around the well with the purpose of determining where to optimally perforate the well-casings.

The second type of coupling occurs when such a field encounters an interface with contrasting medium parameters. An incident electromagnetic field or seis-

mic wave reflects from and transmits through such an interface both electromagnetic and seismic fields. This second type of coupling is referred to as the seismo-electromagnetic conversion or interface response (IR) field. If we focus on the seismic-to-electromagnetic conversion, this second-order coupling effect yields an independent electromagnetic diffusive field, which is generated whenever there is a contrast in mechanical, hydraulic or electrical medium parameters. The electromagnetic diffusion is characterized by the diffusion number, and the velocity-per-frequency is several orders of magnitude higher than the seismic wave velocities. These diffusive electromagnetic events will arrive almost instantaneously at the receiver level and hence these IR events will show up in seismo-electrograms as more or less horizontal events at one-way seismic traveltime (the seismic traveltime from the source to the generating interface). The reciprocal, electromagnetic-to-seismic conversion, also creates ‘flat’ events, but now due to the fact that the incoming diffusive electromagnetic fields have a velocity-per-frequency that is several orders of magnitude higher than the seismic converted field velocity. These converted fields can provide us with information at depth and are therefore of primary interest when exploiting seismo-electromagnetic methods in industry. However, since these fields are second-order coupling effects, their signal strength and signal-to-noise ratio is very low. Furthermore, other secondary effects could take place, such as effects due to gradients in chemical potential and temperature. The IR fields might also be useful in borehole scenarios, if the receivers are then located close to the target area of interest and hence less amplitude losses will occur for the diffusive electromagnetic fields.

In addition to these two types of coupling, seismo-electromagnetic conversion occurs directly at the source, where for example an instantaneous electromagnetic field is being generated upon seismic source impact. This is sometimes referred to as a third-type of seismo-electromagnetic signal (see for example [Revil *et al.* \(2015\)](#)).

These three types of seismo-electromagnetic coupling and their corresponding seismogram and electrogram recordings are schematically illustrated in [Figure 1.1](#).

Throughout this thesis, we will describe both the seismo-electromagnetic and the reciprocal electromagneto-seismic effects with the term ‘seismo-electromagnetic’. The source-receiver combination under consideration will make clear which effect we are looking at.

1.3 Problem statement and thesis objectives

Currently, the major challenge of the seismo-electromagnetic method is the very weak signal-to-noise ratio of the seismo-electromagnetic signals. For shallow subsurface applications, such as ground-water monitoring, field tests have proven that the seismo-electromagnetic method can successfully be applied ([Rosid & Keping, 2005](#); [Dupuis *et al.*, 2007](#)). Despite possible borehole and near-surface applications, in order to make the seismo-electromagnetic method feasible for energy industrial and natural hazard applications, we need to find ways to improve the signal-to-noise ratio of especially the second-order seismo-electromagnetic conversion effect. There are only a few examples of promising field tests with deeper subsurface targets (e.g. [Butler *et al.* \(1996\)](#); [Thompson *et al.* \(2007\)](#)). More field data tests of the seismo-

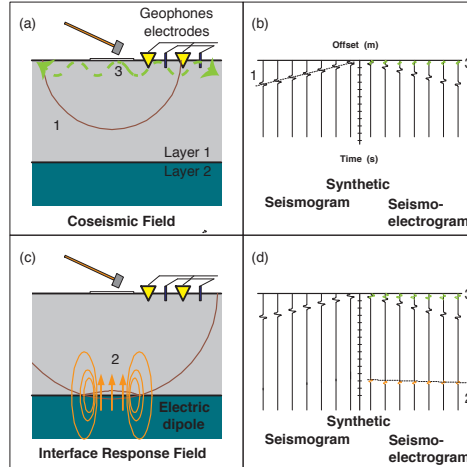


Figure 1.1: Schematic of the types of seismo-electromagnetic coupling (modified from [Schoemaker et al. \(2012\)](#)). A porous layer (layer 1), with some saturation, overlies a porous half-space (layer 2), that has contrasting medium parameters compared to layer 1 (panels (a) and (c)). The seismic source generates a mechanical wave (labelled 1), that is recorded by geophones at the surface (left part of panel (b)). This is the direct seismic wave. This wave also creates a co-propagating coseismic electric field that is registered by the surface electrodes (right part of panel (b)). When the seismic wave arrives at the interface separating the porous layers, the interface response field is generated (labelled 2), that arrives instantaneously at one-way seismic time (orange event), and is only recorded by the surface electrodes (right part of panel (d)). The third event is the source-converted diffusive EM field (green arrows), that arrives around $t = 0$ s, indicated by the green event in panels (b) and (d).

electromagnetic method are certainly required to really bring this method to the next level.

Several different attempts to boost the seismo-electromagnetic signal strength have been made over the last couple of years, all with limited effect. Recently, [Sava & Revil \(2012\)](#); [Revil et al. \(2013\)](#); [Sava et al. \(2014\)](#) have explored to use seismo-electromagnetic focusing techniques to maximize the seismo-electromagnetic conversion. In addition, more specifically dedicated seismo-electromagnetic processing could help, as discussed in for example [Butler & Russell \(1993\)](#); [Warden et al. \(2012\)](#). A brute-force approach is to use commercial hydraulic vibroseis trucks to try and boost the signal-to-noise ratio of the seismo-electromagnetic data by sending large amounts of energy into the subsurface ([Dean & Dupuis, 2011a](#); [Dean et al., 2012](#); [Valuri et al., 2012](#)). Having strong sources is not always possible or desirable and is likely to boost the noise-levels as well. Therefore, it may be beneficial to be able to replace those strong sources by receivers. This is the principle of interferometry. From an imaging point of view, it has been shown effective for a wide class of phenomena, including purely seismic and electromagnetic systems ([Draganov et al., 2006](#); [Wapenaar et al., 2008a](#); [Schuster et al., 2004](#); [Schuster, 2010](#)). When applying interferometry, responses recorded at different receivers are cross-correlated in order to obtain the Green function between these receivers. It can include the responses

of both passive and active sources. The cross-correlation process reorganizes measured data such that it may allow for improved imaging compared to the situations where imaging algorithms are applied to the measured data directly. When having downhole receivers, the virtual source method based on interferometric principles (Bakulin & Calvert, 2006; Mehta *et al.*, 2007a) has been proven useful. This leads to the idea that seismo-electromagnetic interferometry can also help overcoming the weak signal-to-noise ratio challenge. Initial studies applying interferometry by cross-correlation on the SH-TE propagation mode in 1D scenarios, were successful (De Ridder, 2007; De Ridder *et al.*, 2009; Schoemaker *et al.*, 2012).

It is important to realize that even if the signals would be stronger, the fact remains that the seismo-electromagnetic effect is a very complex physical phenomenon and hard to fully understand. Applying existing acoustical geophysical processing, imaging, and inversion techniques to seismo-electromagnetic data can be very challenging, but is not impossible (Jardani *et al.*, 2010; Mahardika *et al.*, 2012; Chen & De Hoop, 2014; Maas *et al.*, 2015).

These two challenges lead to the key aim of this thesis, which is two-fold:

1. Increase our theoretical and physical understanding of the seismo-electromagnetic phenomenon by analytically-based numerical modeling.
2. Investigate the potential of seismo-electromagnetic interferometry.

To be able to model the data for all possible seismo-electromagnetic source-receiver combinations, a requirement for studying interferometry with seismo-electromagnetic fields, we need to develop an analytically-based, layered-Earth modeling code. To this end, we develop ‘ESSEMOD’, which stands for Electromagneto-Seismic and Seismo-Electromagnetic MODeling. Our modeling code is developed in a combined Fortran / C language, and compatible with the ‘Seismic Unix’ parameter interface. To make it possible to compare the modeling results with typical seismo-electromagnetic laboratory wave propagation experiments, we include fluid/porous medium/fluid transitions in our modeling code.

1.4 Thesis outline

We start in Chapter 2 by introducing the theoretical aspects of the seismo-electromagnetic phenomenon. We provide in Section 2.1 an overview of the governing seismo-electromagnetic equations that form the basis of this thesis. In Section 2.2, we rewrite the system of equations to capture the seismo-electromagnetic system in a general differential field equation. We then present in Section 2.3 three different eigenvector sets: a literature eigenvector set according to our preferences, the power-flux normalized version of this eigenvector set, and an independently derived alternative eigenvector set. We finalize this chapter by showing explicit homogeneous-space Green’s function solutions in Section 2.4.

In Chapter 3, we describe the underlying theory applicable to coupled seismo-EM layer-code modeling. Section 3.1 starts with deriving the Global Reflection Scheme that is a crucial part of the algorithm of the layered-Earth modeling code. In Section

3.2, we focus on specific modeling scenarios, by showing theoretically the implications of having a pressure free-surface in the model, or fluid/porous medium/fluid transitions. We then focus in Section 3.3 on how we deal with field composition and the combination of the propagation modes. We also explain how we use Fourier-Bessel transformations to transform the data from the horizontal wavenumber-frequency domain to the space-frequency domain. We explicitly present all Fourier-Bessel transformations for all existing seismo-electromagnetic source-receiver combinations. We finalize this chapter with a note on 3D and 2D modeling with our code ‘ESSEMOD’ (section 3.4).

Chapter 4 is an overview of several numerical studies carried out using seismo-EM layer-code modeling. In Section 4.1, we start by focusing on the numerical validation of the three different eigenvector sets and several accuracy aspects of these sets. We then, in Section 4.2, validate the results of ESSEMOD using the explicit homogeneous-space Green’s function solutions of Section 2.4. We validate different aspects of the global reflection scheme of Section 3.1 using reciprocity tests, shown in Section 4.3. Next, we present in Section 4.6 several numerical results for surface reflection and surface to horizontal borehole measurements. We look at different source-receiver combinations. Furthermore, we carry out a feasibility study focused on signal measurability. Section 4.4 then moves onwards to modeling typical seismo-electromagnetic wave propagation laboratory experiments, where a porous sample is placed in a water tank. We validate our modeling code for fluid/porous medium/fluid transitions by comparing the purely electromagnetic part with an independently developed electromagnetic layered-Earth modeling code. We continue our validation in Section 4.5, by successfully comparing the results of our code ESSEMOD with an independently developed layered-Earth coupled seismo-electromagnetic modeling code (Garambois & Dietrich, 2002). In Section 4.7, we explore the possible natural seismo-electromagnetic signal enhancements due to thin-bed geological settings. After these numerical modeling studies, we move onwards to carefully investigate interferometric synthesis with seismo-electromagnetic fields, using cross-correlation based interferometry applied to the 2D SH-TE propagation mode, presented in Chapter 5. We then discuss some methods and applications of seismo-electromagnetic phenomena in Chapter 6. We first focus on our Multi-Depth-Level Field Decomposition method (Section 6.1), which incorporates the recordings at multiple depth levels in the process of field decomposition into up- and downgoing waves and different field types. In Section 6.2, we then move on towards inversion, studying the seismo-electromagnetic sensitivity using resolution functions. We discuss some other potential applications of the seismo-electromagnetic method in Section 6.3. We finalize the thesis by presenting the main Conclusions of this thesis, as well as a brief Outlook, in Chapter 7.

Chapter 2

Theory of the seismo-electromagnetic phenomenon

2.1 Overview seismo-electromagnetic governing equations

The set of macroscopic governing equations for the seismo-electromagnetic system in an arbitrary inhomogeneous fluid-saturated porous medium were derived by [Pride \(1994\)](#). We briefly recapitulate the starting set of equations used. Next, we express the vertical variations of the field quantities for each propagation mode individually in terms of a system matrix containing the medium parameters and the horizontal partial differentiation operators acting on these field quantities, which forms the basic formulation for seismo-electromagnetic layered-Earth modeling codes ([Woodhouse, 1974](#); [Kennett, 1983](#); [Ursin, 1983](#); [Wapenaar & Grimbergen, 1996](#); [Haartsen & Pride, 1997](#); [Garambois & Dietrich, 2002](#); [Ren *et al.*, 2010](#); [Hu & Gao, 2011](#); [Grobbe & Slob, 2013](#); [Grobbe *et al.*, 2016a,b](#)).

Once we have successfully captured both the SH-TE propagation mode and the P-SV-TM propagation mode in this format, we introduce the power-flux normalized eigenvector system as derived starting from [Haartsen & Pride \(1997\)](#), followed by the derivation of our own independent alternative eigenvector set, starting straight from the system matrices for the SH-TE and P-SV-TM modes. Throughout this thesis we use

$$\hat{f}(x_i, \omega) = \int_{-\infty}^{\infty} f(x_i, t) e^{-j\omega t} dt, \quad (2.1)$$

as the definition for the forward temporal Fourier transform and

$$\tilde{f}(k_1, k_2, x_3, \omega) = \int_{-\infty}^{\infty} \int_{-\infty}^{\infty} \hat{f}(x_i, \omega) e^{jk_\alpha x_\alpha} dx_1 dx_2, \quad (2.2)$$

for the forward spatial Fourier transform. Here, ω denotes the angular frequency in $[\text{rad} \cdot \text{s}^{-1}]$, t is time, j indicates the imaginary unit, x_i indicates the three spatial directions of the right-handed Cartesian coordinate system (with the positive x_3 -direction pointing downwards (depth)), and k_α , with $\alpha = 1$ or 2 , denotes the horizontal wavenumber in those respective directions. The hat indicates a quantity in the space-frequency domain, the tilde sign indicates a quantity in the horizontal wavenumber-frequency domain. Note that these Fourier transform definitions are opposite to the definitions used by e.g. [Haartsen & Pride \(1997\)](#). Throughout this thesis, Latin subscripts can take the values 1, 2 and 3, Greek subscripts can take the values 1 and 2. The Einstein summation convention holds for repeated indices (unless indicated otherwise). Before diving into the world of seismo-electromagnetics, it is important to realize that the propagating electromagnetic parts of the coupled seismo-electromagnetic fields are diffusive fields, and that these diffusive fields behave differently compared to propagating waves (the latter includes the coseismic fields that propagate along with the seismic wave). For instance, the phase term of the frequency-domain homogeneous-space solution to the 3D wave equation has the form $\exp(-j\frac{\omega}{c}R)$, where c denotes the wave propagation velocity (with weak or no dependence on frequency) and R represents the propagation distance $R = |x_i^r - x_i^s|$, where the superscripts s and r indicate the source and receiver locations. The homogeneous-space equivalent for a diffusive electromagnetic field has the form $\exp(-\sqrt{j\omega\sigma\mu}R) = \exp(-\sqrt{\frac{\omega\sigma\mu}{2}}R(1+j))$. Here, σ represents the electric conductivity and μ is the magnetic permeability. We can split this expression in a real part (the damping term) and an imaginary part (phase term), as $\exp(-\sqrt{\frac{\omega\sigma\mu}{2}}R) \exp(-j\sqrt{\frac{\omega\sigma\mu}{2}}R)$. We can cast the imaginary part of this expression in a similar format as is used to describe the phase term for waves, $\exp(-j\frac{\omega}{c_{\text{diff}}}R)$, using $\frac{\omega}{c_{\text{diff}}} = \sqrt{\frac{\omega\sigma\mu}{2}}$, where the diffusion ‘velocity’ c_{diff} is then derived as $c_{\text{diff}} = \sqrt{\frac{2\omega}{\sigma\mu}}$. We can clearly observe that this diffusion ‘velocity’ is proportional to the square root of frequency. As a result, we cannot speak about the ‘velocity’ of a diffusive field. We can only use the term velocity when considering a single frequency, i.e. we can speak of a velocity-per-frequency. Instead of using the term velocity, diffusive fields are characterized by their diffusion number. Slightly counterintuitive, diffusive fields can also be considered to propagate. However, they propagate with very strong attenuation: after one wavelength the amplitude has reduced to $\exp(-2\pi)$. Additionally, where waves scale linearly with length, diffusive fields typically have length scaling with the square root of time ([Mulder *et al.*, 2008](#)).

We can now start with the coupled seismo-electromagnetic theory. We distinguish two equations of motion, two electromagnetic equations and two stress-strain relationships. For notational convenience, we introduce in our notation the Laplace parameter $s = j\omega$.

2.1.1 Pride’s equations of motion

The equations of motion derived by [Pride \(1994\)](#) are an extension of Biot’s proelastic equations of motion: they include a coupling term coupling the mechanical part to

the electric field. Considering an arbitrary, inhomogeneous medium they are given by

$$s\rho^b\hat{v}_i^s + s\rho^f\hat{w}_i - \frac{1}{2}\frac{\partial(\hat{\tau}_{ij}^b + \hat{\tau}_{ji}^b)}{\partial x_j} = \hat{f}_i^b, \quad (2.3)$$

$$s\rho^f\hat{v}_i^s + \frac{\eta}{\hat{k}}\hat{w}_i' + \frac{\partial\hat{p}^f}{\partial x_i} = \hat{f}_i^f, \quad (2.4)$$

where

$$\hat{w}_i' = \hat{w}_i - \hat{\mathcal{L}}\hat{E}_i, \quad (2.5)$$

$$\hat{w}_i = \phi(\hat{v}_i^f - \hat{v}_i^s), \quad (2.6)$$

$$\rho^b = \phi\rho^f + (1 - \phi)\rho^s. \quad (2.7)$$

In the above equations \hat{w}_i is the Biot filtration velocity, \hat{E}_i is the electric field strength, $\hat{\mathcal{L}}$ represents the dynamic seismo-electromagnetic coupling coefficient, which couples the elastodynamic wavefields to the electromagnetic wavefields, η represents the viscosity of the pore fluid, ϕ is the porosity of the medium, and \hat{k} represents the frequency-dependent dynamic permeability. Combining these parameters yields the filtration velocity with coupling denoted by \hat{w}_i' . Furthermore, \hat{v}_i^s and \hat{v}_i^f are the solid and fluid particle velocities, respectively, $\hat{\tau}_{ij}^b$ represents the bulk stress tensor, \hat{p}^f is the fluid pressure, ρ^b , ρ^s and ρ^f are the frequency-independent, isotropic bulk, solid and fluid density, respectively, and \hat{f}_i^b and \hat{f}_i^f denote the volume densities of external force applied to the bulk and fluid phases, respectively. The dynamic coupling coefficient $\hat{\mathcal{L}}$ can be written as follows

$$\hat{\mathcal{L}} = \mathcal{L}_0 \left[1 + \frac{s}{\omega_c} \frac{m}{4} \left(1 - 2\frac{d^l}{\Lambda} \right)^2 \left(1 - d^l \sqrt{\frac{s\rho^f}{\eta}} \right)^2 \right]^{-\frac{1}{2}}. \quad (2.8)$$

In equation (2.8), \mathcal{L}_0 represents the static coupling coefficient, which is defined as (Garambois & Dietrich, 2001; Pride & Garambois, 2005)

$$\mathcal{L}_0 = -\frac{\phi\varepsilon_0\varepsilon_r^f\zeta^p}{\alpha_\infty\eta} \left(1 - 2\frac{d^l}{\Lambda} \right). \quad (2.9)$$

Furthermore, ε_0 and ε_r^f are the electric permittivity of vacuum and the relative electric permittivity of the fluid, respectively. The symbol α_∞ represents the tortuosity of the porous medium. The dynamic coupling coefficient has been experimentally investigated as a function of frequency (e.g. Schoemaker *et al.* (2012)). In (2.8) and (2.9), Λ represents the volume-to-surface ratio of the porous material and d^l the Debye screening length. The Debye screening length represents the characteristic thickness of the electrical double layer (EDL) and is typically on the order of nanometers. Physically, the Debye screening length can be considered as representing the distance over which mobile charge carriers present in the electrolyte screen out the

surface charge present on the grains of the fluid-saturated porous medium (Debye & Hückel, 1923; Pride, 1994; Schoemaker *et al.*, 2012), mathematically described as

$$d^l = \sum_{l=1}^L \sqrt{\frac{\varepsilon_0 \varepsilon_r^f k_B T}{e^2 z_l^2 N_l}}. \quad (2.10)$$

Here, k_B represents the Boltzmann constant, T the temperature (in [K]), N_l is the bulk ionic concentration of species l with valence z_l , for a total of L species present in the system, and e represents the elementary charge. We can calculate N_l using

$$N_l = 10^3 c N_A \|z_l'\|, \quad (2.11)$$

with N_A being Avogadro's constant, c the electrolyte concentration of the pore-fluid in [mol/L], and $\|z_l'\|$ being the absolute value of the valency of the conjugate ion of z_l . However, for realistic Earth scenarios, we typically consider the limit where $\frac{d^l}{\Lambda}$ is small, yielding

$$\mathcal{L}_0 = -\frac{\phi \varepsilon_0 \varepsilon_r^f \zeta^p}{\alpha_\infty \eta}. \quad (2.12)$$

Furthermore, ζ^p represents the zeta potential. Different expressions exist for the zeta potential. However, Pride & Morgan (1991) carried out a literature review on experimental studies of the zeta potential of quartz, showing that

$$\zeta^p = 8 + 26 \log_{10} c, \quad (2.13)$$

is a reasonable approximation of the zeta potential (in [mV]), where c denotes the electrolyte concentration of the pore fluid in [mol/L]. Similar to the dynamic coupling coefficient, the dynamic permeability is defined as

$$\hat{k} = k_0 \left[\left(1 + \frac{s}{\omega_c} \frac{4}{m} \right)^{\frac{1}{2}} + \frac{s}{\omega_c} \right]^{-1}, \quad (2.14)$$

where, k_0 represents the static permeability, which can be related to the porosity cubed using a Carmen-Kozeny relationship, for example

$$k_0 = 2 \cdot 10^{-11} \phi^3, \quad (2.15)$$

for clean Fontainebleau sandstones (Bourbié *et al.*, 1987). Furthermore, m is the similarity parameter, representing a combination of pore-geometry parameters

$$m = \frac{\phi \Lambda^2}{\alpha_\infty k_0}. \quad (2.16)$$

The similarity parameter is a dimensionless number, that will be fixed to a value of 8 (Johnson *et al.*, 1987). Important to notice in both equations (2.8) and (2.14), ω_c

represents the critical frequency separating the low-frequency viscous flow regime from the high-frequency inertial flow regime, defined as

$$\omega_c = \frac{\phi\eta}{\alpha_\infty k_0 \rho^f}. \quad (2.17)$$

For realistic rock and fluid parameters and general field scenarios, this transition frequency lies above the maximum frequency of interest (this maximum being roughly between 10 and 1000 Hz). The frequency dependency of the dynamic coupling coefficient is related to relaxation mechanisms associated with the development of viscous boundary layers in the pores (Pride, 1994). So, when $\omega \ll \omega_c$, viscous boundary layers are not being developed yet, and hence we can neglect the second term of equation (2.8). This reduces the complex, frequency-dependent dynamic coupling coefficient to the static coupling coefficient

$$\hat{\mathcal{L}} = \mathcal{L}_0. \quad (2.18)$$

A similar reasoning holds for the dynamic permeability, which could be approximated by the static permeability for the frequency range under consideration. However, numerically speaking, coding the dynamic permeability is less tedious than coding the dynamic coupling coefficient, and therefore we use equation (2.14) in our numerical schemes.

Note that when the coupling coefficient is equal to zero, equations (2.3) and (2.4) reduce to Biot's poroelasticity equations and the elastodynamic waves decouple from the electromagnetic fields.

2.1.2 Rheology: Stress-strain relations

For an arbitrary, inhomogeneous, isotropic medium, the stress-strain relations are given by:

$$-s\hat{\tau}_{ij}^b + d_{ijkl} \frac{\partial \hat{v}_k^s}{\partial x_l} + C\delta_{ij} \frac{\partial \hat{w}_k}{\partial x_k} = d_{ijkl} \hat{h}_{kl}^b + C\delta_{ij} \hat{q}^i, \quad (2.19)$$

$$s\hat{p}^f + C \frac{\partial \hat{v}_k^s}{\partial x_k} + M \frac{\partial \hat{w}_k}{\partial x_k} = C\hat{h}_{kk}^b + M\hat{q}^i, \quad (2.20)$$

with \hat{h}_{ij}^b representing the density of external deformation rate acting on the bulk and \hat{q}^i being the source volume density of injection rate in the fluid phase. The following symmetry properties hold: $\hat{\tau}_{ij}^b = \hat{\tau}_{ji}^b$, $\hat{h}_{ij}^b = \hat{h}_{ji}^b$ and $\hat{d}_{ijkl} = \hat{d}_{jikl} = \hat{d}_{ijlk} = \hat{d}_{klij}$. Here, M and C are static scalar stiffness parameters and d_{ijkl} is a static stiffness tensor of rank four but, for isotropic media, a function of only two parameters given by

$$d_{ijkl} = \left[K_G - \frac{2}{3}G^{fr} \right] \delta_{ij}\delta_{kl} + G^{fr}(\delta_{ik}\delta_{jl} + \delta_{il}\delta_{jk}), \quad (2.21)$$

where G^{fr} denotes the shear modulus of the solid framework, K_G is Gassmann's bulk modulus and δ_{ij} denotes the Kronecker delta. Isolating the divergence of the

Biot filtration velocity $\frac{\partial \hat{w}_k}{\partial x_k}$ in (2.20), yields

$$\frac{\partial \hat{w}_k}{\partial x_k} = \frac{1}{M} \left[\hat{C} \delta_{kl} \hat{h}_{kl}^b + M \hat{q}^i - s \hat{p}^f - \hat{C} \delta_{kl} \frac{\partial \hat{v}_k^s}{\partial x_l} \right]. \quad (2.22)$$

We can define the stiffness parameters C and M as well as Gassmann's bulk modulus K_G in terms of the fluid, solid and grain framework bulk moduli, yielding

$$K_G = \frac{K^{fr} + \phi K^f + (1 + \phi) K^s \Delta}{1 + \Delta}, \quad (2.23)$$

$$C = \frac{K^f + K^s \Delta}{1 + \Delta}, \quad (2.24)$$

$$M = \frac{K^f}{\phi(1 + \Delta)}. \quad (2.25)$$

Here, K^s is the solid compression modulus, K^f the fluid compression modulus and K^{fr} the compression modulus of the solid framework. Δ is defined as:

$$\Delta = \frac{K^f}{\phi(K^s)^2} [(1 - \phi) K^s - K^{fr}]. \quad (2.26)$$

Rewriting equations (2.19) and (2.22) for the isotropic, frequency-independent case, results in

$$-s \hat{\tau}_{ij}^b + d_{ijkl} \frac{\partial \hat{v}_k^s}{\partial x_l} + C \delta_{ij} \frac{\partial \hat{w}_k}{\partial x_k} = d_{ijkl} \hat{h}_{kl}^b + C \delta_{ij} \hat{q}^i, \quad (2.27)$$

$$\frac{\partial \hat{w}_k}{\partial x_k} = \frac{1}{M} \left[C \hat{h}_{kk}^b + M \hat{q}^i - s \hat{p}^f - C \frac{\partial \hat{v}_k^s}{\partial x_k} \right]. \quad (2.28)$$

Replacing $\frac{\partial \hat{w}_k}{\partial x_k}$ in (2.27) by the expression (2.28) eliminates this term, yielding

$$-s \hat{\tau}_{ij}^b + d_{ijkl} \frac{\partial \hat{v}_k}{\partial x_l} + \frac{C \delta_{ij}}{M} \left[C \delta_{kl} \hat{h}_{kl}^b + M \hat{q}^i - s \hat{p}^f - C \delta_{kl} \frac{\partial \hat{v}_k}{\partial x_l} \right] = d_{ijkl} \hat{h}_{kl}^b + C \delta_{ij} \hat{q}^i. \quad (2.29)$$

Bringing all source terms to the right-hand side and further simplifying yields,

$$-s \hat{\tau}_{ij}^b + \left[d_{ijkl} - \frac{C^2}{M} \delta_{ij} \delta_{kl} \right] \frac{\partial \hat{v}_k}{\partial x_l} - \frac{sC}{M} \delta_{ij} \hat{p} = e_{ijkl} \hat{h}_{kl}^b, \quad (2.30)$$

with $e_{ijkl} = d_{ijkl} - \frac{C^2}{M} \delta_{ij} \delta_{kl}$. Alternatively, $e_{ijkl} = S \delta_{ij} \delta_{kl} + G^{fr} (\delta_{ik} \delta_{jl} + \delta_{il} \delta_{jk})$, where $S = K_G - \frac{2}{3} G^{fr} - \frac{C^2}{M}$, where we can recognize the elastodynamic Lamé constant $\lambda_c = K_G - \frac{2}{3} G^{fr}$. We can also work with the stiffness $H = K_G + \frac{4}{3} G^{fr}$ (e.g. Biot (1962)), which leads to the alternative formulation $d_{ijkl} = (H - 2G^{fr}) \delta_{ij} \delta_{kl} + G^{fr} (\delta_{ik} \delta_{jl} + \delta_{il} \delta_{jk})$. Furthermore, we define $K_c = S + 2G^{fr}$ and we can relate $HM - C^2 = MK_c$.

2.1.3 Maxwell's electromagnetic field equations with coupling to Biot's equations of motion

Now that we have described the governing equations of the mechanical wave-part of the seismo-electromagnetic theory, we focus on the electromagnetic field-part. Below, Maxwell's equations for electromagnetic fields are presented, containing a coupling term to Biot's equations of motion in porous media (Pride, 1994)

$$s\hat{D}_i + \hat{J}_i^{i,e} - \epsilon_{ijk} \frac{\partial \hat{H}_k}{\partial x_j} = -\hat{J}_i^e, \quad (2.31)$$

$$s\hat{B}_i + \hat{J}_i^{i,m} + \epsilon_{ijk} \frac{\partial \hat{E}_k}{\partial x_j} = -\hat{J}_i^m. \quad (2.32)$$

Here, \hat{D}_i denotes the electric flux density and \hat{B}_i the magnetic flux density. \hat{E}_i and \hat{H}_i represent the electric and magnetic field strength, respectively. The right-hand side of these two equations contain the external electric (\hat{J}_i^e) and magnetic (\hat{J}_i^m) current sources. Finally, $\hat{J}_i^{i,e}$ and $\hat{J}_i^{i,m}$ denote the averaged induced electric and magnetic current density, respectively. These induced current densities can be expressed as

$$\hat{J}_i^{i,e} = \hat{\sigma}^e \hat{E}_i - \hat{\mathcal{L}} \left(\frac{\partial \hat{p}^f}{\partial x_i} + s\rho^f \hat{v}_i^s - \hat{f}_i^f \right), \quad (2.33)$$

$$\hat{J}_i^{i,m} = \hat{\sigma}^m \hat{H}_i. \quad (2.34)$$

Here, $\hat{\sigma}^e$ and $\hat{\sigma}^m$ describe the frequency-dependent electric and magnetic conductivity, respectively. These two parameters describe electromagnetic relaxation. For Earth materials, we can ignore the magnetic relaxation losses, $\hat{\sigma}^m = 0$. Recognizing the expression for the equation of motion (2.4) in equation (2.33) and using it to express the induced electric current density in terms of the electric field and the filtration velocity yields

$$\hat{J}_i^{i,e} = \left(\hat{\sigma}^e - \frac{\eta}{\hat{k}} \hat{\mathcal{L}}^2 \right) \hat{E}_i + \frac{\eta}{\hat{k}} \hat{\mathcal{L}} \hat{w}_i. \quad (2.35)$$

In, equations (2.31) and (2.32), ϵ_{ijk} is the Levi-Civita symbol representing the alternating pseudo-tensor used to express (in combination with the spatial partial derivatives) the curls of the magnetic and electric fields, where

$$\epsilon_{ijk} = \begin{cases} 1 & \text{if } i, j, k \text{ is an even permutation of } 1,2,3, \\ -1 & \text{if } i, j, k \text{ is an odd permutation of } 1,2,3, \\ 0 & \text{otherwise.} \end{cases} \quad (2.36)$$

The following constitutive relations hold

$$\hat{D}_i = \epsilon \hat{E}_i, \quad (2.37)$$

$$\hat{B}_i = \mu \hat{H}_i, \quad (2.38)$$

where $\varepsilon = \varepsilon_0 \varepsilon_r$ and $\mu = \mu_0 \mu_r$. Here, μ_0 representing the magnetic permeability of vacuum, μ_r represents the relative magnetic permeability, and ε_r the relative electric permittivity defined as

$$\varepsilon_r = \frac{\phi}{\alpha_\infty} (\varepsilon_r^f - \varepsilon_r^s) + \varepsilon_r^s, \quad (2.39)$$

where ε_r^s and ε_r^f are the relative electric permittivities of the solid and fluid, respectively. We choose $\mu_r = 1$, which is reasonable for Earth materials. In equation (2.35), one can clearly observe what happens with the coupling to Biot's poroelasticity equations when the coupling coefficient is chosen equal to zero.

When we substitute the constitutive relations (2.37) and (2.38) as well as equation (2.35) into Maxwell's electromagnetic field equations with coupling to Biot's equations of motion (2.31) and (2.32), the result reads

$$s\varepsilon \hat{E}_i + \left[\hat{\sigma}^e - \frac{\eta}{\hat{k}} \hat{\mathcal{L}}^2 \right] \hat{E}_i + \frac{\eta}{\hat{k}} \hat{\mathcal{L}} \hat{w}_i - \epsilon_{ijk} \frac{\partial \hat{H}_k}{\partial x_j} = -\hat{J}_i^e, \quad (2.40)$$

$$s\mu_0 \hat{H}_i + \epsilon_{ijk} \frac{\partial \hat{E}_k}{\partial x_j} = -\hat{J}_i^m. \quad (2.41)$$

Following [Pride & Garambois \(2005\)](#), we can use the following reduced static expression (to leading order in $\frac{d^i}{\lambda}$) for the frequency-dependent electrical conductivity

$$\hat{\sigma}^e = \frac{\phi \sigma^f}{\alpha_\infty}, \quad (2.42)$$

where we use the simplified version of the fluid conductivity

$$\sigma^f = (ez)^2 N (b^+ + b^-). \quad (2.43)$$

This expression is based on the assumption that only one valency-type ion is present; therefore the subscript l is removed on z and N . Here, b^+ and b^- represent the ionic mobilities of the cations and anions, respectively. We use a typical value for the ionic mobility of $3.0 \cdot 10^{11} \text{ ms}^{-1} \text{ N}^{-1}$ for inorganic ions ([Haartsen & Pride, 1997](#)).

2.1.4 Seismo-Electromagnetic Theory based on Revil's Assumptions

So far, we have discussed the seismo-electromagnetic theory following the assumptions of [Pride \(1994\)](#). Different underlying theoretical assumptions can lead to different expressions, especially for the dynamic coupling coefficient, the dynamic permeability and the complex conductivity. We now briefly discuss the seismo-electromagnetic model according to [Revil & Mahardika \(2013\)](#). This model could have been used just as easily as the foundation for this thesis. However, the theory was not yet published at the start of this PhD research. In the following discussion, it is important to distinguish two end-member scenarios, based on the size of the electrical double layer with respect to the size of the pores, ([Revil & Mahardika, 2013](#)):

1. A thick double layer, where the counterions of the diffuse layer are uniformly distributed in the pore space
2. A thin double layer, where the thickness of the diffuse layer is much smaller than the size of the pores.

Pride (1994) makes use of a thin double layer theory based on the zeta potential. In contrast, Revil & Mahardika (2013) describe the (thick and thin) double layer theory based on the excess charge density. We here state the main alternative expressions for the dynamic coupling coefficient, permeability and conductivity, as presented by Revil & Mahardika (2013):

$$\underline{\hat{\mathcal{L}}}(\omega, s_w) = \frac{\hat{k}(\omega, s_w)\hat{Q}_V(\omega, s_w)}{\eta_w}, \quad (2.44)$$

where the bar below the symbols indicates that it is a parameter according to Revil & Mahardika (2013). Here, $\underline{\hat{\mathcal{L}}}(\omega, s_w)$ denotes the frequency- and saturation-dependent coupling coefficient, where s_w denotes the water saturation, and η_w the dynamic viscosity of the pore water. The complex frequency- and saturation-dependent permeability $\hat{k}(\omega, s_w)$ is given (for our definition of the Fourier transform) by

$$\hat{k}(\omega, s_w) = \frac{k_r k_0}{1 + j\omega\tau_k}, \quad (2.45)$$

and is used to describe the effect of the inertial force in Darcy's law. Here, τ_k is the relaxation time

$$\tau_k = \frac{k_r k_0 \rho_w F}{\eta_w} s_w^{1-n}, \quad (2.46)$$

characterizing the transition between the viscous laminar flow regime and the inertial laminar flow regime in the frequency-domain Navier-Stokes equation, where n is called the second Archie exponent. The critical angular frequency associated with this relaxation time is $\omega_c = \frac{1}{\tau_k}$. Here, $F = \phi^{-m}$ is the formation factor that is related to the porosity by the first Archie law, where m is the cementation exponent (Archie, 1942). In addition, the relative permeability k_r can be used to express the relationship between the permeability and water saturation, using Brooks & Corey (1964)

$$k_r = s_w^{\frac{2+3\lambda}{\lambda}}, \quad (2.47)$$

where λ forms part of the exponent describing how permeability scales with water saturation, following a power-law behaviour. It is shown in Revil (2013) that $\frac{2+3\lambda}{\lambda}$ can be written as $n + 2$ to be the correct scaling factor when computing the permeability. One of the most important parameters in the model by Revil & Mahardika (2013) is $\hat{Q}(\omega, s_w)$, the frequency- and saturation-dependent excess of charge (or volumetric charge density) that can be dragged by the flow of the pore water through the pore space of the material. The frequency-dependency comes from the

fact that more charges are dragged in the inertial flow regime than in the viscous laminar flow regime, which is in agreement with [Pride \(1994\)](#). We can further distinguish \hat{Q}_V^0 and \hat{Q}_V^∞ , representing the dynamic volumetric charge density dragged in the low-frequency ($\omega\tau_k \ll 1; \omega \ll \omega_c$) and high-frequency ($\omega\tau_k \gg 1; \omega \gg \omega_c$) regimes, respectively. The relaxation time (or similarly the critical frequency) distinguishes the different regimes. Therefore, we can use the following expression to compute the effective charge density as a function of frequency

$$\frac{1}{\hat{Q}_V(\omega)} = \frac{1}{\hat{Q}_V^\infty} + \left(\frac{1}{\hat{Q}_V^0} - \frac{1}{\hat{Q}_V^\infty} \right) \frac{1}{\sqrt{1 + j\omega\tau_k}}. \quad (2.48)$$

In the thick double layer approximation, $\hat{Q}_V^\infty \approx \hat{Q}_V^0$ (i.e. regardless of the frequency, all the counterions of the diffuse layer are dragged by the fluid flow), leading to the following saturation-dependent excess charge density

$$\hat{Q}_V(\omega, s_w) \approx \frac{\hat{Q}_V^0}{s_w}. \quad (2.49)$$

For the thin double layer approximation, it is expected that $\hat{Q}_V^\infty \gg \hat{Q}_V^0$, leading to

$$\hat{Q}_V(\omega, s_w) \approx \hat{Q}_V^0 s_w^{-1} \sqrt{1 + j\omega\tau_k}. \quad (2.50)$$

Another crucial difference between [Pride \(1994\)](#) and [Revil & Mahardika \(2013\)](#) lies in the formulation of the complex conductivity. The frequency-dependency of the complex conductivity can be directly attributed to the fact that the force applied to the charge carriers is not only controlled by the electric field, but also by an electrochemical potential. As a result, diffusion and electromigration are always coupled phenomena in porous media. As a second contribution to the total current density, we can distinguish the advective drag of excess charge of the pore space by the flow of the pore water. Following [Revil & Mahardika \(2013\)](#), we can express their complex conductivity $\hat{\sigma}(\omega)$ as

$$\hat{\sigma} = \sigma' - j\sigma'' = |\hat{\sigma}| \exp(-j\psi), \quad (2.51)$$

with the magnitude of the conductivity described by $|\hat{\sigma}| = \sqrt{(\sigma')^2 + (\sigma'')^2}$, and the phase lag between the electrical current and the resulting electrical field given by $\psi = \text{atan} \frac{\sigma''}{\sigma'}$. Here, σ' denotes the in-phase electrical conductivity, which can be expressed as a function of the pore water conductivity σ_w and the surface conductivity σ_S , as

$$\sigma' = \frac{1}{F} s_w^n \sigma_w + \sigma_S. \quad (2.52)$$

Expressions for the surface conductivity σ_S are discussed in [Revil \(2012, 2013\)](#). Furthermore, σ'' represents the quadrature conductivity, which can be expressed as

$$\sigma'' = -\frac{A(\phi, m)}{F} s_w^{n-1} b_S^+ \left(\frac{f_r}{1 - f_r} \right), \quad (2.53)$$

with f_r representing the fraction of counterions in the diffuse layer, and b_S^\pm denoting the mobility of the counterions in the Stern layer (Revil, 2012, 2013). The frequency-dependence of σ'' is not explicit in equation (2.53) (Revil, 2012). For the quasi-static scenario, this quadrature conductivity should go to zero under DC conditions. The quadrature conductivity typically becomes frequency-dependent below 0.1 Hz (Revil, 2012), a frequency that is below our seismo-electromagnetic range of interest. The above discussed complex conductivity agrees with experimental data. The complex conductivity as used in the model of Pride (1994), also contains frequency-dependency. However, this frequency-dependency is the result of an electro-osmotic contribution which is expected to be negligible (Marshall & Madden, 1959). Pride (1994) ignores induced polarization effects. As a result of all this, the conductivity description based on the assumptions of Pride (1994) will not describe the observed quadrature conductivity of porous clayey materials correctly.

In the above, we have highlighted some important differences between the models of Pride (1994) and Revil & Mahardika (2013). Especially the formulation of Revil & Mahardika (2013) in terms of volumetric charge density and their definitions of the complex conductivity can be considered useful improvements. In addition, the theory as formulated by Revil & Mahardika (2013) allows for investigating seismo-electromagnetic effects in unsaturated porous media. Recently, Jardani & Revil (2015) extended the theory for full coupling in two-phase flow media. The theoretical description of partially-saturated scenarios following the model of Pride (1994) has been presented in Warden *et al.* (2013). Despite obvious differences in the assumptions between the two models, in the low-frequency limit, which is the limit that holds for most seismic scenarios (where the critical frequency lies above the bandwidth of interest), the model based on volumetric charge density as described by Revil & Mahardika (2013) is compatible with the model of Pride (1994), as shown in Appendix A of Revil & Mahardika (2013). This thesis follows the model of Pride (1994), but our seismo-EM layer-code could of course be adjusted to incorporate the assumptions of Revil & Mahardika (2013) instead.

2.2 Capturing the seismo-electromagnetic system in a general differential field equation

2.2.1 Separating horizontal from vertical derivatives

We start with the following mechanical equations of motion (including electromagnetic coupling), stress-strain relations and electromagnetic field equations in space-frequency:

$$s\rho^b\hat{v}_i^s + s\rho^f\hat{w}_i - \partial_j\hat{\tau}_{ij}^b = \hat{f}_i^b, \quad (2.54)$$

$$s\rho^f\hat{v}_i^s + \frac{\eta}{\hat{k}}\left(\hat{w}_i - \hat{\mathcal{L}}\hat{E}_i\right) + \partial_i\hat{p}^f = \hat{f}_i^f, \quad (2.55)$$

$$\partial_k\hat{w}_k = \frac{1}{M}\left(C\hat{h}_{kk}^b + M\hat{q}^i - s\hat{p}^f - C\partial_k\hat{v}_k^s\right), \quad (2.56)$$

$$-s\hat{\tau}_{ij}^b + e_{ijkl}\partial_l\hat{v}_k^s - \frac{sC}{M}\delta_{ij}\hat{p}^f = e_{ijkl}\hat{h}_{kl}^b, \quad (2.57)$$

$$s\varepsilon\hat{E}_i + \left(\sigma^e - \frac{\eta}{\hat{k}}\hat{\mathcal{L}}^2\right)\hat{E}_i + \frac{\eta}{\hat{k}}\hat{\mathcal{L}}\hat{w}_i - \epsilon_{ijk}\partial_j\hat{H}_k = -\hat{J}_i^e, \quad (2.58)$$

$$s\mu_0\hat{H}_i + \epsilon_{ijk}\partial_j\hat{E}_k = -\hat{J}_i^m. \quad (2.59)$$

We now desire to separate the horizontal components from the vertical components. From equation (2.54) we obtain

$$\partial_3\hat{\tau}_{i3}^b = s\rho^b\hat{v}_i + s\rho^f\hat{w}_i - \hat{f}_i^b - \partial_\alpha\hat{\tau}_{i\alpha}^b. \quad (2.60)$$

Using equation (2.56), we find

$$\begin{aligned} \partial_3\hat{w}_3 &= \frac{1}{M}\left(C\hat{h}_{kk}^b + M\hat{q}^i - s\hat{p}^f - C\partial_k\hat{v}_k^s\right) - \partial_\alpha\hat{w}_\alpha \\ &= \frac{1}{M}\left(C\hat{h}_{kk}^b + M\hat{q}^i - s\hat{p}^f - C\partial_\alpha\hat{v}_\alpha^s\right) - \partial_\alpha\hat{w}_\alpha - \frac{C}{M}\partial_3\hat{v}_3^s. \end{aligned} \quad (2.61)$$

Starting from equation (2.57), and separating the horizontal spatial derivatives acting on the particle velocity from the vertical derivatives, we find

$$e_{ijk3}\partial_3\hat{v}_k^s = e_{ijkl}\hat{h}_{kl}^b + s\hat{\tau}_{ij}^b + \frac{sC}{M}\delta_{ij}\hat{p}^f - e_{ijk\alpha}\partial_\alpha\hat{v}_k^s. \quad (2.62)$$

We now select the x_3 -normal component $j = 3$ of the stress-tensor $\hat{\tau}_{ij}^b$, which is the only normal component that we desire in the final field quantity expressions. The other j -components of the stress tensor are eliminated, since they are not continuous over a horizontal interface, and since we are expressing the vertical variations of the field quantities in terms of their horizontal derivatives. We define the compliance tensor, being the inverse \underline{e}_{p3i3} of the stiffness tensor e_{i3k3} , (remember that e_{ijkl} is an

extension of the elastodynamic stiffness tensor d_{ijkl} , often also referred to as c_{ijkl}), as

$$\underline{e}_{p3i3}e_{i3k3} = \delta_{pk}. \quad (2.63)$$

We apply this inverse to both the left-hand side and the right-hand sides of equation (2.62), leading to

$$\partial_3 \hat{v}_p^s = \underline{e}_{p3i3} \left(e_{i3kl} \hat{h}_{kl}^b + s \hat{\tau}_{i3}^b + \frac{sC}{M} \delta_{i3} \hat{p}^f - e_{i3k\alpha} \partial_\alpha \hat{v}_k^s \right). \quad (2.64)$$

The compliance tensor is given explicitly by

$$\underline{e}_{p3i3} = \begin{pmatrix} \underline{e}_{1313} = \frac{1}{G^f r} & \underline{e}_{1323} = 0 & \underline{e}_{1333} = 0 \\ \underline{e}_{2313} = 0 & \underline{e}_{2323} = \frac{1}{G^f r} & \underline{e}_{2333} = 0 \\ \underline{e}_{3313} = 0 & \underline{e}_{3323} = 0 & \underline{e}_{3333} = \frac{1}{s+2G^f r} \end{pmatrix}. \quad (2.65)$$

Therefore, there are only non-zero solutions to equation (2.64) when $p = i$.

Let us now focus on equation (2.60). We can recognize horizontal derivatives of the horizontal normal components of the stress tensor. We only desire vertical normal components of the stress tensor in our final field equations. Therefore, using equation (2.57), we express these horizontal components of the stress tensor in terms of the other field components, as

$$\partial_\alpha \hat{\tau}_{i\alpha}^b = \partial_\alpha \frac{1}{s} \left(e_{i\alpha k\beta} \partial_\beta \hat{v}_k^s + e_{i\alpha k3} \partial_3 \hat{v}_k^s - \frac{sC}{M} \delta_{i\alpha} \hat{p}^f - e_{i\alpha k\beta} \hat{h}_{k\beta}^b - e_{i\alpha k3} \hat{h}_{k3}^b \right). \quad (2.66)$$

We now rewrite equation (2.61), eliminating the vertical derivative of the vertical component particle velocity and the horizontal filtration velocity components using equations (2.64), with $k = 3$ and (2.68), respectively, yielding

$$\begin{aligned} \partial_3 \hat{w}_3 &= \frac{1}{M} \left(C \hat{h}_{kk}^b + M \hat{q}^i - s \hat{p}^f - C \partial_\alpha \hat{v}_\alpha^s \right) \\ &\quad - \frac{C}{M} \left(\underline{e}_{3333} \left[e_{3311} \hat{h}_{11}^b + e_{3322} \hat{h}_{22}^b + e_{3333} \hat{h}_{33}^b + s \hat{\tau}_{33}^b \right. \right. \\ &\quad \left. \left. + \frac{sC}{M} \delta_{33} \hat{p}^f - e_{3311} \partial_1 \hat{v}_1^s - e_{3322} \partial_2 \hat{v}_2^s \right] \right) \\ &\quad - \left(-\frac{s\rho^f \hat{k}}{\eta} \partial_\alpha \hat{v}_\alpha^s + \hat{\mathcal{L}} \partial_\alpha \hat{E}_\alpha - \frac{\hat{k}}{\eta} \partial_\alpha \partial_\alpha \hat{p}^f + \frac{\hat{k}}{\eta} \partial_\alpha \hat{f}_\alpha^f \right). \end{aligned} \quad (2.67)$$

Similarly, from equation (2.55), we can find expressions for the horizontal components of the filtration velocity (since we only desire the vertical component in the final field quantity expressions), as

$$\hat{w}_\alpha = -\frac{s\rho^f \hat{k}}{\eta} \hat{v}_\alpha^s + \hat{\mathcal{L}} \hat{E}_\alpha - \frac{\hat{k}}{\eta} \partial_\alpha \hat{p}^f + \frac{\hat{k}}{\eta} \hat{f}_\alpha^f. \quad (2.68)$$

Combining equations (2.60) and (2.66), we substitute the expressions for the vertical derivative of the particle velocity (equation (2.64)) and the horizontal filtration velocity (equation (2.68)), to obtain for the x_1 -component of the x_3 -normal component of the bulk stress tensor:

$$\begin{aligned} \partial_3 \hat{\tau}_{13}^b &= s\rho^b \hat{v}_1^s + s\rho^f \left(-\frac{s\rho^f \hat{k}}{\eta} \hat{v}_1^s + \hat{\mathcal{L}} \hat{E}_1 - \frac{\hat{k}}{\eta} \partial_1 \hat{p}^f + \frac{\hat{k}}{\eta} \hat{f}_1^f \right) - \hat{f}_1^b \\ &\quad - \frac{1}{s} \partial_\alpha \left\{ e_{1\alpha k\beta} \partial_\beta \hat{v}_k^s + e_{1\alpha k3} \left(e_{i3k3} \left(e_{i3mn} \hat{h}_{mn}^b + s\hat{\tau}_{i3}^b \right. \right. \right. \\ &\quad \left. \left. \left. + \frac{sC}{M} \delta_{i3} \hat{p}^f - e_{i3m\alpha} \partial_\alpha \hat{v}_m^s \right) \right) \right\} \\ &\quad - \frac{sC}{M} \delta_{1\alpha} \hat{p}^f - e_{1\alpha k\beta} \hat{h}_{k\beta}^b - e_{1\alpha k3} \hat{h}_{k3}^b \}. \end{aligned} \quad (2.69)$$

We can observe that the term describing $e_{i\alpha k3} \partial_3 \hat{v}_k^s$ only contributes if $k = 3$ (and hence $i = 3$), leading to

$$\begin{aligned} \partial_3 \hat{\tau}_{13}^b &= s\rho^b \hat{v}_1^s + s\rho^f \left(-\frac{s\rho^f \hat{k}}{\eta} \hat{v}_1^s + \hat{\mathcal{L}} \hat{E}_1 - \frac{\hat{k}}{\eta} \partial_1 \hat{p}^f + \frac{\hat{k}}{\eta} \hat{f}_1^f \right) - \hat{f}_1^b \\ &\quad - \frac{1}{s} \partial_\alpha \left\{ e_{1\alpha k\beta} \partial_\beta \hat{v}_k^s + e_{1\alpha 33} \left(e_{3333} \left(e_{33mn} \hat{h}_{mn}^b + s\hat{\tau}_{33}^b \right. \right. \right. \\ &\quad \left. \left. \left. + \frac{sC}{M} \delta_{33} \hat{p}^f - e_{33m\alpha} \partial_\alpha \hat{v}_m^s \right) \right) \right\} \\ &\quad - \frac{sC}{M} \delta_{1\alpha} \hat{p}^f - e_{1\alpha k\beta} \hat{h}_{k\beta}^b - e_{1\alpha k3} \hat{h}_{k3}^b \}. \end{aligned} \quad (2.70)$$

In a similar way, choosing $i = 2$ in equations (2.60) and (2.66) and combining both equations, followed by substitution of the expressions for the vertical derivative of the particle velocity (equation (2.64)) and the horizontal filtration velocity (equation (2.68)), we obtain the expression for $\partial_3 \hat{\tau}_{23}^b$.

From equation (2.58) we obtain,

$$\partial_3 \hat{H}_1 = s\hat{\epsilon} \hat{E}_2 + \frac{\eta}{\hat{k}} \hat{\mathcal{L}} \hat{w}_2 + \partial_1 \hat{H}_3 + \hat{J}_2^e, \quad (2.71)$$

$$\partial_3 \hat{H}_2 = -s\hat{\epsilon} \hat{E}_1 - \frac{\eta}{\hat{k}} \hat{\mathcal{L}} \hat{w}_1 + \partial_2 \hat{H}_3 - \hat{J}_1^e, \quad (2.72)$$

where we made use of $\hat{\epsilon} = \epsilon + \frac{\hat{\sigma}^e}{s} - \hat{\rho}^E \hat{\mathcal{L}}^2$. Similarly, using equation (2.59), we derive

$$\partial_3 \hat{E}_1 = -s\mu_0 \hat{H}_2 + \partial_1 \hat{E}_3 - \hat{J}_2^m, \quad (2.73)$$

$$\partial_3 \hat{E}_2 = s\mu_0 \hat{H}_1 + \partial_2 \hat{E}_3 + \hat{J}_1^m. \quad (2.74)$$

Now explicitly evaluating $e_{ijkl} = S\delta_{ij}\delta_{kl} + G^{fr}(\delta_{ik}\delta_{jl} + \delta_{il}\delta_{jk})$, as well as using

equation (2.65), yields

$$\partial_3 \hat{v}_1^s = \left(\hat{h}_{31}^b + \hat{h}_{13}^b \right) + \frac{s}{G^{fr}} \hat{\tau}_{13}^b - \partial_1 \hat{v}_3^s, \quad (2.75)$$

$$\partial_3 \hat{v}_2^s = \left(\hat{h}_{32}^b + \hat{h}_{23}^b \right) + \frac{s}{G^{fr}} \hat{\tau}_{23}^b - \partial_2 \hat{v}_3^s, \quad (2.76)$$

$$\partial_3 \hat{v}_3^s = \frac{s}{K_c} \hat{\tau}_{33}^b + \frac{sC}{MK_c} \hat{p}^f - \frac{S}{K_c} (\partial_1 \hat{v}_1^s + \partial_2 \hat{v}_2^s) + \frac{S}{K_c} \left(\hat{h}_{11}^b + \hat{h}_{22}^b \right) + \hat{h}_{33}^b \quad (2.77)$$

$$\begin{aligned} \partial_3 \hat{w}_3 &= -\frac{sC}{MK_c} \hat{\tau}_{33}^b - \frac{s}{M} \left(1 + \frac{C^2}{MK_c} \right) \hat{p}^f + \frac{\hat{k}}{\eta} \partial_\alpha^2 \hat{p}^f \\ &+ \frac{\rho^f}{\hat{\rho}^E} \partial_\alpha \hat{v}_\alpha^s - \hat{\mathcal{L}} \partial_\alpha \hat{E}_\alpha - \frac{\hat{k}}{\eta} \partial_\alpha \hat{f}_\alpha^f - \frac{C}{M} \left(1 - \frac{S}{K_c} \right) \partial_\alpha \hat{v}_\alpha^s \\ &- \frac{C}{M} \frac{S}{K_c} \hat{h}_{\alpha\alpha}^b + \frac{C}{M} \hat{h}_{\alpha\alpha}^b + \hat{q}^i, \end{aligned} \quad (2.78)$$

$$\begin{aligned} \partial_3 \hat{\tau}_{13}^b &= -\partial_1 \frac{S}{K_c} \hat{\tau}_{33}^b - s\rho^f \frac{\hat{k}}{\eta} \partial_1 \hat{p}^f + \frac{1}{s} \partial_1 \left(\frac{sC}{M} \left[1 - \frac{S}{K_c} \right] \hat{p}^f - \right. \\ &\left. \left[\frac{4G^{fr}(S + G^{fr})}{K_c} \partial_1 \hat{v}_1^s + \frac{2SG^{fr}}{K_c} \partial_2 \hat{v}_2^s \right] \right) \\ &+ s\rho^b \hat{v}_1^s - s^2 (\rho^f)^2 \frac{\hat{k}}{\eta} \hat{v}_1^s + s\rho^f \hat{\mathcal{L}} \hat{E}_1 - \hat{f}_1^b + s\rho^f \frac{\hat{k}}{\eta} \hat{f}_1^f \\ &- \frac{1}{s} \partial_1 \left(\frac{S^2}{K_c} \left[\hat{h}_{11}^b + \hat{h}_{22}^b \right] \right) + \frac{1}{s} \partial_1 \left(K_c \hat{h}_{11}^b + S \hat{h}_{22}^b \right) \\ &- \frac{1}{s} \partial_2 \left(G^{fr} [\partial_1 \hat{v}_2^s + \partial_2 \hat{v}_1^s] \right) + \frac{1}{s} \partial_2 \left(G^{fr} \left[\hat{h}_{21}^b + \hat{h}_{12}^b \right] \right), \end{aligned} \quad (2.79)$$

$$\begin{aligned} \partial_3 \hat{\tau}_{23}^b &= -\partial_2 \frac{S}{K_c} \hat{\tau}_{33}^b - s\rho^f \frac{\hat{k}}{\eta} \partial_2 \hat{p}^f + \frac{1}{s} \partial_2 \left(\frac{sC}{M} \left[1 - \frac{S}{K_c} \right] \hat{p}^f - \right. \\ &\left. \left[\frac{2SG^{fr}}{K_c} \partial_1 \hat{v}_1^s + \frac{4G^{fr}(S + G^{fr})}{K_c} \partial_2 \hat{v}_2^s \right] \right) \\ &+ s\rho^b \hat{v}_2^s - s^2 (\rho^f)^2 \frac{\hat{k}}{\eta} \hat{v}_2^s + s\rho^f \hat{\mathcal{L}} \hat{E}_2 - \hat{f}_2^b + s\rho^f \frac{\hat{k}}{\eta} \hat{f}_2^f \\ &- \frac{1}{s} \partial_2 \left(\frac{S^2}{K_c} \left[\hat{h}_{11}^b + \hat{h}_{22}^b \right] \right) + \frac{1}{s} \partial_2 \left(S \hat{h}_{11}^b + K_c \hat{h}_{22}^b \right) \\ &- \frac{1}{s} \partial_1 \left(G^{fr} [\partial_1 \hat{v}_2^s + \partial_2 \hat{v}_1^s] \right) + \frac{1}{s} \partial_1 \left(G^{fr} \left[\hat{h}_{21}^b + \hat{h}_{12}^b \right] \right). \end{aligned} \quad (2.80)$$

From equation (2.60), we also directly obtain

$$\partial_3 \hat{\tau}_{33}^b = s\rho^b \hat{v}_3^s + s\rho^f \hat{w}_3 - \hat{f}_3^b - (\partial_1 \hat{\tau}_{31}^b + \partial_2 \hat{\tau}_{32}^b). \quad (2.81)$$

From equation (2.55), we derive

$$-\partial_3 \hat{p}^f = s\rho^f \hat{v}_3^s + \frac{\eta}{\hat{k}} \left(\hat{w}_3 - \hat{\mathcal{L}} \hat{E}_3 \right) - \hat{f}_3^f. \quad (2.82)$$

Starting from equations (2.71) and (2.72), we eliminate \hat{H}_3 using

$$\hat{H}_3 = \frac{1}{s\mu_0} \left(\partial_2 \hat{E}_1 - \partial_1 \hat{E}_2 - \hat{J}_3^m \right), \quad (2.83)$$

and the horizontal filtration velocity components using equation (2.68) which leads to

$$\begin{aligned} \partial_3 \hat{H}_1 &= s\hat{\epsilon} \hat{E}_2 + \frac{\eta}{\hat{k}} \hat{\mathcal{L}} \left(-\frac{s\rho^f \hat{k}}{\eta} \hat{v}_2^s + \hat{\mathcal{L}} \hat{E}_2 - \frac{\hat{k}}{\eta} \partial_2 \hat{p}^f + \frac{\hat{k}}{\eta} \hat{f}_2^f \right) \\ &\quad + \frac{1}{s\mu_0} \left(\partial_1 \partial_2 \hat{E}_1 - \partial_1^2 \hat{E}_2 - \partial_1 \hat{J}_3^m \right) + \hat{J}_2^e, \end{aligned} \quad (2.84)$$

$$\begin{aligned} \partial_3 \hat{H}_2 &= -s\hat{\epsilon} \hat{E}_1 - \frac{\eta}{\hat{k}} \hat{\mathcal{L}} \left(-\frac{s\rho^f \hat{k}}{\eta} \hat{v}_1^s + \hat{\mathcal{L}} \hat{E}_1 - \frac{\hat{k}}{\eta} \partial_1 \hat{p}^f + \frac{\hat{k}}{\eta} \hat{f}_1^f \right) \\ &\quad + \frac{1}{s\mu_0} \left(\partial_2^2 \hat{E}_1 - \partial_2 \partial_1 \hat{E}_2 - \hat{J}_3^m \right) - \hat{J}_1^e. \end{aligned} \quad (2.85)$$

Finally, starting from equations (2.73) and (2.74), we eliminate \hat{E}_3 using

$$\hat{E}_3 = \frac{1}{s\hat{\epsilon}} \left(-\frac{\eta}{\hat{k}} \hat{\mathcal{L}} \hat{w}_3 + \partial_1 \hat{H}_2 - \partial_2 \hat{H}_1 - \hat{J}_3^e \right), \quad (2.86)$$

which yields

$$\partial_3 \hat{E}_1 = -s\mu_0 \hat{H}_2 + \frac{1}{s\hat{\epsilon}} \left(-\frac{\eta}{\hat{k}} \hat{\mathcal{L}} \partial_1 \hat{w}_3 + \partial_1^2 \hat{H}_2 - \partial_1 \partial_2 \hat{H}_1 - \partial_1 \hat{J}_3^e \right) - \hat{J}_2^m, \quad (2.87)$$

$$\partial_3 \hat{E}_2 = s\mu_0 \hat{H}_1 + \frac{1}{s\hat{\epsilon}} \left(-\frac{\eta}{\hat{k}} \hat{\mathcal{L}} \partial_2 \hat{w}_3 + \partial_2 \partial_1 \hat{H}_2 - \partial_2^2 \hat{H}_1 - \partial_2 \hat{J}_3^e \right) + \hat{J}_1^m. \quad (2.88)$$

We now have expressed the vertical derivatives of the desired field quantities in terms of other fields and horizontal derivatives on other fields.

2.2.2 Taking horizontal derivatives and combining field quantities into mode quantities

Since we are considering a medium that is invariant in two directions (layered-Earth), it can be useful to decouple the total 3D system of equations into two independent seismo-electromagnetic propagation modes: the SH-TE propagation mode, where the horizontally-polarized shear-waves are coupled to the transverse electric mode, and the P-SV-TM propagation mode where the Biot fast and slow pressure waves are coupled to the transverse magnetic mode via the vertically-polarized shear waves. To decouple the system in these two independent propagation modes, we first apply a 2D spatial Fourier transformation to equations (2.75)-(2.88) to obtain the horizontal wavenumber-frequency domain expressions (denoted by the tilde sign). We can express these equations in terms of their mode quantities, by taking the divergence or rotation of the expressions under consideration. To this end, let us first define the following mode quantities:

$$\tilde{v}^{s,H} = -jk_1\tilde{v}_2^s + jk_2\tilde{v}_1^s, \quad (2.89)$$

$$\tilde{\tau}^{b,H} = -jk_1\tilde{\tau}_{23}^b + jk_2\tilde{\tau}_{13}^b, \quad (2.90)$$

$$\tilde{E}^H = -jk_1\tilde{E}_2 + jk_2\tilde{E}_1, \quad (2.91)$$

$$\tilde{H}^H = -jk_1\tilde{H}_1 - jk_2\tilde{H}_2, \quad (2.92)$$

for the SH-TE mode, and

$$\tilde{v}_{norm}^{s,V} = \frac{k_1}{\kappa}\tilde{v}_1^s + \frac{k_2}{\kappa}\tilde{v}_2^s, \quad (2.93)$$

$$\tilde{\tau}_{norm}^{b,V} = \frac{k_1}{\kappa}\tilde{\tau}_{13}^b + \frac{k_2}{\kappa}\tilde{\tau}_{23}^b, \quad (2.94)$$

$$\tilde{E}_{norm}^V = \frac{k_1}{\kappa}\tilde{E}_1 + \frac{k_2}{\kappa}\tilde{E}_2, \quad (2.95)$$

$$\tilde{H}_{norm}^V = \frac{k_1}{\kappa}\tilde{H}_2 - \frac{k_2}{\kappa}\tilde{H}_1, \quad (2.96)$$

for the P-SV-TM mode. Here the radial wavenumber $\kappa = \sqrt{k_1^2 + k_2^2}$. For P-SV-TM, the subscript ‘norm’ indicates that these specific mode quantities have been normalized with a factor $-j\kappa$ (this to obtain favourable symmetry properties in the system matrix later on). Consequently, the factors on the right-hand side, before the field quantities, have also been normalized by $-j\kappa$. The field quantities that are not present in the mode expressions above are purely P-SV-TM field quantities. We can observe for example in equation (2.89), that by taking jk_2 of \tilde{v}_1^s (corresponding to $-\partial_2\hat{v}_1^s$ and adding this to $-jk_1$ of \tilde{v}_2^s yields the SH-TE particle velocity mode quantity. Up till this point, we have eliminated $\hat{\tau}_{\alpha\beta}^b$, \hat{w}_α , \hat{H}_3 , and \hat{E}_3 , using the horizontal wavenumber-frequency versions of equations (2.57), (2.68), (2.83), and

(2.86), respectively, according to

$$\tilde{\tau}_{\alpha\beta}^b = -\frac{1}{s} \left(e_{\alpha\beta k l} j k_l \tilde{v}_\alpha^s + \frac{sC}{M} \delta_{\alpha\beta} \tilde{p}^f + e_{\alpha\beta k l} \tilde{h}_{kl}^b \right), \quad (2.97)$$

$$\tilde{w}_\alpha = -\frac{s\rho^f \hat{k}}{\eta} \tilde{v}_\alpha^s + \hat{\mathcal{L}} \tilde{E}_\alpha + \frac{\hat{k}}{\eta} j k_\alpha \tilde{p}^f + \frac{\hat{k}}{\eta} \tilde{f}_\alpha^f, \quad (2.98)$$

$$\tilde{H}_3 = \frac{1}{s\mu_0} \left(-\tilde{E}^H - \tilde{J}_3^m \right), \quad (2.99)$$

$$\tilde{E}_3 = \frac{1}{s\hat{\epsilon}} \left(-\frac{\eta}{\hat{k}} \hat{\mathcal{L}} \tilde{w}_3 - j\kappa \tilde{H}_{norm}^V - \tilde{J}_3^e \right). \quad (2.100)$$

We now take the derivatives of equations (2.75)-(2.88) and combine according to equations (2.89)-(2.96), yielding two sets of governing equations, one for the SH-TE mode and one for the P-SV-TM mode, expressing the vertical variations of the mode and field quantities in terms of the horizontal variations. For the SH-TE mode, this results in:

$$\partial_3 \tilde{v}^{s,H} = \frac{s}{G^{fr}} \tilde{\tau}^{b,H} - jk_1 \left(\tilde{h}_{23}^b + \tilde{h}_{32}^b \right) + jk_2 \left(\tilde{h}_{13}^b + \tilde{h}_{31}^b \right), \quad (2.101)$$

$$\begin{aligned} \partial_3 \tilde{\tau}^{b,H} = & \frac{G^{fr}}{s} \kappa^2 \tilde{v}^{s,H} + \left(s\rho^b - s^2(\rho^f)^2 \frac{\hat{k}}{\eta} \right) \tilde{v}^{s,H} + s\rho^f \hat{\mathcal{L}} \tilde{E}^H + \\ & jk_1 \left(\tilde{f}_2^b - s\rho^f \frac{\hat{k}}{\eta} \tilde{f}_2^f \right) - jk_2 \left(\tilde{f}_1^b - s\rho^f \frac{\hat{k}}{\eta} \tilde{f}_1^f \right) \\ & + \frac{G^{fr}}{s} (-k_1^2 + k_2^2) \left(\tilde{h}_{21}^b + \tilde{h}_{12}^b \right) - k_1 k_2 \frac{2G^{fr}}{s} \left(-\tilde{h}_{11}^b + \tilde{h}_{22}^b \right) \end{aligned} \quad (2.102)$$

$$\partial_3 \tilde{E}^H = s\mu_0 \tilde{H}^H - jk_\alpha \tilde{J}_\alpha^m, \quad (2.103)$$

$$\begin{aligned} \partial_3 \tilde{H}^H = & s\hat{\epsilon} \tilde{E}^H - s\rho^f \hat{\mathcal{L}} \tilde{v}^{s,H} + \frac{\eta}{\hat{k}} \hat{\mathcal{L}}^2 \tilde{E}^H + \frac{1}{s\mu_0} \kappa^2 \tilde{E}^H \\ & + \hat{\mathcal{L}} \left(-jk_1 \tilde{f}_2^f + jk_2 \tilde{f}_1^f \right) - jk_1 \tilde{J}_2^e + jk_2 \tilde{J}_1^e + \frac{1}{s\mu_0} \kappa^2 \tilde{J}_3^m. \end{aligned} \quad (2.104)$$

Similarly, for the normalized P-SV-TM mode, we obtain

$$\partial_3 \tilde{v}_{norm}^{s,V} = \frac{s}{G^{fr}} \tilde{\tau}_{norm}^{b,V} + j\kappa \tilde{v}_3^s + \frac{k_\alpha}{\kappa} (\tilde{h}_{\alpha 3}^b + \tilde{h}_{3\alpha}^b), \quad (2.105)$$

$$\partial_3 \tilde{v}_3^s = \frac{s}{K_c} \tilde{\tau}_{33}^b + \frac{sC}{MK_c} \tilde{p}^f + \frac{j\kappa S}{K_c} \tilde{v}_{norm}^{s,V} + \frac{S}{K_c} (\tilde{h}_{11}^b + \tilde{h}_{22}^b) + \tilde{h}_{33}^b, \quad (2.106)$$

$$\begin{aligned} \partial_3 \tilde{w}_3 &= -s \frac{C}{MK_c} \tilde{\tau}_{33}^b - \frac{s}{M} \left(1 + \frac{C^2}{MK_c}\right) \tilde{p}^f - \frac{\hat{k}}{\eta} \kappa^2 \tilde{p}^f \\ &\quad - j\kappa \frac{\rho^f}{\hat{\rho}^E} \tilde{v}_{norm}^{s,V} + j\kappa \frac{C}{M} \left(1 - \frac{S}{K_c}\right) \tilde{v}_{norm}^{s,V} + j\kappa \hat{\mathcal{L}} \tilde{E}_{norm}^V \\ &\quad + \frac{\hat{k}}{\eta} j k_\alpha \tilde{f}_\alpha^f - \frac{CS}{MK_c} (\tilde{h}_{11}^b + \tilde{h}_{22}^b) + \frac{C}{M} (\tilde{h}_{11}^b + \tilde{h}_{22}^b) + \tilde{q}^i, \end{aligned} \quad (2.107)$$

$$\partial_3 \tilde{p}^f = -s\rho^f \tilde{v}_3^s - \frac{\eta}{\hat{k}} \left(1 + \frac{\hat{\rho}^E}{\hat{\epsilon}} \hat{\mathcal{L}}^2\right) \tilde{w}_3 - j\kappa \frac{\hat{\rho}^E}{\hat{\epsilon}} \hat{\mathcal{L}} \tilde{H}_{norm}^V - \frac{\hat{\rho}^E}{\hat{\epsilon}} \hat{\mathcal{L}} \tilde{J}_3^e + \tilde{f}_3^f, \quad (2.108)$$

$$\begin{aligned} \partial_3 \tilde{\tau}_{norm}^{b,V} &= j\kappa \frac{S}{K_c} \tilde{\tau}_{33}^b + j\kappa \frac{\rho^f}{\hat{\rho}^E} \tilde{p}^f - j\kappa \frac{C}{M} \left(1 - \frac{S}{K_c}\right) \tilde{p}^f + \kappa^2 \frac{1}{s} \frac{4G^{fr}(S + G^{fr})}{K_c} \tilde{v}_{norm}^{s,V} \\ &\quad + \left(s\rho^b - s^2(\rho^f)^2 \frac{\hat{k}}{\eta}\right) \tilde{v}_{norm}^{s,V} + s\rho^f \hat{\mathcal{L}} \tilde{E}_{norm}^V \\ &\quad + \frac{\rho^f}{\hat{\rho}^E} \frac{k_\alpha}{\kappa} \tilde{f}_\alpha^f - \frac{k_\alpha}{\kappa} \tilde{f}_\alpha^b + \frac{j\kappa S^2}{s K_c} (\tilde{h}_{11}^b + \tilde{h}_{22}^b) + \frac{2G^{fr} k_1 k_2}{sj\kappa} (\tilde{h}_{21}^b + \tilde{h}_{12}^b) \\ &\quad + \frac{k_1^2}{sj\kappa} (K_c \tilde{h}_{11}^b + S \tilde{h}_{22}^b) + \frac{k_2^2}{sj\kappa} (S \tilde{h}_{11}^b + K_c \tilde{h}_{22}^b), \end{aligned} \quad (2.109)$$

$$\partial_3 \tilde{\tau}_{33}^b = j\kappa \tilde{\tau}_{norm}^{b,V} + s\rho^b \tilde{v}_3^s + s\rho^f \tilde{w}_3 - \tilde{f}_3^b, \quad (2.110)$$

$$\partial_3 \tilde{E}_{norm}^V = -s\mu_0 \tilde{H}_{norm}^V - \frac{\kappa^2}{s\hat{\epsilon}} \tilde{H}_{norm}^V + j\kappa \frac{\hat{\rho}^E \hat{\mathcal{L}}}{\hat{\epsilon}} \tilde{w}_3 + \frac{j\kappa}{s\hat{\epsilon}} \tilde{J}_3^e + \frac{k_2}{\kappa} \tilde{J}_1^m - \frac{k_1}{\kappa} \tilde{J}_2^m, \quad (2.111)$$

$$\partial_3 \tilde{H}_{norm}^V = -s\hat{\epsilon} \tilde{E}_{norm}^V + s\rho^f \hat{\mathcal{L}} \tilde{v}_{norm}^{s,V} - \frac{\eta}{\hat{k}} \hat{\mathcal{L}}^2 \tilde{E}_{norm}^V - j\kappa \hat{\mathcal{L}} \tilde{p}^f - \hat{\mathcal{L}} \frac{k_\alpha}{\kappa} \tilde{f}_\alpha^f - \frac{k_\alpha}{\kappa} \tilde{J}_\alpha^e. \quad (2.112)$$

We can now capture these two sets of governing seismo-electromagnetic equations (independently for each propagation mode) in the following matrix-vector representation of the two-way wave equation

$$\partial_3 \tilde{\mathbf{q}}^{H,V}(\mathbf{k}_H, x_3, \omega) = \tilde{\mathbf{A}}^{H,V}(\mathbf{k}_H, x_3, \omega) \tilde{\mathbf{q}}^{H,V}(\mathbf{k}_H, x_3, \omega) + \tilde{\mathbf{d}}^{H,V}(\mathbf{k}_H, x_3, \omega) \delta(x_3 - x_3^s). \quad (2.113)$$

This two-way wave equation can be used for a variety of waves and fields (Wapenaar *et al.*, 2008b). Equation (2.113) expresses, in matrix-vector notation indicated by the boldface symbols, the vertical variations of the field quantities in $\tilde{\mathbf{q}}^{H,V}(\mathbf{k}_H, x_3, \omega)$, in terms of the medium parameters and radial wavenumbers in system matrix $\tilde{\mathbf{A}}^{H,V}(\mathbf{k}_H, x_3, \omega)$ acting on these field quantities (Woodhouse, 1974;

(Kennett, 1983; Ursin, 1983; Wapenaar & Grimbergen, 1996). Furthermore, $\tilde{\mathbf{d}}^{H,V}(\mathbf{k}_H, x_3, \omega)$ represents the source vector containing all source terms of the seismo-electromagnetic SH-TE and P-SV-TM modes. The field quantities for each of these modes in $\tilde{\mathbf{q}}^{H,V}$ are continuous across horizontal interfaces. Considering the fact that in the Earth the major variations occur in the depth direction, it makes sense to take the vertical axis as the direction of preference and separate the vertical variations of the field from the horizontal variations of the same field. We desire to arrange the field quantities in $\tilde{\mathbf{q}}^{H,V}$ in such a way that the corresponding system matrices $\tilde{\mathbf{A}}^{H,V}$ have optimal symmetry properties. This allows for essential simplifications of our eigenvector analysis.

Capturing the SH-TE propagation mode

We use the following arrangement of the field vector for the SH-TE propagation mode

$$\tilde{\mathbf{q}}^H = \begin{pmatrix} \tilde{\mathbf{q}}_1^H \\ \tilde{\mathbf{q}}_2^H \end{pmatrix} = \begin{pmatrix} \tilde{v}^{s,H} \\ \tilde{E}^H \\ \tilde{\tau}^{b,H} \\ -\tilde{H}^H \end{pmatrix}, \quad (2.114)$$

where the superscript H indicates that that respective field quantity is an SH-TE mode quantity.

The corresponding system matrix reads

$$\tilde{\mathbf{A}}^H = \begin{pmatrix} \mathbf{O} & \tilde{\mathbf{A}}_{12} \\ \tilde{\mathbf{A}}_{21} & \mathbf{O} \end{pmatrix}, \quad (2.115)$$

which consists of anti-diagonal symmetric block matrix operators, reading

$$\tilde{\mathbf{A}}_{12}^H = \begin{pmatrix} \beta & 0 \\ 0 & -\zeta \end{pmatrix}, \quad (2.116)$$

$$\tilde{\mathbf{A}}_{21}^H = \begin{pmatrix} \alpha + \frac{\kappa^2}{\beta} & \chi \\ \chi & -(\hat{\rho}^E + \frac{\kappa^2}{\zeta}) \end{pmatrix}. \quad (2.117)$$

In equation (2.115), \mathbf{O} is a two-by-two zero-matrix. Furthermore, the following relations hold between the different variables

$$\alpha = s\hat{\rho}^c, \quad (2.118)$$

$$\hat{\rho}^c = \rho^b - \frac{(\rho^f)^2}{\hat{\rho}^E}, \quad (2.119)$$

$$\hat{\rho}^E = \frac{\eta}{sk}, \quad (2.120)$$

$$\chi = s\rho^f \hat{\mathcal{L}}, \quad (2.121)$$

$$\beta = \frac{s}{G^{fr}}, \quad (2.122)$$

$$\zeta = \hat{\sigma}^m + s\mu, \quad (2.123)$$

$$\hat{\eta}^E = \hat{\sigma}^e + s\varepsilon, \quad (2.124)$$

$$\hat{\varepsilon} = \varepsilon_0\varepsilon_r + \frac{\hat{\sigma}^e}{s} - \hat{\rho}^E \hat{\mathcal{L}}^2 = \varepsilon + \frac{\hat{\sigma}^e}{s} - \hat{\rho}^E \hat{\mathcal{L}}^2 = \frac{\hat{\eta}^E}{s} - \hat{\rho}^E \hat{\mathcal{L}}^2. \quad (2.125)$$

The SH-TE source vector in the horizontal wavenumber-frequency domain then reads

$$\tilde{\mathbf{d}}^H = \left(\tilde{d}_1^H, \tilde{d}_2^H, \tilde{d}_3^H, \tilde{d}_4^H \right)^t, \quad (2.126)$$

where

$$\tilde{d}_1^H = -jk_1 \left[\tilde{h}_{23}^b + \tilde{h}_{32}^b \right] + jk_2 \left[\tilde{h}_{13}^b + \tilde{h}_{31}^b \right], \quad (2.127)$$

$$\tilde{d}_2^H = -jk_\alpha \tilde{J}_\alpha^m, \quad (2.128)$$

$$\begin{aligned} \tilde{d}_3^H = & jk_1 \left[\tilde{f}_2^b - \frac{\rho^f}{\hat{\rho}^E} \tilde{f}_2^f \right] - jk_2 \left[\tilde{f}_1^b - \frac{\rho^f}{\hat{\rho}^E} \tilde{f}_1^f \right] + \frac{1}{s} \left[-k_1^2 + k_2^2 \right] \left[G^{fr} \tilde{h}_{21}^b + G^{fr} \tilde{h}_{12}^b \right] \\ & - \frac{k_1 k_2}{s} \left[-2G^{fr} \tilde{h}_{11}^b + 2G^{fr} \tilde{h}_{22}^b \right], \end{aligned} \quad (2.129)$$

$$\tilde{d}_4^H = -\hat{\mathcal{L}} \left[-jk_1 \tilde{f}_2^f + jk_2 \tilde{f}_1^f \right] + jk_1 \tilde{J}_2^e - jk_2 \tilde{J}_1^e - \frac{1}{s\mu_0} \kappa^2 \tilde{J}_3^m. \quad (2.130)$$

Capturing the P-SV-TM propagation mode

For the P-SV-TM propagation mode, we use the following arrangement of the field vector:

$$\tilde{\mathbf{q}}^V = \begin{pmatrix} \tilde{\mathbf{q}}_1^V \\ \tilde{\mathbf{q}}_2^V \end{pmatrix} = \begin{pmatrix} \tilde{v}_3^s \\ \tilde{w}_3 \\ \tilde{\tau}_{norm}^{b,V} \\ \tilde{H}_{norm}^V \\ \tilde{\tau}_{33}^b \\ -\tilde{p}^f \\ \tilde{v}_{norm}^{s,V} \\ \tilde{E}_{norm}^V \end{pmatrix}, \quad (2.131)$$

where the superscript V indicates that these field quantities are P-SV-TM mode quantities.

These choices result in the following P-SV-TM system matrix

$$\tilde{\mathbf{A}}^V = \begin{pmatrix} \mathbf{O} & \tilde{\mathbf{A}}_{12}^V \\ \tilde{\mathbf{A}}_{21}^V & \mathbf{O} \end{pmatrix}, \quad (2.132)$$

where the submatrices are defined as

$$\tilde{\mathbf{A}}_{12}^V = \begin{pmatrix} \frac{s}{K_c} & -s \frac{C}{MK_c} & \frac{j\kappa S}{K_c} & 0 \\ -s \frac{C}{MK_c} & \frac{s}{M} \left[1 + \frac{C^2}{MK_c} \right] + \frac{\hat{k}}{\eta} \kappa^2 & -j\kappa \frac{\rho^f}{\hat{\rho}^E} + j\kappa \frac{C}{M} \left[1 - \frac{S}{K_c} \right] & j\kappa \hat{\mathcal{L}} \\ \frac{j\kappa S}{K_c} & -j\kappa \frac{\rho^f}{\hat{\rho}^E} + j\kappa \frac{C}{M} \left[1 - \frac{S}{K_c} \right] & \frac{1}{s} \frac{4G_{fr}(S+G_{fr})}{K_c} \kappa^2 + s\hat{\rho}^c & \chi \\ 0 & j\kappa \hat{\mathcal{L}} & \chi & -\hat{\eta}^E \end{pmatrix}, \quad (2.133)$$

and

$$\tilde{\mathbf{A}}_{21}^V = \begin{pmatrix} s\rho^b & s\rho^f & j\kappa & 0 \\ s\rho^f & \frac{s\hat{\rho}^E \hat{\eta}^E}{\hat{\xi}} & 0 & j\kappa \frac{\hat{\xi}}{\hat{\zeta}} \\ j\kappa & 0 & \beta & 0 \\ 0 & j\kappa \frac{\hat{\xi}}{\hat{\zeta}} & 0 & -\zeta - \frac{1}{\hat{\zeta}} \kappa^2 \end{pmatrix}. \quad (2.134)$$

The following additional relations hold between different variables

$$\xi = \frac{\eta}{\hat{k}} \hat{\mathcal{L}} = s\hat{\rho}^E \hat{\mathcal{L}}, \quad (2.135)$$

$$\hat{\zeta} = \hat{\eta}^E - \hat{\xi} \hat{\mathcal{L}}, \quad (2.136)$$

$$\frac{\hat{\eta}^e}{\hat{\zeta}} = 1 + \frac{\hat{\xi} \hat{\mathcal{L}}}{\hat{\zeta}}. \quad (2.137)$$

The corresponding P-SV-TM source vector in the horizontal wavenumber-frequency domain is given by

$$\tilde{\mathbf{d}}^V = \left(\tilde{d}_1^V, \tilde{d}_2^V, \tilde{d}_3^V, \tilde{d}_4^V, \tilde{d}_5^V, \tilde{d}_6^V, \tilde{d}_7^V, \tilde{d}_8^V \right)^t, \quad (2.138)$$

where

$$\tilde{d}_1^V = \frac{S}{(S+2G_{fr})} \left[\tilde{h}_{11}^b + \tilde{h}_{22}^b \right] + \tilde{h}_{33}^b, \quad (2.139)$$

$$\tilde{d}_2^V = \frac{j}{s\hat{\rho}^E} k_\alpha \tilde{f}_\alpha^f + \frac{C}{M} \left[\tilde{h}_{11}^b + \tilde{h}_{22}^b \right] \left[1 - \frac{S}{(S+2G_{fr})} \right] + \tilde{q}^i, \quad (2.140)$$

$$\begin{aligned} \tilde{d}_3^V &= \frac{1}{\kappa} \frac{\rho^f}{\hat{\rho}^E} k_\alpha \tilde{f}_\alpha^f - \frac{1}{\kappa} k_\alpha \tilde{f}_\alpha^b - \frac{2j}{s} \frac{k_1 k_2}{\kappa} \left[G^{fr} \tilde{h}_{21}^b + G^{fr} \tilde{h}_{12}^b \right] \\ &\quad - \frac{j\kappa}{s} \frac{2G^{fr} S}{(S+2G_{fr})} \left[\tilde{h}_{11}^b + \tilde{h}_{22}^b \right] - \frac{2jG^{fr}}{s\kappa} \left[k_1^2 \tilde{h}_{11}^b + k_2^2 \tilde{h}_{22}^b \right], \end{aligned} \quad (2.141)$$

$$\tilde{d}_4^V = -\frac{1}{\kappa} \left[\hat{\mathcal{L}} k_\alpha \tilde{f}_\alpha^f + k_\alpha \tilde{J}_\alpha^e \right] \quad (2.142)$$

$$\tilde{d}_5^V = -\tilde{f}_3^b, \quad (2.143)$$

$$\tilde{d}_6^V = \frac{\hat{\rho}^E}{\hat{\epsilon}} \hat{\mathcal{L}} \tilde{J}_3^e - \tilde{f}_3^f, \quad (2.144)$$

$$\tilde{d}_7^V = \frac{k_\alpha}{\kappa} \left[\tilde{h}_{\alpha 3}^b + \tilde{h}_{3\alpha}^b \right], \quad (2.145)$$

$$\tilde{d}_8^V = \frac{j\kappa}{s\hat{\epsilon}} \tilde{J}_3^e + \frac{1}{\kappa} \left[k_2 \tilde{J}_1^m - k_1 \tilde{J}_2^m \right]. \quad (2.146)$$

2.3 Deriving the eigenvectorsⁱ

Now that we have specified our field vectors $\tilde{\mathbf{q}}^{H,V}$, system matrices $\tilde{\mathbf{A}}^{H,V}$, and source vectors $\tilde{\mathbf{d}}^{H,V}$ for the SH-TE and P-SV-TM propagation modes, we can move onwards to derive and present the eigenvector sets belonging to this specific arrangement of the field vectors. In this section, we derive the eigenvector sets that form the basis for our numerical modeling examples. Before diving into greater detail, let us first evaluate what this eigenvector problem looks like in general. The system matrices above are organized such that they obey the following symmetry relation $\left\{ \tilde{\mathbf{A}}^{H,V} \right\}^t \mathbf{N}^{H,V} = -\mathbf{N}^{H,V} \tilde{\mathbf{A}}^{H,V}$, with

$$\tilde{\mathbf{N}}^{H,V} = \begin{pmatrix} \mathbf{O} & \mathbf{I} \\ -\mathbf{I} & \mathbf{O} \end{pmatrix}, \quad (2.147)$$

where the submatrices are either size 2-by-2 or 4-by-4 for the SH-TE and P-SV-TM mode, respectively. Here, \mathbf{I} is a diagonal identity submatrix, and \mathbf{O} is a null matrix. The system matrix $\tilde{\mathbf{A}}^{H,V}$ can be decomposed into matrices consisting of its eigenvectors and eigenvalues via

$$\tilde{\mathbf{A}}^{H,V} = \tilde{\mathbf{L}}^{H,V} \tilde{\mathbf{\Lambda}}_1^{H,V} \left\{ \tilde{\mathbf{L}}^{H,V} \right\}^{-1}. \quad (2.148)$$

Here, $\tilde{\mathbf{L}}^{H,V}$ and $\left\{ \tilde{\mathbf{L}}^{H,V} \right\}^{-1}$ represent the composition and decomposition matrices, respectively, that consist of the eigenvectors of the SH-TE or P-SV-TM system matrices. The eigenvectors form the basis for wavefield decomposition into one-way wavefields (see [Grobbe *et al.* \(2016b\)](#) for a discussion on seismo-electromagnetic field decomposition).

Furthermore, $\tilde{\mathbf{\Lambda}}_1$ is a diagonal matrix consisting of the eigenvalues of the system, that can be written as

$$\tilde{\mathbf{\Lambda}}_1^{H,V} = \begin{pmatrix} -\tilde{\mathbf{\Lambda}}^{H,V} & \mathbf{O} \\ \mathbf{O} & \tilde{\mathbf{\Lambda}}^{H,V} \end{pmatrix}, \quad (2.149)$$

where

$$\tilde{\mathbf{\Lambda}}^H = \begin{pmatrix} \Gamma_{SH} & 0 \\ 0 & \Gamma_{TE} \end{pmatrix}, \quad (2.150)$$

and

$$\tilde{\mathbf{\Lambda}}^V = \begin{pmatrix} \Gamma_{Pf} & 0 & 0 & 0 \\ 0 & \Gamma_{Ps} & 0 & 0 \\ 0 & 0 & \Gamma_{SV} & 0 \\ 0 & 0 & 0 & \Gamma_{TM} \end{pmatrix}. \quad (2.151)$$

ⁱThis section is part of the journal paper published in *Geophysical Journal International* doi: 10.1093/gji/ggw128 ([Grobbe *et al.*, 2016a](#)). Note that minor changes have been introduced to make the text consistent with the other chapters of this thesis.

The relations between the vertical wavenumbers Γ_w and the spherical wavenumbers γ_w for a certain type of field w are

$$\Gamma_w^2 = \gamma_w^2 + \kappa^2, \quad (2.152)$$

$$\gamma_w^2 = \Gamma_w^2 - \kappa^2, \quad (2.153)$$

with

$$\gamma_w = \frac{s}{\hat{c}_w} \quad (2.154)$$

and where w can be the horizontally polarized shear wave SH , the transverse electric mode TE , the fast compressional wave P_f , the Biot slow compressional wave P_s , the vertically polarized shear wave SV or the transverse magnetic mode TM . In equation (2.154), \hat{c}_w represents the complex wave or field velocity for the specific field type w . To determine the eigenvalues of the system, we need to choose the proper sign of the square root. We choose the positive sign of the square root, based on the fact that for the eigenvalue matrix, we desire that $\Re\{\Gamma_w\} > 0$, based on physical wave propagation constraints (see e.g. Grobbe *et al.* (2016b)).

Pride & Haartsen (1996) have determined the complex velocities for each field type, which we can rewrite for our field quantities and our definition of the Fourier transform as

$$\hat{c}_{SH} = \sqrt{\frac{2}{\frac{\hat{\rho}^c}{Gf\tau} + \frac{\zeta\eta^E}{s^2} + \sqrt{\left[\frac{\hat{\rho}^c}{Gf\tau} - \frac{\zeta\eta^E}{s^2}\right]^2 - \frac{4\zeta\chi^2}{s^3Gf\tau}}}}, \quad (2.155)$$

$$\hat{c}_{TE} = \sqrt{\frac{2}{\frac{\hat{\rho}^c}{Gf\tau} + \frac{\zeta\eta^E}{s^2} - \sqrt{\left[\frac{\hat{\rho}^c}{Gf\tau} - \frac{\zeta\eta^E}{s^2}\right]^2 - \frac{4\zeta\chi^2}{s^3Gf\tau}}}}, \quad (2.156)$$

$$\hat{c}_{P_f} = \sqrt{\frac{2(HM - C^2)}{\hat{\nu} - \sqrt{\hat{\nu}^2 - 4(HM - C^2) \left[\rho^b \frac{\hat{\rho}^E \eta^E}{s\hat{\epsilon}} - (\rho^f)^2\right]}}}}, \quad (2.157)$$

$$\hat{c}_{P_s} = \sqrt{\frac{2(HM - C^2)}{\hat{\nu} + \sqrt{\hat{\nu}^2 - 4(HM - C^2) \left[\rho^b \frac{\hat{\rho}^E \hat{\eta}^E}{\hat{\xi}} - (\rho^f)^2\right]}}}}, \quad (2.158)$$

$$\hat{c}_{SV} = \hat{c}_{SH}, \quad (2.159)$$

$$\hat{c}_{TM} = \hat{c}_{TE}, \quad (2.160)$$

where $\hat{\nu} = \rho^b M + \frac{\hat{\rho}^E \hat{\eta}^E H}{\hat{\xi}} - 2\rho^f C$. Due to the isotropic and lateral invariance of the medium, the horizontally and vertically polarized shear wave velocities are equal to each other. The same holds for the transverse electric and transverse magnetic (diffusive) velocities. Note that the expressions for the velocities contain divisions by s . Numerically, we stabilized the expressions adding a small imaginary number to the angular frequencies, thereby modeling using complex frequencies and in the

Table 2.1: Table showing the required conversions when starting from [Pride & Haartsen \(1996\)](#); [Haartsen & Pride \(1997\)](#).

Haartsen and Pride system	Our system
ωp	κ
$-j\omega$	s
s_s	$\frac{\gamma_s}{s}$
$j\omega\tilde{q}_w$	$-\Gamma_w$
\tilde{q}_w	$\frac{\Gamma_w}{s}$
\mp	\pm
‘EV related to field quantity \tilde{u} ’	‘ $s \cdot$ EV related to field quantity \tilde{u} ’

final step compensating for this small imaginary part in the inverse temporal Fourier transform. Alternatively, one could model the spherical wavenumbers where this problem does not occur.

Now, we present two different eigenvector sets. The first set we derive starting from the published eigenvector sets by [Haartsen & Pride \(1997\)](#), where we adjust those sets to our field quantities and their arrangement in the field vectors and where we apply power-flux normalization. The second set we derive starting directly from the system matrices $\tilde{\mathbf{A}}^{H,V}$, thereby paying special attention to the situation of the coupling coefficient being equal to zero. We again apply power-flux normalization in the final stage.

2.3.1 Power flux-normalizing the Haartsen and Pride-based eigenvectors

Starting from the eigenvectors as published by [Haartsen & Pride \(1997\)](#), we apply the conversions as displayed in Table 1 to comply with our field quantities and Fourier definitions and to express the eigenvectors in terms of wavenumbers.

Here, p denotes the horizontal slowness and \tilde{q}_w the vertical slowness. Since we are dealing with particle velocity fields whereas [Haartsen & Pride \(1997\)](#) use particle displacement, we need to multiply each of the eigenvectors that are directly related to the displacement \tilde{u} with the Laplace parameter s . In addition, for [Haartsen & Pride \(1997\)](#), the $-$ sign indicates downgoing fields and the $+$ sign denotes upgoing fields (which is an opposite definition compared to our notation). Furthermore, there is a typo in [Haartsen & Pride \(1997\)](#): for the first element of the SV/TM eigenvector set the \mp -sign should be a \pm -sign.

SH-TE Propagation Mode We arrange the eigenvector elements according to our preferred field vector organization of equation (6.48). Our composition matrix $\tilde{\mathbf{L}}^H$, where each column corresponds to the eigenvectors of system matrix $\tilde{\mathbf{A}}^H$ for a certain field type, is organized as

$$\tilde{\mathbf{L}}^H = \begin{pmatrix} \tilde{\mathbf{L}}_1^H & \tilde{\mathbf{L}}_1^H \\ \tilde{\mathbf{L}}_2^H & -\tilde{\mathbf{L}}_2^H \end{pmatrix}. \quad (2.161)$$

Let us now use $\tilde{\mathbf{K}}^H$, $\tilde{\mathbf{K}}_1^H$ and $\tilde{\mathbf{K}}_2^H$ (instead of $\tilde{\mathbf{L}}^H$, $\tilde{\mathbf{L}}_1^H$ and $\tilde{\mathbf{L}}_2^H$) to indicate our starting eigenvector matrix and submatrices, i.e. the eigenvector matrices before applying the power-flux normalization procedure. The starting eigenvector submatrices read

$$\tilde{\mathbf{K}}_1^H = \begin{pmatrix} s & s \\ -\frac{s\mu_0\hat{\rho}^E\hat{\mathcal{L}}G^{fr}\phi_{SH}}{\rho^f} & -\frac{s\mu_0\hat{\rho}^E\hat{\mathcal{L}}G^{fr}\phi_{TE}}{\rho^f} \end{pmatrix}, \quad (2.162)$$

and

$$\tilde{\mathbf{K}}_2^H = \begin{pmatrix} -\Gamma_{SH}G^{fr} & -\Gamma_{TE}G^{fr} \\ -\frac{\Gamma_{SH}\hat{\rho}^E\hat{\mathcal{L}}G^{fr}\phi_{SH}}{\rho^f} & -\frac{\Gamma_{TE}\hat{\rho}^E\hat{\mathcal{L}}G^{fr}\phi_{TE}}{\rho^f} \end{pmatrix}, \quad (2.163)$$

where $\phi_{SH,TE}$ is a certain scaling factor that depends on the field type, defined as

$$\phi_{SH,TE} = -\frac{\gamma_{SH,TE}^2 - \frac{s^2\rho^b}{G^{fr}}}{\gamma_{SH,TE}^2 - \hat{\zeta}\zeta}. \quad (2.164)$$

Now that we have obtained the SH-TE eigenvector set according to our preferences and based on velocity field normalization, we demonstrate how we can power-flux normalize these eigenvectors in an effective way. We can find the power-flux normalized eigenvector matrix by requiring that

$$\left\{ \tilde{\mathbf{L}}^H \right\}^{-1}(\kappa, x_3, \omega) = -\left\{ \tilde{\mathbf{N}}^H \right\}^{-1} \left\{ \tilde{\mathbf{L}}^H \right\}^t(\kappa, x_3, \omega) \tilde{\mathbf{N}}^H. \quad (2.165)$$

The details on how to derive the power-flux normalized eigenvector matrix that satisfies this condition are given in Appendix 2.3.A. Through this procedure, we end-up with the following power-flux normalized composition matrix:

$$\tilde{\mathbf{L}}^H = \begin{pmatrix} sd_1 & sd_2 \\ -\frac{s\mu_0\hat{\rho}^E\hat{\mathcal{L}}G^{fr}\phi_{SH}}{\rho^f}d_1 & -\frac{s\mu_0\hat{\rho}^E\hat{\mathcal{L}}G^{fr}\phi_{TE}}{\rho^f}d_2 \\ -\Gamma_{SH}G^{fr}d_1 & -\Gamma_{TE}G^{fr}d_2 \\ -\frac{\Gamma_{SH}\hat{\rho}^E\hat{\mathcal{L}}G^{fr}\phi_{SH}}{\rho^f}d_1 & -\frac{\Gamma_{TE}\hat{\rho}^E\hat{\mathcal{L}}G^{fr}\phi_{TE}}{\rho^f}d_2 \\ sd_1 & sd_2 \\ -\frac{s\mu_0\hat{\rho}^E\hat{\mathcal{L}}G^{fr}\phi_{SH}}{\rho^f}d_1 & -\frac{s\mu_0\hat{\rho}^E\hat{\mathcal{L}}G^{fr}\phi_{TE}}{\rho^f}d_2 \\ \Gamma_{SH}G^{fr}d_1 & \Gamma_{TE}G^{fr}d_2 \\ \frac{\Gamma_{SH}\hat{\rho}^E\hat{\mathcal{L}}G^{fr}\phi_{SH}}{\rho^f}d_1 & \frac{\Gamma_{TE}\hat{\rho}^E\hat{\mathcal{L}}G^{fr}\phi_{TE}}{\rho^f}d_2 \end{pmatrix}. \quad (2.166)$$

Looking at equation (2.228), it can be observed that the decomposition matrix $\left\{ \tilde{\mathbf{L}}^H \right\}^{-1}$ can be written as

$$\left\{ \tilde{\mathbf{L}}^H \right\}^{-1} = \frac{1}{2} \begin{pmatrix} \left\{ \tilde{\mathbf{L}}_1^H \right\}^{-1} & \left\{ \tilde{\mathbf{L}}_2^H \right\}^{-1} \\ \left\{ \tilde{\mathbf{L}}_1^H \right\}^{-1} & -\left\{ \tilde{\mathbf{L}}_2^H \right\}^{-1} \end{pmatrix}. \quad (2.167)$$

However, using equation (2.165), we can determine the power-flux normalized decomposition matrix $\{\tilde{\mathbf{L}}^H\}^{-1}$. In a general notation, this power-flux normalized decomposition matrix is organized as follows

$$\{\tilde{\mathbf{L}}^H\}^{-1} = \begin{pmatrix} \left\{ \tilde{\mathbf{L}}_2^H \right\}^t & \left\{ \tilde{\mathbf{L}}_1^H \right\}^t \\ \left\{ \tilde{\mathbf{L}}_2^H \right\}^t & -\left\{ \tilde{\mathbf{L}}_1^H \right\}^t \end{pmatrix}. \quad (2.168)$$

Comparing the expressions (2.167) and (2.168) we can observe that for power-flux normalized eigenvector systems, we can use the transpose of a submatrix as the inverse of the other submatrix, via

$$\left\{ \tilde{\mathbf{L}}_1^H(\kappa, x_3, \omega) \right\}^{-1} = 2 \left\{ \tilde{\mathbf{L}}_2^H(\kappa, x_3, \omega) \right\}^t \quad (2.169)$$

$$\left\{ \tilde{\mathbf{L}}_2^H(\kappa, x_3, \omega) \right\}^{-1} = 2 \left\{ \tilde{\mathbf{L}}_1^H(\kappa, x_3, \omega) \right\}^t. \quad (2.170)$$

P-SV-TM Propagation Mode Starting from the published eigenvector set of [Haartsen & Pride \(1997\)](#), corresponding to our arrangement of the field vector and applying the same conversions as discussed for the SH-TE mode (Table 1), we find the P-SV-TM eigenvectors that meet our conditions. In order to let our composition matrix $\tilde{\mathbf{K}}^V$ obey the following structure,

$$\tilde{\mathbf{K}}^V = \begin{pmatrix} \tilde{\mathbf{K}}_1^V & \tilde{\mathbf{K}}_1^V \\ \tilde{\mathbf{K}}_2^V & -\tilde{\mathbf{K}}_2^V \end{pmatrix}, \quad (2.171)$$

we introduce an additional minus sign for the outgoing fast and slow compressional wave related eigenvectors, as described in [Haartsen & Pride \(1997\)](#). This does not change the field vector $\tilde{\mathbf{q}}^V$, but will introduce a minus sign difference when looking at the one-way wavefields corresponding to these two wavytypes. Our starting P-SV-TM submatrices, before the flux-normalization procedure, now read

$$\tilde{\mathbf{K}}_1^V = \begin{pmatrix} \frac{s\Gamma_{Pf}}{\gamma_{Pf}} & \frac{s\Gamma_{Ps}}{\gamma_{Ps}} \\ \frac{s\Gamma_{Pf}\phi_{Pf}}{\gamma_{Pf}} & \frac{s\Gamma_{Ps}\phi_{Ps}}{\gamma_{Ps}} \\ -\frac{2G^{fr}j\kappa\Gamma_{Pf}}{\gamma_{Pf}} & -\frac{2G^{fr}j\kappa\Gamma_{Ps}}{\gamma_{Ps}} \\ 0 & 0 \\ \frac{-sj\kappa}{\gamma_{SV}} & \frac{-sj\kappa}{\gamma_{TM}} \\ -\frac{G^{fr}}{\rho^f} \left(\frac{\gamma_{SV}^2}{s^2} - \frac{\rho^b}{G^{fr}} \right) \frac{sj\kappa}{\gamma_{SV}} & -\frac{G^{fr}}{\rho^f} \left(\frac{\gamma_{TM}^2}{s^2} - \frac{\rho^b}{G^{fr}} \right) \frac{sj\kappa}{\gamma_{TM}} \\ -\frac{G^{fr}(\Gamma_{SV}^2 + \kappa^2)}{G^{fr}(\Gamma_{SV}^2 + \kappa^2)} & -\frac{G^{fr}(\Gamma_{TM}^2 + \kappa^2)}{G^{fr}(\Gamma_{TM}^2 + \kappa^2)} \\ -\gamma_{SV} \frac{\hat{\rho}^E}{\rho^f} \hat{\mathcal{L}} G^{fr} \phi_{SV} & -\gamma_{TM} \frac{\hat{\rho}^E}{\rho^f} \hat{\mathcal{L}} G^{fr} \phi_{TM} \end{pmatrix}, \quad (2.172)$$

and

$$\tilde{\mathbf{K}}_2^V = \begin{pmatrix} -\gamma_{Pf} \left(H + \frac{2G^{fr}\kappa^2}{\gamma_{Pf}^2} + \phi_{Pf}C \right) & -\gamma_{Ps} \left(H + \frac{2G^{fr}\kappa^2}{\gamma_{Ps}^2} + \phi_{Ps}C \right) \\ -\gamma_{Pf} (C + \phi_{Pf}M) & -\gamma_{Ps} (C + \phi_{Ps}M) \\ \frac{s j \kappa}{\gamma_{Pf}} & \frac{s j \kappa}{\gamma_{Ps}} \\ -\frac{\hat{\rho}^E \hat{\mathcal{L}} \phi_{Pf} s j \kappa}{\gamma_{Pf} \hat{\epsilon}} & -\frac{\hat{\rho}^E \hat{\mathcal{L}} \phi_{Ps} s j \kappa}{\gamma_{Ps} \hat{\epsilon}} \\ \frac{2G^{fr} j \kappa \Gamma_{SV}}{\gamma_{SV}} & \frac{2G^{fr} j \kappa \Gamma_{TM}}{\gamma_{TM}} \\ \mathbf{0} & \mathbf{0} \\ \frac{s \Gamma_{SV}}{\gamma_{SV}} & \frac{s \Gamma_{TM}}{\gamma_{TM}} \\ \frac{\Gamma_{SV} \mu_0 \frac{\hat{\rho}^E}{\rho^f} \hat{\mathcal{L}} G^{fr} \phi_{SV} s}{\gamma_{SV}} & \frac{\Gamma_{TM} \mu_0 \frac{\hat{\rho}^E}{\rho^f} \hat{\mathcal{L}} G^{fr} \phi_{TM} s}{\gamma_{TM}} \end{pmatrix}, \quad (2.173)$$

where ϕ_w is again a certain scaling factor, depending on the wavetypes w , defined as

$$\phi_{Pf,Ps} = -\frac{s^2 \rho^b - H \gamma_{Pf,Ps}^2}{s^2 \rho^f - C \gamma_{Pf,Ps}^2}, \quad (2.174)$$

and where $\phi_{SV,TM}$ is equal to the scaling factor discussed for the SH-TE mode, equation (2.164).

To find the P-SV-TM power-flux normalization factors, we can again follow the same procedure as discussed for the SH-TE system. Following this procedure provides us in the end with the desired power-flux normalization factors. We omit the precise details of this derivation since it is similar to the procedure discussed extensively for the SH-TE propagation mode. The power-flux normalization factors read

$$d_1^V = d_5^V = \frac{1}{\sqrt{2s\Gamma_{Pf} \left(-H - 2\phi_{Pf}C - \phi_{Pf}^2 M \right)}}, \quad (2.175)$$

$$d_2^V = d_6^V = \frac{1}{\sqrt{2s\Gamma_{Ps} \left(-H - 2\phi_{Ps}C - \phi_{Ps}^2 M \right)}}, \quad (2.176)$$

$$d_3^V = d_7^V = \frac{1}{\sqrt{2s\Gamma_{SV} \left(-G^{fr} + \mu_0 \left[\frac{\hat{\rho}^E \hat{\mathcal{L}} G^{fr} \phi_{SV}}{\rho^f} \right]^2 \right)}}, \quad (2.177)$$

$$d_4^V = d_8^V = \frac{1}{\sqrt{2s\Gamma_{TM} \left(-G^{fr} + \mu_0 \left[\frac{\hat{\rho}^E \hat{\mathcal{L}} G^{fr} \phi_{TM}}{\rho^f} \right]^2 \right)}}, \quad (2.178)$$

where we recognize identical factors for SH versus SV, and TE versus TM, equations (2.247) versus (2.177), and (2.248) versus (2.178), respectively. Again, we choose the positive sign of the square root.

These normalization factors are again elements of the diagonal matrix $\tilde{\mathbf{D}}^V$, and using $\tilde{\mathbf{L}}^V = \tilde{\mathbf{K}}^V \tilde{\mathbf{D}}^V$ we obtain the desired power-flux normalized eigenvector matrices for the P-SV-TM mode.

We can observe that when the seismo-electromagnetic coupling coefficient $\hat{\mathcal{L}}$ is equal to zero, the fourth row of composition submatrix, equation (2.172), and the fourth row of composition submatrix, equation (2.173), are zero for all elements. These rows are involved when composing the two-way electromagnetic P-SV-TM mode field quantities (\tilde{H}_{norm}^V and \tilde{E}_{norm}^V , respectively) from one-way wavefields, via $\tilde{\mathbf{q}}^V = \tilde{\mathbf{L}}^V \tilde{\mathbf{p}}^V$, where $\tilde{\mathbf{p}}^V$ contains the downgoing and upgoing wavefields (see also for example [Grobbe et al. \(2016b\)](#)). When there is no coupling between mechanical and electromagnetic fields, we expect columns one, two and three of the composition submatrices to be equal to zero, whereas the fourth column (corresponding to the TM field type) should be non-zero, generating the electromagnetic fields. We can see that for the [Haartsen & Pride \(1997\)](#)-based eigenvector set, also this fourth column is equal to zero. Furthermore, we can observe that the fourth, electromagnetically-associated column is non-zero for most of the other rows (which correspond to mechanical field quantities) when there is no seismo-electromagnetic coupling. This is physically not what we expect; we expect zero values for these elements since there is no coupling between mechanical and electromagnetic fields. We investigate numerically the zero-valued coupling coefficient scenario more closely later on.

2.3.2 Deriving alternative power-flux normalized eigenvector sets

Now that we have our power-flux normalized eigenvectors sets for both the SH-TE and P-SV-TM modes, starting from the published eigenvector sets by [Haartsen & Pride \(1997\)](#), we now show how we can derive the eigenvectors directly from the system matrices $\tilde{\mathbf{A}}^H$ and $\tilde{\mathbf{A}}^V$, equations (2.115) and (2.132), respectively. Thereby, we construct our eigenvector matrices in such a way that the eigenvector matrices get the correct shape when the coupling coefficient $\hat{\mathcal{L}} = 0$. For the eigenvector matrices, this means that the rows corresponding to for example an electromagnetic field quantity in $\tilde{\mathbf{q}}^V$, should automatically obtain zero elements in their columns corresponding to the mechanical wave types when $\hat{\mathcal{L}}$ is equal to zero.

Let us start by looking at equations (2.115), (2.132), (2.148), and (2.149). We can observe that the following relations hold between the system submatrices, the composition and decomposition submatrices and the eigenvalues submatrices

$$\tilde{\mathbf{A}}_{12}^{H,V} = -\tilde{\mathbf{L}}_1^{H,V} \tilde{\mathbf{\Lambda}}^{H,V} \left\{ \tilde{\mathbf{L}}_2^{H,V} \right\}^{-1}, \quad (2.179)$$

$$\tilde{\mathbf{A}}_{21}^{H,V} = -\tilde{\mathbf{L}}_2^{H,V} \tilde{\mathbf{\Lambda}}^{H,V} \left\{ \tilde{\mathbf{L}}_1^{H,V} \right\}^{-1}, \quad (2.180)$$

with the eigenvalue submatrices for the SH-TE and P-SV-TM modes described by equations (2.150) and (2.151), respectively. Let us now focus on the specific choices

made in deriving the SH-TE and P-SV-TM eigenvector sets. Please note that we follow slightly different procedures while deriving the eigenvectors for both propagation modes. We could for example apply the same steps for the SH-TE mode as we describe for the P-SV-TM mode. However, from experience we have noticed that the end-result of this procedure yields numerically less stable results for the SH-TE mode than the alternative way of deriving described here. Vice versa, we cannot apply the SH-TE procedure when deriving the P-SV-TM mode since the size of the system is way bigger and in addition the system is more complicated, making the derivations tedious. On the contrary, the P-SV-TM procedure described here is more straightforward and less tedious, plus it yields numerically stable results for this propagation mode.

SH-TE Propagation Mode Let us start by focusing on the SH-TE system. We start by rewriting equation (2.179) to find an expression for $\tilde{\mathbf{L}}_2^H$ as

$$\tilde{\mathbf{L}}_2^H = - \left\{ \tilde{\mathbf{A}}_{12}^H \right\}^{-1} \tilde{\mathbf{L}}_1^H \tilde{\mathbf{A}}^H. \quad (2.181)$$

We can easily find the inverse of $\tilde{\mathbf{A}}_{12}^H$ since this is a diagonal matrix. We choose $\tilde{\mathbf{L}}_1^H$ in such a way that we obtain the desired structure for $\hat{\mathcal{L}} = 0$ as well as fulfill the physics of the seismo-electromagnetic system. Writing equation (2.181) in explicit matrix notation yields

$$\begin{aligned} \tilde{\mathbf{L}}_2^H &= \begin{pmatrix} -\frac{1}{\beta} & 0 \\ 0 & -\frac{1}{\zeta} \end{pmatrix} \begin{pmatrix} d_1^H & d_2^H \chi \\ d_1^H A \chi & d_2^H B \end{pmatrix} \begin{pmatrix} \Gamma_{SH} & 0 \\ 0 & \Gamma_{TE} \end{pmatrix} = \\ &= \begin{pmatrix} \frac{d_1^H \Gamma_{SH}}{\beta} & \frac{d_2^H \chi \Gamma_{TE}}{\beta} \\ \frac{d_1^H A \chi \Gamma_{SH}}{\zeta} & \frac{d_2^H B \Gamma_{TE}}{\zeta} \end{pmatrix}. \end{aligned} \quad (2.182)$$

Now using equation (2.180), we can obtain four equations for solving for two unknowns (A and B).

$$\left(\alpha + \frac{\kappa^2}{\beta} \right) d_1^H + d_1^H A \chi^2 = \frac{d_1^H \Gamma_{SH}^2}{\beta}, \quad (2.183)$$

$$\left(\alpha + \frac{\kappa^2}{\beta} \right) d_2^H \chi + d_2^H B \chi = \frac{d_2^H \chi \Gamma_{TE}^2}{\beta}, \quad (2.184)$$

$$d_1^H \chi - \left(\eta^E + \frac{\kappa^2}{\zeta} \right) d_1^H A \chi = -\frac{d_1^H A \chi \Gamma_{SH}^2}{\zeta}, \quad (2.185)$$

$$d_2^H \chi^2 - \left(\eta^E + \frac{\kappa^2}{\zeta} \right) d_2^H B = -\frac{d_2^H B \Gamma_{TE}^2}{\zeta}. \quad (2.186)$$

Dividing out the terms that occur both at the left- and right-hand sides (amongst which are the scaling factors d_1^H and d_2^H), isolating the unknowns A and B and using the relations between spherical and radial wavenumbers (equations (2.152))

and (2.153)) yields two possible expressions for each of the two unknowns:

$$A = \frac{\gamma_{SH}^2 - \alpha\beta}{\chi^2\beta}, \quad (2.187)$$

$$B = \frac{\gamma_{TE}^2 - \alpha\beta}{\beta}, \quad (2.188)$$

$$A = -\frac{\zeta}{\gamma_{SH}^2 - \eta^E\zeta}, \quad (2.189)$$

$$B = -\frac{\chi^2\zeta}{\gamma_{TE}^2 - \eta^E\zeta}. \quad (2.190)$$

Remember, we want expressions that are stable when no seismo-electromagnetic coupling occurs (i.e. no divisions by $\hat{\mathcal{L}}$ only). Therefore, we use equation (2.189) as the expression for A. For B, the selection is ambiguous. We choose equation (2.188) as the expression for B. By equating equation (2.187) to (2.189) and (2.188) to (2.190), the following interesting relations can be found

$$(\gamma_{SH}^2 - \alpha\beta)(\gamma_{SH}^2 - \eta^E\zeta) = -\chi^2\beta\zeta, \quad (2.191)$$

$$(\gamma_{TE}^2 - \alpha\beta)(\gamma_{TE}^2 - \eta^E\zeta) = -\chi^2\beta\zeta. \quad (2.192)$$

Now that we have solved for the two unknown parameters A and B of the eigenvector matrix, we can normalize the eigenvectors with respect to different quantities. Note that in the whole derivation so far the normalization factors d_1^H and d_2^H dropped out of the equations, meaning that the expressions for the two unknown parameters are normalization independent. Due to the way we have organized our system matrix $\tilde{\mathbf{A}}^H$ (symmetry), and due to the specific structure of the composition matrix $\tilde{\mathbf{L}}^H$ in terms of its submatrices $\tilde{\mathbf{L}}_1^H$ and $\tilde{\mathbf{L}}_2^H$, we can find our power-flux normalization factors, by requiring that

$$\tilde{\mathbf{L}}_1^H \left\{ \tilde{\mathbf{L}}_2^H \right\}^t = \frac{1}{2} \tilde{\mathbf{I}}^H, \quad (2.193)$$

where we make use of the relations between the transverse and the inverse of certain composition submatrices (equations (2.169) and (2.170)).

By requiring equation (2.193) to hold we can solve for the flux-normalization scaling factors $d_{1,2}^H$. We combine the expressions for the diagonal elements of $\frac{1}{2}\tilde{\mathbf{I}}^H$ with the expressions for the off-diagonals, yielding expressions containing solely d_1^H or d_2^H . Furthermore, we recognize and apply the relations (2.191) and (2.192). Depending on which one of these relations we apply, different end-results for d_1^H and d_2^H are obtained. We choose to use the following end-results as power-flux normalization factors

$$d_1^H = \sqrt{-\frac{\beta(\gamma_{SH}^2 - \eta^E\zeta)}{2[\Gamma_{SH}(\gamma_{SH}^2 - \gamma_{TE}^2)]}}, \quad (2.194)$$

$$d_2^H = \sqrt{-\frac{\beta^2\zeta}{2[\Gamma_{TE}(\gamma_{SH}^2 - \gamma_{TE}^2)(\gamma_{TE}^2 - \alpha\beta)]}}. \quad (2.195)$$

Substituting equations (2.194) and (2.195) in the expressions for $\tilde{\mathbf{L}}_1^H$ and $\tilde{\mathbf{L}}_2^H$ (see equation (2.182)), yields

$$\tilde{\mathbf{L}}_1^H = \begin{pmatrix} \sqrt{-\frac{\beta(\gamma_{SH}^2 - \eta^E \zeta)}{2\Gamma_{SH}(\gamma_{SH}^2 - \gamma_{TE}^2)}} & \sqrt{-\frac{\beta^2 \zeta \chi^2}{2\Gamma_{TE}(\gamma_{SH}^2 - \gamma_{TE}^2)(\gamma_{TE}^2 - \alpha\beta)}} \\ \sqrt{-\frac{\beta \zeta^2 \chi^2}{2\Gamma_{SH}(\gamma_{SH}^2 - \eta^E \zeta)(\gamma_{SH}^2 - \gamma_{TE}^2)}} & \sqrt{-\frac{\zeta(\gamma_{TE}^2 - \alpha\beta)}{2\Gamma_{TE}(\gamma_{SH}^2 - \gamma_{TE}^2)}} \end{pmatrix}, \quad (2.196)$$

and

$$\tilde{\mathbf{L}}_2^H = - \begin{pmatrix} \sqrt{-\frac{\Gamma_{SH}(\gamma_{SH}^2 - \eta^E \zeta)}{2\beta(\gamma_{SH}^2 - \gamma_{TE}^2)}} & \sqrt{-\frac{\zeta \chi^2 \Gamma_{TE}}{2(\gamma_{SH}^2 - \gamma_{TE}^2)(\gamma_{TE}^2 - \alpha\beta)}} \\ \sqrt{-\frac{\beta \chi^2 \Gamma_{SH}}{2(\gamma_{SH}^2 - \gamma_{TE}^2)(\gamma_{SH}^2 - \eta^E \zeta)}} & \sqrt{-\frac{\Gamma_{TE}(\gamma_{TE}^2 - \alpha\beta)}{2\zeta(\gamma_{SH}^2 - \gamma_{TE}^2)}} \end{pmatrix}. \quad (2.197)$$

We refer to this eigenvector set as the GST SH-TE set.

P-SV-TM Propagation Mode For the P-SV-TM system, we take a slightly different approach, since we cannot easily invert $\tilde{\mathbf{A}}_{12}^V$. We could of course have used the inverse of $\tilde{\mathbf{A}}_{21}^V$, however, experience has taught us this does not result in the desired stable final eigenvector expressions. The approach expressed here shows great similarities with the approach presented for the SH-TE mode (and could have also been used for the SH-TE mode). We start by rewriting equation (2.180) to find an expression for $\tilde{\mathbf{L}}_2^V$ as

$$\tilde{\mathbf{L}}_2^V = -\tilde{\mathbf{A}}_{21}^V \tilde{\mathbf{L}}_1^V \left\{ \tilde{\mathbf{A}}^V \right\}^{-1}. \quad (2.198)$$

Let us now choose $\tilde{\mathbf{L}}_1^V$ in such a way that we obtain the desired structure for $\hat{\mathcal{L}} = 0$ as well as fulfill the physics of the seismo-electromagnetic system. We therefore choose $\tilde{\mathbf{L}}_1^V$ as follows

$$\tilde{\mathbf{L}}_1^V = \begin{pmatrix} d_1^V & d_2^V A & d_3^V B & d_4^V D\chi \\ d_1^V E & d_2^V & d_3^V F & d_4^V G\chi \\ d_1^V N & d_2^V O & d_3^V & d_4^V P\chi \\ 0 & 0 & d_3^V T\chi & d_4^V \end{pmatrix}. \quad (2.199)$$

As can be observed, we have added the factor χ , containing $\hat{\mathcal{L}}$, to the elements of $\tilde{\mathbf{L}}_1^V$ such that the correct elements of $\tilde{\mathbf{L}}_1^V$ are equal to zero if $\hat{\mathcal{L}}$ equals zero (i.e. that no coupling between the mechanical and electromagnetic parts occurs). What can also be recognized, is that two elements (elements (4,1) and (4,2)) are explicitly defined as zero. They correspond to the P-SV-TM mode magnetic field due to the fast and slow compressional waves. As has been shown in various laboratory experiments [Bordes *et al.* \(2008\)](#), the magnetic field is purely associated with shear waves or of course electromagnetic fields. Furthermore, as we see later on when determining the $\tilde{\mathbf{L}}_2^V$ submatrix, these zero elements will move to positions (2,3) and (2,4) in $\tilde{\mathbf{L}}_2^V$,

which correspond to the fluid pressure due to SV waves and TM fields. Since the fluid pressure is only associated with the fast and slow pressure waves, these SV and TM elements must be zero, which proves that by choosing the discussed elements equal to zero, the physics of the seismo-electromagnetic phenomenon are correctly preserved. Here, $d_{1;4}^V$ denotes a still to be determined (or chosen) scaling factor that for example power flux-normalizes the whole system. Again, $d_{1;4}^V$ can be seen as elements of a diagonal scaling matrix $\tilde{\mathbf{D}}^V$.

As can be observed in equation (2.198), we need the inverse of (2.151) to find $\tilde{\mathbf{L}}_2^V$. This inverse reads

$$\{\tilde{\mathbf{A}}^V\}^{-1} = \begin{pmatrix} \frac{1}{\Gamma_{Pf}} & 0 & 0 & 0 \\ 0 & \frac{1}{\Gamma_{Ps}} & 0 & 0 \\ 0 & 0 & \frac{1}{\Gamma_{SV}} & 0 \\ 0 & 0 & 0 & \frac{1}{\Gamma_{TM}} \end{pmatrix}. \quad (2.200)$$

Using equation (2.198) we can express $\tilde{\mathbf{L}}_2^V$ in terms of $\tilde{\mathbf{L}}_1^V$ and the known values for the elements of the system submatrix $\tilde{\mathbf{A}}_{21}^V$ and the inverse of the eigenvalues $\{\tilde{\mathbf{A}}^V\}^{-1}$, yielding

$$\tilde{\mathbf{L}}_2 = - \begin{pmatrix} \frac{d_1^V}{\Gamma_{Pf}} [s\rho^b + s\rho^f E + j\kappa N] & \frac{d_2^V}{\Gamma_{Ps}} [s\rho^b A + s\rho^f + j\kappa O] \\ \frac{d_1^V}{\Gamma_{Pf}} [s\rho^f + s\hat{\rho}^E \left(1 + \frac{\hat{\xi}\hat{\zeta}}{\zeta}\right) E] & \frac{d_2^V}{\Gamma_{Ps}} [s\rho^f A + s\hat{\rho}^E \left(1 + \frac{\hat{\xi}\hat{\zeta}}{\zeta}\right)] \\ \frac{d_1^V}{\Gamma_{Pf}} [j\kappa + \beta N] & \frac{d_2^V}{\Gamma_{Ps}} [j\kappa A + \beta O] \\ \frac{d_1^V}{\Gamma_{Pf}} [j\kappa \frac{\hat{\xi}}{\zeta} E] & \frac{d_2^V}{\Gamma_{Ps}} [j\kappa \frac{\hat{\xi}}{\zeta}] \\ \frac{d_3^V}{\Gamma_{SV}} [s\rho^b B + s\rho^f F + j\kappa] & \frac{d_4^V}{\Gamma_{TM}} [s\rho^b D\chi + s\rho^f G\chi + j\kappa P\chi] \\ 0 & 0 \\ \frac{d_3^V}{\Gamma_{SV}} [j\kappa B + \beta] & \frac{d_4^V}{\Gamma_{TM}} [j\kappa D\chi + \beta P\chi] \\ \frac{d_3^V}{\Gamma_{SV}} [j\kappa \frac{\hat{\xi}}{\zeta} F + \left(-\zeta - \frac{\kappa^2}{\zeta}\right) T\chi] & \frac{d_4^V}{\Gamma_{TM}} [j\kappa \frac{\hat{\xi}}{\zeta} G\chi + \left(-\zeta - \frac{\kappa^2}{\zeta}\right)] \end{pmatrix}. \quad (2.201)$$

We can indeed observe that elements (2,3) and (2,4) are zero, as required from a physical point of view.

Now that we have defined and consistently determined the composition submatrices $\tilde{\mathbf{L}}_1^V$ and $\tilde{\mathbf{L}}_2^V$ in general terms, respectively, we can use the other equation, equation (2.179), to determine a set of equations that contains all necessary information to solve for the unknown parameters of these composition submatrices. To this end, we rewrite equation (2.179) as

$$\tilde{\mathbf{A}}_{12}^V \tilde{\mathbf{L}}_2^V = -\tilde{\mathbf{L}}_1^V \tilde{\mathbf{A}}^V. \quad (2.202)$$

Writing out equation (2.202) explicitly will yield four sets of four equations, one set for each field type (Pf, Ps, SV and TM), which can be used to solve for the unknown

parameters. The details of this derivation are presented in Appendix 2.3.B. Solving for the unknown parameters in this way yields

$$N = \frac{-2j\kappa}{\beta}, \quad (2.203)$$

$$E = \frac{\frac{K_c M \hat{\xi}}{c_{P_f}^2} - \rho^b M \hat{\xi} + \rho^f C \hat{\xi}}{M \hat{\xi} \rho^f - \hat{\rho}^E C \eta^E}, \quad (2.204)$$

$$A = \frac{-\rho^f M \hat{\xi} + \hat{\rho}^E C \eta^E}{\rho^b M \hat{\xi} - \rho^f C \hat{\xi} - \frac{K_c M \hat{\xi}}{c_{P_s}^2}}, \quad (2.205)$$

$$O = NA \quad (2.206)$$

$$B_1 = s^2 \rho^b - \frac{s^2 (\rho^f)^2 \hat{\xi}}{\hat{\rho}^E \eta^E} - 2(S + G^{fr}) \kappa^2 - K_c \gamma_{SV}^2, \quad (2.207)$$

$$T_1 = \frac{-2s^3 \kappa^2 (\rho^f)^2 \hat{\mathcal{L}}^2}{\eta^E B_1} - \frac{\kappa^2}{\hat{\xi}} (s \hat{\rho}^E \hat{\mathcal{L}}^2 + \eta^E - \hat{\xi}) + \eta^E \hat{\xi} - \gamma_{SV}^2, \quad (2.208)$$

$$T = \frac{\frac{-2s\kappa^2(1+\frac{S}{G^{fr}})}{B_1} - \frac{s}{G^{fr}}}{T_1}, \quad (2.209)$$

$$B = \frac{sj\kappa}{B_1} \left[\frac{\rho^f \hat{\xi} \chi T}{\hat{\rho}^E \eta^E} - \left(1 + \frac{S}{G^{fr}} \right) \right], \quad (2.210)$$

$$F = \frac{-s\rho^f \hat{\xi} B - j\kappa \hat{\xi} \chi T}{s \hat{\rho}^E \eta^E}, \quad (2.211)$$

$$D_1 = \left[s^2 \rho^b - \frac{s^2 (\rho^f)^2 \hat{\xi}}{\hat{\rho}^E \eta^E} - 2(S + G^{fr}) \kappa^2 - K_c \gamma_{TM}^2 \right], \quad (2.212)$$

$$D_2 = \left[-K_c \left(-\hat{\xi} - \frac{\kappa^2}{\hat{\xi}} \right) - \frac{S \kappa^2}{\eta^E} - \frac{K_c \xi \chi \kappa^2}{s \rho^f \eta^E \hat{\xi}} \right], \quad (2.213)$$

$$D_3 = \left[s^2 \rho^b S - \frac{s^2 (\rho^f)^2 S \hat{\xi}}{\hat{\rho}^E \eta^E} + 4G^{fr} (S + G^{fr}) \kappa^2 + s^2 \hat{\rho}^c K_c - \frac{s \rho^f K_c \xi \chi}{\hat{\rho}^E \eta^E} \right], \quad (2.214)$$

$$P_1 = \left[\frac{s^2 \hat{\rho}^c K_c}{G^{fr}} + 2(S + G^{fr}) \kappa^2 - K_c \gamma_{TM}^2 \right], \quad (2.215)$$

$$P = \frac{\left[D_1 D_2 + \frac{\kappa^2}{\eta^E} D_3 \right]}{\left[P_1 D_1 + \kappa^2 \left(1 + \frac{S}{G^{fr}} \right) D_3 \right]}, \quad (2.216)$$

$$D = \frac{sj\kappa \left[\frac{1}{\eta^E} - P \left(1 + \frac{S}{G^{fr}} \right) \right]}{D_1}, \quad (2.217)$$

$$G = \frac{-s(\rho^f)^2 \hat{\xi} D - j\kappa \hat{\rho}^E}{s \hat{\rho}^E \eta^E \rho^f}. \quad (2.218)$$

Now that we have solved for all ten unknown parameters of the eigenvector

matrix, we can normalize the eigenvectors with respect to different quantities. Note that in the whole derivation so far the normalization factors d_1^V , d_2^V , d_3^V and d_4^V dropped out of the equations, meaning that the expressions for the ten unknown parameters are normalization independent. Where [Haartsen & Pride \(1997\)](#) have used displacement normalization, we here choose for power-flux normalization. Due to the way we have organized our system matrix $\tilde{\mathbf{A}}^V$, and due to the specific structure of the composition matrix $\tilde{\mathbf{L}}^V$ in terms of its submatrices $\tilde{\mathbf{L}}_1^V$ and $\tilde{\mathbf{L}}_2^V$, we can find power-flux normalization factors, by requiring that

$$\left\{ \tilde{\mathbf{L}}_1^V \right\}^t \tilde{\mathbf{L}}_2^V = \frac{1}{2} \tilde{\mathbf{I}}^V, \quad (2.219)$$

where we make use of the relations between the transverse and the inverse of submatrices (similar to equations (2.169) and (2.170)). By requiring equation (2.219) to hold and explicitly writing out these submatrix multiplications in general terms, we can solve for the flux-normalization scaling factors $d_{1:4}^V$, yielding

$$d_1^V = \sqrt{-\frac{\Gamma_{Pf}}{2s \left[\rho^b + E \left(2\rho^f + \frac{\hat{\rho}^E \eta^E E}{\xi} \right) \right]}}, \quad (2.220)$$

$$d_2^V = \sqrt{-\frac{\Gamma_{Ps}}{2s \left[A(\rho^b A + 2\rho^f) + \frac{\hat{\rho}^E \eta^E E}{\xi} \right]}}, \quad (2.221)$$

$$d_3^V = \sqrt{-\frac{\Gamma_{SV}}{2 \left[B(s\rho^b B + 2j\kappa) - \frac{s\hat{\rho}^E \eta^E F^2}{\xi} + \beta + \Psi \chi^2 T^2 \right]}}, \quad (2.222)$$

$$d_4^V = \sqrt{-\frac{\Gamma_{TM}}{2 \left[\chi^2 (s\rho^b D^2 + 2j\kappa PD + \beta P^2) - \frac{s\hat{\rho}^E \eta^E \chi^2 G^2}{\xi} + \Psi \right]}}, \quad (2.223)$$

with $\Psi = -\zeta - \frac{\kappa^2}{\xi}$. We have now found expressions for the power-flux normalized eigenvectors of the P-SV-TM system, straight from the system matrices and defined and derived in such a way that they obey the physics of fully decoupled poroelastic and electromagnetic systems when $\hat{\mathcal{L}} = 0$ and remain numerically stable. We refer to this eigenvector set as the GST P-SV-TM set.

Appendix

2.3.A Details of the Power-flux Normalization Procedure for the SH-TE HP Eigenvector Set

This appendix presents the details on how to effectively power-flux normalize the HP eigenvector set for the SH-TE propagation mode. Starting from the velocity field normalized eigenvector set for the SH-TE propagation mode, we can derive the

power-flux normalized eigenvector matrix by requiring that equation (2.165) must hold. Having $\tilde{\mathbf{N}}^H$ as described in (2.147), its inverse reads

$$\left\{ \tilde{\mathbf{N}}^H \right\}^{-1} = \begin{pmatrix} \mathbf{O} & -\mathbf{I} \\ \mathbf{I} & \mathbf{O} \end{pmatrix} = \begin{pmatrix} 0 & 0 & -1 & 0 \\ 0 & 0 & 0 & -1 \\ 1 & 0 & 0 & 0 \\ 0 & 1 & 0 & 0 \end{pmatrix}. \quad (2.224)$$

From this, it can be easily seen that the following relation holds between \mathbf{N} and its inverse:

$$-\left\{ \tilde{\mathbf{N}}^H \right\}^{-1} = \tilde{\mathbf{N}}^H. \quad (2.225)$$

However, the flux-normalized $\tilde{\mathbf{L}}^H$ for which (2.165) holds is not yet known. To find the correct flux-normalized composition matrix $\tilde{\mathbf{L}}^H$, the following steps are performed. Let us first define $\tilde{\mathbf{L}}^H$ as

$$\tilde{\mathbf{L}}^H = \tilde{\mathbf{K}}^H \tilde{\mathbf{D}}^H, \quad (2.226)$$

where $\tilde{\mathbf{D}}^H$ can be an arbitrary invertible diagonal matrix, in this case chosen as

$$\tilde{\mathbf{D}}^H = \begin{pmatrix} \tilde{\mathbf{D}}_1^H & \mathbf{O} \\ \mathbf{O} & \tilde{\mathbf{D}}_2^H \end{pmatrix} = \begin{pmatrix} d_1^H & 0 & 0 & 0 \\ 0 & d_2^H & 0 & 0 \\ 0 & 0 & d_3^H & 0 \\ 0 & 0 & 0 & d_4^H \end{pmatrix}. \quad (2.227)$$

By making this choice, and knowing that for the resulting composition matrix $\tilde{\mathbf{L}}^H$ (via (2.226)) the following organization must still hold

$$\tilde{\mathbf{L}}^H = \begin{pmatrix} \tilde{\mathbf{L}}_1^H & \tilde{\mathbf{L}}_1^H \\ \tilde{\mathbf{L}}_2^H & -\tilde{\mathbf{L}}_2^H \end{pmatrix}, \quad (2.228)$$

which is also the structure of $\tilde{\mathbf{K}}^H$, this already leads to the following requirement for $\tilde{\mathbf{D}}^H$, $\tilde{\mathbf{D}}_1^H = \tilde{\mathbf{D}}_2^H$. More specifically, d_3^H and d_4^H are required to be equal to d_1^H and d_2^H , respectively.

We now explicitly write out the composition matrix $\tilde{\mathbf{K}}^H$ in general terms, where we have replaced all elements, except for the first row, by general symbols a, b, c, d, e and f

$$\tilde{\mathbf{K}}^H = \begin{pmatrix} s & s & s & s \\ e & f & e & f \\ a & b & -a & -b \\ c & d & -c & -d \end{pmatrix}. \quad (2.229)$$

The transpose of the composition matrix, $\left\{ \tilde{\mathbf{K}}^H \right\}^t$ then reads:

$$\left\{ \tilde{\mathbf{K}}^H \right\}^t = \begin{pmatrix} \left\{ \tilde{\mathbf{K}}_1^H \right\}^t & \left\{ \tilde{\mathbf{K}}_2^H \right\}^t \\ \left\{ \tilde{\mathbf{K}}_1^H \right\}^t & -\left\{ \tilde{\mathbf{K}}_2^H \right\}^t \end{pmatrix}. \quad (2.230)$$

To obtain the flux-normalized composition matrix $\tilde{\mathbf{L}}^H$, (2.165) is rewritten in terms of $\tilde{\mathbf{K}}^H$, using $\tilde{\mathbf{L}}^H = \tilde{\mathbf{K}}^H \tilde{\mathbf{D}}^H$

$$\left(\tilde{\mathbf{K}}^H \tilde{\mathbf{D}}^H\right)^{-1} = -\left\{\tilde{\mathbf{N}}^H\right\}^{-1}\left(\tilde{\mathbf{K}}^H \tilde{\mathbf{D}}^H\right)^t \tilde{\mathbf{N}}^H = \tilde{\mathbf{N}}^H\left(\tilde{\mathbf{K}}^H \tilde{\mathbf{D}}^H\right)^t \tilde{\mathbf{N}}^H. \quad (2.231)$$

In addition,

$$\tilde{\mathbf{L}}\tilde{\mathbf{L}}^{-1} = \tilde{\mathbf{L}}^{-1}\tilde{\mathbf{L}} = \mathbf{I}, \quad (2.232)$$

holds, of course, as well. Hence, combining (2.231) and (2.232) results in

$$\tilde{\mathbf{N}}^H\left(\tilde{\mathbf{K}}^H \tilde{\mathbf{D}}^H\right)^t \tilde{\mathbf{N}}^H \tilde{\mathbf{K}} \tilde{\mathbf{D}} = \tilde{\mathbf{N}}^H\left\{\tilde{\mathbf{D}}^H\right\}^t\left\{\tilde{\mathbf{K}}^H\right\}^t \tilde{\mathbf{N}}^H \tilde{\mathbf{K}}^H \tilde{\mathbf{D}}^H = \mathbf{I}^H. \quad (2.233)$$

Let us now for notational convenience drop the superscript H . Explicitly expressing equation (2.233) in full matrix-notation yields

$$\begin{aligned} \tilde{\mathbf{N}}\tilde{\mathbf{D}}^t\tilde{\mathbf{K}}^t\mathbf{N}\tilde{\mathbf{K}}\tilde{\mathbf{D}} &= \begin{pmatrix} \tilde{\mathbf{D}}_1\left(\tilde{\mathbf{K}}_2^t\tilde{\mathbf{K}}_1 + \tilde{\mathbf{K}}_1^t\tilde{\mathbf{K}}_2\right)\tilde{\mathbf{D}}_1 & \tilde{\mathbf{D}}_1\left(\tilde{\mathbf{K}}_2^t\tilde{\mathbf{K}}_1 - \tilde{\mathbf{K}}_1^t\tilde{\mathbf{K}}_2\right)\tilde{\mathbf{D}}_1 \\ \tilde{\mathbf{D}}_1\left(\tilde{\mathbf{K}}_2^t\tilde{\mathbf{K}}_1 - \tilde{\mathbf{K}}_1^t\tilde{\mathbf{K}}_2\right)\tilde{\mathbf{D}}_1 & \tilde{\mathbf{D}}_1\left(\tilde{\mathbf{K}}_2^t\tilde{\mathbf{K}}_1 + \tilde{\mathbf{K}}_1^t\tilde{\mathbf{K}}_2\right)\tilde{\mathbf{D}}_2 \end{pmatrix} \\ &= \begin{pmatrix} \mathbf{I} & \mathbf{O} \\ \mathbf{O} & \mathbf{I} \end{pmatrix}. \end{aligned} \quad (2.234)$$

Using the general expressions for $\tilde{\mathbf{K}}_1$ and $\tilde{\mathbf{K}}_2$ (equation (2.229)) the following terms are evaluated

$$\tilde{\mathbf{K}}_2^t\tilde{\mathbf{K}}_1 + \tilde{\mathbf{K}}_1^t\tilde{\mathbf{K}}_2 = \begin{pmatrix} 2(as + ec) & as + fc + bs + ed \\ as + fc + bs + ed & 2(bs + fd) \end{pmatrix}, \quad (2.235)$$

and

$$\tilde{\mathbf{K}}_2^t\tilde{\mathbf{K}}_1 - \tilde{\mathbf{K}}_1^t\tilde{\mathbf{K}}_2 = \begin{pmatrix} 0 & as + fc - bs - ed \\ -as - fc + bs + ed & 0 \end{pmatrix}. \quad (2.236)$$

Let us for simplicity introduce a new parameter $\varpi = as + fc - bs - ed$. From (2.234) it turns out that the following condition must hold

$$\tilde{\mathbf{D}}_1\left(\tilde{\mathbf{K}}_2^t\tilde{\mathbf{K}}_1 - \tilde{\mathbf{K}}_1^t\tilde{\mathbf{K}}_2\right)\tilde{\mathbf{D}}_1 = \mathbf{O}. \quad (2.237)$$

Evaluating equation (2.237) results in:

$$\tilde{\mathbf{D}}_1\left(\tilde{\mathbf{K}}_2^t\tilde{\mathbf{K}}_1 - \tilde{\mathbf{K}}_1^t\tilde{\mathbf{K}}_2\right)\tilde{\mathbf{D}}_1 = \begin{pmatrix} 0 & d_1^H d_2^H \varpi \\ -d_1^H d_2^H \varpi & 0 \end{pmatrix}. \quad (2.238)$$

From both equations (2.234) and (2.238) it follows that, in order for the required conditions to hold, ϖ must be equal to 0. Hence, after filling in the expressions for the different terms making up ϖ , the following expression has to hold:

$$\left[-G_{fr} + \mu_0\left(\frac{\hat{\rho}^E G_{fr} \hat{\mathcal{L}}}{\rho^f}\right)^2 \phi_{sh} \phi_{te}\right] (s\Gamma_{SH} + s\Gamma_{TE}) = 0. \quad (2.239)$$

In order for this condition to be satisfied, we require

$$-1 + \mu_0 \left(\frac{\hat{\rho}^E \hat{\mathcal{L}}}{\rho^f} \right)^2 G^{fr} \phi_{sh} \phi_{te} = 0. \quad (2.240)$$

Hence,

$$\mu_0 \left(\frac{\hat{\rho}^E \hat{\mathcal{L}}}{\rho^f} \right)^2 G^{fr} \phi_{sh} \phi_{te} = 1. \quad (2.241)$$

For equation (2.241) to be satisfied,

$$\phi_{sh} \phi_{te} = \frac{1}{\mu_0 \left(\frac{\hat{\rho}^E \hat{\mathcal{L}}}{\rho^f} \right)^2 G^{fr}}, \quad (2.242)$$

must hold. This condition is checked and proven to be satisfied.

Furthermore, for equation (2.234) to hold, the following condition must be satisfied

$$\tilde{\mathbf{D}}_1 \left(\tilde{\mathbf{K}}_2^t \tilde{\mathbf{K}}_1 + \tilde{\mathbf{K}}_1^t \tilde{\mathbf{K}}_2 \right) \tilde{\mathbf{D}}_1 = \mathbf{I}. \quad (2.243)$$

Writing out this condition in its general terms shows that the following must hold

$$\tilde{\mathbf{D}}_1 \left(\tilde{\mathbf{K}}_2^t \tilde{\mathbf{K}}_1 + \tilde{\mathbf{K}}_1^t \tilde{\mathbf{K}}_2 \right) \tilde{\mathbf{D}}_1 = \begin{pmatrix} 2 (d_1^H)^2 (as + ec) & d_1^H d_2^H (as + bs + fc + ed) \\ d_1^H d_2^H (as + bs + fc + ed) & 2 (d_2^H)^2 (bs + fd) \end{pmatrix}. \quad (2.244)$$

It turns out that the same condition (2.241) needs to be satisfied in order for the anti-diagonal of (2.244) to be zero. The only conditions that still need to be satisfied are:

$$2 (d_1^H)^2 (as + ec) = 1, \quad (2.245)$$

$$2 (d_2^H)^2 (bs + fd) = 1. \quad (2.246)$$

This is where the actual power-flux normalization will take place.

From equations (2.245) and (2.246), using equation (2.241), it follows that

$$d_1^H = \frac{1}{\sqrt{2s\Gamma_{sh} \left[-G^{fr} + \mu_0 \left(\frac{\hat{\rho}^E \hat{\mathcal{L}} G^{fr} \phi_{sh}}{\rho^f} \right)^2 \right]}} = \left(-2s\Gamma_{sh} G^{fr} \left[1 - \frac{\phi_{sh}}{\phi_{te}} \right] \right)^{-\frac{1}{2}}, \quad (2.247)$$

$$d_2^H = \frac{1}{\sqrt{2s\Gamma_{te} \left[-G^{fr} + \mu_0 \left(\frac{\hat{\rho}^E \hat{\mathcal{L}} G^{fr} \phi_{te}}{\rho^f} \right)^2 \right]}} = \left(-2s\Gamma_{te} G^{fr} \left[1 - \frac{\phi_{te}}{\phi_{sh}} \right] \right)^{-\frac{1}{2}}. \quad (2.248)$$

We choose the positive sign of the square root, based on the fact that for the eigenvalue matrix, we desire that $\Re\{\Gamma_w\} > 0$. We can now evaluate $\tilde{\mathbf{L}}^H = \tilde{\mathbf{K}}^H \tilde{\mathbf{D}}^H$ yielding the flux-normalized composition matrix $\tilde{\mathbf{L}}^H$ of equation (2.166).

2.3.B Details of the Alternatively Derived Power-Flux Normalized P-SV-TM GST Eigenvector Set

This appendix presents the details for deriving the GST P-SV-TM eigenvector set as presented in this thesis. We start from equation (2.202). Since both the right-hand side and the left-hand side of equation (2.202) (implicitly in $\tilde{\mathbf{L}}_2^V$) contain a minus sign, these will cancel and will be ignored in the derivations below. Explicitly writing out equation (2.202) yields four sets of four equations each, one set for each field type (Pf, Ps, SV and TM):

Set 1:

$$\begin{aligned}
& \frac{s}{K_c} \frac{d_1^V}{\Gamma_{Pf}} [s\rho^b + s\rho^f E + j\kappa N] \\
& -s \frac{C}{MK_c} \frac{d_1^V}{\Gamma_{Pf}} \left[s\rho^f + s\hat{\rho}^E \left(1 + \frac{\hat{\xi}\hat{\mathcal{L}}}{\hat{\zeta}} \right) E \right] \\
& + j\kappa \frac{S}{K_c} \frac{d_1^V}{\Gamma_{Pf}} [j\kappa + \beta N] = d_1^V \Gamma_{Pf}, \tag{2.249}
\end{aligned}$$

$$\begin{aligned}
& -s \frac{C}{MK_c} \frac{d_1^V}{\Gamma_{Pf}} [s\rho^b + s\rho^f E + j\kappa N] + \\
& \left(\frac{s}{M} \left[1 + \frac{C^2}{MK_c} \right] + \frac{\hat{k}}{\eta} \kappa^2 \right) \left(\frac{d_1^V}{\Gamma_{Pf}} \left[s\rho^f + s\hat{\rho}^E \left(1 + \frac{\hat{\xi}\hat{\mathcal{L}}}{\hat{\zeta}} \right) E \right] \right) \\
& + (-j\kappa \frac{\rho^f}{\hat{\rho}^E} + j\kappa \frac{C}{M} \left[1 - \frac{S}{K_c} \right]) \left(\frac{d_1^V}{\Gamma_{Pf}} [j\kappa + \beta N] \right) \\
& + j\kappa \hat{\mathcal{L}} \left(\frac{d_1^V}{\Gamma_{Pf}} \left[j\kappa \frac{\hat{\xi}}{\hat{\zeta}} E \right] \right) = d_1^V E \Gamma_{Pf}, \tag{2.250}
\end{aligned}$$

$$\begin{aligned}
& \frac{j\kappa S}{K_c} \frac{d_1^V}{\Gamma_{Pf}} [s\rho^b + s\rho^f E + j\kappa N] \\
& + (-j\kappa \frac{\rho^f}{\hat{\rho}^E} + j\kappa \frac{C}{M} \left[1 - \frac{S}{K_c} \right]) \left(\frac{d_1^V}{\Gamma_{Pf}} \left[s\rho^f + s\hat{\rho}^E \left(1 + \frac{\hat{\xi}\hat{\mathcal{L}}}{\hat{\zeta}} \right) E \right] \right) \\
& + \left(\frac{1}{s} \frac{4G_{fr}(S + G_{fr})}{K_c} \kappa^2 + s\hat{\rho}^c \right) \left(\frac{d_1^V}{\Gamma_{Pf}} [j\kappa + \beta N] \right) \\
& + \chi \left(\frac{d_1^V}{\Gamma_{Pf}} \left[j\kappa \frac{\hat{\xi}}{\hat{\zeta}} E \right] \right) = d_1^V N \Gamma_{Pf}, \tag{2.251}
\end{aligned}$$

$$\begin{aligned}
& (j\kappa \hat{\mathcal{L}}) \left(\frac{d_1^V}{\Gamma_{Pf}} \left[s\rho^f + s\hat{\rho}^E \left(1 + \frac{\hat{\xi}\hat{\mathcal{L}}}{\hat{\zeta}} \right) E \right] \right) \\
& + \chi \left(\frac{d_1^V}{\Gamma_{Pf}} [j\kappa + \beta N] \right) \\
& - \eta^E \left(\frac{d_1^V}{\Gamma_{Pf}} \left[j\kappa \frac{\hat{\xi}}{\hat{\zeta}} E \right] \right) = 0, \tag{2.252}
\end{aligned}$$

Set 2:

$$\begin{aligned}
& \left(\frac{s}{K_c}\right)\left(\frac{d_2^V}{\Gamma_{Ps}} [s\rho^b A + s\rho^f + j\kappa O]\right) \\
& + \left(-s\frac{C}{MK_c}\right)\left(\frac{d_2^V}{\Gamma_{Ps}} \left[s\rho^f A + s\hat{\rho}^E \left(1 + \frac{\hat{\xi}\hat{\mathcal{L}}}{\hat{\zeta}}\right) \right]\right) \\
& \quad + \frac{j\kappa S}{K_c} \frac{d_2^V}{\Gamma_{Ps}} [j\kappa A + \beta O] = d_2^V A \Gamma_{Ps}, \tag{2.253}
\end{aligned}$$

$$\begin{aligned}
& \left(-s\frac{C}{MK_c}\right)\left(\frac{d_2^V}{\Gamma_{Ps}} [s\rho^b A + s\rho^f + j\kappa O]\right) \\
& + \left(\frac{s}{M} \left[1 + \frac{C^2}{MK_c}\right] + \frac{\hat{k}}{\eta} \kappa^2\right)\left(\frac{d_2^V}{\Gamma_{Ps}} \left[s\rho^f A + s\hat{\rho}^E \frac{\eta^E}{\hat{\zeta}} \right]\right) \\
& + \left(-j\kappa \frac{\rho^f}{\hat{\rho}^E} + j\kappa \frac{C}{M} \left[1 - \frac{S}{K_c}\right]\right)\left(\frac{d_2^V}{\Gamma_{Ps}} [j\kappa A + \beta O]\right) \\
& \quad + (j\kappa \hat{\mathcal{L}})\left(\frac{d_2^V}{\Gamma_{Ps}} \left[j\kappa \frac{\hat{\xi}}{\hat{\zeta}} \right]\right) = d_2^V \Gamma_{Ps}, \tag{2.254}
\end{aligned}$$

$$\begin{aligned}
& \left(\frac{j\kappa S}{K_c}\right)\left(\frac{d_2^V}{\Gamma_{Ps}} [s\rho^b A + s\rho^f + j\kappa O]\right) \\
& + \left(-j\kappa \frac{\rho^f}{\hat{\rho}^E}\right) + j\kappa \frac{C}{M} \left[1 - \frac{S}{K_c}\right]\left(\frac{d_2^V}{\Gamma_{Ps}} \left[s\rho^f A + s\hat{\rho}^E \left(1 + \frac{\hat{\xi}\hat{\mathcal{L}}}{\hat{\zeta}}\right) \right]\right) \\
& + \left(\frac{1}{s} \frac{4G_{fr}(S + G_{fr})}{K_c} \kappa^2 + s\hat{\rho}^c\right)\left(\frac{d_2^V}{\Gamma_{Ps}} [j\kappa A + \beta O]\right) \\
& \quad + \chi \left(\frac{d_2^V}{\Gamma_{Ps}} \left[j\kappa \frac{\hat{\xi}}{\hat{\zeta}} \right]\right) = O \Gamma_{Ps}, \tag{2.255}
\end{aligned}$$

$$\begin{aligned}
& (j\kappa \hat{\mathcal{L}})\left(\frac{d_2^V}{\Gamma_{Ps}} \left[s\rho^f A + s\hat{\rho}^E \left(1 + \frac{\hat{\xi}\hat{\mathcal{L}}}{\hat{\zeta}}\right) \right]\right) \\
& \quad + (\chi)\left(\frac{d_2^V}{\Gamma_{Ps}} [j\kappa A + \beta O]\right) \\
& \quad - \eta^E \left(\frac{d_2^V}{\Gamma_{Ps}} \left[j\kappa \frac{\hat{\xi}}{\hat{\zeta}} \right]\right) = 0, \tag{2.256}
\end{aligned}$$

Set 3:

$$\begin{aligned} \left(\frac{s}{K_c}\right) \frac{d_3^V}{\Gamma_{SV}} [s\rho^b B + s\rho^f F + j\kappa] \\ + \frac{j\kappa S}{K_c} \frac{d_3^V}{\Gamma_{SV}} [j\kappa B + \beta] = d_3^V B \Gamma_{SV}, \end{aligned} \quad (2.257)$$

$$\begin{aligned} \left(-s \frac{C}{MK_c}\right) \left(\frac{d_3^V}{\Gamma_{SV}} [s\rho^b B + s\rho^f F + j\kappa]\right) \\ + \left(-j\kappa \frac{\rho^f}{\hat{\rho}^E} + j\kappa \frac{C}{M} \left[1 - \frac{S}{K_c}\right]\right) \left(\frac{d_3^V}{\Gamma_{SV}} [j\kappa B + \beta]\right) \\ + (j\kappa \hat{\mathcal{L}}) \left(\frac{d_3^V}{\Gamma_{SV}} \left[j\kappa \frac{\hat{\xi}}{\hat{\zeta}} F + \left(-\zeta - \frac{\kappa^2}{\hat{\zeta}}\right) T\chi \right]\right) = d_3^V F \Gamma_{SV}, \end{aligned} \quad (2.258)$$

$$\begin{aligned} \left(\frac{j\kappa S}{K_c}\right) \left(\frac{d_3^V}{\Gamma_{SV}} [s\rho^b B + s\rho^f F + j\kappa]\right) \\ + \left(\frac{1}{s} \frac{4G_{fr}(S + G_{fr})}{K_c} \kappa^2 + s\hat{\rho}^c\right) \left(\frac{d_3^V}{\Gamma_{SV}} [j\kappa B + \beta]\right) \\ + \chi \left(\frac{d_3^V}{\Gamma_{SV}} \left[j\kappa \frac{\hat{\xi}}{\hat{\zeta}} F + \left(-\zeta - \frac{\kappa^2}{\hat{\zeta}}\right) T\chi \right]\right) = d_3^V \Gamma_{SV}, \end{aligned} \quad (2.259)$$

$$(2.260)$$

$$\begin{aligned} \chi \frac{d_3^V}{\Gamma_{SV}} [j\kappa B + \beta] \\ - \eta^E \left(\frac{d_3^V}{\Gamma_{SV}} \left[j\kappa \frac{\hat{\xi}}{\hat{\zeta}} F + \left(-\zeta - \frac{\kappa^2}{\hat{\zeta}}\right) T\chi \right]\right) = d_3^V T\chi \Gamma_{SV}, \end{aligned} \quad (2.261)$$

Set 4:

$$\begin{aligned} & \left(\frac{s}{K_c}\right)\left(\frac{d_4^V}{\Gamma_{TM}} [s\rho^b D\chi + s\rho^f G\chi + j\kappa P\chi]\right) \\ & \quad + \left(\frac{j\kappa S}{K_c}\right)\left(\frac{d_4^V}{\Gamma_{TM}} [j\kappa D\chi + \beta P\chi]\right) = d_4^V D\chi \Gamma_{TM}, \end{aligned} \quad (2.262)$$

(2.263)

$$\begin{aligned} & \left(-s\frac{C}{MK_c}\right)\left(\frac{d_4^V}{\Gamma_{TM}} [s\rho^b D\chi + s\rho^f G\chi + j\kappa P\chi]\right) \\ & + \left(-j\kappa\frac{\rho^f}{\hat{\rho}^E} + j\kappa\frac{C}{M}\left[1 - \frac{S}{K_c}\right]\right)\left(\frac{d_4^V}{\Gamma_{TM}} [j\kappa D\chi + \beta P\chi]\right) \\ & \quad + \left(j\kappa\hat{\mathcal{L}}\right)\left(\frac{d_4^V}{\Gamma_{TM}} \left[j\kappa\frac{\hat{\xi}}{\hat{\zeta}}G\chi + \left(-\zeta - \frac{\kappa^2}{\hat{\zeta}}\right)\right]\right) = d_4^V G\chi \Gamma_{TM}, \end{aligned} \quad (2.264)$$

$$\begin{aligned} & \left(\frac{j\kappa S}{K_c}\right)\left(\frac{d_4^V}{\Gamma_{TM}} [s\rho^b D\chi + s\rho^f G\chi + j\kappa P\chi]\right) \\ & + \left(\frac{1}{s}\frac{4G_{fr}(S + G_{fr})}{K_c}\kappa^2 + s\hat{\rho}^c\right)\left(\frac{d_4^V}{\Gamma_{TM}} [j\kappa D\chi + \beta P\chi]\right) \\ & \quad + \chi\left(\frac{d_4^V}{\Gamma_{TM}} \left[j\kappa\frac{\hat{\xi}}{\hat{\zeta}}G\chi + \left(-\zeta - \frac{\kappa^2}{\hat{\zeta}}\right)\right]\right) = d_4^V P\chi \Gamma_{TM}, \end{aligned} \quad (2.265)$$

$$\begin{aligned} & \quad \chi\left(\frac{d_4^V}{\Gamma_{TM}} [j\kappa D\chi + \beta P\chi]\right) \\ & \quad - \eta^E\left(\frac{d_4^V}{\Gamma_{TM}} \left[j\kappa\frac{\hat{\xi}}{\hat{\zeta}}G\chi + \left(-\zeta - \frac{\kappa^2}{\hat{\zeta}}\right)\right]\right) = d_4^V \Gamma_{TM}. \end{aligned} \quad (2.266)$$

The first two sets, corresponding to the *Pf* and *Ps* eigenvectors, have two unknown parameters that need to be solved for, whereas the second two sets, corresponding to the *SV* and *TM* eigenvectors, contain three unknown parameters. Since each set consists of four equations, it is obvious the system that needs to be solved for has a certain amount of redundancy. We require the final expressions for the unknown parameters to be as concise as possible, in order to minimize numerical round-off errors. Furthermore, care must be taken that no divisions by the radial wavenumber κ or the coupling coefficient $\hat{\mathcal{L}}$ take place, since we want the system to be numerically stable for scenarios where $\kappa = 0$ and / or with no coupling between the mechanical and electromagnetic systems. Taking these aspects into consideration, the following expressions for the unknown parameters have been found. For set 1, corresponding to the *Pf* eigenvectors, we have used equations (2.249) and (2.252), to solve for the two unknowns *N* and *E*, yielding

$$N = \frac{-2j\kappa}{\beta}, \quad (2.267)$$

$$E = \frac{1}{s^2} \frac{\left[K_c \Gamma_{Pf}^2 - s^2 \rho^b + \frac{s^2 \rho^f C}{M} - S \kappa^2 - 2\kappa^2 G_{fr}\right]}{\left[\rho^f - \frac{\hat{\rho}^E C \eta^E}{M \hat{\xi}}\right]}. \quad (2.268)$$

Parameter E can be further simplified as

$$E = \frac{\frac{K_c M \hat{\xi}}{\hat{c}_{Pf}^2} - \rho^b M \hat{\xi} + \rho^f C \hat{\xi}}{M \hat{\xi} \rho^f - \hat{\rho}^E C \eta^E}. \quad (2.269)$$

For set 2, corresponding to the Ps eigenvectors, we have used equations (2.253) and (2.256) to solve for the two unknown parameters A and O

$$A = \frac{\left[-s^2 \rho^f + \frac{s^2 \hat{\rho}^E C \eta^E}{M \hat{\xi}} \right]}{\left[s^2 \rho^b - \frac{s^2 \rho^f C}{M} - K_c \Gamma_{Ps}^2 + 2\kappa^2 G^{fr} + \kappa^2 S \right]}, \quad (2.270)$$

$$O = \frac{-2j\kappa A}{\beta} = NA. \quad (2.271)$$

We can simplify A as

$$A = \frac{-\rho^f M \hat{\xi} + \hat{\rho}^E C \eta^E}{\rho^b M \hat{\xi} - \rho^f C \hat{\xi} - \frac{K_c M \hat{\xi}}{\hat{c}_{Ps}^2}}. \quad (2.272)$$

As can be seen, the expression for A is similar to E : $A = -1/E$ with the velocity of the Biot slow P-wave instead of the Biot fast P-wave.

To determine the three unknown parameters B , F and T of set 3, corresponding to the SV eigenvectors, we need three equations. To obtain stable solutions without divisions by solely κ or L (which can be zero and cause instabilities) we use equations (2.257), (2.261) and the equation following from the fact that we require $\tilde{L}_2(2, 3) = 0$,

$$\tilde{L}_2(2, 3) = - \left(\frac{s \rho^f d_3^V B}{\Gamma_{SV}} + \frac{s \hat{\rho}^E \eta^E d_3^V F}{\hat{\xi} \Gamma_{SV}} + \frac{j \kappa \hat{\xi} d_3^V \chi T}{\hat{\xi} \Gamma_{SV}} \right) = 0. \quad (2.273)$$

We use equation (2.273) to express F in terms of B and T , then subsequently equation (2.257) to find an expression of B in terms of T and finally equation (2.261) to express T in terms of solely known variables. As far as we are aware of, this order of applying the superposition principle yields the most compact and stable expressions for B , F and T . This results in the following expressions

$$B_1 = s^2 \rho^b - \frac{s^2 (\rho^f)^2 \hat{\xi}}{\hat{\rho}^E \eta^E} - 2(S + G^{fr}) \kappa^2 - K_c \gamma_{SV}^2, \quad (2.274)$$

$$T_1 = \frac{-2s^3 \kappa^2 (\rho^f)^2 \hat{L}^2}{\eta^E B_1} - \frac{\kappa^2}{\hat{\xi}} \left(s \hat{\rho}^E \hat{L}^2 + \eta^E - \hat{\xi} \right) + \eta^E \zeta - \gamma_{SV}^2, \quad (2.275)$$

$$T = \frac{-2s\kappa^2 \left(1 + \frac{S}{G^{fr}}\right)}{B_1} - \frac{s}{G^{fr}}, \quad (2.276)$$

$$B = \frac{s j \kappa}{B_1} \left[\frac{\rho^f \hat{\xi} \chi T}{\hat{\rho}^E \eta^E} - \left(1 + \frac{S}{G^{fr}}\right) \right], \quad (2.277)$$

$$F = \frac{-s \rho^f \hat{\xi} B - j \kappa \hat{\xi} \chi T}{s \hat{\rho}^E \eta^E}. \quad (2.278)$$

Finally, we try to derive numerically stable expressions for the three unknown parameters of set 4, D, G and P, using equations (2.262), (2.265) and again the equation following from the fact that we require that also $\tilde{L}_2(2, 4) = 0$

$$\tilde{L}_2(2, 4) = -\frac{d_4^V}{\Gamma_{TM}} [s\rho^f \hat{\zeta} \chi D + s\hat{\rho}^E \eta^E \chi G + j\kappa \xi] = 0. \quad (2.279)$$

We use equation (2.279) to express G in terms of D, subsequently equation (2.262) to express D in terms of P, and finally equation (2.265) to express P in terms of solely known variables. Again, this order of applying the superposition principle yields the most compact and stable expressions for D, G and P, as far as we are aware of. This results in

$$D_1 = \left[s^2 \rho^b - \frac{s^2 (\rho^f)^2 \hat{\zeta}}{\hat{\rho}^E \eta^E} - 2(S + G^{fr}) \kappa^2 - K_c \gamma_{TM}^2 \right], \quad (2.280)$$

$$D_2 = \left[-K_c \left(-\zeta - \frac{\kappa^2}{\hat{\zeta}} \right) - \frac{S \kappa^2}{\eta^E} - \frac{K_c \xi \chi \kappa^2}{s \rho^f \eta^E \hat{\zeta}} \right], \quad (2.281)$$

$$D_3 = \left[s^2 \rho^b S - \frac{s^2 (\rho^f)^2 S \hat{\zeta}}{\hat{\rho}^E \eta^E} + 4G^{fr} (S + G^{fr}) \kappa^2 + s^2 \hat{\rho}^c K_c - \frac{s \rho^f K_c \xi \chi}{\hat{\rho}^E \eta^E} \right], \quad (2.282)$$

$$P_1 = \left[\frac{s^2 \hat{\rho}^c K_c}{G^{fr}} + 2(S + G^{fr}) \kappa^2 - K_c \gamma_{TM}^2 \right], \quad (2.283)$$

$$P = \frac{\left[D_1 D_2 + \frac{\kappa^2}{\eta^E} D_3 \right]}{\left[P_1 D_1 + \kappa^2 \left(1 + \frac{S}{G^{fr}} \right) D_3 \right]}, \quad (2.284)$$

$$D = \frac{s j \kappa \left[\frac{1}{\eta^E} - P \left(1 + \frac{S}{G^{fr}} \right) \right]}{D_1}, \quad (2.285)$$

$$G = \frac{-s (\rho^f)^2 \hat{\zeta} D - j \kappa \hat{\rho}^E}{s \hat{\rho}^E \eta^E \rho^f}. \quad (2.286)$$

2.4 Explicit homogeneous space Green's function solutions

We have seen that for layered-Earth geometries, we can capture the expressions for both the SH-TE and the P-SV-TM propagation modes separately into the following matrix differential equation

$$\partial_3 \tilde{\mathbf{F}}^{H,V} - \tilde{\mathbf{A}}^{H,V} \tilde{\mathbf{F}}^{H,V} = \tilde{\mathbf{S}}^{H,V} \delta(x_3 - x_3^s), \quad (2.287)$$

where the tilde denotes that the expressions are given in the horizontal wavenumber-frequency domain. Here, $\tilde{\mathbf{F}}$ denotes the two-way field vector, $\tilde{\mathbf{A}}$ is the two-way operator or system matrix and $\tilde{\mathbf{S}}$ contains the two-way source quantities. The system matrix for the SH-TE system is of size 4x4, whereas the size of the P-SV-TM system matrix is 8x8. We follow an approach different from that of [Pride & Haartsen \(1996\)](#) to obtain the homogeneous space Green's functions. Where [Pride & Haartsen \(1996\)](#) inverted a subset of equations to derive a few homogeneous space-solutions, we model all seismoelectric and electroseismic source-receiver combinations both in ESSEMOD and with homogeneous space Green's function solutions. We make use of power flux-normalized composition and decomposition matrices. Due to the power-flux normalization, we use the transpose of the composition (sub)matrices as the inverse for the decomposition (sub)matrices. We start by transforming equation (2.287) to the three-dimensional wavenumber domain (denoted by the breve) using $\partial_3 \iff -jk_3$, from which we obtain

$$\begin{pmatrix} jk_3 \mathbf{I} & \check{\mathbf{A}}_{12}^{H,V} \\ \check{\mathbf{A}}_{21}^{H,V} & jk_3 \mathbf{I} \end{pmatrix} \begin{pmatrix} \check{F}_1^{H,V} \\ \check{F}_2^{H,V} \end{pmatrix} = - \begin{pmatrix} \check{S}_1^{H,V} \\ \check{S}_2^{H,V} \end{pmatrix}, \quad (2.288)$$

which can be solved as

$$\begin{pmatrix} \check{F}_1^{H,V} \\ \check{F}_2^{H,V} \end{pmatrix} = - \begin{pmatrix} \check{\mathbf{G}}_{11}^{H,V} & \check{\mathbf{G}}_{12}^{H,V} \\ \check{\mathbf{G}}_{21}^{H,V} & \check{\mathbf{G}}_{22}^{H,V} \end{pmatrix} \begin{pmatrix} \check{S}_1^{H,V} \\ \check{S}_2^{H,V} \end{pmatrix}, \quad (2.289)$$

where the following expressions hold for the Green function matrices

$$\check{\mathbf{G}}_{11}^{H,V} = -2jk_3 \check{\mathbf{L}}_1^{H,V} (k_3^2 \mathbf{I} + (\boldsymbol{\Lambda}^{H,V})^2)^{-1} \left(\check{\mathbf{L}}_2^{H,V} \right)^t, \quad (2.290)$$

$$\check{\mathbf{G}}_{12}^{H,V} = 2\check{\mathbf{A}}_{12}^{H,V} \check{\mathbf{L}}_2^{H,V} (k_3^2 \mathbf{I} + (\boldsymbol{\Lambda}^{H,V})^2)^{-1} \left(\check{\mathbf{L}}_1^{H,V} \right)^t, \quad (2.291)$$

$$\check{\mathbf{G}}_{21}^{H,V} = 2\check{\mathbf{A}}_{21}^{H,V} \check{\mathbf{L}}_1^{H,V} (k_3^2 \mathbf{I} + (\boldsymbol{\Lambda}^{H,V})^2)^{-1} \left(\check{\mathbf{L}}_2^{H,V} \right)^t, \quad (2.292)$$

$$\check{\mathbf{G}}_{22}^{H,V} = -2jk_3 \check{\mathbf{L}}_2^{H,V} (k_3^2 \mathbf{I} + (\boldsymbol{\Lambda}^{H,V})^2)^{-1} \left(\check{\mathbf{L}}_1^{H,V} \right)^t. \quad (2.293)$$

To arrive at this result, we made use of inversion by partitioning ([Press et al., 1988](#)),

$$\begin{pmatrix} \mathbf{A} & \mathbf{B} \\ \mathbf{C} & \mathbf{D} \end{pmatrix} \begin{pmatrix} \mathbf{P} & \mathbf{Q} \\ \mathbf{R} & \mathbf{S} \end{pmatrix} = \begin{pmatrix} \mathbf{I} & \mathbf{O} \\ \mathbf{O} & \mathbf{I} \end{pmatrix}, \quad (2.294)$$

where

$$\begin{pmatrix} \mathbf{P} & \mathbf{Q} \\ \mathbf{R} & \mathbf{S} \end{pmatrix} = \begin{pmatrix} (\mathbf{A} - \mathbf{B}\mathbf{D}^{-1}\mathbf{C})^{-1} & -\mathbf{A}^{-1}\mathbf{B}(\mathbf{D} - \mathbf{C}\mathbf{A}^{-1}\mathbf{B})^{-1} \\ -\mathbf{D}^{-1}\mathbf{C}(\mathbf{A} - \mathbf{B}\mathbf{D}^{-1}\mathbf{C})^{-1} & (\mathbf{D} - \mathbf{C}\mathbf{A}^{-1}\mathbf{B})^{-1} \end{pmatrix}. \quad (2.295)$$

We take

$$\mathbf{A} = \mathbf{D} = jk_3\mathbf{I}, \quad \mathbf{B} = \check{\mathbf{A}}_{12}, \quad \mathbf{C} = \check{\mathbf{A}}_{21}, \quad (2.296)$$

and make use of the fact that \mathbf{A} and \mathbf{D} are unit diagonal matrices except for the scalar constant jk_3 , such that we arrive at the expressions for the Green function matrices. Note that the eigenvalue matrix contains the vertical wavenumbers on the diagonal and the matrix $(k_3^2\mathbf{I} + \mathbf{\Lambda}^2)$ is easily invertible. The matrices $\check{\mathbf{A}}_{12}$ and $\check{\mathbf{A}}_{21}$ and the composition matrices do not depend on jk_3 . Hence, the Green function matrices do not depend on jk_3 except in the diagonal matrix that has to be inverted and the factor itself that appears in the expressions for $\check{\mathbf{G}}_{11}$ and $\check{\mathbf{G}}_{22}$. We can rewrite the system matrices using equation (2.148), and using $\check{\mathbf{G}}^{H,V} = (k_3^2\mathbf{I} + (\check{\mathbf{\Lambda}}^{H,V})^2)^{-1}$, where $\check{\mathbf{G}}^{H,V}$ is a diagonal Green's function matrix containing the scalar Green's functions for the different field types for the mode under consideration. This leads to:

$$\check{\mathbf{G}}_{11}^{H,V} = -2jk_3\check{\mathbf{L}}_1^{H,V}\check{\mathbf{G}}^{H,V}\left(\check{\mathbf{L}}_2^{H,V}\right)^t, \quad (2.297)$$

$$\check{\mathbf{G}}_{12}^{H,V} = -2\check{\mathbf{L}}_1^{H,V}\check{\mathbf{\Lambda}}^{H,V}\check{\mathbf{G}}^{H,V}\left(\check{\mathbf{L}}_1^{H,V}\right)^t, \quad (2.298)$$

$$\check{\mathbf{G}}_{21}^{H,V} = -2\check{\mathbf{L}}_2^{H,V}\check{\mathbf{\Lambda}}^{H,V}\check{\mathbf{G}}^{H,V}\left(\check{\mathbf{L}}_2^{H,V}\right)^t, \quad (2.299)$$

$$\check{\mathbf{G}}_{22}^{H,V} = -2jk_3\check{\mathbf{L}}_2^{H,V}\check{\mathbf{G}}^{H,V}\left(\check{\mathbf{L}}_1^{H,V}\right)^t. \quad (2.300)$$

We can now select which source-receiver combination we want to model in a homogeneous space, in order to validate the results obtained from ESSEMOD. We can express all source-receiver combinations in terms of homogeneous space-solutions. When certain field quantities are present in the field vectors of both propagation modes, the SH-TE and P-SV-TM results need to be combined in the end to find the total Green's function solution for these fields. We will start with a comprehensive example and focus on a combined field E_1 due to a pure P-SV-TM source-type: \hat{f}_3^b being the bulk force in the x_3 -direction (depth), where the hat denotes a space-frequency domain quantity. For the arrangement of the field vector as used in our seismo-EM layer-code, the expression for the electric field belonging to the P-SV-TM propagation mode due to \hat{f}_3^b reads

$$\check{E}_{norm}^{V;J_3^b} = -2jk_3J_3^b \sum_{k=1}^4 \check{L}_{2,4k}^V \check{G}_{kk}^V \check{L}_{1,1k}^V. \quad (2.301)$$

The following relation holds between the electric fields for the P-SV-TM mode and the SH-TE mode and the electric field component in the x_1 -direction

$$\check{E}_1 = -jk_1\check{E}_{norm}^V/\kappa + jk_2\check{E}_{norm}^H/\kappa, \quad (2.302)$$

where κ is the radial wavenumber, $\kappa = \sqrt{k_1^2 + k_2^2}$, and where the subscript 'norm' refers to the fact that the field quantities of both propagation modes have been normalized with a factor $-\kappa$. In the case of a pure P-SV-TM source type (like the \hat{f}_3^b), the SH-TE contribution to the expression (2.302) is zero. Using this relation, filling in the correct components of the composition matrices in (2.301) and transforming analytically back to the space-frequency domain, the necessary homogeneous Green's function solution for $E_1^{J_3^b}$ can be obtained. We omit the exact expressions here for brevity. In this way, all possible seismoelectric and electroseismic source-receiver combinations can be expressed in terms of their homogeneous space solution and can be compared with the numerical homogeneous results from layer-code modeling. To further illustrate this, we will look at $v_1^{J_1^e}$, the particle velocity in the x_1 -direction due to an electric dipole source in the x_1 -direction, and $v_1^{f_1^b}$, the particle velocity in the x_1 -direction due to a bulk force source in the x_1 -direction. For the arrangement of the field vector as used in our seismo-EM layer-code, the expressions for the particle velocity field belonging to the P-SV-TM propagation mode due to \hat{J}_1^e and \hat{f}_1^b , read

$$\check{v}_{norm}^{V;J_1^e} = \frac{2jk_1}{\kappa} \hat{J}_1^e \sum_{k=1}^4 \check{L}_{2,3k}^V \check{\Gamma}_{kk}^V \check{G}_{kk}^V \check{L}_{2,4k}^V, \quad (2.303)$$

$$\check{v}_{norm}^{V;f_1^b} = \frac{2jk_1}{\kappa} \hat{f}_1^b \sum_{k=1}^4 \check{L}_{2,3k}^V \check{\Gamma}_{kk}^V \check{G}_{kk}^V \check{L}_{2,3k}^V, \quad (2.304)$$

respectively. Similarly, the expressions for the particle velocity field belonging to the SH-TE propagation mode due to \hat{J}_1^e and \hat{f}_1^b , are

$$\check{v}_{norm}^{H;J_1^e} = -\frac{2jk_2}{\kappa} \hat{J}_1^e \sum_{k=1}^2 \check{L}_{1,1k}^H \check{\Gamma}_{kk}^H \check{G}_{kk}^H \check{L}_{1,2k}^H, \quad (2.305)$$

$$\check{v}_{norm}^{H;f_1^b} = -\frac{2jk_2}{\kappa} \hat{f}_1^b \sum_{k=1}^2 \check{L}_{1,1k}^H \check{\Gamma}_{kk}^H \check{G}_{kk}^H \check{L}_{1,1k}^H, \quad (2.306)$$

respectively. We can combine the particle velocity fields of both propagation modes into the particle velocity field in the x_1 -direction, via

$$\check{v}_1 = -jk_1 \check{v}_{norm}^V / \kappa + jk_2 \check{v}_{norm}^H / \kappa. \quad (2.307)$$

Combining equations (2.303), (2.305), and (2.307), as well as (2.304), (2.306), and (2.307), yields again the required analytical homogeneous space solution, which can be directly modeled and compared with the numerical results for a homogeneous medium as generated by seismo-EM layer-code modeling.

Chapter 3

The model: Theory of seismo-EM layer-code modeling

3.1 Global reflection scheme for seismo-EM layer-code modeling

3.1.1 Two-way and one-way fields

As we have seen, we can decompose the system matrix $\tilde{\mathbf{A}}^{H,V}$ into matrices consisting of its eigenvectors and eigenvalues, for both the SH-TE and the P-SV-TM propagation modes independently. The eigenvector matrices are also referred to as composition matrices, since they compose two-way field quantities from one-way fields. Vice versa, the inverse of the composition matrices are referred to as decomposition matrices, since they decompose two-way fields into one-way fields. The following general relation holds between the recorded two-way fields and the decomposed one-way fields

$$\begin{pmatrix} \tilde{\mathbf{q}}_1 \\ \tilde{\mathbf{q}}_2 \end{pmatrix} = \begin{pmatrix} \tilde{\mathbf{L}}_1 & \tilde{\mathbf{L}}_1 \\ \tilde{\mathbf{L}}_2 & -\tilde{\mathbf{L}}_2 \end{pmatrix} \begin{pmatrix} \tilde{\mathbf{p}}^+ \\ \tilde{\mathbf{p}}^- \end{pmatrix}, \quad (3.1)$$

where the + sign indicates downgoing fields (in the positive x_3 -direction) and the - sign indicates upgoing fields. In this chapter, we have omitted the superscripts H and V indicating the SH-TE and P-SV-TM propagation modes, respectively, for notational convenience. Be aware that each equation presented holds for both the SH-TE and P-SV-TM modes independently, since we have decoupled both modes in Section 2.2.2. For wavefields, $\tilde{\mathbf{p}}^+$ represents the one-way, decomposed downgoing field and $\tilde{\mathbf{p}}^-$ the one-way, decomposed upgoing field at a certain level of decomposition. For diffusive fields, $\tilde{\mathbf{p}}^+$ is the field that decays in the positive x_3 -direction and $\tilde{\mathbf{p}}^-$ is the field that decays in the negative x_3 -direction. Decomposed fields are not uniquely defined. The fields can be normalized with respect to different quantities. In principle any normalization of the composition matrix will work. We use power-flux normalized composition matrices. One of the advantages of using

power flux-normalization is that favourable reciprocity relations hold for the flux-normalized one-way fields (Frasier (1970), Wapenaar (1998)). In equation (3.1), $\tilde{\mathbf{q}}_1$ represents a subvector of the two-way field quantity vector $\tilde{\mathbf{q}}$, being composed from one-way fields by applying the $\tilde{\mathbf{L}}_1$ submatrices to the one-way fields $\tilde{\mathbf{p}}^\pm$. Similarly, $\tilde{\mathbf{q}}_2$ is the subvector being composed from one-way fields by applying the $\pm\tilde{\mathbf{L}}_2$ submatrices to the one-way fields $\tilde{\mathbf{p}}^\pm$.

In multi-component (MC) field decomposition schemes, the downgoing and upgoing one-way fields can be obtained by left-multiplying the recorded two-way field vector with the inverse of the composition matrix, where we make use of the power-flux normalization transpose-to-inverse property (e.g. equations (2.169) and (2.170)), yielding

$$\begin{pmatrix} \tilde{\mathbf{p}}^+ \\ \tilde{\mathbf{p}}^- \end{pmatrix} = \begin{pmatrix} \tilde{\mathbf{L}}_2^t & \tilde{\mathbf{L}}_1^t \\ \tilde{\mathbf{L}}_2^t & -\tilde{\mathbf{L}}_1^t \end{pmatrix} \begin{pmatrix} \tilde{\mathbf{q}}_1 \\ \tilde{\mathbf{q}}_2 \end{pmatrix}. \quad (3.2)$$

For a more extensive discussion on field decomposition, including the introduction of the Multi-Depth-Level Field Decomposition Scheme, the reader is referred to Section 6.1.

In our seismo-EM layer-code, we start by directly modeling one-way fields generated at the source-level, which are then propagating/diffusing through the layered-Earth model, and are finally composed into two-way fields at the receiver level. To correctly describe the propagation/diffusion of the fields through the layered-Earth model, we make use of a Global Reflection Scheme (based on the three-layer scalar reflection scheme by Airy (1833)). In the electromagnetic community, Redheffer (1961) solved the layered-Earth problem using the scattering matrix for electromagnetic waves, thereby introducing the so-called Redheffer star product. The reflectivity method of Kennett (1983) is basically built upon this work, and is well-known in the seismic community for modeling layered-Earth responses. There are some important differences between the reflectivity method of Kennett (1983) and our global reflection scheme. To solve the layered-Earth problem, Kennett (1983) uses the full scattering matrices, thereby explicitly requiring to calculate and store (computationally-speaking) both the upgoing and downgoing global reflection and transmission matrices at the interfaces in the model. To solve the layered-Earth problem, the method of Kennett (1983) requires his numerical scheme to calculate these matrices iteratively, stepping through the layered-model more than once. In our global reflection scheme, we express the system in terms of reflection matrices only. We distinguish local reflection matrices from global reflection matrices. This allows our iterative scheme to step through the layered-model more effectively. Our scheme also only requires calculation and storage of the global reflection matrices. In the presentation of our global reflection scheme, we will refer to the vertical spatial (depth) direction x_3 as z , for notational convenience.

3.1.2 Local and global reflection matrices

The local reflection operators, indicated by $\tilde{\mathbf{r}}$, describe the generation of outgoing fields from an incoming field due to the reflection at an interface between contrasting media. We define the local downgoing reflection matrix as follows

$$\tilde{\mathbf{p}}_n^-(z_{n+1}) = \tilde{\mathbf{r}}_n^{+}(z_{n+1})\tilde{\mathbf{W}}^+(z_{n+1}, z_n)\tilde{\mathbf{p}}_n^+(z_n), \quad (3.3)$$

where z_{n+1} is the depth of the interface under consideration, at the bottom of layer n and above layer $n+1$ (see also Figure 3.1). Equation (3.3) holds for wavefields generated above the interface under consideration. We read the superscript $-+$ from right to left, indicating that a downgoing one-way field ($\tilde{\mathbf{p}}_n^+$) reflects into an upgoing one-way field ($\tilde{\mathbf{p}}_n^-$) at that specific interface.

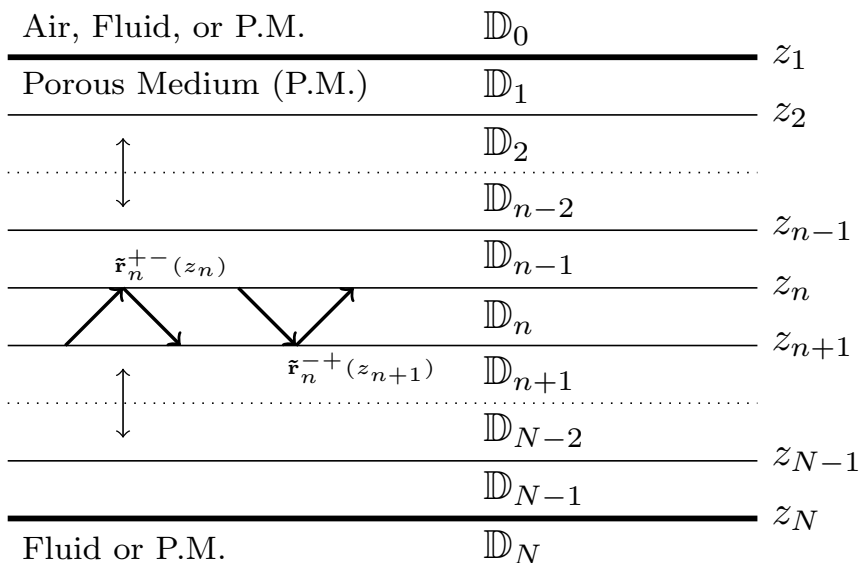


Figure 3.1: Schematic overview of the layered-Earth configurations used in ESSEMOD, indicating the interface- and layer-counting notational system. Here, \mathbb{D}_n indicates the layer counting (which corresponds to the subscript n under the quantities in the equations) and z_n denotes the interface counting (which corresponds to the z_n -arguments of the quantities in the equations). In addition, $\tilde{\mathbf{r}}_n^{+-}$ denotes a downgoing to upgoing local reflection coefficient, and $\tilde{\mathbf{r}}_n^{-+}$ an upgoing to downgoing local reflection coefficient. The same superscript notation holds for the global reflection coefficients.

The forward extrapolation operator $\tilde{\mathbf{W}}^+(z_{n+1}, z_n)$, extrapolates the downgoing fields downwards, from interface z_n to interface z_{n+1} . When using these extrapolation operators, it is implicitly assumed that the medium between the two depth levels is source-free and homogeneous. The downgoing and upgoing forward extrapolation operators $\tilde{\mathbf{W}}^+(z_{n+1}, z_n)$ and $\tilde{\mathbf{W}}^-(z_n, z_{n+1})$ are defined as

$$\tilde{\mathbf{W}}^+(z_{n+1}, z_n) = \tilde{\mathbf{W}}^-(z_n, z_{n+1}) = \exp(-\tilde{\mathbf{L}}(z_{n+1} - z_n)), \quad (3.4)$$

where $\tilde{\mathbf{\Lambda}}$ represents an n -by- n diagonal matrix containing the eigenvalues for each of the n -field types present in the system under consideration (for example $n = 2$ for the SH-TE mode, where SH and TE are the field types under consideration). Note that the above equation (3.4) is a symbolic notation (due to the use of a matrix in the argument of the exponent). Effectively, the exponent of each of the individual elements in diagonal matrix $\tilde{\mathbf{\Lambda}}$ is taken. Since we are dealing with laterally invariant media, $\tilde{\mathbf{\Lambda}}$ is a purely diagonal matrix as we have seen in Section 2.3. Note that it is crucial to define the sign of the field extrapolation operators in such a way that evanescent and diffusive fields decay. As discussed, we choose the positive sign of the square root, based on the fact that for the eigenvalue matrix, we desire that $\Re\{\Gamma_w\} > 0$, based on physical wave propagation constraints (Grobbe *et al.*, 2016b).

Similar to equation (3.3), the local upgoing reflection matrix, for wavefields generated below the interface under consideration, is defined as

$$\tilde{\mathbf{p}}_n^+(z_n) = \tilde{\mathbf{r}}_n^{+-}(z_n)\tilde{\mathbf{W}}^-(z_n, z_{n+1})\tilde{\mathbf{p}}_n^-(z_{n+1}). \quad (3.5)$$

The term *local* reflection matrix already indicates that these matrices only account for one reflection at one specific interface. To account for all multiple reflections behind the locally reflecting interface, a *global* reflection matrix $\tilde{\mathbf{R}}$ is defined as

$$\tilde{\mathbf{p}}_n^-(z_{n+1}) = \tilde{\mathbf{R}}_n^{-(z_{n+1})}\tilde{\mathbf{W}}^+(z_{n+1}, z_n)\tilde{\mathbf{p}}_n^+(z_n), \quad (3.6)$$

$$\tilde{\mathbf{p}}_n^+(z_n) = \tilde{\mathbf{R}}_n^{+(z_n)}\tilde{\mathbf{W}}^-(z_n, z_{n+1})\tilde{\mathbf{p}}_n^-(z_{n+1}), \quad (3.7)$$

with equation (3.6) describing the downgoing global reflection matrix and equation (3.7) representing the upgoing global reflection matrix. Equation (3.6) holds for locations z below the source location z_s , i.e. for $z > z_s$. On the contrary, equation (3.7) holds for locations z above the source location z_s , i.e. for $z < z_s$.

To extrapolate the local or global reflection matrices away from the interface to an arbitrary depth level z in a homogeneous source-free subdomain, between z_n and z_{n+1} , the wavefield extrapolators $\tilde{\mathbf{W}}$ (equation (3.4)) are used as follows

$$\tilde{\mathbf{p}}_n^-(z) = \tilde{\mathbf{W}}^-(z, z_{n+1})\tilde{\mathbf{p}}_n^-(z_{n+1}), \quad (3.8)$$

$$\tilde{\mathbf{p}}_n^+(z) = \tilde{\mathbf{W}}^+(z, z_n)\tilde{\mathbf{p}}_n^+(z_n). \quad (3.9)$$

Now, recognizing and substituting equations (3.6) and (3.7), yields

$$\tilde{\mathbf{p}}_n^-(z) = \tilde{\mathbf{W}}^-(z, z_{n+1})\tilde{\mathbf{R}}_n^{-(z_{n+1})}\tilde{\mathbf{W}}^+(z_{n+1}, z_n)\tilde{\mathbf{p}}_n^+(z_n), \quad (3.10)$$

$$\tilde{\mathbf{p}}_n^+(z) = \tilde{\mathbf{W}}^+(z, z_n)\tilde{\mathbf{R}}_n^{+(z_n)}\tilde{\mathbf{W}}^-(z_n, z_{n+1})\tilde{\mathbf{p}}_n^-(z_{n+1}). \quad (3.11)$$

Using the relations

$$\tilde{\mathbf{W}}^-(z, z_{n+1}) = \tilde{\mathbf{W}}^+(z_{n+1}, z), \quad (3.12)$$

$$\tilde{\mathbf{W}}^+(z, z_n) = \tilde{\mathbf{W}}^-(z_n, z), \quad (3.13)$$

yields

$$\tilde{\mathbf{p}}_n^-(z) = \tilde{\mathbf{W}}^+(z_{n+1}, z)\tilde{\mathbf{R}}_n^{-(z_{n+1})}\tilde{\mathbf{W}}^+(z_{n+1}, z_n)\tilde{\mathbf{p}}_n^+(z_n), \quad (3.14)$$

$$\tilde{\mathbf{p}}_n^+(z) = \tilde{\mathbf{W}}^-(z_n, z)\tilde{\mathbf{R}}_n^{+(z_n)}\tilde{\mathbf{W}}^-(z_n, z_{n+1})\tilde{\mathbf{p}}_n^-(z_{n+1}). \quad (3.15)$$

From these two equations, we can extract expressions for the global down- and upgoing reflection matrices at an arbitrary depth level z in layer n , $\tilde{\mathbf{R}}_n^{-+,+-}$:

$$\tilde{\mathbf{R}}_n^{-+}(z) = \tilde{\mathbf{W}}^+(z_{n+1}, z) \tilde{\mathbf{R}}_n^{-+}(z_{n+1}) \tilde{\mathbf{W}}^+(z_{n+1}, z_n), \quad (3.16)$$

$$\tilde{\mathbf{R}}_n^{+-}(z) = \tilde{\mathbf{W}}^-(z_n, z) \tilde{\mathbf{R}}_n^{+-}(z_n) \tilde{\mathbf{W}}^-(z_n, z_{n+1}), \quad (3.17)$$

where the calligraphic font $\tilde{\mathbf{R}}$ denotes that these global reflection matrices are ‘special’ in the sense that they are the result of extrapolation operators acting upon the ‘standard’ global reflection matrices defined at the interfaces.

3.1.3 Calculating the global reflection matrices outside the source layer

Considering the boundary conditions at an interface z_{n+1}

$$\lim_{z \downarrow z_{n+1}} \tilde{\mathbf{q}}_{n+1}(z) - \lim_{z \uparrow z_{n+1}} \tilde{\mathbf{q}}_n(z) = 0, \quad (3.18)$$

and evaluating the limits yields

$$\tilde{\mathbf{q}}_n(z_{n+1}) = \tilde{\mathbf{q}}_{n+1}(z_{n+1}). \quad (3.19)$$

Substitution of $\tilde{\mathbf{q}}_n = \tilde{\mathbf{L}} \tilde{\mathbf{p}}_n$ results in

$$\tilde{\mathbf{L}}_n \tilde{\mathbf{p}}_n(z_{n+1}) = \tilde{\mathbf{L}}_{n+1} \tilde{\mathbf{p}}_{n+1}(z_{n+1}). \quad (3.20)$$

As shown before (e.g equation (2.161)), the flux-normalized composition matrix $\tilde{\mathbf{L}}$ is organized as

$$\tilde{\mathbf{L}} = \begin{pmatrix} \tilde{\mathbf{L}}_1 & \tilde{\mathbf{L}}_1 \\ \tilde{\mathbf{L}}_2 & -\tilde{\mathbf{L}}_2 \end{pmatrix}. \quad (3.21)$$

Using this property of $\tilde{\mathbf{L}}$, separating the down- and upgoing one-way fields and substituting it into (3.20) results in

$$\tilde{\mathbf{L}}_{1,n} \tilde{\mathbf{p}}_n^+(z_{n+1}) + \tilde{\mathbf{L}}_{1,n} \tilde{\mathbf{p}}_n^-(z_{n+1}) = \tilde{\mathbf{L}}_{1,n+1} \tilde{\mathbf{p}}_{n+1}^+(z_{n+1}) + \tilde{\mathbf{L}}_{1,n+1} \tilde{\mathbf{p}}_{n+1}^-(z_{n+1}), \quad (3.22)$$

$$\tilde{\mathbf{L}}_{2,n} \tilde{\mathbf{p}}_n^+(z_{n+1}) - \tilde{\mathbf{L}}_{2,n} \tilde{\mathbf{p}}_n^-(z_{n+1}) = \tilde{\mathbf{L}}_{2,n+1} \tilde{\mathbf{p}}_{n+1}^+(z_{n+1}) - \tilde{\mathbf{L}}_{2,n+1} \tilde{\mathbf{p}}_{n+1}^-(z_{n+1}). \quad (3.23)$$

We use equations (3.6) and (3.14) (and recognize equation (3.16)), and we evaluate the fields at $z = z_{n+1}$, leading to

$$\tilde{\mathbf{p}}_n^-(z_{n+1}) = \tilde{\mathbf{R}}_n^{-+}(z_{n+1})\tilde{\mathbf{p}}_n^+(z_{n+1}), \quad (3.24)$$

$$\tilde{\mathbf{p}}_{n+1}^-(z_{n+1}) = \tilde{\mathbf{R}}_{n+1}^{-+}(z_{n+1})\tilde{\mathbf{p}}_{n+1}^+(z_{n+1}). \quad (3.25)$$

Here, $\tilde{\mathbf{p}}_n^-(z_{n+1})$ is the upgoing one-way field in the n^{th} -layer (above the interface), at interface z_{n+1} , whereas $\tilde{\mathbf{p}}_{n+1}^-(z_{n+1})$ is the upgoing field in layer $n+1$ (below the interface), at interface z_{n+1} . Substituting equations (3.24) and (3.25) into equations (3.22) and (3.23), results in

$$\tilde{\mathbf{L}}_{1,n} [\mathbf{I} + \mathbf{R}_n^{-+}(z_{n+1})] \tilde{\mathbf{p}}_n^+(z_{n+1}) = \tilde{\mathbf{L}}_{1,n+1} [\mathbf{I} + \tilde{\mathbf{R}}_{n+1}^{-+}(z_{n+1})] \tilde{\mathbf{p}}_{n+1}^+(z_{n+1}), \quad (3.26)$$

$$\tilde{\mathbf{L}}_{2,n} [\mathbf{I} - \mathbf{R}_n^{-+}(z_{n+1})] \tilde{\mathbf{p}}_n^+(z_{n+1}) = \tilde{\mathbf{L}}_{2,n+1} [\mathbf{I} - \tilde{\mathbf{R}}_{n+1}^{-+}(z_{n+1})] \tilde{\mathbf{p}}_{n+1}^+(z_{n+1}). \quad (3.27)$$

Using equations (3.26) and (3.27), we express the global, downgoing reflection matrix $\tilde{\mathbf{R}}_n^{-+}(z_{n+1})$ in terms of $\tilde{\mathbf{R}}_{n+1}^{-+}(z_{n+1})$:

$$\begin{aligned} \tilde{\mathbf{R}}_n^{-+}(z_{n+1}) = & \left[\left(\tilde{\mathbf{L}}_{1,n}^{\text{down}} - \tilde{\mathbf{L}}_{2,n}^{\text{down}} \right) + \left(\tilde{\mathbf{L}}_{1,n}^{\text{down}} + \tilde{\mathbf{L}}_{2,n}^{\text{down}} \right) \tilde{\mathbf{R}}_{n+1}^{-+}(z_{n+1}) \right] \times \\ & \left[\left(\tilde{\mathbf{L}}_{1,n}^{\text{down}} + \tilde{\mathbf{L}}_{2,n}^{\text{down}} \right) + \left(\tilde{\mathbf{L}}_{1,n}^{\text{down}} - \tilde{\mathbf{L}}_{2,n}^{\text{down}} \right) \tilde{\mathbf{R}}_{n+1}^{-+}(z_{n+1}) \right]^{-1}, \end{aligned} \quad (3.28)$$

where the cross-symbol (\times) simply denotes a matrix-matrix multiplication and where

$$\tilde{\mathbf{L}}_{1,n}^{\text{down}} = \left[\tilde{\mathbf{L}}_{1,n} \right]^{-1} \tilde{\mathbf{L}}_{1,n+1} = 2\tilde{\mathbf{L}}_{2,n}^t \tilde{\mathbf{L}}_{1,n+1}, \quad (3.29)$$

$$\tilde{\mathbf{L}}_{2,n}^{\text{down}} = \left[\tilde{\mathbf{L}}_{2,n} \right]^{-1} \tilde{\mathbf{L}}_{2,n+1} = 2\tilde{\mathbf{L}}_{1,n}^t \tilde{\mathbf{L}}_{2,n+1}. \quad (3.30)$$

Here, we have exploited the fact that we have power-flux normalized the composition and decomposition matrices, enabling us to write the inverse of a composition submatrix as the transpose of another composition submatrix. This expression can be used for reflectors below the source level.

Equation (3.28) is the matrix-vector equivalent of an equation presented by Fokkema & Ziolkowski (1987). Using equation (3.28), we can calculate the global downgoing reflection matrix at any interface, starting from the bottom interface of the model and recursively updating the operator upwards. There will be no reflections created from below the bottom interface of the model, located at z_N . In other words, $\tilde{\mathbf{R}}_N^{-+}(z > z_N) = 0$, changing equation (3.28) for the bottom interface into

$$\tilde{\mathbf{R}}_{N-1}^{-+}(z_N) = \tilde{\mathbf{r}}_{N-1}^{-+}(z_N) = \left(\tilde{\mathbf{L}}_{1,N-1}^{\text{down}} - \tilde{\mathbf{L}}_{2,N-1}^{\text{down}} \right) \left(\tilde{\mathbf{L}}_{1,N-1}^{\text{down}} + \tilde{\mathbf{L}}_{2,N-1}^{\text{down}} \right)^{-1}. \quad (3.31)$$

The reflection at the bottom interface can be purely described by a local downgoing reflection matrix. We use this definition of the local reflection matrix (equation

(3.31)), that holds for each individual interface, to rewrite equation (3.28) as

$$\begin{aligned} \tilde{\mathbf{R}}_n^{++}(z_{n+1}) = & \left[\tilde{\mathbf{r}}_n^{++}(z_{n+1}) + \left(\tilde{\mathbf{L}}_{1,n}^{down} + \tilde{\mathbf{L}}_{2,n}^{down} \right) \tilde{\mathbf{R}}_{n+1}^{++}(z_{n+1}) \left(\tilde{\mathbf{L}}_{1,n}^{down} + \tilde{\mathbf{L}}_{2,n}^{down} \right)^{-1} \right] \times \\ & \left[\mathbf{I} + \left(\tilde{\mathbf{L}}_{1,n}^{down} - \tilde{\mathbf{L}}_{2,n}^{down} \right) \tilde{\mathbf{R}}_{n+1}^{++}(z_{n+1}) \left(\tilde{\mathbf{L}}_{1,n}^{down} + \tilde{\mathbf{L}}_{2,n}^{down} \right)^{-1} \right]^{-1}. \end{aligned} \quad (3.32)$$

We can derive a similar expression for the global upgoing reflection matrix (for reflectors above the source level). We start with

$$\tilde{\mathbf{L}}_{1,n} \left[\tilde{\mathbf{R}}_n^{+-}(z_{n+1}) + \mathbf{I} \right] \tilde{\mathbf{p}}_n^-(z_{n+1}) = \tilde{\mathbf{L}}_{1,n+1} \left[\tilde{\mathbf{R}}_{n+1}^{+-}(z_{n+1}) + \mathbf{I} \right] \tilde{\mathbf{p}}_{n+1}^-(z_{n+1}), \quad (3.33)$$

$$\tilde{\mathbf{L}}_{2,n} \left[\tilde{\mathbf{R}}_n^{+-}(z_{n+1}) - \mathbf{I} \right] \tilde{\mathbf{p}}_n^-(z_{n+1}) = \tilde{\mathbf{L}}_{2,n+1} \left[\tilde{\mathbf{R}}_{n+1}^{+-}(z_{n+1}) - \mathbf{I} \right] \tilde{\mathbf{p}}_{n+1}^-(z_{n+1}). \quad (3.34)$$

Using equations (3.33) and (3.34), we express the global, upgoing reflection matrix $\tilde{\mathbf{R}}_{n+1}^{+-}(z_{n+1})$ in terms of $\tilde{\mathbf{R}}_n^{+-}(z_{n+1})$:

$$\begin{aligned} \tilde{\mathbf{R}}_{n+1}^{+-}(z_{n+1}) = & \left[\left(\tilde{\mathbf{L}}_{1,n}^{up} - \tilde{\mathbf{L}}_{2,n}^{up} \right) + \left(\tilde{\mathbf{L}}_{1,n}^{up} + \tilde{\mathbf{L}}_{2,n}^{up} \right) \tilde{\mathbf{R}}_n^{+-}(z_{n+1}) \right] \times \\ & \left[\left(\tilde{\mathbf{L}}_{1,n}^{up} + \tilde{\mathbf{L}}_{2,n}^{up} \right) + \left(\tilde{\mathbf{L}}_{1,n}^{up} - \tilde{\mathbf{L}}_{2,n}^{up} \right) \tilde{\mathbf{R}}_n^{+-}(z_{n+1}) \right]^{-1}, \end{aligned} \quad (3.35)$$

where

$$\tilde{\mathbf{L}}_{1,n}^{up} = \left[\tilde{\mathbf{L}}_{1,n+1} \right]^{-1} \tilde{\mathbf{L}}_{1,n} = 2\tilde{\mathbf{L}}_{2,n+1}^t \tilde{\mathbf{L}}_{1,n}, \quad (3.36)$$

$$\tilde{\mathbf{L}}_{2,n}^{up} = \left[\tilde{\mathbf{L}}_{2,n+1} \right]^{-1} \tilde{\mathbf{L}}_{2,n} = 2\tilde{\mathbf{L}}_{1,n+1}^t \tilde{\mathbf{L}}_{2,n}, \quad (3.37)$$

and

$$\tilde{\mathbf{R}}_n^{+-}(z_{n+1}) = \tilde{\mathbf{W}}^-(z_n, z_{n+1}) \tilde{\mathbf{R}}_n^{+-}(z_n) \tilde{\mathbf{W}}^-(z_n, z_{n+1}). \quad (3.38)$$

We can use equation (3.35) to iteratively determine the global upgoing reflection matrix, starting at the upper interface of the model and moving downwards. There are no reflections occurring above the upper interface of the model. In other words, $\tilde{\mathbf{R}}_1^{+-}(z < z_1) = 0$ in equation (3.35), yielding

$$\tilde{\mathbf{R}}_1^{+-}(z_1) = \tilde{\mathbf{r}}_1^{+-}(z_1) = \left(\tilde{\mathbf{L}}_{1,0}^{up} - \tilde{\mathbf{L}}_{2,0}^{up} \right) \left(\tilde{\mathbf{L}}_{1,0}^{up} + \tilde{\mathbf{L}}_{2,0}^{up} \right)^{-1}, \quad (3.39)$$

for the upper interface. Recognizing this definition of the local upgoing reflection matrix (for each individual interface) in equation (3.35), yields

$$\begin{aligned} \tilde{\mathbf{R}}_{n+1}^{+-}(z_{n+1}) &= \left[\tilde{\mathbf{r}}_{n+1}^{+-}(z_{n+1}) + \left(\tilde{\mathbf{L}}_{1,n}^{up} + \tilde{\mathbf{L}}_{2,n}^{up} \right) \tilde{\mathcal{R}}_n^{+-}(z_{n+1}) \left(\tilde{\mathbf{L}}_{1,n}^{up} + \tilde{\mathbf{L}}_{2,n}^{up} \right)^{-1} \right] \times \\ &\quad \left[\mathbf{I} + \left(\tilde{\mathbf{L}}_{1,n}^{up} - \tilde{\mathbf{L}}_{2,n}^{up} \right) \tilde{\mathcal{R}}_n^{+-}(z_{n+1}) \left(\tilde{\mathbf{L}}_{1,n}^{up} + \tilde{\mathbf{L}}_{2,n}^{up} \right)^{-1} \right]^{-1}. \end{aligned} \quad (3.40)$$

Equations (3.32) and (3.40) form the basis of the recursive global reflection scheme.

3.1.4 Calculating the global reflection matrices in a homogeneous bounded subdomain with sources

Imagine a homogeneous bounded subdomain with a source at source level $z = z_s$, where z_s is not the depth of an interface. Fields above the source level are denoted with a superscript a and fields below the source level with superscript b . Evaluating the boundary condition at this source level z_s , results in

$$\lim_{z \downarrow z_s} \tilde{\mathbf{q}}_n^b(z) - \lim_{z \uparrow z_s} \tilde{\mathbf{q}}_n^a(z) = \tilde{\mathbf{d}}_n(z_s). \quad (3.41)$$

Writing this equation in terms of one-way fields/sources, gives

$$\tilde{\mathbf{L}}_n \tilde{\mathbf{p}}_n^b(z_s) - \tilde{\mathbf{L}}_n \tilde{\mathbf{p}}_n^a(z_s) = \tilde{\mathbf{L}}_n \tilde{\mathbf{b}}_n(z_s). \quad (3.42)$$

As can be seen, the composition matrix $\tilde{\mathbf{L}}_n$ can be divided out on the left-hand and right-hand sides. By writing the up- and downgoing one-way fields explicitly, the following relations are obtained:

$$\tilde{\mathbf{p}}_n^{b,+}(z_s) = \tilde{\mathbf{p}}_n^{a,+}(z_s) + \tilde{\mathbf{b}}_n^+(z_s), \quad (3.43)$$

$$\tilde{\mathbf{p}}_n^{b,-}(z_s) = \tilde{\mathbf{p}}_n^{a,-}(z_s) + \tilde{\mathbf{b}}_n^-(z_s). \quad (3.44)$$

Using equation (3.8) to obtain the upgoing one-way fields (from below) at the source level z_s and writing it in terms of downgoing one-way fields below the source level, yields

$$\begin{aligned} \tilde{\mathbf{p}}_n^{b,-}(z_s) &= \tilde{\mathbf{W}}^-(z_s, z_{n+1}) \tilde{\mathbf{R}}_n^{+}(z_{n+1}) \tilde{\mathbf{W}}^+(z_{n+1}, z_s) \tilde{\mathbf{p}}_n^{b,+}(z_s) \\ &= \tilde{\mathbf{W}}^+(z_{n+1}, z_s) \tilde{\mathbf{R}}_n^{+}(z_{n+1}) \tilde{\mathbf{W}}^+(z_{n+1}, z_s) \tilde{\mathbf{p}}_n^{b,+}(z_s) \\ &= \tilde{\mathbf{R}}_n^{+}(z_s) \tilde{\mathbf{p}}_n^{b,+}(z_s). \end{aligned} \quad (3.45)$$

In a similar way the downgoing one-way fields (from above) at the source level can be written in terms of the upgoing one-way fields above the source level as

$$\begin{aligned}
\tilde{\mathbf{p}}_n^{a,+}(z_s) &= \tilde{\mathbf{W}}^+(z_s, z_n) \tilde{\mathbf{R}}_n^{+-}(z_n) \tilde{\mathbf{W}}^-(z_n, z_s) \tilde{\mathbf{p}}_n^{a,-}(z_s) \\
&= \tilde{\mathbf{W}}^-(z_n, z_s) \tilde{\mathbf{R}}_n^{+-}(z_n) \tilde{\mathbf{W}}^-(z_n, z_s) \tilde{\mathbf{p}}_n^{a,-}(z_s) \\
&= \tilde{\mathbf{R}}_n^{+-}(z_s) \tilde{\mathbf{p}}_n^{a,-}(z_s).
\end{aligned} \tag{3.46}$$

Combining equations (3.43), (3.44), (3.45) and (3.46) results in the following expressions for the four possible one-way wavefields (up- and downgoing, above and below the source level):

$$\begin{aligned}
\tilde{\mathbf{p}}_n^{a,+}(z_s) &= \left[\mathbf{I} - \tilde{\mathbf{R}}_n^{+-}(z_s) \tilde{\mathbf{R}}_n^{-+}(z_s) \right]^{-1} \times \\
&\quad \left[\tilde{\mathbf{R}}_n^{+-}(z_s) \tilde{\mathbf{R}}_n^{-+}(z_s) \tilde{\mathbf{b}}^+(z_s) - \tilde{\mathbf{R}}_n^{+-}(z_s) \tilde{\mathbf{b}}^-(z_s) \right],
\end{aligned} \tag{3.47}$$

$$\begin{aligned}
\tilde{\mathbf{p}}_n^{a,-}(z_s) &= \left[\mathbf{I} - \tilde{\mathbf{R}}_n^{-+}(z_s) \tilde{\mathbf{R}}_n^{+-}(z_s) \right]^{-1} \times \\
&\quad \left[\tilde{\mathbf{R}}_n^{-+}(z_s) \tilde{\mathbf{b}}^+(z_s) - \tilde{\mathbf{b}}^-(z_s) \right],
\end{aligned} \tag{3.48}$$

$$\begin{aligned}
\tilde{\mathbf{p}}_n^{b,+}(z_s) &= \left[\mathbf{I} - \tilde{\mathbf{R}}_n^{+-}(z_s) \tilde{\mathbf{R}}_n^{-+}(z_s) \right]^{-1} \times \\
&\quad \left[\tilde{\mathbf{b}}^+(z_s) - \tilde{\mathbf{R}}_n^{+-}(z_s) \tilde{\mathbf{b}}^-(z_s) \right],
\end{aligned} \tag{3.49}$$

$$\begin{aligned}
\tilde{\mathbf{p}}_n^{b,-}(z_s) &= \left[\mathbf{I} - \tilde{\mathbf{R}}_n^{-+}(z_s) \tilde{\mathbf{R}}_n^{+-}(z_s) \right]^{-1} \times \\
&\quad \left[\tilde{\mathbf{R}}_n^{-+}(z_s) \tilde{\mathbf{b}}^+(z_s) - \tilde{\mathbf{R}}_n^{-+}(z_s) \tilde{\mathbf{R}}_n^{+-}(z_s) \tilde{\mathbf{b}}^-(z_s) \right].
\end{aligned} \tag{3.50}$$

We can clearly recognize the multiple-generator, the terms on the right-hand side between the brackets indicating the inverse. We now consider three possible modeling scenarios:

1. Source and Receivers in the same layer (with receivers (slightly) above or below the source), in ESSEMOD referred to as ‘above=0’
2. Source and Receivers in different layers, with receivers below the source, in ESSEMOD referred to as ‘above=-1’
3. Source and Receivers in different layers, with receivers above the source, in ESSEMOD referred to as ‘above=1’.

Let us first consider scenario 1. In this case, we treat the direct field separately, using homogeneous-space Green’s function solutions which we add to the final solution in the space-frequency domain. Therefore, we can skip equations (3.48) and (3.49), and only need equations (3.47) and (3.50). We define the receiver depth level as z_r , and rewrite the equations such that we record the one-way down- or upgoing fields of the left-hand side of the equations at z_r , generated by a one-way down- or

upgoing source on the right-hand side at z_s :

$$\tilde{\mathbf{p}}_n^{a,++}(z_r) = \left[\mathbf{I} - \tilde{\mathbf{R}}_n^{+-}(z_n, z_{n+1}) \tilde{\mathbf{R}}_n^{-+}(z_{n+1}, z_n) \right]^{-1} \times \left[\tilde{\mathbf{R}}_n^{+-}(z_r, z_s) \tilde{\mathbf{R}}_n^{-+}(z_s, z_s) \tilde{\mathbf{b}}^+(z_s) \right], \quad (3.51)$$

$$\tilde{\mathbf{p}}_n^{a,+^-}(z_r) = \left[\mathbf{I} - \tilde{\mathbf{R}}_n^{+-}(z_n, z_{n+1}) \tilde{\mathbf{R}}_n^{-+}(z_{n+1}, z_n) \right]^{-1} \times \left[-\tilde{\mathbf{R}}_n^{+-}(z_r, z_s) \tilde{\mathbf{b}}^-(z_s) \right], \quad (3.52)$$

$$\tilde{\mathbf{p}}_n^{b,-+}(z_r) = \left[\mathbf{I} - \tilde{\mathbf{R}}_n^{-+}(z_{n+1}, z_n) \tilde{\mathbf{R}}_n^{+-}(z_n, z_{n+1}) \right]^{-1} \times \left[\tilde{\mathbf{R}}_n^{-+}(z_r, z_s) \tilde{\mathbf{b}}^+(z_s) \right], \quad (3.53)$$

$$\tilde{\mathbf{p}}_n^{b,-^-}(z_r) = \left[\mathbf{I} - \tilde{\mathbf{R}}_n^{-+}(z_{n+1}, z_n) \tilde{\mathbf{R}}_n^{+-}(z_n, z_{n+1}) \right]^{-1} \times \left[-\tilde{\mathbf{R}}_n^{-+}(z_r, z_s) \tilde{\mathbf{R}}_n^{+-}(z_s, z_s) \tilde{\mathbf{b}}^-(z_s) \right], \quad (3.54)$$

where

$$\tilde{\mathbf{R}}_n^{+-}(z_n, z_{n+1}) = \tilde{\mathbf{R}}_n^{+-}(z_n) \tilde{\mathbf{W}}^-(z_n, z_{n+1}), \quad (3.55)$$

$$\tilde{\mathbf{R}}_n^{-+}(z_{n+1}, z_n) = \tilde{\mathbf{R}}_n^{-+}(z_{n+1}) \tilde{\mathbf{W}}^+(z_{n+1}, z_n), \quad (3.56)$$

$$\tilde{\mathbf{R}}_n^{+-}(z_r, z_s) = \tilde{\mathbf{W}}^+(z_r, z_n) \tilde{\mathbf{R}}_n^{+-}(z_n) \tilde{\mathbf{W}}^-(z_n, z_s), \quad (3.57)$$

$$\tilde{\mathbf{R}}_n^{-+}(z_s, z_s) = \tilde{\mathbf{W}}^-(z_s, z_{n+1}) \tilde{\mathbf{R}}_n^{-+}(z_{n+1}) \tilde{\mathbf{W}}^+(z_{n+1}, z_s). \quad (3.58)$$

$$(3.59)$$

For scenario 2, we only require equation (3.49). Since in this case, the receivers are located in a layer below the source layer, we describe the one-way fields until the lower interface of the source layer:

$$\tilde{\mathbf{p}}_n^{b,++}(z_{n+1}) = \tilde{\mathbf{W}}^+(z_{n+1}, z_s) \left[\mathbf{I} - \tilde{\mathbf{R}}_n^{+-}(z_n, z_{n+1}) \tilde{\mathbf{R}}_n^{-+}(z_{n+1}, z_n) \right]^{-1} \tilde{\mathbf{b}}^+(z_s), \quad (3.60)$$

$$\tilde{\mathbf{p}}_n^{b,+^-}(z_{n+1}) = \left[\mathbf{I} - \tilde{\mathbf{R}}_n^{+-}(z_{n+1}, z_n) \tilde{\mathbf{R}}_n^{-+}(z_n, z_{n+1}) \right]^{-1} \left[-\tilde{\mathbf{R}}_n^{+-}(z_{n+1}, z_s) \tilde{\mathbf{b}}^-(z_s) \right], \quad (3.61)$$

where

$$\tilde{\mathbf{R}}_n^{+-}(z_{n+1}, z_s) = \tilde{\mathbf{W}}^+(z_{n+1}, z_n) \tilde{\mathbf{R}}_n^{+-}(z_n) \tilde{\mathbf{W}}^-(z_n, z_s). \quad (3.62)$$

From here onwards, either full layer propagation will take place (through one or multiple layers, dependent on the receiver location), or propagation over a small distance in the receiver layer to the receiver level. Let us briefly take a closer look at the multiple generator, e.g $\left[\mathbf{I} - \tilde{\mathbf{R}}_n^{+-}(z_n, z_{n+1}) \tilde{\mathbf{R}}_n^{-+}(z_{n+1}, z_n) \right]^{-1}$. We can expand this function as

$$\begin{aligned}
& \left[\mathbf{I} - \tilde{\mathbf{R}}_n^{+-}(z_n, z_{n+1}) \tilde{\mathbf{R}}_n^{-+}(z_{n+1}, z_n) \right]^{-1} = \left[\mathbf{I} - \tilde{\mathbf{R}}_n^{+-}(z_n, z_{n+1}) \tilde{\mathbf{R}}_n^{-+}(z_{n+1}, z_n) \right]^{-1} \times \\
& \left(\left[\mathbf{I} - \tilde{\mathbf{R}}_n^{+-}(z_n, z_{n+1}) \tilde{\mathbf{R}}_n^{-+}(z_{n+1}, z_n) \right] + \tilde{\mathbf{R}}_n^{+-}(z_n, z_{n+1}) \tilde{\mathbf{R}}_n^{-+}(z_{n+1}, z_n) \right) \\
& = \mathbf{I} + \left[\mathbf{I} - \tilde{\mathbf{R}}_n^{+-}(z_n, z_{n+1}) \tilde{\mathbf{R}}_n^{-+}(z_{n+1}, z_n) \right]^{-1} \tilde{\mathbf{R}}_n^{+-}(z_n, z_{n+1}) \tilde{\mathbf{R}}_n^{-+}(z_{n+1}, z_n). \quad (3.63)
\end{aligned}$$

Substituting this in equation (3.60), leads to

$$\begin{aligned}
\tilde{\mathbf{p}}_n^{b,++}(z_{n+1}) &= \tilde{\mathbf{W}}^+(z_{n+1}, z_s) \tilde{\mathbf{b}}^+(z_s) + \\
& \tilde{\mathbf{W}}^+(z_{n+1}, z_s) \left[\mathbf{I} - \tilde{\mathbf{R}}_n^{+-}(z_n, z_{n+1}) \tilde{\mathbf{R}}_n^{-+}(z_{n+1}, z_n) \right]^{-1} \times \\
& \tilde{\mathbf{R}}_n^{+-}(z_n, z_{n+1}) \tilde{\mathbf{R}}_n^{-+}(z_{n+1}, z_n) \tilde{\mathbf{b}}^+(z_s), \quad (3.64)
\end{aligned}$$

where we clearly recognize the expression for $\tilde{\mathbf{p}}_n^{a,++}$ of equation (3.51) (with adjusted arguments). In addition, comparing equations (3.52) and (3.61), we can observe that they are identical (with adjusted arguments). This shows that we do not require the other two expressions, since they are implicitly present.

Similarly, for scenario 3, we only require equation (3.48). Since in this case, the receivers are located in a layer above the source layer, we describe the one-way fields until the upper interface of the source layer:

$$\tilde{\mathbf{p}}_n^{a,-}(z_n) = \tilde{\mathbf{W}}^-(z_n, z_s) \left[\mathbf{I} - \tilde{\mathbf{R}}_n^{+-}(z_{n+1}, z_n) \tilde{\mathbf{R}}_n^{-+}(z_n, z_{n+1}) \right]^{-1} \tilde{\mathbf{b}}^-(z_s), \quad (3.65)$$

$$\tilde{\mathbf{p}}_n^{a,+}(z_{n+1}) = \left[\mathbf{I} - \tilde{\mathbf{R}}_n^{-+}(z_{n+1}, z_n) \tilde{\mathbf{R}}_n^{+-}(z_n, z_{n+1}) \right]^{-1} \left[-\tilde{\mathbf{R}}_n^{-+}(z_n, z_s) \tilde{\mathbf{b}}^+(z_s) \right], \quad (3.66)$$

where

$$\tilde{\mathbf{R}}_n^{-+}(z_n, z_s) = \tilde{\mathbf{W}}^-(z_n, z_{n+1}) \tilde{\mathbf{R}}_n^{-+}(z_{n+1}) \tilde{\mathbf{W}}^+(z_{n+1}, z_s). \quad (3.67)$$

From here onwards, these fields can be transmitted across the interface, after which either full layer propagation will take place (through one or multiple layers, dependent on the receiver location), or propagation over a small distance (in the receiver layer) to the receiver level. The proper transmission of fields across interfaces will be addressed next.

3.1.5 Calculating the one-way fields outside the source layer

Thusfar, we have considered the reflection of fields from the interfaces in the model. However, the transmission of fields across interfaces also needs to be properly addressed. Let us start by considering a geometry where the source is located above the receiver level. We know the downgoing field $\tilde{\mathbf{p}}_n^+(z_{n+1})$ and can express the upgoing field as:

$$\tilde{\mathbf{p}}_n^-(z_{n+1}) = \tilde{\mathbf{R}}_n^{-+}(z_{n+1}) \tilde{\mathbf{p}}_n^+(z_{n+1}). \quad (3.68)$$

Similarly, we can express the upgoing field at the other side of the interface as

$$\tilde{\mathbf{p}}_{n+1}^-(z_{n+1}) = \tilde{\mathbf{R}}_{n+1}^{+}(z_{n+1})\tilde{\mathbf{p}}_{n+1}^+(z_{n+1}). \quad (3.69)$$

In this geometry, the only ‘unknown’ field is $\tilde{\mathbf{p}}_{n+1}^+(z_{n+1})$.

Let us consider again the boundary conditions at a source-free interface at depth $z = z_{n+1}$, below the source level $z = z_s$,

$$\lim_{z \downarrow z_{n+1}} \tilde{\mathbf{q}}_{n+1}(z) - \lim_{z \uparrow z_{n+1}} \tilde{\mathbf{q}}_n(z) = \mathbf{0}. \quad (3.70)$$

We express the limit of equation (3.70) in terms of one-way fields and bring one term to the other side of the equation, yielding

$$\tilde{\mathbf{L}}_{n+1}\tilde{\mathbf{p}}_{n+1}(z_{n+1}) = \tilde{\mathbf{L}}_n\tilde{\mathbf{p}}_n(z_{n+1}). \quad (3.71)$$

Expressing everything in terms of the downgoing fields, and isolating the unknown field $\tilde{\mathbf{p}}_{n+1}^+(z_{n+1})$, yields

$$\begin{aligned} \tilde{\mathbf{p}}_{n+1}^+(z_{n+1}) &= \left[\mathbf{I} + \tilde{\mathbf{R}}_{n+1}^{+}(z_{n+1}) \right]^{-1} \tilde{\mathbf{L}}_{1,n+1}^{-1} \tilde{\mathbf{L}}_{1,n} \left[\mathbf{I} + \tilde{\mathbf{R}}_n^{+}(z_{n+1}) \right] \tilde{\mathbf{p}}_n^+(z_{n+1}) \\ &= \left[\mathbf{I} + \tilde{\mathbf{R}}_{n+1}^{+}(z_{n+1}) \right]^{-1} 2\tilde{\mathbf{L}}_{2,n+1}^t \tilde{\mathbf{L}}_{1,n} \left[\mathbf{I} + \tilde{\mathbf{R}}_n^{+}(z_{n+1}) \right] \tilde{\mathbf{p}}_n^+(z_{n+1}), \end{aligned} \quad (3.72)$$

where we have used the general rule for matrix inversion: $(\mathbf{AB})^{-1} = \mathbf{B}^{-1}\mathbf{A}^{-1}$. In this way the downgoing field can be transmitted across the interfaces and determined in each subsequent layer. Once the layer containing the receivers is reached, the global downgoing reflection matrix in that layer can be used again to determine the upgoing fields.

Similarly, we can derive an expression for properly transmitting fields across interfaces in the upgoing direction, which is of use when the receivers are located above the source level. In this case, we express the downgoing fields in terms of upgoing fields and isolate the unknown field $\tilde{\mathbf{p}}_n^-(z_{n+1})$, yielding

$$\begin{aligned} \tilde{\mathbf{p}}_n^-(z_{n+1}) &= \left[\mathbf{I} + \tilde{\mathbf{R}}_n^{+-}(z_{n+1}) \right]^{-1} \tilde{\mathbf{L}}_{1,n}^{-1} \tilde{\mathbf{L}}_{1,n+1} \left[\mathbf{I} + \tilde{\mathbf{R}}_{n+1}^{+-}(z_{n+1}) \right] \tilde{\mathbf{p}}_{n+1}^-(z_{n+1}) \\ &= \left[\mathbf{I} + \tilde{\mathbf{R}}_n^{+-}(z_{n+1}) \right]^{-1} 2\tilde{\mathbf{L}}_{2,n}^t \tilde{\mathbf{L}}_{1,n+1} \left[\mathbf{I} + \tilde{\mathbf{R}}_{n+1}^{+-}(z_{n+1}) \right] \tilde{\mathbf{p}}_{n+1}^-(z_{n+1}). \end{aligned} \quad (3.73)$$

We now have all the ingredients required to successfully apply the Global Reflection Scheme in seismo-EM layer-code modeling. As we have seen, to determine the global downgoing reflection matrices, we start at the bottom interface in the model, whereas for determining the global upgoing reflection matrices, we start at the top interface in the model. In certain scenarios, we can desire specific boundary conditions to hold at these model boundaries. These conditions affect the local reflection matrices at these interfaces, and in certain scenarios also the global reflection matrices. We now discuss for both the SH-TE and P-SV-TM propagation modes the implications of desiring a free-surface at the top of the model, and fluid/porous medium or porous medium/fluid transitions at the top or bottom of the model, respectively.

3.2 Including a pressure-free surface and fluid/porous medium/fluid boundaries

3.2.1 SH-TE scattering matrix at a free-surface

We approximate the surface of the Earth as a free-surface, i.e. the air is approximated as a vacuum. As a consequence, only electromagnetic fields can diffuse across this surface and there are no seismic waves present in the vacuum. These boundary conditions have clear implications on the local reflection matrices at this free-surface. Let us first consider this scenario for the SH-TE propagation mode. The boundary conditions at the free-surface ($z = z_1$) are:

- $\tilde{\tau}^{b,H}$ is zero
- \tilde{E}^H is continuous
- \tilde{H}^H is continuous.

We now evaluate the incoming and outgoing one-way fields at the free-surface, via

$$\tilde{\mathbf{p}}^{H,out} = \tilde{\mathbf{S}}^H \tilde{\mathbf{p}}^{H,in}, \quad (3.74)$$

where $\tilde{\mathbf{S}}^H$ represents the scattering matrix at the free-surface. Explicitly, this results in:

$$\begin{pmatrix} \tilde{p}_{0,TE}^-(z_1) \\ \tilde{p}_{1,SH}^+(z_1) \\ \tilde{p}_{1,TE}^+(z_1) \end{pmatrix} = \begin{pmatrix} \tilde{r}_{TE-TE}^{+-}(z_1) & \tilde{t}_{TE-SH}^-(z_1) \\ \tilde{t}_{SH-TE}^+(z_1) & \tilde{r}_{SH-SH}^{+-}(z_1) \\ \tilde{t}_{TE-TE}^+(z_1) & \tilde{r}_{TE-SH}^{+-}(z_1) \end{pmatrix} \begin{pmatrix} \tilde{p}_{0,TE}^+(z_1) \\ \tilde{p}_{1,SH}^-(z_1) \\ \tilde{p}_{1,TE}^-(z_1) \end{pmatrix}. \quad (3.75)$$

In the scattering matrix, the first subscript denotes the outgoing field type, the second subscript the incoming field type. To solve this system, we require three boundary conditions. Expressed in terms of two-way field quantities, we use:

$$\begin{pmatrix} \tilde{E}^H \\ 0 \\ -\tilde{H}^H \end{pmatrix}_{vacuum} = \begin{pmatrix} \tilde{E}^H \\ \tilde{\tau}^{b,H} \\ -\tilde{H}^H \end{pmatrix}_{p.m.}, \quad (3.76)$$

where *p.m.* stands for ‘porous medium’. Before we can express these two-way field boundary conditions in terms of eigenvector-composition matrices and one-way fields, we need to derive the eigenvectors for the vacuum.

For

$$\tilde{\mathbf{q}}_{vacuum}^H = \begin{pmatrix} \tilde{E}^H \\ -\tilde{H}^H \end{pmatrix}, \quad (3.77)$$

the SH-TE system matrix reduces to

$$\tilde{\mathbf{A}}_{vacuum}^H = \begin{pmatrix} 0 & -\zeta \\ -\left(\hat{\eta}^E + \frac{\kappa^2}{\zeta}\right) & 0 \end{pmatrix}. \quad (3.78)$$

We know that the wavenumber is related to the velocity via $\|\mathbf{k}\| = \frac{s}{j\hat{e}}$, where $\mathbf{k} = (k_1, k_2, k_3)$. We now express k_3 in terms of the velocity and the radial wavenumber as $k_3^2 = \frac{-s^2}{\hat{e}^2} - \kappa^2$. If $k_3 = 0$, $\frac{-s^2}{\hat{e}^2} = \kappa^2$. We can now solve the zero-eigenvalue problem (where $k_3 = 0$) by solving the problem where determinant of the system matrix is equal to zero, leading to $-\zeta\hat{\eta}^E - \kappa^2 = 0$. We can recognize that $\frac{-s^2}{\hat{e}^2} = -\zeta\hat{\eta}^E = -s^2\mu_0\epsilon_0$, since the electric conductivity of vacuum is zero and the relative magnetic permeability in vacuum is equal to one. This leads to the well-known electromagnetic velocity of vacuum: $\hat{c}_{EM,vacuum} = \sqrt{\frac{1}{\mu_0\epsilon_0}}$. This can be written in terms of vertical wavenumbers Γ_{EM} . We now derive the SH-TE eigenvectors for a vacuum, by solving $\tilde{\mathbf{A}}_{vacuum}^H \tilde{\mathbf{L}}_{vacuum}^H = \tilde{\mathbf{L}}_{vacuum}^H \tilde{\mathbf{\Lambda}}_1^{vacuum;H}$ and the flux-normalization condition $\tilde{\mathbf{L}}_1^H \left(\tilde{\mathbf{L}}_2^H\right)^t = \frac{1}{2}\mathbf{I}$:

$$\begin{pmatrix} 0 & -\zeta \\ -\left(\hat{\eta}^E + \frac{\kappa^2}{\zeta}\right) & 0 \end{pmatrix} \begin{pmatrix} d_{1,EM}^H & d_{1,EM}^H \\ B_{EM}^H d_{1,EM}^H & -B_{EM}^H d_{1,EM}^H \end{pmatrix} = \begin{pmatrix} d_{1,EM}^H & d_{1,EM}^H \\ B_{EM}^H d_{1,EM}^H & -B_{EM}^H d_{1,EM}^H \end{pmatrix} \begin{pmatrix} -\Gamma_{EM} & 0 \\ 0 & \Gamma_{EM} \end{pmatrix}, \quad (3.79)$$

leading to

$$B_{EM}^H = \frac{\Gamma_{EM}}{\zeta}, \quad (3.80)$$

$$d_{1,EM}^H = \sqrt{\frac{\zeta}{2\Gamma_{EM}}}. \quad (3.81)$$

We can now express equation (3.76) in terms of the eigenvectors and one-way fields, as

$$\begin{pmatrix} d_{1,EM}^H & d_{1,EM}^H \\ 0 & 0 \\ B_{EM}^H d_{1,EM}^H & -B_{EM}^H d_{1,EM}^H \end{pmatrix} \begin{pmatrix} \tilde{p}_{0,TE}^+ \\ \tilde{p}_{0,TE}^- \end{pmatrix} = \begin{pmatrix} \tilde{L}_{1;21}^H & \tilde{L}_{1;22}^H & \tilde{L}_{1;21}^H & \tilde{L}_{1;22}^H \\ \tilde{L}_{2;11}^H & \tilde{L}_{2;12}^H & -\tilde{L}_{2;11}^H & -\tilde{L}_{2;12}^H \\ \tilde{L}_{2;21}^H & \tilde{L}_{2;22}^H & -\tilde{L}_{2;21}^H & -\tilde{L}_{2;22}^H \end{pmatrix} \begin{pmatrix} \tilde{p}_{1,SH}^+ \\ \tilde{p}_{1,TE}^+ \\ \tilde{p}_{1,SH}^- \\ \tilde{p}_{1,TE}^- \end{pmatrix}. \quad (3.82)$$

Separating the incoming and outgoing fields at the free-surface, mimicking equation (3.75), yields

$$\begin{pmatrix} -d_{1,EM}^H & \tilde{L}_{1;21}^H & \tilde{L}_{1;22}^H \\ 0 & \tilde{L}_{2;11}^H & \tilde{L}_{2;12}^H \\ B_{EM}^H d_{1,EM}^H & \tilde{L}_{2;21}^H & \tilde{L}_{2;22}^H \end{pmatrix} \begin{pmatrix} \tilde{p}_{0,TE}^- \\ \tilde{p}_{1,SH}^+ \\ \tilde{p}_{1,TE}^+ \end{pmatrix} = \begin{pmatrix} d_{1,EM}^H & -\tilde{L}_{1;21}^H & -\tilde{L}_{1;22}^H \\ 0 & \tilde{L}_{2;11}^H & \tilde{L}_{2;12}^H \\ B_{EM}^H d_{1,EM}^H & \tilde{L}_{2;21}^H & \tilde{L}_{2;22}^H \end{pmatrix} \begin{pmatrix} \tilde{p}_{0,TE}^+ \\ \tilde{p}_{1,SH}^- \\ \tilde{p}_{1,TE}^- \end{pmatrix}. \quad (3.83)$$

Multiplying the left- and right-hand sides of equation (3.83) with the inverse of the matrix on the left-hand side, yields the scattering matrix $\tilde{\mathbf{S}}^H$ we are after

$$\tilde{\mathbf{S}}^H = \begin{pmatrix} -d_{1,EM}^H & \tilde{L}_{1;21}^H & \tilde{L}_{1;22}^H \\ 0 & \tilde{L}_{2;11}^H & \tilde{L}_{2;12}^H \\ B_{EM}^H d_{1,EM}^H & \tilde{L}_{2;21}^H & \tilde{L}_{2;22}^H \end{pmatrix}^{-1} \begin{pmatrix} d_{1,EM}^H & -\tilde{L}_{1;21}^H & -\tilde{L}_{1;22}^H \\ 0 & \tilde{L}_{2;11}^H & \tilde{L}_{2;12}^H \\ B_{EM}^H d_{1,EM}^H & \tilde{L}_{2;21}^H & \tilde{L}_{2;22}^H \end{pmatrix}. \quad (3.84)$$

We now have all required expressions for the local SH-TE transmission and reflection coefficients at the free-surface.

3.2.2 P-SV-TM scattering matrix at a free-surface

In a similar way, we can derive the free-surface scattering matrix for the P-SV-TM mode. The boundary conditions at the free-surface ($z = z_1$) now read:

- $\tilde{\tau}_{norm}^{b,V}$ and $\tilde{\tau}_{33}^b$ are zero
- \tilde{p}^f is zero
- \tilde{E}_{norm}^V is continuous
- \tilde{H}_{norm}^V is continuous.

Evaluating the incoming and outgoing one-way wavefields at the free-surface via

$$\tilde{\mathbf{p}}^{V,out} = \tilde{\mathbf{S}}^V \tilde{\mathbf{p}}^{V,in}, \quad (3.85)$$

where $\tilde{\mathbf{S}}^V$ represents the scattering matrix. Explicitly, this results in

$$\begin{pmatrix} \tilde{p}_{0,TM}^-(z_1) \\ \tilde{p}_{1,Pf}^+(z_1) \\ \tilde{p}_{1,Ps}^+(z_1) \\ \tilde{p}_{1,SV}^+(z_1) \\ \tilde{p}_{1,TM}^+(z_1) \end{pmatrix} = \begin{pmatrix} \tilde{r}_{TM-TM}^{--}(z_1) & \tilde{t}_{TM-Pf}^-(z_1) & \tilde{t}_{TM-Ps}^-(z_1) \\ \tilde{t}_{Pf-TM}^+(z_1) & \tilde{r}_{Pf-Pf}^{+-}(z_1) & \tilde{r}_{Pf-Ps}^{+-}(z_1) \\ \tilde{t}_{Ps-TM}^+(z_1) & \tilde{r}_{Ps-Pf}^{+-}(z_1) & \tilde{r}_{Ps-Ps}^{+-}(z_1) \\ \tilde{t}_{SV-TM}^+(z_1) & \tilde{r}_{SV-Pf}^{+-}(z_1) & \tilde{r}_{SV-Ps}^{+-}(z_1) \\ \tilde{t}_{TM-TM}^+(z_1) & \tilde{r}_{TM-Pf}^{+-}(z_1) & \tilde{r}_{TM-Ps}^{+-}(z_1) \end{pmatrix} \begin{pmatrix} \tilde{t}_{TM-SV}^-(z_1) & \tilde{t}_{TM-TM}^-(z_1) \\ \tilde{r}_{Pf-SV}^{+-}(z_1) & \tilde{r}_{Pf-TM}^{+-}(z_1) \\ \tilde{r}_{Ps-SV}^{+-}(z_1) & \tilde{r}_{Ps-TM}^{+-}(z_1) \\ \tilde{r}_{SV-SV}^{+-}(z_1) & \tilde{r}_{SV-TM}^{+-}(z_1) \\ \tilde{r}_{TM-SV}^{+-}(z_1) & \tilde{r}_{TM-TM}^{+-}(z_1) \end{pmatrix} \begin{pmatrix} \tilde{p}_{0,TM}^+(z_1) \\ \tilde{p}_{1,Pf}^-(z_1) \\ \tilde{p}_{1,Ps}^-(z_1) \\ \tilde{p}_{1,SV}^-(z_1) \\ \tilde{p}_{1,TM}^-(z_1) \end{pmatrix}. \quad (3.86)$$

To solve this system, 5 boundary conditions are needed. We consider the following boundary conditions:

$$\begin{pmatrix} 0 \\ \tilde{H}_{norm}^V \\ 0 \\ 0 \\ \tilde{E}_{norm}^V \end{pmatrix}_{vacuum} = \begin{pmatrix} \tilde{\tau}_{norm}^{b,V} \\ \tilde{H}_{norm}^V \\ \tilde{\tau}_{33}^b \\ -\tilde{p}^f \\ \tilde{E}_{norm}^V \end{pmatrix}_{p.m.}. \quad (3.87)$$

For

$$\tilde{\mathbf{q}}_{vacuum}^V = \begin{pmatrix} \tilde{H}_{norm}^V \\ \tilde{E}_{norm}^V \end{pmatrix}, \quad (3.88)$$

the P-SV-TM system matrix reduces to

$$\tilde{\mathbf{A}}_{vacuum}^V = \begin{pmatrix} 0 & -\hat{\eta}^E \\ -\zeta - \frac{\kappa^2}{\hat{\eta}^E} & 0 \end{pmatrix}. \quad (3.89)$$

We again solve the problem where the determinant of the system matrix is equal to zero, yielding $-\hat{\eta}^E \zeta - \kappa^2 = -s^2 \varepsilon_0 \mu_0 - \kappa^2 = 0$, since in the vacuum, there is no coupling, i.e. $\hat{\mathbf{L}} = 0$, reducing $\hat{\zeta}$ to $\hat{\eta}^E$. We again find the expression for the electromagnetic velocity in vacuum. We now derive the P-SV-TM eigenvectors for a vacuum, by solving $\tilde{\mathbf{A}}_{vacuum}^V \tilde{\mathbf{L}}_{vacuum}^V = \tilde{\mathbf{L}}_{vacuum}^V \tilde{\mathbf{\Lambda}}_1^{vacuum,V}$ and the flux-normalization condition $\tilde{\mathbf{L}}_1^V (\tilde{\mathbf{L}}_2^V)^t = \frac{1}{2} \mathbf{I}$:

$$\begin{pmatrix} 0 & -\hat{\eta}^E \\ -\zeta - \frac{\kappa^2}{\hat{\eta}^E} & 0 \end{pmatrix} \begin{pmatrix} d_{1,EM}^V & d_{1,EM}^V \\ B_{EM}^V d_{1,EM}^V & -B_{EM}^V d_{1,EM}^V \end{pmatrix} = \begin{pmatrix} d_{1,EM}^V & d_{1,EM}^V \\ B_{EM}^V d_{1,EM}^V & -B_{EM}^V d_{1,EM}^V \end{pmatrix} \begin{pmatrix} -\Gamma_{EM} & 0 \\ 0 & \Gamma_{EM} \end{pmatrix}, \quad (3.90)$$

leading to

$$B_{EM}^V = \frac{\Gamma_{EM}}{\hat{\eta}^E}, \quad (3.91)$$

$$d_{1,EM}^V = \sqrt{\frac{\hat{\eta}^E}{2\Gamma_{EM}}}. \quad (3.92)$$

It is important to realize that the electric conductivity in vacuum is zero. We can now express equation (3.87) in terms of the eigenvectors and one-way fields, as

$$\begin{pmatrix} 0 & 0 \\ d_{1,EM}^V & d_{1,EM}^V \\ 0 & 0 \\ 0 & 0 \\ B_{EM}^V d_{1,EM}^V & -B_{EM}^V d_{1,EM}^V \end{pmatrix} \begin{pmatrix} \tilde{p}_{0,TM}^+(z_1) \\ \tilde{p}_{0,TM}^-(z_1) \end{pmatrix} = \begin{pmatrix} \tilde{L}_{1;31}^V & \tilde{L}_{1;32}^V & \tilde{L}_{1;33}^V & \tilde{L}_{1;34}^V \\ \tilde{L}_{1;41}^V & \tilde{L}_{1;42}^V & \tilde{L}_{1;43}^V & \tilde{L}_{1;44}^V \\ \tilde{L}_{2;11}^V & \tilde{L}_{2;12}^V & \tilde{L}_{2;13}^V & \tilde{L}_{2;14}^V \\ \tilde{L}_{2;21}^V & \tilde{L}_{2;22}^V & \tilde{L}_{2;23}^V & \tilde{L}_{2;24}^V \\ \tilde{L}_{2;41}^V & \tilde{L}_{2;42}^V & \tilde{L}_{2;43}^V & \tilde{L}_{2;44}^V \end{pmatrix} \begin{pmatrix} \tilde{p}_{1,Pf}^+(z_1) \\ \tilde{p}_{1,Ps}^+(z_1) \\ \tilde{p}_{1,SV}^+(z_1) \\ \tilde{p}_{1,TM}^+(z_1) \\ \tilde{p}_{1,Pf}^-(z_1) \\ \tilde{p}_{1,Ps}^-(z_1) \\ \tilde{p}_{1,SV}^-(z_1) \\ \tilde{p}_{1,TM}^-(z_1) \end{pmatrix}. \quad (3.93)$$

Separating the incoming and outgoing fields at the free-surface, mimicking equation (3.86), yields

$$\begin{pmatrix} 0 & \tilde{L}_{1;31}^V & \tilde{L}_{1;32}^V & \tilde{L}_{1;33}^V & \tilde{L}_{1;34}^V \\ -d_{1,EM}^V & \tilde{L}_{1;41}^V & \tilde{L}_{1;42}^V & \tilde{L}_{1;43}^V & \tilde{L}_{1;44}^V \\ 0 & \tilde{L}_{2;11}^V & \tilde{L}_{2;12}^V & \tilde{L}_{2;13}^V & \tilde{L}_{2;14}^V \\ 0 & \tilde{L}_{2;21}^V & \tilde{L}_{2;22}^V & \tilde{L}_{2;23}^V & \tilde{L}_{2;24}^V \\ B_{EM}^V d_{1,EM}^V & \tilde{L}_{2;41}^V & \tilde{L}_{2;42}^V & \tilde{L}_{2;43}^V & \tilde{L}_{2;44}^V \end{pmatrix} \begin{pmatrix} \tilde{p}_{0,TM}^-(z_1) \\ \tilde{p}_{1,Pf}^+(z_1) \\ \tilde{p}_{1,Ps}^+(z_1) \\ \tilde{p}_{1,SV}^+(z_1) \\ \tilde{p}_{1,TM}^+(z_1) \end{pmatrix} = \begin{pmatrix} 0 & -\tilde{L}_{1;31}^V & -\tilde{L}_{1;32}^V & -\tilde{L}_{1;33}^V & -\tilde{L}_{1;34}^V \\ d_{1,EM}^V & -\tilde{L}_{1;41}^V & -\tilde{L}_{1;42}^V & -\tilde{L}_{1;43}^V & -\tilde{L}_{1;44}^V \\ 0 & \tilde{L}_{2;11}^V & \tilde{L}_{2;12}^V & \tilde{L}_{2;13}^V & \tilde{L}_{2;14}^V \\ 0 & \tilde{L}_{2;21}^V & \tilde{L}_{2;22}^V & \tilde{L}_{2;23}^V & \tilde{L}_{2;24}^V \\ B_{EM}^V d_{1,EM}^V & \tilde{L}_{2;41}^V & \tilde{L}_{2;42}^V & \tilde{L}_{2;43}^V & \tilde{L}_{2;44}^V \end{pmatrix} \begin{pmatrix} \tilde{p}_{0,TM}^+(z_1) \\ \tilde{p}_{1,Pf}^-(z_1) \\ \tilde{p}_{1,Ps}^-(z_1) \\ \tilde{p}_{1,SV}^-(z_1) \\ \tilde{p}_{1,TM}^-(z_1) \end{pmatrix}. \quad (3.94)$$

Next, left-multiplying the left- and right-hand side of (3.94) with the inverse of the matrix on the left-hand side gives the desired form of (3.86). We now have all required expressions for the local P-SV-TM transmission and reflection coefficients at the free-surface.

3.2.3 SH-TE local scattering matrix at a porous medium/fluid interface

Consider we have a fluid halfspace (indicated by superscript *fl* or subscript *fluid*) below a porous medium. For the SH-TE propagation mode, the interface separating both layers has significant effects on the propagating wavefields, since the fluid layer does not sustain shear waves. We again desire to derive the correct scattering matrix at such an interface. We start again by writing the problem under consideration as follows

$$\tilde{\mathbf{p}}_{out}^H = \tilde{\mathbf{S}}^{p.m./fl;H} \tilde{\mathbf{p}}_{in}^H. \quad (3.95)$$

For the contrast under consideration, this means

$$\begin{pmatrix} \tilde{P}_{0,SH}^- \\ \tilde{P}_{0,TE}^- \\ \tilde{P}_{1,EM}^+ \end{pmatrix} = \begin{pmatrix} \tilde{r}_{SH-SH}^{-+} & \tilde{r}_{SH-TE}^{-+} & \tilde{t}_{SH-EM}^- \\ \tilde{r}_{TE-SH}^{-+} & \tilde{r}_{TE-TE}^{-+} & \tilde{t}_{TE-EM}^- \\ \tilde{t}_{EM-SH}^+ & \tilde{t}_{EM-TE}^+ & \tilde{r}_{EM-EM}^+ \end{pmatrix} \begin{pmatrix} \tilde{P}_{0,SH}^+ \\ \tilde{P}_{0,TE}^+ \\ \tilde{P}_{1,EM}^- \end{pmatrix}. \quad (3.96)$$

For this porous medium/fluid interface, we would like to solve for \tilde{r}^{-+} , the local downgoing reflection coefficient. As can be seen, in order to solve for this scattering matrix, 3 boundary conditions are required. For the SH-TE system under consideration, the following boundary conditions apply for porous medium/fluid interfaces:

- \tilde{E}^H is continuous across the interface
- $-\tilde{H}^H$ is continuous across the interface
- $\tilde{\tau}^{b,H}$ is zero in the fluid
- $\tilde{v}^{s,H}$ is ‘free’.

We select the first three boundary conditions to solve this problem. In terms of a two-way field-equality, this reads

$$\tilde{\mathbf{q}}_{p.m.}^H = \begin{pmatrix} \tilde{E}^H \\ \tilde{\tau}^{b,H} \\ -\tilde{H}^H \end{pmatrix} = \tilde{\mathbf{q}}_{fluid}^H = \begin{pmatrix} \tilde{E}^H \\ 0 \\ -\tilde{H}^H \end{pmatrix}. \quad (3.97)$$

The composition matrix for the porous medium is already known (see Section 2.3). However, the composition matrix for the fluid layer needs to be derived in order to solve the system correctly. Let us consider the following problem

$$\begin{pmatrix} \tilde{E}^H \\ -\tilde{H}^H \end{pmatrix} = \begin{pmatrix} d_{1,EM}^{fl,H} & d_{1,EM}^{fl,H} \\ B_{EM}^{fl,H} d_{1,EM}^{fl,H} & -B_{EM}^{fl,H} d_{1,EM}^{fl,H} \end{pmatrix} \begin{pmatrix} \tilde{P}_{EM}^+ \\ \tilde{P}_{EM}^- \end{pmatrix}, \quad (3.98)$$

where $d_{1;EM}^{fl,H}$ is the power flux-normalization factor for the fluid layer, which needs to be determined, and $B_{EM}^{fl,H}$ is a certain scaling factor for the system in the fluid. The system matrix $\tilde{\mathbf{A}}_{fluid;EM}^H$ corresponding to this system reads

$$\tilde{\mathbf{A}}_{fluid;EM}^H = \begin{pmatrix} 0 & -\zeta \\ -\left(\eta^e + \frac{\kappa^2}{\zeta}\right) & 0 \end{pmatrix}. \quad (3.99)$$

In order to obtain the expressions for these unknown factors, the relation between system matrix, eigenvectors and eigenvalues needs to be solved again. For this, the expression for the electromagnetic velocity in the fluid layer needs to be derived as well. We can do so by solving

$$\tilde{\mathbf{A}}_{fluid;EM}^H \begin{vmatrix} 0 & -\zeta \\ -\left(\eta^e + \frac{\kappa^2}{\zeta}\right) & 0 \end{vmatrix} = 0. \quad (3.100)$$

Writing out each of the terms in its individual constituents, and using

$$\frac{\kappa^2}{-s^2} = \frac{1}{\hat{c}_{EM}^2}, \quad (3.101)$$

yields

$$\hat{c}_{EM} = \sqrt{\frac{1}{\mu_0 \left(\frac{\sigma^e}{s} + \epsilon_0 \epsilon_r\right)}}, \quad (3.102)$$

where the electric conductivity is non-zero. Now, we solve for

$$\tilde{\mathbf{A}}_{fluid;EM}^H \tilde{\mathbf{L}}_{fluid;EM}^H = \tilde{\mathbf{L}}_{fluid;EM}^H \tilde{\mathbf{\Lambda}}_{1;EM}^{fl,H}, \quad (3.103)$$

reading

$$\begin{pmatrix} 0 & -\zeta \\ -\left(\eta^e + \frac{\kappa^2}{\zeta}\right) & 0 \end{pmatrix} \begin{pmatrix} d_{1,EM}^{fl,H} & d_{1,EM}^{fl,H} \\ B_{EM}^{fl,H} d_{1,EM}^{fl,H} & -B_{EM}^{fl,H} d_{1,EM}^{fl,H} \end{pmatrix} = \begin{pmatrix} d_{1,EM}^{fl,H} & d_{1,EM}^{fl,H} \\ B_{EM}^{fl,H} d_{1,EM}^{fl,H} & -B_{EM}^{fl,H} d_{1,EM}^{fl,H} \end{pmatrix} \begin{pmatrix} -\Gamma_{EM} & 0 \\ 0 & \Gamma_{EM} \end{pmatrix}. \quad (3.104)$$

Using first row-first column we find $B_{EM}^{fl,H} = \frac{\Gamma_{EM}}{\zeta}$. Now using $\tilde{\mathbf{L}}_1^{fl,H} (\tilde{\mathbf{L}}_2^{fl,H})^t = \frac{1}{2} \mathbf{I}$, we find $B_{EM}^{fl,H} (d_{1,EM}^{fl,H})^2 = \frac{1}{2}$, yielding $d_{1,EM}^{fl,H} = \sqrt{\frac{1}{2B_{EM}^{fl,H}}} = \sqrt{\frac{\zeta}{2\Gamma_{EM}}}$. This leads to the following composition matrix for the SH-TE propagation mode in a fluid

$$\tilde{\mathbf{L}}^{fl,H} = \begin{pmatrix} d_{1,EM}^{fl,H} & d_{1,EM}^{fl,H} \\ B_{EM}^{fl,H} d_{1,EM}^{fl,H} & -B_{EM}^{fl,H} d_{1,EM}^{fl,H} \end{pmatrix}. \quad (3.105)$$

Now, all information is available for applying the correct boundary conditions at the porous medium/fluid interface, following

$$\tilde{\mathbf{L}}_{fluid}^H \tilde{\mathbf{p}}_{fluid}^H = \tilde{\mathbf{L}}_{p.m.}^H \tilde{\mathbf{p}}_{p.m.}^H. \quad (3.106)$$

Writing this equation explicitly, yields

$$\begin{pmatrix} d_{1,EM}^{fl,H} & d_{1,EM}^{fl,H} \\ 0 & 0 \\ B_{EM}^{fl,H} d_{1,EM}^{fl,H} & B_{EM}^{fl,H} d_{1,EM}^{fl,H} \end{pmatrix} \begin{pmatrix} \tilde{p}_{EM}^+ \\ \tilde{p}_{EM}^- \end{pmatrix} = \begin{pmatrix} \tilde{L}_{1;21}^H & \tilde{L}_{1;22}^H & \tilde{L}_{1;21}^H & \tilde{L}_{1;22}^H \\ \tilde{L}_{2;11}^H & \tilde{L}_{2;12}^H & -\tilde{L}_{2;11}^H & -\tilde{L}_{2;12}^H \\ \tilde{L}_{2;21}^H & \tilde{L}_{2;22}^H & -\tilde{L}_{2;21}^H & -\tilde{L}_{2;22}^H \end{pmatrix} \begin{pmatrix} \tilde{p}_{SH}^+ \\ \tilde{p}_{TE}^+ \\ \tilde{p}_{SH}^- \\ \tilde{p}_{TE}^- \end{pmatrix}. \quad (3.107)$$

Now, mimicking the format of equation (3.100), we obtain

$$\begin{pmatrix} -\tilde{L}_{1;21}^H & -\tilde{L}_{1;22}^H & d_{1,EM}^{fl,H} \\ \tilde{L}_{2;11}^H & \tilde{L}_{2;12}^H & 0 \\ \tilde{L}_{2;21}^H & \tilde{L}_{2;22}^H & B_{EM}^{fl,H} d_{1,EM}^{fl,H} \end{pmatrix} \begin{pmatrix} \tilde{p}_{0,SH}^- \\ \tilde{p}_{0,TE}^- \\ \tilde{p}_{1,EM}^+ \end{pmatrix} = \begin{pmatrix} \tilde{L}_{1;11}^H & \tilde{L}_{1;12}^H & -d_{1,EM}^{fl,H} \\ \tilde{L}_{1;21}^H & \tilde{L}_{1;22}^H & 0 \\ \tilde{L}_{2;21}^H & \tilde{L}_{2;22}^H & B_{EM}^{fl,H} d_{1,EM}^{fl,H} \end{pmatrix} \begin{pmatrix} \tilde{p}_{0,SH}^+ \\ \tilde{p}_{0,TE}^+ \\ \tilde{p}_{1,EM}^- \end{pmatrix}. \quad (3.108)$$

Now, to obtain the desired scattering matrix $\tilde{\mathbf{S}}^{p.m./fl;H}$, we need to left multiply at both sides with the inverse of the composition matrix on the left-hand side. Elements $\tilde{S}_{\alpha\beta}^H$ then correspond with the local reflection matrix we are after.

3.2.4 SH-TE local scattering matrix at a fluid/porous medium interface

In a similar way, a fluid/p.m. interface scattering matrix can be derived, where the fluid halfspace is located on top of the porous medium. The expression $\tilde{\mathbf{p}}_{out}^H = \tilde{\mathbf{S}}^{fl/p.m.;H} \tilde{\mathbf{p}}_{in}^H$ then reads

$$\begin{pmatrix} \tilde{p}_{0,EM}^- \\ \tilde{p}_{1,SH}^+ \\ \tilde{p}_{1,TE}^+ \end{pmatrix} = \begin{pmatrix} \tilde{r}_{EM-EM}^{+-} & \tilde{t}_{EM-SH}^- & \tilde{t}_{EM-TE}^- \\ \tilde{t}_{SH-EM}^+ & \tilde{r}_{SH-SH}^{+-} & \tilde{r}_{SH-TE}^{+-} \\ \tilde{t}_{TE-EM}^+ & \tilde{r}_{TE-SH}^{+-} & \tilde{r}_{TE-TE}^{+-} \end{pmatrix} \begin{pmatrix} \tilde{p}_{0,EM}^+ \\ \tilde{p}_{1,SH}^- \\ \tilde{p}_{1,TE}^- \end{pmatrix}. \quad (3.109)$$

The expression for the electromagnetic field velocity remains the same, also the scaling factors determined previously for the SH-TE fluid layer composition matrix are identical. Using the same set of boundary conditions and setting up the equation for the two-way fields at the fluid/porous medium interface, using the format of

equation (3.109), yields

$$\begin{pmatrix} d_{1,EM}^{fl,H} & -L_{1;21}^{fl,H} & -L_{1;22}^{fl,H} \\ 0 & -L_{2;11}^{fl,H} & -L_{2;12}^{fl,H} \\ -B_{EM}^{fl,H} d_{1,EM}^{fl,H} & -L_{2;21}^{fl,H} & -L_{2;22}^{fl,H} \end{pmatrix} \begin{pmatrix} \tilde{p}_{0,EM}^- \\ \tilde{p}_{1,SH}^+ \\ \tilde{p}_{1,TE}^+ \end{pmatrix} = \begin{pmatrix} -d_{1,EM}^{fl,H} & L_{1;21}^{fl,H} & L_{1;22}^{fl,H} \\ 0 & -L_{2;11}^{fl,H} & -L_{2;12}^{fl,H} \\ -B_{EM}^{fl,H} d_{1,EM}^{fl,H} & -L_{2;21}^{fl,H} & -L_{2;22}^{fl,H} \end{pmatrix} \begin{pmatrix} \tilde{p}_{0,EM}^+ \\ \tilde{p}_{1,SH}^- \\ \tilde{p}_{1,TE}^- \end{pmatrix}. \quad (3.110)$$

Now, left-multiplying both sides again with the inverse of the matrix on the left-hand side, yields the desired scattering matrix at the fluid/porous medium interface. Here, the elements of the second and third column on the second and third row of $\tilde{\mathbf{S}}^{fl/p.m.;H}$ correspond to the desired local reflection coefficient matrix $\tilde{\mathbf{r}}^{+-}$.

3.2.5 P-SV-TM scattering matrix at a porous medium/fluid interface

For the P-SV-TM propagation mode, a similar scattering matrix needs to be derived for the porous medium/fluid transition. However, the boundary conditions at the porous medium/fluid interface are slightly different from the ones for the SH-TE propagation mode, since pressure waves can propagate through a fluid as well as electromagnetic fields. However, since the shear waves are not sustained in the fluid layers, the pressure waves and electromagnetic fields travel independently (non-coupled) from each other. Let us start again writing the problem under consideration as follows

$$\tilde{\mathbf{p}}_{out}^V = \tilde{\mathbf{S}}^{p.m./fl;V} \tilde{\mathbf{p}}_{in}^V. \quad (3.111)$$

For the contrast under consideration, this means

$$\begin{pmatrix} \tilde{p}_{0,Pf}^- \\ \tilde{p}_{0,Ps}^- \\ \tilde{p}_{0,SV}^- \\ \tilde{p}_{0,TM}^- \\ \tilde{p}_{1,P}^+ \\ \tilde{p}_{1,EM}^+ \end{pmatrix} = \begin{pmatrix} \tilde{r}_{Pf-Pf}^{-+} & \tilde{r}_{Pf-Ps}^{-+} & \tilde{r}_{Pf-SV}^{-+} \\ \tilde{r}_{Ps-Pf}^{-+} & \tilde{r}_{Ps-Ps}^{-+} & \tilde{r}_{Ps-SV}^{-+} \\ \tilde{r}_{SV-Pf}^{-+} & \tilde{r}_{SV-Ps}^{-+} & \tilde{r}_{SV-SV}^{-+} \\ \tilde{r}_{TM-Pf}^{-+} & \tilde{r}_{TM-Ps}^{-+} & \tilde{r}_{TM-SV}^{-+} \\ \tilde{t}_{P-Pf}^+ & \tilde{t}_{P-Ps}^+ & \tilde{t}_{P-SV}^+ \\ \tilde{t}_{EM-Pf}^+ & \tilde{t}_{EM-Ps}^+ & \tilde{t}_{EM-SV}^+ \end{pmatrix} \begin{pmatrix} \tilde{p}_{0,Pf}^+ \\ \tilde{p}_{0,Ps}^+ \\ \tilde{p}_{0,SV}^+ \\ \tilde{p}_{0,TM}^+ \\ \tilde{p}_{1,P}^- \\ \tilde{p}_{1,EM}^- \end{pmatrix}. \quad (3.112)$$

For this interface, we would like to solve for \tilde{r}^{-+} , the local reflection coefficient expressing the reflection of a downgoing field into an upgoing field. As can be seen,

in order to solve for this scattering matrix, 6 boundary conditions are required. Consider we have a fluid layer below a solid material layer. For the P-SV-TM propagation mode, the interface separating both layers has significant effects on the propagating wavefields. The boundary conditions for this propagation mode are a bit more tedious than the ones for the SH-TE system. We here consider open-pore boundary conditions according to [Deresiewicz & Skalak \(1963\)](#); [Pride & Haartsen \(1996\)](#); [Schakel & Smeulders \(2010\)](#). The following relations hold:

$$(1 - \phi)\tilde{v}_3^s + \phi\tilde{v}_3^f = \tilde{v}_3^{fluid}, \quad (3.113)$$

$$-\tilde{p}^f = -\tilde{p}^{fluid}, \quad (3.114)$$

$$\tilde{\sigma}_{13} = \tilde{\sigma}_{33} = 0; \quad \text{intergranular stress}, \quad (3.115)$$

$$\tilde{H}_{norm}^V = \tilde{H}_{norm}^V, \quad (3.116)$$

$$\tilde{E}_{norm}^V = \tilde{E}_{norm}^V. \quad (3.117)$$

Furthermore, the following relation between bulk stress and intergranular stress holds ([Pride & Haartsen, 1996](#); [Schakel & Smeulders, 2010](#))

$$\tilde{\tau}^b = -\tilde{\sigma} - \tilde{p}\mathbf{I}. \quad (3.118)$$

Also, [Van Dalen \(2011\)](#) shows this relation as follows

$$\tau_{ij} = -\sigma_{ij} - (1 - \phi)p\delta_{ij}. \quad (3.119)$$

When encountering a fluid, where porosity $\phi = 1$, Van Dalen shows that

$$\tau_{ij} = -\sigma_{ij} - (1 - \phi)p\delta_{ij} = -\phi p. \quad (3.120)$$

Effectively, for the vertical bulk stress τ_{33}^b , this yields,

$$\tau_{33}^b = -\sigma_{33} - p + \phi p = -\phi p. \quad (3.121)$$

When encountering a fluid, $\sigma_{33} = 0$, and $\phi = 1$, yielding indeed

$$\tilde{\tau}_{33}^b = -\tilde{p}. \quad (3.122)$$

For the P-SV-TM system under consideration, the following boundary conditions apply for fluid-porous medium interfaces:

- \tilde{E}_{norm}^V is continuous across the interface
- \tilde{H}_{norm}^V is continuous across the interface
- \tilde{p}^f is continuous across the interface
- $\tilde{v}_3^s + \tilde{w}_3$ is continuous across the interface and forms \tilde{v}_3^{fluid}
- $\tilde{\tau}_{norm}^{b,V}$ is zero in the fluid layer
- $\tilde{\tau}_{33}^b + \tilde{p}^f$ is zero in the fluid layer

- \tilde{v}_{norm}^V is ‘free’.

We select the first six boundary conditions to solve this problem. The conditions for the horizontal particle velocities \tilde{v}^V are then free.

Recall that the relation between two-way recorded wavefield quantities and the one-way decomposed wavefields reads

$$\tilde{\mathbf{q}}^V = \tilde{\mathbf{L}}^V \tilde{\mathbf{p}}^V, \quad (3.123)$$

where

$$\tilde{\mathbf{q}}_{p.m.}^V = \begin{pmatrix} \tilde{v}_3^s \\ \tilde{w}_3 \\ \tilde{\tau}_{norm}^{b,V} \\ \tilde{H}_{norm}^V \\ \tilde{\tau}_{33}^b \\ -\tilde{p}^f \\ \tilde{v}_{norm}^{s,V} \\ \tilde{E}_{norm}^V \end{pmatrix}. \quad (3.124)$$

Applying the correct fluid-porous medium boundary conditions, yields the following equality across the interface

$$\tilde{\mathbf{q}}_{p.m.}^V = \begin{pmatrix} \tilde{v}_3^s + \tilde{w}_3 \\ \tilde{\tau}_{norm}^{b,V} \\ \tilde{H}_{norm}^V \\ \tilde{\tau}_{33}^b + \tilde{p}^f \\ -\tilde{p}^f \\ \tilde{E}_{norm}^V \end{pmatrix} = \tilde{\mathbf{q}}_{fluid}^V = \begin{pmatrix} \tilde{v}_3^{fluid} \\ 0 \\ \tilde{H}_{norm}^V \\ 0 \\ -\tilde{p}^{fluid} \\ \tilde{E}_{norm}^V \end{pmatrix}. \quad (3.125)$$

The composition matrix for the porous medium is already known (see Section 2.3). However, the composition matrix for the fluid layer needs to be derived in order to solve the system correctly. As mentioned before, the pressure waves and the electromagnetic fields are uncoupled in the fluid layer, meaning $\hat{\mathcal{L}} = 0$. Therefore, we can derive scaling factors and composition matrices for the seismic and electromagnetic systems independently.

We can derive the system matrix $\tilde{\mathbf{A}}_{fluid;P}^V$ corresponding to the acoustic system in a fluid straight from the basic acoustic wave equation. The system matrix for the field vector $(\tilde{\mathbf{q}}_{fluid}^V)^t = (\tilde{v}_3^{fluid}, -\tilde{p}^{fluid})$, reads

$$\tilde{\mathbf{A}}_P^{fl;V} = \begin{pmatrix} 0 & \frac{s}{K^f} + \frac{\kappa^2}{s\rho^f} \\ s\rho^f & 0 \end{pmatrix}. \quad (3.126)$$

Again, the system matrix for the P-SV-TM electromagnetic system in a fluid is given by:

$$\tilde{\mathbf{A}}_{EM}^{fl;V} = \begin{pmatrix} 0 & -\hat{\eta}^E \\ -\zeta - \frac{\kappa^2}{\hat{\eta}^E} & 0 \end{pmatrix}. \quad (3.127)$$

Solving the zero-eigenvalue problem for both cases yields the acoustic velocity in a fluid, $\hat{c}_P = \sqrt{\frac{K^f}{\rho^f}}$, and the electromagnetic velocity in a fluid, $\hat{c}_{EM} = \sqrt{\frac{1}{\mu_0(\frac{\hat{\sigma}^e}{s} + \varepsilon)}}$. Next, we solve for

$$\tilde{\mathbf{A}}_{fluid;P}^V \tilde{\mathbf{L}}_{fluid;P}^V = \tilde{\mathbf{L}}_{fluid;P}^V \tilde{\mathbf{A}}_{1;P}^{fl,V}, \quad (3.128)$$

and

$$\tilde{\mathbf{A}}_{fluid;EM}^V \tilde{\mathbf{L}}_{fluid;EM}^V = \tilde{\mathbf{L}}_{fluid;EM}^V \tilde{\mathbf{A}}_{1;EM}^{fl,V}, \quad (3.129)$$

explicitly reading as

$$\begin{pmatrix} 0 & \frac{s}{K^f} + \frac{\kappa^2}{s\rho^f} \\ s\rho^f & 0 \end{pmatrix} \begin{pmatrix} d_{1,P}^{fl,V} & d_{1,P}^{fl,V} \\ B_P^{fl,V} d_{1,P}^{fl,V} & -B_P^{fl,V} d_{1,P}^{fl,V} \end{pmatrix} = \\ \begin{pmatrix} d_{1,P}^{fl,V} & d_{1,P}^{fl,V} \\ B_P^{fl,V} d_{1,P}^{fl,V} & -B_P^{fl,V} d_{1,P}^{fl,V} \end{pmatrix} \begin{pmatrix} -\Gamma_P & 0 \\ 0 & \Gamma_P \end{pmatrix}, \quad (3.130)$$

and

$$\begin{pmatrix} 0 & -\hat{\eta}^E \\ -\zeta - \frac{\kappa^2}{\hat{\eta}^E} & 0 \end{pmatrix} \begin{pmatrix} d_{1,EM}^{fl,V} & d_{1,EM}^{fl,V} \\ B_{EM}^{fl,V} d_{1,EM}^{fl,V} & -B_{EM}^{fl,V} d_{1,EM}^{fl,V} \end{pmatrix} = \\ \begin{pmatrix} d_{1,EM}^{fl,V} & d_{1,EM}^{fl,V} \\ B_{EM}^{fl,V} d_{1,EM}^{fl,V} & -B_{EM}^{fl,V} d_{1,EM}^{fl,V} \end{pmatrix} \begin{pmatrix} -\Gamma_{EM} & 0 \\ 0 & \Gamma_{EM} \end{pmatrix}. \quad (3.131)$$

We find for the seismic scaling factors $B_P^{fl,V} = -\frac{s\rho^f}{\Gamma_P}$ and for the electromagnetic scaling $B_{EM}^{fl,V} = \frac{\Gamma_{EM}}{\hat{\eta}^E}$. Solving for the power-flux normalization factors, we derive $d_{1,P}^{fl,V} = \sqrt{-\frac{\Gamma_P}{2s\rho^f}}$, and $d_{1,EM}^{fl,V} = \sqrt{\frac{\hat{\eta}^e}{2\Gamma_{EM}}}$.

Now, all information is available for applying the correct boundary conditions of equation (3.125) at the porous medium/fluid interface, written in terms of eigen-

vectors and one-way fields as:

$$\begin{pmatrix} d_{1,P}^{fl,V} & 0 & d_{1,P}^{fl,V} & 0 \\ 0 & 0 & 0 & 0 \\ 0 & d_{1,EM}^{fl,V} & 0 & d_{1,EM}^{fl,V} \\ 0 & 0 & 0 & 0 \\ B_P^{fl,V} d_{1,P}^{fl,V} & 0 & -B_P^{fl,V} d_{1,P}^{fl,V} & 0 \\ 0 & B_{EM}^{fl,V} d_{1,EM}^{fl,V} & 0 & -B_{EM}^{fl,V} d_{1,EM}^{fl,V} \end{pmatrix} \begin{pmatrix} \tilde{p}_P^+ \\ \tilde{p}_{EM}^+ \\ \tilde{p}_P^- \\ \tilde{p}_{EM}^- \end{pmatrix} =$$

$$\begin{pmatrix} \tilde{L}_{1;11}^V + \tilde{L}_{1;21}^V & \tilde{L}_{1;12}^V + \tilde{L}_{1;22}^V & \tilde{L}_{1;13}^V + \tilde{L}_{1;23}^V & \tilde{L}_{1;14}^V + \tilde{L}_{1;24}^V \\ \tilde{L}_{1;31}^V & \tilde{L}_{1;32}^V & \tilde{L}_{1;33}^V & \tilde{L}_{1;34}^V \\ \tilde{L}_{1;41}^V & \tilde{L}_{1;42}^V & \tilde{L}_{1;43}^V & \tilde{L}_{1;44}^V \\ \tilde{L}_{2;11}^V - \tilde{L}_{2;21}^V & \tilde{L}_{2;12}^V - \tilde{L}_{2;22}^V & \tilde{L}_{2;13}^V - \tilde{L}_{2;23}^V & \tilde{L}_{2;14}^V - \tilde{L}_{2;24}^V \\ \tilde{L}_{2;21}^V & \tilde{L}_{2;22}^V & \tilde{L}_{2;23}^V & \tilde{L}_{2;24}^V \\ \tilde{L}_{2;41}^V & \tilde{L}_{2;42}^V & \tilde{L}_{2;43}^V & \tilde{L}_{2;44}^V \end{pmatrix}$$

$$\begin{pmatrix} \tilde{L}_{1;11}^V + \tilde{L}_{1;21}^V & \tilde{L}_{1;12}^V + \tilde{L}_{1;22}^V & \tilde{L}_{1;13}^V + \tilde{L}_{1;23}^V & \tilde{L}_{1;14}^V + \tilde{L}_{1;24}^V \\ \tilde{L}_{1;31}^V & \tilde{L}_{1;32}^V & \tilde{L}_{1;33}^V & \tilde{L}_{1;34}^V \\ \tilde{L}_{1;41}^V & \tilde{L}_{1;42}^V & \tilde{L}_{1;43}^V & \tilde{L}_{1;44}^V \\ -(\tilde{L}_{2;11}^V - \tilde{L}_{2;21}^V) & -(\tilde{L}_{2;12}^V - \tilde{L}_{2;22}^V) & -(\tilde{L}_{2;13}^V - \tilde{L}_{2;23}^V) & -(\tilde{L}_{2;14}^V - \tilde{L}_{2;24}^V) \\ -\tilde{L}_{2;21}^V & -\tilde{L}_{2;22}^V & -\tilde{L}_{2;23}^V & -\tilde{L}_{2;24}^V \\ -\tilde{L}_{2;41}^V & -\tilde{L}_{2;42}^V & -\tilde{L}_{2;43}^V & -\tilde{L}_{2;44}^V \end{pmatrix} \begin{pmatrix} \tilde{p}_{Pf}^+ \\ \tilde{p}_{Ps}^+ \\ \tilde{p}_{Sv}^+ \\ \tilde{p}_{Tm}^+ \\ \tilde{p}_{Pf}^- \\ \tilde{p}_{Ps}^- \\ \tilde{p}_{Sv}^- \\ \tilde{p}_{Tm}^- \end{pmatrix}.$$

(3.132)

Now separating incoming and outgoing fields, mimicking the format of equation

(3.112), we obtain

$$\begin{pmatrix}
 -(\tilde{L}_{1;11}^V + \tilde{L}_{1;21}^V) & -(\tilde{L}_{1;12}^V + \tilde{L}_{1;22}^V) & -(\tilde{L}_{1;13}^V + \tilde{L}_{1;23}^V) & -(\tilde{L}_{1;14}^V + \tilde{L}_{1;24}^V) \\
 -\tilde{L}_{1;31}^V & -\tilde{L}_{1;32}^V & -\tilde{L}_{1;33}^V & -\tilde{L}_{1;34}^V \\
 -\tilde{L}_{1;41}^V & -\tilde{L}_{1;42}^V & -\tilde{L}_{1;43}^V & -\tilde{L}_{1;44}^V \\
 (\tilde{L}_{2;11}^V - \tilde{L}_{2;21}^V) & (\tilde{L}_{2;12}^V - \tilde{L}_{2;22}^V) & (\tilde{L}_{2;13}^V - \tilde{L}_{2;23}^V) & (\tilde{L}_{2;14}^V - \tilde{L}_{2;24}^V) \\
 \tilde{L}_{2;21}^V & \tilde{L}_{2;22}^V & \tilde{L}_{2;23}^V & \tilde{L}_{2;24}^V \\
 \tilde{L}_{2;41}^V & \tilde{L}_{1;42}^V & \tilde{L}_{2;43}^V & \tilde{L}_{2;44}^V \\
 d_{1,P}^{fl,V} & 0 & & \\
 0 & 0 & & \\
 0 & d_{1,EM}^{fl,V} & & \\
 0 & 0 & & \\
 B_P^{fl,V} d_{1,P}^{fl,V} & 0 & & \\
 0 & B_{EM}^{fl,V} d_{1,EM}^{fl,V} & &
 \end{pmatrix}
 \begin{pmatrix}
 \tilde{p}_{Pf}^- \\
 \tilde{p}_{Ps}^- \\
 \tilde{p}_{SV}^- \\
 \tilde{p}_{TM}^- \\
 \tilde{p}_P^+ \\
 \tilde{p}_{EM}^+
 \end{pmatrix}
 =
 \begin{pmatrix}
 \tilde{L}_{1;11}^V + \tilde{L}_{1;21}^V & \tilde{L}_{1;12}^V + \tilde{L}_{1;22}^V & \tilde{L}_{1;13}^V + \tilde{L}_{1;23}^V & \tilde{L}_{1;14}^V + \tilde{L}_{1;24}^V \\
 \tilde{L}_{1;31}^V & \tilde{L}_{1;32}^V & \tilde{L}_{1;33}^V & \tilde{L}_{1;34}^V \\
 \tilde{L}_{1;41}^V & \tilde{L}_{1;42}^V & \tilde{L}_{1;43}^V & \tilde{L}_{1;44}^V \\
 \tilde{L}_{2;11}^V - \tilde{L}_{2;21}^V & \tilde{L}_{2;12}^V - \tilde{L}_{2;22}^V & \tilde{L}_{2;13}^V - \tilde{L}_{2;23}^V & \tilde{L}_{2;14}^V - \tilde{L}_{2;24}^V \\
 \tilde{L}_{2;21}^V & \tilde{L}_{2;22}^V & \tilde{L}_{2;23}^V & \tilde{L}_{2;24}^V \\
 \tilde{L}_{2;41}^V & \tilde{L}_{2;42}^V & \tilde{L}_{2;43}^V & \tilde{L}_{2;44}^V \\
 -d_{1,P}^{fl,V} & 0 & & \\
 0 & 0 & & \\
 0 & -d_{1,EM}^{fl,V} & & \\
 0 & 0 & & \\
 B_P^{fl,V} d_{1,P}^{fl,V} & 0 & & \\
 0 & B_{EM}^{fl,V} d_{1,EM}^{fl,V} & &
 \end{pmatrix}
 \begin{pmatrix}
 \tilde{p}_{Pf}^+ \\
 \tilde{p}_{Ps}^+ \\
 \tilde{p}_{SV}^+ \\
 \tilde{p}_{TM}^+ \\
 \tilde{p}_P^- \\
 \tilde{p}_{EM}^-
 \end{pmatrix}. \tag{3.133}$$

Now, to obtain the desired scattering matrix $\tilde{\mathbf{S}}^{p.m/fl;V}$, we need to left multiply at both sides with the inverse of the composition matrix on the left-hand side.

3.2.6 P-SV-TM scattering matrix at a fluid/porous medium interface

In a similar way, we can derive the P-SV-TM scattering matrix at a fluid/porous medium interface. For the contrast under consideration, we start with

$$\begin{pmatrix} \tilde{p}_P^- \\ \tilde{p}_{EM}^- \\ \tilde{p}_{Pf}^+ \\ \tilde{p}_{Ps}^+ \\ \tilde{p}_{SV}^+ \\ \tilde{p}_{TM}^+ \end{pmatrix} = \begin{pmatrix} \tilde{r}_{P-P}^{-+} & \tilde{r}_{P-EM}^{-+} & \tilde{t}_{P-Pf}^- \\ \tilde{r}_{EM-P}^{-+} & \tilde{r}_{EM-EM}^{-+} & \tilde{t}_{EM-Pf}^- \\ \tilde{t}_{Pf-P}^+ & \tilde{t}_{Pf-EM}^+ & \tilde{r}_{Pf-Pf}^{+-} \\ \tilde{t}_{Ps-P}^+ & \tilde{t}_{Ps-EM}^+ & \tilde{r}_{Ps-Pf}^{+-} \\ \tilde{t}_{SV-P}^+ & \tilde{t}_{SV-EM}^+ & \tilde{r}_{SV-Pf}^{+-} \\ \tilde{t}_{TM-P}^+ & \tilde{t}_{TM-EM}^+ & \tilde{r}_{TM-Pf}^{+-} \end{pmatrix} \begin{pmatrix} \tilde{t}_{P-Ps}^- & \tilde{t}_{P-SV}^- & \tilde{t}_{P-TM}^- \\ \tilde{t}_{EM-Ps}^- & \tilde{t}_{EM-SV}^- & \tilde{t}_{EM-TM}^- \\ \tilde{r}_{Pf-Ps}^+ & \tilde{r}_{Pf-SV}^+ & \tilde{r}_{Pf-TM}^+ \\ \tilde{r}_{Ps-Ps}^{+-} & \tilde{r}_{Ps-SV}^{+-} & \tilde{r}_{Ps-TM}^{+-} \\ \tilde{r}_{SV-Ps}^{+-} & \tilde{r}_{SV-SV}^{+-} & \tilde{r}_{SV-TM}^{+-} \\ \tilde{r}_{TM-Ps}^{+-} & \tilde{r}_{TM-SV}^{+-} & \tilde{r}_{TM-TM}^{+-} \end{pmatrix} \begin{pmatrix} \tilde{p}_P^+ \\ \tilde{p}_{EM}^+ \\ \tilde{p}_{Pf}^- \\ \tilde{p}_{Ps}^- \\ \tilde{p}_{SV}^- \\ \tilde{p}_{TM}^- \end{pmatrix}. \quad (3.134)$$

For this interface, we would like to solve for \tilde{r}^{+-} , the local reflection coefficient expressing the reflection of an upgoing field into a downgoing field. Again, in order to solve for this scattering matrix, 6 boundary conditions are required. We select the same boundary conditions as for the porous medium/fluid P-SV-TM scenario. All acoustic and EM velocities, system matrices, scaling factors and power-flux normalization factors remain also the same. So, all information is available for applying the correct boundary conditions of equation (3.125) at the fluid/porous medium interface. Separating incoming and outgoing fields, mimicking the format of equation (3.134), we obtain

$$\begin{pmatrix}
-d_{1,P}^{fl,V} & 0 \\
0 & 0 \\
0 & -d_{1,EM}^{fl,V} \\
0 & 0 \\
B_P^{fl,V} d_{1,P}^{fl,V} & 0 \\
0 & B_{EM}^{fl,V} d_{1,EM}^{fl,V} \\
\tilde{L}_{1;11}^V + \tilde{L}_{1;21}^V & \tilde{L}_{1;12}^V + \tilde{L}_{1;22}^V & \tilde{L}_{1;13}^V + \tilde{L}_{1;23}^V & \tilde{L}_{1;14}^V + \tilde{L}_{1;24}^V \\
\tilde{L}_{1;31}^V & \tilde{L}_{1;32}^V & \tilde{L}_{1;33}^V & \tilde{L}_{1;34}^V \\
\tilde{L}_{1;41}^V & \tilde{L}_{1;42}^V & \tilde{L}_{1;43}^V & \tilde{L}_{1;44}^V \\
(\tilde{L}_{2;11}^V - \tilde{L}_{2;21}^V) & (\tilde{L}_{2;12}^V - \tilde{L}_{2;22}^V) & (\tilde{L}_{2;13}^V - \tilde{L}_{2;23}^V) & (\tilde{L}_{2;14}^V - \tilde{L}_{2;24}^V) \\
\tilde{L}_{2;21}^V & \tilde{L}_{2;22}^V & \tilde{L}_{2;23}^V & \tilde{L}_{2;24}^V \\
\tilde{L}_{2;41}^V & \tilde{L}_{2;42}^V & \tilde{L}_{2;43}^V & \tilde{L}_{2;44}^V
\end{pmatrix}
\begin{pmatrix}
\tilde{p}_P^- \\
\tilde{p}_{EM}^- \\
\tilde{p}_{Pf}^- \\
\tilde{p}_{Ps}^- \\
\tilde{p}_{SV}^- \\
\tilde{p}_{TM}^-
\end{pmatrix} =
\begin{pmatrix}
d_{1,P}^{fl,V} & 0 \\
0 & 0 \\
0 & d_{1,EM}^{fl,V} \\
0 & 0 \\
B_P^{fl,V} d_{1,P}^{fl,V} & 0 \\
0 & B_{EM}^{fl,V} d_{1,EM}^{fl,V} \\
-(\tilde{L}_{1;11}^V + \tilde{L}_{1;21}^V) & -(\tilde{L}_{1;12}^V + \tilde{L}_{1;22}^V) & -(\tilde{L}_{1;13}^V + \tilde{L}_{1;23}^V) & -(\tilde{L}_{1;14}^V + \tilde{L}_{1;24}^V) \\
-\tilde{L}_{1;31}^V & -\tilde{L}_{1;32}^V & -\tilde{L}_{1;33}^V & -\tilde{L}_{1;34}^V \\
-\tilde{L}_{1;41}^V & -\tilde{L}_{1;42}^V & -\tilde{L}_{1;43}^V & -\tilde{L}_{1;44}^V \\
\tilde{L}_{2;11}^V - \tilde{L}_{2;21}^V & \tilde{L}_{2;12}^V - \tilde{L}_{2;22}^V & \tilde{L}_{2;13}^V - \tilde{L}_{2;23}^V & \tilde{L}_{2;14}^V - \tilde{L}_{2;24}^V \\
\tilde{L}_{2;21}^V & \tilde{L}_{2;22}^V & \tilde{L}_{2;23}^V & \tilde{L}_{2;24}^V \\
\tilde{L}_{2;41}^V & \tilde{L}_{2;42}^V & \tilde{L}_{2;43}^V & \tilde{L}_{2;44}^V
\end{pmatrix}
\begin{pmatrix}
\tilde{p}_P^+ \\
\tilde{p}_{EM}^+ \\
\tilde{p}_{Pf}^+ \\
\tilde{p}_{Ps}^- \\
\tilde{p}_{SV}^- \\
\tilde{p}_{TM}^-
\end{pmatrix}. \tag{3.135}$$

Now, to obtain the desired scattering matrix $\tilde{\mathbf{S}}^{fl/p.m.:V}$, we need to left multiply at both sides with the inverse of the composition matrix on the left-hand side.

3.2.7 SH-TE global downgoing reflection matrix at a fluid/porous medium interface

Thus far, we have considered the effects of porous medium/fluid and fluid/porous medium interfaces on the local scattering matrices. However, these interfaces also have an effect on the global reflection matrices, that need to be properly updated across these interfaces in the recursive scheme. In the following sections, we will describe the expressions required for correctly updating the global reflection matrices across these interfaces.

Let us start with the scenario where we have a fluid halfspace above a porous medium, for the SH-TE propagation mode. We desire to correctly update the global downgoing reflection matrix across the fluid/porous medium interface. We again select the same boundary conditions as discussed before for the SH-TE system in porous medium/fluid and fluid/porous medium transitions, to solve the problem.

Applying the correct fluid-porous medium boundary conditions, yields the fol-

lowing equality across the interface

$$\tilde{\mathbf{q}}_{p.m.}^H = \begin{pmatrix} \tilde{\mathbf{E}}^H \\ \tilde{\tau}^{b,H} \\ -\tilde{\mathbf{H}}^H \end{pmatrix} = \tilde{\mathbf{q}}_{fluid}^H = \begin{pmatrix} \tilde{\mathbf{E}}^H \\ 0 \\ -\tilde{\mathbf{H}}^H \end{pmatrix}. \quad (3.136)$$

We already know the required composition matrices for the SH-TE system in a porous medium and in a fluid. Writing the equality (3.145) in terms of one-way fields yields

$$\tilde{\mathbf{L}}_{fluid}^H \tilde{\mathbf{P}}_{fluid}^H = \tilde{\mathbf{L}}_{p.m.}^H \tilde{\mathbf{P}}_{p.m.}^H, \quad (3.137)$$

or explicitly

$$\begin{pmatrix} d_{1;EM}^{fl,H} & d_{1;EM}^{fl,H} \\ 0 & 0 \\ B_{EM}^{fl,H} d_{1;EM}^{fl,H} & -B_{EM}^{fl,H} d_{1;EM}^{fl,H} \end{pmatrix} \begin{pmatrix} \tilde{p}_{EM}^+ \\ \tilde{p}_{EM}^- \end{pmatrix} = \begin{pmatrix} \tilde{L}_{1;21}^H & v_{1;22}^H & \tilde{L}_{1;21}^H & \tilde{L}_{1;22}^H \\ \tilde{L}_{2;11}^H & \tilde{L}_{2;12}^H & -\tilde{L}_{2;11}^H & -\tilde{L}_{2;12}^H \\ \tilde{L}_{2;21}^H & \tilde{L}_{2;22}^H & -\tilde{L}_{2;21}^H & -\tilde{L}_{2;22}^H \end{pmatrix} \begin{pmatrix} \tilde{p}_{SH}^+ \\ \tilde{p}_{TE}^+ \\ \tilde{p}_{SH}^- \\ \tilde{p}_{TE}^- \end{pmatrix}. \quad (3.138)$$

Here, we want to find the global downgoing reflection matrix ($\tilde{\mathbf{R}}_n^-(z_{n+1})$) at the fluid side of the interface. In order to find this reflection matrix, we need to express it in terms of the global reflection matrix at the porous medium side of the interface $\tilde{\mathbf{R}}_{n+1}^{-+}(z_{n+1})$. On the fluid side of the interface, the following relation holds

$$\tilde{\mathbf{p}}_{fluid}^- = \tilde{\mathbf{R}}_n^-(z_{n+1}) \tilde{\mathbf{p}}_{fluid}^+. \quad (3.139)$$

Similarly, in the porous medium, the upgoing fields can be expressed as

$$\tilde{\mathbf{p}}_{p.m.}^- = \tilde{\mathbf{R}}_{n+1}^{-+}(z_{n+1}) \tilde{\mathbf{p}}_{p.m.}^+. \quad (3.140)$$

We can now express the one-way upgoing fields in the porous medium in terms of the downgoing fields in the porous medium times the global reflection matrix at the porous medium side of the interface, $\tilde{\mathbf{R}}_{n+1}^{-+}(z_{n+1})$, as

$$\begin{pmatrix} \tilde{p}_{SH}^-(z_{n+1}) \\ \tilde{p}_{TE}^-(z_{n+1}) \end{pmatrix} = \begin{pmatrix} \tilde{\mathcal{R}}_{SH-SH}^{-+} & \tilde{\mathcal{R}}_{SH-TE}^{-+} \\ \tilde{\mathcal{R}}_{TE-SH}^{-+} & \tilde{\mathcal{R}}_{TE-TE}^{-+} \end{pmatrix} \begin{pmatrix} \tilde{p}_{SH}^+(z_{n+1}) \\ \tilde{p}_{TE}^+(z_{n+1}) \end{pmatrix}. \quad (3.141)$$

Using these expressions, we can rewrite equation (3.138) in terms of only downgoing

fields at the porous medium side:

$$\begin{aligned}
 & \begin{pmatrix} \tilde{L}_{1;21}^H [1 + \tilde{\mathcal{R}}_{11}^{-+}] + \tilde{L}_{1;22}^H \tilde{\mathcal{R}}_{21}^{-+} & \tilde{L}_{1;22}^H [1 + \tilde{\mathcal{R}}_{22}^{-+}] + \tilde{L}_{1;21}^H \tilde{\mathcal{R}}_{12}^{-+} \\ \tilde{L}_{2;11}^H [1 - \tilde{\mathcal{R}}_{11}^{-+}] - \tilde{L}_{2;12}^H \tilde{\mathcal{R}}_{21}^{-+} & \tilde{L}_{2;12}^H [1 - \tilde{\mathcal{R}}_{22}^{-+}] - \tilde{L}_{2;11}^H \tilde{\mathcal{R}}_{12}^{-+} \\ \tilde{L}_{2;21}^H [1 - \tilde{\mathcal{R}}_{11}^{-+}] - \tilde{L}_{2;22}^H \tilde{\mathcal{R}}_{21}^{-+} & \tilde{L}_{2;22}^H [1 - \tilde{\mathcal{R}}_{22}^{-+}] - \tilde{L}_{2;21}^H \tilde{\mathcal{R}}_{12}^{-+} \end{pmatrix} \begin{pmatrix} \tilde{p}_{SH}^+ \\ \tilde{p}_{TE}^+ \end{pmatrix} \\
 & = \begin{pmatrix} d_{1;EM}^{fl,H} & d_{1;EM}^{fl,H} \\ 0 & 0 \\ B_{EM}^{fl,H} d_{1;EM}^{fl,H} & -B_{EM}^{fl,H} d_{1;EM}^{fl,H} \end{pmatrix} \begin{pmatrix} \tilde{p}_{EM}^+ \\ \tilde{p}_{EM}^- \end{pmatrix}. \tag{3.142}
 \end{aligned}$$

We now first reorganize this expression separating the unknown, outgoing one-way fields from the incoming one-way fields, as

$$\begin{aligned}
 & \begin{pmatrix} \tilde{L}_{1;21}^H [1 + \tilde{\mathcal{R}}_{11}^{-+}] + \tilde{L}_{1;22}^H \tilde{\mathcal{R}}_{21}^{-+} & \tilde{L}_{1;22}^H [1 + \tilde{\mathcal{R}}_{22}^{-+}] + \tilde{L}_{1;21}^H \tilde{\mathcal{R}}_{12}^{-+} \\ \tilde{L}_{2;11}^H [1 - \tilde{\mathcal{R}}_{11}^{-+}] - \tilde{L}_{2;12}^H \tilde{\mathcal{R}}_{21}^{-+} & \tilde{L}_{2;12}^H [1 - \tilde{\mathcal{R}}_{22}^{-+}] - \tilde{L}_{2;11}^H \tilde{\mathcal{R}}_{12}^{-+} \\ \tilde{L}_{2;21}^H [1 - \tilde{\mathcal{R}}_{11}^{-+}] - \tilde{L}_{2;22}^H \tilde{\mathcal{R}}_{21}^{-+} & \tilde{L}_{2;22}^H [1 - \tilde{\mathcal{R}}_{22}^{-+}] - \tilde{L}_{2;21}^H \tilde{\mathcal{R}}_{12}^{-+} \\ -d_{1;EM}^{fl,H} \\ 0 \\ B_{EM}^{fl,H} d_{1;EM}^{fl,H} \end{pmatrix} \begin{pmatrix} \tilde{p}_{SH}^+ \\ \tilde{p}_{TE}^+ \\ \tilde{p}_{EM}^- \end{pmatrix} = \begin{pmatrix} d_{1;EM}^{fl,H} \\ 0 \\ B_{EM}^{fl,H} d_{1;EM}^{fl,H} \end{pmatrix} \begin{pmatrix} \tilde{p}_{EM}^+ \end{pmatrix}. \tag{3.143}
 \end{aligned}$$

Now, we can solve for the unknown one-way fields on the left-hand side, by multiplying both sides with the inverse of the matrix on the left-hand side, yielding

$$\begin{pmatrix} \tilde{p}_{SH}^+ \\ \tilde{p}_{TE}^+ \\ \tilde{p}_{EM}^- \end{pmatrix} = \begin{pmatrix} \tilde{T}_{SH-TE}^+ \\ \tilde{T}_{TE-TE}^+ \\ \tilde{R}_n^{-+}(z_{n+1}) \end{pmatrix} \tilde{p}_{EM}^+, \tag{3.144}$$

where $\tilde{R}_n^{-+}(z_{n+1})$ is the global reflection coefficient at the fluid side we were after, correctly updated across the interface in the recursive scheme. We also recognize the global transmission coefficients that are required for example when the source is located in the fluid and the receivers in the porous medium.

3.2.8 SH-TE global upgoing reflection matrix at a porous medium/fluid interface

We now consider the scenario where we have a fluid halfspace below a porous medium, for the SH-TE propagation mode, and desire to correctly update the global

upgoing reflection matrix across the porous medium/fluid interface. We again select the same boundary conditions as discussed before for the SH-TE system in porous medium/fluid and fluid/porous medium transitions, to solve the problem.

Applying the correct fluid/porous medium boundary conditions, yields the following equality across the interface

$$\tilde{\mathbf{q}}_{p.m.}^H = \begin{pmatrix} \tilde{E}^H \\ \tilde{\tau}^{b,H} \\ -\tilde{H}^H \end{pmatrix} = \tilde{\mathbf{q}}_{fluid}^H = \begin{pmatrix} \tilde{E}^H \\ 0 \\ -\tilde{H}^H \end{pmatrix}. \quad (3.145)$$

We already know the required composition matrices for the SH-TE system in a porous medium and in a fluid.

Writing the equality (3.145) in terms of one-way fields yields

$$\tilde{\mathbf{L}}_{fluid}^H \tilde{\mathbf{P}}_{fluid}^H = \tilde{\mathbf{L}}_{p.m.}^H \tilde{\mathbf{P}}_{p.m.}^H, \quad (3.146)$$

or explicitly

$$\begin{pmatrix} d_{1;EM}^{fl,H} & d_{1;EM}^{fl,H} \\ 0 & 0 \\ B_{EM}^{fl,H} d_{1;EM}^{fl,H} & -B_{EM}^{fl,H} d_{1;EM}^{fl,H} \end{pmatrix} \begin{pmatrix} \tilde{p}_{EM}^+ \\ \tilde{p}_{EM}^- \end{pmatrix} = \begin{pmatrix} \tilde{L}_{1;21}^H & \tilde{L}_{1;22}^H & \tilde{L}_{1;21}^H & \tilde{L}_{1;22}^H \\ \tilde{L}_{2;11}^H & \tilde{L}_{2;12}^H & -\tilde{L}_{2;11}^H & -\tilde{L}_{2;12}^H \\ \tilde{L}_{2;21}^H & \tilde{L}_{2;22}^H & -\tilde{L}_{2;21}^H & -\tilde{L}_{2;22}^H \end{pmatrix} \begin{pmatrix} \tilde{p}_{SH}^+ \\ \tilde{p}_{TE}^+ \\ \tilde{p}_{SH}^- \\ \tilde{p}_{TE}^- \end{pmatrix}. \quad (3.147)$$

Here, we want to find the global upgoing reflection matrix $\tilde{\mathbf{R}}_{n+1}^{+-}(z_{n+1})$ at the fluid side of the interface. In order to find this reflection matrix, we need to express it in terms of the global upgoing reflection matrix at the porous medium side of the interface $\tilde{\mathbf{R}}_n^{+-}(z_{n+1})$. On the fluid side of the interface, the following relation holds

$$\tilde{\mathbf{p}}_{fluid}^+ = \tilde{\mathbf{R}}_{n+1}^{+-}(z_{n+1}) \tilde{\mathbf{p}}_{fluid}^-. \quad (3.148)$$

Similarly, in the porous medium, the downgoing fields can be expressed as

$$\tilde{\mathbf{p}}_{p.m.}^+ = \tilde{\mathbf{R}}_n^{+-}(z_{n+1}) \tilde{\mathbf{p}}_{p.m.}^-. \quad (3.149)$$

We can now express the one-way downgoing fields in the porous medium in terms of the upgoing fields in the porous medium times the global reflection matrix at the porous medium side of the interface, $\tilde{\mathbf{R}}_n^{+-}(z_{n+1})$, as

$$\begin{pmatrix} \tilde{p}_{SH}^+(z_{n+1}) \\ \tilde{p}_{TE}^+(z_{n+1}) \end{pmatrix} = \begin{pmatrix} \tilde{\mathcal{R}}_{SH-SH}^{+-} & \tilde{\mathcal{R}}_{SH-TE}^{+-} \\ \tilde{\mathcal{R}}_{TE-SH}^{+-} & \tilde{\mathcal{R}}_{TE-TE}^{+-} \end{pmatrix} \begin{pmatrix} \tilde{p}_{SH}^-(z_{n+1}) \\ \tilde{p}_{TE}^-(z_{n+1}) \end{pmatrix}. \quad (3.150)$$

Using these expressions, we can rewrite equation (3.147) in terms of only upgoing fields at the porous medium side:

$$\begin{aligned} & \begin{pmatrix} \tilde{L}_{1;21}^H [1 + \tilde{\mathcal{R}}_{11}^{+-}] + \tilde{L}_{1;22}^H \tilde{\mathcal{R}}_{21}^{+-} & \tilde{L}_{1;22}^H [1 + \tilde{\mathcal{R}}_{22}^{+-}] + \tilde{L}_{1;21}^H \tilde{\mathcal{R}}_{12}^{+-} \\ -\tilde{L}_{2;11}^H [1 - \tilde{\mathcal{R}}_{11}^{+-}] + \tilde{L}_{2;12}^H \tilde{\mathcal{R}}_{21}^{+-} & -\tilde{L}_{2;12}^H [1 - \tilde{\mathcal{R}}_{22}^{+-}] + \tilde{L}_{2;11}^H \tilde{\mathcal{R}}_{12}^{+-} \\ -\tilde{L}_{2;21}^H [1 - \tilde{\mathcal{R}}_{11}^{+-}] + \tilde{L}_{2;22}^H \tilde{\mathcal{R}}_{21}^{+-} & -\tilde{L}_{2;22}^H [1 - \tilde{\mathcal{R}}_{22}^{+-}] + \tilde{L}_{2;21}^H \tilde{\mathcal{R}}_{12}^{+-} \end{pmatrix} \begin{pmatrix} \tilde{p}_{SH}^- \\ \tilde{p}_{TE}^- \end{pmatrix} \\ &= \begin{pmatrix} d_{1;EM}^{fl,H} & d_{1;EM}^{fl,H} \\ 0 & 0 \\ B_{EM}^{fl,H} d_{1;EM}^{fl,H} & -B_{EM}^{fl,H} d_{1;EM}^{fl,H} \end{pmatrix} \begin{pmatrix} \tilde{p}_{EM}^+ \\ \tilde{p}_{EM}^- \end{pmatrix}. \end{aligned} \quad (3.151)$$

We now first reorganize this expression separating the unknown, outgoing one-way fields from the incoming one-way fields, as

$$\begin{aligned} & \begin{pmatrix} \tilde{L}_{1;21}^H [1 + \tilde{\mathcal{R}}_{11}^{+-}] + \tilde{L}_{1;22}^H \tilde{\mathcal{R}}_{21}^{+-} & \tilde{L}_{1;22}^H [1 + \tilde{\mathcal{R}}_{22}^{+-}] + \tilde{L}_{1;21}^H \tilde{\mathcal{R}}_{12}^{+-} \\ -\tilde{L}_{2;11}^H [1 - \tilde{\mathcal{R}}_{11}^{+-}] + \tilde{L}_{2;12}^H \tilde{\mathcal{R}}_{21}^{+-} & -\tilde{L}_{2;12}^H [1 - \tilde{\mathcal{R}}_{22}^{+-}] + \tilde{L}_{2;11}^H \tilde{\mathcal{R}}_{12}^{+-} \\ -\tilde{L}_{2;21}^H [1 - \tilde{\mathcal{R}}_{11}^{+-}] + \tilde{L}_{2;22}^H \tilde{\mathcal{R}}_{21}^{+-} & -\tilde{L}_{2;22}^H [1 - \tilde{\mathcal{R}}_{22}^{+-}] + \tilde{L}_{2;21}^H \tilde{\mathcal{R}}_{12}^{+-} \\ -d_{1,EM}^{fl,H} \\ 0 \\ -B_{EM}^{fl,H} d_{1,EM}^{fl,H} \end{pmatrix} \begin{pmatrix} \tilde{p}_{SH}^- \\ \tilde{p}_{TE}^- \\ \tilde{p}_{EM}^+ \end{pmatrix} = \begin{pmatrix} d_{1,EM}^{fl,H} \\ 0 \\ -B_{EM}^{fl,H} d_{1,EM}^{fl,H} \end{pmatrix} \begin{pmatrix} \tilde{p}_{EM}^- \end{pmatrix}. \end{aligned} \quad (3.152)$$

Now, we can solve for the unknown one-way fields on the left-hand side, by multiplying both sides with the inverse of the matrix on the left-hand side, yielding

$$\begin{pmatrix} \tilde{p}_{SH}^- \\ \tilde{p}_{TE}^- \\ \tilde{p}_{EM}^+ \end{pmatrix} = \begin{pmatrix} \tilde{T}_{SH-TE}^- \\ \tilde{T}_{TE-TE}^- \\ \tilde{R}_{n+1}^{+-}(z_{n+1}) \end{pmatrix} \tilde{p}_{EM}^-, \quad (3.153)$$

where $\tilde{R}_{n+1}^{+-}(z_{n+1})$ is the global upgoing reflection coefficient at the fluid side we were after, correctly updated across the interface in the recursive scheme. We also recognize the global transmission coefficients that are required for example when the source is located in the fluid and the receivers in the porous medium.

3.2.9 P-SV-TM global downgoing reflection matrix at a fluid/porous medium interface

Similar to the SH-TE scenario, we also require expressions for the P-SV-TM propagation mode to correctly update the global reflection coefficients across fluid/porous

medium interfaces. We consider the scenario where a fluid halfspace is located above a porous medium, and we desire to correctly update the downgoing global reflection matrix in our recursive scheme. We select the same boundary conditions as discussed before for the P-SV-TM system in porous medium/fluid and fluid/porous medium transitions, to solve the problem.

We again apply the P-SV-TM fluid-solid boundary conditions of equation (3.125). We already know the required composition matrices for the P-SV-TM system in a porous medium and in a fluid. Writing equality (3.125) in terms of one-way fields yields

$$\begin{pmatrix} d_{1,P}^{fl,V} & 0 & d_{1,P}^{fl,V} & 0 \\ 0 & 0 & 0 & 0 \\ 0 & d_{1,EM}^{fl,V} & 0 & d_{1,EM}^{fl,V} \\ 0 & 0 & 0 & 0 \\ B_P^{fl,V} d_{1,P}^{fl,V} & 0 & -B_P^{fl,V} d_{1,P}^{fl,V} & 0 \\ 0 & B_{EM}^{fl,V} d_{1,EM}^{fl,V} & 0 & -B_{EM}^{fl,V} d_{1,EM}^{fl,V} \end{pmatrix} \begin{pmatrix} \tilde{p}_P^+ \\ \tilde{p}_{EM}^+ \\ \tilde{p}_P^- \\ \tilde{p}_{EM}^- \end{pmatrix} = \begin{pmatrix} \tilde{L}_{1;11}^V + \tilde{L}_{1;21}^V & \tilde{L}_{1;12}^V + \tilde{L}_{1;22}^V & \tilde{L}_{1;13}^V + \tilde{L}_{1;23}^V & \tilde{L}_{1;14}^V + \tilde{L}_{1;24}^V \\ \tilde{L}_{1;31}^V & \tilde{L}_{1;32}^V & \tilde{L}_{1;33}^V & \tilde{L}_{1;34}^V \\ \tilde{L}_{1;41}^V & \tilde{L}_{1;42}^V & \tilde{L}_{1;43}^V & \tilde{L}_{1;44}^V \\ \tilde{L}_{2;11}^V - \tilde{L}_{2;21}^V & \tilde{L}_{2;12}^V - \tilde{L}_{2;22}^V & \tilde{L}_{2;13}^V - \tilde{L}_{2;23}^V & \tilde{L}_{2;14}^V - \tilde{L}_{2;24}^V \\ \tilde{L}_{2;21}^V & \tilde{L}_{2;22}^V & \tilde{L}_{2;23}^V & \tilde{L}_{2;24}^V \\ \tilde{L}_{2;41}^V & \tilde{L}_{2;42}^V & \tilde{L}_{2;43}^V & \tilde{L}_{2;44}^V \end{pmatrix} \begin{pmatrix} \tilde{p}_{Pf}^+ \\ \tilde{p}_{Ps}^+ \\ \tilde{p}_{SV}^+ \\ \tilde{p}_{TM}^+ \\ \tilde{p}_{Pf}^- \\ \tilde{p}_{Ps}^- \\ \tilde{p}_{SV}^- \\ \tilde{p}_{TM}^- \end{pmatrix}. \quad (3.154)$$

Here, we want to find the global downgoing reflection matrix ($\tilde{\mathbf{R}}_n^+(z_{n+1})$) at the fluid side of the interface. In order to find this reflection matrix, we need to express it in terms of the global reflection coefficient at the porous medium side of the interface $\tilde{\mathbf{R}}_{n+1}^+(z_{n+1})$. On the fluid side of the interface, the following relation holds

$$\tilde{\mathbf{p}}_{fl}^- = \tilde{\mathbf{R}}_n^+(z_{n+1}) \tilde{\mathbf{p}}_{fl}^+. \quad (3.155)$$

Similarly, in the porous medium, the upgoing fields can be expressed as

$$\tilde{\mathbf{p}}_{p.m.}^- = \tilde{\mathbf{R}}_{n+1}^+(z_{n+1}) \tilde{\mathbf{p}}_{p.m.}^+. \quad (3.156)$$

We can now express the one-way upgoing fields in the porous medium in terms of the downgoing fields in the porous medium times the global reflection matrix at the porous medium side $\tilde{\mathbf{R}}_{n+1}^+(z_{n+1})$:

$$\begin{pmatrix} \tilde{p}_{Pf}^- \\ \tilde{p}_{Ps}^- \\ \tilde{p}_{SV}^- \\ \tilde{p}_{TM}^- \end{pmatrix} = \begin{pmatrix} \tilde{\mathcal{R}}_{Pf-Pf}^{-+} & \tilde{\mathcal{R}}_{Pf-Ps}^{-+} & \tilde{\mathcal{R}}_{Pf-SV}^{-+} & \tilde{\mathcal{R}}_{Pf-TM}^{-+} \\ \tilde{\mathcal{R}}_{Ps-Pf}^{-+} & \tilde{\mathcal{R}}_{Ps-Ps}^{-+} & \tilde{\mathcal{R}}_{Ps-SV}^{-+} & \tilde{\mathcal{R}}_{Ps-TM}^{-+} \\ \tilde{\mathcal{R}}_{SV-Pf}^{-+} & \tilde{\mathcal{R}}_{SV-Ps}^{-+} & \tilde{\mathcal{R}}_{SV-SV}^{-+} & \tilde{\mathcal{R}}_{SV-TM}^{-+} \\ \tilde{\mathcal{R}}_{TM-Pf}^{-+} & \tilde{\mathcal{R}}_{TM-Ps}^{-+} & \tilde{\mathcal{R}}_{TM-SV}^{-+} & \tilde{\mathcal{R}}_{TM-TM}^{-+} \end{pmatrix} \begin{pmatrix} \tilde{p}_{Pf}^+ \\ \tilde{p}_{Ps}^+ \\ \tilde{p}_{SV}^+ \\ \tilde{p}_{TM}^+ \end{pmatrix}. \quad (3.157)$$

Using these expressions, we can rewrite equation (3.154) in terms of only down-going fields at the porous medium side

$$\begin{pmatrix} \tilde{L}_{11} & \tilde{L}_{12} & \tilde{L}_{13} & \tilde{L}_{14} \\ \tilde{L}_{21} & \tilde{L}_{22} & \tilde{L}_{23} & \tilde{L}_{24} \\ \tilde{L}_{31} & \tilde{L}_{32} & \tilde{L}_{33} & \tilde{L}_{34} \\ \tilde{L}_{41} & \tilde{L}_{42} & \tilde{L}_{43} & \tilde{L}_{44} \\ \tilde{L}_{51} & \tilde{L}_{52} & \tilde{L}_{53} & \tilde{L}_{54} \\ \tilde{L}_{61} & \tilde{L}_{62} & \tilde{L}_{63} & \tilde{L}_{64} \end{pmatrix} \begin{pmatrix} \tilde{p}_{Pf}^+ \\ \tilde{p}_{Ps}^+ \\ \tilde{p}_{SV}^+ \\ \tilde{p}_{TM}^+ \end{pmatrix} \\ = \begin{pmatrix} d_{1,P}^{fl,V} & 0 & d_{1,P}^{fl,V} & 0 \\ 0 & 0 & 0 & 0 \\ 0 & d_{1,EM}^{fl,V} & 0 & d_{1,EM}^{fl,V} \\ 0 & 0 & 0 & 0 \\ B_P^{fl,V} d_{1,P}^{fl,V} & 0 & -B_P^{fl,V} d_{1,P}^{fl,V} & 0 \\ 0 & B_{EM}^{fl,V} d_{1,EM}^{fl,V} & 0 & -B_{EM}^{fl,V} d_{1,EM}^{fl,V} \end{pmatrix} \begin{pmatrix} \tilde{p}_P^+ \\ \tilde{p}_{EM}^+ \\ \tilde{p}_P^- \\ \tilde{p}_{EM}^- \end{pmatrix}, \quad (3.158)$$

Here,

$$\tilde{L}_{1J} = (\tilde{L}_{1;1I} + \tilde{L}_{1;2I})(\delta_{IJ} + \tilde{\mathcal{R}}_{IJ}^{-+}), \quad (3.159)$$

$$\tilde{L}_{2J} = \tilde{L}_{1;3I}(\delta_{IJ} + \tilde{\mathcal{R}}_{IJ}^{-+}), \quad (3.160)$$

$$\tilde{L}_{3J} = \tilde{L}_{1;4I}(\delta_{IJ} + \tilde{\mathcal{R}}_{IJ}^{-+}), \quad (3.161)$$

$$\tilde{L}_{4J} = (\tilde{L}_{2;1I} - \tilde{L}_{2;2I})(\delta_{IJ} - \tilde{\mathcal{R}}_{IJ}^{-+}), \quad (3.162)$$

$$\tilde{L}_{5J} = \tilde{L}_{2;2I}(\delta_{IJ} - \tilde{\mathcal{R}}_{IJ}^{-+}), \quad (3.163)$$

$$\tilde{L}_{6J} = \tilde{L}_{2;4I}(\delta_{IJ} - \tilde{\mathcal{R}}_{IJ}^{-+}), \quad (3.164)$$

where in this case the capital subscripts I and J can take the values 1 to 4 and the Einstein summation convention holds for repeated indices.

We separate the unknown, outgoing one-way fields from the incoming one-way

fields, yielding:

$$\begin{pmatrix} \tilde{L}_{11} & \tilde{L}_{12} & \tilde{L}_{13} & \tilde{L}_{14} & -d_{1,P}^{fl,V} & 0 \\ \tilde{L}_{21} & \tilde{L}_{22} & \tilde{L}_{23} & \tilde{L}_{24} & 0 & 0 \\ \tilde{L}_{31} & \tilde{L}_{32} & \tilde{L}_{33} & \tilde{L}_{34} & 0 & -d_{1,EM}^{fl,V} \\ \tilde{L}_{41} & \tilde{L}_{42} & \tilde{L}_{43} & \tilde{L}_{44} & 0 & 0 \\ \tilde{L}_{51} & \tilde{L}_{52} & \tilde{L}_{53} & \tilde{L}_{54} & B_P^{fl,V} d_{1,P}^{fl,V} & 0 \\ \tilde{L}_{61} & \tilde{L}_{62} & \tilde{L}_{63} & \tilde{L}_{64} & 0 & B_{EM}^{fl,V} d_{1,EM}^{fl,V} \end{pmatrix} \begin{pmatrix} \tilde{p}_{Pf}^+ \\ \tilde{p}_{Ps}^+ \\ \tilde{p}_{SV}^+ \\ \tilde{p}_{TM}^+ \\ \tilde{p}_P^- \\ \tilde{p}_{EM}^- \end{pmatrix} = \quad (3.165)$$

$$\begin{pmatrix} d_{1,P}^{fl,V} & 0 \\ 0 & 0 \\ 0 & d_{1,EM}^{fl,V} \\ 0 & 0 \\ B_P^{fl,V} d_{1,P}^{fl,V} & 0 \\ 0 & B_{EM}^{fl,V} d_{1,EM}^{fl,V} \end{pmatrix} \begin{pmatrix} \tilde{p}_P^+ \\ \tilde{p}_{EM}^+ \end{pmatrix}. \quad (3.166)$$

We solve for the unknown one-way fields on the left-hand side by left-multiplying both sides with the inverse of the matrix on the left-hand side, yielding

$$\begin{pmatrix} \tilde{p}_{Pf}^+ \\ \tilde{p}_{Ps}^+ \\ \tilde{p}_{SV}^+ \\ \tilde{p}_{TM}^+ \\ \tilde{p}_P^- \\ \tilde{p}_{EM}^- \end{pmatrix} = \begin{pmatrix} \tilde{T}_{Pf-P}^+ & \tilde{T}_{Pf-EM}^+ \\ \tilde{T}_{Ps-P}^+ & \tilde{T}_{Ps-EM}^+ \\ \tilde{T}_{SV-P}^+ & \tilde{T}_{SV-EM}^+ \\ \tilde{T}_{EM-P}^+ & \tilde{T}_{EM-EM}^+ \\ \tilde{R}_{P-P;n}^{-+}(z_{n+1}) & \tilde{R}_{P-EM;n}^{-+}(z_{n+1}) \\ \tilde{R}_{EM-P;n}^{-+}(z_{n+1}) & \tilde{R}_{EM-EM;n}^{-+}(z_{n+1}) \end{pmatrix} \begin{pmatrix} \tilde{p}_P^+ \\ \tilde{p}_{EM}^+ \end{pmatrix}, \quad (3.167)$$

where $\tilde{R}_n^{-+}(z_{n+1})$ represent the global reflection coefficients at the fluid-side that we were after.

3.2.10 P-SV-TM global upgoing reflection matrix at a porous medium/fluid interface

We now consider the scenario where a fluid halfspace is located below a porous medium, and we desire to correctly update the upgoing global reflection matrix in our recursive scheme. The procedure is similar as for the case where a fluid halfspace is located above a porous medium. We select the same boundary conditions as discussed before for the P-SV-TM system in porous medium/fluid and fluid/porous medium transitions, to solve the problem.

We again apply the P-SV-TM fluid-porous medium boundary conditions of equation (3.125). We already know the required composition matrices for the P-SV-TM system in a porous medium and in a fluid. Writing the equality (3.125) in terms of one-way fields yields

$$\begin{pmatrix}
d_{1,P}^{fl,V} & 0 & d_{1,P}^{fl,V} & 0 \\
0 & 0 & 0 & 0 \\
0 & d_{1,EM}^{fl,V} & 0 & d_{1,EM}^{fl,V} \\
0 & 0 & 0 & 0 \\
B_P^{fl,V} d_{1,P}^{fl,V} & 0 & -B_P^{fl,V} d_{1,P}^{fl,V} & 0 \\
0 & B_{EM}^{fl,V} d_{1,EM}^{fl,V} & 0 & -B_{EM}^{fl,V} d_{1,EM}^{fl,V}
\end{pmatrix}
\begin{pmatrix}
\tilde{p}_P^+ \\
\tilde{p}_{EM}^+ \\
\tilde{p}_P^- \\
\tilde{p}_{EM}^-
\end{pmatrix} =
\begin{pmatrix}
\tilde{L}_{1;11}^V + \tilde{L}_{1;21}^V & \tilde{L}_{1;12}^V + \tilde{L}_{1;22}^V & \tilde{L}_{1;13}^V + \tilde{L}_{1;23}^V & \tilde{L}_{1;14}^V + \tilde{L}_{1;24}^V \\
\tilde{L}_{1;31}^V & \tilde{L}_{1;32}^V & \tilde{L}_{1;33}^V & \tilde{L}_{1;34}^V \\
\tilde{L}_{1;41}^V & \tilde{L}_{1;42}^V & \tilde{L}_{1;43}^V & \tilde{L}_{1;44}^V \\
\tilde{L}_{2;11}^V - \tilde{L}_{2;21}^V & \tilde{L}_{2;12}^V - \tilde{L}_{2;22}^V & \tilde{L}_{2;13}^V - \tilde{L}_{2;23}^V & \tilde{L}_{2;14}^V - \tilde{L}_{2;24}^V \\
\tilde{L}_{2;21}^V & \tilde{L}_{2;22}^V & \tilde{L}_{2;23}^V & \tilde{L}_{2;24}^V \\
\tilde{L}_{2;41}^V & \tilde{L}_{2;42}^V & \tilde{L}_{2;43}^V & \tilde{L}_{2;44}^V
\end{pmatrix}
\begin{pmatrix}
\tilde{L}_{1;11}^V + \tilde{L}_{1;21}^V & \tilde{L}_{1;12}^V + \tilde{L}_{1;22}^V & \tilde{L}_{1;13}^V + \tilde{L}_{1;23}^V & \tilde{L}_{1;14}^V + \tilde{L}_{1;24}^V \\
\tilde{L}_{1;31}^V & \tilde{L}_{1;32}^V & \tilde{L}_{1;33}^V & \tilde{L}_{1;34}^V \\
\tilde{L}_{1;41}^V & \tilde{L}_{1;42}^V & \tilde{L}_{1;43}^V & \tilde{L}_{1;44}^V \\
-(\tilde{L}_{2;11}^V - \tilde{L}_{2;21}^V) & -(\tilde{L}_{2;12}^V - \tilde{L}_{2;22}^V) & -(\tilde{L}_{2;13}^V - \tilde{L}_{2;23}^V) & -(\tilde{L}_{2;14}^V - \tilde{L}_{2;24}^V) \\
-\tilde{L}_{2;21}^V & -\tilde{L}_{2;22}^V & -\tilde{L}_{2;23}^V & -\tilde{L}_{2;24}^V \\
-\tilde{L}_{2;41}^V & -\tilde{L}_{2;42}^V & -\tilde{L}_{2;43}^V & -\tilde{L}_{2;44}^V
\end{pmatrix}
\begin{pmatrix}
\tilde{p}_{Pf}^+ \\
\tilde{p}_{Ps}^+ \\
\tilde{p}_{SV}^+ \\
\tilde{p}_{TM}^+ \\
\tilde{p}_{Pf}^- \\
\tilde{p}_{Ps}^- \\
\tilde{p}_{SV}^- \\
\tilde{p}_{TM}^-
\end{pmatrix}. \tag{3.168}$$

Here, we want to find the global upgoing reflection matrix ($\tilde{\mathbf{R}}_{n+1}^{+-}(z_{n+1})$) at the fluid side of the interface. In order to find this reflection matrix, we need to express it in terms of the global reflection coefficient at the porous medium side of the interface $\tilde{\mathbf{R}}_n^{+-}(z_{n+1})$. On the fluid side of the interface, the following relation holds

$$\tilde{\mathbf{p}}_{fl}^+ = \tilde{\mathbf{R}}_{n+1}^{+-}(z_{n+1})\tilde{\mathbf{p}}_{fl}^-. \tag{3.169}$$

Similarly, in the porous medium, the downgoing fields can be expressed as

$$\tilde{\mathbf{p}}_{p.m.}^+ = \tilde{\mathbf{R}}_n^{+-}(z_{n+1})\tilde{\mathbf{p}}_{p.m.}^-. \tag{3.170}$$

We can now express the one-way downgoing fields in the porous medium in terms of the upgoing fields in the porous medium times the global reflection matrix at the porous medium side $\tilde{\mathbf{R}}_n^{+-}(z_{n+1})$:

$$\begin{pmatrix}
\tilde{p}_{Pf}^+ \\
\tilde{p}_{Ps}^+ \\
\tilde{p}_{SV}^+ \\
\tilde{p}_{TM}^+
\end{pmatrix} =
\begin{pmatrix}
\tilde{\mathcal{R}}_{Pf-Pf}^{+-} & \tilde{\mathcal{R}}_{Pf-Ps}^{+-} & \tilde{\mathcal{R}}_{Pf-SV}^{+-} & \tilde{\mathcal{R}}_{Pf-TM}^{+-} \\
\tilde{\mathcal{R}}_{Ps-Pf}^{+-} & \tilde{\mathcal{R}}_{Ps-Ps}^{+-} & \tilde{\mathcal{R}}_{Ps-SV}^{+-} & \tilde{\mathcal{R}}_{Ps-TM}^{+-} \\
\tilde{\mathcal{R}}_{SV-Pf}^{+-} & \tilde{\mathcal{R}}_{SV-Ps}^{+-} & \tilde{\mathcal{R}}_{SV-SV}^{+-} & \tilde{\mathcal{R}}_{SV-TM}^{+-} \\
\tilde{\mathcal{R}}_{TM-Pf}^{+-} & \tilde{\mathcal{R}}_{TM-Ps}^{+-} & \tilde{\mathcal{R}}_{TM-SV}^{+-} & \tilde{\mathcal{R}}_{TM-TM}^{+-}
\end{pmatrix}
\begin{pmatrix}
\tilde{p}_{Pf}^- \\
\tilde{p}_{Ps}^- \\
\tilde{p}_{SV}^- \\
\tilde{p}_{TM}^-
\end{pmatrix}. \tag{3.171}$$

Using these expressions, we can rewrite equation (3.168) in terms of only upgoing

fields at the porous medium side

$$\begin{aligned}
 & \begin{pmatrix} \tilde{L}_{11} & \tilde{L}_{12} & \tilde{L}_{13} & \tilde{L}_{14} \\ \tilde{L}_{21} & \tilde{L}_{22} & \tilde{L}_{23} & \tilde{L}_{24} \\ \tilde{L}_{31} & \tilde{L}_{32} & \tilde{L}_{33} & \tilde{L}_{34} \\ \tilde{L}_{41} & \tilde{L}_{42} & \tilde{L}_{43} & \tilde{L}_{44} \\ \tilde{L}_{51} & \tilde{L}_{52} & \tilde{L}_{53} & \tilde{L}_{54} \\ \tilde{L}_{61} & \tilde{L}_{62} & \tilde{L}_{63} & \tilde{L}_{64} \end{pmatrix} \begin{pmatrix} \tilde{p}_{Pf}^- \\ \tilde{p}_{Ps}^- \\ \tilde{p}_{SV}^- \\ \tilde{p}_{TM}^- \end{pmatrix} \\
 = & \begin{pmatrix} d_{1,P}^{fl,V} & 0 & d_{1,P}^{fl,V} & 0 \\ 0 & 0 & 0 & 0 \\ 0 & d_{1,EM}^{fl,V} & 0 & d_{1,EM}^{fl,V} \\ 0 & 0 & 0 & 0 \\ B_P^{fl,V} d_{1,P}^{fl,V} & 0 & -B_P^{fl,V} d_{1,P}^{fl,V} & 0 \\ 0 & B_{EM}^{fl,V} d_{1,EM}^{fl,V} & 0 & -B_{EM}^{fl,V} d_{1,EM}^{fl,V} \end{pmatrix} \begin{pmatrix} \tilde{p}_P^+ \\ \tilde{p}_{EM}^+ \\ \tilde{p}_P^- \\ \tilde{p}_{EM}^- \end{pmatrix}, \tag{3.172}
 \end{aligned}$$

where the expressions for $\tilde{L}_{(1:6)J}$ are identical to the expressions for the P-SV-TM global downgoing reflection matrix (3.159)-(3.164), except for the fact that $\tilde{\mathcal{R}}_{IJ}^{-+}$ should be replaced by $\tilde{\mathcal{R}}_{IJ}^{+-}$, and that equations (3.162)-(3.164) should be multiplied by minus one.

We separate the unknown, outgoing one-way fields from the incoming one-way fields, yielding:

$$\begin{aligned}
 & \begin{pmatrix} \tilde{L}_{11} & \tilde{L}_{12} & \tilde{L}_{13} & \tilde{L}_{14} & -d_{1,P}^{fl,V} & 0 \\ \tilde{L}_{21} & \tilde{L}_{22} & \tilde{L}_{23} & \tilde{L}_{24} & 0 & 0 \\ \tilde{L}_{31} & \tilde{L}_{32} & \tilde{L}_{33} & \tilde{L}_{34} & 0 & -d_{1,EM}^{fl,V} \\ \tilde{L}_{41} & \tilde{L}_{42} & \tilde{L}_{43} & \tilde{L}_{44} & 0 & 0 \\ \tilde{L}_{51} & \tilde{L}_{52} & \tilde{L}_{53} & \tilde{L}_{54} & -B_P^{fl,V} d_{1,P}^{fl,V} & 0 \\ \tilde{L}_{61} & \tilde{L}_{62} & \tilde{L}_{63} & \tilde{L}_{64} & 0 & -B_{EM}^{fl,V} d_{1,EM}^{fl,V} \end{pmatrix} \begin{pmatrix} \tilde{p}_{Pf}^- \\ \tilde{p}_{Ps}^- \\ \tilde{p}_{SV}^- \\ \tilde{p}_{TM}^- \\ \tilde{p}_P^+ \\ \tilde{p}_{EM}^+ \end{pmatrix} = \\
 & \tag{3.173}
 \end{aligned}$$

$$\begin{aligned}
 & \begin{pmatrix} d_{1,P}^{fl,V} & 0 \\ 0 & 0 \\ 0 & d_{1,EM}^{fl,V} \\ 0 & 0 \\ -B_P^{fl,V} d_{1,P}^{fl,V} & 0 \\ 0 & -B_{EM}^{fl,V} d_{1,EM}^{fl,V} \end{pmatrix} \begin{pmatrix} \tilde{p}_P^- \\ \tilde{p}_{EM}^- \end{pmatrix}. \\
 & \tag{3.174}
 \end{aligned}$$

We solve for the unknown one-way fields on the left-hand side by left-multiplying

both sides with the inverse of the matrix on the left-hand side, yielding

$$\begin{pmatrix} \tilde{p}_{Pf}^- \\ \tilde{p}_{Ps}^- \\ \tilde{p}_{SV}^- \\ \tilde{p}_{TM}^- \\ \tilde{p}_P^+ \\ \tilde{p}_{EM}^+ \end{pmatrix} = \begin{pmatrix} \tilde{T}_{Pf-P}^- & \tilde{T}_{Pf-EM}^- \\ \tilde{T}_{Ps-P}^- & \tilde{T}_{Ps-EM}^- \\ \tilde{T}_{SV-P}^- & \tilde{T}_{SV-EM}^- \\ \tilde{T}_{EM-P}^- & \tilde{T}_{EM-EM}^- \\ \tilde{R}_{P-P;n+1}^{+-}(z_{n+1}) & \tilde{R}_{P-EM;n+1}^{+-}(z_{n+1}) \\ \tilde{R}_{EM-P;n+1}^{+-}(z_{n+1}) & \tilde{R}_{EM-EM;n+1}^{+-}(z_{n+1}) \end{pmatrix} \begin{pmatrix} \tilde{p}_P^- \\ \tilde{p}_{EM}^- \end{pmatrix}, \quad (3.175)$$

where $\tilde{R}_{n+1}^{+-}(z_{n+1})$ represent the global upgoing reflection coefficients at the fluid-side that we were after. We now have obtained all required expressions (for both the SH-TE and P-SV-TM propagation mode), for modeling scenarios with a free-surface, and scenarios with fluid/porous medium/fluid transitions.

3.3 Field composition, combining modes and Fourier-Bessel transformations

For layered-Earth geometries, we have carried out all calculations and corresponding seismo-EM layer-code modeling in the horizontal wavenumber-frequency domain. However, we would like to obtain data in the space-time domain as the final output from our layer-code modeling. For the frequency-to-time transformation, we make use of a temporal inverse Fourier transformation. The horizontal wavenumber expressions cannot be analytically transformed back to the space domain; the inverse spatial transformation has to be computed numerically. We could of course make use of a 2D spatial inverse Fourier Transformation. However, numerically speaking, this is quite an expensive procedure. We therefore choose to rewrite the set of equations in such a way, that the use of Fourier-Bessel transformations is possible.

3.3.1 Field decomposition and composition

Before diving into the details of the Fourier-Bessel transformations, let us first focus on field decomposition and composition. As we have seen, we can capture the 3D governing set of seismo-electromagnetic equations for horizontally layered, 1D media in the format of equation 2.113, which reads (slightly adjusted)

$$\frac{\partial \tilde{\mathbf{q}}^{H,V}}{\partial x_3} - \tilde{\mathbf{A}}^{H,V} \tilde{\mathbf{q}}^{H,V} = \tilde{\mathbf{d}}^{H,V} \delta(x_3 - x_3^s), \quad (3.176)$$

where x_3^s denotes the vertical spatial coordinate of the source. We can decompose the two-way fields into one-way fields by applying field decomposition (see e.g. [Grobbe et al. \(2016a\)](#)). We can write equation (3.176) for decomposed, one-way fields as

$$\frac{\partial \tilde{\mathbf{p}}^{H,V}}{\partial x_3} - \tilde{\mathbf{\Lambda}}^{H,V} \tilde{\mathbf{p}}^{H,V} = (\tilde{\mathbf{L}}^{H,V})^{-1} \tilde{\mathbf{d}}^{H,V} \delta(x_3 - x_3^s). \quad (3.177)$$

Here, we have made use of the fact that we have explicit expressions for the composition matrix $\tilde{\mathbf{L}}^{H,V}$, the eigenvectors of the two propagation modes, such that $\tilde{\mathbf{A}}^{H,V} = \tilde{\mathbf{L}}^{H,V} \tilde{\mathbf{\Lambda}}^{H,V} (\tilde{\mathbf{L}}^{H,V})^{-1}$ holds (which we also used in the derivation of the eigenvector sets in Section 2.3).

We use the following relationship between the one-way fields due to two-way source types:

$$\tilde{\mathbf{p}}^{H,V} = \tilde{\mathcal{G}}^{H,V} (\tilde{\mathbf{L}}^{H,V})^{-1} \tilde{\mathbf{d}}^{H,V}, \quad (3.178)$$

where $\tilde{\mathcal{G}}$ is the Green function matrix containing the one-way impulse responses of the layered medium. Composing the two-way fields from one-way fields via

$$\tilde{\mathbf{q}}^{H,V} = \tilde{\mathbf{L}}^{H,V} \tilde{\mathbf{p}}^{H,V}, \quad (3.179)$$

we obtain a general equation for two-way wavefields due to two-way source types for each individual propagation mode:

$$\tilde{\mathbf{q}}^{H,V} = \tilde{\mathbf{L}}^{H,V} \tilde{\mathcal{G}}^{H,V} (\tilde{\mathbf{L}}^{H,V})^{-1} \tilde{\mathbf{d}}^{H,V}. \quad (3.180)$$

This equation forms the basis for the composition of two-way physical field quantities at the receiver level in layer-code modeling. If we now replace the two-way source vector $\tilde{\mathbf{d}}^{H,V}$ in equation 3.177 by a unit matrix \mathbf{I} , we can express equation 3.177 in terms of the Green matrices, as

$$\frac{\partial \tilde{\mathbf{g}}^{H,V}}{\partial x_3} - \tilde{\mathbf{\Lambda}}^{H,V} \tilde{\mathbf{g}}^{H,V} = \mathbf{I} \delta(x_3 - x_3^s). \quad (3.181)$$

We have implicitly chosen point sources at $\mathbf{x}_H = (0.0, 0.0)$, which is reasonable since we are dealing with a laterally-invariant layered medium. Let us now drop the superscripts defining the two modes for convenience. The Green function matrix is organized as

$$\tilde{\mathbf{g}} = \begin{pmatrix} \tilde{\mathbf{g}}^{++} & \tilde{\mathbf{g}}^{+-} \\ \tilde{\mathbf{g}}^{-+} & \tilde{\mathbf{g}}^{--} \end{pmatrix}, \quad (3.182)$$

where for example $\tilde{\mathbf{g}}^{+-}$ denotes the Green function submatrix for downgoing fields (+ superscript) at the receiver level generated by an upgoing source (- superscript). Similar meanings can be given to the other Green's function submatrices. As we know, the composition and decomposition matrices of equation 3.180 are defined as

$$\tilde{\mathbf{L}} = \begin{pmatrix} \tilde{\mathbf{L}}_1 & \tilde{\mathbf{L}}_1 \\ \tilde{\mathbf{L}}_2 & -\tilde{\mathbf{L}}_2 \end{pmatrix}, \quad (3.183)$$

$$\tilde{\mathbf{L}}^{-1} = \begin{pmatrix} \tilde{\mathbf{L}}_2^t & \tilde{\mathbf{L}}_1^t \\ \tilde{\mathbf{L}}_2^t & -\tilde{\mathbf{L}}_1^t \end{pmatrix}. \quad (3.184)$$

We can redefine equation 3.180 in terms of two-way Green's matrices as

$$\tilde{\mathbf{q}} = \tilde{\mathbf{G}} \tilde{\mathbf{d}}, \quad (3.185)$$

where $\tilde{\mathbf{G}} = \tilde{\mathbf{L}} \tilde{\mathbf{g}} \tilde{\mathbf{L}}^{-1}$, or more explicitly as

$$\tilde{\mathbf{q}}_1 = \tilde{\mathbf{G}}_{11} \tilde{\mathbf{d}}_1 + \tilde{\mathbf{G}}_{12} \tilde{\mathbf{d}}_2, \quad (3.186)$$

$$\tilde{\mathbf{q}}_2 = \tilde{\mathbf{G}}_{21} \tilde{\mathbf{d}}_1 + \tilde{\mathbf{G}}_{22} \tilde{\mathbf{d}}_2, \quad (3.187)$$

with

$$\tilde{\mathbf{G}}_{11} = \tilde{\mathbf{L}}_1 \left[\tilde{\mathbf{g}}^{++} + \tilde{\mathbf{g}}^{+-} + \tilde{\mathbf{g}}^{-+} + \tilde{\mathbf{g}}^{--} \right] \tilde{\mathbf{L}}_1^t, \quad (3.188)$$

$$\tilde{\mathbf{G}}_{12} = \tilde{\mathbf{L}}_1 \left[\tilde{\mathbf{g}}^{++} - \tilde{\mathbf{g}}^{+-} + \tilde{\mathbf{g}}^{-+} - \tilde{\mathbf{g}}^{--} \right] \tilde{\mathbf{L}}_1^t, \quad (3.189)$$

$$\tilde{\mathbf{G}}_{21} = \tilde{\mathbf{L}}_2 \left[\tilde{\mathbf{g}}^{++} + \tilde{\mathbf{g}}^{+-} - \tilde{\mathbf{g}}^{-+} - \tilde{\mathbf{g}}^{--} \right] \tilde{\mathbf{L}}_2^t, \quad (3.190)$$

$$\tilde{\mathbf{G}}_{22} = \tilde{\mathbf{L}}_2 \left[\tilde{\mathbf{g}}^{++} - \tilde{\mathbf{g}}^{+-} - \tilde{\mathbf{g}}^{-+} + \tilde{\mathbf{g}}^{--} \right] \tilde{\mathbf{L}}_2^t. \quad (3.191)$$

This formulation can be used for both 2D and 3D models. For 2D, we simply apply a 1D spatial inverse Fourier transformation to obtain the space-frequency results, whereas in 3D scenarios we apply Fourier-Bessel transformations as derived in the next sections. Before explicitly deriving the Fourier-Bessel transformations for each seismo-electromagnetic source-receiver combination, let us quickly recapitulate the theory of propagation modes. Please note that now that we have assumed point sources and express everything in terms of Green's functions, the source vector $\tilde{\mathbf{d}}^{H,V}$ looks slightly different. To explain this, let us look at how we defined the sources thus far. In the space-time domain, the electric current source in the x_1 -direction is defined as

$$J_1^e(\mathbf{x}, t) = \mathcal{J}_1^e(t)\delta(\mathbf{x} - \mathbf{x}^s). \quad (3.192)$$

In the space-frequency domain, where we started our seismo-electromagnetic governing equations, this source term reads

$$\hat{J}_1^e(\mathbf{x}, \omega) = \hat{\mathcal{J}}_1^e(\omega)\delta(\mathbf{x} - \mathbf{x}^s), \quad (3.193)$$

where we can see that the source terms implicitly contain a spatial delta function. In the horizontal wavenumber-frequency domain, this leads to

$$\tilde{J}_1^e(\mathbf{k}_H, x_3, \omega) = \hat{\mathcal{J}}_1^e(\omega)\exp(jk_\alpha x_\alpha^s)\delta(x_3 - x_3^s). \quad (3.194)$$

Similar definitions hold for the other source terms. For the point sources, where we choose $\mathbf{x}_H^s = (0, 0)$ as the horizontal source location, equation 3.194 reduces to

$$\tilde{J}_1^e(\mathbf{k}_H, x_3, \omega) = \hat{\mathcal{J}}_1^e(\omega)\delta(x_3 - x_3^s). \quad (3.195)$$

We use this since we are considering a horizontally invariant medium. By looking at the Green function solutions (the responses to the delta-functions), the source vectors (like the one in equation 3.185) read

$$\tilde{\mathbf{d}}^H = \left(\tilde{d}_1^H, \tilde{d}_2^H, \tilde{d}_3^H, \tilde{d}_4^H \right)^t, \quad (3.196)$$

for the SH-TE mode, where

$$\tilde{d}_1^H = -jk_1 \left[\hat{\mathcal{H}}_{23}^b + \hat{\mathcal{H}}_{32}^b \right] + jk_2 \left[\hat{\mathcal{H}}_{13}^b + \hat{\mathcal{H}}_{13}^b \right], \quad (3.197)$$

$$\tilde{d}_2^H = -jk_\alpha \hat{\mathcal{J}}_\alpha^m, \quad (3.198)$$

$$\begin{aligned} \tilde{d}_3^H &= jk_1 \left[\hat{\mathcal{F}}_2^b - \frac{\rho^f}{\rho_E} \hat{\mathcal{F}}_2^f \right] - jk_2 \left[\hat{\mathcal{F}}_1^b - \frac{\rho^f}{\rho_E} \hat{\mathcal{F}}_1^f \right] \\ &+ \frac{G^{fr}}{s} \left[-k_1^2 + k_2^2 \right] \left[\hat{\mathcal{H}}_{12}^b + \hat{\mathcal{H}}_{21}^b \right] - \frac{2G^{fr}k_1k_2}{s} \left[-\hat{\mathcal{H}}_{11}^b + \hat{\mathcal{H}}_{22}^b \right], \end{aligned} \quad (3.199)$$

$$\tilde{d}_4^H = -\hat{\mathcal{L}} \left[-jk_1 \hat{\mathcal{F}}_2^f + jk_2 \hat{\mathcal{F}}_1^f \right] + jk_1 \hat{\mathcal{J}}_2^e - jk_2 \hat{\mathcal{J}}_1^e - \frac{1}{s\mu_0} \kappa^2 \hat{\mathcal{J}}_3^m, \quad (3.200)$$

and

$$\tilde{\mathbf{d}}^V = \left(\tilde{d}_1^V, \tilde{d}_2^V, \tilde{d}_3^V, \tilde{d}_4^V, \tilde{d}_5^V, \tilde{d}_6^V, \tilde{d}_7^V, \tilde{d}_8^V \right)^t, \quad (3.201)$$

for the P-SV-TM mode, where

$$\tilde{d}_1^V = \frac{S}{(S + 2G^{fr})} \left[\hat{\mathcal{H}}_{11}^b + \hat{\mathcal{H}}_{22}^b \right] + \hat{\mathcal{H}}_{33}^b, \quad (3.202)$$

$$\tilde{d}_2^V = \frac{j}{s\hat{\rho}^E} k_\alpha \hat{\mathcal{F}}_\alpha^f + \frac{C}{M} \left[\hat{\mathcal{H}}_{11}^b + \hat{\mathcal{H}}_{22}^b \right] \left[1 - \frac{S}{(S + 2G^{fr})} \right] + \hat{\mathcal{Q}}^i, \quad (3.203)$$

$$\begin{aligned} \tilde{d}_3^V &= \frac{1}{\kappa} \frac{\rho^f}{\hat{\rho}^E} k_\alpha \hat{\mathcal{F}}_\alpha^f - \frac{1}{\kappa} k_\alpha \hat{\mathcal{F}}_\alpha^b - \frac{2j}{s} \frac{k_1 k_2}{\kappa} \left[G^{fr} \hat{\mathcal{H}}_{21}^b + G^{fr} \hat{\mathcal{H}}_{12}^b \right] \\ &- \frac{j\kappa}{s} \frac{2G^{fr} S}{(S + 2G^{fr})} \left[\hat{\mathcal{H}}_{11}^b + \hat{\mathcal{H}}_{22}^b \right] - \frac{2jG^{fr}}{s\kappa} \left[k_1^2 \hat{\mathcal{H}}_{11}^b + k_2^2 \hat{\mathcal{H}}_{22}^b \right], \end{aligned} \quad (3.204)$$

$$\tilde{d}_4^V = -\frac{1}{\kappa} \left[\hat{\mathcal{L}}_{k_\alpha} \hat{\mathcal{F}}_\alpha^f + k_\alpha \hat{\mathcal{J}}_\alpha^e \right], \quad (3.205)$$

$$\tilde{d}_5^V = -\hat{\mathcal{F}}_3^b, \quad (3.206)$$

$$\tilde{d}_6^V = \frac{\hat{\rho}^E}{\hat{\epsilon}} \hat{\mathcal{L}} \hat{\mathcal{J}}_3^e - \hat{\mathcal{F}}_3^f, \quad (3.207)$$

$$\tilde{d}_7^V = \frac{k_\alpha}{\kappa} \left[\hat{\mathcal{H}}_{\alpha 3}^b + \hat{\mathcal{H}}_{3\alpha}^b \right], \quad (3.208)$$

$$\tilde{d}_8^V = \frac{j\kappa}{s\hat{\epsilon}} \hat{\mathcal{J}}_3^e + \frac{1}{\kappa} \left[k_2 \hat{\mathcal{J}}_1^m - k_1 \hat{\mathcal{J}}_2^m \right]. \quad (3.209)$$

We can recognize the symbols indicating the purely frequency-dependent source functions (which act as a temporal filter).

3.3.2 Mode theory and combining the modes

When dealing with the governing equations of the seismo-electromagnetic system, physical field quantities were combined by taking either the divergence or rotation of the expressions under consideration, yielding different mode field quantities for both the SH-TE and P-SV-TM propagation modes. We composed the different mode quantities, in the horizontal wavenumber-frequency domain, as

$$\tilde{v}^{s,H} = -jk_1 \tilde{v}_2^s + jk_2 \tilde{v}_1^s, \quad (3.210)$$

$$\tilde{\tau}^{b,H} = -jk_1 \tilde{\tau}_{23}^b + jk_2 \tilde{\tau}_{13}^b, \quad (3.211)$$

$$\tilde{E}^H = -jk_1 \tilde{E}_2 + jk_2 \tilde{E}_1, \quad (3.212)$$

$$\tilde{H}^H = -jk_1 \tilde{H}_1 - jk_2 \tilde{H}_2, \quad (3.213)$$

for the SH-TE mode, and as

$$\tilde{v}_{norm}^{s,V} = \frac{k_1}{\kappa} \tilde{v}_1^s + \frac{k_2}{\kappa} \tilde{v}_2^s, \quad (3.214)$$

$$\tilde{\tau}_{norm}^{b,V} = \frac{k_1}{\kappa} \tilde{\tau}_{13}^b + \frac{k_2}{\kappa} \tilde{\tau}_{23}^b, \quad (3.215)$$

$$\tilde{E}_{norm}^V = \frac{k_1}{\kappa} \tilde{E}_1 + \frac{k_2}{\kappa} \tilde{E}_2, \quad (3.216)$$

$$\tilde{H}_{norm}^V = \frac{k_1}{\kappa} \tilde{H}_2 - \frac{k_2}{\kappa} \tilde{H}_1, \quad (3.217)$$

for the P-SV-TM mode, where the subscript ‘norm’ indicates that the mode quantities have been normalized with a factor $-j\kappa$, such that the system matrix $\tilde{\mathbf{A}}^V$ has favourable symmetry properties. Consequently, the factors before the field quantities have also been normalized by $-j\kappa$.

At the receiver level, both propagation modes and their mode quantities, that were thus far treated independently in the layered-Earth system, need to be combined to obtain the individual physical field quantities that compose these mode quantities. We combine the expressions for a certain mode quantity-type (for example equations 3.212 and 3.216), in such a way that one of the two physical field quantities (\tilde{E}_1 or \tilde{E}_2) remains. As an explicit example, we consider combining the electric mode quantities \tilde{E}^H and \tilde{E}^V into the physical electric field quantity in the x_1 -direction, \tilde{E}_1 . We start by multiplying equation 3.212 at both the left- and right-hand side with jk_2 , yielding

$$\begin{aligned} jk_2\tilde{E}^H &= jk_2 \left[-jk_1\tilde{E}_2 + jk_2\tilde{E}_1 \right] \\ &= k_1k_2\tilde{E}_2 - k_2^2\tilde{E}_1. \end{aligned} \quad (3.218)$$

Similarly, we write the P-SV-TM mode expression, equation 3.216, as

$$-j\kappa\tilde{E}_{norm}^V = -jk_1\tilde{E}_1 - jk_2\tilde{E}_2, \quad (3.219)$$

and multiply both the left-hand side and the right-hand side with jk_1 , yielding

$$\begin{aligned} k_1\kappa\tilde{E}_{norm}^V &= jk_1 \left[-jk_1\tilde{E}_1 - jk_2\tilde{E}_2 \right] \\ &= k_1^2\tilde{E}_1 + k_1k_2\tilde{E}_2. \end{aligned} \quad (3.220)$$

We now subtract equation 3.218 from equation 3.220, leaving us with the desired physical field quantity \tilde{E}_1 :

$$\begin{aligned} k_1\kappa\tilde{E}_{norm}^V - jk_2\tilde{E}^H &= k_1^2\tilde{E}_1 + k_1k_2\tilde{E}_2 - k_1k_2\tilde{E}_2 + k_2^2\tilde{E}_1 \\ &= [k_1^2 + k_2^2]\tilde{E}_1 = \kappa^2\tilde{E}_1. \end{aligned} \quad (3.221)$$

$$\tilde{E}_1 = \frac{k_1}{\kappa}\tilde{E}_{norm}^V - \frac{jk_2}{\kappa^2}\tilde{E}^H. \quad (3.222)$$

Similarly, we can multiply the SH-TE mode expression at both sides with jk_1 and the P-SV-TM mode expression with jk_2 . When we now add the final expressions we end up with the other physical quantity that composes these mode quantities, \tilde{E}_2 :

$$\tilde{E}_2 = \frac{k_2}{\kappa}\tilde{E}_{norm}^V + \frac{jk_1}{\kappa^2}\tilde{E}^H. \quad (3.223)$$

We can clearly recognize two core expressions for mode combination, referred to as type \tilde{E}_1 and ‘receiver’-type \tilde{E}_2 . All other physical quantities that compose a mode quantity can be derived via one of these two types. A third type can be defined as well, corresponding to the purely P-SV-TM field quantities that do not need to be combined with the SH-TE mode quantities. We refer to this type as the

\tilde{v}_3 -type. The complete list of final mode-combining expressions, reads

$$\tilde{E}_1 = \frac{k_1}{\kappa} \tilde{E}_{norm}^V - \frac{jk_2}{\kappa^2} \tilde{E}^H, \quad (3.224)$$

$$\tilde{\tau}_{13}^b = \frac{k_1}{\kappa} \tilde{\tau}_{norm}^{b,V} - \frac{jk_2}{\kappa^2} \tilde{\tau}^{b,H}, \quad (3.225)$$

$$\tilde{H}_2 = \frac{k_1}{\kappa} \tilde{H}_{norm}^V + \frac{jk_2}{\kappa^2} \tilde{H}^H, \quad (3.226)$$

$$\tilde{v}_1^s = \frac{k_1}{\kappa} \tilde{v}_{norm}^{s,V} - \frac{jk_2}{\kappa^2} \tilde{v}^{s,H}, \quad (3.227)$$

$$\tilde{E}_2 = \frac{k_2}{\kappa} \tilde{E}_{norm}^V + \frac{jk_1}{\kappa^2} \tilde{E}^H, \quad (3.228)$$

$$\tilde{\tau}_{23}^b = \frac{k_2}{\kappa} \tilde{\tau}_{norm}^{b,V} + \frac{jk_1}{\kappa^2} \tilde{\tau}^{b,H}, \quad (3.229)$$

$$\tilde{H}_1 = -\frac{k_2}{\kappa} \tilde{H}_{norm}^V + \frac{jk_1}{\kappa^2} \tilde{H}^H, \quad (3.230)$$

$$\tilde{v}_2^s = \frac{k_2}{\kappa} \tilde{v}_{norm}^{s,V} + \frac{jk_1}{\kappa^2} \tilde{v}^{s,H}. \quad (3.231)$$

We can generalize these expressions in terms of the elements of the two-way field vectors $\tilde{\mathbf{q}}^{H,V}$ as defined in equations (6.48) and (6.49) of Section 2.2. For completeness, we here add the \tilde{v}_3^s -type expressions, leading to

$$\tilde{E}_1 = \frac{k_1}{\kappa} \tilde{q}_8^V - \frac{jk_2}{\kappa^2} \tilde{q}_2^H, \quad (3.232)$$

$$\tilde{\tau}_{13}^b = \frac{k_1}{\kappa} \tilde{q}_3^V - \frac{jk_2}{\kappa^2} \tilde{q}_3^H, \quad (3.233)$$

$$\tilde{H}_2 = \frac{k_1}{\kappa} \tilde{q}_4^V - \frac{jk_2}{\kappa^2} \tilde{q}_4^H, \quad (3.234)$$

$$\tilde{v}_1^s = \frac{k_1}{\kappa} \tilde{q}_7^V - \frac{jk_2}{\kappa^2} \tilde{q}_1^H, \quad (3.235)$$

$$\tilde{E}_2 = \frac{k_2}{\kappa} \tilde{q}_8^V + \frac{jk_1}{\kappa^2} \tilde{q}_2^H, \quad (3.236)$$

$$\tilde{\tau}_{23}^b = \frac{k_2}{\kappa} \tilde{q}_3^V + \frac{jk_1}{\kappa^2} \tilde{q}_3^H, \quad (3.237)$$

$$\tilde{H}_1 = -\left[\frac{k_2}{\kappa} \tilde{q}_4^V + \frac{jk_1}{\kappa^2} \tilde{q}_4^H \right], \quad (3.238)$$

$$\tilde{v}_2^s = \frac{k_2}{\kappa} \tilde{q}_7^V + \frac{jk_1}{\kappa^2} \tilde{q}_1^H, \quad (3.239)$$

$$\tilde{v}_3^s = \tilde{q}_1^V, \quad (3.240)$$

$$\tilde{w}_3^s = \tilde{q}_2^V, \quad (3.241)$$

$$\tilde{\tau}_{33}^b = \tilde{q}_5^V, \quad (3.242)$$

$$-\tilde{p}^f = \tilde{q}_6^V, \quad (3.243)$$

where the subscripts in the right-hand side correspond to the elements of the two-way field vector $\tilde{\mathbf{q}}^{H,V}$.

3.3.3 Explicit Fourier-Bessel transformations

At the receiver level, we now compose the different two-way seismo-electromagnetic source-receiver combinations by combining equations (3.232)-(3.243) with equation (3.180). We select both the desired field quantity (row of $\tilde{\mathbf{L}}^{H,V}$ and the generating source-type (column of $(\tilde{\mathbf{L}}^{H,V})^{-1}$). In our derivations, we make use of the notation of equation (3.180) instead of the Green matrix notation, since this one-way field notation corresponds with the algorithm of our seismo-EM layer-code. We explicitly derive the Fourier-Bessel Transformations required to transform the data from the horizontal wavenumber-frequency domain to the space-frequency domain. Before diving into the details, we briefly present some useful Bessel function relations. After that, we demonstrate the derivations for each source-type by focusing on one of the three ‘receiver’-type expressions.

Some useful derivatives of Bessel functions

We here present some important relations for Bessel functions and their spatial derivatives, which we need in the explicit derivations of the Fourier-Bessel transformations. In the horizontal wavenumber domain expressions we can expect product factors $(jk_\alpha)^n$, with $n = 1, 2, 3$. Also, factors like $jk_1k_2^2$ can occur but in essence they are not different. Factors containing the radial wavenumber κ do not play a role. Factors like $(-jk_\alpha)^n$ in the horizontal wavenumber domain transform to operators ∂_α^n in the space domain. These differentiation operators can act on the Bessel functions in the Fourier-Bessel integrals. We can numerically evaluate these integrals, or first obtain the space domain expressions and then subsequently evaluate the derivatives. We define the radial distance r and angle ϕ as $r = \sqrt{(x_1 - x_1^s)^2 + (x_2 - x_2^s)^2}$ and $\phi = \text{atan}(\frac{x_2}{x_1})$, with $r \geq 0$ and $-\pi < \phi \leq \pi$. We aim to obtain expressions without explicit divisions by the radial distance r , since r can be equal to zero. We use the following rules from Abramowitz & Stegun (1965),

$$J_{-n}(\kappa r) = (-1)^n J_n(\kappa r), \quad (3.244)$$

$$J'_n(\kappa r) = \frac{1}{2} (J_{n-1}(\kappa r) - J_{n+1}(\kappa r)), \quad (3.245)$$

$$\frac{2n}{\kappa r} J_n(\kappa r) = J_{n-1}(\kappa r) + J_{n+1}(\kappa r), \quad (3.246)$$

to derive

$$\partial_\alpha J_0(\kappa r) = -\frac{x_\alpha}{r} \kappa J_1(\kappa r), \quad (3.247)$$

where $J_0(\kappa r)$ is the Bessel function of the first kind and order zero, with argument κr . Be aware that the chain-rule applies to the argument of the Bessel functions as well. Furthermore, we can obtain

$$\partial_1^2 J_0(\kappa r) = -\frac{\kappa^2}{2} \left(J_0(\kappa r) - \frac{x_1^2 - x_2^2}{r^2} J_2(\kappa r) \right), \quad (3.248)$$

and similarly

$$\partial_2^2 J_0(\kappa r) = -\frac{\kappa^2}{2} \left(J_0(\kappa r) + \frac{x_1^2 - x_2^2}{r^2} J_2(\kappa r) \right). \quad (3.249)$$

We also derive

$$\partial_1 \partial_2 J_0(\kappa r) = \frac{\kappa^2 x_1 x_2}{r^2} J_2(\kappa r), \quad (3.250)$$

$$\partial_1 \partial_2^2 J_0(\kappa r) = \frac{\kappa^3}{4} \frac{x_1}{r} \left[J_1(\kappa r) - \left(1 - 2 \left(\frac{x_1^2 - x_2^2}{r^2} \right) \right) J_3(\kappa r) \right], \quad (3.251)$$

$$\partial_1^2 \partial_2 J_0(\kappa r) = \frac{\kappa^3}{4} \frac{x_2}{r} \left[J_1(\kappa r) - \left(1 + 2 \left(\frac{x_1^2 - x_2^2}{r^2} \right) \right) J_3(\kappa r) \right], \quad (3.252)$$

$$\begin{aligned} \partial_1^3 J_0(\kappa r) &= -\frac{\kappa^2}{2} \left(\partial_1 J_0(\kappa r) - \partial_1 \left[\frac{x_1^2 - x_2^2}{r^2} J_2(\kappa r) \right] \right) \\ &= \frac{\kappa^3}{4} \frac{x_1}{r} \left(3J_1(\kappa r) + \left(1 - 2 \frac{x_1^2 - x_2^2}{r^2} \right) J_3(\kappa r) \right), \end{aligned} \quad (3.253)$$

$$\begin{aligned} \partial_2^3 J_0(\kappa r) &= -\frac{\kappa^2}{2} \left(\partial_2 J_0(\kappa r) + \partial_2 \left[\frac{x_1^2 - x_2^2}{r^2} J_2(\kappa r) \right] \right) \\ &= \frac{\kappa^3}{4} \frac{x_2}{r} \left(3J_1(\kappa r) + \left(1 + 2 \frac{x_1^2 - x_2^2}{r^2} \right) J_3(\kappa r) \right). \end{aligned} \quad (3.254)$$

In cylindrical coordinates, we can use directional cosines to calculate the Cartesian solutions:

$$\cos(\phi) = \frac{x_1}{r}, \quad (3.255)$$

$$\sin(\phi) = \frac{x_2}{r}, \quad (3.256)$$

$$\cos(\phi)\sin(\phi) = \frac{x_1 x_2}{r^2}, \quad (3.257)$$

$$\cos(2\phi) = \frac{x_1^2 - x_2^2}{r^2}. \quad (3.258)$$

This leads to

$$\partial_1 J_0(\kappa r) = -\kappa \cos(\phi) J_1(\kappa r), \quad (3.259)$$

$$\partial_2 J_0(\kappa r) = -\kappa \sin(\phi) J_1(\kappa r), \quad (3.260)$$

$$\partial_1^2 J_0(\kappa r) = -\frac{\kappa^2}{2} [J_0(\kappa r) - \cos(2\phi) J_2(\kappa r)], \quad (3.261)$$

$$\partial_2^2 J_0(\kappa r) = -\frac{\kappa^2}{2} [J_0(\kappa r) + \cos(2\phi) J_2(\kappa r)], \quad (3.262)$$

$$\partial_1 \partial_2 J_0(\kappa r) = \kappa^2 \cos(\phi) \sin(\phi) J_2(\kappa r), \quad (3.263)$$

$$\partial_1 \partial_2^2 J_0(\kappa r) = \frac{\kappa^3}{4} \cos(\phi) [J_1(\kappa r) - (1 - 2\cos(2\phi)) J_3(\kappa r)], \quad (3.264)$$

$$\partial_1^2 \partial_2 J_0(\kappa r) = \frac{\kappa^3}{4} \sin(\phi) [J_1(\kappa r) - (1 + 2\cos(2\phi)) J_3(\kappa r)], \quad (3.265)$$

$$\partial_1^3 J_0(\kappa r) = \frac{\kappa^3}{4} \cos(\phi) [3J_1(\kappa r) + (1 - 2\cos(2\phi)) J_3(\kappa r)], \quad (3.266)$$

$$\partial_2^3 J_0(\kappa r) = \frac{\kappa^3}{4} \sin(\phi) [3J_1(\kappa r) + (1 + 2\cos(2\phi)) J_3(\kappa r)]. \quad (3.267)$$

It can be seen that no explicit divisions by the radial distance need to occur, since everything can be expressed in terms of directional sines and cosines, and integer order Bessel functions. There still seem to occur singularities for $r = 0$ in the directional sines and cosines. However, this is only an apparent problem since these angle-dependent terms only occur together with J_n with $n = 1, 2, \dots$. For these Bessel functions, $J_n(0) = 0$ (i.e. for a zero argument, when $r = 0$), and hence no singularity problems occur at $r = 0$.

Example: The Fourier-Bessel transformation for $E_1^{J_e}$

We here present the Fourier-Bessel transformations for each source-type for receiver-type E_1 , by explicitly focusing on the \tilde{E}_1 fields. By selecting a different row of $\tilde{\mathbf{L}}^{H,V}$, we can obtain the expressions for $\tilde{\tau}_{13}^b$, \tilde{H}_2 , and \tilde{v}_1^s . Combining (3.224) with (3.180) and selecting specific columns of $(\tilde{\mathbf{L}}^{H,V})^{-1}$ corresponding to different source-types, yields different relations for the horizontal electric field component in the x_1 -direction due to different two-way sources, expressed in terms of the one-way fields (or Green's functions as denoted in equations 3.188-3.191). Note that again $s = j\omega$. We start with the expression for $\tilde{E}_1^{J_e}$, representing the two-way field \tilde{E}_1 recorded at

the receiver level due to a two-way source \tilde{J}_1^e at the source level,

$$\begin{aligned}
\tilde{E}_1^{J_1^e}(\mathbf{k}_H, x_3, \omega) &= \frac{k_1}{\kappa} \tilde{E}_{norm}^V(\kappa, x_3, \omega) - \frac{jk_2}{\kappa^2} \tilde{E}^H(\kappa, x_3, \omega) \\
&= \frac{k_1}{\kappa} \tilde{q}_8^V(\kappa, x_3, \omega) - \frac{jk_2}{\kappa^2} \tilde{q}_2^H(\kappa, x_3, \omega) \\
&= \frac{k_1}{\kappa} \left[\tilde{\mathbf{L}}_{8,J}^V(\kappa, x_3, \omega) \tilde{\mathcal{G}}_{J,K}^V(\kappa, x_3, \omega) (\tilde{\mathbf{L}}^V)_{K,4}^{-1}(\kappa, x_3, \omega) \right] \tilde{d}_4^V(\kappa, x_3, \omega) \\
&\quad - \frac{jk_2}{\kappa^2} \left[\tilde{\mathbf{L}}_{2,J}^H(\kappa, x_3, \omega) \tilde{\mathcal{G}}_{J,K}^H(\kappa, x_3, \omega) (\tilde{\mathbf{L}}^H)_{K,4}^{-1}(\kappa, x_3, \omega) \right] \tilde{d}_4^H(\kappa, x_3, \omega) \\
&= \frac{k_1}{\kappa} \left[\tilde{\mathbf{L}}_{8,J}^V(\kappa, x_3, \omega) \tilde{\mathcal{G}}_{J,K}^V(\kappa, x_3, \omega) (\tilde{\mathbf{L}}^V)_{K,4}^{-1}(\kappa, x_3, \omega) \right] \left(\frac{-1}{\kappa} k_1 \hat{J}_1^e(\omega) \right) \\
&\quad - \frac{jk_2}{\kappa^2} \left[\tilde{\mathbf{L}}_{2,J}^H(\kappa, x_3, \omega) \tilde{\mathcal{G}}_{J,K}^H(\kappa, x_3, \omega) (\tilde{\mathbf{L}}^H)_{K,4}^{-1}(\kappa, x_3, \omega) \right] \left(-jk_2 \hat{J}_1^e(\omega) \right) \\
&= \left\{ \frac{-k_1^2}{\kappa^2} \left[\tilde{\mathbf{L}}_{8,J}^V(\kappa, x_3, \omega) \tilde{\mathcal{G}}_{J,K}^V(\kappa, x_3, \omega) (\tilde{\mathbf{L}}^V)_{K,4}^{-1}(\kappa, x_3, \omega) \right] \right. \\
&\quad \left. - \frac{k_2^2}{\kappa^2} \left[\tilde{\mathbf{L}}_{2,J}^H(\kappa, x_3, \omega) \tilde{\mathcal{G}}_{J,K}^H(\kappa, x_3, \omega) (\tilde{\mathbf{L}}^H)_{K,4}^{-1}(\kappa, x_3, \omega) \right] \right\} \hat{J}_1^e(\omega) \\
&= \tilde{G}_{11}^{ee}(\mathbf{k}_H, x_3, x_3^s, \omega) \hat{J}_1^e(\omega). \tag{3.268}
\end{aligned}$$

Here, $\tilde{G}_{11}^{ee}(\mathbf{k}_H, x_3, x_3^s, \omega)$ is the two-way Green's function in the horizontal wavenumber-frequency domain, where the superscripts denote field type and source type, respectively, and the subscripts the components of this field type and source type. For this case, this means the Green function describing an electric field in the x_1 direction due to an electric current source in the same direction. This expression cannot be analytically transformed back to space-time, but the inverse spatial Fourier transformation has to be computed numerically. We can write the space-frequency solution as

$$\begin{aligned}
\hat{E}_1^{J_1^e}(\mathbf{x}, \omega) &= \hat{G}_{11}^{ee}(\mathbf{x}, \mathbf{x}^s, \omega) \hat{J}_1^e(\omega) \\
&= \frac{\hat{J}_1^e(\omega)}{4\pi^2} \int_{\mathbf{k}_H=-\infty}^{\infty} \tilde{G}_{11}^{ee}(\mathbf{k}_H, x_3, x_3^s, \omega) \exp(-j(\mathbf{k}_H \cdot \Delta \mathbf{x}_H)) dk_1 dk_2, \tag{3.269}
\end{aligned}$$

where $\mathbf{k}_H = k_1 \hat{\mathbf{x}}_1 + k_2 \hat{\mathbf{x}}_2$, with $\hat{\mathbf{x}}_\alpha$ denoting unit vectors in the indicated direction. Similarly $\Delta \mathbf{x}_H = (x_1^r) \hat{\mathbf{x}}_1 + (x_2^r) \hat{\mathbf{x}}_2$, with the superscript r denoting the receiver-related positions. We now drop the superscript indicating the receiver. We also drop the explicit horizontal wavenumber-frequency arguments in the right-hand side of the equations. We take

$$k_1 = \kappa \cos(\psi + \phi), \quad x_1 = r \cos(\phi) = |\mathbf{x}_H| \cos(\phi), \tag{3.270}$$

$$k_2 = \kappa \sin(\psi + \phi), \quad x_2 = r \sin(\phi) = |\mathbf{x}_H| \sin(\phi), \tag{3.271}$$

such that

$$dk_1 dk_2 = \kappa d\kappa d\psi, \quad 0 < \kappa < \infty, \quad 0 < \psi < 2\pi, \tag{3.272}$$

and change to cylindrical coordinates in \mathbf{k}_H -space:

$$\mathbf{k}_H \cdot \mathbf{x}_H \equiv |\mathbf{k}_H| |\mathbf{x}_H| \cos(\psi) = \kappa |\mathbf{x}_H| \cos(\psi), \quad (3.273)$$

where ψ is the angle between \mathbf{k}_H and \mathbf{x}_H . We can write

$$\begin{aligned} \mathbf{k}_H \cdot \mathbf{x}_H &= k_1 x_1 + k_2 x_2 = \kappa \cos(\psi + \phi) \|\mathbf{x}_H\| \cos(\phi) \\ &+ \kappa \sin(\psi + \phi) |\mathbf{x}_H| \\ &= \kappa [\cos(\psi) \cos(\phi) - \sin(\psi) \sin(\phi)] |\mathbf{x}_H| \cos(\phi) \\ &+ \kappa [\sin(\psi) \cos(\phi) + \cos(\psi) \sin(\phi)] |\mathbf{x}_H| \sin(\phi) \\ &= \kappa |\mathbf{x}_H| \cos(\psi) [(\sin(\phi))^2 + (\cos(\phi))^2] \\ &= \kappa |\mathbf{x}_H| \cos(\psi) \\ &= \kappa r \cos(\psi). \end{aligned} \quad (3.274)$$

Substituting these expressions in equation 3.269, making use of $k_1^2 \xrightarrow{FT^{-1}} -\partial_1^2$ and $k_2^2 \xrightarrow{FT^{-1}} -\partial_2^2$, and recognizing and substituting the expression for the Bessel function of the first kind and order zero,

$$J_0(\kappa r) = \frac{1}{2\pi} \int_{\psi=0}^{2\pi} \exp(-j\kappa r \cos\psi) d\psi, \quad (3.275)$$

yields, combined with equations 3.261 and 3.262:

$$\begin{aligned} \hat{E}_1^{j_1^e}(\mathbf{x}, \omega) &= \\ &\frac{\hat{J}_1^e(\omega)}{2\pi} \int_{\kappa=0}^{\infty} \left[\frac{\partial_1^2}{\kappa^2} \left(\tilde{\mathbf{L}}_{8,J}^V \tilde{\mathcal{G}}_{J,K}^V (\tilde{\mathbf{L}}^V)_{K,4}^{-1} \right) + \frac{\partial_2^2}{\kappa^2} \left(\tilde{\mathbf{L}}_{2,J}^H \tilde{\mathcal{G}}_{J,K}^H (\tilde{\mathbf{L}}^H)_{K,4}^{-1} \right) \right] J_0(\kappa r) \kappa d\kappa \\ &= \frac{\hat{J}_1^e(\omega)}{2\pi} \int_{\kappa=0}^{\infty} \left[-\frac{1}{2} (J_0(\kappa r) - \cos(2\phi) J_2(\kappa r)) \left(\tilde{\mathbf{L}}_{8,J}^V \tilde{\mathcal{G}}_{J,K}^V (\tilde{\mathbf{L}}^V)_{K,4}^{-1} \right) \right. \\ &\quad \left. - \frac{1}{2} (J_0(\kappa r) + \cos(2\phi) J_2(\kappa r)) \left(\tilde{\mathbf{L}}_{2,J}^H \tilde{\mathcal{G}}_{J,K}^H (\tilde{\mathbf{L}}^H)_{K,4}^{-1} \right) \right] \kappa d\kappa. \end{aligned} \quad (3.276)$$

We can write this equation such that the directional cosines are outside of the integral

$$\begin{aligned} \hat{E}_1^{j_1^e}(\mathbf{x}, \omega) &= \\ &-\frac{\hat{J}_1^e(\omega)}{4\pi} \int_{\kappa=0}^{\infty} \left[J_0(\kappa r) \left(\tilde{\mathbf{L}}_{8,J}^V \tilde{\mathcal{G}}_{J,K}^V (\tilde{\mathbf{L}}^V)_{K,4}^{-1} + \tilde{\mathbf{L}}_{2,J}^H \tilde{\mathcal{G}}_{J,K}^H (\tilde{\mathbf{L}}^H)_{K,4}^{-1} \right) \right] \kappa d\kappa \\ &+ \frac{\hat{J}_1^e(\omega)}{4\pi} \cos(2\phi) \int_{\kappa=0}^{\infty} \left[J_2(\kappa r) \left(\tilde{\mathbf{L}}_{8,J}^V \tilde{\mathcal{G}}_{J,K}^V (\tilde{\mathbf{L}}^V)_{K,4}^{-1} - \tilde{\mathbf{L}}_{2,J}^H \tilde{\mathcal{G}}_{J,K}^H (\tilde{\mathbf{L}}^H)_{K,4}^{-1} \right) \right] \kappa d\kappa. \end{aligned} \quad (3.277)$$

This form can be used because there are no separate divisions by factors of κ inside $\tilde{\mathbf{L}}_{2,J}^{H,V}$ and $(\tilde{\mathbf{L}}^{H,V})_{K,4}^{-1}$. Otherwise these factors would have to be taken out explicitly.

For all other seismo-electromagnetic source-receiver combinations, we will present the result until the form of equation 3.276. Bear in mind that each of these expressions can be rewritten such that the directional cosines are outside the integral (like in equation (3.277)). This is also how the Fourier-Bessel transformations are coded in ESSEMOD.

Appendix

3.3.A Explicit Fourier-Bessel transformations for all source-receiver combinations

In this appendix, we present the explicit Fourier-Bessel transformations for all other independent seismo-electromagnetic source-receiver combinations. We do not present the explicit expressions for the eliminated fields of equations (2.97)-(2.100). We skip the explicit transformation to cylindrical coordinates followed by the recognition of the Bessel function of the first kind and order zero and we directly jump from equations of the horizontal wavenumber-frequency form of equation 3.268 to the space-frequency form of equation 3.276. We have reduced the fontsize of the equations for a more compact presentation.

E_1 -type two-way field quantity expressions

For $\tilde{E}_1^{J_2^e}$, we transform

$$\begin{aligned}
 \tilde{E}_1^{J_2^e}(\mathbf{k}_H, x_3, \omega) &= \frac{k_1}{\kappa} \tilde{E}_{norm}^V(\kappa, x_3, \omega) - \frac{jk_2}{\kappa^2} \tilde{E}^H(\kappa, x_3, \omega) \\
 &= \frac{k_1}{\kappa} \tilde{q}_8^V(\kappa, x_3, \omega) - \frac{jk_2}{\kappa^2} \tilde{q}_2^H(\kappa, x_3, \omega) \\
 &= \left\{ \frac{-k_1 k_2}{\kappa^2} \left[\tilde{\mathbf{L}}_{8,J}^V(\kappa, x_3, \omega) \tilde{\mathcal{G}}_{J,K}^V(\kappa, x_3, \omega) (\tilde{\mathbf{L}}^V)_{K,4}^{-1}(\kappa, x_3, \omega) \right] \right. \\
 &\quad \left. + \frac{k_1 k_2}{\kappa^2} \left[\tilde{\mathbf{L}}_{2,J}^H(\kappa, x_3, \omega) \tilde{\mathcal{G}}_{J,K}^H(\kappa, x_3, \omega) (\tilde{\mathbf{L}}^H)_{K,4}^{-1}(\kappa, x_3, \omega) \right] \right\} \hat{\mathcal{J}}_2^e(\omega),
 \end{aligned} \tag{3.278}$$

to

$$\begin{aligned}
 \hat{E}_1^{J_2^e}(\mathbf{x}, \omega) &= \frac{\hat{\mathcal{J}}_2^e(\omega)}{2\pi} \int_{\kappa=0}^{\infty} \left[\frac{\partial_1 \partial_2}{\kappa^2} \left(\tilde{\mathbf{L}}_{8,J}^V \tilde{\mathcal{G}}_{J,K}^V (\tilde{\mathbf{L}}^V)_{K,4}^{-1} \right) \right. \\
 &\quad \left. - \frac{\partial_1 \partial_2}{\kappa^2} \left(\tilde{\mathbf{L}}_{2,J}^H \tilde{\mathcal{G}}_{J,K}^H (\tilde{\mathbf{L}}^H)_{K,4}^{-1} \right) \right] J_0(\kappa r) \kappa d\kappa \\
 &= \frac{\hat{\mathcal{J}}_2^e(\omega)}{2\pi} \int_{\kappa=0}^{\infty} \left[\cos(\phi) \sin(\phi) \left(\tilde{\mathbf{L}}_{8,J}^V \tilde{\mathcal{G}}_{J,K}^V (\tilde{\mathbf{L}}^V)_{K,4}^{-1} \right) \right. \\
 &\quad \left. - \cos(\phi) \sin(\phi) \left(\tilde{\mathbf{L}}_{2,J}^H \tilde{\mathcal{G}}_{J,K}^H (\tilde{\mathbf{L}}^H)_{K,4}^{-1} \right) \right] J_2(\kappa r) \kappa d\kappa.
 \end{aligned} \tag{3.279}$$

For $\tilde{E}_1^{J_3^e}$, we transform

$$\begin{aligned}
\tilde{E}_1^{J_3^e}(\mathbf{k}_H, x_3, \omega) &= \frac{k_1}{\kappa} \tilde{E}_{norm}^V(\kappa, x_3, \omega) - \frac{jk_2}{\kappa^2} \tilde{E}^H(\kappa, x_3, \omega) \\
&= \frac{k_1}{\kappa} \tilde{q}_8^V(\kappa, x_3, \omega) - \frac{jk_2}{\kappa^2} \tilde{q}_2^H(\kappa, x_3, \omega) \\
&= \frac{k_1}{\kappa} \left[\tilde{\mathbf{L}}_{8,J}^V(\kappa, x_3, \omega) \tilde{\mathcal{G}}_{J,K}^V(\kappa, x_3, \omega) (\tilde{\mathbf{L}}^V)_{K,6}^{-1}(\kappa, x_3, \omega) \right] \left(\frac{\hat{\rho}^E \hat{\mathcal{L}}}{\hat{\epsilon}} \hat{J}_3^e(\omega) \right) \\
&\quad + \frac{jk_1}{s\hat{\epsilon}} \left[\tilde{\mathbf{L}}_{8,J}^V(\kappa, x_3, \omega) \tilde{\mathcal{G}}_{J,K}^V(\kappa, x_3, \omega) (\tilde{\mathbf{L}}^V)_{K,6}^{-1}(\kappa, x_3, \omega) \right] \hat{J}_3^e(\omega), \quad (3.280)
\end{aligned}$$

to

$$\begin{aligned}
\hat{E}_1^{J_3^e}(\mathbf{x}, \omega) &= \frac{\hat{J}_3^e(\omega)}{2\pi} \int_{\kappa=0}^{\infty} \left[\frac{j\partial_1}{\kappa} \left(\tilde{\mathbf{L}}_{8,J}^V \tilde{\mathcal{G}}_{J,K}^V (\tilde{\mathbf{L}}^V)_{K,6}^{-1} \right) \frac{\hat{\rho}^E \hat{\mathcal{L}}}{\hat{\epsilon}} \right. \\
&\quad \left. - \partial_1 \left(\tilde{\mathbf{L}}_{8,J}^V \tilde{\mathcal{G}}_{J,K}^V (\tilde{\mathbf{L}}^V)_{K,8}^{-1} \right) \frac{1}{s\hat{\epsilon}} \right] J_0(\kappa r) \kappa d\kappa \\
&= \frac{\hat{J}_3^e(\omega)}{2\pi} \int_{\kappa=0}^{\infty} \left[-j\cos(\phi) \left(\tilde{\mathbf{L}}_{8,J}^V \tilde{\mathcal{G}}_{J,K}^V (\tilde{\mathbf{L}}^V)_{K,6}^{-1} \right) \frac{\hat{\rho}^E \hat{\mathcal{L}}}{\hat{\epsilon}} \right. \\
&\quad \left. + \kappa \cos(\phi) \left(\tilde{\mathbf{L}}_{8,J}^V \tilde{\mathcal{G}}_{J,K}^V (\tilde{\mathbf{L}}^V)_{K,8}^{-1} \right) \frac{1}{s\hat{\epsilon}} \right] J_1(\kappa r) \kappa d\kappa. \quad (3.281)
\end{aligned}$$

The imaginary number j under the integral is compensated by an explicit factor j inside the $\tilde{\mathbf{L}}_{8,J}^V \tilde{\mathcal{G}}_{J,K}^V (\tilde{\mathbf{L}}^V)_{K,6}^{-1}$ term, making the expression physical. Note that \hat{J}_3^e is a purely P-SV-TM source-type. Hence, we can compose the true field quantity using only the P-SV-TM mode. This holds for all other source types that are purely existing in the P-SV-TM mode. For $\tilde{E}_1^{J_1^m}$, we transform

$$\begin{aligned}
\tilde{E}_1^{J_1^m}(\mathbf{k}_H, x_3, \omega) &= \frac{k_1}{\kappa} \tilde{E}_{norm}^V(\kappa, x_3, \omega) - \frac{jk_2}{\kappa^2} \tilde{E}^H(\kappa, x_3, \omega) \\
&= \frac{k_1}{\kappa} \tilde{q}_8^V(\kappa, x_3, \omega) - \frac{jk_2}{\kappa^2} \tilde{q}_2^H(\kappa, x_3, \omega) \\
&= \left\{ \frac{k_1 k_2}{\kappa^2} \left[\tilde{\mathbf{L}}_{8,J}^V(\kappa, x_3, \omega) \tilde{\mathcal{G}}_{J,K}^V(\kappa, x_3, \omega) (\tilde{\mathbf{L}}^V)_{K,8}^{-1}(\kappa, x_3, \omega) \right] \right. \\
&\quad \left. - \frac{k_1 k_2}{\kappa^2} \left[\tilde{\mathbf{L}}_{2,J}^H(\kappa, x_3, \omega) \tilde{\mathcal{G}}_{J,K}^H(\kappa, x_3, \omega) (\tilde{\mathbf{L}}^H)_{K,2}^{-1}(\kappa, x_3, \omega) \right] \right\} \hat{J}_1^m(\omega), \quad (3.282)
\end{aligned}$$

to

$$\begin{aligned}
 \hat{E}_1^{J^m}(\mathbf{x}, \omega) &= \frac{\hat{J}_1^m(\omega)}{2\pi} \int_{\kappa=0}^{\infty} \left[-\frac{\partial_1 \partial_2}{\kappa^2} \left(\tilde{\mathbf{L}}_{8,J}^V \tilde{\mathcal{G}}_{J,K}^V (\tilde{\mathbf{L}}^V)_{K,8}^{-1} \right) \right. \\
 &\quad \left. + \frac{\partial_1 \partial_2}{\kappa^2} \left(\tilde{\mathbf{L}}_{2,J}^H \tilde{\mathcal{G}}_{J,K}^H (\tilde{\mathbf{L}}^H)_{K,2}^{-1} \right) \right] J_0(\kappa r) \kappa d\kappa \\
 &= \frac{\hat{J}_1^m(\omega)}{2\pi} \int_{\kappa=0}^{\infty} \left[-\cos(\phi) \sin(\phi) \left(\tilde{\mathbf{L}}_{8,J}^V \tilde{\mathcal{G}}_{J,K}^V (\tilde{\mathbf{L}}^V)_{K,8}^{-1} \right) \right. \\
 &\quad \left. + \cos(\phi) \sin(\phi) \left(\tilde{\mathbf{L}}_{2,J}^H \tilde{\mathcal{G}}_{J,K}^H (\tilde{\mathbf{L}}^H)_{K,2}^{-1} \right) \right] J_2(\kappa r) \kappa d\kappa.
 \end{aligned} \tag{3.283}$$

For $\tilde{E}_1^{J^m}$, we transform

$$\begin{aligned}
 \tilde{E}_1^{J^m}(\mathbf{k}_H, x_3, \omega) &= \frac{k_1}{\kappa} \tilde{E}_{norm}^V(\kappa, x_3, \omega) - \frac{jk_2}{\kappa^2} \tilde{E}^H(\kappa, x_3, \omega) \\
 &= \frac{k_1}{\kappa} \tilde{q}_8^V(\kappa, x_3, \omega) - \frac{jk_2}{\kappa^2} \tilde{q}_2^H(\kappa, x_3, \omega) \\
 &= \left\{ \frac{-k_1^2}{\kappa^2} \left[\tilde{\mathbf{L}}_{8,J}^V(\kappa, x_3, \omega) \tilde{\mathcal{G}}_{J,K}^V(\kappa, x_3, \omega) (\tilde{\mathbf{L}}^V)_{K,8}^{-1}(\kappa, x_3, \omega) \right] \right. \\
 &\quad \left. - \frac{k_2^2}{\kappa^2} \left[\tilde{\mathbf{L}}_{2,J}^H(\kappa, x_3, \omega) \tilde{\mathcal{G}}_{J,K}^H(\kappa, x_3, \omega) (\tilde{\mathbf{L}}^H)_{K,2}^{-1}(\kappa, x_3, \omega) \right] \right\} \hat{J}_2^m(\omega),
 \end{aligned} \tag{3.284}$$

to

$$\begin{aligned}
 \hat{E}_1^{J^m}(\mathbf{x}, \omega) &= \frac{\hat{J}_2^m(\omega)}{2\pi} \int_{\kappa=0}^{\infty} \left[\frac{\partial_1^2}{\kappa^2} \left(\tilde{\mathbf{L}}_{8,J}^V \tilde{\mathcal{G}}_{J,K}^V (\tilde{\mathbf{L}}^V)_{K,8}^{-1} \right) \right. \\
 &\quad \left. + \frac{\partial_2^2}{\kappa^2} \left(\tilde{\mathbf{L}}_{2,J}^H \tilde{\mathcal{G}}_{J,K}^H (\tilde{\mathbf{L}}^H)_{K,2}^{-1} \right) \right] J_0(\kappa r) \kappa d\kappa \\
 &= \frac{\hat{J}_2^m(\omega)}{2\pi} \int_{\kappa=0}^{\infty} \left\{ -\frac{1}{2} \left(\tilde{\mathbf{L}}_{8,J}^V \tilde{\mathcal{G}}_{J,K}^V (\tilde{\mathbf{L}}^V)_{K,8}^{-1} \right) (J_0(\kappa r) - \cos(2\phi) J_2(\kappa r)) \right. \\
 &\quad \left. - \frac{1}{2} \left(\tilde{\mathbf{L}}_{2,J}^H \tilde{\mathcal{G}}_{J,K}^H (\tilde{\mathbf{L}}^H)_{K,2}^{-1} \right) (J_0(\kappa r) + \cos(2\phi) J_2(\kappa r)) \right\} \kappa d\kappa.
 \end{aligned} \tag{3.285}$$

For $\tilde{E}_1^{J^m}$, we transform

$$\begin{aligned}
 \tilde{E}_1^{J^m}(\mathbf{k}_H, x_3, \omega) &= \frac{k_1}{\kappa} \tilde{E}_{norm}^V(\kappa, x_3, \omega) - \frac{jk_2}{\kappa^2} \tilde{E}^H(\kappa, x_3, \omega) \\
 &= \frac{k_1}{\kappa} \tilde{q}_8^V(\kappa, x_3, \omega) - \frac{jk_2}{\kappa^2} \tilde{q}_2^H(\kappa, x_3, \omega) \\
 &= jk_2 \left(\tilde{\mathbf{L}}_{2,J}^H(\kappa, x_3, \omega) \tilde{\mathcal{G}}_{J,K}^H(\kappa, x_3, \omega) (\tilde{\mathbf{L}}^H)_{K,4}^{-1}(\kappa, x_3, \omega) \right) \left(\frac{1}{s\mu_0} \hat{J}_3^m(\omega) \right),
 \end{aligned} \tag{3.286}$$

to

$$\begin{aligned}
\hat{E}_2^{J_3^m}(\mathbf{x}, \omega) &= \frac{\hat{J}_3^m(\omega)}{2\pi} \int_{\kappa=0}^{\infty} \left[-\partial_2 \left(\tilde{\mathbf{L}}_{2,J}^H \tilde{\mathcal{G}}_{J,K}^H (\tilde{\mathbf{L}}^H)_{K,4}^{-1} \right) \left(\frac{1}{s\mu_0} \right) \right] J_0(\kappa r) \kappa d\kappa \\
&= \frac{\hat{J}_3^m(\omega)}{2\pi} \int_{\kappa=0}^{\infty} \kappa \sin(\phi) \left(\tilde{\mathbf{L}}_{2,J}^H \tilde{\mathcal{G}}_{J,K}^H (\tilde{\mathbf{L}}^H)_{K,4}^{-1} \right) \left(\frac{1}{s\mu_0} \right) J_1(\kappa r) \kappa d\kappa.
\end{aligned} \tag{3.287}$$

For $\tilde{E}_1^{f_1^b}$, we transform

$$\begin{aligned}
\tilde{E}_1^{f_1^b}(\mathbf{k}_H, x_3, \omega) &= \frac{k_1}{\kappa} \tilde{E}_{norm}^V(\kappa, x_3, \omega) - \frac{jk_2}{\kappa^2} \tilde{E}^H(\kappa, x_3, \omega) \\
&= \frac{k_1}{\kappa} \tilde{q}_8^V(\kappa, x_3, \omega) - \frac{jk_2}{\kappa^2} \tilde{q}_2^H(\kappa, x_3, \omega) \\
&= -\frac{k_1^2}{\kappa^2} \left[\tilde{\mathbf{L}}_{8,J}^V(\kappa, x_3, \omega) \tilde{\mathcal{G}}_{J,K}^V (\tilde{\mathbf{L}}^V)_{K,3}^{-1}(\kappa, x_3, \omega) \right] \hat{\mathcal{F}}_1^b(\omega) \\
&\quad - \frac{k_2^2}{\kappa^2} \left[\tilde{\mathbf{L}}_{2,J}^H(\kappa, x_3, \omega) \tilde{\mathcal{G}}_{J,K}^H (\tilde{\mathbf{L}}^H)_{K,3}^{-1}(\kappa, x_3, \omega) \right] \hat{\mathcal{F}}_1^b(\omega), \tag{3.288}
\end{aligned}$$

to

$$\begin{aligned}
\hat{E}_1^{f_1^b}(\mathbf{x}, \omega) &= \frac{\hat{\mathcal{F}}_1^b(\omega)}{2\pi} \int_{\kappa=0}^{\infty} \left[\frac{\partial_1^2}{\kappa^2} \left(\tilde{\mathbf{L}}_{8,J}^V \tilde{\mathcal{G}}_{J,K}^V (\tilde{\mathbf{L}}^V)_{K,3}^{-1} \right) \right. \\
&\quad \left. + \frac{\partial_2^2}{\kappa^2} \left(\tilde{\mathbf{L}}_{2,J}^H(\kappa, x_3, \omega) \tilde{\mathcal{G}}_{J,K}^H (\tilde{\mathbf{L}}^H)_{K,3}^{-1} \right) \right] J_0(\kappa r) \kappa d\kappa \\
&= \frac{\hat{\mathcal{F}}_1^b(\omega)}{2\pi} \int_{\kappa=0}^{\infty} \left[-\frac{1}{2} \left(\tilde{\mathbf{L}}_{8,J}^V \tilde{\mathcal{G}}_{J,K}^V (\tilde{\mathbf{L}}^V)_{K,3}^{-1} \right) (J_0(\kappa r) - \cos(2\phi) J_2(\kappa r)) \right. \\
&\quad \left. - \frac{1}{2} \left(\tilde{\mathbf{L}}_{2,J}^H(\kappa, x_3, \omega) \tilde{\mathcal{G}}_{J,K}^H (\tilde{\mathbf{L}}^H)_{K,3}^{-1} \right) (J_0(\kappa r) + \cos(2\phi) J_2(\kappa r)) \right] \kappa d\kappa. \\
&= \frac{\hat{\mathcal{F}}_1^b(\omega)}{4\pi} \int_{\kappa=0}^{\infty} \left\{ -J_0(\kappa r) \left[\left(\tilde{\mathbf{L}}_{8,J}^V \tilde{\mathcal{G}}_{J,K}^V (\tilde{\mathbf{L}}^V)_{K,3}^{-1} \right) \right. \right. \\
&\quad \left. \left. + \left(\tilde{\mathbf{L}}_{2,J}^H(\kappa, x_3, \omega) \tilde{\mathcal{G}}_{J,K}^H (\tilde{\mathbf{L}}^H)_{K,3}^{-1} \right) \right] \right. \\
&\quad \left. + \cos(2\phi) J_2(\kappa r) \left[\left(\tilde{\mathbf{L}}_{8,J}^V \tilde{\mathcal{G}}_{J,K}^V (\tilde{\mathbf{L}}^V)_{K,3}^{-1} \right) \right. \right. \\
&\quad \left. \left. - \left(\tilde{\mathbf{L}}_{2,J}^H(\kappa, x_3, \omega) \tilde{\mathcal{G}}_{J,K}^H (\tilde{\mathbf{L}}^H)_{K,3}^{-1} \right) \right] \right\} \kappa d\kappa. \tag{3.289}
\end{aligned}$$

For $\tilde{E}_1^{f_1^f}$, we transform

$$\begin{aligned}
 \tilde{E}_1^{f1}(\mathbf{k}_H, x_3, \omega) &= \frac{k_1}{\kappa} \tilde{E}_{norm}^V(\kappa, x_3, \omega) - \frac{jk_2}{\kappa^2} \tilde{E}^H(\kappa, x_3, \omega) \\
 &= \frac{k_1}{\kappa} \tilde{q}_8^V(\kappa, x_3, \omega) - \frac{jk_2}{\kappa^2} \tilde{q}_2^H(\kappa, x_3, \omega) \\
 &= \frac{jk_1^2}{\kappa} \left[\tilde{\mathbf{L}}_{8,J}^V(\kappa, x_3, \omega) \tilde{\mathbf{G}}_{J,K}^V(\kappa, x_3, \omega) (\tilde{\mathbf{L}}^V)_{K,2}^{-1}(\kappa, x_3, \omega) \left(\frac{1}{s\hat{\rho}^E} \hat{\mathcal{F}}_1^f(\omega) \right) \right] \\
 &\quad + \frac{k_1^2}{\kappa^2} \left[\tilde{\mathbf{L}}_{8,J}^V(\kappa, x_3, \omega) \tilde{\mathbf{G}}_{J,K}^V(\kappa, x_3, \omega) (\tilde{\mathbf{L}}^V)_{K,3}^{-1}(\kappa, x_3, \omega) \left(\frac{\rho^f}{\hat{\rho}^E} \hat{\mathcal{F}}_1^f(\omega) \right) \right. \\
 &\quad \left. - \tilde{\mathbf{L}}_{8,J}^V(\kappa, x_3, \omega) \tilde{\mathbf{G}}_{J,K}^V(\kappa, x_3, \omega) (\tilde{\mathbf{L}}^V)_{K,4}^{-1}(\kappa, x_3, \omega) \left(\hat{\mathcal{L}} \hat{\mathcal{F}}_1^f(\omega) \right) \right] \\
 &\quad + \frac{k_2^2}{\kappa^2} \left[\tilde{\mathbf{L}}_{2,J}^H(\kappa, x_3, \omega) \tilde{\mathbf{G}}_{J,K}^H(\kappa, x_3, \omega) (\tilde{\mathbf{L}}^H)_{K,3}^{-1}(\kappa, x_3, \omega) \left(\frac{\rho^f}{\hat{\rho}^E} \hat{\mathcal{F}}_1^f(\omega) \right) \right. \\
 &\quad \left. - \tilde{\mathbf{L}}_{2,J}^H(\kappa, x_3, \omega) \tilde{\mathbf{G}}_{J,K}^H(\kappa, x_3, \omega) (\tilde{\mathbf{L}}^H)_{K,4}^{-1}(\kappa, x_3, \omega) \left(\hat{\mathcal{L}} \hat{\mathcal{F}}_1^f(\omega) \right) \right], \quad (3.290)
 \end{aligned}$$

to

$$\begin{aligned}
 \hat{E}_1^{f1}(\mathbf{x}, \omega) &= \frac{\hat{\mathcal{F}}_1^f(\omega)}{2\pi} \int_{\kappa=0}^{\infty} \left[-j \frac{\partial_1^2}{\kappa} \left(\tilde{\mathbf{L}}_{8,J}^V \tilde{\mathbf{G}}_{J,K}^V (\tilde{\mathbf{L}}^V)_{K,2}^{-1} \right) \left(\frac{1}{s\hat{\rho}^E} \right) \right. \\
 &\quad \left. - \frac{\partial_1^2}{\kappa^2} \left(\tilde{\mathbf{L}}_{8,J}^V(\kappa, x_3, \omega) \tilde{\mathbf{G}}_{J,K}^V(\kappa, x_3, \omega) (\tilde{\mathbf{L}}^V)_{K,3}^{-1}(\kappa, x_3, \omega) \right) \left(\frac{\rho^f}{\hat{\rho}^E} \right) \right. \\
 &\quad \left. + \frac{\partial_1^2}{\kappa^2} \left(\tilde{\mathbf{L}}_{8,J}^V \tilde{\mathbf{G}}_{J,K}^V (\tilde{\mathbf{L}}^V)_{K,4}^{-1} \right) \hat{\mathcal{L}} \right. \\
 &\quad \left. - \frac{\partial_2^2}{\kappa^2} \left(\tilde{\mathbf{L}}_{2,J}^H(\kappa, x_3, \omega) \tilde{\mathbf{G}}_{J,K}^H(\kappa, x_3, \omega) (\tilde{\mathbf{L}}^H)_{K,3}^{-1}(\kappa, x_3, \omega) \right) \left(\frac{\rho^f}{\hat{\rho}^E} \right) \right. \\
 &\quad \left. + \frac{\partial_2^2}{\kappa^2} \left(\tilde{\mathbf{L}}_{2,J}^H(\kappa, x_3, \omega) \tilde{\mathbf{G}}_{J,K}^H(\kappa, x_3, \omega) (\tilde{\mathbf{L}}^H)_{K,4}^{-1} \right) \hat{\mathcal{L}} \right] J_0(\kappa r) \kappa d\kappa \\
 &= \frac{\hat{\mathcal{F}}_1^b(\omega)}{2\pi} \int_{\kappa=0}^{\infty} \left\{ \frac{jk}{2} \left(\tilde{\mathbf{L}}_{8,J}^V \tilde{\mathbf{G}}_{J,K}^V (\tilde{\mathbf{L}}^V)_{K,2}^{-1} \right) \left(\frac{1}{s\hat{\rho}^E} \right) (J_0(\kappa r) - \cos(2\phi) J_2(\kappa r)) \right. \\
 &\quad \left. + \frac{1}{2} \left[\left(\tilde{\mathbf{L}}_{8,J}^V \tilde{\mathbf{G}}_{J,K}^V (\tilde{\mathbf{L}}^V)_{K,3}^{-1} \right) \frac{\rho^f}{\hat{\rho}^E} - \left(\tilde{\mathbf{L}}_{8,J}^V \tilde{\mathbf{G}}_{J,K}^V (\tilde{\mathbf{L}}^V)_{K,4}^{-1} \right) \hat{\mathcal{L}} \right] (J_0(\kappa r) - \cos(2\phi) J_2(\kappa r)) \right. \\
 &\quad \left. + \frac{1}{2} \left[\left(\tilde{\mathbf{L}}_{2,J}^H(\kappa, x_3, \omega) \tilde{\mathbf{G}}_{J,K}^H(\kappa, x_3, \omega) (\tilde{\mathbf{L}}^H)_{K,3}^{-1} \right) \frac{\rho^f}{\hat{\rho}^E} \right. \right. \\
 &\quad \left. \left. - \left(\tilde{\mathbf{L}}_{2,J}^H(\kappa, x_3, \omega) \tilde{\mathbf{G}}_{J,K}^H(\kappa, x_3, \omega) (\tilde{\mathbf{L}}^H)_{K,4}^{-1} \right) \hat{\mathcal{L}} \right] (J_0(\kappa r) + \cos(2\phi) J_2(\kappa r)) \right\} \kappa d\kappa. \\
 &= \frac{\hat{\mathcal{F}}_1^b(\omega)}{2\pi} \int_{\kappa=0}^{\infty} \left\{ \frac{1}{2} \left[\left(\tilde{\mathbf{L}}_{8,J}^V \tilde{\mathbf{G}}_{J,K}^V (\tilde{\mathbf{L}}^V)_{K,2}^{-1} \right) \left(\frac{jk}{s\hat{\rho}^E} \right) \right. \right. \\
 &\quad \left. \left. + \left(\tilde{\mathbf{L}}_{8,J}^V \tilde{\mathbf{G}}_{J,K}^V (\tilde{\mathbf{L}}^V)_{K,3}^{-1} \right) \frac{\rho^f}{\hat{\rho}^E} - \left(\tilde{\mathbf{L}}_{8,J}^V \tilde{\mathbf{G}}_{J,K}^V (\tilde{\mathbf{L}}^V)_{K,4}^{-1} \right) \hat{\mathcal{L}} \right] (J_0(\kappa r) - \cos(2\phi) J_2(\kappa r)) \right. \\
 &\quad \left. + \frac{1}{2} \left[\left(\tilde{\mathbf{L}}_{2,J}^H(\kappa, x_3, \omega) \tilde{\mathbf{G}}_{J,K}^H(\kappa, x_3, \omega) (\tilde{\mathbf{L}}^H)_{K,3}^{-1} \right) \frac{\rho^f}{\hat{\rho}^E} \right. \right. \\
 &\quad \left. \left. - \left(\tilde{\mathbf{L}}_{2,J}^H(\kappa, x_3, \omega) \tilde{\mathbf{G}}_{J,K}^H(\kappa, x_3, \omega) (\tilde{\mathbf{L}}^H)_{K,4}^{-1} \right) \hat{\mathcal{L}} \right] (J_0(\kappa r) + \cos(2\phi) J_2(\kappa r)) \right\} \kappa d\kappa. \quad (3.291)
 \end{aligned}$$

For \tilde{E}_1^{fb} , we transform

$$\begin{aligned}
\tilde{E}_1^{fb}(\mathbf{k}_H, x_3, \omega) &= \frac{k_1}{\kappa} \tilde{E}_{norm}^V(\kappa, x_3, \omega) - \frac{jk_2}{\kappa^2} \tilde{E}^H(\kappa, x_3, \omega) \\
&= \frac{k_1}{\kappa} \tilde{q}_8^V(\kappa, x_3, \omega) - \frac{jk_2}{\kappa^2} \tilde{q}_2^H(\kappa, x_3, \omega) \\
&= -\frac{k_1 k_2}{\kappa^2} \left[\tilde{\mathbf{L}}_{8,J}^V(\kappa, x_3, \omega) \tilde{\mathcal{G}}_{J,K}^V(\kappa, x_3, \omega) (\tilde{\mathbf{L}}^V)_{K,3}^{-1}(\kappa, x_3, \omega) \right] \hat{\mathcal{F}}_2^b(\omega) \\
&\quad + \frac{k_1 k_2}{\kappa^2} \left[\tilde{\mathbf{L}}_{2,J}^H(\kappa, x_3, \omega) \tilde{\mathcal{G}}_{J,K}^H(\kappa, x_3, \omega) (\tilde{\mathbf{L}}^H)_{K,3}^{-1}(\kappa, x_3, \omega) \right] \hat{\mathcal{F}}_2^b(\omega),
\end{aligned} \tag{3.292}$$

to

$$\begin{aligned}
\hat{E}_1^{fb}(\mathbf{x}, \omega) &= \frac{\hat{\mathcal{F}}_2^b(\omega)}{2\pi} \int_{\kappa=0}^{\infty} \left[\frac{\partial_1 \partial_2}{\kappa^2} \left(\tilde{\mathbf{L}}_{8,J}^V \tilde{\mathcal{G}}_{J,K}^V (\tilde{\mathbf{L}}^V)_{K,3}^{-1} \right) \right. \\
&\quad \left. - \frac{\partial_1 \partial_2}{\kappa^2} \left(\tilde{\mathbf{L}}_{2,J}^H(\kappa, x_3, \omega) \tilde{\mathcal{G}}_{J,K}^H(\kappa, x_3, \omega) (\tilde{\mathbf{L}}^H)_{K,3}^{-1} \right) \right] J_0(\kappa r) \kappa d\kappa \\
&= \frac{\hat{\mathcal{F}}_1^b(\omega)}{4\pi} \int_{\kappa=0}^{\infty} \left[\cos(\phi) \sin(\phi) \left(\tilde{\mathbf{L}}_{8,J}^V \tilde{\mathcal{G}}_{J,K}^V (\tilde{\mathbf{L}}^V)_{K,3}^{-1} \right) \right. \\
&\quad \left. - \cos(\phi) \sin(\phi) \left(\tilde{\mathbf{L}}_{2,J}^H(\kappa, x_3, \omega) \tilde{\mathcal{G}}_{J,K}^H(\kappa, x_3, \omega) (\tilde{\mathbf{L}}^H)_{K,3}^{-1} \right) \right] J_2(\kappa r) \kappa d\kappa.
\end{aligned} \tag{3.293}$$

For \tilde{E}_1^{ff} , we transform

$$\begin{aligned}
\tilde{E}_1^{ff}(\mathbf{k}_H, x_3, \omega) &= \frac{k_1}{\kappa} \tilde{E}_{norm}^V(\kappa, x_3, \omega) - \frac{jk_2}{\kappa^2} \tilde{E}^H(\kappa, x_3, \omega) \\
&= \frac{k_1}{\kappa} \tilde{q}_8^V(\kappa, x_3, \omega) - \frac{jk_2}{\kappa^2} \tilde{q}_2^H(\kappa, x_3, \omega) \\
&= \frac{jk_1 k_2}{\kappa} \left[\tilde{\mathbf{L}}_{8,J}^V(\kappa, x_3, \omega) \tilde{\mathcal{G}}_{J,K}^V(\kappa, x_3, \omega) (\tilde{\mathbf{L}}^V)_{K,2}^{-1}(\kappa, x_3, \omega) \left(\frac{1}{s \hat{\rho}^E} \hat{\mathcal{F}}_2^f(\omega) \right) \right] \\
&\quad + \frac{k_1 k_2}{\kappa^2} \left[\tilde{\mathbf{L}}_{8,J}^V(\kappa, x_3, \omega) \tilde{\mathcal{G}}_{J,K}^V(\kappa, x_3, \omega) (\tilde{\mathbf{L}}^V)_{K,3}^{-1}(\kappa, x_3, \omega) \left(\frac{\rho^f}{\hat{\rho}^E} \hat{\mathcal{F}}_2^f(\omega) \right) \right. \\
&\quad \left. - \tilde{\mathbf{L}}_{8,J}^V(\kappa, x_3, \omega) \tilde{\mathcal{G}}_{J,K}^V(\kappa, x_3, \omega) (\tilde{\mathbf{L}}^V)_{K,4}^{-1}(\kappa, x_3, \omega) \left(\hat{\mathcal{L}} \hat{\mathcal{F}}_2^f(\omega) \right) \right] \\
&\quad - \frac{k_1 k_2}{\kappa^2} \left[\tilde{\mathbf{L}}_{2,J}^H(\kappa, x_3, \omega) \tilde{\mathcal{G}}_{J,K}^H(\kappa, x_3, \omega) (\tilde{\mathbf{L}}^H)_{K,3}^{-1}(\kappa, x_3, \omega) \left(\frac{\rho^f}{\hat{\rho}^E} \hat{\mathcal{F}}_2^f(\omega) \right) \right. \\
&\quad \left. - \tilde{\mathbf{L}}_{2,J}^H(\kappa, x_3, \omega) \tilde{\mathcal{G}}_{J,K}^H(\kappa, x_3, \omega) (\tilde{\mathbf{L}}^H)_{K,4}^{-1}(\kappa, x_3, \omega) \left(\hat{\mathcal{L}} \hat{\mathcal{F}}_2^f(\omega) \right) \right],
\end{aligned} \tag{3.294}$$

to

$$\begin{aligned}
 \hat{E}_1^{f_2}(\mathbf{x}, \omega) &= \frac{\hat{\mathcal{F}}_2^f(\omega)}{2\pi} \int_{\kappa=0}^{\infty} \left[-j \frac{\partial_1 \partial_2}{\kappa} \left(\tilde{\mathbf{L}}_{8,J}^V \tilde{\mathcal{G}}_{J,K}^V (\tilde{\mathbf{L}}^V)_{K,2}^{-1} \right) \left(\frac{1}{s \hat{\rho}^E} \right) \right. \\
 &\quad - \frac{\partial_1 \partial_2}{\kappa^2} \left(\tilde{\mathbf{L}}_{8,J}^V \tilde{\mathcal{G}}_{J,K}^V (\tilde{\mathbf{L}}^V)_{K,3}^{-1} \right) \frac{\rho^f}{\hat{\rho}^E} \\
 &\quad + \frac{\partial_1 \partial_2}{\kappa^2} \left(\tilde{\mathbf{L}}_{8,J}^V \tilde{\mathcal{G}}_{J,K}^V (\tilde{\mathbf{L}}^V)_{K,4}^{-1} \right) \hat{\mathcal{L}} \\
 &\quad + \frac{\partial_1 \partial_2}{\kappa^2} \left(\tilde{\mathbf{L}}_{2,J}^H(\kappa, x_3, \omega) \tilde{\mathcal{G}}_{J,K}^H(\kappa, x_3, \omega) (\tilde{\mathbf{L}}^H)_{K,3}^{-1} \right) \frac{\rho^f}{\hat{\rho}^E} \\
 &\quad \left. - \frac{\partial_1 \partial_2}{\kappa^2} \left(\tilde{\mathbf{L}}_{2,J}^H(\kappa, x_3, \omega) \tilde{\mathcal{G}}_{J,K}^H(\kappa, x_3, \omega) (\tilde{\mathbf{L}}^H)_{K,4}^{-1} \right) \hat{\mathcal{L}} \right] J_0(\kappa r) \kappa d\kappa \\
 &= \frac{\hat{\mathcal{F}}_2^b(\omega)}{2\pi} \int_{\kappa=0}^{\infty} \left[-j \kappa \left(\tilde{\mathbf{L}}_{8,J}^V \tilde{\mathcal{G}}_{J,K}^V (\tilde{\mathbf{L}}^V)_{K,2}^{-1} \right) \frac{1}{s \hat{\rho}^E} \right. \\
 &\quad - \left(\tilde{\mathbf{L}}_{8,J}^V \tilde{\mathcal{G}}_{J,K}^V (\tilde{\mathbf{L}}^V)_{K,3}^{-1} \right) \frac{\rho^f}{\hat{\rho}^E} \\
 &\quad + \left(\tilde{\mathbf{L}}_{8,J}^V \tilde{\mathcal{G}}_{J,K}^V (\tilde{\mathbf{L}}^V)_{K,4}^{-1} \right) \hat{\mathcal{L}} \\
 &\quad + \left(\tilde{\mathbf{L}}_{2,J}^H(\kappa, x_3, \omega) \tilde{\mathcal{G}}_{J,K}^H(\kappa, x_3, \omega) (\tilde{\mathbf{L}}^H)_{K,3}^{-1} \right) \frac{\rho^f}{\hat{\rho}^E} \\
 &\quad \left. - \left(\tilde{\mathbf{L}}_{2,J}^H(\kappa, x_3, \omega) \tilde{\mathcal{G}}_{J,K}^H(\kappa, x_3, \omega) (\tilde{\mathbf{L}}^H)_{K,4}^{-1} \right) \hat{\mathcal{L}} \right] \cos(\phi) \sin(\phi) J_2(\kappa r) \kappa d\kappa.
 \end{aligned} \tag{3.295}$$

For $\tilde{E}_1^{f_3^b}$, we transform

$$\begin{aligned}
 \tilde{E}_1^{f_3^b}(\mathbf{k}_H, x_3, \omega) &= \frac{k_1}{\kappa} \tilde{E}_{norm}^V(\kappa, x_3, \omega) - \frac{jk_2}{\kappa^2} \tilde{E}^H(\kappa, x_3, \omega) \\
 &= \frac{k_1}{\kappa} \tilde{q}_8^V(\kappa, x_3, \omega) - \frac{jk_2}{\kappa^2} \tilde{q}_2^H(\kappa, x_3, \omega) \\
 &= \frac{-k_1}{\kappa} \left[\tilde{\mathbf{L}}_{8,J}^V(\kappa, x_3, \omega) \tilde{\mathcal{G}}_{J,K}^V(\kappa, x_3, \omega) (\tilde{\mathbf{L}}^V)_{K,5}^{-1}(\kappa, x_3, \omega) \right] \left(\hat{\mathcal{F}}_3^b(\omega) \right),
 \end{aligned} \tag{3.296}$$

to

$$\begin{aligned}
 \hat{E}_1^{f_3^b}(\mathbf{x}, \omega) &= \frac{\hat{\mathcal{F}}_3^b(\omega)}{2\pi} \int_{\kappa=0}^{\infty} \left[-\frac{j \partial_1}{\kappa} \left(\tilde{\mathbf{L}}_{8,J}^V \tilde{\mathcal{G}}_{J,K}^V (\tilde{\mathbf{L}}^V)_{K,5}^{-1} \right) \right] J_0(\kappa r) \kappa d\kappa \\
 &= \frac{\hat{\mathcal{F}}_3^b(\omega)}{2\pi} \int_{\kappa=0}^{\infty} \left[j \cos(\phi) \left(\tilde{\mathbf{L}}_{8,J}^V \tilde{\mathcal{G}}_{J,K}^V (\tilde{\mathbf{L}}^V)_{K,5}^{-1} \right) \right] J_1(\kappa r) \kappa d\kappa.
 \end{aligned} \tag{3.297}$$

For $\tilde{E}_1^{f_3^f}$, we transform

$$\begin{aligned}
\tilde{E}_1^{f3}(\mathbf{k}_H, x_3, \omega) &= \frac{k_1}{\kappa} \tilde{E}_{norm}^V(\kappa, x_3, \omega) - \frac{jk_2}{\kappa^2} \tilde{E}^H(\kappa, x_3, \omega) \\
&= \frac{k_1}{\kappa} \tilde{q}_8^V(\kappa, x_3, \omega) - \frac{jk_2}{\kappa^2} \tilde{q}_2^H(\kappa, x_3, \omega) \\
&= \frac{-k_1}{\kappa} \left[\tilde{\mathbf{L}}_{8,J}^V(\kappa, x_3, \omega) \tilde{\mathcal{G}}_{J,K}^V(\kappa, x_3, \omega) (\tilde{\mathbf{L}}^V)_{K,6}^{-1}(\kappa, x_3, \omega) \right] \left(\hat{\mathcal{F}}_3^f(\omega) \right),
\end{aligned} \tag{3.298}$$

to

$$\begin{aligned}
\hat{E}_1^{f3}(\mathbf{x}, \omega) &= \frac{\hat{\mathcal{F}}_3^f(\omega)}{2\pi} \int_{\kappa=0}^{\infty} \left[-\frac{j\partial_1}{\kappa} \left(\tilde{\mathbf{L}}_{8,J}^V \tilde{\mathcal{G}}_{J,K}^V (\tilde{\mathbf{L}}^V)_{K,6}^{-1} \right) \right] J_0(\kappa r) \kappa d\kappa \\
&= \frac{\hat{\mathcal{F}}_3^f(\omega)}{2\pi} \int_{\kappa=0}^{\infty} \left[j\cos(\phi) \left(\tilde{\mathbf{L}}_{8,J}^V \tilde{\mathcal{G}}_{J,K}^V (\tilde{\mathbf{L}}^V)_{K,6}^{-1} \right) \right] J_1(\kappa r) \kappa d\kappa.
\end{aligned} \tag{3.299}$$

For \tilde{E}_1^{qi} , we transform

$$\begin{aligned}
\tilde{E}_1^{qi}(\mathbf{k}_H, x_3, \omega) &= \frac{k_1}{\kappa} \tilde{E}_{norm}^V(\kappa, x_3, \omega) - \frac{jk_2}{\kappa^2} \tilde{E}^H(\kappa, x_3, \omega) \\
&= \frac{k_1}{\kappa} \tilde{q}_8^V(\kappa, x_3, \omega) - \frac{jk_2}{\kappa^2} \tilde{q}_2^H(\kappa, x_3, \omega) \\
&= \frac{k_1}{\kappa} \left[\tilde{\mathbf{L}}_{8,J}^V(\kappa, x_3, \omega) \tilde{\mathcal{G}}_{J,K}^V(\kappa, x_3, \omega) (\tilde{\mathbf{L}}^V)_{K,2}^{-1}(\kappa, x_3, \omega) \right] \left(\hat{\mathcal{Q}}^i(\omega) \right),
\end{aligned} \tag{3.300}$$

to

$$\begin{aligned}
\hat{E}_1^{qi}(\mathbf{x}, \omega) &= \frac{\hat{\mathcal{Q}}^i(\omega)}{2\pi} \int_{\kappa=0}^{\infty} \left[\frac{j\partial_1}{\kappa} \left(\tilde{\mathbf{L}}_{8,J}^V \tilde{\mathcal{G}}_{J,K}^V (\tilde{\mathbf{L}}^V)_{K,2}^{-1} \right) \right] J_0(\kappa r) \kappa d\kappa \\
&= \frac{\hat{\mathcal{Q}}^i(\omega)}{2\pi} \int_{\kappa=0}^{\infty} \left[-j\cos(\phi) \left(\tilde{\mathbf{L}}_{8,J}^V \tilde{\mathcal{G}}_{J,K}^V (\tilde{\mathbf{L}}^V)_{K,2}^{-1} \right) \right] J_1(\kappa r) \kappa d\kappa.
\end{aligned} \tag{3.301}$$

For \tilde{E}_1^{hb} , we transform

$$\begin{aligned}
 \tilde{E}_1^{h^b}(\mathbf{k}_H, x_3, \omega) &= \frac{k_1}{\kappa} \tilde{E}_{norm}^V(\kappa, x_3, \omega) - \frac{jk_2}{\kappa^2} \tilde{E}^H(\kappa, x_3, \omega) \\
 &= \frac{k_1}{\kappa} \tilde{q}_8^V(\kappa, x_3, \omega) - \frac{jk_2}{\kappa^2} \tilde{q}_2^H(\kappa, x_3, \omega) \\
 &= \frac{k_1}{\kappa} \left[\tilde{\mathbf{L}}_{8,J}^V(\kappa, x_3, \omega) \tilde{\mathcal{G}}_{J,K}^V(\kappa, x_3, \omega) (\tilde{\mathbf{L}}^V)_{K,1}^{-1}(\kappa, x_3, \omega) \left(\frac{S}{K_c} \right) \right. \\
 &\quad \left. + \tilde{\mathbf{L}}_{8,J}^V(\kappa, x_3, \omega) \tilde{\mathcal{G}}_{J,K}^V(\kappa, x_3, \omega) (\tilde{\mathbf{L}}^V)_{K,2}^{-1}(\kappa, x_3, \omega) \left(\frac{C}{M} \left(1 - \frac{S}{K_c} \right) \right) \right] \hat{\mathcal{H}}_{11}^b(\omega) \\
 &\quad - jk_1 \left[\tilde{\mathbf{L}}_{8,J}^V(\kappa, x_3, \omega) \tilde{\mathcal{G}}_{J,K}^V(\kappa, x_3, \omega) (\tilde{\mathbf{L}}^V)_{K,3}^{-1}(\kappa, x_3, \omega) \frac{2G^{fr}S}{sK_c} \right] \hat{\mathcal{H}}_{11}^b(\omega) \\
 &\quad - \frac{jk_1^3}{\kappa^2} \left[\tilde{\mathbf{L}}_{8,J}^V(\kappa, x_3, \omega) \tilde{\mathcal{G}}_{J,K}^V(\kappa, x_3, \omega) (\tilde{\mathbf{L}}^V)_{K,3}^{-1}(\kappa, x_3, \omega) \frac{2G^{fr}}{s} \right] \hat{\mathcal{H}}_{11}^b(\omega) \\
 &\quad - \frac{jk_1 k_2^2}{\kappa^2} \left[\tilde{\mathbf{L}}_{2,J}^H(\kappa, x_3, \omega) \tilde{\mathcal{G}}_{J,K}^H(\kappa, x_3, \omega) (\tilde{\mathbf{L}}^H)_{K,1}^{-1}(\kappa, x_3, \omega) \frac{2G^{fr}}{s} \right] \hat{\mathcal{H}}_{11}^b(\omega),
 \end{aligned} \tag{3.302}$$

to

$$\begin{aligned}
 \tilde{E}_1^{h^b}(\mathbf{k}_H, x_3, \omega) &= \frac{\hat{\mathcal{H}}_{11}^b(\omega)}{2\pi} \int_{\kappa=0}^{\infty} \left\{ \frac{j\partial_1}{\kappa} \left[\tilde{\mathbf{L}}_{8,J}^V(\kappa, x_3, \omega) \tilde{\mathcal{G}}_{J,K}^V(\kappa, x_3, \omega) (\tilde{\mathbf{L}}^V)_{K,1}^{-1}(\kappa, x_3, \omega) \left(\frac{S}{K_c} \right) \right. \right. \\
 &\quad \left. \left. + \tilde{\mathbf{L}}_{8,J}^V(\kappa, x_3, \omega) \tilde{\mathcal{G}}_{J,K}^V(\kappa, x_3, \omega) (\tilde{\mathbf{L}}^V)_{K,2}^{-1}(\kappa, x_3, \omega) \left(\frac{C}{M} \left(1 - \frac{S}{K_c} \right) \right) \right] \right. \\
 &\quad \left. + \partial_1 \left[\tilde{\mathbf{L}}_{8,J}^V(\kappa, x_3, \omega) \tilde{\mathcal{G}}_{J,K}^V(\kappa, x_3, \omega) (\tilde{\mathbf{L}}^V)_{K,3}^{-1}(\kappa, x_3, \omega) \frac{2G^{fr}S}{sK_c} \right] \right. \\
 &\quad \left. - \frac{\partial_1^3}{\kappa^2} \left[\tilde{\mathbf{L}}_{8,J}^V(\kappa, x_3, \omega) \tilde{\mathcal{G}}_{J,K}^V(\kappa, x_3, \omega) (\tilde{\mathbf{L}}^V)_{K,3}^{-1}(\kappa, x_3, \omega) \frac{2G^{fr}}{s} \right] \right. \\
 &\quad \left. - \frac{\partial_1 \partial_2^2}{\kappa^2} \left[\tilde{\mathbf{L}}_{2,J}^H(\kappa, x_3, \omega) \tilde{\mathcal{G}}_{J,K}^H(\kappa, x_3, \omega) (\tilde{\mathbf{L}}^H)_{K,1}^{-1}(\kappa, x_3, \omega) \frac{2G^{fr}}{s} \right] \right\} J_0(\kappa r) \kappa d\kappa. \\
 &= \frac{\hat{\mathcal{H}}_{11}^b(\omega)}{2\pi} \int_{\kappa=0}^{\infty} -j \cos(\phi) \left[\tilde{\mathbf{L}}_{8,J}^V(\kappa, x_3, \omega) \tilde{\mathcal{G}}_{J,K}^V(\kappa, x_3, \omega) (\tilde{\mathbf{L}}^V)_{K,1}^{-1}(\kappa, x_3, \omega) \left(\frac{S}{K_c} \right) \right. \\
 &\quad \left. + \tilde{\mathbf{L}}_{8,J}^V(\kappa, x_3, \omega) \tilde{\mathcal{G}}_{J,K}^V(\kappa, x_3, \omega) (\tilde{\mathbf{L}}^V)_{K,2}^{-1}(\kappa, x_3, \omega) \left(\frac{C}{M} \left(1 - \frac{S}{K_c} \right) \right) \right] J_1(\kappa r) \\
 &\quad - \kappa \cos(\phi) \left[\tilde{\mathbf{L}}_{8,J}^V(\kappa, x_3, \omega) \tilde{\mathcal{G}}_{J,K}^V(\kappa, x_3, \omega) (\tilde{\mathbf{L}}^V)_{K,3}^{-1}(\kappa, x_3, \omega) \frac{2G^{fr}S}{sK_c} \right] J_1(\kappa r) \\
 &\quad - \frac{\kappa}{4} \cos(\phi) \left[\tilde{\mathbf{L}}_{8,J}^V(\kappa, x_3, \omega) \tilde{\mathcal{G}}_{J,K}^V(\kappa, x_3, \omega) (\tilde{\mathbf{L}}^V)_{K,3}^{-1}(\kappa, x_3, \omega) \frac{2G^{fr}}{s} \right] (3J_1(\kappa r) \\
 &\quad + (1 - 2\cos(2\phi)) J_3(\kappa r)) \\
 &\quad - \frac{\kappa}{4} \cos(\phi) \left[\tilde{\mathbf{L}}_{2,J}^H(\kappa, x_3, \omega) \tilde{\mathcal{G}}_{J,K}^H(\kappa, x_3, \omega) (\tilde{\mathbf{L}}^H)_{K,1}^{-1}(\kappa, x_3, \omega) \frac{2G^{fr}}{s} \right] (J_1(\kappa r) \\
 &\quad - (1 - 2\cos(2\phi)) J_3(\kappa r)) \kappa d\kappa.
 \end{aligned} \tag{3.303}$$

For $\tilde{E}_1^{h^b}$, we transform

$$\begin{aligned}
\tilde{E}_1^{h^b}(\mathbf{k}_H, x_3, \omega) &= \frac{k_1}{\kappa} \tilde{E}_{norm}^V(\kappa, x_3, \omega) - \frac{jk_2}{\kappa^2} \tilde{E}^H(\kappa, x_3, \omega) \\
&= \frac{k_1}{\kappa} \tilde{q}_8^V(\kappa, x_3, \omega) - \frac{jk_2}{\kappa^2} \tilde{q}_2^H(\kappa, x_3, \omega) \\
&= \frac{k_1}{\kappa} \left[\tilde{\mathbf{L}}_{8,J}^V(\kappa, x_3, \omega) \tilde{\mathcal{G}}_{J,K}^V(\kappa, x_3, \omega) (\tilde{\mathbf{L}}^V)_{K,1}^{-1}(\kappa, x_3, \omega) \left(\frac{S}{K_c} \right) \right. \\
&\quad \left. + \tilde{\mathbf{L}}_{8,J}^V(\kappa, x_3, \omega) \tilde{\mathcal{G}}_{J,K}^V(\kappa, x_3, \omega) (\tilde{\mathbf{L}}^V)_{K,2}^{-1}(\kappa, x_3, \omega) \left(\frac{C}{M} \left(1 - \frac{S}{K_c} \right) \right) \right] \hat{\mathcal{H}}_{22}^b(\omega) \\
&\quad - jk_1 \left[\tilde{\mathbf{L}}_{8,J}^V(\kappa, x_3, \omega) \tilde{\mathcal{G}}_{J,K}^V(\kappa, x_3, \omega) (\tilde{\mathbf{L}}^V)_{K,3}^{-1}(\kappa, x_3, \omega) \frac{2G^{fr}S}{sK_c} \right] \hat{\mathcal{H}}_{22}^b(\omega) \\
&\quad - \frac{jk_1 k_2^2}{\kappa^2} \left[\tilde{\mathbf{L}}_{8,J}^V(\kappa, x_3, \omega) \tilde{\mathcal{G}}_{J,K}^V(\kappa, x_3, \omega) (\tilde{\mathbf{L}}^V)_{K,3}^{-1}(\kappa, x_3, \omega) \frac{2G^{fr}}{s} \right] \hat{\mathcal{H}}_{22}^b(\omega) \\
&\quad + \frac{jk_1 k_2^2}{\kappa^2} \left[\tilde{\mathbf{L}}_{2,J}^H(\kappa, x_3, \omega) \tilde{\mathcal{G}}_{J,K}^H(\kappa, x_3, \omega) (\tilde{\mathbf{L}}^H)_{K,1}^{-1}(\kappa, x_3, \omega) \frac{2G^{fr}}{s} \right] \hat{\mathcal{H}}_{22}^b(\omega),
\end{aligned} \tag{3.304}$$

to

$$\begin{aligned}
\tilde{E}_1^{h^b}(\mathbf{k}_H, x_3, \omega) &= \frac{\hat{\mathcal{H}}_{22}^b(\omega)}{2\pi} \int_{\kappa=0}^{\infty} \left\{ \frac{j\partial_1}{\kappa} \left[\tilde{\mathbf{L}}_{8,J}^V(\kappa, x_3, \omega) \tilde{\mathcal{G}}_{J,K}^V(\kappa, x_3, \omega) (\tilde{\mathbf{L}}^V)_{K,1}^{-1}(\kappa, x_3, \omega) \left(\frac{S}{K_c} \right) \right. \right. \\
&\quad \left. \left. + \tilde{\mathbf{L}}_{8,J}^V(\kappa, x_3, \omega) \tilde{\mathcal{G}}_{J,K}^V(\kappa, x_3, \omega) (\tilde{\mathbf{L}}^V)_{K,2}^{-1}(\kappa, x_3, \omega) \left(\frac{C}{M} \left(1 - \frac{S}{K_c} \right) \right) \right] \right. \\
&\quad \left. + \partial_1 \left[\tilde{\mathbf{L}}_{8,J}^V(\kappa, x_3, \omega) \tilde{\mathcal{G}}_{J,K}^V(\kappa, x_3, \omega) (\tilde{\mathbf{L}}^V)_{K,3}^{-1}(\kappa, x_3, \omega) \frac{2G^{fr}S}{sK_c} \right] \right. \\
&\quad \left. - \frac{\partial_1 \partial_2^2}{\kappa^2} \left[\tilde{\mathbf{L}}_{8,J}^V(\kappa, x_3, \omega) \tilde{\mathcal{G}}_{J,K}^V(\kappa, x_3, \omega) (\tilde{\mathbf{L}}^V)_{K,3}^{-1}(\kappa, x_3, \omega) \frac{2G^{fr}}{s} \right] \right. \\
&\quad \left. + \frac{\partial_1 \partial_2^2}{\kappa^2} \left[\tilde{\mathbf{L}}_{2,J}^H(\kappa, x_3, \omega) \tilde{\mathcal{G}}_{J,K}^H(\kappa, x_3, \omega) (\tilde{\mathbf{L}}^H)_{K,1}^{-1}(\kappa, x_3, \omega) \frac{2G^{fr}}{s} \right] \right\} J_0(\kappa r) \kappa d\kappa. \\
&= \frac{\hat{\mathcal{H}}_{11}^b(\omega)}{2\pi} \int_{\kappa=0}^{\infty} -j\cos(\phi) \left[\tilde{\mathbf{L}}_{8,J}^V(\kappa, x_3, \omega) \tilde{\mathcal{G}}_{J,K}^V(\kappa, x_3, \omega) (\tilde{\mathbf{L}}^V)_{K,1}^{-1}(\kappa, x_3, \omega) \left(\frac{S}{K_c} \right) \right. \\
&\quad \left. + \tilde{\mathbf{L}}_{8,J}^V(\kappa, x_3, \omega) \tilde{\mathcal{G}}_{J,K}^V(\kappa, x_3, \omega) (\tilde{\mathbf{L}}^V)_{K,2}^{-1}(\kappa, x_3, \omega) \left(\frac{C}{M} \left(1 - \frac{S}{K_c} \right) \right) \right] J_1(\kappa r) \\
&\quad - \kappa \cos(\phi) \left[\tilde{\mathbf{L}}_{8,J}^V(\kappa, x_3, \omega) \tilde{\mathcal{G}}_{J,K}^V(\kappa, x_3, \omega) (\tilde{\mathbf{L}}^V)_{K,3}^{-1}(\kappa, x_3, \omega) \frac{2G^{fr}S}{sK_c} \right] J_1(\kappa r) \\
&\quad - \frac{\kappa}{4} \cos(\phi) \left[\tilde{\mathbf{L}}_{8,J}^V(\kappa, x_3, \omega) \tilde{\mathcal{G}}_{J,K}^V(\kappa, x_3, \omega) (\tilde{\mathbf{L}}^V)_{K,3}^{-1}(\kappa, x_3, \omega) \frac{2G^{fr}}{s} \right] (J_1(\kappa r) \\
&\quad - (1 - 2\cos(2\phi)) J_3(\kappa r)) \\
&\quad + \frac{\kappa}{4} \cos(\phi) \left[\tilde{\mathbf{L}}_{2,J}^H(\kappa, x_3, \omega) \tilde{\mathcal{G}}_{J,K}^H(\kappa, x_3, \omega) (\tilde{\mathbf{L}}^H)_{K,1}^{-1}(\kappa, x_3, \omega) \frac{2G^{fr}}{s} \right] (J_1(\kappa r) \\
&\quad - (1 - 2\cos(2\phi)) J_3(\kappa r)) \kappa d\kappa.
\end{aligned} \tag{3.305}$$

For $\tilde{E}_1^{h^b}$, we transform

$$\begin{aligned}
 \tilde{E}_1^{h_{33}^b}(\mathbf{k}_H, x_3, \omega) &= \frac{k_1}{\kappa} \tilde{E}_{norm}^V(\kappa, x_3, \omega) - \frac{jk_2}{\kappa^2} \tilde{E}^H(\kappa, x_3, \omega) \\
 &= \frac{k_1}{\kappa} \tilde{q}_8^V(\kappa, x_3, \omega) - \frac{jk_2}{\kappa^2} \tilde{q}_2^H(\kappa, x_3, \omega) \\
 &= \frac{k_1}{\kappa} \left[\tilde{\mathbf{L}}_{8,J}^V(\kappa, x_3, \omega) \tilde{\mathcal{G}}_{J,K}^V(\kappa, x_3, \omega) (\tilde{\mathbf{L}}^V)_{K,1}^{-1}(\kappa, x_3, \omega) \right] \hat{\mathcal{H}}_{33}^b(\omega),
 \end{aligned} \tag{3.306}$$

to

$$\begin{aligned}
 \hat{E}_1^{h_{33}^b}(\mathbf{x}, \omega) &= \frac{\hat{\mathcal{H}}_{33}^b(\omega)}{2\pi} \int_{\kappa=0}^{\infty} \left[\frac{j\partial_1}{\kappa} \left(\tilde{\mathbf{L}}_{8,J}^V \tilde{\mathcal{G}}_{J,K}^V (\tilde{\mathbf{L}}^V)_{K,1}^{-1} \right) \right] J_0(\kappa r) \kappa d\kappa \\
 &= \frac{\hat{\mathcal{H}}_{33}^b(\omega)}{2\pi} \int_{\kappa=0}^{\infty} \left[-j\cos(\phi) \left(\tilde{\mathbf{L}}_{8,J}^V \tilde{\mathcal{G}}_{J,K}^V (\tilde{\mathbf{L}}^V)_{K,1}^{-1} \right) \right] J_1(\kappa r) \kappa d\kappa.
 \end{aligned} \tag{3.307}$$

For $\tilde{E}_1^{h_{13}^b}$, we transform

$$\begin{aligned}
 \tilde{E}_1^{h_{13}^b}(\mathbf{k}_H, x_3, \omega) &= \frac{k_1}{\kappa} \tilde{E}_{norm}^V(\kappa, x_3, \omega) - \frac{jk_2}{\kappa^2} \tilde{E}^H(\kappa, x_3, \omega) \\
 &= \frac{k_1}{\kappa} \tilde{q}_8^V(\kappa, x_3, \omega) - \frac{jk_2}{\kappa^2} \tilde{q}_2^H(\kappa, x_3, \omega) \\
 &= \frac{k_1^2}{\kappa^2} \left[\tilde{\mathbf{L}}_{8,J}^V(\kappa, x_3, \omega) \tilde{\mathcal{G}}_{J,K}^V(\kappa, x_3, \omega) (\tilde{\mathbf{L}}^V)_{K,7}^{-1}(\kappa, x_3, \omega) \right] \left(\hat{\mathcal{H}}_{13}^b(\omega) + \hat{\mathcal{H}}_{31}^b(\omega) \right) \\
 &\quad + \frac{k_2^2}{\kappa^2} \left(\tilde{\mathbf{L}}_{2,J}^H(\kappa, x_3, \omega) \tilde{\mathcal{G}}_{J,K}^H(\kappa, x_3, \omega) (\tilde{\mathbf{L}}^H)_{K,1}^{-1}(\kappa, x_3, \omega) \right) \left(\hat{\mathcal{H}}_{13}^b(\omega) + \hat{\mathcal{H}}_{31}^b(\omega) \right),
 \end{aligned} \tag{3.308}$$

to

$$\begin{aligned}
 \hat{E}_1^{h_{13}^b}(\mathbf{x}, \omega) &= \frac{\left(\hat{\mathcal{H}}_{13}^b(\omega) + \hat{\mathcal{H}}_{31}^b(\omega) \right)}{2\pi} \int_{\kappa=0}^{\infty} \left[\frac{-\partial_1^2}{\kappa^2} \left(\tilde{\mathbf{L}}_{8,J}^V \tilde{\mathcal{G}}_{J,K}^V (\tilde{\mathbf{L}}^V)_{K,7}^{-1} \right) \right. \\
 &\quad \left. - \frac{\partial_2^2}{\kappa^2} \left(\tilde{\mathbf{L}}_{2,J}^H \tilde{\mathcal{G}}_{J,K}^H (\tilde{\mathbf{L}}^H)_{K,1}^{-1} \right) \right] J_0(\kappa r) \kappa d\kappa \\
 &= \frac{\left(\hat{\mathcal{H}}_{13}^b(\omega) + \hat{\mathcal{H}}_{31}^b(\omega) \right)}{2\pi} \int_{\kappa=0}^{\infty} \left[\frac{1}{2} \left(\tilde{\mathbf{L}}_{8,J}^V \tilde{\mathcal{G}}_{J,K}^V (\tilde{\mathbf{L}}^V)_{K,7}^{-1} \right) (J_0(\kappa r) - \cos(2\phi) J_2(\kappa r)) \right. \\
 &\quad \left. + \frac{1}{2} \left(\tilde{\mathbf{L}}_{2,J}^H \tilde{\mathcal{G}}_{J,K}^H (\tilde{\mathbf{L}}^H)_{K,1}^{-1} \right) (J_0(\kappa r) + \cos(2\phi) J_2(\kappa r)) \right] \kappa d\kappa.
 \end{aligned} \tag{3.309}$$

For $\tilde{E}_1^{h_{23}^b}$, we transform

$$\begin{aligned}
\tilde{E}_1^{h^b_{23}}(\mathbf{k}_H, x_3, \omega) &= \frac{k_1}{\kappa} \tilde{E}_{norm}^V(\kappa, x_3, \omega) - \frac{jk_2}{\kappa^2} \tilde{E}^H(\kappa, x_3, \omega) \\
&= \frac{k_1}{\kappa} \tilde{q}_8^V(\kappa, x_3, \omega) - \frac{jk_2}{\kappa^2} \tilde{q}_2^H(\kappa, x_3, \omega) \\
&= \frac{k_1 k_2}{\kappa^2} \left[\tilde{\mathbf{L}}_{8,J}^V(\kappa, x_3, \omega) \tilde{\mathbf{G}}_{J,K}^V(\kappa, x_3, \omega) (\tilde{\mathbf{L}}^V)_{K,7}^{-1}(\kappa, x_3, \omega) \right] \left(\hat{\mathcal{H}}_{23}^b(\omega) + \hat{\mathcal{H}}_{32}^b(\omega) \right) \\
&\quad - \frac{k_1 k_2}{\kappa^2} \left(\tilde{\mathbf{L}}_{2,J}^H(\kappa, x_3, \omega) \tilde{\mathbf{G}}_{J,K}^H(\kappa, x_3, \omega) (\tilde{\mathbf{L}}^H)_{K,1}^{-1}(\kappa, x_3, \omega) \right) \left(\hat{\mathcal{H}}_{23}^b(\omega) + \hat{\mathcal{H}}_{32}^b(\omega) \right),
\end{aligned} \tag{3.310}$$

to

$$\begin{aligned}
\hat{E}_1^{h^b_{23}}(\mathbf{x}, \omega) &= \frac{\left(\hat{\mathcal{H}}_{23}^b(\omega) + \hat{\mathcal{H}}_{32}^b(\omega) \right)}{2\pi} \int_{\kappa=0}^{\infty} \left[\frac{-\partial_1 \partial_2}{\kappa^2} \left(\tilde{\mathbf{L}}_{8,J}^V \tilde{\mathbf{G}}_{J,K}^V (\tilde{\mathbf{L}}^V)_{K,7}^{-1} \right) \right. \\
&\quad \left. + \frac{\partial_1 \partial_2}{\kappa^2} \left(\tilde{\mathbf{L}}_{2,J}^H \tilde{\mathbf{G}}_{J,K}^H (\tilde{\mathbf{L}}^H)_{K,1}^{-1} \right) \right] J_0(\kappa r) \kappa d\kappa \\
&= \frac{\left(\hat{\mathcal{H}}_{23}^b(\omega) + \hat{\mathcal{H}}_{32}^b(\omega) \right)}{2\pi} \int_{\kappa=0}^{\infty} \left[- \left(\tilde{\mathbf{L}}_{8,J}^V \tilde{\mathbf{G}}_{J,K}^V (\tilde{\mathbf{L}}^V)_{K,7}^{-1} \right) \right. \\
&\quad \left. + \left(\tilde{\mathbf{L}}_{2,J}^H \tilde{\mathbf{G}}_{J,K}^H (\tilde{\mathbf{L}}^H)_{K,1}^{-1} \right) \right] \cos(\phi) \sin(\phi) J_2(\kappa r) \kappa d\kappa.
\end{aligned} \tag{3.311}$$

For $\tilde{E}_1^{h^b_{12}}$, we transform

$$\begin{aligned}
\tilde{E}_1^{h^b_{12}}(\mathbf{k}_H, x_3, \omega) &= \frac{k_1}{\kappa} \tilde{E}_{norm}^V(\kappa, x_3, \omega) - \frac{jk_2}{\kappa^2} \tilde{E}^H(\kappa, x_3, \omega) \\
&= \frac{k_1}{\kappa} \tilde{q}_8^V(\kappa, x_3, \omega) - \frac{jk_2}{\kappa^2} \tilde{q}_2^H(\kappa, x_3, \omega) \\
&= -\frac{jk_1^2 k_2}{\kappa^2} \left[\tilde{\mathbf{L}}_{8,J}^V(\kappa, x_3, \omega) \tilde{\mathbf{G}}_{J,K}^V(\kappa, x_3, \omega) (\tilde{\mathbf{L}}^V)_{K,3}^{-1}(\kappa, x_3, \omega) \right] \left(\frac{2}{s} \left[G^{fr} \hat{\mathcal{H}}_{21}^b(\omega) \right. \right. \\
&\quad \left. \left. + G^{fr} \hat{\mathcal{H}}_{12}^b(\omega) \right] \right) \\
&\quad + \frac{jk_1^2 k_2}{\kappa^2} \left[\tilde{\mathbf{L}}_{2,J}^H(\kappa, x_3, \omega) \tilde{\mathbf{G}}_{J,K}^H(\kappa, x_3, \omega) (\tilde{\mathbf{L}}^H)_{K,3}^{-1}(\kappa, x_3, \omega) \right] \\
&\quad \frac{1}{s} \left[G^{fr} \hat{\mathcal{H}}_{21}^b(\omega) + G^{fr} \hat{\mathcal{H}}_{12}^b(\omega) \right] \\
&\quad - \frac{jk_2^3}{\kappa^2} \left[\tilde{\mathbf{L}}_{2,J}^H(\kappa, x_3, \omega) \tilde{\mathbf{G}}_{J,K}^H(\kappa, x_3, \omega) (\tilde{\mathbf{L}}^H)_{K,3}^{-1}(\kappa, x_3, \omega) \right] \\
&\quad \frac{1}{s} \left[G^{fr} \hat{\mathcal{H}}_{21}^b(\omega) + G^{fr} \hat{\mathcal{H}}_{12}^b(\omega) \right],
\end{aligned} \tag{3.312}$$

to

$$\begin{aligned}
 \hat{E}_1^{h,b}(\mathbf{x}, \omega) &= \frac{(\hat{\mathcal{H}}_{12}^b(\omega) + \hat{\mathcal{H}}_{21}^b(\omega))}{2\pi} \int_{\kappa=0}^{\infty} \left[-\frac{\partial_1^2 \partial_2}{\kappa^2} \left(\tilde{\mathbf{L}}_{8,J}^V \tilde{\mathcal{G}}_{J,K}^V (\tilde{\mathbf{L}}^V)_{K,3}^{-1} \right) \frac{2G^{fr}}{s} \right. \\
 &\quad + \frac{\partial_1^2 \partial_2}{\kappa^2} \left(\tilde{\mathbf{L}}_{2,J}^H \tilde{\mathcal{G}}_{J,K}^H (\tilde{\mathbf{L}}^H)_{K,3}^{-1} \right) \frac{G^{fr}}{s} \\
 &\quad \left. - \frac{\partial_2^3}{\kappa^2} \left(\tilde{\mathbf{L}}_{2,J}^H \tilde{\mathcal{G}}_{J,K}^H (\tilde{\mathbf{L}}^H)_{K,3}^{-1} \right) \frac{G^{fr}}{s} \right] J_0(\kappa r) \kappa d\kappa \\
 &= \frac{(\hat{\mathcal{H}}_{12}^b(\omega) + \hat{\mathcal{H}}_{21}^b(\omega))}{2\pi} \int_{\kappa=0}^{\infty} \left\{ \frac{\kappa}{4} \sin(\phi) \left[- \left(\tilde{\mathbf{L}}_{8,J}^V \tilde{\mathcal{G}}_{J,K}^V (\tilde{\mathbf{L}}^V)_{K,3}^{-1} \right) \frac{2G^{fr}}{s} \right. \right. \\
 &\quad \left. \left. + \left(\tilde{\mathbf{L}}_{2,J}^H \tilde{\mathcal{G}}_{J,K}^H (\tilde{\mathbf{L}}^H)_{K,3}^{-1} \right) \frac{G^{fr}}{s} \right] (J_1(\kappa r) - (1 + 2\cos(2\phi)) J_3(\kappa r)) \right. \\
 &\quad \left. - \frac{\kappa}{4} \sin(\phi) \left(\tilde{\mathbf{L}}_{2,J}^H \tilde{\mathcal{G}}_{J,K}^H (\tilde{\mathbf{L}}^H)_{K,3}^{-1} \right) \frac{G^{fr}}{s} (3J_1(\kappa r) + (1 + 2\cos(2\phi)) J_3(\kappa r)) \right\} \kappa d\kappa.
 \end{aligned} \tag{3.313}$$

E_2 -type two-way field quantity expressions

We here present the Fourier-Bessel transformations for each source-type for receiver-type E_2 , by explicitly focusing on the \tilde{E}_2 fields. By selecting different rows of $\tilde{\mathbf{L}}^{H,V}$, we can obtain the expressions for $\tilde{\tau}_{23}^b$, \tilde{H}_1 , and \tilde{v}_2^s .

For $\tilde{E}_2^{J_1^e}$, we transform

$$\begin{aligned}
 \tilde{E}_2^{J_1^e}(\mathbf{k}_H, x_3, \omega) &= \frac{k_2}{\kappa} \tilde{E}_{norm}^V(\kappa, x_3, \omega) + \frac{jk_1}{\kappa^2} \tilde{E}^H(\kappa, x_3, \omega) \\
 &= \frac{k_2}{\kappa} \tilde{q}_8^V(\kappa, x_3, \omega) + \frac{jk_1}{\kappa^2} \tilde{q}_2^H(\kappa, x_3, \omega) \\
 &= \left\{ \frac{-k_1 k_2}{\kappa^2} \left[\tilde{\mathbf{L}}_{8,J}^V(\kappa, x_3, \omega) \tilde{\mathcal{G}}_{J,K}^V(\kappa, x_3, \omega) (\tilde{\mathbf{L}}^V)_{K,4}^{-1}(\kappa, x_3, \omega) \right] \right. \\
 &\quad \left. + \frac{k_1 k_2}{\kappa^2} \left[\tilde{\mathbf{L}}_{2,J}^H(\kappa, x_3, \omega) \tilde{\mathcal{G}}_{J,K}^H(\kappa, x_3, \omega) (\tilde{\mathbf{L}}^H)_{K,4}^{-1}(\kappa, x_3, \omega) \right] \right\} \hat{\mathcal{J}}_1^e(\omega, \mathbf{x}, \omega)
 \end{aligned} \tag{3.314}$$

to

$$\begin{aligned}
 \hat{E}_2^{J_1^e}(\mathbf{x}, \omega) &= \frac{\hat{\mathcal{J}}_1^e(\omega)}{2\pi} \int_{\kappa=0}^{\infty} \left[\frac{\partial_1 \partial_2}{\kappa^2} \left(\tilde{\mathbf{L}}_{8,J}^V \tilde{\mathcal{G}}_{J,K}^V (\tilde{\mathbf{L}}^V)_{K,4}^{-1} \right) \right. \\
 &\quad \left. - \frac{\partial_1 \partial_2}{\kappa^2} \left(\tilde{\mathbf{L}}_{2,J}^H \tilde{\mathcal{G}}_{J,K}^H (\tilde{\mathbf{L}}^H)_{K,4}^{-1} \right) \right] J_0(\kappa r) \kappa d\kappa \\
 &= \frac{\hat{\mathcal{J}}_1^e(\omega)}{2\pi} \int_{\kappa=0}^{\infty} \left[\cos(\phi) \sin(\phi) \left(\tilde{\mathbf{L}}_{8,J}^V \tilde{\mathcal{G}}_{J,K}^V (\tilde{\mathbf{L}}^V)_{K,4}^{-1} \right) \right. \\
 &\quad \left. - \cos(\phi) \sin(\phi) \left(\tilde{\mathbf{L}}_{2,J}^H \tilde{\mathcal{G}}_{J,K}^H (\tilde{\mathbf{L}}^H)_{K,4}^{-1} \right) \right] J_2(\kappa r) \kappa d\kappa.
 \end{aligned} \tag{3.315}$$

For $\tilde{E}_2^{J_2^e}$, we transform

$$\begin{aligned}
\tilde{E}_2^{J_2^e}(\mathbf{k}_H, x_3, \omega) &= \frac{k_2}{\kappa} \tilde{E}_{norm}^V(\kappa, x_3, \omega) + \frac{jk_1}{\kappa^2} \tilde{E}^H(\kappa, x_3, \omega) \\
&= \frac{k_2}{\kappa} \tilde{q}_8^V(\kappa, x_3, \omega) + \frac{jk_1}{\kappa^2} \tilde{q}_2^H(\kappa, x_3, \omega) \\
&= \left\{ \frac{-k_2^2}{\kappa^2} \left[\tilde{\mathbf{L}}_{8,J}^V(\kappa, x_3, \omega) \tilde{\mathcal{G}}_{J,K}^V(\kappa, x_3, \omega) (\tilde{\mathbf{L}}^V)_{K,4}^{-1}(\kappa, x_3, \omega) \right] \right. \\
&\quad \left. - \frac{k_1^2}{\kappa^2} \left[\tilde{\mathbf{L}}_{2,J}^H(\kappa, x_3, \omega) \tilde{\mathcal{G}}_{J,K}^H(\kappa, x_3, \omega) (\tilde{\mathbf{L}}^H)_{K,4}^{-1}(\kappa, x_3, \omega) \right] \right\} \hat{\mathcal{J}}_2^e(\omega) \quad (3.316)
\end{aligned}$$

to

$$\begin{aligned}
\hat{E}_2^{J_2^e}(\mathbf{x}, \omega) &= \frac{\hat{\mathcal{J}}_2^e(\omega)}{2\pi} \int_{\kappa=0}^{\infty} \left[\frac{\partial_2^2}{\kappa^2} \left(\tilde{\mathbf{L}}_{8,J}^V \tilde{\mathcal{G}}_{J,K}^V (\tilde{\mathbf{L}}^V)_{K,4}^{-1} \right) \right. \\
&\quad \left. + \frac{\partial_1^2}{\kappa^2} \left(\tilde{\mathbf{L}}_{2,J}^H \tilde{\mathcal{G}}_{J,K}^H (\tilde{\mathbf{L}}^H)_{K,4}^{-1} \right) \right] J_0(\kappa r) \kappa d\kappa \\
&= \frac{\hat{\mathcal{J}}_2^e(\omega)}{2\pi} \int_{\kappa=0}^{\infty} \left\{ -\frac{1}{2} \left(\tilde{\mathbf{L}}_{8,J}^V \tilde{\mathcal{G}}_{J,K}^V (\tilde{\mathbf{L}}^V)_{K,4}^{-1} \right) (J_0(\kappa r) + \cos(2\phi) J_2(\kappa r)) \right. \\
&\quad \left. - \frac{1}{2} \left(\tilde{\mathbf{L}}_{2,J}^H \tilde{\mathcal{G}}_{J,K}^H (\tilde{\mathbf{L}}^H)_{K,4}^{-1} \right) (J_0(\kappa r) - \cos(2\phi) J_2(\kappa r)) \right\} \kappa d\kappa. \quad (3.317)
\end{aligned}$$

For $\tilde{E}_2^{J_3^e}$, we transform

$$\begin{aligned}
\tilde{E}_2^{J_3^e}(\mathbf{k}_H, x_3, \omega) &= \frac{k_2}{\kappa} \tilde{E}_{norm}^V(\kappa, x_3, \omega) + \frac{jk_1}{\kappa^2} \tilde{E}^H(\kappa, x_3, \omega) \\
&= \frac{k_2}{\kappa} \tilde{q}_8^V(\kappa, x_3, \omega) + \frac{jk_1}{\kappa^2} \tilde{q}_2^H(\kappa, x_3, \omega) \\
&= \frac{k_2}{\kappa} \left[\tilde{\mathbf{L}}_{8,J}^V(\kappa, x_3, \omega) \tilde{\mathcal{G}}_{J,K}^V(\kappa, x_3, \omega) (\tilde{\mathbf{L}}^V)_{K,6}^{-1}(\kappa, x_3, \omega) \right] \left(\frac{\hat{\rho}^E \hat{\mathcal{L}}}{\hat{\epsilon}} \hat{\mathcal{J}}_3^e(\omega) \right) \\
&\quad + \frac{jk_2}{s\hat{\epsilon}} \left[\tilde{\mathbf{L}}_{8,J}^V(\kappa, x_3, \omega) \tilde{\mathcal{G}}_{J,K}^V(\kappa, x_3, \omega) (\tilde{\mathbf{L}}^V)_{K,8}^{-1}(\kappa, x_3, \omega) \right] \hat{\mathcal{J}}_3^e(\omega), \quad (3.318)
\end{aligned}$$

to

$$\begin{aligned}
\hat{E}_2^{J_3^e}(\mathbf{x}, \omega) &= \frac{\hat{\mathcal{J}}_3^e(\omega)}{2\pi} \int_{\kappa=0}^{\infty} \left[\frac{j\partial_2}{\kappa} \left(\tilde{\mathbf{L}}_{8,J}^V \tilde{\mathcal{G}}_{J,K}^V (\tilde{\mathbf{L}}^V)_{K,6}^{-1} \right) \frac{\hat{\rho}^E \hat{\mathcal{L}}}{\hat{\epsilon}} \right. \\
&\quad \left. - \partial_2 \left(\tilde{\mathbf{L}}_{8,J}^V \tilde{\mathcal{G}}_{J,K}^V (\tilde{\mathbf{L}}^V)_{K,8}^{-1} \right) \frac{1}{s\hat{\epsilon}} \right] J_0(\kappa r) \kappa d\kappa \\
&= \frac{\hat{\mathcal{J}}_3^e(\omega)}{2\pi} \int_{\kappa=0}^{\infty} \left[-j\sin(\phi) \left(\tilde{\mathbf{L}}_{8,J}^V \tilde{\mathcal{G}}_{J,K}^V (\tilde{\mathbf{L}}^V)_{K,6}^{-1} \right) \frac{\hat{\rho}^E \hat{\mathcal{L}}}{\hat{\epsilon}} \right. \\
&\quad \left. + \kappa \sin(\phi) \left(\tilde{\mathbf{L}}_{8,J}^V \tilde{\mathcal{G}}_{J,K}^V (\tilde{\mathbf{L}}^V)_{K,8}^{-1} \right) \frac{1}{s\hat{\epsilon}} \right] J_1(\kappa r) \kappa d\kappa. \quad (3.319)
\end{aligned}$$

For $\tilde{E}_2^{J_1^m}$, we transform

$$\begin{aligned}
 \tilde{E}_2^{J_1^m}(\mathbf{k}_H, x_3, \omega) &= \frac{k_2}{\kappa} \tilde{E}_{norm}^V(\kappa, x_3, \omega) + \frac{jk_1}{\kappa^2} \tilde{E}^H(\kappa, x_3, \omega) \\
 &= \frac{k_2}{\kappa} \tilde{q}_8^V(\kappa, x_3, \omega) + \frac{jk_1}{\kappa^2} \tilde{q}_2^H(\kappa, x_3, \omega) \\
 &= \left\{ \frac{k_2^2}{\kappa^2} \left[\tilde{\mathbf{L}}_{8,J}^V(\kappa, x_3, \omega) \tilde{\mathcal{G}}_{J,K}^V(\kappa, x_3, \omega) (\tilde{\mathbf{L}}^V)_{K,8}^{-1}(\kappa, x_3, \omega) \right] \right. \\
 &\quad \left. + \frac{k_1^2}{\kappa^2} \left[\tilde{\mathbf{L}}_{2,J}^H(\kappa, x_3, \omega) \tilde{\mathcal{G}}_{J,K}^H(\kappa, x_3, \omega) (\tilde{\mathbf{L}}^H)_{K,2}^{-1}(\kappa, x_3, \omega) \right] \right\} \hat{\mathcal{J}}_1^m(\omega) \quad (3.320)
 \end{aligned}$$

to

$$\begin{aligned}
 \hat{E}_2^{J_1^m}(\mathbf{x}, \omega) &= \frac{\hat{\mathcal{J}}_1^m(\omega)}{2\pi} \int_{\kappa=0}^{\infty} \left[-\frac{\partial_2^2}{\kappa^2} \left(\tilde{\mathbf{L}}_{8,J}^V \tilde{\mathcal{G}}_{J,K}^V (\tilde{\mathbf{L}}^V)_{K,8}^{-1} \right) \right. \\
 &\quad \left. - \frac{\partial_1^2}{\kappa^2} \left(\tilde{\mathbf{L}}_{2,J}^H \tilde{\mathcal{G}}_{J,K}^H (\tilde{\mathbf{L}}^H)_{K,2}^{-1} \right) \right] J_0(\kappa r) \kappa d\kappa \\
 &= \frac{\hat{\mathcal{J}}_1^m(\omega)}{2\pi} \int_{\kappa=0}^{\infty} \left\{ \frac{1}{2} \left(\tilde{\mathbf{L}}_{8,J}^V \tilde{\mathcal{G}}_{J,K}^V (\tilde{\mathbf{L}}^V)_{K,8}^{-1} \right) (J_0(\kappa r) + \cos(2\phi) J_2(\kappa r)) \right. \\
 &\quad \left. + \frac{1}{2} \left(\tilde{\mathbf{L}}_{2,J}^H \tilde{\mathcal{G}}_{J,K}^H (\tilde{\mathbf{L}}^H)_{K,2}^{-1} \right) (J_0(\kappa r) - \cos(2\phi) J_2(\kappa r)) \right\} \kappa d\kappa. \quad (3.321)
 \end{aligned}$$

For $\tilde{E}_2^{J_2^m}$, we transform

$$\begin{aligned}
 \tilde{E}_2^{J_2^m}(\mathbf{k}_H, x_3, \omega) &= \frac{k_2}{\kappa} \tilde{E}_{norm}^V(\kappa, x_3, \omega) + \frac{jk_1}{\kappa^2} \tilde{E}^H(\kappa, x_3, \omega) \\
 &= \frac{k_2}{\kappa} \tilde{q}_8^V(\kappa, x_3, \omega) + \frac{jk_1}{\kappa^2} \tilde{q}_2^H(\kappa, x_3, \omega) \\
 &= \left\{ \frac{-k_1 k_2}{\kappa^2} \left[\tilde{\mathbf{L}}_{8,J}^V(\kappa, x_3, \omega) \tilde{\mathcal{G}}_{J,K}^V(\kappa, x_3, \omega) (\tilde{\mathbf{L}}^V)_{K,8}^{-1}(\kappa, x_3, \omega) \right] \right. \\
 &\quad \left. + \frac{k_1 k_2}{\kappa^2} \left[\tilde{\mathbf{L}}_{2,J}^H(\kappa, x_3, \omega) \tilde{\mathcal{G}}_{J,K}^H(\kappa, x_3, \omega) (\tilde{\mathbf{L}}^H)_{K,2}^{-1}(\kappa, x_3, \omega) \right] \right\} \hat{\mathcal{J}}_2^m(\omega), \quad (3.322)
 \end{aligned}$$

to

$$\begin{aligned}
 \hat{E}_2^{J_2^m}(\mathbf{x}, \omega) &= \frac{\hat{\mathcal{J}}_2^m(\omega)}{2\pi} \int_{\kappa=0}^{\infty} \left[\frac{\partial_1 \partial_2}{\kappa^2} \left(\tilde{\mathbf{L}}_{8,J}^V \tilde{\mathcal{G}}_{J,K}^V (\tilde{\mathbf{L}}^V)_{K,8}^{-1} \right) \right. \\
 &\quad \left. - \frac{\partial_1 \partial_2}{\kappa^2} \left(\tilde{\mathbf{L}}_{2,J}^H \tilde{\mathcal{G}}_{J,K}^H (\tilde{\mathbf{L}}^H)_{K,2}^{-1} \right) \right] J_0(\kappa r) \kappa d\kappa \\
 &= \frac{\hat{\mathcal{J}}_2^m(\omega)}{2\pi} \int_{\kappa=0}^{\infty} \left\{ \cos(\phi) \sin(\phi) \left[\left(\tilde{\mathbf{L}}_{8,J}^V \tilde{\mathcal{G}}_{J,K}^V (\tilde{\mathbf{L}}^V)_{K,8}^{-1} \right) \right. \right. \\
 &\quad \left. \left. - \left(\tilde{\mathbf{L}}_{2,J}^H \tilde{\mathcal{G}}_{J,K}^H (\tilde{\mathbf{L}}^H)_{K,2}^{-1} \right) \right] J_2(\kappa r) \right\} \kappa d\kappa. \quad (3.323)
 \end{aligned}$$

For $\tilde{E}_2^{J_3^m}$, we transform

$$\begin{aligned}
\tilde{E}_2^{J_3^m}(\mathbf{k}_H, x_3, \omega) &= \frac{k_2}{\kappa} \tilde{E}_{norm}^V(\kappa, x_3, \omega) + \frac{jk_1}{\kappa^2} \tilde{E}^H(\kappa, x_3, \omega) \\
&= \frac{k_2}{\kappa} \tilde{q}_8^V(\kappa, x_3, \omega) + \frac{jk_1}{\kappa^2} \tilde{q}_2^H(\kappa, x_3, \omega) \\
&= -jk_1 \left(\tilde{\mathbf{L}}_{2,J}^H(\kappa, x_3, \omega) \tilde{\mathcal{G}}_{J,K}^H(\kappa, x_3, \omega) (\tilde{\mathbf{L}}^H)_{K,4}^{-1}(\kappa, x_3, \omega) \right) \left(\frac{1}{s\mu_0} \hat{\mathcal{J}}_3^m(\omega) \right),
\end{aligned} \tag{3.324}$$

to

$$\begin{aligned}
\hat{E}_2^{J_3^m}(\mathbf{x}, \omega) &= \frac{\hat{\mathcal{J}}_3^m(\omega)}{2\pi} \int_{\kappa=0}^{\infty} \left[\partial_1 \left(\tilde{\mathbf{L}}_{2,J}^H \tilde{\mathcal{G}}_{J,K}^H (\tilde{\mathbf{L}}^H)_{K,4}^{-1} \right) \left(\frac{1}{s\mu_0} \right) \right] J_0(\kappa r) \kappa d\kappa \\
&= \frac{\hat{\mathcal{J}}_3^m(\omega)}{2\pi} \int_{\kappa=0}^{\infty} -\kappa \cos(\phi) \left(\tilde{\mathbf{L}}_{2,J}^H \tilde{\mathcal{G}}_{J,K}^H (\tilde{\mathbf{L}}^H)_{K,4}^{-1} \right) \left(\frac{1}{s\mu_0} \right) J_1(\kappa r) \kappa d\kappa.
\end{aligned} \tag{3.325}$$

For $\tilde{E}_2^{f_1^b}$, we transform

$$\begin{aligned}
\tilde{E}_2^{f_1^b}(\mathbf{k}_H, x_3, \omega) &= \frac{k_2}{\kappa} \tilde{E}_{norm}^V(\kappa, x_3, \omega) + \frac{jk_1}{\kappa^2} \tilde{E}^H(\kappa, x_3, \omega) \\
&= \frac{k_2}{\kappa} \tilde{q}_8^V(\kappa, x_3, \omega) + \frac{jk_1}{\kappa^2} \tilde{q}_2^H(\kappa, x_3, \omega) \\
&= -\frac{k_1 k_2}{\kappa^2} \left[\tilde{\mathbf{L}}_{8,J}^V(\kappa, x_3, \omega) \tilde{\mathcal{G}}_{J,K}^V(\kappa, x_3, \omega) (\tilde{\mathbf{L}}^V)_{K,3}^{-1}(\kappa, x_3, \omega) \right] \hat{\mathcal{F}}_1^b(\omega) \\
&\quad + \frac{k_1 k_2}{\kappa^2} \left[\tilde{\mathbf{L}}_{2,J}^H(\kappa, x_3, \omega) \tilde{\mathcal{G}}_{J,K}^H(\kappa, x_3, \omega) (\tilde{\mathbf{L}}^H)_{K,3}^{-1}(\kappa, x_3, \omega) \right] \hat{\mathcal{F}}_1^b(\omega),
\end{aligned} \tag{3.326}$$

to

$$\begin{aligned}
\hat{E}_2^{f_1^b}(\mathbf{x}, \omega) &= \frac{\hat{\mathcal{F}}_1^b(\omega)}{2\pi} \int_{\kappa=0}^{\infty} \left[\frac{\partial_1 \partial_2}{\kappa^2} \left(\tilde{\mathbf{L}}_{8,J}^V \tilde{\mathcal{G}}_{J,K}^V (\tilde{\mathbf{L}}^V)_{K,3}^{-1} \right) \right. \\
&\quad \left. - \frac{\partial_1 \partial_2}{\kappa^2} \left(\tilde{\mathbf{L}}_{2,J}^H(\kappa, x_3, \omega) \tilde{\mathcal{G}}_{J,K}^H(\kappa, x_3, \omega) (\tilde{\mathbf{L}}^H)_{K,3}^{-1} \right) \right] J_0(\kappa r) \kappa d\kappa \\
&= \frac{\hat{\mathcal{F}}_1^b(\omega)}{2\pi} \int_{\kappa=0}^{\infty} \left\{ \cos(\phi) \sin(\phi) \left[\left(\tilde{\mathbf{L}}_{8,J}^V \tilde{\mathcal{G}}_{J,K}^V (\tilde{\mathbf{L}}^V)_{K,3}^{-1} \right) \right. \right. \\
&\quad \left. \left. - \left(\tilde{\mathbf{L}}_{2,J}^H(\kappa, x_3, \omega) \tilde{\mathcal{G}}_{J,K}^H(\kappa, x_3, \omega) (\tilde{\mathbf{L}}^H)_{K,3}^{-1} \right) \right] J_2(\kappa r) \right\} \kappa d\kappa.
\end{aligned} \tag{3.327}$$

For \tilde{E}_2^{f1} , we transform

$$\begin{aligned}
 \tilde{E}_2^{f1}(\mathbf{k}_H, x_3, \omega) &= \frac{k_2}{\kappa} \tilde{E}_{norm}^V(\kappa, x_3, \omega) + \frac{jk_1}{\kappa^2} \tilde{E}^H(\kappa, x_3, \omega) \\
 &= \frac{k_2}{\kappa} \tilde{q}_8^V(\kappa, x_3, \omega) + \frac{jk_1}{\kappa^2} \tilde{q}_2^H(\kappa, x_3, \omega) \\
 &= \frac{jk_1 k_2}{\kappa} \left[\tilde{\mathbf{L}}_{8,J}^V(\kappa, x_3, \omega) \tilde{\mathcal{G}}_{J,K}^V(\kappa, x_3, \omega) (\tilde{\mathbf{L}}^V)_{K,2}^{-1}(\kappa, x_3, \omega) \left(\frac{1}{s\hat{\rho}^E} \hat{\mathcal{F}}_1^f(\omega) \right) \right] \\
 &\quad + \frac{k_1 k_2}{\kappa^2} \left[\tilde{\mathbf{L}}_{8,J}^V(\kappa, x_3, \omega) \tilde{\mathcal{G}}_{J,K}^V(\kappa, x_3, \omega) (\tilde{\mathbf{L}}^V)_{K,3}^{-1}(\kappa, x_3, \omega) \left(\frac{\rho^f}{\hat{\rho}^E} \hat{\mathcal{F}}_1^f(\omega) \right) \right. \\
 &\quad \left. - \tilde{\mathbf{L}}_{8,J}^V(\kappa, x_3, \omega) \tilde{\mathcal{G}}_{J,K}^V(\kappa, x_3, \omega) (\tilde{\mathbf{L}}^V)_{K,4}^{-1}(\kappa, x_3, \omega) \left(\hat{\mathcal{L}} \hat{\mathcal{F}}_1^f(\omega) \right) \right] \\
 &\quad - \frac{k_1 k_2}{\kappa^2} \left[\tilde{\mathbf{L}}_{2,J}^H(\kappa, x_3, \omega) \tilde{\mathcal{G}}_{J,K}^H(\kappa, x_3, \omega) (\tilde{\mathbf{L}}^H)_{K,3}^{-1}(\kappa, x_3, \omega) \left(\frac{\rho^f}{\hat{\rho}^E} \hat{\mathcal{F}}_1^f(\omega) \right) \right. \\
 &\quad \left. - \tilde{\mathbf{L}}_{2,J}^H(\kappa, x_3, \omega) \tilde{\mathcal{G}}_{J,K}^H(\kappa, x_3, \omega) (\tilde{\mathbf{L}}^H)_{K,4}^{-1}(\kappa, x_3, \omega) \left(\hat{\mathcal{L}} \hat{\mathcal{F}}_1^f(\omega) \right) \right], \quad (3.328)
 \end{aligned}$$

to

$$\begin{aligned}
 \hat{E}_2^{f1}(\mathbf{x}, \omega) &= \frac{\hat{\mathcal{F}}_1^f(\omega)}{2\pi} \int_{\kappa=0}^{\infty} \left[-j \frac{\partial_1 \partial_2}{\kappa} \left(\tilde{\mathbf{L}}_{8,J}^V \tilde{\mathcal{G}}_{J,K}^V (\tilde{\mathbf{L}}^V)_{K,2}^{-1} \right) \left(\frac{1}{s\hat{\rho}^E} \right) \right. \\
 &\quad \left. - \frac{\partial_1 \partial_2}{\kappa^2} \left(\tilde{\mathbf{L}}_{8,J}^V(\kappa, x_3, \omega) \tilde{\mathcal{G}}_{J,K}^V(\kappa, x_3, \omega) (\tilde{\mathbf{L}}^V)_{K,3}^{-1}(\kappa, x_3, \omega) \right) \left(\frac{\rho^f}{\hat{\rho}^E} \right) \right. \\
 &\quad \left. + \frac{\partial_1 \partial_2}{\kappa^2} \left(\tilde{\mathbf{L}}_{8,J}^V \tilde{\mathcal{G}}_{J,K}^V (\tilde{\mathbf{L}}^V)_{K,4}^{-1} \right) \hat{\mathcal{L}} \right. \\
 &\quad \left. + \frac{\partial_1 \partial_2}{\kappa^2} \left(\tilde{\mathbf{L}}_{2,J}^H(\kappa, x_3, \omega) \tilde{\mathcal{G}}_{J,K}^H(\kappa, x_3, \omega) (\tilde{\mathbf{L}}^H)_{K,3}^{-1}(\kappa, x_3, \omega) \right) \left(\frac{\rho^f}{\hat{\rho}^E} \right) \right. \\
 &\quad \left. - \frac{\partial_1 \partial_2}{\kappa^2} \left(\tilde{\mathbf{L}}_{2,J}^H(\kappa, x_3, \omega) \tilde{\mathcal{G}}_{J,K}^H(\kappa, x_3, \omega) (\tilde{\mathbf{L}}^H)_{K,4}^{-1} \right) \hat{\mathcal{L}} \right] J_0(\kappa r) \kappa d \kappa \\
 &= \frac{\hat{\mathcal{F}}_1^b(\omega)}{2\pi} \int_{\kappa=0}^{\infty} \left\{ \cos(\phi) \sin(\phi) \left[\left(\tilde{\mathbf{L}}_{8,J}^V \tilde{\mathcal{G}}_{J,K}^V (\tilde{\mathbf{L}}^V)_{K,2}^{-1} \right) \left(\frac{-j\kappa}{s\hat{\rho}^E} \right) \right. \right. \\
 &\quad \left. \left. - \left(\tilde{\mathbf{L}}_{8,J}^V \tilde{\mathcal{G}}_{J,K}^V (\tilde{\mathbf{L}}^V)_{K,3}^{-1} \right) \frac{\rho^f}{\hat{\rho}^E} + \left(\tilde{\mathbf{L}}_{8,J}^V \tilde{\mathcal{G}}_{J,K}^V (\tilde{\mathbf{L}}^V)_{K,4}^{-1} \right) \hat{\mathcal{L}} \right. \right. \\
 &\quad \left. \left. + \left(\tilde{\mathbf{L}}_{2,J}^H(\kappa, x_3, \omega) \tilde{\mathcal{G}}_{J,K}^H(\kappa, x_3, \omega) (\tilde{\mathbf{L}}^H)_{K,3}^{-1} \right) \frac{\rho^f}{\hat{\rho}^E} \right. \right. \\
 &\quad \left. \left. - \left(\tilde{\mathbf{L}}_{2,J}^H(\kappa, x_3, \omega) \tilde{\mathcal{G}}_{J,K}^H(\kappa, x_3, \omega) (\tilde{\mathbf{L}}^H)_{K,4}^{-1} \right) \hat{\mathcal{L}} \right] J_2(\kappa r) \right\} \kappa d \kappa. \quad (3.329)
 \end{aligned}$$

For \tilde{E}_2^{f2} , we transform

$$\begin{aligned}
\tilde{E}_2^{fb}(\mathbf{k}_H, x_3, \omega) &= \frac{k_2}{\kappa} \tilde{E}_{norm}^V(\kappa, x_3, \omega) + \frac{jk_1}{\kappa^2} \tilde{E}^H(\kappa, x_3, \omega) \\
&= \frac{k_2}{\kappa} \tilde{q}_8^V(\kappa, x_3, \omega) + \frac{jk_1}{\kappa^2} \tilde{q}_2^H(\kappa, x_3, \omega) \\
&= -\frac{k_2^2}{\kappa^2} \left[\tilde{\mathbf{L}}_{8,J}^V(\kappa, x_3, \omega) \tilde{\mathbf{G}}_{J,K}^V(\kappa, x_3, \omega) (\tilde{\mathbf{L}}^V)_{K,3}^{-1}(\kappa, x_3, \omega) \right] \hat{\mathcal{F}}_2^b(\omega) \\
&\quad - \frac{k_1^2}{\kappa^2} \left[\tilde{\mathbf{L}}_{2,J}^H(\kappa, x_3, \omega) \tilde{\mathbf{G}}_{J,K}^H(\kappa, x_3, \omega) (\tilde{\mathbf{L}}^H)_{K,3}^{-1}(\kappa, x_3, \omega) \right] \hat{\mathcal{F}}_2^b(\omega), \quad (3.330)
\end{aligned}$$

to

$$\begin{aligned}
\hat{E}_2^{fb}(\mathbf{x}, \omega) &= \frac{\hat{\mathcal{F}}_2^b(\omega)}{2\pi} \int_{\kappa=0}^{\infty} \left[\frac{\partial^2}{\kappa^2} \left(\tilde{\mathbf{L}}_{8,J}^V \tilde{\mathbf{G}}_{J,K}^V (\tilde{\mathbf{L}}^V)_{K,3}^{-1} \right) \right. \\
&\quad \left. + \frac{\partial^2}{\kappa^2} \left(\tilde{\mathbf{L}}_{2,J}^H \tilde{\mathbf{G}}_{J,K}^H (\tilde{\mathbf{L}}^H)_{K,3}^{-1} \right) \right] J_0(\kappa r) \kappa d\kappa \\
&= \frac{\hat{\mathcal{F}}_2^b(\omega)}{4\pi} \int_{\kappa=0}^{\infty} \left[-\frac{1}{2} \left(\tilde{\mathbf{L}}_{8,J}^V \tilde{\mathbf{G}}_{J,K}^V (\tilde{\mathbf{L}}^V)_{K,3}^{-1} \right) (J_0(\kappa r) + \cos(2\phi) J_2(\kappa r)) \right. \\
&\quad \left. - \frac{1}{2} \left(\tilde{\mathbf{L}}_{2,J}^H \tilde{\mathbf{G}}_{J,K}^H (\tilde{\mathbf{L}}^H)_{K,3}^{-1} \right) (J_0(\kappa r) - \cos(2\phi) J_2(\kappa r)) \right] \kappa d\kappa. \quad (3.331)
\end{aligned}$$

For \tilde{E}_2^{ff} , we transform

$$\begin{aligned}
\tilde{E}_2^{ff}(\mathbf{k}_H, x_3, \omega) &= \frac{k_2}{\kappa} \tilde{E}_{norm}^V(\kappa, x_3, \omega) + \frac{jk_1}{\kappa^2} \tilde{E}^H(\kappa, x_3, \omega) \\
&= \frac{k_2}{\kappa} \tilde{q}_8^V(\kappa, x_3, \omega) + \frac{jk_1}{\kappa^2} \tilde{q}_2^H(\kappa, x_3, \omega) \\
&= \frac{jk_2^2}{\kappa} \left[\tilde{\mathbf{L}}_{8,J}^V(\kappa, x_3, \omega) \tilde{\mathbf{G}}_{J,K}^V(\kappa, x_3, \omega) (\tilde{\mathbf{L}}^V)_{K,2}^{-1}(\kappa, x_3, \omega) \left(\frac{1}{s_{\hat{\rho}^E}} \hat{\mathcal{F}}_2^f(\omega) \right) \right] \\
&\quad + \frac{k_2^2}{\kappa^2} \left[\tilde{\mathbf{L}}_{8,J}^V(\kappa, x_3, \omega) \tilde{\mathbf{G}}_{J,K}^V(\kappa, x_3, \omega) (\tilde{\mathbf{L}}^V)_{K,3}^{-1}(\kappa, x_3, \omega) \left(\frac{\rho^f}{\hat{\rho}^E} \hat{\mathcal{F}}_2^f(\omega) \right) \right. \\
&\quad \left. - \tilde{\mathbf{L}}_{8,J}^V(\kappa, x_3, \omega) \tilde{\mathbf{G}}_{J,K}^V(\kappa, x_3, \omega) (\tilde{\mathbf{L}}^V)_{K,4}^{-1}(\kappa, x_3, \omega) \left(\hat{\mathcal{L}} \hat{\mathcal{F}}_2^f(\omega) \right) \right] \\
&\quad + \frac{k_1^2}{\kappa^2} \left[\tilde{\mathbf{L}}_{2,J}^H(\kappa, x_3, \omega) \tilde{\mathbf{G}}_{J,K}^H(\kappa, x_3, \omega) (\tilde{\mathbf{L}}^H)_{K,3}^{-1}(\kappa, x_3, \omega) \left(\frac{\rho^f}{\hat{\rho}^E} \hat{\mathcal{F}}_2^f(\omega) \right) \right. \\
&\quad \left. - \tilde{\mathbf{L}}_{2,J}^H(\kappa, x_3, \omega) \tilde{\mathbf{G}}_{J,K}^H(\kappa, x_3, \omega) (\tilde{\mathbf{L}}^H)_{K,4}^{-1}(\kappa, x_3, \omega) \left(\hat{\mathcal{L}} \hat{\mathcal{F}}_2^f(\omega) \right) \right], \quad (3.332)
\end{aligned}$$

to

$$\begin{aligned}
 \hat{E}_2^{f_2}(\mathbf{x}, \omega) &= \frac{\hat{\mathcal{F}}_2^f(\omega)}{2\pi} \int_{\kappa=0}^{\infty} \left[-j \frac{\partial_2^2}{\kappa} \left(\tilde{\mathbf{L}}_{8,J}^V \tilde{\mathcal{G}}_{J,K}^V (\tilde{\mathbf{L}}^V)_{K,2}^{-1} \right) \left(\frac{1}{s\hat{\rho}E} \right) \right. \\
 &\quad - \frac{\partial_2^2}{\kappa^2} \left(\tilde{\mathbf{L}}_{8,J}^V \tilde{\mathcal{G}}_{J,K}^V (\tilde{\mathbf{L}}^V)_{K,3}^{-1} \right) \frac{\rho^f}{\hat{\rho}E} \\
 &\quad + \frac{\partial_2^2}{\kappa^2} \left(\tilde{\mathbf{L}}_{8,J}^V \tilde{\mathcal{G}}_{J,K}^V (\tilde{\mathbf{L}}^V)_{K,4}^{-1} \right) \hat{\mathcal{L}} \\
 &\quad \left. - \frac{\partial_2^2}{\kappa^2} \left(\tilde{\mathbf{L}}_{2,J}^H(\kappa, x_3, \omega) \tilde{\mathcal{G}}_{J,K}^H(\kappa, x_3, \omega) (\tilde{\mathbf{L}}^H)_{K,3}^{-1} \right) \frac{\rho^f}{\hat{\rho}E} \right. \\
 &\quad \left. + \frac{\partial_2^2}{\kappa^2} \left(\tilde{\mathbf{L}}_{2,J}^H(\kappa, x_3, \omega) \tilde{\mathcal{G}}_{J,K}^H(\kappa, x_3, \omega) (\tilde{\mathbf{L}}^H)_{K,4}^{-1} \right) \hat{\mathcal{L}} \right] J_0(\kappa r) \kappa d\kappa \\
 &= \frac{\hat{\mathcal{F}}_2^b(\omega)}{2\pi} \int_{\kappa=0}^{\infty} \left\{ \frac{1}{2} \left[-j\kappa \left(\tilde{\mathbf{L}}_{8,J}^V \tilde{\mathcal{G}}_{J,K}^V (\tilde{\mathbf{L}}^V)_{K,2}^{-1} \right) \frac{1}{s\hat{\rho}E} \right. \right. \\
 &\quad + \left(\tilde{\mathbf{L}}_{8,J}^V \tilde{\mathcal{G}}_{J,K}^V (\tilde{\mathbf{L}}^V)_{K,3}^{-1} \right) \frac{\rho^f}{\hat{\rho}E} \\
 &\quad \left. - \left(\tilde{\mathbf{L}}_{8,J}^V \tilde{\mathcal{G}}_{J,K}^V (\tilde{\mathbf{L}}^V)_{K,4}^{-1} \right) \hat{\mathcal{L}} \right] (J_0(\kappa r) + \cos(2\phi) J_2(\kappa r)) \\
 &\quad + \frac{1}{2} \left[\left(\tilde{\mathbf{L}}_{2,J}^H(\kappa, x_3, \omega) \tilde{\mathcal{G}}_{J,K}^H(\kappa, x_3, \omega) (\tilde{\mathbf{L}}^H)_{K,3}^{-1} \right) \frac{\rho^f}{\hat{\rho}E} \right. \\
 &\quad \left. - \left(\tilde{\mathbf{L}}_{2,J}^H(\kappa, x_3, \omega) \tilde{\mathcal{G}}_{J,K}^H(\kappa, x_3, \omega) (\tilde{\mathbf{L}}^H)_{K,4}^{-1} \right) \hat{\mathcal{L}} \right] (J_0(\kappa r) - \cos(2\phi) J_2(\kappa r)) \right\} \kappa d\kappa.
 \end{aligned} \tag{3.333}$$

For $\tilde{E}_2^{f_3^b}$, we transform

$$\begin{aligned}
 \tilde{E}_2^{f_3^b}(\mathbf{k}_H, x_3, \omega) &= \frac{k_2}{\kappa} \tilde{E}_{norm}^V(\kappa, x_3, \omega) + \frac{jk_1}{\kappa^2} \tilde{E}^H(\kappa, x_3, \omega) \\
 &= \frac{k_2}{\kappa} \tilde{q}_8^V(\kappa, x_3, \omega) + \frac{jk_1}{\kappa^2} \tilde{q}_2^H(\kappa, x_3, \omega) \\
 &= \frac{-k_2}{\kappa} \left[\tilde{\mathbf{L}}_{8,J}^V(\kappa, x_3, \omega) \tilde{\mathcal{G}}_{J,K}^V(\kappa, x_3, \omega) (\tilde{\mathbf{L}}^V)_{K,5}^{-1}(\kappa, x_3, \omega) \right] \left(\hat{\mathcal{F}}_3^b(\omega) \right),
 \end{aligned} \tag{3.334}$$

to

$$\begin{aligned}
 \hat{E}_2^{f_3^b}(\mathbf{x}, \omega) &= \frac{\hat{\mathcal{F}}_3^b(\omega)}{2\pi} \int_{\kappa=0}^{\infty} \left[-j \frac{\partial_2}{\kappa} \left(\tilde{\mathbf{L}}_{8,J}^V \tilde{\mathcal{G}}_{J,K}^V (\tilde{\mathbf{L}}^V)_{K,5}^{-1} \right) \right] J_0(\kappa r) \kappa d\kappa \\
 &= \frac{\hat{\mathcal{F}}_3^b(\omega)}{2\pi} \int_{\kappa=0}^{\infty} \left[j \sin(\phi) \left(\tilde{\mathbf{L}}_{8,J}^V \tilde{\mathcal{G}}_{J,K}^V (\tilde{\mathbf{L}}^V)_{K,5}^{-1} \right) \right] J_1(\kappa r) \kappa d\kappa.
 \end{aligned} \tag{3.335}$$

For $\tilde{E}_2^{f_3^f}$, we transform

$$\begin{aligned}
\tilde{E}_2^{f_3}(\mathbf{k}_H, x_3, \omega) &= \frac{k_2}{\kappa} \tilde{E}_{norm}^V(\kappa, x_3, \omega) + \frac{jk_1}{\kappa^2} \tilde{E}^H(\kappa, x_3, \omega) \\
&= \frac{k_2}{\kappa} \tilde{q}_8^V(\kappa, x_3, \omega) + \frac{jk_1}{\kappa^2} \tilde{q}_2^H(\kappa, x_3, \omega) \\
&= \frac{-k_2}{\kappa} \left[\tilde{\mathbf{L}}_{8,J}^V(\kappa, x_3, \omega) \tilde{\mathbf{G}}_{J,K}^V(\kappa, x_3, \omega) (\tilde{\mathbf{L}}^V)_{K,6}^{-1}(\kappa, x_3, \omega) \right] \left(\hat{\mathcal{F}}_3^f(\omega) \right),
\end{aligned} \tag{3.336}$$

to

$$\begin{aligned}
\hat{E}_2^{f_3}(\mathbf{x}, \omega) &= \frac{\hat{\mathcal{F}}_3^f(\omega)}{2\pi} \int_{\kappa=0}^{\infty} \left[-\frac{j\partial_2}{\kappa} \left(\tilde{\mathbf{L}}_{8,J}^V \tilde{\mathbf{G}}_{J,K}^V (\tilde{\mathbf{L}}^V)_{K,6}^{-1} \right) \right] J_0(\kappa r) \kappa d\kappa \\
&= \frac{\hat{\mathcal{F}}_3^f(\omega)}{2\pi} \int_{\kappa=0}^{\infty} \left[j\sin(\phi) \left(\tilde{\mathbf{L}}_{8,J}^V \tilde{\mathbf{G}}_{J,K}^V (\tilde{\mathbf{L}}^V)_{K,6}^{-1} \right) \right] J_1(\kappa r) \kappa d\kappa.
\end{aligned} \tag{3.337}$$

For $\tilde{E}_2^{q_i}$, we transform

$$\begin{aligned}
\tilde{E}_2^{q_i}(\mathbf{k}_H, x_3, \omega) &= \frac{k_2}{\kappa} \tilde{E}_{norm}^V(\kappa, x_3, \omega) + \frac{jk_1}{\kappa^2} \tilde{E}^H(\kappa, x_3, \omega) \\
&= \frac{k_2}{\kappa} \tilde{q}_8^V(\kappa, x_3, \omega) + \frac{jk_1}{\kappa^2} \tilde{q}_2^H(\kappa, x_3, \omega) \\
&= \frac{k_2}{\kappa} \left[\tilde{\mathbf{L}}_{8,J}^V(\kappa, x_3, \omega) \tilde{\mathbf{G}}_{J,K}^V(\kappa, x_3, \omega) (\tilde{\mathbf{L}}^V)_{K,2}^{-1}(\kappa, x_3, \omega) \right] \left(\hat{\mathcal{Q}}^i(\omega) \right),
\end{aligned} \tag{3.338}$$

to

$$\begin{aligned}
\hat{E}_2^{q_i}(\mathbf{x}, \omega) &= \frac{\hat{\mathcal{Q}}^i(\omega)}{2\pi} \int_{\kappa=0}^{\infty} \left[\frac{j\partial_2}{\kappa} \left(\tilde{\mathbf{L}}_{8,J}^V \tilde{\mathbf{G}}_{J,K}^V (\tilde{\mathbf{L}}^V)_{K,2}^{-1} \right) \right] J_0(\kappa r) \kappa d\kappa \\
&= \frac{\hat{\mathcal{Q}}^i(\omega)}{2\pi} \int_{\kappa=0}^{\infty} \left[-j\sin(\phi) \left(\tilde{\mathbf{L}}_{8,J}^V \tilde{\mathbf{G}}_{J,K}^V (\tilde{\mathbf{L}}^V)_{K,2}^{-1} \right) \right] J_1(\kappa r) \kappa d\kappa.
\end{aligned} \tag{3.339}$$

For $\tilde{E}_2^{h_{11}^b}$, we transform

$$\begin{aligned}
 \tilde{E}_2^{h^b_{11}}(\mathbf{k}_H, x_3, \omega) &= \frac{k_2}{\kappa} \tilde{E}_{norm}^V(\kappa, x_3, \omega) + \frac{jk_1}{\kappa^2} \tilde{E}^H(\kappa, x_3, \omega) \\
 &= \frac{k_2}{\kappa} \tilde{q}_8^V(\kappa, x_3, \omega) + \frac{jk_1}{\kappa^2} \tilde{q}_2^H(\kappa, x_3, \omega) \\
 &= \frac{k_2}{\kappa} \left[\tilde{\mathbf{L}}_{8,J}^V(\kappa, x_3, \omega) \tilde{\mathcal{G}}_{J,K}^V(\kappa, x_3, \omega) (\tilde{\mathbf{L}}^V)_{K,1}^{-1}(\kappa, x_3, \omega) \left(\frac{S}{K_c} \right) \right. \\
 &\quad \left. + \tilde{\mathbf{L}}_{8,J}^V(\kappa, x_3, \omega) \tilde{\mathcal{G}}_{J,K}^V(\kappa, x_3, \omega) (\tilde{\mathbf{L}}^V)_{K,2}^{-1}(\kappa, x_3, \omega) \left(\frac{C}{M} \left(1 - \frac{S}{K_c} \right) \right) \right] \hat{\mathcal{H}}_{11}^b(\omega) \\
 &\quad - jk_2 \left[\tilde{\mathbf{L}}_{8,J}^V(\kappa, x_3, \omega) \tilde{\mathcal{G}}_{J,K}^V(\kappa, x_3, \omega) (\tilde{\mathbf{L}}^V)_{K,3}^{-1}(\kappa, x_3, \omega) \frac{2G^{fr}S}{sK_c} \right] \hat{\mathcal{H}}_{11}^b(\omega) \\
 &\quad - \frac{jk_1^2 k_2}{\kappa^2} \left[\tilde{\mathbf{L}}_{8,J}^V(\kappa, x_3, \omega) \tilde{\mathcal{G}}_{J,K}^V(\kappa, x_3, \omega) (\tilde{\mathbf{L}}^V)_{K,3}^{-1}(\kappa, x_3, \omega) \frac{2G^{fr}}{s} \right] \hat{\mathcal{H}}_{11}^b(\omega) \\
 &\quad + \frac{jk_1^2 k_2}{\kappa^2} \left[\tilde{\mathbf{L}}_{2,J}^H(\kappa, x_3, \omega) \tilde{\mathcal{G}}_{J,K}^H(\kappa, x_3, \omega) (\tilde{\mathbf{L}}^H)_{K,1}^{-1}(\kappa, x_3, \omega) \frac{2G^{fr}}{s} \right] \hat{\mathcal{H}}_{11}^b(\omega),
 \end{aligned} \tag{3.340}$$

to

$$\begin{aligned}
 \tilde{E}_2^{h^b_{11}}(\mathbf{k}_H, x_3, \omega) &= \frac{\hat{\mathcal{H}}_{11}^b(\omega)}{2\pi} \int_{\kappa=0}^{\infty} \left\{ \frac{j\partial_2}{\kappa} \left[\tilde{\mathbf{L}}_{8,J}^V(\kappa, x_3, \omega) \tilde{\mathcal{G}}_{J,K}^V(\kappa, x_3, \omega) (\tilde{\mathbf{L}}^V)_{K,1}^{-1}(\kappa, x_3, \omega) \left(\frac{S}{K_c} \right) \right. \right. \\
 &\quad \left. \left. + \tilde{\mathbf{L}}_{8,J}^V(\kappa, x_3, \omega) \tilde{\mathcal{G}}_{J,K}^V(\kappa, x_3, \omega) (\tilde{\mathbf{L}}^V)_{K,2}^{-1}(\kappa, x_3, \omega) \left(\frac{C}{M} \left(1 - \frac{S}{K_c} \right) \right) \right] \right. \\
 &\quad \left. + \partial_2 \left[\tilde{\mathbf{L}}_{8,J}^V(\kappa, x_3, \omega) \tilde{\mathcal{G}}_{J,K}^V(\kappa, x_3, \omega) (\tilde{\mathbf{L}}^V)_{K,3}^{-1}(\kappa, x_3, \omega) \frac{2G^{fr}S}{sK_c} \right] \right. \\
 &\quad \left. - \frac{\partial_1^2 \partial_2}{\kappa^2} \left[\tilde{\mathbf{L}}_{8,J}^V(\kappa, x_3, \omega) \tilde{\mathcal{G}}_{J,K}^V(\kappa, x_3, \omega) (\tilde{\mathbf{L}}^V)_{K,3}^{-1}(\kappa, x_3, \omega) \frac{2G^{fr}}{s} \right] \right. \\
 &\quad \left. + \frac{\partial_1^2 \partial_2}{\kappa^2} \left[\tilde{\mathbf{L}}_{2,J}^H(\kappa, x_3, \omega) \tilde{\mathcal{G}}_{J,K}^H(\kappa, x_3, \omega) (\tilde{\mathbf{L}}^H)_{K,1}^{-1}(\kappa, x_3, \omega) \frac{2G^{fr}}{s} \right] \right\} J_0(\kappa r) \kappa d\kappa. \\
 &= \frac{\hat{\mathcal{H}}_{11}^b(\omega)}{2\pi} \int_{\kappa=0}^{\infty} -j \sin(\phi) \left[\tilde{\mathbf{L}}_{8,J}^V(\kappa, x_3, \omega) \tilde{\mathcal{G}}_{J,K}^V(\kappa, x_3, \omega) (\tilde{\mathbf{L}}^V)_{K,1}^{-1}(\kappa, x_3, \omega) \left(\frac{S}{K_c} \right) \right. \\
 &\quad \left. + \tilde{\mathbf{L}}_{8,J}^V(\kappa, x_3, \omega) \tilde{\mathcal{G}}_{J,K}^V(\kappa, x_3, \omega) (\tilde{\mathbf{L}}^V)_{K,2}^{-1}(\kappa, x_3, \omega) \left(\frac{C}{M} \left(1 - \frac{S}{K_c} \right) \right) \right] J_1(\kappa r) \\
 &\quad - \kappa \sin(\phi) \left[\tilde{\mathbf{L}}_{8,J}^V(\kappa, x_3, \omega) \tilde{\mathcal{G}}_{J,K}^V(\kappa, x_3, \omega) (\tilde{\mathbf{L}}^V)_{K,3}^{-1}(\kappa, x_3, \omega) \frac{2G^{fr}S}{sK_c} \right] J_1(\kappa r) \\
 &\quad - \frac{\kappa}{4} \sin(\phi) \left[\tilde{\mathbf{L}}_{8,J}^V(\kappa, x_3, \omega) \tilde{\mathcal{G}}_{J,K}^V(\kappa, x_3, \omega) (\tilde{\mathbf{L}}^V)_{K,3}^{-1}(\kappa, x_3, \omega) \frac{2G^{fr}}{s} \right] (J_1(\kappa r) \\
 &\quad - (1 + 2\cos(2\phi)) J_3(\kappa r)) \\
 &\quad + \frac{\kappa}{4} \sin(\phi) \left[\tilde{\mathbf{L}}_{2,J}^H(\kappa, x_3, \omega) \tilde{\mathcal{G}}_{J,K}^H(\kappa, x_3, \omega) (\tilde{\mathbf{L}}^H)_{K,1}^{-1}(\kappa, x_3, \omega) \frac{2G^{fr}}{s} \right] (J_1(\kappa r) \\
 &\quad - (1 + 2\cos(2\phi)) J_3(\kappa r)) \kappa d\kappa.
 \end{aligned} \tag{3.341}$$

For $\tilde{E}_2^{h^b_{22}}$, we transform

$$\begin{aligned}
\tilde{E}_2^{hb_{22}}(\mathbf{k}_H, x_3, \omega) &= \frac{k_2}{\kappa} \tilde{E}_{norm}^V(\kappa, x_3, \omega) + \frac{jk_1}{\kappa^2} \tilde{E}^H(\kappa, x_3, \omega) \\
&= \frac{k_2}{\kappa} \tilde{q}_8^V(\kappa, x_3, \omega) + \frac{jk_1}{\kappa^2} \tilde{q}_2^H(\kappa, x_3, \omega) \\
&= \frac{k_2}{\kappa} \left[\tilde{\mathbf{L}}_{8,J}^V(\kappa, x_3, \omega) \tilde{\mathcal{G}}_{J,K}^V(\kappa, x_3, \omega) (\tilde{\mathbf{L}}^V)_{K,1}^{-1}(\kappa, x_3, \omega) \left(\frac{S}{K_c} \right) \right. \\
&\quad \left. + \tilde{\mathbf{L}}_{8,J}^V(\kappa, x_3, \omega) \tilde{\mathcal{G}}_{J,K}^V(\kappa, x_3, \omega) (\tilde{\mathbf{L}}^V)_{K,2}^{-1}(\kappa, x_3, \omega) \left(\frac{C}{M} \left(1 - \frac{S}{K_c} \right) \right) \right] \hat{\mathcal{H}}_{22}^b(\omega) \\
&\quad - jk_2 \left[\tilde{\mathbf{L}}_{8,J}^V(\kappa, x_3, \omega) \tilde{\mathcal{G}}_{J,K}^V(\kappa, x_3, \omega) (\tilde{\mathbf{L}}^V)_{K,3}^{-1}(\kappa, x_3, \omega) \frac{2G^{fr}S}{sK_c} \right] \hat{\mathcal{H}}_{22}^b(\omega) \\
&\quad - \frac{jk_2^3}{\kappa^2} \left[\tilde{\mathbf{L}}_{8,J}^V(\kappa, x_3, \omega) \tilde{\mathcal{G}}_{J,K}^V(\kappa, x_3, \omega) (\tilde{\mathbf{L}}^V)_{K,3}^{-1}(\kappa, x_3, \omega) \frac{2G^{fr}}{s} \right] \hat{\mathcal{H}}_{22}^b(\omega) \\
&\quad - \frac{jk_1^2 k_2}{\kappa^2} \left[\tilde{\mathbf{L}}_{2,J}^H(\kappa, x_3, \omega) \tilde{\mathcal{G}}_{J,K}^H(\kappa, x_3, \omega) (\tilde{\mathbf{L}}^H)_{K,1}^{-1}(\kappa, x_3, \omega) \frac{2G^{fr}}{s} \right] \hat{\mathcal{H}}_{22}^b(\omega),
\end{aligned} \tag{3.342}$$

to

$$\begin{aligned}
\tilde{E}_2^{hb_{22}}(\mathbf{k}_H, x_3, \omega) &= \frac{\hat{\mathcal{H}}_{22}^b(\omega)}{2\pi} \int_{\kappa=0}^{\infty} \left\{ \frac{j\partial_2}{\kappa} \left[\tilde{\mathbf{L}}_{8,J}^V(\kappa, x_3, \omega) \tilde{\mathcal{G}}_{J,K}^V(\kappa, x_3, \omega) (\tilde{\mathbf{L}}^V)_{K,1}^{-1}(\kappa, x_3, \omega) \left(\frac{S}{K_c} \right) \right. \right. \\
&\quad \left. \left. + \tilde{\mathbf{L}}_{8,J}^V(\kappa, x_3, \omega) \tilde{\mathcal{G}}_{J,K}^V(\kappa, x_3, \omega) (\tilde{\mathbf{L}}^V)_{K,2}^{-1}(\kappa, x_3, \omega) \left(\frac{C}{M} \left(1 - \frac{S}{K_c} \right) \right) \right] \right. \\
&\quad \left. + \partial_2 \left[\tilde{\mathbf{L}}_{8,J}^V(\kappa, x_3, \omega) \tilde{\mathcal{G}}_{J,K}^V(\kappa, x_3, \omega) (\tilde{\mathbf{L}}^V)_{K,3}^{-1}(\kappa, x_3, \omega) \frac{2G^{fr}S}{sK_c} \right] \right. \\
&\quad \left. - \frac{\partial_2^3}{\kappa^2} \left[\tilde{\mathbf{L}}_{8,J}^V(\kappa, x_3, \omega) \tilde{\mathcal{G}}_{J,K}^V(\kappa, x_3, \omega) (\tilde{\mathbf{L}}^V)_{K,3}^{-1}(\kappa, x_3, \omega) \frac{2G^{fr}}{s} \right] \right. \\
&\quad \left. - \frac{\partial_1^2 \partial_2}{\kappa^2} \left[\tilde{\mathbf{L}}_{2,J}^H(\kappa, x_3, \omega) \tilde{\mathcal{G}}_{J,K}^H(\kappa, x_3, \omega) (\tilde{\mathbf{L}}^H)_{K,1}^{-1}(\kappa, x_3, \omega) \frac{2G^{fr}}{s} \right] \right\} J_0(\kappa r) \kappa dk. \\
&= \frac{\hat{\mathcal{H}}_{11}^b(\omega)}{2\pi} \int_{\kappa=0}^{\infty} -j \sin(\phi) \left[\tilde{\mathbf{L}}_{8,J}^V(\kappa, x_3, \omega) \tilde{\mathcal{G}}_{J,K}^V(\kappa, x_3, \omega) (\tilde{\mathbf{L}}^V)_{K,1}^{-1}(\kappa, x_3, \omega) \left(\frac{S}{K_c} \right) \right. \\
&\quad \left. + \tilde{\mathbf{L}}_{8,J}^V(\kappa, x_3, \omega) \tilde{\mathcal{G}}_{J,K}^V(\kappa, x_3, \omega) (\tilde{\mathbf{L}}^V)_{K,2}^{-1}(\kappa, x_3, \omega) \left(\frac{C}{M} \left(1 - \frac{S}{K_c} \right) \right) \right] J_1(\kappa r) \\
&\quad - \kappa \sin(\phi) \left[\tilde{\mathbf{L}}_{8,J}^V(\kappa, x_3, \omega) \tilde{\mathcal{G}}_{J,K}^V(\kappa, x_3, \omega) (\tilde{\mathbf{L}}^V)_{K,3}^{-1}(\kappa, x_3, \omega) \frac{2G^{fr}S}{sK_c} \right] J_1(\kappa r) \\
&\quad - \frac{\kappa}{4} \sin(\phi) \left[\tilde{\mathbf{L}}_{8,J}^V(\kappa, x_3, \omega) \tilde{\mathcal{G}}_{J,K}^V(\kappa, x_3, \omega) (\tilde{\mathbf{L}}^V)_{K,3}^{-1}(\kappa, x_3, \omega) \frac{2G^{fr}}{s} \right] (3J_1(\kappa r) \\
&\quad + (1 + 2\cos(2\phi)) J_3(\kappa r)) \\
&\quad - \frac{\kappa}{4} \sin(\phi) \left[\tilde{\mathbf{L}}_{2,J}^H(\kappa, x_3, \omega) \tilde{\mathcal{G}}_{J,K}^H(\kappa, x_3, \omega) (\tilde{\mathbf{L}}^H)_{K,1}^{-1}(\kappa, x_3, \omega) \frac{2G^{fr}}{s} \right] (J_1(\kappa r) \\
&\quad - (1 + 2\cos(2\phi)) J_3(\kappa r)) \kappa dk.
\end{aligned} \tag{3.343}$$

For $\tilde{E}_2^{hb_{33}}$, we transform

$$\begin{aligned}
 \tilde{E}_2^{h_{33}^b}(\mathbf{k}_H, x_3, \omega) &= \frac{k_2}{\kappa} \tilde{E}_{norm}^V(\kappa, x_3, \omega) + \frac{jk_1}{\kappa^2} \tilde{E}^H(\kappa, x_3, \omega) \\
 &= \frac{k_2}{\kappa} \tilde{q}_8^V(\kappa, x_3, \omega) + \frac{jk_1}{\kappa^2} \tilde{q}_2^H(\kappa, x_3, \omega) \\
 &= \frac{k_2}{\kappa} \left[\tilde{\mathbf{L}}_{8,J}^V(\kappa, x_3, \omega) \tilde{\mathcal{G}}_{J,K}^V(\kappa, x_3, \omega) (\tilde{\mathbf{L}}^V)_{K,1}^{-1}(\kappa, x_3, \omega) \right] \hat{\mathcal{H}}_{33}^b(\omega),
 \end{aligned} \tag{3.344}$$

to

$$\begin{aligned}
 \hat{E}_2^{h_{33}^b}(\mathbf{x}, \omega) &= \frac{\hat{\mathcal{H}}_{33}^b(\omega)}{2\pi} \int_{\kappa=0}^{\infty} \left[\frac{j\partial_2}{\kappa} \left(\tilde{\mathbf{L}}_{8,J}^V \tilde{\mathcal{G}}_{J,K}^V (\tilde{\mathbf{L}}^V)_{K,1}^{-1} \right) \right] J_0(\kappa r) \kappa d\kappa \\
 &= \frac{\hat{\mathcal{H}}_{33}^b(\omega)}{2\pi} \int_{\kappa=0}^{\infty} \left[-j\sin(\phi) \left(\tilde{\mathbf{L}}_{8,J}^V \tilde{\mathcal{G}}_{J,K}^V (\tilde{\mathbf{L}}^V)_{K,1}^{-1} \right) \right] J_1(\kappa r) \kappa d\kappa.
 \end{aligned} \tag{3.345}$$

For $\tilde{E}_2^{h_{13}^b}$, we transform

$$\begin{aligned}
 \tilde{E}_2^{h_{13}^b}(\mathbf{k}_H, x_3, \omega) &= \frac{k_2}{\kappa} \tilde{E}_{norm}^V(\kappa, x_3, \omega) + \frac{jk_1}{\kappa^2} \tilde{E}^H(\kappa, x_3, \omega) \\
 &= \frac{k_2}{\kappa} \tilde{q}_8^V(\kappa, x_3, \omega) + \frac{jk_1}{\kappa^2} \tilde{q}_2^H(\kappa, x_3, \omega) \\
 &= \frac{k_1 k_2}{\kappa^2} \left[\tilde{\mathbf{L}}_{8,J}^V(\kappa, x_3, \omega) \tilde{\mathcal{G}}_{J,K}^V(\kappa, x_3, \omega) (\tilde{\mathbf{L}}^V)_{K,7}^{-1}(\kappa, x_3, \omega) \right] \left(\hat{\mathcal{H}}_{13}^b(\omega) + \hat{\mathcal{H}}_{31}^b(\omega) \right) \\
 &\quad - \frac{k_1 k_2}{\kappa^2} \left(\tilde{\mathbf{L}}_{2,J}^H(\kappa, x_3, \omega) \tilde{\mathcal{G}}_{J,K}^H(\kappa, x_3, \omega) (\tilde{\mathbf{L}}^H)_{K,1}^{-1}(\kappa, x_3, \omega) \right) \left(\hat{\mathcal{H}}_{13}^b(\omega) + \hat{\mathcal{H}}_{31}^b(\omega) \right),
 \end{aligned} \tag{3.346}$$

to

$$\begin{aligned}
 \hat{E}_2^{h_{13}^b}(\mathbf{x}, \omega) &= \frac{\left(\hat{\mathcal{H}}_{13}^b(\omega) + \hat{\mathcal{H}}_{31}^b(\omega) \right)}{2\pi} \int_{\kappa=0}^{\infty} \left[\frac{-\partial_1 \partial_2}{\kappa^2} \left(\tilde{\mathbf{L}}_{8,J}^V \tilde{\mathcal{G}}_{J,K}^V (\tilde{\mathbf{L}}^V)_{K,7}^{-1} \right) \right. \\
 &\quad \left. + \frac{\partial_1 \partial_2}{\kappa^2} \left(\tilde{\mathbf{L}}_{2,J}^H \tilde{\mathcal{G}}_{J,K}^H (\tilde{\mathbf{L}}^H)_{K,1}^{-1} \right) \right] J_0(\kappa r) \kappa d\kappa \\
 &= \frac{\left(\hat{\mathcal{H}}_{13}^b(\omega) + \hat{\mathcal{H}}_{31}^b(\omega) \right)}{2\pi} \int_{\kappa=0}^{\infty} \left\{ \cos(\phi) \sin(\phi) \left[- \left(\tilde{\mathbf{L}}_{8,J}^V \tilde{\mathcal{G}}_{J,K}^V (\tilde{\mathbf{L}}^V)_{K,7}^{-1} \right) \right. \right. \\
 &\quad \left. \left. + \left(\tilde{\mathbf{L}}_{2,J}^H \tilde{\mathcal{G}}_{J,K}^H (\tilde{\mathbf{L}}^H)_{K,1}^{-1} \right) \right] J_2(\kappa r) \right\} \kappa d\kappa.
 \end{aligned} \tag{3.347}$$

For $\tilde{E}_2^{h_{23}^b}$, we transform

$$\begin{aligned}
\tilde{E}_2^{h^b}(\mathbf{k}_H, x_3, \omega) &= \frac{k_2}{\kappa} \tilde{E}_{norm}^V(\kappa, x_3, \omega) + \frac{jk_1}{\kappa^2} \tilde{E}^H(\kappa, x_3, \omega) \\
&= \frac{k_2}{\kappa} \tilde{q}_8^V(\kappa, x_3, \omega) + \frac{jk_1}{\kappa^2} \tilde{q}_2^H(\kappa, x_3, \omega) \\
&= \frac{k_2^2}{\kappa^2} \left[\tilde{\mathbf{L}}_{8,J}^V(\kappa, x_3, \omega) \tilde{\mathcal{G}}_{J,K}^V(\kappa, x_3, \omega) (\tilde{\mathbf{L}}^V)_{K,7}^{-1}(\kappa, x_3, \omega) \right] \left(\hat{\mathcal{H}}_{23}^b(\omega) + \hat{\mathcal{H}}_{32}^b(\omega) \right) \\
&\quad + \frac{k_1^2}{\kappa^2} \left(\tilde{\mathbf{L}}_{2,J}^H(\kappa, x_3, \omega) \tilde{\mathcal{G}}_{J,K}^H(\kappa, x_3, \omega) (\tilde{\mathbf{L}}^H)_{K,1}^{-1}(\kappa, x_3, \omega) \right) \left(\hat{\mathcal{H}}_{23}^b(\omega) + \hat{\mathcal{H}}_{32}^b(\omega) \right),
\end{aligned} \tag{3.348}$$

to

$$\begin{aligned}
\tilde{E}_2^{h^b}(\mathbf{x}, \omega) &= \frac{\left(\hat{\mathcal{H}}_{23}^b(\omega) + \hat{\mathcal{H}}_{32}^b(\omega) \right)}{2\pi} \int_{\kappa=0}^{\infty} \left[\frac{-\partial_2^2}{\kappa^2} \left(\tilde{\mathbf{L}}_{8,J}^V \tilde{\mathcal{G}}_{J,K}^V (\tilde{\mathbf{L}}^V)_{K,7}^{-1} \right) \right. \\
&\quad \left. - \frac{\partial_1^2}{\kappa^2} \left(\tilde{\mathbf{L}}_{2,J}^H \tilde{\mathcal{G}}_{J,K}^H (\tilde{\mathbf{L}}^H)_{K,1}^{-1} \right) \right] J_0(\kappa r) \kappa d\kappa \\
&= \frac{\left(\hat{\mathcal{H}}_{23}^b(\omega) + \hat{\mathcal{H}}_{32}^b(\omega) \right)}{2\pi} \int_{\kappa=0}^{\infty} \left\{ \frac{1}{2} \left(\tilde{\mathbf{L}}_{8,J}^V \tilde{\mathcal{G}}_{J,K}^V (\tilde{\mathbf{L}}^V)_{K,7}^{-1} \right) (J_0(\kappa r) + \cos(2\phi) J_2(\kappa r)) \right. \\
&\quad \left. + \frac{1}{2} \left(\tilde{\mathbf{L}}_{2,J}^H \tilde{\mathcal{G}}_{J,K}^H (\tilde{\mathbf{L}}^H)_{K,1}^{-1} \right) (J_0(\kappa r) - \cos(2\phi) J_2(\kappa r)) \right\} \kappa d\kappa.
\end{aligned} \tag{3.349}$$

For $\tilde{E}_2^{h^b}$, we transform

$$\begin{aligned}
\tilde{E}_2^{h^b}(\mathbf{k}_H, x_3, \omega) &= \frac{k_2}{\kappa} \tilde{E}_{norm}^V(\kappa, x_3, \omega) + \frac{jk_1}{\kappa^2} \tilde{E}^H(\kappa, x_3, \omega) \\
&= \frac{k_2}{\kappa} \tilde{q}_8^V(\kappa, x_3, \omega) + \frac{jk_1}{\kappa^2} \tilde{q}_2^H(\kappa, x_3, \omega) \\
&= -\frac{jk_1 k_2^2}{\kappa^2} \left[\tilde{\mathbf{L}}_{8,J}^V(\kappa, x_3, \omega) \tilde{\mathcal{G}}_{J,K}^V(\kappa, x_3, \omega) (\tilde{\mathbf{L}}^V)_{K,3}^{-1}(\kappa, x_3, \omega) \right] \left(\frac{2}{s} \left[G^{fr} \hat{\mathcal{H}}_{21}^b(\omega) \right. \right. \\
&\quad \left. \left. + G^{fr} \hat{\mathcal{H}}_{12}^b(\omega) \right] \right) \\
&\quad - \frac{jk_1^3}{\kappa^2} \left[\tilde{\mathbf{L}}_{2,J}^H(\kappa, x_3, \omega) \tilde{\mathcal{G}}_{J,K}^H(\kappa, x_3, \omega) (\tilde{\mathbf{L}}^H)_{K,3}^{-1}(\kappa, x_3, \omega) \right] \\
&\quad \frac{1}{s} \left[G^{fr} \hat{\mathcal{H}}_{21}^b(\omega) + G^{fr} \hat{\mathcal{H}}_{12}^b(\omega) \right] \\
&\quad + \frac{jk_1 k_2^2}{\kappa^2} \left[\tilde{\mathbf{L}}_{2,J}^H(\kappa, x_3, \omega) \tilde{\mathcal{G}}_{J,K}^H(\kappa, x_3, \omega) (\tilde{\mathbf{L}}^H)_{K,3}^{-1}(\kappa, x_3, \omega) \right] \\
&\quad \frac{1}{s} \left[G^{fr} \hat{\mathcal{H}}_{21}^b(\omega) + G^{fr} \hat{\mathcal{H}}_{12}^b(\omega) \right],
\end{aligned} \tag{3.350}$$

to

$$\begin{aligned}
 \hat{E}_2^{Hb}(\mathbf{x}, \omega) &= \frac{(\hat{\mathcal{H}}_{12}^b(\omega) + \hat{\mathcal{H}}_{21}^b(\omega))}{2\pi} \int_{\kappa=0}^{\infty} \left[-\frac{\partial_1 \partial_2^2}{\kappa^2} \left(\tilde{\mathbf{L}}_{8,J}^V \tilde{\mathcal{G}}_{J,K}^V (\tilde{\mathbf{L}}^V)_{K,3}^{-1} \right) \frac{2G^{fr}}{s} \right. \\
 &\quad - \frac{\partial_1^3}{\kappa^2} \left(\tilde{\mathbf{L}}_{2,J}^H \tilde{\mathcal{G}}_{J,K}^H (\tilde{\mathbf{L}}^H)_{K,3}^{-1} \right) \frac{G^{fr}}{s} \\
 &\quad \left. + \frac{\partial_1 \partial_2^2}{\kappa^2} \left(\tilde{\mathbf{L}}_{2,J}^H \tilde{\mathcal{G}}_{J,K}^H (\tilde{\mathbf{L}}^H)_{K,3}^{-1} \right) \frac{G^{fr}}{s} \right] J_0(\kappa r) \kappa d\kappa \\
 &= \frac{(\hat{\mathcal{H}}_{12}^b(\omega) + \hat{\mathcal{H}}_{21}^b(\omega))}{2\pi} \int_{\kappa=0}^{\infty} \left\{ \frac{\kappa}{4} \cos(\phi) \left[- \left(\tilde{\mathbf{L}}_{8,J}^V \tilde{\mathcal{G}}_{J,K}^V (\tilde{\mathbf{L}}^V)_{K,3}^{-1} \right) \frac{2G^{fr}}{s} \right. \right. \\
 &\quad \left. \left. + \left(\tilde{\mathbf{L}}_{2,J}^H \tilde{\mathcal{G}}_{J,K}^H (\tilde{\mathbf{L}}^H)_{K,3}^{-1} \right) \frac{G^{fr}}{s} \right] (J_1(\kappa r) - (1 - 2\cos(2\phi)) J_3(\kappa r)) \right. \\
 &\quad \left. - \frac{\kappa}{4} \cos(\phi) \left(\tilde{\mathbf{L}}_{2,J}^H \tilde{\mathcal{G}}_{J,K}^H (\tilde{\mathbf{L}}^H)_{K,3}^{-1} \right) \frac{G^{fr}}{s} (3J_1(\kappa r) + (1 - 2\cos(2\phi)) J_3(\kappa r)) \right\} \kappa d\kappa.
 \end{aligned} \tag{3.351}$$

v_3^s -type two-way field quantity expressions

We here present the Fourier-Bessel transformations for each source-type for receiver-type v_3^s , by explicitly focusing on the \tilde{v}_3^s fields. By selecting different rows of $\tilde{\mathbf{L}}^{H,V}$, we can obtain the expressions for \tilde{w}_3 , $\tilde{\tau}_{33}^b$, and $-\tilde{p}^f$. In this section, we drop the superscript s , denoting ‘solid’, for notational convenience.

For $\tilde{v}_3^{J_1^e}$, we transform

$$\begin{aligned}
 \tilde{v}_3^{J_1^e}(\mathbf{k}_H, x_3, \omega) &= \tilde{q}_1^V(\kappa, x_3, \omega) \\
 &= \left\{ \frac{-k_1}{\kappa} \left[\tilde{\mathbf{L}}_{1,J}^V(\kappa, x_3, \omega) \tilde{\mathcal{G}}_{J,K}^V(\kappa, x_3, \omega) (\tilde{\mathbf{L}}^V)_{K,4}^{-1}(\kappa, x_3, \omega) \right] \right\} \hat{\mathcal{J}}_1^e(\omega),
 \end{aligned} \tag{3.352}$$

to

$$\begin{aligned}
 \tilde{v}_3^{J_1^e}(\mathbf{x}, \omega) &= \frac{\hat{\mathcal{J}}_1^e(\omega)}{2\pi} \int_{\kappa=0}^{\infty} \left[-\frac{j\partial_1}{\kappa} \left(\tilde{\mathbf{L}}_{1,J}^V \tilde{\mathcal{G}}_{J,K}^V (\tilde{\mathbf{L}}^V)_{K,4}^{-1} \right) \right] J_0(\kappa r) \kappa d\kappa \\
 &= \frac{\hat{\mathcal{J}}_1^e(\omega)}{2\pi} \int_{\kappa=0}^{\infty} \left[\left(\tilde{\mathbf{L}}_{1,J}^V \tilde{\mathcal{G}}_{J,K}^V (\tilde{\mathbf{L}}^V)_{K,4}^{-1} \right) j\cos(\phi) J_1(\kappa r) \right] \kappa d\kappa.
 \end{aligned} \tag{3.353}$$

For $\tilde{v}_3^{J_2^e}$, we transform

$$\begin{aligned}
 \tilde{v}_3^{J_2^e}(\mathbf{k}_H, x_3, \omega) &= \tilde{q}_1^V(\kappa, x_3, \omega) \\
 &= \left\{ \frac{-k_2}{\kappa} \left[\tilde{\mathbf{L}}_{1,J}^V(\kappa, x_3, \omega) \tilde{\mathcal{G}}_{J,K}^V(\kappa, x_3, \omega) (\tilde{\mathbf{L}}^V)_{K,4}^{-1}(\kappa, x_3, \omega) \right] \right\} \hat{\mathcal{J}}_2^e(\omega),
 \end{aligned} \tag{3.354}$$

to

$$\begin{aligned}
 \hat{v}_3^{J_2^e}(\mathbf{x}, \omega) &= \frac{\hat{J}_2^e(\omega)}{2\pi} \int_{\kappa=0}^{\infty} \left[-\frac{j\partial_2}{\kappa^2} \left(\tilde{\mathbf{L}}_{1,J}^V \tilde{\mathcal{G}}_{J,K}^V (\tilde{\mathbf{L}}^V)_{K,4}^{-1} \right) \right] J_0(\kappa r) \kappa d\kappa \\
 &= \frac{\hat{J}_2^e(\omega)}{2\pi} \int_{\kappa=0}^{\infty} \left[j\sin(\phi) \left(\tilde{\mathbf{L}}_{1,J}^V \tilde{\mathcal{G}}_{J,K}^V (\tilde{\mathbf{L}}^V)_{K,4}^{-1} \right) \right] J_1(\kappa r) \kappa d\kappa.
 \end{aligned} \tag{3.355}$$

For $\tilde{v}_3^{J_3^e}$, we transform

$$\begin{aligned}
 \tilde{v}_3^{J_3^e}(\mathbf{k}_H, x_3, \omega) &= \tilde{q}_1^V(\kappa, x_3, \omega) \\
 &= \left[\tilde{\mathbf{L}}_{1,J}^V(\kappa, x_3, \omega) \tilde{\mathcal{G}}_{J,K}^V(\kappa, x_3, \omega) (\tilde{\mathbf{L}}^V)_{K,6}^{-1}(\kappa, x_3, \omega) \right] \left(\frac{\hat{\rho}^E \hat{\mathcal{L}}}{\hat{\epsilon}} \hat{J}_3^e(\omega) \right) \\
 &\quad + \left[\tilde{\mathbf{L}}_{1,J}^V(\kappa, x_3, \omega) \tilde{\mathcal{G}}_{J,K}^V(\kappa, x_3, \omega) (\tilde{\mathbf{L}}^V)_{K,8}^{-1}(\kappa, x_3, \omega) \right] \left(\frac{j\kappa}{s\hat{\epsilon}} \hat{J}_3^e(\omega) \right),
 \end{aligned} \tag{3.356}$$

to

$$\begin{aligned}
 \tilde{v}_3^{J_3^e}(\mathbf{x}, \omega) &= \frac{\hat{J}_3^e(\omega)}{2\pi} \int_{\kappa=0}^{\infty} \left[\left(\tilde{\mathbf{L}}_{1,J}^V \tilde{\mathcal{G}}_{J,K}^V (\tilde{\mathbf{L}}^V)_{K,6}^{-1} \right) \frac{\hat{\rho}^E \hat{\mathcal{L}}}{\hat{\epsilon}} \right. \\
 &\quad \left. + \left(\tilde{\mathbf{L}}_{1,J}^V \tilde{\mathcal{G}}_{J,K}^V (\tilde{\mathbf{L}}^V)_{K,8}^{-1} \right) \frac{j\kappa}{s\hat{\epsilon}} \right] J_0(\kappa r) \kappa d\kappa.
 \end{aligned} \tag{3.357}$$

For $\tilde{v}_3^{J_1^m}$, we transform

$$\begin{aligned}
 \tilde{v}_3^{J_1^m}(\mathbf{k}_H, x_3, \omega) &= \tilde{q}_1^V(\kappa, x_3, \omega) \\
 &= \left\{ \frac{k_2}{\kappa} \left[\tilde{\mathbf{L}}_{1,J}^V(\kappa, x_3, \omega) \tilde{\mathcal{G}}_{J,K}^V(\kappa, x_3, \omega) (\tilde{\mathbf{L}}^V)_{K,8}^{-1}(\kappa, x_3, \omega) \right] \right\} \hat{J}_1^m(\omega),
 \end{aligned} \tag{3.358}$$

to

$$\begin{aligned}
 \hat{v}_3^{J_1^m}(\mathbf{x}, \omega) &= \frac{\hat{J}_1^m(\omega)}{2\pi} \int_{\kappa=0}^{\infty} \left[\frac{j\partial_2}{\kappa} \left(\tilde{\mathbf{L}}_{1,J}^V \tilde{\mathcal{G}}_{J,K}^V (\tilde{\mathbf{L}}^V)_{K,8}^{-1} \right) \right] J_0(\kappa r) \kappa d\kappa \\
 &= \frac{\hat{J}_1^m(\omega)}{2\pi} \int_{\kappa=0}^{\infty} -j\sin(\phi) \left(\tilde{\mathbf{L}}_{1,J}^V \tilde{\mathcal{G}}_{J,K}^V (\tilde{\mathbf{L}}^V)_{K,8}^{-1} \right) J_1(\kappa r) \kappa d\kappa.
 \end{aligned} \tag{3.359}$$

For $\tilde{v}_3^{J_2^m}$, we transform

$$\begin{aligned}\tilde{v}_3^{J_2^m}(\mathbf{k}_H, x_3, \omega) &= \tilde{q}_1^V(\kappa, x_3, \omega) \\ &= \left\{ \frac{-k_1}{\kappa} \left[\tilde{\mathbf{L}}_{1,J}^V(\kappa, x_3, \omega) \tilde{\mathcal{G}}_{J,K}^V(\kappa, x_3, \omega) (\tilde{\mathbf{L}}^V)_{K,8}^{-1}(\kappa, x_3, \omega) \right] \right\} \hat{\mathcal{J}}_2^m(\omega),\end{aligned}\tag{3.360}$$

to

$$\begin{aligned}\tilde{v}_3^{J_2^m}(\mathbf{x}, \omega) &= \frac{\hat{\mathcal{J}}_2^m(\omega)}{2\pi} \int_{\kappa=0}^{\infty} -\frac{j\partial_1}{\kappa} \left(\tilde{\mathbf{L}}_{1,J}^V \tilde{\mathcal{G}}_{J,K}^V (\tilde{\mathbf{L}}^V)_{K,8}^{-1} \right) J_0(\kappa r) \kappa d\kappa \\ &= \frac{\hat{\mathcal{J}}_2^m(\omega)}{2\pi} \int_{\kappa=0}^{\infty} j\cos(\phi) \left(\tilde{\mathbf{L}}_{1,J}^V \tilde{\mathcal{G}}_{J,K}^V (\tilde{\mathbf{L}}^V)_{K,8}^{-1} \right) J_1(\kappa r) \kappa d\kappa.\end{aligned}\tag{3.361}$$

Note that we here do not present the v_3^s response due to a J_3^m source: J_3^m is a pure SHTE source-type. Since v_3^s is purely a PSVTM field-type, we do not need to evaluate this specific source-receiver combination.

For $\tilde{v}_3^{f_1^b}$, we transform

$$\begin{aligned}\tilde{v}_3^{f_1^b}(\mathbf{k}_H, x_3, \omega) &= \tilde{q}_1^V(\kappa, x_3, \omega) \\ &= -\frac{k_1}{\kappa} \left[\tilde{\mathbf{L}}_{1,J}^V(\kappa, x_3, \omega) \tilde{\mathcal{G}}_{J,K}^V(\kappa, x_3, \omega) (\tilde{\mathbf{L}}^V)_{K,3}^{-1}(\kappa, x_3, \omega) \right] \hat{\mathcal{F}}_1^b(\omega),\end{aligned}\tag{3.362}$$

to

$$\begin{aligned}\tilde{v}_3^{f_1^b}(\mathbf{x}, \omega) &= \frac{\hat{\mathcal{F}}_1^b(\omega)}{2\pi} \int_{\kappa=0}^{\infty} \left[-\frac{j\partial_1}{\kappa} \left(\tilde{\mathbf{L}}_{1,J}^V \tilde{\mathcal{G}}_{J,K}^V (\tilde{\mathbf{L}}^V)_{K,3}^{-1} \right) \right] J_0(\kappa r) \kappa d\kappa \\ &= \frac{\hat{\mathcal{F}}_1^b(\omega)}{4\pi} \int_{\kappa=0}^{\infty} j\cos(\phi) \left(\tilde{\mathbf{L}}_{1,J}^V \tilde{\mathcal{G}}_{J,K}^V (\tilde{\mathbf{L}}^V)_{K,3}^{-1} \right) J_1(\kappa r) \kappa d\kappa.\end{aligned}\tag{3.363}$$

For $\tilde{v}_3^{f_1^f}$, we transform

$$\begin{aligned}\tilde{v}_3^{f_1^f}(\mathbf{k}_H, x_3, \omega) &= \tilde{q}_1^V(\kappa, x_3, \omega) \\ &= jk_1 \left[\tilde{\mathbf{L}}_{1,J}^V(\kappa, x_3, \omega) \tilde{\mathcal{G}}_{J,K}^V(\kappa, x_3, \omega) (\tilde{\mathbf{L}}^V)_{K,2}^{-1}(\kappa, x_3, \omega) \left(\frac{1}{s\hat{\rho}^E} \hat{\mathcal{F}}_1^f(\omega) \right) \right] \\ &\quad + \frac{k_1}{\kappa} \left[\tilde{\mathbf{L}}_{1,J}^V(\kappa, x_3, \omega) \tilde{\mathcal{G}}_{J,K}^V(\kappa, x_3, \omega) (\tilde{\mathbf{L}}^V)_{K,3}^{-1}(\kappa, x_3, \omega) \left(\frac{\rho^f}{\hat{\rho}^E} \hat{\mathcal{F}}_1^f(\omega) \right) \right. \\ &\quad \left. - \tilde{\mathbf{L}}_{1,J}^V(\kappa, x_3, \omega) \tilde{\mathcal{G}}_{J,K}^V(\kappa, x_3, \omega) (\tilde{\mathbf{L}}^V)_{K,4}^{-1}(\kappa, x_3, \omega) \left(\hat{\mathcal{L}} \hat{\mathcal{F}}_1^f(\omega) \right) \right],\end{aligned}\tag{3.364}$$

to

$$\begin{aligned}
\hat{v}_3^{f^f}(\mathbf{x}, \omega) &= \frac{\hat{\mathcal{F}}_1^f(\omega)}{2\pi} \int_{\kappa=0}^{\infty} \left[-\partial_1 \left(\tilde{\mathbf{L}}_{1,J}^V \tilde{\mathcal{G}}_{J,K}^V (\tilde{\mathbf{L}}^V)_{K,2}^{-1} \right) \left(\frac{1}{s\hat{\rho}^E} \right) \right. \\
&\quad + \frac{j\partial_1}{\kappa} \left(\tilde{\mathbf{L}}_{1,J}^V(\kappa, x_3, \omega) \tilde{\mathcal{G}}_{J,K}^V(\kappa, x_3, \omega) (\tilde{\mathbf{L}}^V)_{K,3}^{-1}(\kappa, x_3, \omega) \right) \left(\frac{\rho^f}{\hat{\rho}^E} \right) \\
&\quad \left. - \frac{j\partial_1}{\kappa} \left(\tilde{\mathbf{L}}_{1,J}^V \tilde{\mathcal{G}}_{J,K}^V (\tilde{\mathbf{L}}^V)_{K,4}^{-1} \right) \hat{\mathcal{L}} \right] J_0(\kappa r) \kappa d\kappa \\
&= \frac{\hat{\mathcal{F}}_1^b(\omega)}{2\pi} \int_{\kappa=0}^{\infty} \left\{ \kappa \cos(\phi) \left(\tilde{\mathbf{L}}_{1,J}^V \tilde{\mathcal{G}}_{J,K}^V (\tilde{\mathbf{L}}^V)_{K,2}^{-1} \right) \left(\frac{1}{s\hat{\rho}^E} \right) \right. \\
&\quad \left. - j \cos(\phi) \left[\left(\tilde{\mathbf{L}}_{1,J}^V \tilde{\mathcal{G}}_{J,K}^V (\tilde{\mathbf{L}}^V)_{K,3}^{-1} \right) \frac{\rho^f}{\hat{\rho}^E} - \left(\tilde{\mathbf{L}}_{1,J}^V \tilde{\mathcal{G}}_{J,K}^V (\tilde{\mathbf{L}}^V)_{K,4}^{-1} \right) \hat{\mathcal{L}} \right] \right\} J_1(\kappa r) \kappa d\kappa.
\end{aligned} \tag{3.365}$$

For $\tilde{v}_3^{f^b}$, we transform

$$\begin{aligned}
\tilde{v}_3^{f^b}(\mathbf{k}_H, x_3, \omega) &= \tilde{q}_1^V(\kappa, x_3, \omega) \\
&= -\frac{k_2}{\kappa} \left(\tilde{\mathbf{L}}_{1,J}^V(\kappa, x_3, \omega) \tilde{\mathcal{G}}_{J,K}^V(\kappa, x_3, \omega) (\tilde{\mathbf{L}}^V)_{K,3}^{-1}(\kappa, x_3, \omega) \right) \hat{\mathcal{F}}_2^b(\omega),
\end{aligned} \tag{3.366}$$

to

$$\begin{aligned}
\tilde{v}_3^{f^b}(\mathbf{x}, \omega) &= \frac{\hat{\mathcal{F}}_2^b(\omega)}{2\pi} \int_{\kappa=0}^{\infty} \left[-\frac{j\partial_2}{\kappa} \left(\tilde{\mathbf{L}}_{1,J}^V \tilde{\mathcal{G}}_{J,K}^V (\tilde{\mathbf{L}}^V)_{K,3}^{-1} \right) \right] J_0(\kappa r) \kappa d\kappa, \\
&= \frac{\hat{\mathcal{F}}_2^b(\omega)}{4\pi} \int_{\kappa=0}^{\infty} j \sin(\phi) \left(\tilde{\mathbf{L}}_{1,J}^V \tilde{\mathcal{G}}_{J,K}^V (\tilde{\mathbf{L}}^V)_{K,3}^{-1} \right) J_1(\kappa r) \kappa d\kappa.
\end{aligned} \tag{3.367}$$

For $\tilde{v}_3^{f^f}$, we transform

$$\begin{aligned}
\tilde{v}_3^{f^f}(\mathbf{k}_H, x_3, \omega) &= \tilde{q}_1^V(\kappa, x_3, \omega) \\
&= jk_2 \left[\tilde{\mathbf{L}}_{1,J}^V(\kappa, x_3, \omega) \tilde{\mathcal{G}}_{J,K}^V(\kappa, x_3, \omega) (\tilde{\mathbf{L}}^V)_{K,2}^{-1}(\kappa, x_3, \omega) \left(\frac{1}{s\hat{\rho}^E} \hat{\mathcal{F}}_2^f(\omega) \right) \right] \\
&\quad + \frac{k_2}{\kappa} \left[\tilde{\mathbf{L}}_{1,J}^V(\kappa, x_3, \omega) \tilde{\mathcal{G}}_{J,K}^V(\kappa, x_3, \omega) (\tilde{\mathbf{L}}^V)_{K,3}^{-1}(\kappa, x_3, \omega) \left(\frac{\rho^f}{\hat{\rho}^E} \hat{\mathcal{F}}_2^f(\omega) \right) \right. \\
&\quad \left. - \tilde{\mathbf{L}}_{1,J}^V(\kappa, x_3, \omega) \tilde{\mathcal{G}}_{J,K}^V(\kappa, x_3, \omega) (\tilde{\mathbf{L}}^V)_{K,4}^{-1}(\kappa, x_3, \omega) \left(\hat{\mathcal{L}} \hat{\mathcal{F}}_2^f(\omega) \right) \right],
\end{aligned} \tag{3.368}$$

to

$$\begin{aligned}
 \tilde{v}_3^{f^f}(\mathbf{x}, \omega) &= \frac{\hat{\mathcal{F}}_2^f(\omega)}{2\pi} \int_{\kappa=0}^{\infty} \left[-\partial_2 \left(\tilde{\mathbf{L}}_{1,J}^V \tilde{\mathcal{G}}_{J,K}^V (\tilde{\mathbf{L}}^V)_{K,2}^{-1} \right) \left(\frac{1}{s\hat{\rho}^E} \right) \right. \\
 &\quad + \frac{j\partial_2}{\kappa} \left(\tilde{\mathbf{L}}_{1,J}^V \tilde{\mathcal{G}}_{J,K}^V (\tilde{\mathbf{L}}^V)_{K,3}^{-1} \right) \frac{\rho^f}{\hat{\rho}^E} \\
 &\quad \left. - \frac{j\partial_2}{\kappa} \left(\tilde{\mathbf{L}}_{1,J}^V \tilde{\mathcal{G}}_{J,K}^V (\tilde{\mathbf{L}}^V)_{K,4}^{-1} \right) \hat{\mathcal{L}} \right] J_0(\kappa r) \kappa d\kappa \\
 &= \frac{\hat{\mathcal{F}}_2^b(\omega)}{2\pi} \int_{\kappa=0}^{\infty} \left[\kappa \sin(\phi) \left(\tilde{\mathbf{L}}_{1,J}^V \tilde{\mathcal{G}}_{J,K}^V (\tilde{\mathbf{L}}^V)_{K,2}^{-1} \right) \frac{1}{s\hat{\rho}^E} \right. \\
 &\quad - j\sin(\phi) \left(\tilde{\mathbf{L}}_{1,J}^V \tilde{\mathcal{G}}_{J,K}^V (\tilde{\mathbf{L}}^V)_{K,3}^{-1} \right) \frac{\rho^f}{\hat{\rho}^E} \\
 &\quad \left. + j\sin(\phi) \left(\tilde{\mathbf{L}}_{1,J}^V \tilde{\mathcal{G}}_{J,K}^V (\tilde{\mathbf{L}}^V)_{K,4}^{-1} \right) \hat{\mathcal{L}} \right] J_1(\kappa r) \kappa d\kappa.
 \end{aligned} \tag{3.369}$$

For $\tilde{v}_3^{f^b}$, we transform

$$\begin{aligned}
 \tilde{v}_3^{f^b}(\mathbf{k}_H, x_3, \omega) &= \tilde{q}_1^V(\kappa, x_3, \omega) \\
 &= \left[\tilde{\mathbf{L}}_{1,J}^V(\kappa, x_3, \omega) \tilde{\mathcal{G}}_{J,K}^V(\kappa, x_3, \omega) (\tilde{\mathbf{L}}^V)_{K,5}^{-1}(\kappa, x_3, \omega) \right] \left(-\hat{\mathcal{F}}_3^b(\omega) \right),
 \end{aligned} \tag{3.370}$$

to

$$\tilde{v}_3^{f^b}(\mathbf{x}, \omega) = \frac{\hat{\mathcal{F}}_3^b(\omega)}{2\pi} \int_{\kappa=0}^{\infty} - \left(\tilde{\mathbf{L}}_{1,J}^V \tilde{\mathcal{G}}_{J,K}^V (\tilde{\mathbf{L}}^V)_{K,5}^{-1} \right) J_0(\kappa r) \kappa d\kappa. \tag{3.371}$$

For $\tilde{v}_3^{f^f}$, we transform

$$\begin{aligned}
 \tilde{v}_3^{f^f}(\mathbf{k}_H, x_3, \omega) &= \tilde{q}_1^V(\kappa, x_3, \omega) \\
 &= \left[\tilde{\mathbf{L}}_{1,J}^V(\kappa, x_3, \omega) \tilde{\mathcal{G}}_{J,K}^V(\kappa, x_3, \omega) (\tilde{\mathbf{L}}^V)_{K,6}^{-1}(\kappa, x_3, \omega) \right] \left(-\hat{\mathcal{F}}_3^f(\omega) \right),
 \end{aligned} \tag{3.372}$$

to

$$\tilde{v}_3^{f^f}(\mathbf{x}, \omega) = \frac{\hat{\mathcal{F}}_3^f(\omega)}{2\pi} \int_{\kappa=0}^{\infty} - \left(\tilde{\mathbf{L}}_{1,J}^V \tilde{\mathcal{G}}_{J,K}^V (\tilde{\mathbf{L}}^V)_{K,6}^{-1} \right) J_0(\kappa r) \kappa d\kappa. \tag{3.373}$$

For $\tilde{v}_3^{q^i}$, we transform

$$\begin{aligned}\tilde{v}_3^{q^i}(\mathbf{k}_H, x_3, \omega) &= \tilde{q}_1^V(\kappa, x_3, \omega) \\ &= \left[\tilde{\mathbf{L}}_{1,J}^V(\kappa, x_3, \omega) \tilde{\mathcal{G}}_{J,K}^V(\kappa, x_3, \omega) (\tilde{\mathbf{L}}^V)_{K,2}^{-1}(\kappa, x_3, \omega) \right] \left(\hat{\mathcal{Q}}^i(\omega) \right),\end{aligned}\tag{3.374}$$

to

$$\hat{v}_3^{q^i}(\mathbf{x}, \omega) = \frac{\hat{\mathcal{Q}}^i(\omega)}{2\pi} \int_{\kappa=0}^{\infty} \left(\tilde{\mathbf{L}}_{1,J}^V \tilde{\mathcal{G}}_{J,K}^V (\tilde{\mathbf{L}}^V)_{K,2}^{-1} \right) J_0(\kappa r) \kappa d\kappa\tag{3.375}$$

For $\tilde{v}_3^{h^b}$, we transform

$$\begin{aligned}\tilde{v}_3^{h^b}(\mathbf{k}_H, x_3, \omega) &= \tilde{q}_1^V(\kappa, x_3, \omega) \\ &= \left[\tilde{\mathbf{L}}_{1,J}^V(\kappa, x_3, \omega) \tilde{\mathcal{G}}_{J,K}^V(\kappa, x_3, \omega) (\tilde{\mathbf{L}}^V)_{K,1}^{-1}(\kappa, x_3, \omega) \left(\frac{S}{K_c} \right) \right. \\ &\quad \left. + \tilde{\mathbf{L}}_{1,J}^V(\kappa, x_3, \omega) \tilde{\mathcal{G}}_{J,K}^V(\kappa, x_3, \omega) (\tilde{\mathbf{L}}^V)_{K,2}^{-1}(\kappa, x_3, \omega) \left(\frac{C}{M} \left(1 - \frac{S}{K_c} \right) \right) \right] \hat{\mathcal{H}}_{11}^b(\omega) \\ &\quad + \left[\tilde{\mathbf{L}}_{1,J}^V(\kappa, x_3, \omega) \tilde{\mathcal{G}}_{J,K}^V(\kappa, x_3, \omega) (\tilde{\mathbf{L}}^V)_{K,3}^{-1}(\kappa, x_3, \omega) \frac{-2j\kappa G^{fr} S}{s K_c} \right] \hat{\mathcal{H}}_{11}^b(\omega) \\ &\quad - \frac{jk_1^2}{\kappa} \left[\tilde{\mathbf{L}}_{1,J}^V(\kappa, x_3, \omega) \tilde{\mathcal{G}}_{J,K}^V(\kappa, x_3, \omega) (\tilde{\mathbf{L}}^V)_{K,3}^{-1}(\kappa, x_3, \omega) \frac{2G^{fr}}{s} \right] \hat{\mathcal{H}}_{11}^b(\omega),\end{aligned}\tag{3.376}$$

to

$$\begin{aligned}
 \tilde{v}_3^{h_{11}^b}(\mathbf{k}_H, x_3, \omega) &= \frac{\hat{H}_{11}^b(\omega)}{2\pi} \int_{\kappa=0}^{\infty} \left\{ \left(\tilde{\mathbf{L}}_{1,J}^V(\kappa, x_3, \omega) \tilde{\mathcal{G}}_{J,K}^V(\kappa, x_3, \omega) (\tilde{\mathbf{L}}^V)^{-1}_{K,1}(\kappa, x_3, \omega) \right) \left(\frac{S}{K_c} \right) \right. \\
 &\quad + \left(\tilde{\mathbf{L}}_{1,J}^V(\kappa, x_3, \omega) \tilde{\mathcal{G}}_{J,K}^V(\kappa, x_3, \omega) (\tilde{\mathbf{L}}^V)^{-1}_{K,2}(\kappa, x_3, \omega) \right) \left(\frac{C}{M} \left(1 - \frac{S}{K_c} \right) \right) \\
 &\quad + \left(\tilde{\mathbf{L}}_{1,J}^V(\kappa, x_3, \omega) \tilde{\mathcal{G}}_{J,K}^V(\kappa, x_3, \omega) (\tilde{\mathbf{L}}^V)^{-1}_{K,3}(\kappa, x_3, \omega) \right) \frac{-2j\kappa G^{fr} S}{sK_c} \\
 &\quad \left. + \frac{j\partial^2}{\kappa} \left(\tilde{\mathbf{L}}_{1,J}^V(\kappa, x_3, \omega) \tilde{\mathcal{G}}_{J,K}^V(\kappa, x_3, \omega) (\tilde{\mathbf{L}}^V)^{-1}_{K,3}(\kappa, x_3, \omega) \right) \frac{2G^{fr}}{s} \right\} J_0(\kappa r) \kappa d\kappa, \\
 &= \frac{\hat{H}_{11}^b(\omega)}{2\pi} \int_{\kappa=0}^{\infty} \left\{ \left[\left(\tilde{\mathbf{L}}_{1,J}^V(\kappa, x_3, \omega) \tilde{\mathcal{G}}_{J,K}^V(\kappa, x_3, \omega) (\tilde{\mathbf{L}}^V)^{-1}_{K,1}(\kappa, x_3, \omega) \right) \left(\frac{S}{K_c} \right) \right. \right. \\
 &\quad + \left(\tilde{\mathbf{L}}_{1,J}^V(\kappa, x_3, \omega) \tilde{\mathcal{G}}_{J,K}^V(\kappa, x_3, \omega) (\tilde{\mathbf{L}}^V)^{-1}_{K,2}(\kappa, x_3, \omega) \right) \left(\frac{C}{M} \left(1 - \frac{S}{K_c} \right) \right) \\
 &\quad \left. + \left(\tilde{\mathbf{L}}_{1,J}^V(\kappa, x_3, \omega) \tilde{\mathcal{G}}_{J,K}^V(\kappa, x_3, \omega) (\tilde{\mathbf{L}}^V)^{-1}_{K,3}(\kappa, x_3, \omega) \right) \frac{-2j\kappa G^{fr} S}{sK_c} \right] J_0(\kappa r) \\
 &\quad - \frac{j\kappa}{2} \left(\tilde{\mathbf{L}}_{1,J}^V(\kappa, x_3, \omega) \tilde{\mathcal{G}}_{J,K}^V(\kappa, x_3, \omega) (\tilde{\mathbf{L}}^V)^{-1}_{K,3}(\kappa, x_3, \omega) \right) \frac{2G^{fr}}{s} \\
 &\quad \left. \left(J_0(\kappa r) - \cos(2\phi) J_2(\kappa r) \right) \right\} \kappa d\kappa.
 \end{aligned} \tag{3.377}$$

For $\tilde{v}_3^{h_{22}^b}$, we transform

$$\begin{aligned}
 \tilde{v}_3^{h_{22}^b}(\mathbf{k}_H, x_3, \omega) &= \tilde{q}_1^V(\kappa, x_3, \omega) \\
 &= \left[\tilde{\mathbf{L}}_{1,J}^V(\kappa, x_3, \omega) \tilde{\mathcal{G}}_{J,K}^V(\kappa, x_3, \omega) (\tilde{\mathbf{L}}^V)^{-1}_{K,1}(\kappa, x_3, \omega) \left(\frac{S}{K_c} \right) \right. \\
 &\quad \left. + \tilde{\mathbf{L}}_{1,J}^V(\kappa, x_3, \omega) \tilde{\mathcal{G}}_{J,K}^V(\kappa, x_3, \omega) (\tilde{\mathbf{L}}^V)^{-1}_{K,2}(\kappa, x_3, \omega) \left(\frac{C}{M} \left(1 - \frac{S}{K_c} \right) \right) \right] \hat{H}_{22}^b(\omega) \\
 &\quad + \left[\tilde{\mathbf{L}}_{1,J}^V(\kappa, x_3, \omega) \tilde{\mathcal{G}}_{J,K}^V(\kappa, x_3, \omega) (\tilde{\mathbf{L}}^V)^{-1}_{K,3}(\kappa, x_3, \omega) \frac{-2j\kappa G^{fr} S}{sK_c} \right] \hat{H}_{22}^b(\omega) \\
 &\quad - \frac{jk_2^2}{\kappa} \left[\tilde{\mathbf{L}}_{1,J}^V(\kappa, x_3, \omega) \tilde{\mathcal{G}}_{J,K}^V(\kappa, x_3, \omega) (\tilde{\mathbf{L}}^V)^{-1}_{K,3}(\kappa, x_3, \omega) \frac{2G^{fr}}{s} \right] \hat{H}_{22}^b(\omega),
 \end{aligned} \tag{3.378}$$

to

$$\begin{aligned}
\tilde{v}_3^{h^b_{22}}(\mathbf{k}_H, x_3, \omega) &= \frac{\hat{h}_{22}^b(\omega)}{2\pi} \int_{\kappa=0}^{\infty} \left[\left(\tilde{\mathbf{L}}_{1,J}^V(\kappa, x_3, \omega) \tilde{\mathcal{G}}_{J,K}^V(\kappa, x_3, \omega) (\tilde{\mathbf{L}}^V)_{K,1}^{-1}(\kappa, x_3, \omega) \right) \left(\frac{S}{K_c} \right) \right. \\
&\quad + \left(\tilde{\mathbf{L}}_{1,J}^V(\kappa, x_3, \omega) \tilde{\mathcal{G}}_{J,K}^V(\kappa, x_3, \omega) (\tilde{\mathbf{L}}^V)_{K,2}^{-1}(\kappa, x_3, \omega) \right) \left(\frac{C}{M} \left(1 - \frac{S}{K_c} \right) \right) \\
&\quad + \left(\tilde{\mathbf{L}}_{1,J}^V(\kappa, x_3, \omega) \tilde{\mathcal{G}}_{J,K}^V(\kappa, x_3, \omega) (\tilde{\mathbf{L}}^V)_{K,3}^{-1}(\kappa, x_3, \omega) \right) \frac{-2j\kappa G^{fr} S}{sK_c} \\
&\quad \left. + \frac{j\partial_2^2}{\kappa} \left(\tilde{\mathbf{L}}_{1,J}^V(\kappa, x_3, \omega) \tilde{\mathcal{G}}_{J,K}^V(\kappa, x_3, \omega) (\tilde{\mathbf{L}}^V)_{K,3}^{-1}(\kappa, x_3, \omega) \frac{2G^{fr}}{s} \right) \right] J_0(\kappa r) \kappa d\kappa \\
&= \frac{\hat{h}_{22}^b(\omega)}{2\pi} \int_{\kappa=0}^{\infty} \left\{ \left[\left(\tilde{\mathbf{L}}_{1,J}^V(\kappa, x_3, \omega) \tilde{\mathcal{G}}_{J,K}^V(\kappa, x_3, \omega) (\tilde{\mathbf{L}}^V)_{K,1}^{-1}(\kappa, x_3, \omega) \right) \left(\frac{S}{K_c} \right) \right. \right. \\
&\quad + \left(\tilde{\mathbf{L}}_{1,J}^V(\kappa, x_3, \omega) \tilde{\mathcal{G}}_{J,K}^V(\kappa, x_3, \omega) (\tilde{\mathbf{L}}^V)_{K,2}^{-1}(\kappa, x_3, \omega) \right) \left(\frac{C}{M} \left(1 - \frac{S}{K_c} \right) \right) \\
&\quad + \left(\tilde{\mathbf{L}}_{1,J}^V(\kappa, x_3, \omega) \tilde{\mathcal{G}}_{J,K}^V(\kappa, x_3, \omega) (\tilde{\mathbf{L}}^V)_{K,3}^{-1}(\kappa, x_3, \omega) \right) \frac{-2j\kappa G^{fr} S}{sK_c} \left. \right] J_0(\kappa r) \\
&\quad \left. - \frac{j\kappa}{2} \left(\tilde{\mathbf{L}}_{1,J}^V(\kappa, x_3, \omega) \tilde{\mathcal{G}}_{J,K}^V(\kappa, x_3, \omega) (\tilde{\mathbf{L}}^V)_{K,3}^{-1}(\kappa, x_3, \omega) \frac{2G^{fr}}{s} \right) \right. \\
&\quad \left. (J_0(\kappa r) + \cos(2\phi)J_2(\kappa r)) \right\} \kappa d\kappa.
\end{aligned} \tag{3.379}$$

For $\tilde{v}_3^{h^b_{33}}$, we transform

$$\begin{aligned}
\tilde{v}_3^{h^b_{33}}(\mathbf{k}_H, x_3, \omega) &= \hat{q}_1^V(\kappa, x_3, \omega) \\
&= \left[\tilde{\mathbf{L}}_{1,J}^V(\kappa, x_3, \omega) \tilde{\mathcal{G}}_{J,K}^V(\kappa, x_3, \omega) (\tilde{\mathbf{L}}^V)_{K,1}^{-1}(\kappa, x_3, \omega) \right] \hat{h}_{33}^b(\omega),
\end{aligned} \tag{3.380}$$

to

$$\tilde{v}_3^{h^b_{33}}(\mathbf{x}, \omega) = \frac{\hat{h}_{33}^b(\omega)}{2\pi} \int_{\kappa=0}^{\infty} \left(\tilde{\mathbf{L}}_{1,J}^V \tilde{\mathcal{G}}_{J,K}^V (\tilde{\mathbf{L}}^V)_{K,1}^{-1} \right) J_0(\kappa r) \kappa d\kappa. \tag{3.381}$$

For $\tilde{v}_3^{h^b_{13}}$, we transform

$$\begin{aligned}
\tilde{v}_3^{h^b_{13}}(\mathbf{k}_H, x_3, \omega) &= \hat{q}_1^V(\kappa, x_3, \omega) \\
&= \frac{k_1}{\kappa} \left[\tilde{\mathbf{L}}_{1,J}^V(\kappa, x_3, \omega) \tilde{\mathcal{G}}_{J,K}^V(\kappa, x_3, \omega) (\tilde{\mathbf{L}}^V)_{K,7}^{-1}(\kappa, x_3, \omega) \right] \left(\hat{h}_{13}^b(\omega) + \hat{h}_{31}^b(\omega) \right),
\end{aligned} \tag{3.382}$$

to

$$\begin{aligned}
 \hat{v}_3^{h^b_{13}}(\mathbf{x}, \omega) &= \frac{(\hat{\mathcal{H}}_{13}^b(\omega) + \hat{\mathcal{H}}_{31}^b(\omega))}{2\pi} \int_{\kappa=0}^{\infty} \frac{j\partial_1}{\kappa} \left(\tilde{\mathbf{L}}_{1,J}^V \tilde{\mathcal{G}}_{J,K}^V (\tilde{\mathbf{L}}^V)_{K,7}^{-1} \right) J_0(\kappa r) \kappa d\kappa \\
 &= \frac{(\hat{\mathcal{H}}_{13}^b(\omega) + \hat{\mathcal{H}}_{31}^b(\omega))}{2\pi} \int_{\kappa=0}^{\infty} -j\cos(\phi) \left(\tilde{\mathbf{L}}_{1,J}^V \tilde{\mathcal{G}}_{J,K}^V (\tilde{\mathbf{L}}^V)_{K,7}^{-1} \right) J_1(\kappa r) \kappa d\kappa.
 \end{aligned} \tag{3.383}$$

For $\tilde{v}_3^{h^b_{23}}$, we transform

$$\begin{aligned}
 \tilde{v}_3^{h^b_{23}}(\mathbf{k}_H, x_3, \omega) &= \tilde{q}_1^V(\kappa, x_3, \omega) \\
 &= \frac{k_2}{\kappa} \left[\tilde{\mathbf{L}}_{1,J}^V(\kappa, x_3, \omega) \tilde{\mathcal{G}}_{J,K}^V(\kappa, x_3, \omega) (\tilde{\mathbf{L}}^V)_{K,7}^{-1}(\kappa, x_3, \omega) \right] \left(\hat{\mathcal{H}}_{23}^b(\omega) + \hat{\mathcal{H}}_{32}^b(\omega) \right),
 \end{aligned} \tag{3.384}$$

to

$$\begin{aligned}
 \hat{v}_3^{h^b_{23}}(\mathbf{x}, \omega) &= \frac{(\hat{\mathcal{H}}_{23}^b(\omega) + \hat{\mathcal{H}}_{32}^b(\omega))}{2\pi} \int_{\kappa=0}^{\infty} \frac{j\partial_2}{\kappa} \left(\tilde{\mathbf{L}}_{1,J}^V \tilde{\mathcal{G}}_{J,K}^V (\tilde{\mathbf{L}}^V)_{K,7}^{-1} \right) J_0(\kappa r) \kappa d\kappa \\
 &= \frac{(\hat{\mathcal{H}}_{23}^b(\omega) + \hat{\mathcal{H}}_{32}^b(\omega))}{2\pi} \int_{\kappa=0}^{\infty} -j\sin(\phi) \left(\tilde{\mathbf{L}}_{1,J}^V \tilde{\mathcal{G}}_{J,K}^V (\tilde{\mathbf{L}}^V)_{K,7}^{-1} \right) J_1(\kappa r) \kappa d\kappa.
 \end{aligned} \tag{3.385}$$

For $\tilde{v}_3^{h^b_{12}}$, we transform

$$\begin{aligned}
 \tilde{v}_3^{h^b_{12}}(\mathbf{k}_H, x_3, \omega) &= \tilde{q}_1^V(\kappa, x_3, \omega) \\
 &= -\frac{jk_1 k_2}{\kappa} \left[\tilde{\mathbf{L}}_{1,J}^V(\kappa, x_3, \omega) \tilde{\mathcal{G}}_{J,K}^V(\kappa, x_3, \omega) (\tilde{\mathbf{L}}^V)_{K,3}^{-1}(\kappa, x_3, \omega) \right] \left(\frac{2}{s} \left[G^{fr} \hat{\mathcal{H}}_{21}^b(\omega) \right. \right. \\
 &\quad \left. \left. + G^{fr} \hat{\mathcal{H}}_{12}^b(\omega) \right] \right),
 \end{aligned} \tag{3.386}$$

to

$$\begin{aligned}
 \hat{v}_3^{h^b_{12}}(\mathbf{x}, \omega) &= \frac{(\hat{\mathcal{H}}_{12}^b(\omega) + \hat{\mathcal{H}}_{21}^b(\omega))}{2\pi} \int_{\kappa=0}^{\infty} \frac{j\partial_1 \partial_2}{\kappa} \left(\tilde{\mathbf{L}}_{1,J}^V \tilde{\mathcal{G}}_{J,K}^V (\tilde{\mathbf{L}}^V)_{K,3}^{-1} \right) \frac{2G^{fr}}{s} J_0(\kappa r) \kappa d\kappa \\
 &= \frac{(\hat{\mathcal{H}}_{12}^b(\omega) + \hat{\mathcal{H}}_{21}^b(\omega))}{2\pi} \int_{\kappa=0}^{\infty} j\kappa \cos(\phi) \sin(\phi) \left(\tilde{\mathbf{L}}_{1,J}^V \tilde{\mathcal{G}}_{J,K}^V (\tilde{\mathbf{L}}^V)_{K,3}^{-1} \right) \frac{2G^{fr}}{s} J_2(\kappa r) \kappa d\kappa.
 \end{aligned} \tag{3.387}$$

3.4 2D and 3D numerical modeling with ESSEMOD

Based on the previous presented theory, we have developed an analytically-based, numerical modeling code for modeling all electromagneto-seismic and seismo-electromagnetic source-receiver combinations in layered-Earth geometries. We have named our modeling code ‘ESSEMOD’, which stands for Electromagneto-Seismic and Seismo-Electromagnetic MODELing. Our seismo-EM layer-code is developed in a combined Fortran / C language, and compatible with the ‘Seismic Unix’ parameter interface. The code can model both 2D and 3D situations, in 1D layered-Earth geometries. In 2D, the SH-TE and P-SV-TM propagation modes are naturally decoupled (see e.g. [Grobbe *et al.* \(2016b\)](#)). We use a 1D spatial inverse Fourier transformation to transform the data from the horizontal wavenumber-frequency domain to the space-frequency domain. Care must be taken that proper spatial sampling occurs in the 2D modeling, such that aliasing, and effects due to the periodicity related to the discrete inverse fast Fourier transformation, are avoided ([Bracewell, 2000](#)). In 3D, the two propagation modes need to be combined, as discussed earlier. We use the presented Fourier-Bessel transformations to transform the data from the horizontal wavenumber-frequency domain to the space-frequency domain. Proper radial distance-radial wavenumber sampling needs to occur in this case, such that the Bessel functions damp out sufficiently and the data is correctly transformed to the space-frequency domain.

Chapter 4

The model: Numerical results of seismo-EM layer-code modeling

4.1 Numerical tests with different eigenvector setsⁱ

In this section we present the numerical results of seismo-electromagnetic layered-Earth modeling, using different eigenvector sets. For our tests, we use our layer-code ESSEMOD. First, we focus on the numerical stability of each of the eigenvector sets. We investigate both the stability and internal consistency of the eigenvector sets using two different tests:

1. A numerical stability analysis based on the fact that the combination of system matrix, eigenvectors and eigenvalues should yield a zero result.
2. A numerical stability test of the flux-normalized eigenvector systems by investigating the preciseness and correctness of using the transpose of the submatrices as its inverse.

We use $N_t = 2048$ time-samples with a time-sampling step of $\Delta t = 0.001$ s. We use the same, two-halfspace model for all numerical stability tests, consisting of halfspace (medium) A over halfspace (medium) B. The relevant model parameters are specified in Table 4.1. Note that velocity ranges (the real parts of the complex velocities) are displayed in Table 4.1 for the bandwidth under consideration. We use a Ricker wavelet with a peak frequency of 30 Hz and a peak amplitude of $1 \cdot 10^9$ N/m³. The source is located at $x_3 = 100$ m and the receivers are placed at $x_3 = 770$ m depth. The subsurface contains one interface, at $x_3 = 1000$ m depth, such that both coseismic / coelectric fields as well as interface response fields (or seismo-electromagnetic conversion) are generated. In the appendices, we present radial wavenumber-radial frequency (κ - ω) images for each submatrix element, corresponding to certain row-column combinations of the consistency and stability checks.

ⁱThis section is part of the journal paper published in *Geophysical Journal International* doi: 10.1093/gji/ggw128 (Grobbe *et al.*, 2016a). Note that minor changes have been introduced to make the text consistent with the other chapters of this thesis.

Table 4.1: Overview of the velocities in [m/s], (static) coupling coefficients in [$m^2 \cdot s \cdot V^{-1}$], and porosity [-] values for each of the different media. To illustrate the frequency-dependency of certain wave/field-types, velocity ranges (the real parts of the complex velocities) are displayed for the bandwidth under consideration, presenting the values for the lowest and highest frequency. Note that the EM-velocities are proportional to the square-root of frequency.

Phys. quantity	Medium A	Medium B	Medium C	Medium D
P_f -vel. [m/s]	3159.81-3159.84	3153.67-3153.68	3145.83-3145.84	4388.43-4388.43
P_s -vel. [m/s]	2.89-92.96	3.98-131.09	3.92-129.12	3.12-4.25
S -vel. [m/s]	2110.79-2110.87	1952.83-1953.03	1959.91-1960.09	1825.74-1825.74
EM -vel. [m/s]	$31796.34-1.01 \cdot 10^6$	$4496.68-1.42 \cdot 10^5$	$4388.31-1.39 \cdot 10^5$	$1.0 \cdot 10^7-2.84 \cdot 10^7$
$\hat{\mathcal{L}}_0$ [m^2s/V]	$9.07 \cdot 10^{-9}$	$2.08 \cdot 10^{-9}$	$2.18 \cdot 10^{-9}$	$9.07 \cdot 10^{-14}$
ϕ [-]	0.4	0.2	0.21	$4 \cdot 10^{-6}$

Next, we investigate what impact the different numerical stabilities have on the modeling results. We start with a validating comparison between the Haartsen and Pride (1997)-based particle velocity normalized eigenvector set (referred to as the ‘HP’ set), the Haartsen and Pride (1997)-based flux-normalized eigenvector set (referred to as the ‘HPF’ set) and our flux-normalized eigenvector set (referred to as the ‘GST’ set) is made. We use the same model as for the numerical stability tests and prove that all eigenvector sets yield similar results for this model under consideration.

We also consider the special case scenario for this model, where the seismo-electromagnetic coupling coefficient $\hat{\mathcal{L}}$ is chosen equal to zero, resulting in a decoupling of the poroelastic and the electromagnetic parts of the seismo-electromagnetic system. In other words, in this case purely poroelastic and purely electromagnetic systems are modeled, without coupling between electromagnetic and mechanical fields. We investigate the differences between the HPF set and the GST set, for both a purely poroelastic wavefield and a purely electromagnetic field.

We finalize by presenting the results for two different models, that demonstrate the true impact of these numerical stability issues, and issues with low coupling coefficients, on the seismo-electromagnetic modeling results.

4.1.1 Numerical Stability

We now test the different eigenvector sets on their numerical stability and consistency. To this end, we carry out two different tests: a system consistency test and a flux-normalization identity test. We display the results of these checks for each individual submatrix element, for all radial wavenumber-frequency combinations in Appendices 4.1.A-4.1.E, where Appendices 4.1.A-4.1.C display the results of the system consistency tests and Appendices 4.1.D and 4.1.E present the results of the flux-normalization identity tests. Theoretically, all plots should present a zero-value. The computations are carried out in double precision with 15-17 significant decimal places. The results are plotted on a logarithmic scale, running from 10^{-6} to 10^{-22} . We define 10^{-6} as our absolute threshold-value, where values greater than this threshold are considered to be unacceptable errors (not anymore below numerical precision).

System Consistency Tests

To check the numerical consistency and stability of the seismo-electromagnetic systems under consideration, we investigate a modified version of equation (2.148)

$$\tilde{\mathbf{A}}^{H,V} \tilde{\mathbf{L}}^{H,V} - \tilde{\mathbf{L}}^{H,V} \tilde{\mathbf{A}}_1^{H,V} = 0. \quad (4.1)$$

Since the system matrix $\tilde{\mathbf{A}}^{H,V}$ is anti-diagonal we can carry-out this check per submatrix. This yields two independent equations that can be used to check the system matrix, eigenvector, and eigenvalue inter-consistency and accuracy:

$$\tilde{\mathbf{A}}_{12}^{H,V} \tilde{\mathbf{L}}_2^{H,V} + \tilde{\mathbf{L}}_1^{H,V} \tilde{\mathbf{A}}^{H,V} = 0, \quad (4.2)$$

$$\tilde{\mathbf{A}}_{21}^{H,V} \tilde{\mathbf{L}}_1^{H,V} + \tilde{\mathbf{L}}_2^{H,V} \tilde{\mathbf{A}}^{H,V} = 0. \quad (4.3)$$

The results of equations (4.2) and (4.3) are referred to as H1 and H2 (for the SH-TE system), respectively, and as V1 and V2 (for the P-SV-TM system), respectively.

Let us first focus on the SH-TE system. We can observe that for the GST set (Figures 4.9 and 4.10), the diagonal elements (1,1) and (2,2) of the H2 system (Figures 4.10(a) and 4.10(d)) have the largest error. However, all deviations from the expected zero-value result are around the acceptable order of 10^{-10} . This means that the observed variations in deviation from zero are displaying the numerical noise levels.

When we look at the results from the HP set (Figures 4.13 and 4.14), we observe that H1 element (2,2) (Figures 4.13(d)) and H2 elements (1,1), (1,2) and (2,2) (Figures 4.10(a), 4.10(b) and 4.10(d), respectively) all have values in the order of 10^{-6} or more, where H2 elements (1,2) and (2,2) (Figures 4.10(b) and 4.10(d)) show values in the order of 10^4 and 10^3 , respectively.

When we then look at the flux-normalized version of this eigenvector set, HPF (Figures 4.17 and 4.18), we can clearly see that the values have decreased significantly. Except H2 element (1,2) (Figure 4.18(b)), which shows a value in the order of 10^{-7} , all elements have values of 10^{-10} or smaller. The way the eigenvectors are normalized plays an important role in the numerical precision and stability of modeling seismo-electromagnetic phenomena. The GST eigenvector set is shown to perform numerically stable for all elements.

Next, we take a closer look at the numerical consistency of the P-SV-TM system. Again, we start by looking at the results of the GST set, displayed in Figures 4.11 and 4.12. Most of the elements of both the V1 and V2 systems show values in the order of the numerical noise levels. There is only one visible outlier: V1 element (4,3) (Figures 4.11(o)) with a value in the order of 10^{-8} , but it is still below the threshold of 10^{-6} . This error level is mainly caused due to ‘spikes’ that occur at specific wavenumber-frequency combinations (e.g. around $\kappa = 0.3 \text{ m}^{-1}$ at 100Hz). This is visible as the red ‘peak’ slope in element (4,3) of Figure 4.11(o).

Looking at the results from eigenvector set HP (Figures 4.15 and 4.16), we can clearly observe larger errors, in multiple elements: V1 elements (2,4) (Figures 4.15(h)), (3,1)-(3,4) (Figures 4.15(i)-4.15(l)), (4,2) (Figures 4.15(n)) and (4,4) (Figures 4.15(p)) and V2 elements (1,1)-(1,4) (Figures 4.16(a)-4.16(d)), (2,1)-(2,4) (Figures 4.16(e)-4.16(h)), (4,1) (Figures 4.16(m)), (4,3) (Figures 4.16(o)) and (4,4)

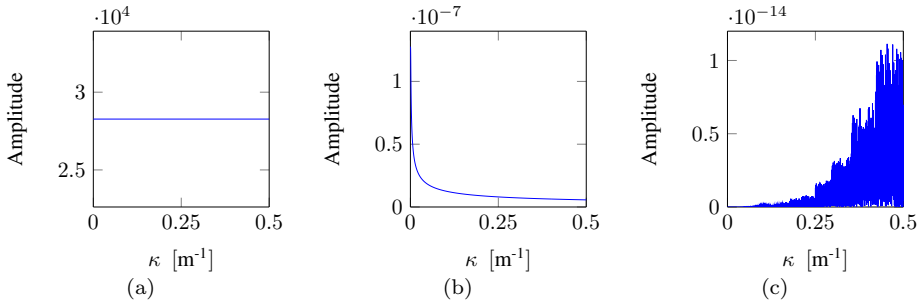


Figure 4.1: *H2* system check, for submatrix element (1,2), plotted for 100 Hz as a function of radial wavenumber κ . (a) HP eigenvector set (b) HPF eigenvector set (c) GST eigenvector set

(Figures 4.16(p)). Some of the elements again show huge deviations from the theoretically expected zero-value, resulting in unacceptable error levels (in the order of $1 \cdot 10^{-6}$ or higher).

When flux-normalizing this eigenvector set, resulting in the HPF set, we can again observe a significant improvement in numerical consistency and stability. Now, only 4 elements show a significant error: V1 element (3,4) (Figures 4.19(i)) (order 10^{-8}) and V2 elements (2,1), (2,3) and (2,4) (Figures 4.20(e), 4.20(g) and 4.20(h)). Again, flux-normalizing the eigenvector sets is proven to stabilize the numerical results and improve numerical accuracy. In addition, it is again shown that the GST set overall results in the best numerical stability and precision. The numerical consistency errors of the HP and HPF may have implications on finding small amplitude signals when there are also strong signals in the data. The HP and HPF sets may generate disturbing numerical noise that partially masks the small amplitude events (for example interface response fields) that can be correctly modeled with the more stable and precise GST set.

Figure 4.1 displays the system consistency results for element (1,2) of the *H2* system, for the HP, HPF and GST eigenvector sets (corresponding to Figures 4.1a, 4.1b, and 4.1c, respectively), for a single frequency of 100 Hz as a function of radial wavenumber. These plots provide clear insight in the numerical variations with different wavenumbers. We can clearly observe that the GST set is numerically consistent for this element, the HP set shows unacceptable error levels and the flux-normalizing this HP set results in slightly better consistency, but still less than the GST set.

Flux-Normalization Identity Tests

Now that we have shown that power flux-normalizing the eigenvector sets improves numerical stability/precision and internal system consistency, we focus with our second test only on the power-flux normalized eigenvector sets HPF and GST. We know that for flux-normalized systems, we can express the inverse of the composition matrix in terms of the transposes of the composition submatrices (see for example

equation (2.168)). We make use of this knowledge to carry out the following two numerical checks

$$2 \left\{ \tilde{\mathbf{L}}_2^{H,V} \right\}^t \tilde{\mathbf{L}}_1^{H,V} - \tilde{\mathbf{I}}^{H,V} = 0, \quad (4.4)$$

$$2 \left\{ \tilde{\mathbf{L}}_1^{H,V} \right\}^t \tilde{\mathbf{L}}_2^{H,V} - \tilde{\mathbf{I}}^{H,V} = 0. \quad (4.5)$$

The results of equation (4.4) will be again referred to as H1 and V1 for the SH-TE and P-SV-TM modes, respectively. Similarly, the results of equation (4.5) will be referred to as H2 and V2 for the SH-TE and P-SV-TM systems, respectively.

We start again with the SH-TE system. Figures 4.21 and 4.22 show that for the GST set, all elements have values less than 10^{-15} , which is beyond numerical precision and hence only displays numerical noise.

For the HPF set, displayed in Figures 4.25 and 4.26, we can observe that all elements still show acceptable error levels. However, the maximum values are now in the order of 10^{-10} , slightly higher than the GST set. We can nevertheless conclude that for both flux-normalized eigenvector sets, we can correctly use the transpose of the composition submatrices as an inverse. Another observation is the fact that the matrix of elements of the figures corresponding to H1, Figures 4.21 and 4.25, are the transpose of the matrix of elements of the Figures 4.22 and 4.26 corresponding to H2, for both the GST and HPF sets.

Let us now look at the P-SV-TM propagation mode. The results for the GST set are presented in Figures 4.23 and 4.24. We can observe that most of the elements have values below or around numerical precision. There are a few elements that display slightly higher values: elements (3,4) and (4,3) for V1 (Figures 4.23(l) and 4.23(o)) (having values in the order of 10^{-7} and 10^{-8} , respectively) and for V2 the elements (3,4) and (4,3) (Figures 4.24(l) and 4.24(o)) (but now having values the other way around; in the order of 10^{-8} and 10^{-7} , respectively). So once again, the figures of V1 and V2 are each others transpose. The value in the order of 10^{-7} is caused mainly due to the spike around $\kappa = 0.3$ for 100 Hz. In contrast, looking at the results for the HPF set (Figures 4.27 and 4.28), we can observe that element (3,4) in V1 (Figure 4.27(l)) and hence (4,3) in V2 (Figure 4.28(o)) have lower values compared to the ones for the GST eigenvector set for these elements. However, other elements, for example element (1,4) (Figure 4.27(d)) and (2,4) (Figure 4.27(h)) in V1 (and hence (4,1) (Figure 4.28(m)) and (4,2) (Figure 4.28(n)) for V2) display larger values than for the GST set and element (4,3) of V1 (Figure 4.27(o)) and hence (3,4) of V2 (Figure 4.28(o)) for V2 have similar values as the GST set. In conclusion, both flux-normalized eigenvector sets perform also well enough for the P-SV-TM mode when using the transpose of the composition submatrices as an inverse. The GST and HPF sets result in larger and smaller values for different elements. Overall, the GST eigenvector set seems to be slightly more stable for the P-SV-TM mode than the HPF set, but both sets yield acceptable results.

A clear example can be seen in Figure 4.2, displaying the flux-normalization identity checks for all radial wavenumbers for a single frequency of 100 Hz. Figure 4.2(a) displays the results of the HPF set, Figure 4.2(b) of the GST set. We can observe that the GST set results in random deviations from zero in the order of 10^{-18} ,

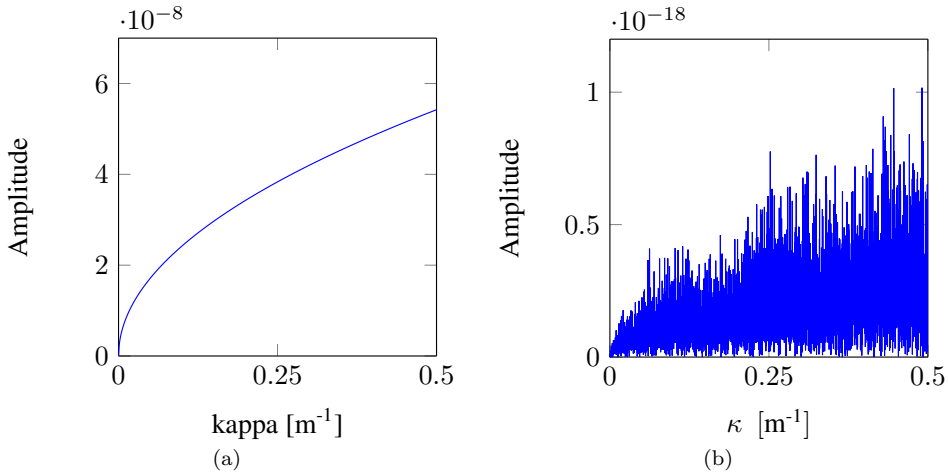


Figure 4.2: V_2 identity check, for submatrix element (4,2), plotted for 100 Hz as a function of radial wavenumber κ . (a) HPF eigenvector set (b) GST eigenvector set

which is around numerical precision. In contrast, the HPF set shows correlated deviations in the order of 10^{-8} , which might still be acceptable but is obviously numerically less stable and precise.

4.1.2 Implications for the Seismo-Electromagnetic Modeling Results

Validating Comparisons between the Three Eigenvector Sets

We here compare the seismo-electromagnetic modeling results of layer-code modeling for an electric field component in the x_1 -direction, generated by a seismic dipole bulk force source in the x_1 -direction, for the model under consideration. We compare the results of using the HPF set (Figure 4.3(a)), the HP set (Figure 4.3(b)) and the GST set (Figure 4.3(c)). Using the logarithmic plotting scale, we can clearly observe the different seismo-electromagnetic events and we can observe that there is a perfect match between the three eigenvector sets in both phase and amplitude for all events. The logarithmic scale displays the base-10 logarithm of the absolute value of the data. To illustrate this further, a plot showing a trace-overlay between the HPF set (black-dashed), the HP set (blue-dotted) and the GST set (red solid) is presented in Figure 4.3(c). However, differences in the numerical noise levels are visible (e.g. the noise for $t > 0.7$ s). The HP and HPF sets display higher numerical noise levels than the GST eigenvector set. This is an indicator for differences in numerical stability for the different eigenvector sets.

These numerical results serve as a validation for each of the individual eigenvector sets.

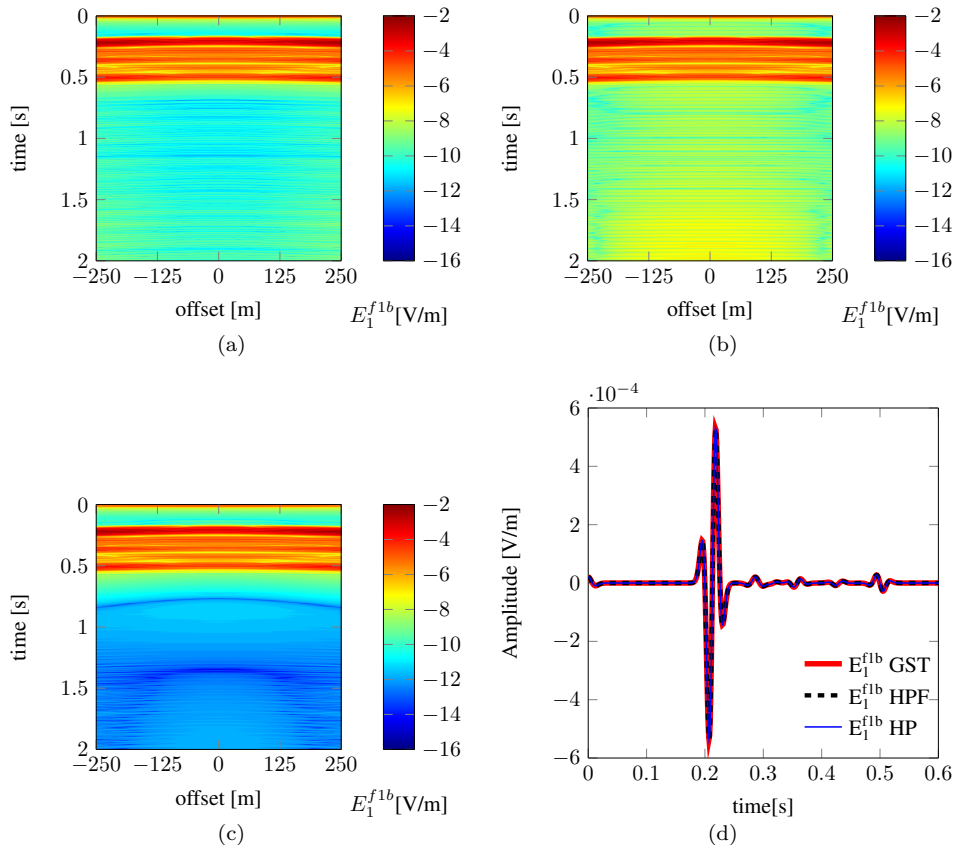


Figure 4.3: Eigenvector validation comparison of seismo-electromagnetic shot records for a shot at $x_3 = 100$ m depth registered at depth level $x_3 = 770$ m, in a model with an interface at $x_3 = 1000$ m. The displayed fields are the electric field component in the x_1 -direction due to a seismic bulk force source component in the same direction. The results of Figures a-c are plotted on a logarithmic scale. The logarithmic scale displays the base-10 logarithm of the absolute value of the data. (a) seismo-electromagnetic shot records modeled with the HP eigenvector set. (b) seismo-electromagnetic shot records modeled with the HPF eigenvector set. (c) seismo-electromagnetic shot records modeled with the GST eigenvector set. (d) Zero-offset trace-overlay of the HPF modeling result displayed with the black-dashed line, the HP result in blue solid and the GST results displayed in red solid.

Numerical inaccuracy: strong and weak events

We have seen that each eigenvector set visibly generates the same results for the two-halfspace model under consideration. But what are then the implications of the obvious differences in numerical stability and consistency between the HP, HPF and GST eigenvector sets? To this end, we study a model where an additional second interface is placed 1000 m below the first interface (at a depth of 2000 m) of the numerical consistency model used thusfar. The interface separates the upper medium B from the lower medium C, resulting in only a 5% porosity contrast over this interface (and of course a resulting contrast in medium parameters that depend on the porosity). The results are presented in Figures 4.4 and 4.5. Looking at Figure 4.4, we clearly see that the GST set (Figure 4.4c) results in a very clean shot record. The HP set is already less clean (Figure 4.4a), and the HPF set shows a lot of numerical noise for the later arrival times (Figure 4.4b). We can observe that the strong events arriving roughly in the first 0.5 s, are modeled consistently by the HP, HPF, and GST sets. However, in Figure 4.4b, we can clearly observe in the HPF results, that the weak events arriving at later times, related mainly to multiple reflections and conversions between the two interfaces, are of similar amplitude as the noise levels. The top inset figure of the trace overlay presented in Figure 4.5, clearly shows that after roughly $t = 1$ s, the events modeled with the HPF set (black, dashed) strongly deviate from the GST results (red, solid). These deviations occur for the smaller amplitude events, in this model events with amplitudes in the order of 10^{-7} V/m. Due to numerical instability, additional wiggles are visible, amplitude and waveform differences can be observed, and the noise levels reach values that are similar or even higher than the amplitudes of the events. For the HP eigenvector set (blue, solid), the results match better with the GST set, also for these weaker events at later times in the order of 10^{-7} V/m. However, for the very weak events in the order of 10^{-10} V/m, so 3 orders of magnitude weaker, obvious erroneous modeling results can be observed for the HP set (bottom inset figure of Figure 4.5, whereas the GST set still models these events numerically stable and clean.

The Limiting Case of No Seismo-Electromagnetic Coupling

We now investigate the effect of taking $\hat{\mathcal{L}} = 0$ (i.e. no seismo-electromagnetic coupling occurs) on the numerical stability of each eigenvector set. We first explore what happens if we set the seismo-electromagnetic coupling coefficient equal to zero. In other words, we model situations where there is no coupling between poroelastic and electromagnetic fields. In this way, we can model the purely poroelastic and purely electromagnetic fields independently.

We start by focusing on the purely electromagnetic part by looking at the electric field response in the x_1 -direction generated by an electric current source in the x_1 -direction. Theoretically, we expect only the direct electromagnetic event and its reflection at the interface at depth. Both events will arrive at almost identical times on the seismic time scale (around $t=0$). The results are presented in Figure 4.6(a), a trace overlay for zero-offset. The results of the GST set are presented with the solid red line, and the results using the HPF set are plotted in black-dashed. We can

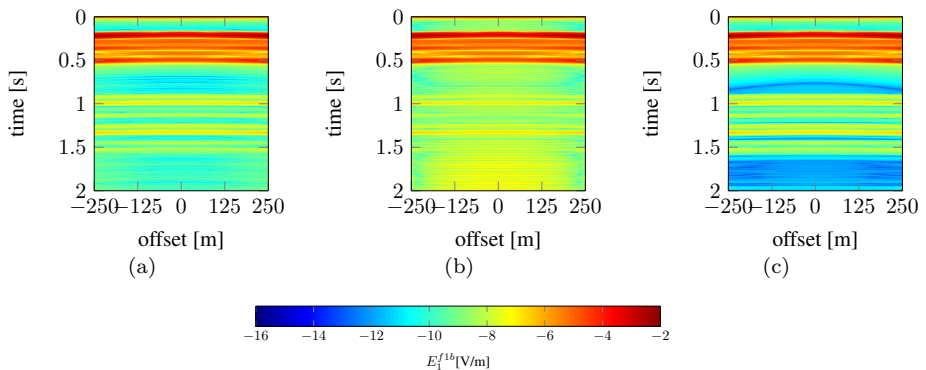


Figure 4.4: Eigenvector comparison of seismo-electromagnetic shot records for a shot at $x_3 = 100$ m depth registered at depth level $x_3 = 770$ m, in a model with an interface separating medium A from medium B at $x_3 = 1000$ m and an additional interface with only a 5% porosity contrast, separating medium B from medium C, at $x_3 = 2000$ m. The displayed fields are the electric field component in the x_1 -direction due to a seismic bulk force source component in the same direction. The results are plotted on a logarithmic scale. (a) seismo-electromagnetic shot records modeled with the HP eigenvector set. (b) seismo-electromagnetic shot records modeled with the HPF eigenvector set. (c) seismo-electromagnetic shot records modeled with the GST eigenvector set.

clearly observe that no electromagnetic events are being generated, when using the HPF set, i.e. the result is zero whereas we theoretically expect two events. The result of the GST set clearly does show an electromagnetic event around $t=0$. The two expected events show up as one event on a seismic time scale. Similar observations can be made for the other offsets. We have already predicted this behaviour by looking at equations (2.172) and (2.173). For additional electromagnetic comparisons of seismo-EM layer-code modeling using the GST eigenvector set with independent electromagnetic modeling codes, the reader is referred to Grobbe *et al.* (2014) and Maas *et al.* (2015).

This electromagnetic test already shows that the HPF set does not correctly model the purely electromagnetic scenario when the coupling coefficient is zero. So how about the purely poroelastic scenario? To answer this question, we look at the results of the x_1 -component of the particle velocity generated by a seismic bulk force source in the same direction. Figure 4.6(b) shows the zero-offset comparison between the HPF set in black-dashed and the GST set in solid red for this purely poroelastic scenario. The result of the HPF set has been reduced by a factor of 1000. One can clearly see that the HPF set does not model the purely poroelastic scenario correctly either. In contrast, for the results using the GST set we can clearly identify the different events at the correct arrival times that we theoretically expect for this purely poroelastic scenario (direct and reflected fields). Similar observations can be made for the other offsets. To truly validate the correctness in both amplitude and phase, a comparison with an independent poroelastic code can be made. However, for the purpose of this section, it is sufficient to acknowledge the differences in mod-

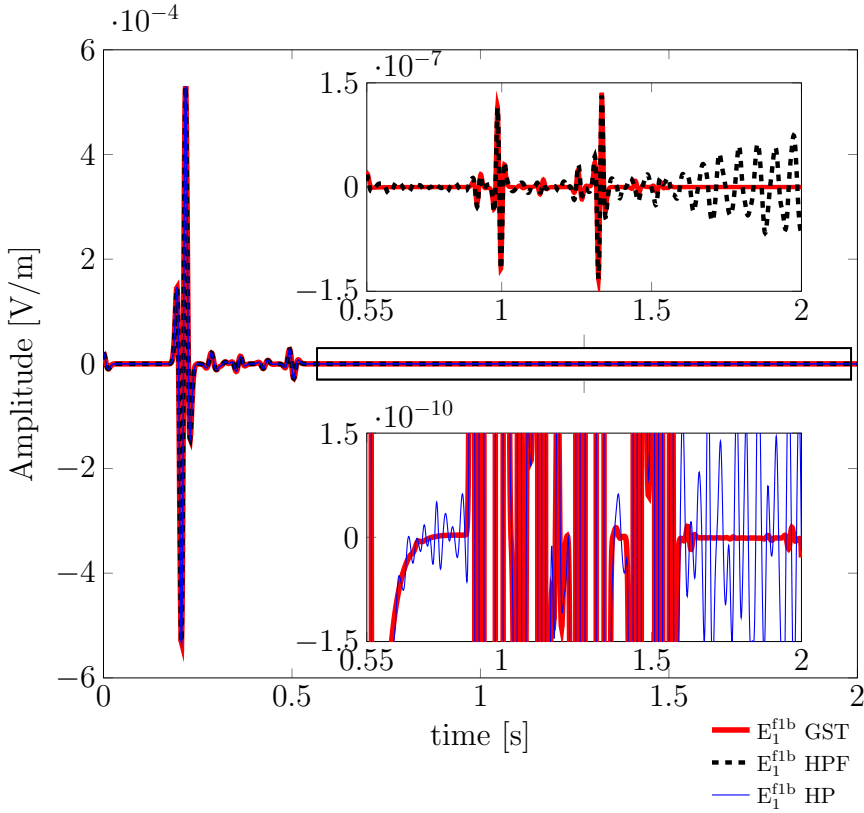


Figure 4.5: Zero-offset trace overlay plot of seismo-electromagnetic modeling with three different eigenvector sets. The plots show the results for a shot at $x_3 = 100$ m depth registered at depth level $x_3 = 770$ m, in a model with an interface separating medium A from medium B at $x_3 = 1000$ m and an additional interface with only a 5% porosity contrast, separating medium B from medium C, at $x_3 = 2000$ m. The displayed fields are the electric field component in the x_1 -direction due to a seismic bulk force source component in the same direction. The blue-solid line shows the results for the HP set (also the lower zoom inset), the black-dashed line for the HPF set (also the upper zoom inset) and the red-solid line for the GST set.

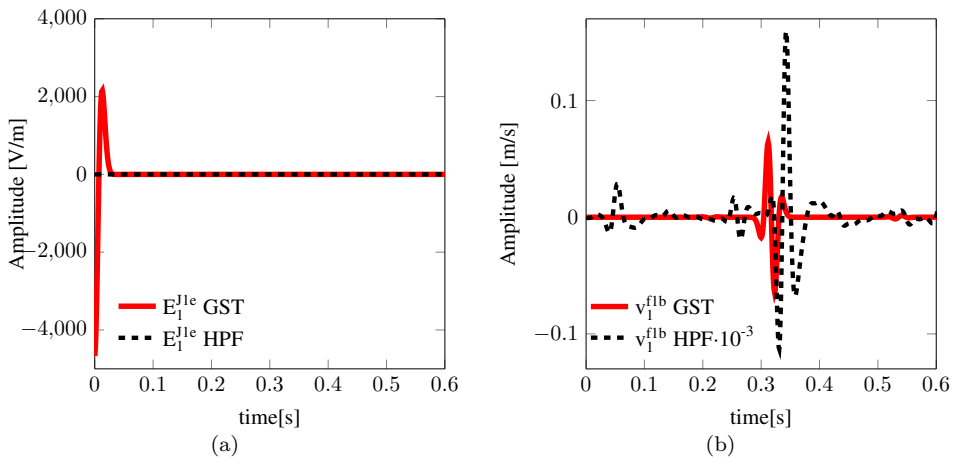


Figure 4.6: Electric field component in the x_1 -direction due to a seismic bulk force source in the same direction, for a shot at $x_3 = 100$ m depth registered at depth level $x_3 = 770$ m in a situation with no seismo-electromagnetic coupling (the coupling coefficient is equal to zero). The results shown are obtained using the GST eigenvector set in red solid, and the HPF set in black-dashed. (a) Zero-offset trace comparison for a purely electromagnetic scenario: the electric field in the x_1 -direction due to an electric current source in the same direction. (b) Zero-offset trace comparison for a purely poroelastic scenario: the horizontal particle velocity field component in the x_1 -direction due to a dipole bulk force source in the same direction.

eling results between the HPF eigenvector set and the GST eigenvector set in case of decoupled mechanical and electromagnetic fields, recognizing that the GST set correctly models these scenarios whereas the HPF set fails. Do the eigenvector sets yield a correct zero-valued result in case of no seismo-electromagnetic coupling for a seismo-electromagnetic source-receiver combination: the x_1 electric field component generated by a seismic bulk force source in the x_1 -direction? Theoretically, this should yield a zero-valued result since no coupling should occur between poroelastic and electromagnetic fields. Comparisons between the HPF set and the GST set indeed showed a zero-valued result at all offsets for both sets (not shown).

We now know that the HPF set (and hence also the HP set), is not correctly modeling the decoupled, purely poroelastic and electromagnetic scenarios when the seismo-electromagnetic coupling coefficient is equal to zero. So, what happens if we model coupled seismo-electromagnetic scenarios in media containing layers with very small coupling coefficients? To this end, we model seismo-electromagnetic phenomena in a two half-space model, where the upper half-space (originally medium A) now has a very low porosity (almost approaching a pure solid), and hence a very small coupling coefficient (properties of medium D, see Table 2). The parameters dependent on the porosity of course change accordingly. Figures 4.7 and 4.8 show the results of this scenario. In Figure 4.7, we can observe that the GST eigenvector set (Figure 4.7a) models the seismo-electromagnetic fields correctly and numerically

stable. In contrast, the HP eigenvector set fails to correctly model this scenario in a numerically stable fashion (Figure 4.7b). Looking at the trace overlay in Figure 4.8, we can see that the major events still match reasonably for all three eigenvector sets. However, zooming in to the weaker events in the first 0.7 s, we can observe differences in the amplitude of for example the direct source converted EM field at $t=0$ s. In addition, we can observe that the GST set has very low noise levels (red, solid), whereas the noise levels of the HP set are quite high (blue, solid). As an example, compare the weak amplitude of the arrival around 0.5 s with the noise levels of the HP and HPF sets at earlier and later times (Figure 4.8). So for models containing small, multiple arrivals, these arrivals will be masked by the noise levels of the HP set (and the HPF set), and visible in the GST set. Figure 4.7c shows that the HPF eigenvector set, when exploiting the power flux-normalized transpose property for the inverse, completely fails to model this scenario correctly. However, when the HPF set is used with a numerical inverse instead of making use of this transposition property (equations (2.169) and (2.170)), the modeling results are identical to the HP results (compare Figures 4.7b and 4.7d). We can conclude that for modeling scenarios with small coupling coefficients (due to for example low porosity values or high electrolyte concentrations), the HP and HPF eigenvector sets can seriously fail to correctly model all the events, especially weaker events (such as certain seismo-electromagnetic interface response fields or multiples). The GST eigenvector set remains stable at all times and always yields clean results.

4.1.3 Discussion

The validating results of Figure 4.3 have shown that the HP and HPF sets suffer from higher numerical noise levels than the GST set. The HP set shows about 6 orders of magnitude difference between the strongest events in the shot record and the noise levels, the HPF set about 5 orders of magnitude difference and the GST set about 10 orders of magnitude difference. Although this might indicate that the HP set performs slightly better than its flux-normalized HPF version, the numerical stability tests have proven that the HPF set overall has better numerical stability and precision than the HP set. The HPF set makes use of the power flux-normalized transpose property to obtain the decomposition matrix (equations (2.169) and (2.170)), whereas the HP set was always modeled using a numerical inverse to obtain the decomposition matrix. This numerical inverse probably smooths out numerical inaccuracies and instabilities that can be the consequence of a badly scaled or badly organized composition (eigenvector) matrix, whereas the transposition operation simply reorganizes the values of the composition matrix to obtain the decomposition matrix. This fact is nicely illustrated in Figure 4.7, where the HPF set yields exactly the same results as the HP set when a numerical inverse is used. The results for the GST set in Figure 4.3 display a 10-orders of magnitude difference between signal and numerical noise, already providing a first indication that the GST set yields the best numerical stability and precision. In addition, the two-interface model and the low-porosity model have proven that the GST set yields stable and clean results at all times, whereas the HPF set and the HP set

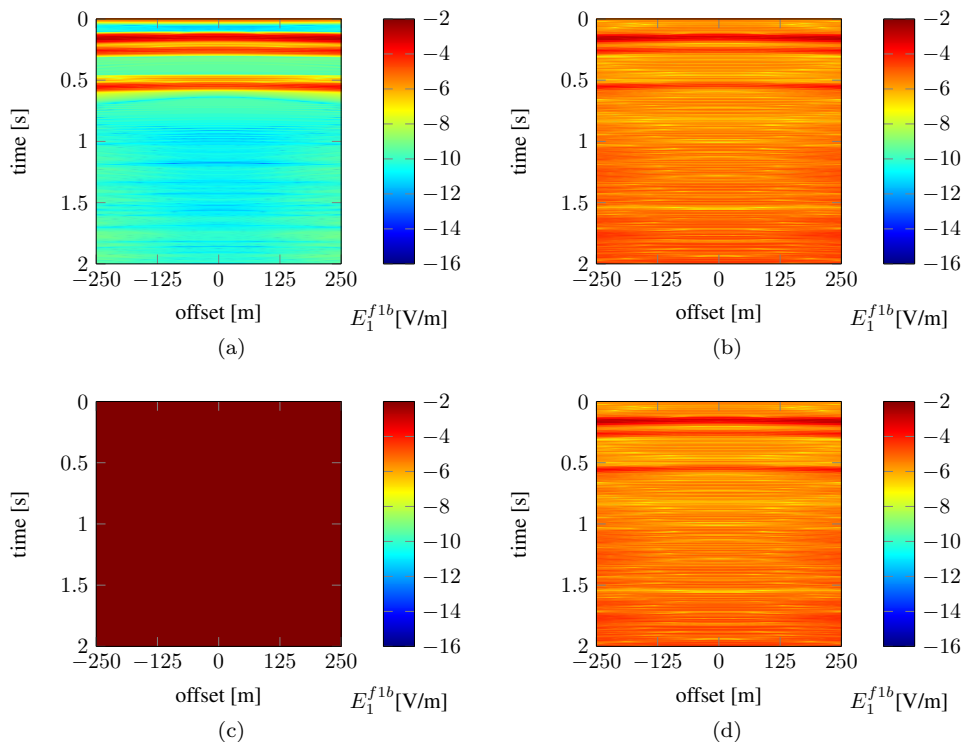


Figure 4.7: Eigenvector comparison of seismo-electromagnetic shot records for a shot at $x_3 = 100$ m depth registered at depth level $x_3 = 770$ m, in a model with an interface at $x_3 = 1000$ m, separating medium D from medium B. The displayed fields are the electric field component in the x_1 -direction due to a seismic bulk force source component in the same direction. The results are plotted on a logarithmic scale. (a) seismo-electromagnetic shot records modeled with the GST eigenvector set. (b) seismo-electromagnetic shot records modeled with the HP eigenvector set. (c) seismo-electromagnetic shot records modeled with the HPF eigenvector set, when the inverse of the eigenvector matrix is obtained from the transposition equivalence property. (d) seismo-electromagnetic shot records modeled with the HPF eigenvector set, when the inverse of the eigenvector matrix is computed numerically.

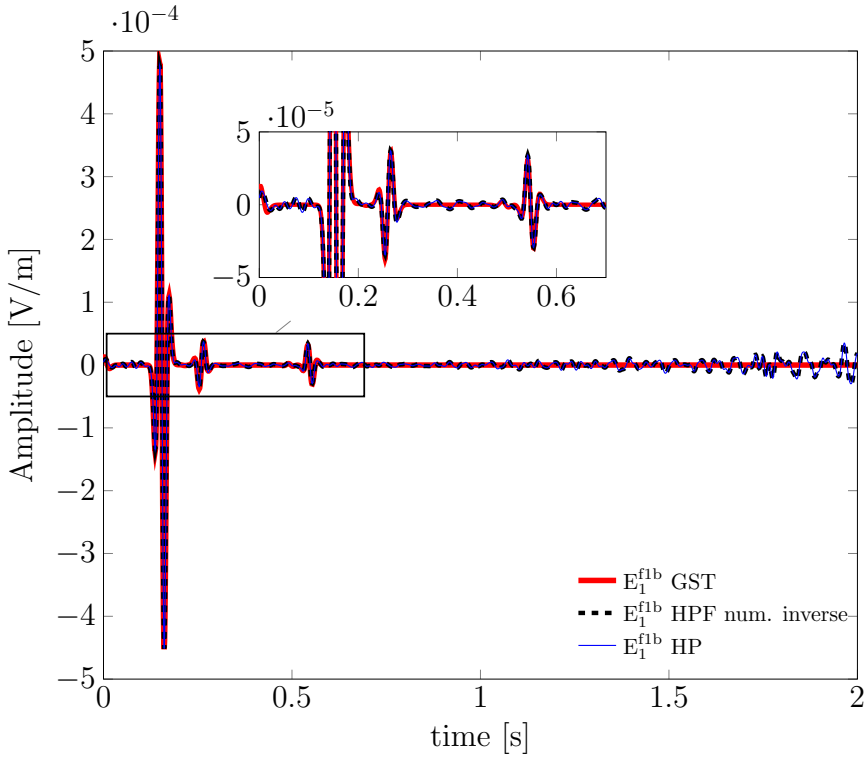


Figure 4.8: Zero-offset trace overlay plot of seismo-electromagnetic modeling with three different eigenvector sets. The plots show the results for a shot at $x_3 = 100$ m registered at depth level $x_3 = 770$ m, in a model with an interface at $x_3 = 1000$ m, separating medium D from medium B. The displayed fields are the electric field component in the x_1 -direction due to a seismic bulk force source component in the same direction. The blue-solid line shows the results for the HP set, the black-dashed line for the HPF set, when the inverse of the eigenvector matrix is computed numerically, and the red-solid line for the GST set.

break down.

So what are these numerical instabilities and inaccuracies caused by? The seismo-electromagnetic composition matrices consist of different parameters and their columns represent different field types (the fast P-wave, slow P-wave, SV-wave, TM-field, SH-wave, and the TE-field). The wide variety of seismo-electromagnetic medium parameters can have a wide variety in terms of orders of magnitude: the shear modulus has for example relatively large values, whereas the permeability has small values. Also, looking at the wave/field velocities, the Biot slow P-wave has much smaller velocity values than the electromagnetic field velocities. These big and small values interact with each other, for example in the computation of the global reflection coefficients of the layered-Earth numerical algorithm for each interface in the model. The relative magnitude of the variables in the computations can dictate the severity of round-off errors that are introduced. For example, a loss of numerical precision can occur due to the addition of a large number with a small number. We have seen that power flux-normalizing the HP set (leading to the HPF set), visibly improves the numerical consistency of the eigenvector set. This normalization based on the power of the system adjusts the composition matrix in such a way, that the relative magnitude of the different variables varies less. The GST eigenvector set is designed completely independently, taking the underlying physics explicitly into account. In addition, the GST set is power flux-normalized, balancing the composition matrix even further. Therefore, the relative magnitude of different variables is more consistent, and varies even less. We must note that the final expressions of the GST eigenvector set for the P-SV-TM mode as presented in this thesis are more complicated and extensive than the HPF eigenvector set.

As we have shown, the numerical stability differences have obvious implications on finding small amplitude signals when there are also strong signals in the data. Especially, later arriving, weak events (for example multiples and interface response fields) are masked by numerical noise levels of the HP and HPF sets, whereas these events are correctly modeled with the more stable and precise GST set. Furthermore, the fact that the GST set is capable of correctly modeling scenarios with no seismo-electromagnetic coupling at all (i.e. modeling the independent poroelastic and electromagnetic fields), is an additional benefit. It is also an indication that the physics of the HP and HPF sets are not correctly taken into account. In addition, as soon as there is little coupling between the mechanical and electromagnetic fields (for example low porosity values or high electrolyte concentration), the modeling results of the GST set compared to the HP and HPF sets, behave differently. Our modeling scenario clearly shows that the GST set remains stable and models all events correctly and clean, whereas the HP and HPF sets show numerical noise levels that are of similar amplitude as the weak events in the data. This makes distinguishing between noise and physical weak events impossible. The seismo-electromagnetic interface response fields that we are mainly after, since those fields can provide us with information at depth, often have very weak amplitudes. We therefore desire that our numerical modeling codes model all events correctly and as clean as possible, enabling better interface response interpretation of our modeling results.

In the model with two interfaces, as well as the model with weak seismo-

electromagnetic coupling, we have only changed the porosity values of the medium compared to the model used for the validation of the eigenvector sets (see Table 2). Of course, many other parameters or parameter combinations, as well as model geometries can yield small seismo-electromagnetic coupling coefficients, weak, late arriving events or big contrasts between large and small amplitude events. Also, in this section we have only studied the horizontal electric field due to a seismic bulk force source. There are many other seismo-electromagnetic source-receiver combinations. The numerical effects and instabilities of the HP and HPF eigenvector sets might be even more pronounced for other source-receiver combinations, dependent on for example the model scenario under consideration. Furthermore, for the seismic frequency bandwidth, the Biot slow wave is actually a diffusive field that decays very rapidly and diffuses at very low velocities. It almost never shows up in the seismo-electromagnetic shot records. However, when studying seismo-electromagnetic phenomena in for example the ultrasonic frequency range, the Biot slow wave becomes a propagating wave and can show up in the records. Numerical instabilities associated with these parts of the eigenvector sets might become more pronounced for these frequency bandwidths as well. Typical seismo-electromagnetic laboratory wave propagation experiments (Schakel *et al.*, 2011; Smeulders *et al.*, 2014; Zhu *et al.*, 2000; Zhu & Toksöz, 2005) make use of ultrasonic frequencies due to the small scale of the experiments. Validating such physical experiments by correct, complete, and precise numerical modeling is crucial for our further understanding of the seismo-electromagnetic phenomena and the absolute and relative amplitudes that are to be expected from the different seismo-electromagnetic coupling mechanisms.

One can argue how crucial the discussed errors in the modeling of the weak events are for the overall picture. It is true that all three eigenvector sets model the major events correctly. However, the HPF set already models events that have a magnitude in the order of 10^{-3} weaker than these major events, not correctly. The HP set models events that are 10^{-6} weaker than the largest events incorrectly, and these events are masked by the noise levels. These are serious errors for numerical modeling, and not negligible. Of course it might be difficult to measure these weaker events in field experiments, but with numerical modeling, we desire our results to be complete, correct, clean and numerically stable. The GST set yields such results at all times. It is therefore strongly recommended to use this newly developed eigenvector set for future layered-Earth seismo-electromagnetic modeling experiments.

4.1.4 Conclusions

We have shown how to effectively flux-normalize the Haartsen & Pride (1997) eigenvector sets (with particle velocity instead of displacement). In addition, we have derived an alternative flux-normalized eigenvector set directly from the system matrices, thereby imposing specific physical conditions that guarantee correct modeling of the independent poroelastic and electromagnetic systems as well, when the seismo-electromagnetic coupling coefficient is equal to zero. Our approach is in principle applicable to any physical wave or field phenomenon that can be captured in the presented system matrix format.

We have carried out two different numerical stability tests: the first test focused on the internal consistency of the system matrix, its eigenvectors and eigenvalues and the second test focused on the stability and preciseness of the flux-normalized systems.

From the first test we conclude that flux-normalizing the eigenvector sets stabilizes the numerical results and improves numerical accuracy, for both the SH-TE and P-SV-TM propagation modes. Flux-normalizing the HP eigenvector set, resulting in the HPF set, drastically improves the numerical stability, but still there are stability issues. Our GST set results overall in the best numerical performance both in terms of stability and preciseness. The HP and HPF sets showed significant numerical consistency errors for specific matrix elements and certain radial wavenumber-frequency combinations.

The second test focused on how well we can express the inverse of the composition matrix in terms of the transposes of the composition submatrices. For the SH-TE mode, the GST eigenvector set results in slightly smaller errors than the HPF eigenvector set. However, both error levels are acceptable. For the P-SV-TM mode, the GST and HPF sets have larger and smaller errors at different elements. Overall, the GST set seems to be slightly more stable for the P-SV-TM mode, but again both eigenvector sets yield acceptable results. We can conclude that for both flux-normalized eigenvector sets, we can correctly use the transpose of the composition submatrices as an inverse.

We have validated the results using the different eigenvector sets in our seismo-EM layer-code ESSEMOD. From the validating comparisons using a two-halfspace model we conclude that each eigenvector set generates identical results for all the major events in the model under consideration. However, the proven differences in numerical stability and precision between the HP, HPF and GST sets play an important role for different scenarios. As we have shown, the differences have obvious implications on finding small amplitude signals when there are also strong signals in the data. Especially, later arriving, weak events (for example multiples and interface response fields) are masked by numerical noise levels of the HP and HPF sets, whereas these events are correctly modeled with the more stable and precise GST set.

When the seismo-electromagnetic coupling coefficient is equal to zero (i.e. when there is no coupling between mechanical and electromagnetic fields), it turns out that only the GST set models the purely poroelastic and purely electromagnetic systems correctly. The incorrect modeling of the independent mechanical and electromagnetic fields by the HP and HPF sets has been explained by theoretically looking at the eigenvector sets as well. It is also an indication that the physics of the HP and HPF sets are not correctly taken into account. Our approach of explicitly enforcing the physics in our derivation of the GST eigenvector set results in correctly modeling of the decoupled purely poroelastic and purely electromagnetic scenarios as well.

In addition, we have shown that as soon as there is little coupling between the mechanical and electromagnetic fields (for example low porosity values or high electrolyte concentrations), the modeling results of the GST set compared to the HP and HPF sets, behave differently. Our modeling scenario clearly shows that the

GST set remains stable at all times and models all coupled seismo-electromagnetic events correctly and clean, whereas the HP and HPF sets show clearly numerical noise levels that are of similar amplitude as the weak events in the data, making a distinction between noise and physical weak events impossible.

Although it might be difficult to measure the physically weak events in actual field experiments, in numerical modeling, we desire our results to be complete, correct, clean, and numerically stable to obtain optimal insights in the physics of seismo-electromagnetic phenomena. The GST set is proven to yield such results at all times, and we therefore recommend to use this newly developed eigenvector set for future layered-Earth seismo-electromagnetic modeling experiments.

Appendix

4.1.A System Consistency Test using GST Eigenvectors

This appendix shows the results of the system consistency tests according to equation (4.2), for H1 and V1, and equation (4.3), for H2 and V2, respectively. These tests were carried out using the GST eigenvector sets.

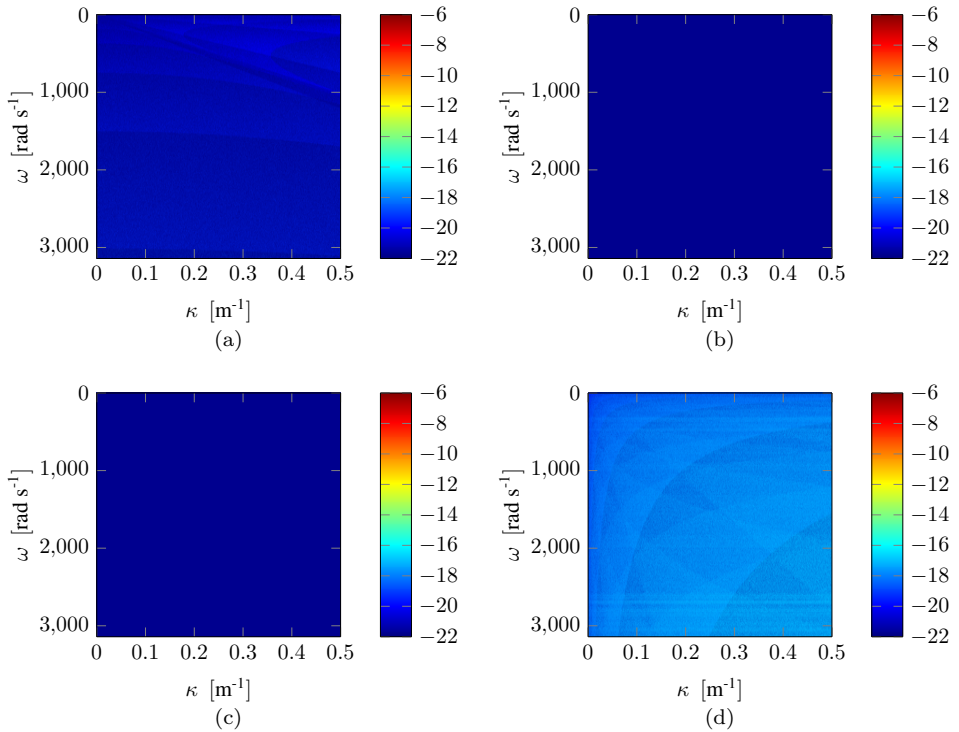


Figure 4.9: *H1* system check with the GST set for all radial wavenumber-angular frequency combinations. (a) submatrix element (1,1) (b) submatrix element (1,2) (c) submatrix element (2,1) (d) submatrix element (2,2)

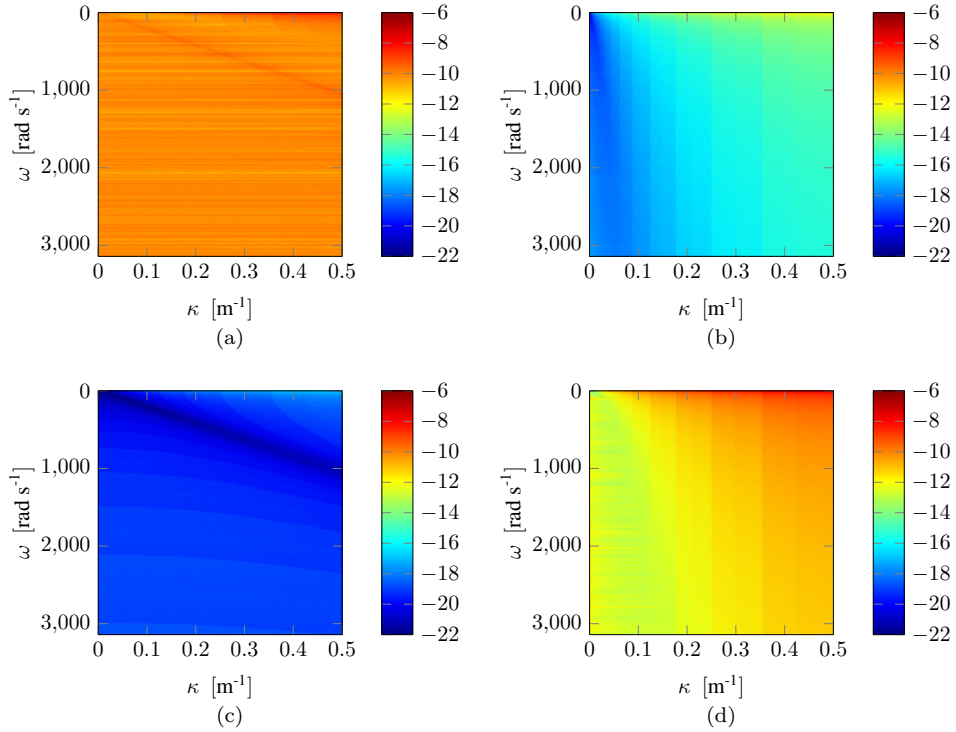


Figure 4.10: *H2* system check with the GST set for all radial wavenumber-angular frequency combinations. (a) submatrix element (1,1) (b) submatrix element (1,2) (c) submatrix element (2,1) (d) submatrix element (2,2)

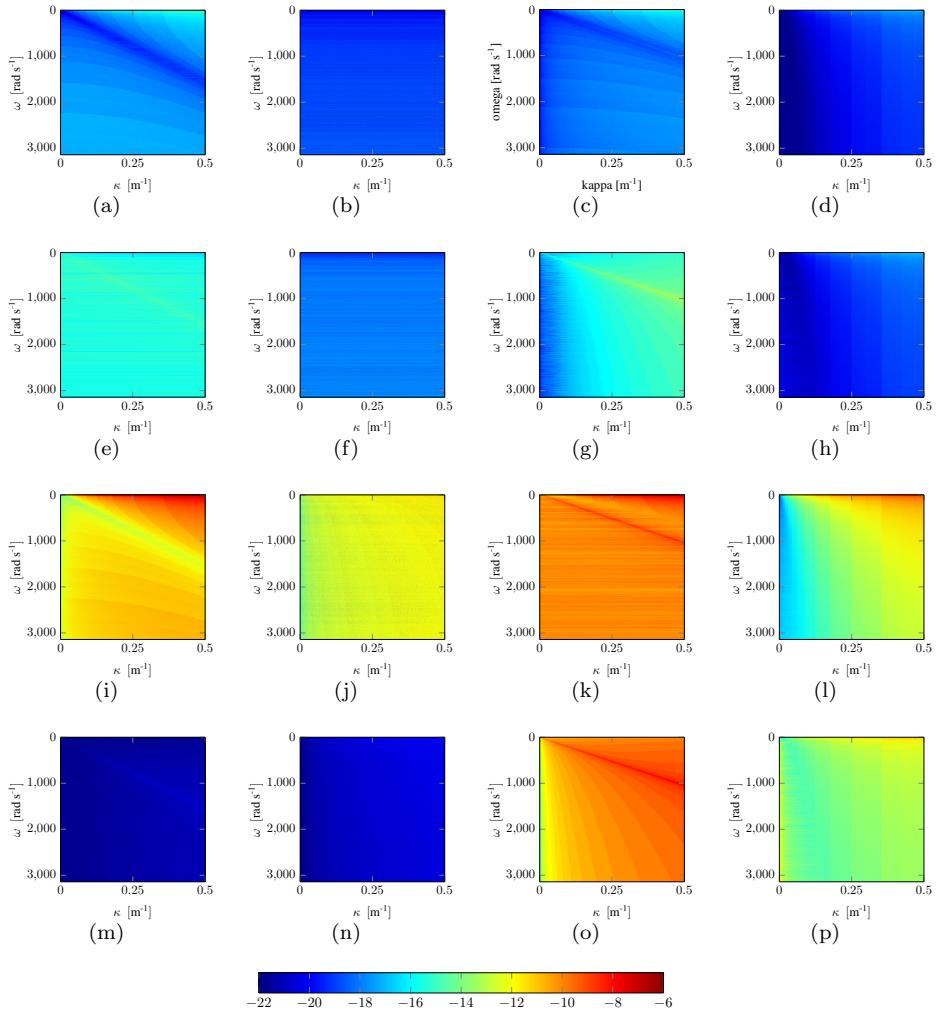


Figure 4.11: *V1* system check with the GST set for all radial wavenumber-angular frequency combinations. (a) submatrix element (1,1) (b) submatrix element (1,2) (c) submatrix element (1,3) (d) submatrix element (1,4) (e) submatrix element (2,1) (f) submatrix element (2,2) (g) submatrix element (2,3) (h) submatrix element (2,4) (i) submatrix element (3,1) (j) submatrix element (3,2) (k) submatrix element (3,3) (l) submatrix element (3,4) (m) submatrix element (4,1) (n) submatrix element (4,2) (o) submatrix element (4,3) (p) submatrix element (4,4)

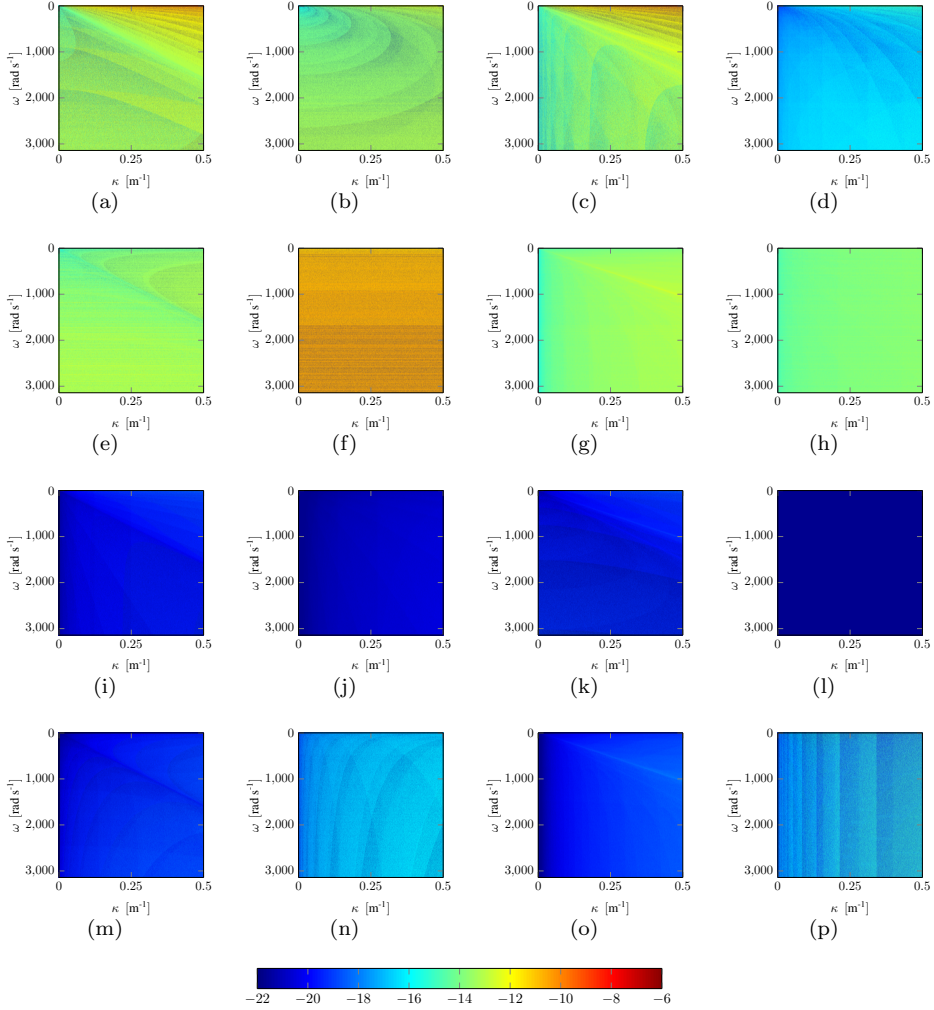


Figure 4.12: V_2 system check with the GST set for all radial wavenumber-angular frequency combinations. (a) submatrix element (1,1) (b) submatrix element (1,2) (c) submatrix element (1,3) (d) submatrix element (1,4) (e) submatrix element (2,1) (f) submatrix element (2,2) (g) submatrix element (2,3) (h) submatrix element (2,4) (i) submatrix element (3,1) (j) submatrix element (3,2) (k) submatrix element (3,3) (l) submatrix element (3,4) (m) submatrix element (4,1) (n) submatrix element (4,2) (o) submatrix element (4,3) (p) submatrix element (4,4)

4.1.B System Consistency Test using HP Eigenvectors

This appendix shows the results of the system consistency tests according to equation (4.2), for H1 and V1, and equation (4.3), for H2 and V2, respectively. These tests were carried out using the HP eigenvector sets.

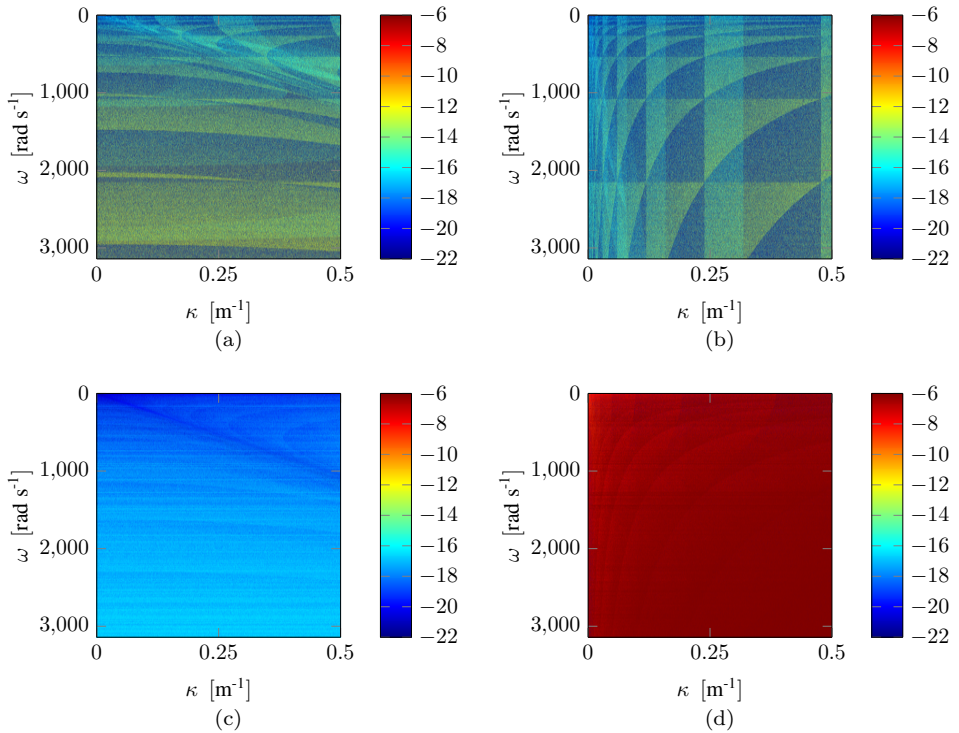


Figure 4.13: *H1* system check with the HP set for all radial wavenumber-angular frequency combinations. (a) submatrix element (1,1) (b) submatrix element (1,2) (c) submatrix element (2,1) (d) submatrix element (2,2)

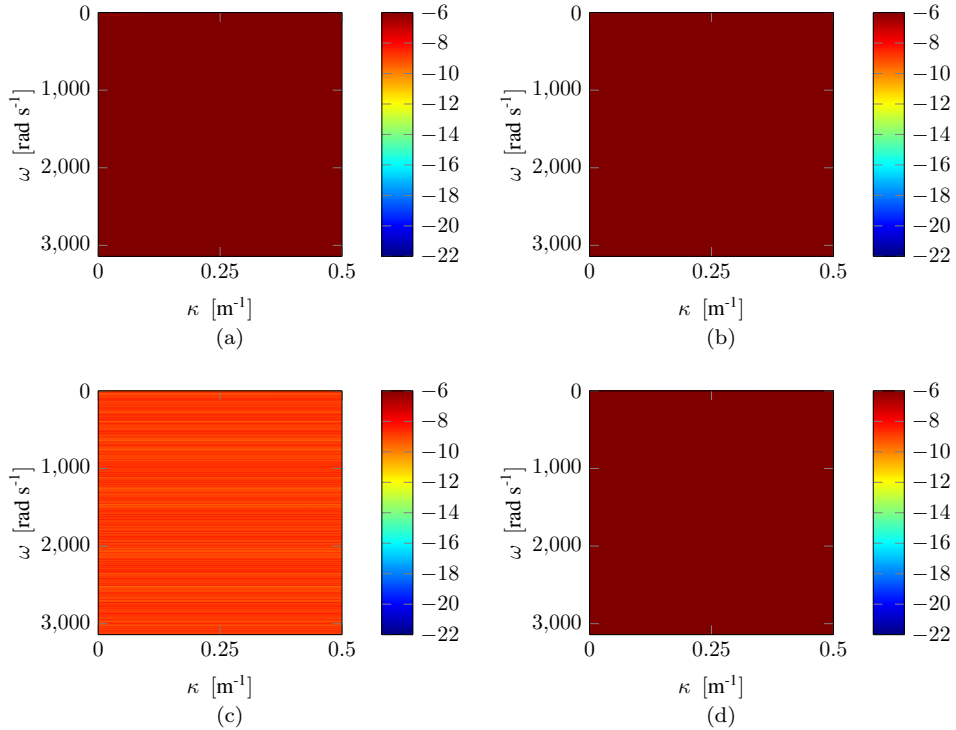


Figure 4.14: H_2 system check with the HP set for all radial wavenumber-angular frequency combinations. (a) submatrix element (1,1) (b) submatrix element (1,2) (c) submatrix element (2,1) (d) submatrix element (2,2)

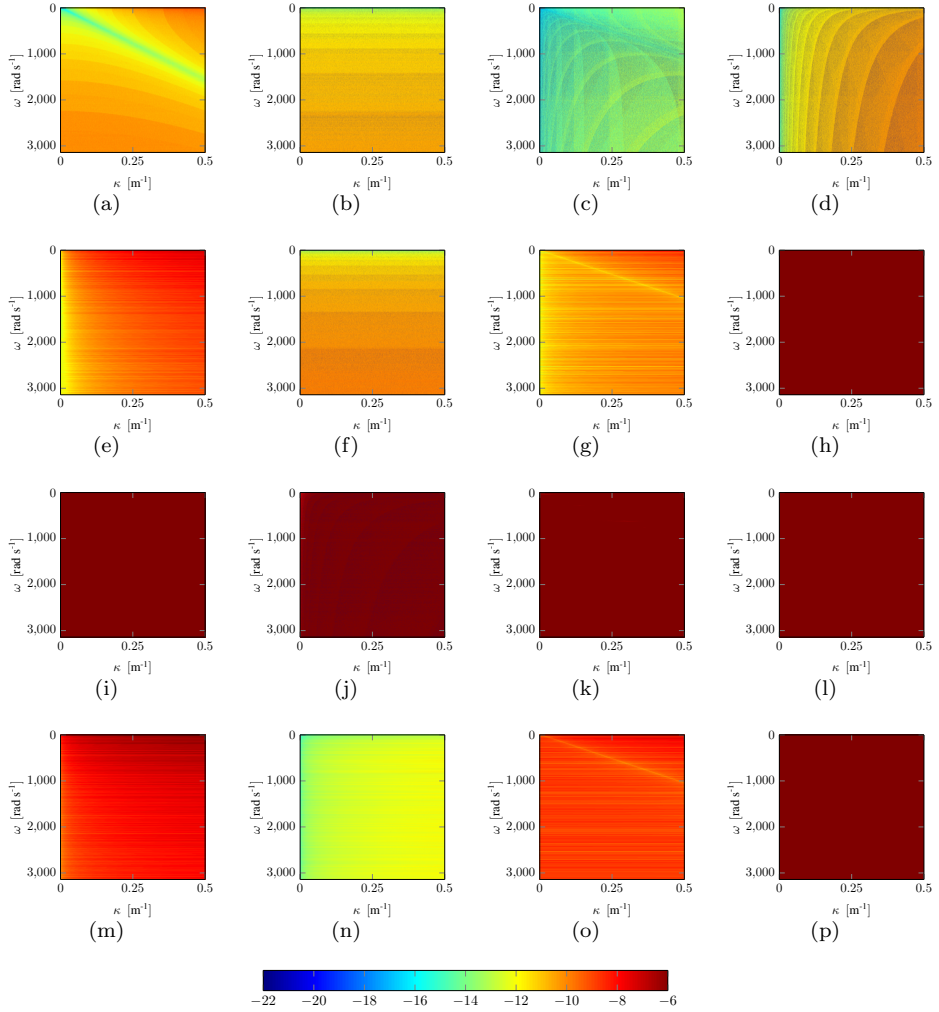


Figure 4.15: V_1 system check with the HP set for all radial wavenumber-angular frequency combinations. (a) submatrix element (1,1) (b) submatrix element (1,2) (c) submatrix element (1,3) (d) submatrix element (1,4) (e) submatrix element (2,1) (f) submatrix element (2,2) (g) submatrix element (2,3) (h) submatrix element (2,4) (i) submatrix element (3,1) (j) submatrix element (3,2) (k) submatrix element (3,3) (l) submatrix element (3,4) (m) submatrix element (4,1) (n) submatrix element (4,2) (o) submatrix element (4,3) (p) submatrix element (4,4)

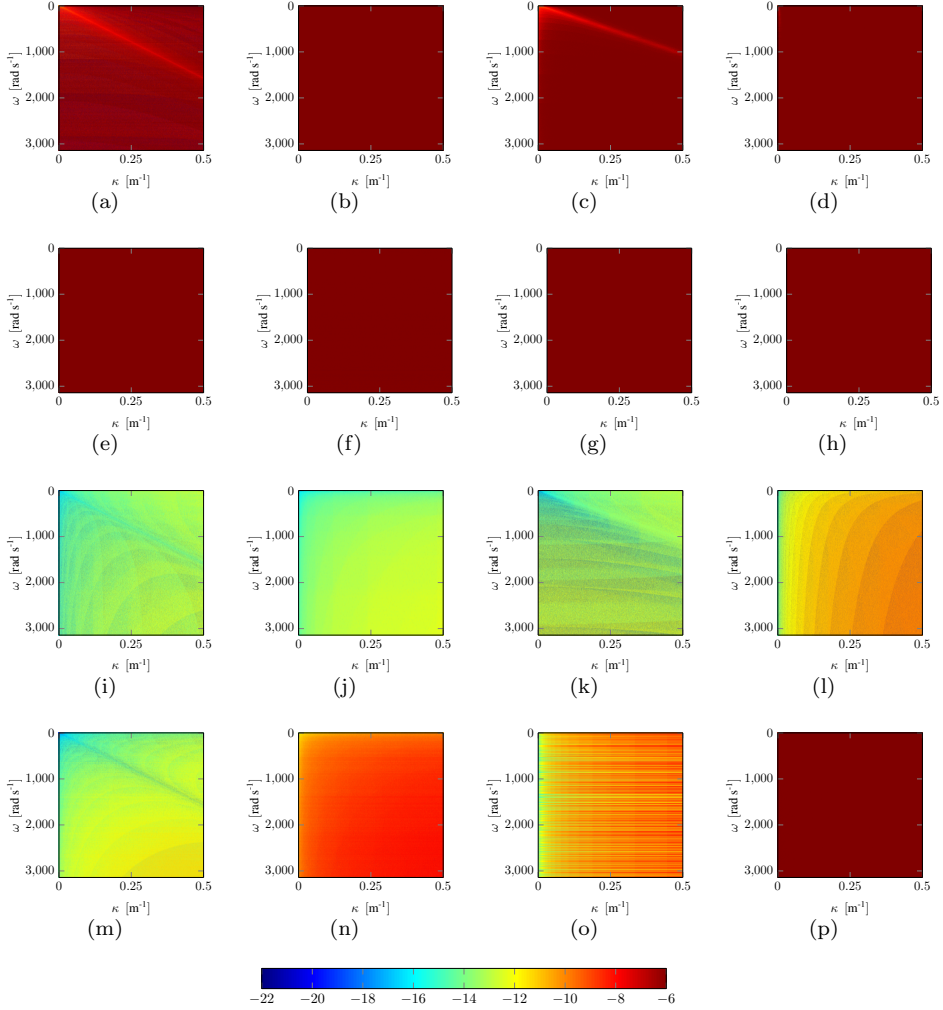


Figure 4.16: V_2 system check with the HP set for all radial wavenumber-angular frequency combinations. (a) submatrix element (1,1) (b) submatrix element (1,2) (c) submatrix element (1,3) (d) submatrix element (1,4) (e) submatrix element (2,1) (f) submatrix element (2,2) (g) submatrix element (2,3) (h) submatrix element (2,4) (i) submatrix element (3,1) (j) submatrix element (3,2) (k) submatrix element (3,3) (l) submatrix element (3,4) (m) submatrix element (4,1) (n) submatrix element (4,2) (o) submatrix element (4,3) (p) submatrix element (4,4)

4.1.C System Consistency Test using HPF Eigenvectors

This appendix shows the results of the system consistency tests according to equation (4.2), for H1 and V1, and equation (4.3), for H2 and V2, respectively. These tests were carried out using the HPF eigenvector sets.

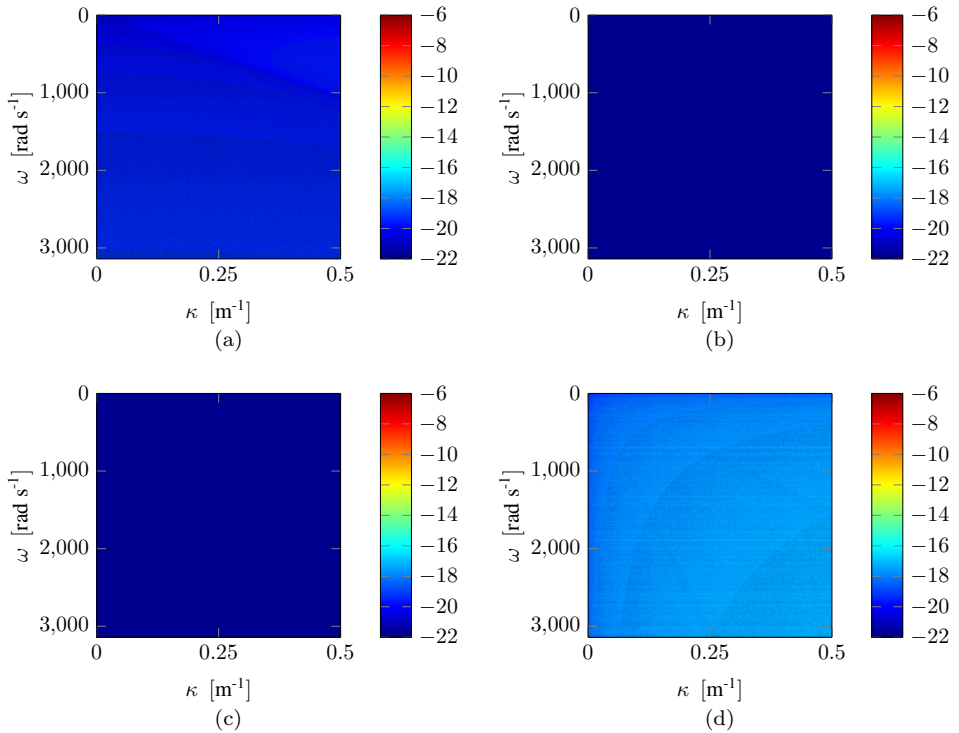


Figure 4.17: *H1* system check with the HPF set for all radial wavenumber-angular frequency combinations. (a) submatrix element (1,1) (b) submatrix element (1,2) (c) submatrix element (2,1) (d) submatrix element (2,2)

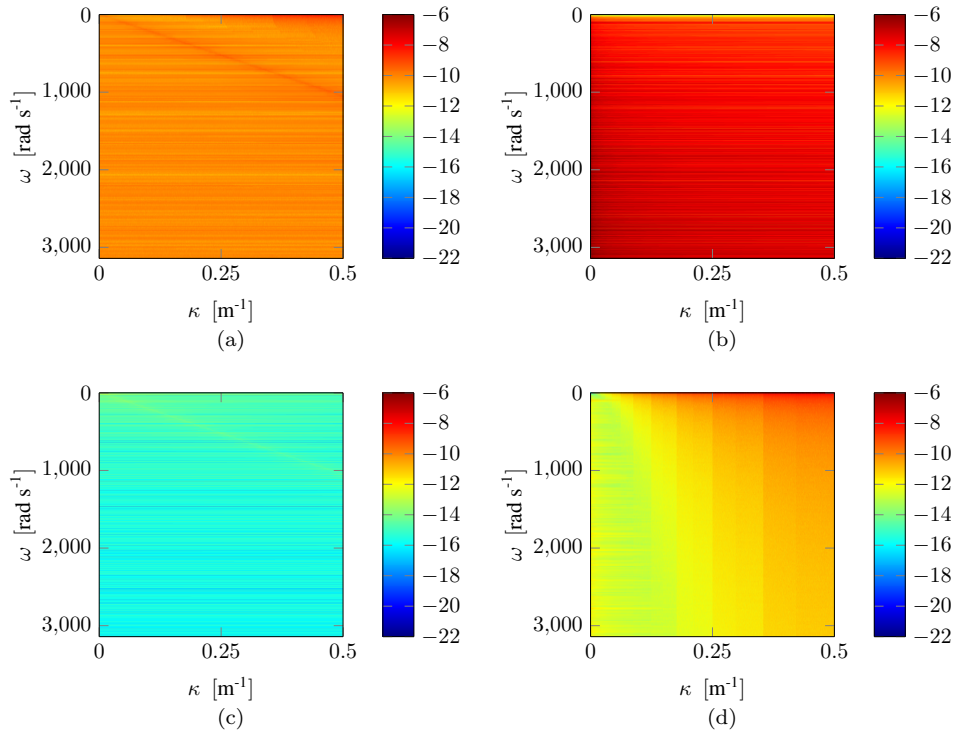


Figure 4.18: *H2* system check with the HPF set for all radial wavenumber-angular frequency combinations. (a) submatrix element (1,1) (b) submatrix element (1,2) (c) submatrix element (2,1) (d) submatrix element (2,2)

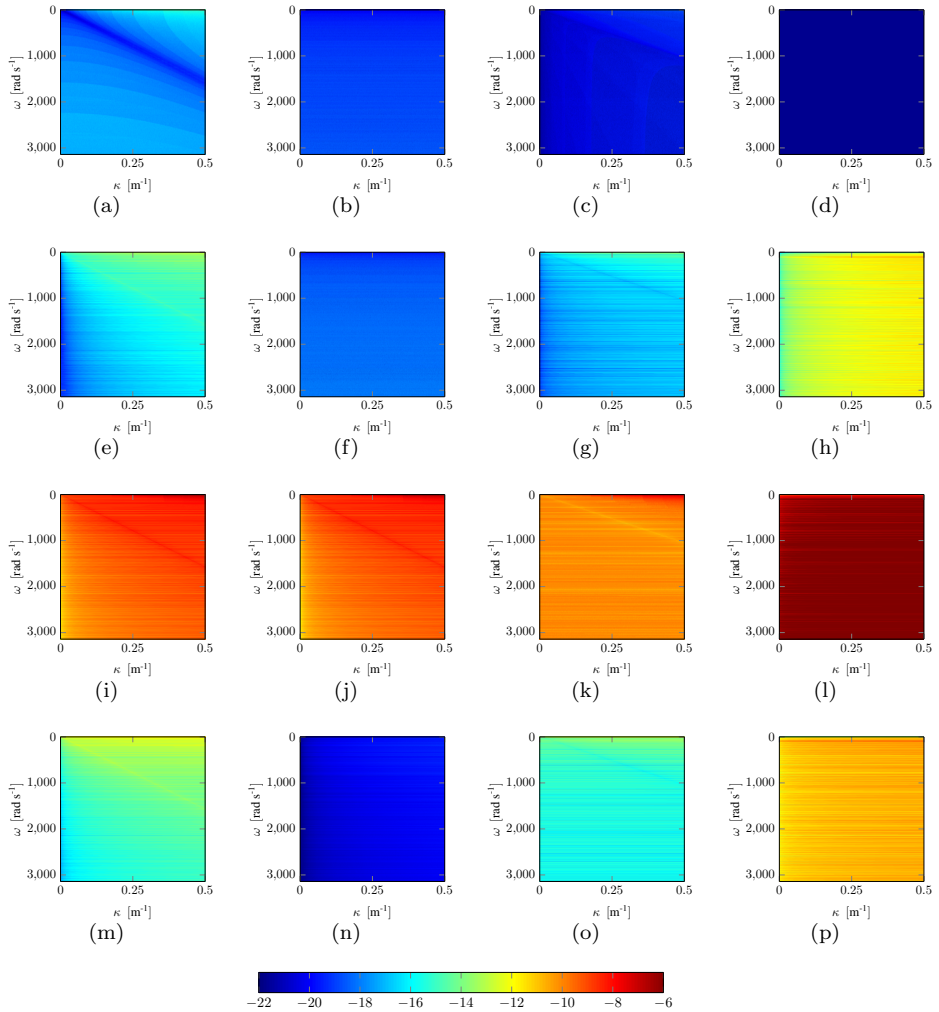


Figure 4.19: *V1* system check with the HPF set for all radial wavenumber-angular frequency combinations. (a) submatrix element (1,1) (b) submatrix element (1,2) (c) submatrix element (1,3) (d) submatrix element (1,4) (e) submatrix element (2,1) (f) submatrix element (2,2) (g) submatrix element (2,3) (h) submatrix element (2,4) (i) submatrix element (3,1) (j) submatrix element (3,2) (k) submatrix element (3,3) (l) submatrix element (3,4) (m) submatrix element (4,1) (n) submatrix element (4,2) (o) submatrix element (4,3) (p) submatrix element (4,4)

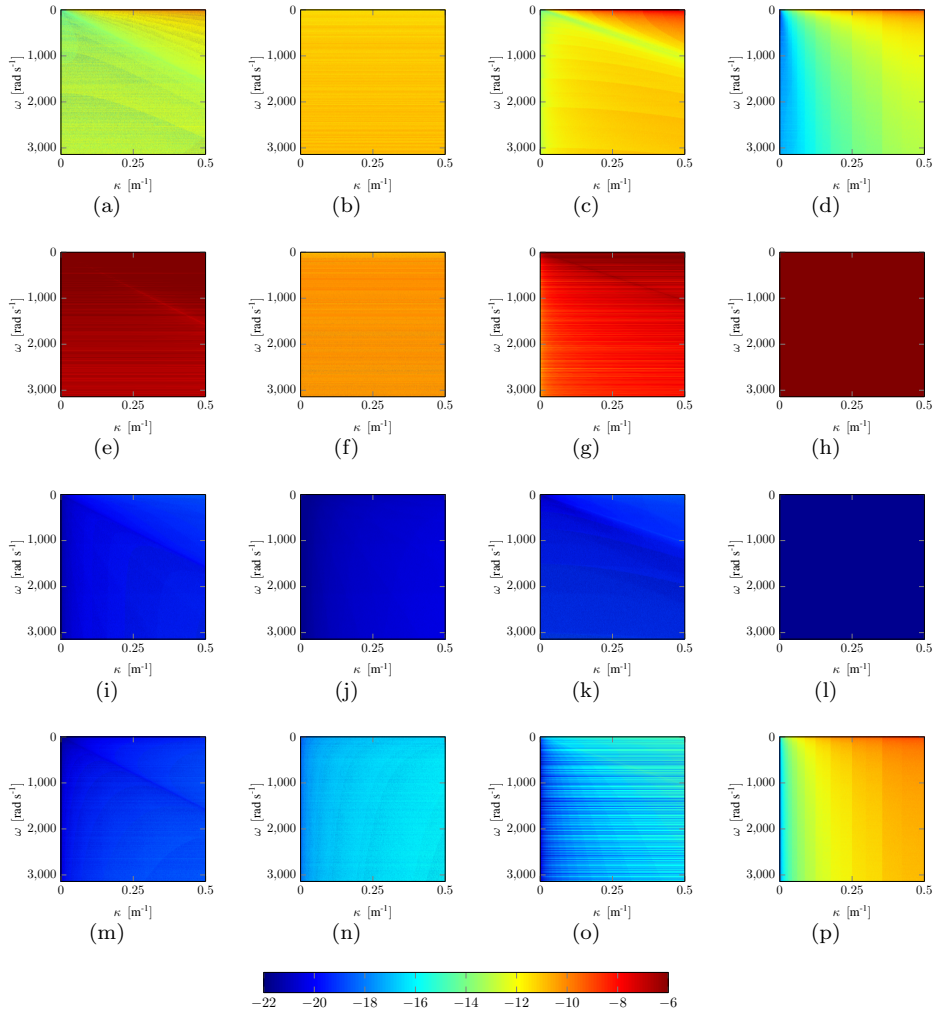


Figure 4.20: *V2* system check with the HPF set for all radial wavenumber-angular frequency combinations. (a) submatrix element (1,1) (b) submatrix element (1,2) (c) submatrix element (1,3) (d) submatrix element (1,4) (e) submatrix element (2,1) (f) submatrix element (2,2) (g) submatrix element (2,3) (h) submatrix element (2,4) (i) submatrix element (3,1) (j) submatrix element (3,2) (k) submatrix element (3,3) (l) submatrix element (3,4) (m) submatrix element (4,1) (n) submatrix element (4,2) (o) submatrix element (4,3) (p) submatrix element (4,4)

4.1.D Flux-Normalization Identity Test using GST eigenvectors

This appendix shows the results of the flux-normalization identity tests according to equation (4.4), for H1 and V1, and equation (4.5), for H2 and V2, respectively. These tests were carried out using the GST eigenvector sets.

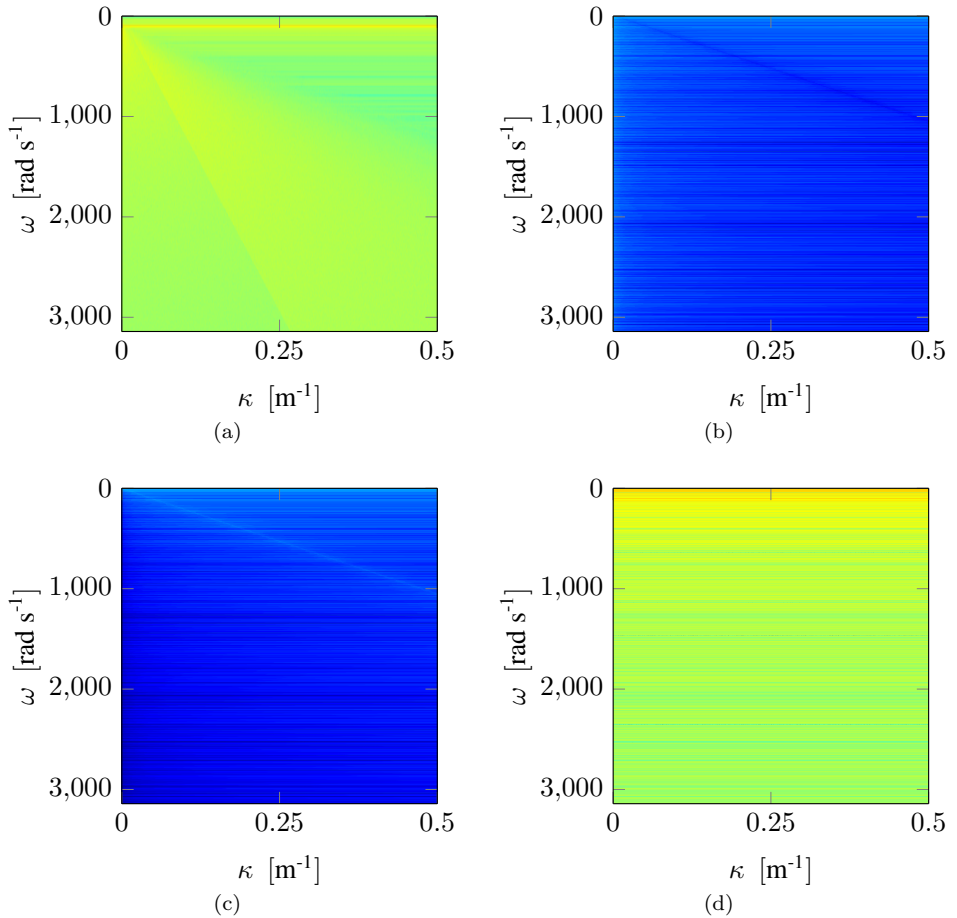


Figure 4.21: H1 Identity check with the GST set for all radial wavenumber-angular frequency combinations. (a) submatrix element (1,1) (b) submatrix element (1,2) (c) submatrix element (2,1) (d) submatrix element (2,2)

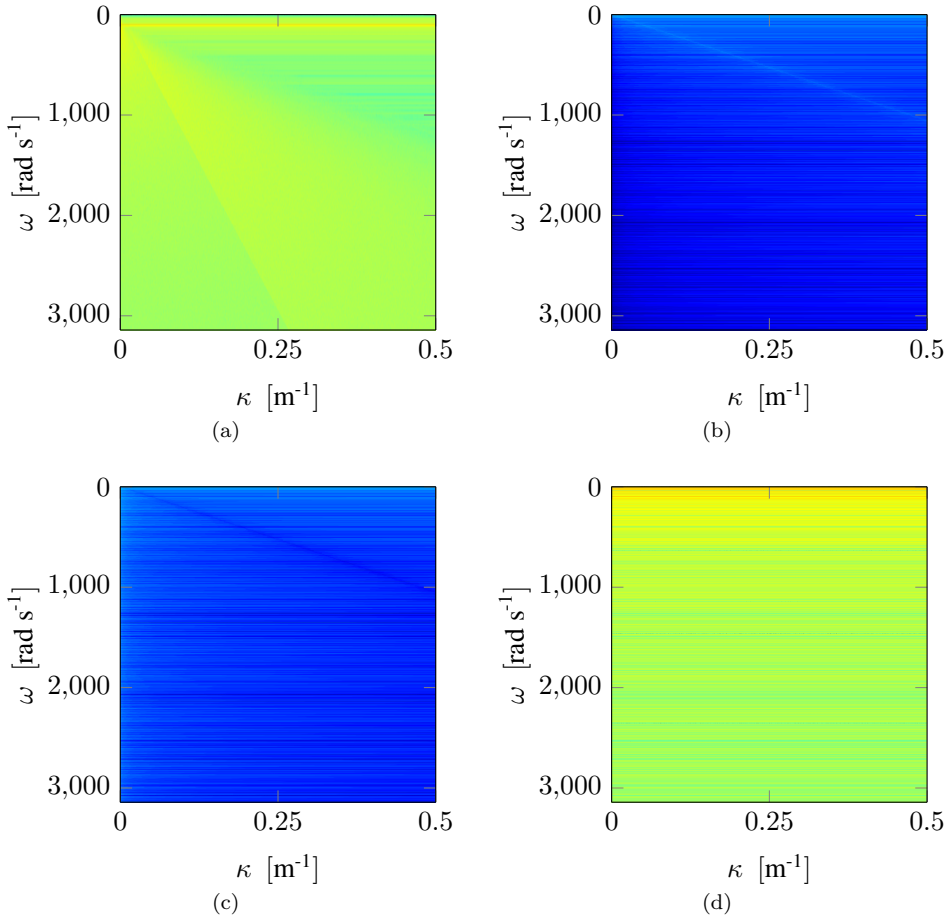


Figure 4.22: *H2 Identity check with the GST set for all radial wavenumber-angular frequency combinations. (a) submatrix element (1,1) (b) submatrix element (1,2) (c) submatrix element (2,1) (d) submatrix element (2,2)*

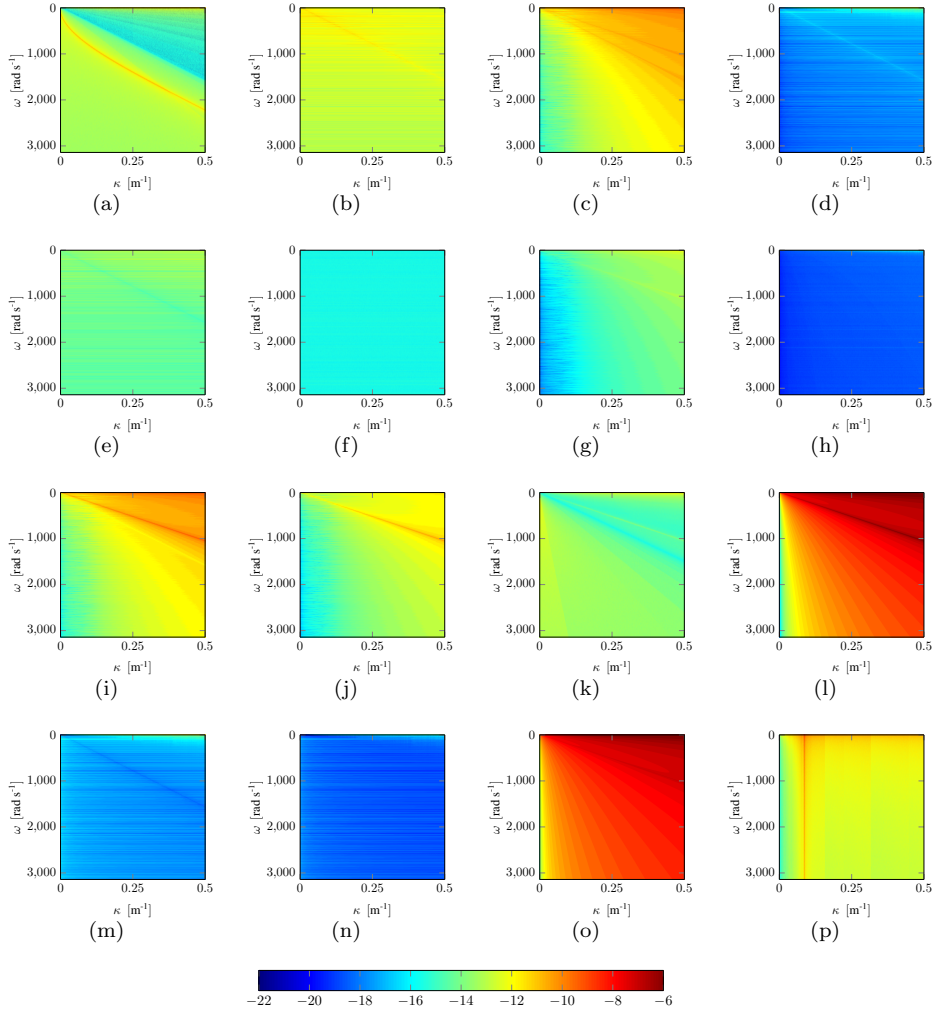


Figure 4.23: *V1 Identity Check with the GST set for all radial wavenumber-angular frequency combinations. (a) submatrix element (1,1) (b) submatrix element (1,2) (c) submatrix element (1,3) (d) submatrix element (1,4) (e) submatrix element (2,1) (f) submatrix element (2,2) (g) submatrix element (2,3) (h) submatrix element (2,4) (i) submatrix element (3,1) (j) submatrix element (3,2) (k) submatrix element (3,3) (l) submatrix element (3,4) (m) submatrix element (4,1) (n) submatrix element (4,2) (o) submatrix element (4,3) (p) submatrix element (4,4)*

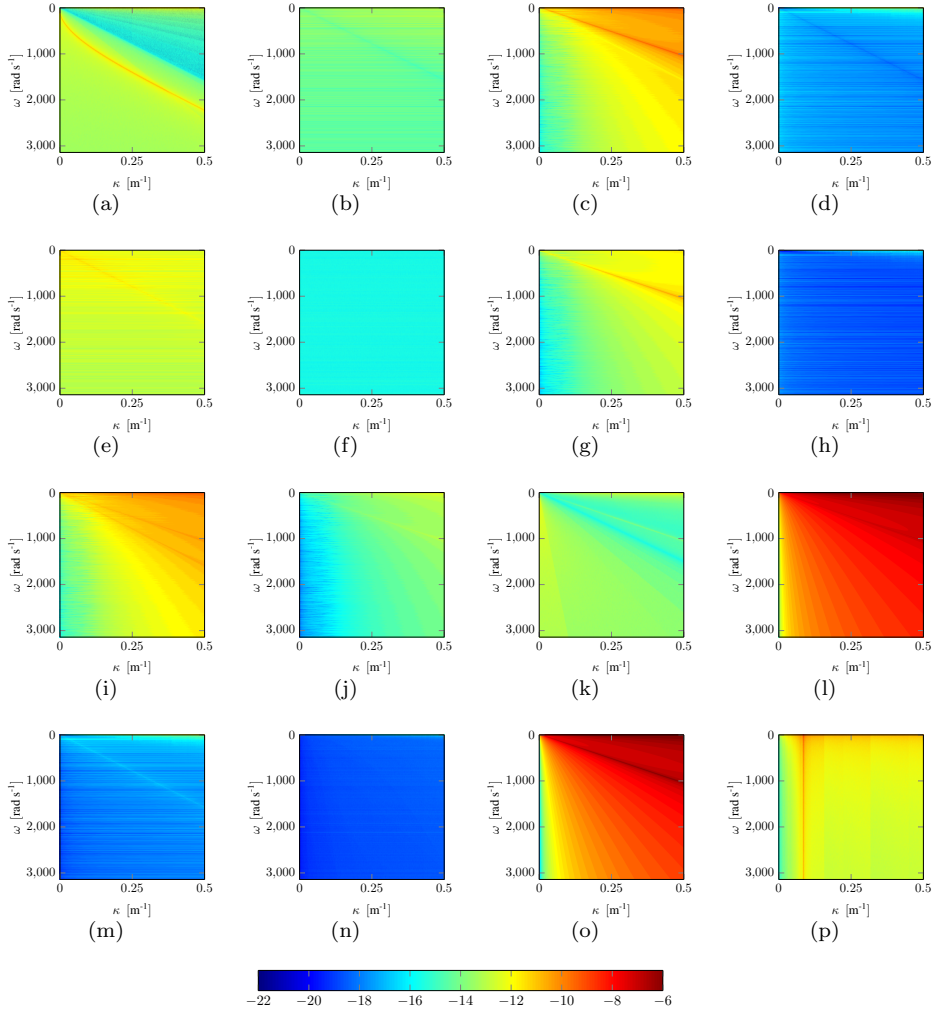


Figure 4.24: *V2 Identity Check with the GST set for all radial wavenumber-angular frequency combinations. (a) submatrix element (1,1) (b) submatrix element (1,2) (c) submatrix element (1,3) (d) submatrix element (1,4) (e) submatrix element (2,1) (f) submatrix element (2,2) (g) submatrix element (2,3) (h) submatrix element (2,4) (i) submatrix element (3,1) (j) submatrix element (3,2) (k) submatrix element (3,3) (l) submatrix element (3,4) (m) submatrix element (4,1) (n) submatrix element (4,2) (o) submatrix element (4,3) (p) submatrix element (4,4)*

4.1.E Flux-Normalization Identity Test using HPF Eigenvectors

This appendix shows the results of the flux-normalization identity tests according to equation (4.4), for H1 and V1, and equation (4.5), for H2 and V2, respectively. These tests were carried out using the HPF eigenvector sets.

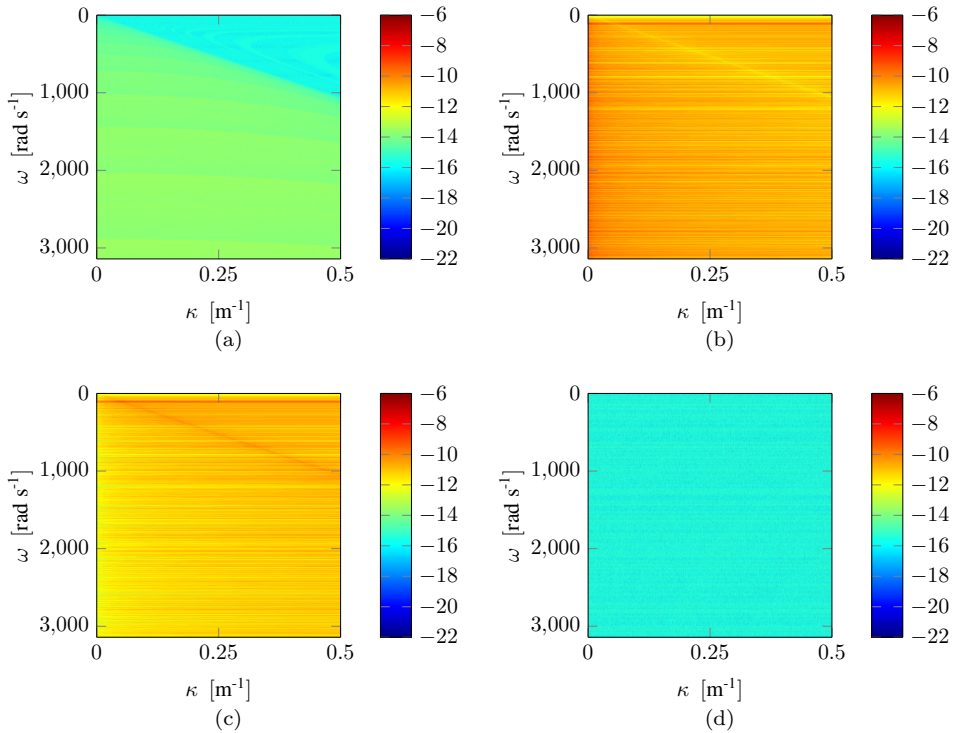


Figure 4.25: *H1 Identity Check with the HPF set for all radial wavenumber-angular frequency combinations. (a) submatrix element (1,1) (b) submatrix element (1,2) (c) submatrix element (2,1) (d) submatrix element (2,2)*

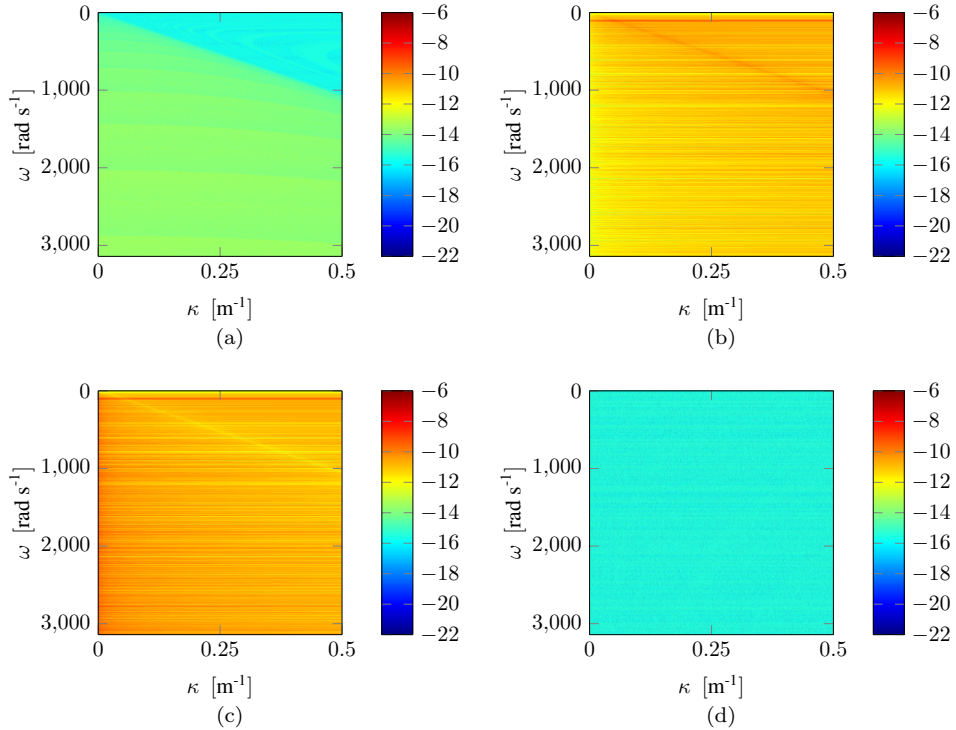


Figure 4.26: *H2 Identity Check with the HPF set for all radial wavenumber-angular frequency combinations. (a) submatrix element (1,1) (b) submatrix element (1,2) (c) submatrix element (2,1) (d) submatrix element (2,2)*

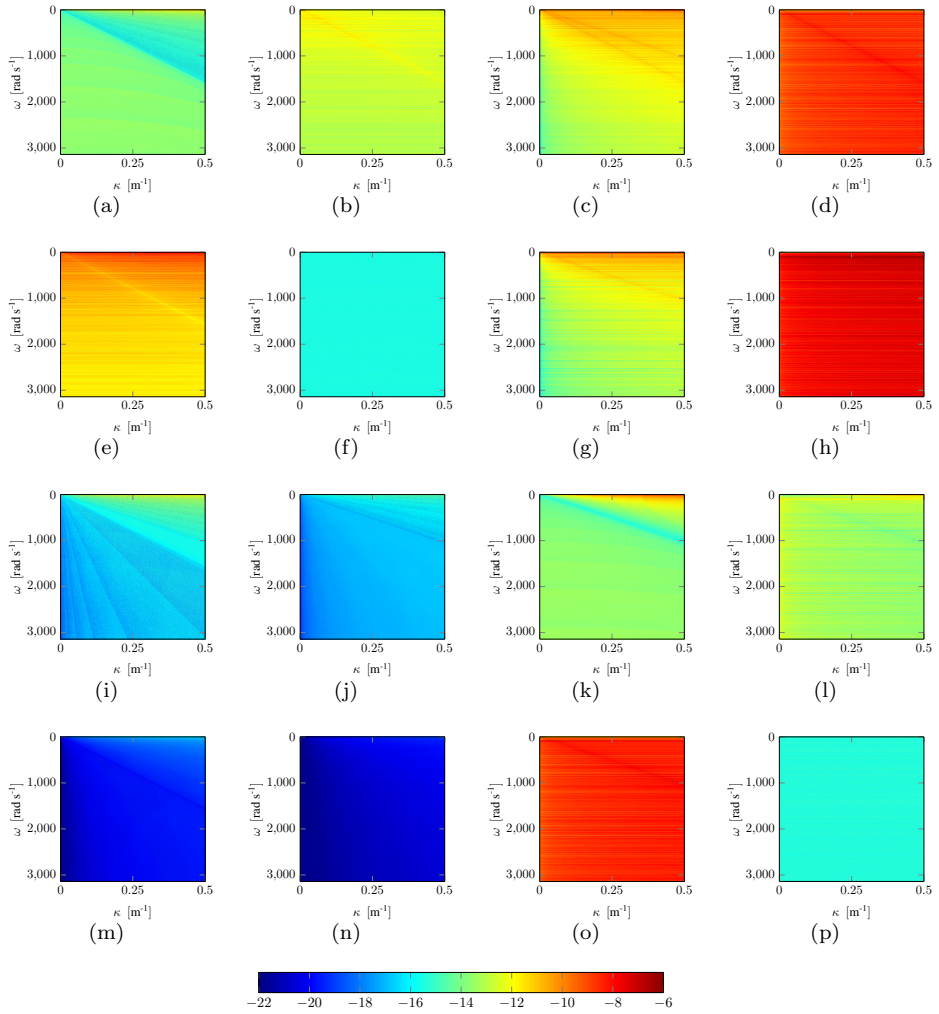


Figure 4.27: *V1 Identity Check with the HPF set for all radial wavenumber-angular frequency combinations. (a) submatrix element (1,1) (b) submatrix element (1,2) (c) submatrix element (1,3) (d) submatrix element (1,4) (e) submatrix element (2,1) (f) submatrix element (2,2) (g) submatrix element (2,3) (h) submatrix element (2,4) (i) submatrix element (3,1) (j) submatrix element (3,2) (k) submatrix element (3,3) (l) submatrix element (3,4) (m) submatrix element (4,1) (n) submatrix element (4,2) (o) submatrix element (4,3) (p) submatrix element (4,4)*

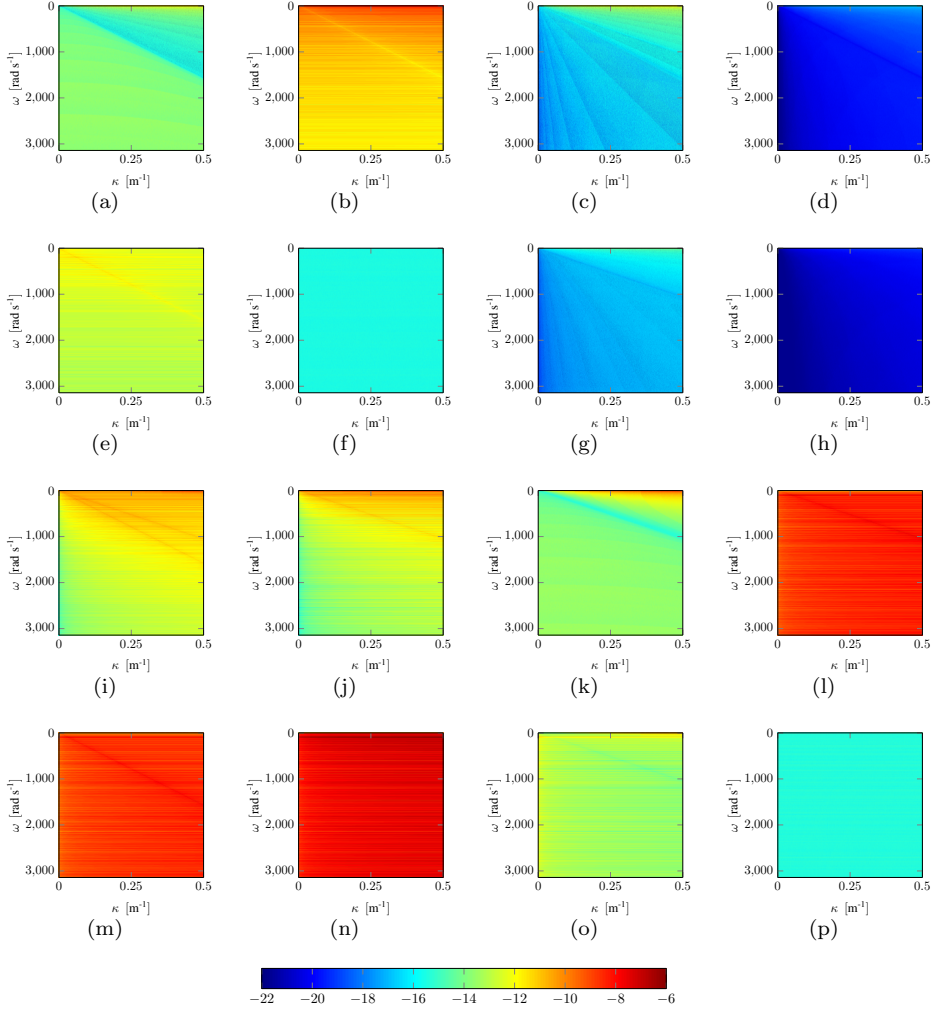


Figure 4.28: *V2 Identity Check with the HPF set for all radial wavenumber-angular frequency combinations. (a) submatrix element (1,1) (b) submatrix element (1,2) (c) submatrix element (1,3) (d) submatrix element (1,4) (e) submatrix element (2,1) (f) submatrix element (2,2) (g) submatrix element (2,3) (h) submatrix element (2,4) (i) submatrix element (3,1) (j) submatrix element (3,2) (k) submatrix element (3,3) (l) submatrix element (3,4) (m) submatrix element (4,1) (n) submatrix element (4,2) (o) submatrix element (4,3) (p) submatrix element (4,4)*

4.2 Homogeneous Space Green's Function Validation

4.2.1 Introduction

In recent years, quite some numerical finite-element and finite-difference codes have been developed for modeling the seismoelectric effect in 2D (e.g. [Haines & Pride \(2006\)](#), [Zyserman *et al.* \(2010\)](#)). Furthermore, [Haartsen & Pride \(1997\)](#) and [Garambois & Dietrich \(2002\)](#) have used an analytically-based code to model some 3D seismoelectric source-receiver combinations in horizontally layered, radially symmetric media. With our code ESSEMOD, we are capable of modeling the wave propagation of *all* existing **Electromagneto-Seismic** and **Seismo-Electromagnetic** source-receiver combinations in layered-Earth scenarios. Our layer-code makes use of global reflection coefficients, leading to an efficient numerical scheme due to the fact that explicit computation of the scattering matrices is not required. Fourier-Bessel transformations are used to go back from the horizontal wavenumber-frequency domain to the space-frequency domain. We compare the results of several of these modeled source-receiver combinations in a homogeneous medium with explicitly derived analytical homogeneous space Green's function solutions, as presented in section 2.4, to validate the results of our seismo-EM layer-code modeling in both arrival times and amplitudes. Especially the amplitudes are important due to the fact that the main reason seismoelectric phenomena are not yet used in industry, are the weak amplitudes of these phenomena (e.g. [Dean & Dupuis \(2011a\)](#), [Thompson *et al.* \(2007\)](#)). By validating our layer-code with homogeneous space Green's function solutions, we obtain certainty in our modeling results and can get better insights in which parameters affect the amplitudes most. Furthermore, ESSEMOD can then be used to validate existing seismo-electromagnetic layered-Earth numerical modeling codes (e.g. [Garambois & Dietrich \(2002\)](#), [Haartsen & Pride \(1997\)](#)). When compared and validated with these codes, our layer-code can be used for testing finite element and finite difference codes, as well as for further investigation of all parameters and coupling effects that play a role in this complex physical phenomenon.

4.2.2 Results

We have directly modeled the homogeneous space expressions for the source-receiver combinations as presented in section 2.4, in order to check the results that are generated by layer-code modeling for a homogeneous medium (referred to as 'ESSEMOD'). To simulate a homogeneous medium in the seismo-EM layer-code, all medium parameters in the different layers are chosen equal to each other, such that all reflection coefficients are zero. For the modeling geometry we have placed a source at $\mathbf{x}_S = (0, 0, 100)$ m, the receivers at 770 m depth and we consider a receiver grid of 51 receivers in both the x_1 - and x_2 -directions with a spacing of 10 m. For the source, we use a Ricker wavelet with a peak frequency of 30 Hz, a phase shift of -0.1 s to visualize the direct source converted EM event arriving around $t=0$ more clearly, and an amplitude of 0.1 GPa/m (for the seismic source types) and 0.1 GA/m² (for

the electrical current source). An overview of the relevant symbols, their physical meaning and the values used for the numerical modeling experiments are presented in Table 4.2. In both numerical schemes (layer-code modeling and the analytical Green's function solutions), all seismo-electromagnetic parameters and their mutual relations are used as input variables, as formulated in Pride (1994). We start by looking at the $v_1^{J_1^e}$ source-receiver combination. We have derived the explicit analytical Green's function solutions using the more compact, HPF eigenvector set. Of course we could also derive the Green function solutions using the GST set. Figure 4.29 displays the results of the $v_1^{J_1^e}$ source-receiver combination for Figure 4.29a, the analytical Green's function solution, Figure 4.29b, the ESSEMOD HPF solution and Figure 4.29c the ESSEMOD GST solution. We can clearly observe the three different events that are to be expected: the direct source-converted EM field, the direct fast P-wave and the direct S-wave coseismic fields. We have used the logarithmic scale in order to be able to see most of the generated fields. All three solutions show a perfect match of the events in both amplitude and phase. This is emphasized in the trace-overlay comparison for zero-offset, presented in Figure 4.30. We see the result obtained from ESSEMOD using the GST set in red, the ESSEMOD result using the HPF set is displayed in black-dashed and we use blue dots for the analytical result.

However, we can also clearly observe differences in numerical noise levels between the HPF set and the GST set, by looking at Figure 4.29. The GST set yields a much cleaner shot record and is once again proven to be preferred for seismo-electromagnetic layered-Earth modeling. We can also see that the GST set matches perfectly with the analytically derived Green's function solutions (which are based on the HPF set). To truly compare 'apples' with 'apples', we will only present the comparison with the HPF-based ESSEMOD results for the other source-receiver combinations under consideration. We will also adjust the scale of the figures such that we purely can focus on the events.

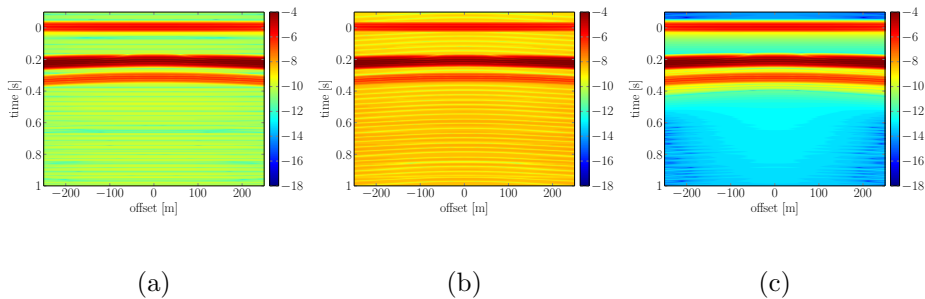


Figure 4.29: Comparison between the analytical Green's function solution and the results of ESSEMOD using the HPF and the GST eigenvector sets, for the $v_1^{J_1^e}$ source-receiver combination. The amplitudes are plotted on a logarithmic scale, in order to clearly visualize all generated events. (a) The analytical Green's function solution (b) Result of ESSEMOD using the HPF set (c) Result of ESSEMOD using the GST set

Let us examine the homogeneous space solutions compared to ESSEMOD more closely, by looking at a purely P-SV-TM source-receiver combination: $E_1^{f_3^b}$.

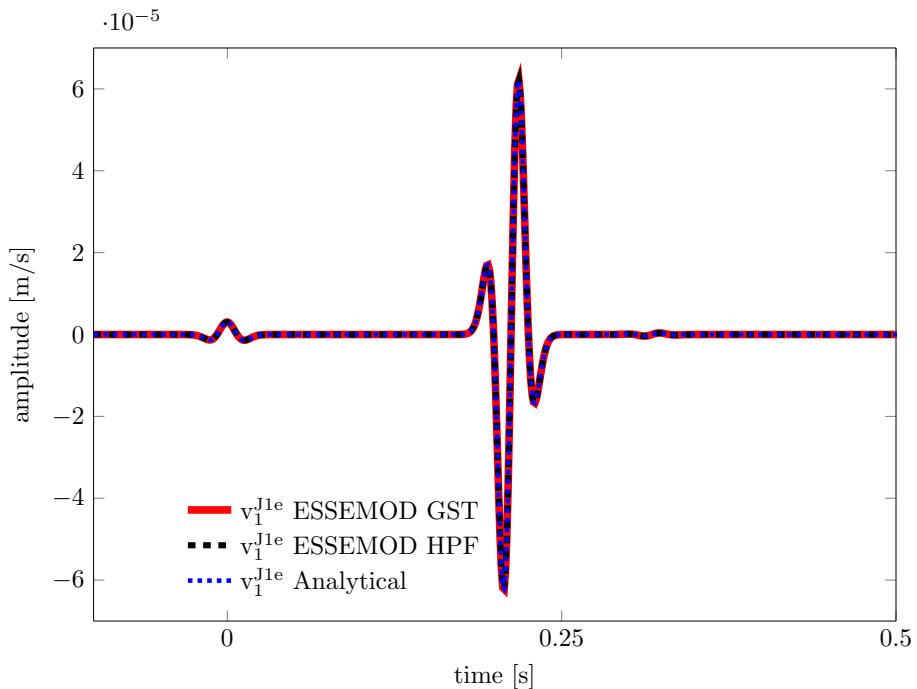


Figure 4.30: Single, zero-offset trace comparison for $v_1^{J_1^e}$ for ESSEMOD GST in red, ESSEMOD HPF in black-dashed and the analytical result blue-dotted.

Figure 4.30 shows the comparison between the analytical result (Figure 4.30a) and ESSEMOD (Figure 4.30b), for this combination. We can again observe that both the timing and the amplitudes of the different fields are identical for the analytical case and ESSEMOD. A direct flat EM event is visible at $t=0$ s, which corresponds to the part of equation 2.301 describing the \hat{G}_{TM} Green's function expression. This is again the source-converted direct EM-wave. Around $t=0.2$ s we can observe a hyperbola with an arrival time corresponding to the fast P-wave velocity, a coseismic field. The contribution in the analytical case comes from the part of equation (2.301) describing the \hat{G}_{Pf} Green's function. Around $t=0.3$ s we observe another hyperbola with a steeper curvature, meaning a slower propagation velocity. The arrival time of this event, another coseismic field, corresponds to the vertically polarized shear-wave velocity, described in the analytical case by the part of equation (2.301) dealing with \hat{G}_{SV} . All individual contributions of the different fields for different medium parameters or fluid properties can be modeled and checked separately using the corresponding field parts of the analytical Green's function solutions. Using this analysis, it can be seen that the slow P-wave does not contribute in this time window,

which makes sense due to its very low propagation velocity.

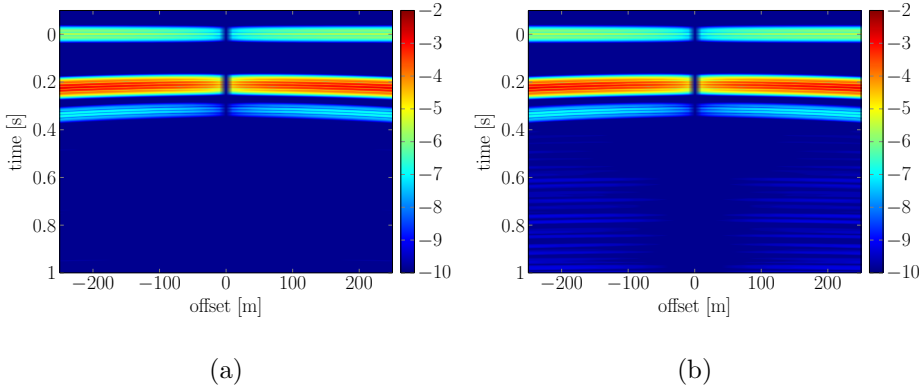


Figure 4.31: (a) Comparison between the analytical Green's function solution and the HPF ESSEMOD result, for the E_1^{f3} source-receiver combination. The amplitudes are plotted on a logarithmic scale, in order to clearly visualize all generated events. (a) The analytical Green's function solution (b) Result of ESSEMOD using the HPF set.

Figure 4.32 shows a trace comparison per offset for this dataset, where we have selected each 5th trace for plotting, and we have amplified the direct EM event with a factor of 100 and the direct S-wave with a factor of 1000. Again the result of ESSEMOD HPF is shown with red solid lines, and the analytical result in black-dashed. One can clearly see that the phase, amplitude and waveform all match perfectly.

Finally, Figure 4.33 shows the shot records on a logarithmic scale for the v_1^{fb} and the H_2^{f1} source-receiver combinations, respectively.

Figure 4.33 displays the result for the v_1^{fb} source-receiver combination. As we now consider a seismic wave quantity due to a seismic source type, one can expect higher amplitudes than in the previous two examples, due to the fact that a complete field type conversion is not required to generate the desired field. Looking at Figure 4.33a, these higher expected amplitudes can indeed be observed. One can observe that in this case the slower, SV-wave related event has a higher amplitude than the fast pressure wave related event. This seems logical, since the source is a dipole bulk force source in the horizontal x_1 -direction, generating mainly shear waves. Figure 4.34 shows the result for the H_2^{f1} source-receiver combination, the magnetic field due to the same dipole bulk force source as used to obtain the result of Figure 4.33. We now observe a direct source converted EM field and only a direct S-wave coseismic field. This is what we expect, since the magnetic field is purely associated with shear waves (see also e.g. Garambois & Dietrich (2002)).

We again observe for both the v_1^{fb} and the H_2^{f1} source-receiver combinations, that the analytical Green's function solutions and the modeling of ESSEMOD using the HPF set in a homogeneous domain, match perfectly in both phase and amplitude.

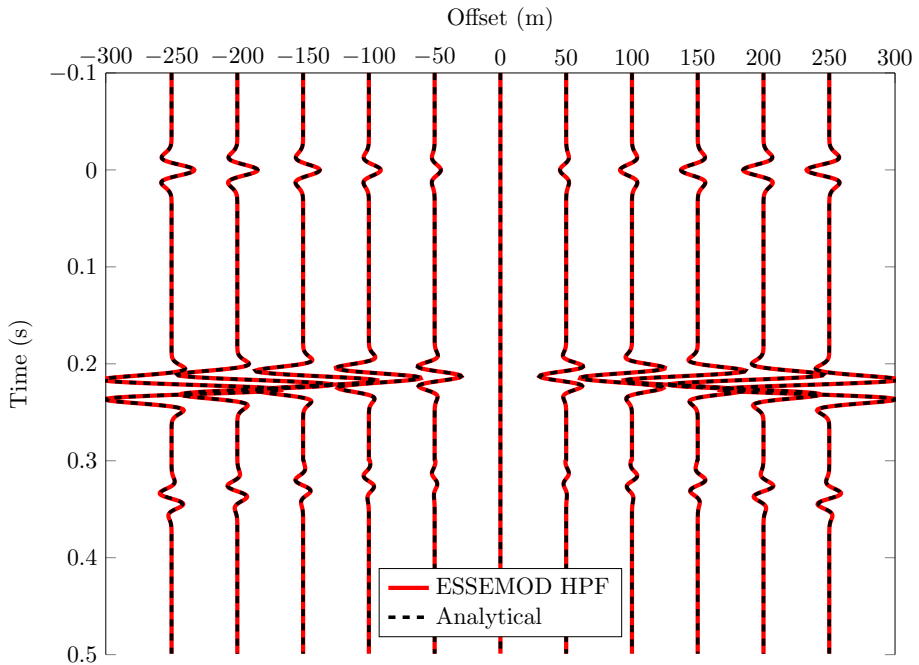


Figure 4.32: Trace comparison for $E_1^{f_3^b}$ for ESSEMOD HPF in red and the analytical result in black-dashed. We have amplified the direct EM event with a factor of 100 and the direct S-wave with a factor of 1000.

4.2.3 Conclusions

We have shown by comparison with explicit homogeneous space Green's function solutions that our seismo-EM layer-code ESSEMOD correctly models the propagation of a particle velocity field component in the x_1 -direction due to both a J_1^e and an f_1^b source type, the electric field component in the x_1 -direction due to an f_3^b source type and the magnetic field component in the x_2 -direction due to an f_1^b source type. We are capable of validating both the amplitudes and arrival times of the results of layer-code modeling for all electromagneto-seismic and seismoelectromagnetic source-receiver combinations in homogeneous media. Hereby, we reduce uncertainty in the obtained numerical results. From the explicit expressions we have obtained insight in the strength of the contributions of the four different possible wave types. Once all sources and receivers are validated, ESSEMOD can be used to compare numerical results obtained with other seismo-electromagnetic layered-Earth codes and afterwards also to validate existing seismo-electromagnetic finite-difference and finite-element codes.

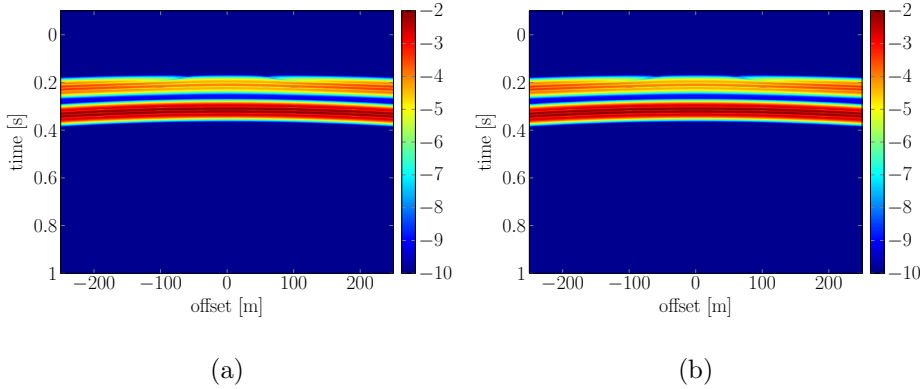


Figure 4.33: (a) Comparison between the analytical Green's function solution and the HPF ESSEMOD result, for the v_1^{fb} source-receiver combination. The amplitudes are plotted on a logarithmic scale, in order to clearly visualize all generated events. (a) The analytical Green's function solution (b) Result of ESSEMOD using the HPF set.

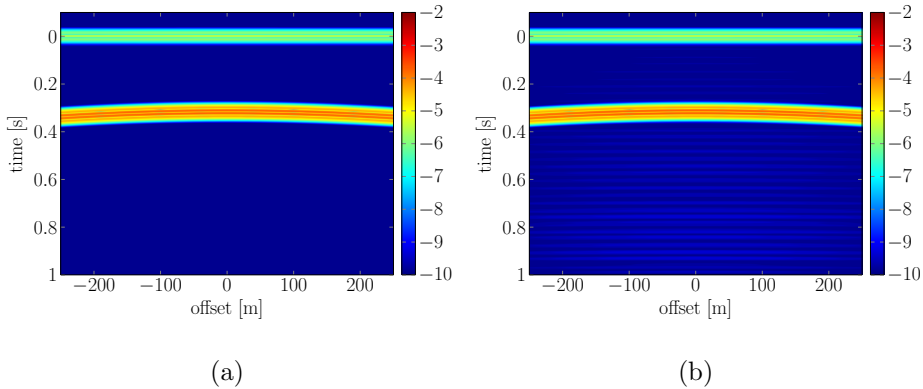


Figure 4.34: (a) Comparison between the analytical Green's function solution and the HPF ESSEMOD result, for the H_2^{fb} source-receiver combination. The amplitudes are plotted on a logarithmic scale, in order to clearly visualize all generated events. (a) The analytical Green's function solution (b) Result of ESSEMOD using the HPF set.

4.3 Numerical reciprocity checks

In this section, we test the algorithm of our seismo-EM layer-code by carrying out seismo-electromagnetic reciprocity checks. For the reciprocal experiment, every receiver of the 'normal' experiment is turned into a source in the reciprocal experiment. At the same time, in the reciprocal experiment there is only one receiver at the location of the source in the 'normal' experiment. The source types and receiver types are switching as well: in the reciprocal experiment the source type becomes the re-

Table 4.2: Overview of the relevant medium parameters used for both modeling schemes.

Property	symbol	Value	Dimension
Porosity	φ	0.4	[-]
Pore fluid density	ρ^f	$1.0 \cdot 10^3$	[kg/m ³]
Bulk density	ρ^b	$2.7 \cdot 10^3$	[kg/m ³]
Shear modulus framework of grains	G^{fr}	$9.0 \cdot 10^9$	[Pa]
Pore fluid viscosity	η	$1.0 \cdot 10^{-3}$	[kg/(m s)]
Tortuosity	α_∞	3.0	[-]
Static permeability	k_0	$1.3 \cdot 10^{-12}$	[m ²]
Static electrokinetic coupling	$\hat{\mathcal{L}}$	$9.07 \cdot 10^{-9}$	[m ² /(s V)]
Dynamic permeability	\hat{k}	ω -dependent	[m ²]
Effective fluid density	$\hat{\rho}^E$	ω -dependent	[kg m ⁻³ s ⁻¹]
Magnetic permeability of vacuum	μ_0	$4.0 \cdot 10^{-7}\pi$	[H m ⁻¹]
Velocity of light in free-space	c_0	299792458	[m s ⁻¹]
Dielectric permittivity of vacuum	ε_0	$8.85 \cdot 10^{-12}$	[F m ⁻¹]
Relative dielectric permittivity	ε_r	14.13	[F m ⁻¹]
Bulk electric conductivity	σ^e	$1.2 \cdot 10^{-3}$	[S m ⁻¹]
Eff. electr. permittivity incl. coupling	$\hat{\varepsilon}$	ω -dependent	[F m ⁻¹]

ceiver type and vice versa. Depending on the relevant reciprocity relations, there can be sign switches between the normal and the reciprocal experiments. We here compare different source-receiver combinations, for different modeling scenarios. Our source is in the ‘normal’ experiment located at 100 m depth, the receivers at 770 m depth. We start by looking at a purely homogeneous space scenario, for medium A. This is the same medium as used for our homogeneous space validations in Section 4.2, Table 4.2. After that, we introduce a free surface and test for correct reciprocal behaviour of the modeling code. Next, we introduce an interface at 1000 m, creating a contrast medium A over medium B. Medium B varies from medium A having a porosity of 0.2, a static permeability of $1.6 \cdot 10^{-12}$ [m²] and a concentration of $1.0 \cdot 10^{-2}$ [mol/L]. We finalize by looking at models with multiple interfaces, by adding another interface at 1100 m, where the contrast is medium B over medium A.

4.3.1 Homogeneous space reciprocity results

We start by looking at the $v_1^{J_1^e}$ combination and its reciprocal $E_1^{J_1^b}$, displayed in Figure 4.35a. Figure 4.35b displays the opposite modeling scenario. We can observe that for both scenarios, the ‘normal’ modeling results displayed in solid red and the reciprocal modeling results displayed in black-dashed, perfectly match in both phase and amplitude. Since we are modeling in homogeneous space, both scenarios yield identical results. In a layered-Earth, the results of Figure 4.35a and Figure 4.35b would be different. For this source-receiver combination, we have amplified both the direct EM and the direct shear waves by a factor of 100, for visualization purposes.

We now compare the $H_2^{J_2^b}$ results of the ‘normal’ model run with the $-v_1^{J_2^m}$ results of the reciprocal model. The results are presented in Figure 4.36. In this case, we have amplified the direct EM event with a factor of 10. We can observe that the ‘normal’ model and the reciprocal model are identical, but polarity reversed. This

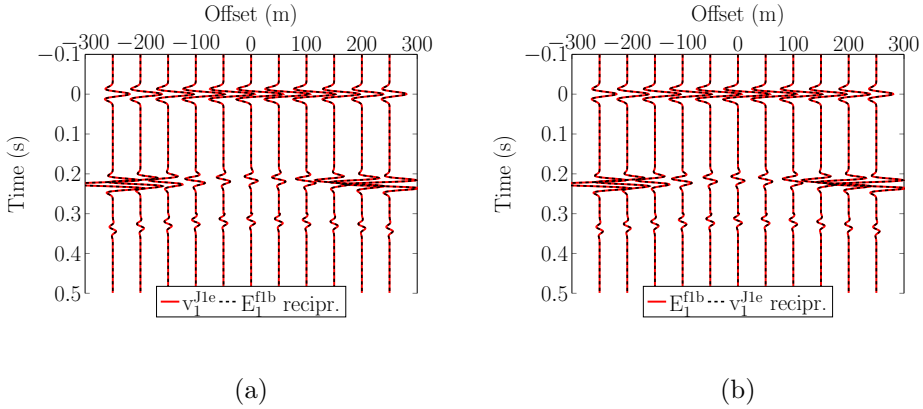


Figure 4.35: Reciprocity trace comparison with offset (a) $v_1^{J_1^e}$ combination for the ‘normal’ experiment, $E_1^{J_1^b}$ for its reciprocal (b) $E_1^{J_1^b}$ combination for the ‘normal’ experiment, $v_1^{J_1^e}$ for its reciprocal

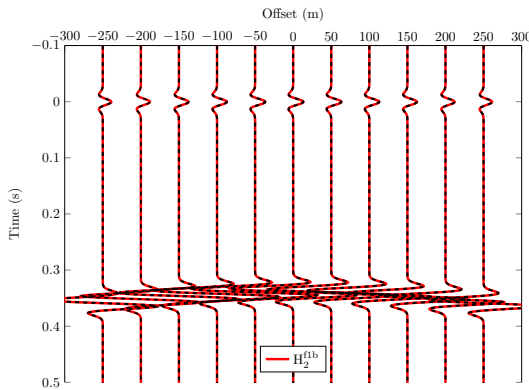


Figure 4.36: Reciprocity trace comparison with offset. $H_2^{f_1^b}$ combination for the ‘normal’ experiment in solid red, $-v_1^{J_2^m}$ for its reciprocal in black-dashed.

is due to the fact that the reciprocity relation between these two source-receiver combinations introduces also an additional minus sign, which we did not yet correct for in this model.

In order to easily see all generated events in the following, more complicated models, we will now display the shot records again on a logarithmic scale. We now introduce a free surface in the homogeneous space models. We look at the $E_1^{J_1^b}$ combination and its reciprocal $v_1^{J_1^e}$. Figure 4.37a displays the shot record for $E_1^{J_1^b}$

and Figure 4.37b shows the reciprocal result for $v_1^{J_1^e}$. We again observe a perfect dynamic match.

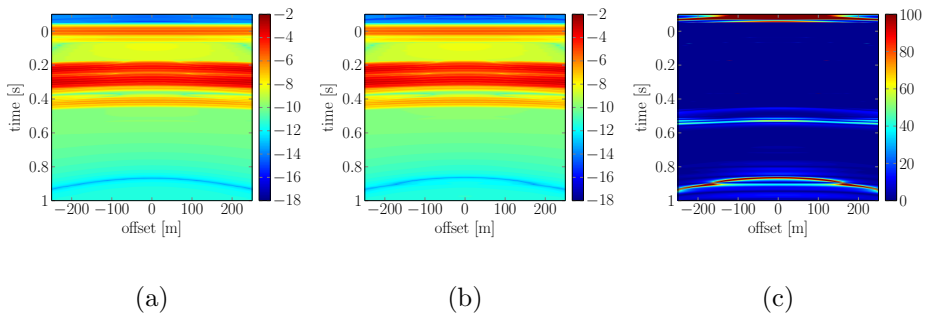


Figure 4.37: (a) Reciprocity shot record comparison on a logarithmic scale, for a homogeneous model with a free surface. (a) $E_1^{f_b}$ combination for the ‘normal’ experiment, (b) $v_1^{J_1^e}$ for the reciprocal experiment. (c) The difference plot (a)-(b), normalized with (b) and multiplied with a factor 100, displaying the relative error in percentage.

We can observe each of the expected events: the direct coseismic fields and their source-side ghosts. Some of the events are masked by the direct P- and S-wave arrivals, since their arrival time is similar to these direct coseismic fields. This modeling experiment shows that the free surface is correctly implemented. Since it is difficult to compare figures in small detail on a logarithmic scale, we also look at the relative difference between the forward model and the reciprocal result. The difference plot in Figure 4.37c, displays the subtraction of the forward model minus the reciprocal model, normalized by the reciprocal model and multiplied with a factor of 100, to result in the relative error in percentage. We can clearly see that at the locations where the events occur, the relative difference is 0 %. However, a small difference is observable in Figure 4.37c just before $t = 0.5$ s, which is probably related to the weak tail of the event starting around $t = 0.4$ s in Figures 4.37a and 4.37b. The higher relative errors occur at locations where no events are visible. This is to be expected since when there are minor differences occurring for the values that are very small (close to zero), the corresponding relative error grows quickly. The difference plot clearly displays a perfect match between the forward and reciprocal models. For the following results, we will not display these difference plots anymore, but we have checked the results in this manner.

4.3.2 Models with interfaces

We start by looking at the reciprocity tests for models with a single interface at 1000 m depth. We look again at the $E_1^{f_b}$ combination and its reciprocal $v_1^{J_1^e}$. Comparing Figure 4.38a and Figure 4.38b, we can observe as good as identical results in both phase and amplitude. The shot records contain besides coseismic/coelectric fields, also flat events corresponding to interface responses. However, these are hard to see

for this model, due to the fact that they are masked by the coseismic fields.

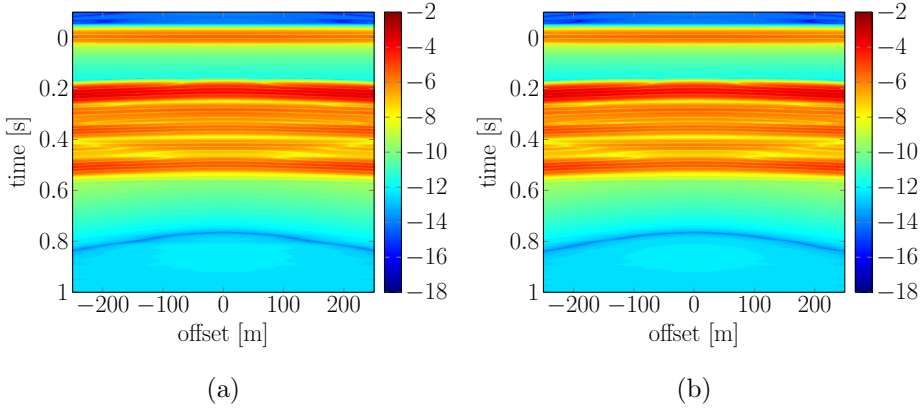


Figure 4.38: (a) Reciprocity shot record comparison on a logarithmic scale, for a model with a single interface at 1000 m depth. (a) $E_1^{f_1^b}$ combination for the ‘normal’ experiment, (b) $v_1^{J_1^e}$ for its reciprocal.

Figures 4.38a and 4.38b show that by adding another layer, additional multiples are observable, due to bounces of the fields in the layer between 1000 and 1100 m depth. Again, a perfect dynamic match is visible.

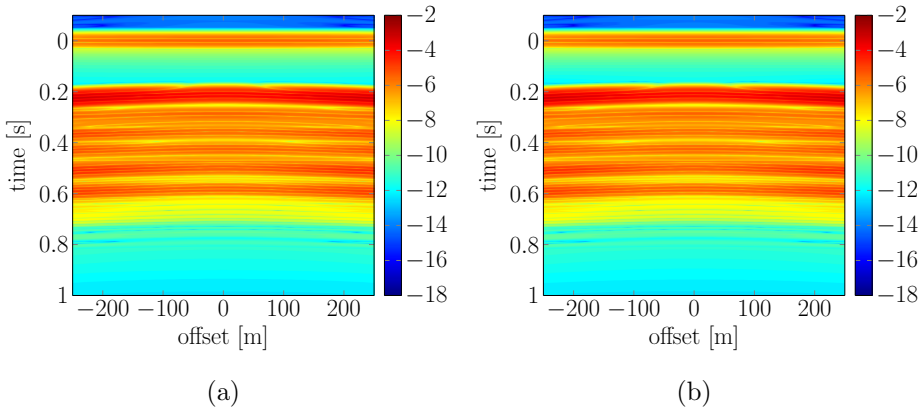


Figure 4.39: (a) Reciprocity shot record comparison on a logarithmic scale, for a model with an interface at 1000 m and a second interface at 1100 m depth. (a) $E_1^{f_1^b}$ combination for the normal experiment, (b) $v_1^{J_1^e}$ for its reciprocal.

For the same model, Figure 4.40a shows the result for the $H_2^{f_1^b}$ combination, whereas Figure 4.40b displays the reciprocal results for $-v_1^{J_2^m}$. Again we observe a

perfect dynamic match.

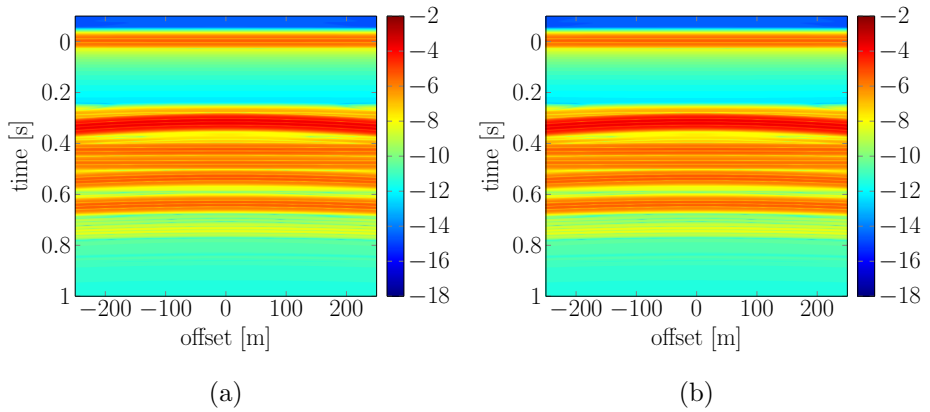


Figure 4.40: (a) Reciprocity shot record comparison on a logarithmic scale, for a model with an interface at 1000 m and a second interface at 1100 m depth. (a) $H_2^{f_1^b}$ combination for the normal experiment, (b) $-v_1^{J_2^n}$ for its reciprocal.

All figures in this section display identical results for both the ‘normal’ and reciprocal scenarios, for multiple source-receiver combinations, indicating that the underlying algorithm of ESSEMOD models both geometrical configurations (source above or below the receivers) consistently.

4.4 Seismo-electromagnetic wave propagation modeling in configurations with fluid/porous medium/fluid transitions: A numerical validation

4.4.1 Abstract

Based on the theory of Chapter 3, Sections 3.2.3-3.2.9, we have extended our layer-code to be able to model seismo-electromagnetic wave propagation in arbitrarily layered Earth geometries with fluid / porous medium / (fluid) interfaces. In this way, we are capable of effectively simulating full seismo-electromagnetic wave propagation, i.e. all existing seismoelectromagnetic and electromagneto-seismic source-receiver combinations, in typical laboratory configurations. We validate the underlying global reflection scheme by comparing it with an independently developed layered-Earth modeling code for purely electromagnetic fields. The results show a perfect match in both amplitude and phase, indicating that ESSEMOD is correctly modeling the electromagnetic parts of the seismo-electromagnetic wave propagation in horizontally layered media with fluid / porous medium / fluid transitions. We finalize with a seismo-electromagnetic reciprocal modeling experiment, proving that also the full seismo-electromagnetic wave propagation through fluid / porous medium transitions is modeled consistently.

4.4.2 Introduction

The main reason why seismo-electromagnetic techniques are not yet widely applied in industry, is that the seismo-electromagnetic conversion has a very low signal-to-noise ratio. In addition, very little is still understood of this complex physical phenomenon. Therefore, it is crucial to be able to perform numerical modeling experiments to carefully investigate the effect and the parameters that play a role. However, to really make a step towards successful application of seismo-electromagnetic methods in the field, the numerical modeling results have to be compared and validated using laboratory experiments.

Over the last couple of years, several seismo-electromagnetic laboratory experiments have been carried out in an attempt to validate the posed theory by [Pride \(1994\)](#) and to better understand this complex physical phenomenon (e.g., [Zhu *et al.* \(2000\)](#), [Zhu & Toksöz \(2005\)](#), [Schoemaker *et al.* \(2012\)](#)). Typically, the laboratory experiments are carried out using water-tanks in which the sources, receivers and sample under consideration can be deployed. In order to successfully model these kinds of configurations, the numerical algorithm must be able to handle configurations with fluid / porous medium interfaces correctly. Some recent examples of comparisons between laboratory measurements and theoretical numerical predictions are [Schakel *et al.* \(2011\)](#) and [Smeulders *et al.* \(2014\)](#). However, the numerical modeling scheme used in these articles was specifically designed for the laboratory configuration at use. The schemes make use of an explicitly defined seismo-electromagnetic reflec-

tion coefficient at a certain interface (Schakel & Smeulders, 2010). Furthermore, only the electric field components due to an acoustic pressure source could be modeled, thereby only considering the seismo-electromagnetic P-SV-TM propagation mode.

We have extended our layer-code to be able to model seismo-electromagnetic wave propagation in arbitrarily layered Earth geometries with fluid / porous medium / (fluid) interfaces. In this way, we are capable of effectively simulating full seismo-electromagnetic wave propagation (i.e. all existing seismo-electromagnetic source-receiver combinations) in typical laboratory configurations, meaning a porous sample in a water tank.

The theoretical details can be found in Chapter 3, Sections 3.2.3-3.2.9. We will present a first aspect of the actual validation of the numerical code itself: the comparison with an independently developed layered-Earth modeling code for purely electromagnetic fields (Hunziker *et al.*, 2015). By putting the coupling coefficient in our modeling code to zero, the poroelastic system completely decouples from the electromagnetic system. In this way, the seismo-EM layer-code can also be used to model poroelastic and electromagnetic wave phenomena in layered Earth models. In addition, the decoupled system provides us with the means to reduce the complexity of the recordings, thereby enabling to validate specific parts of the algorithm, in this case the reflection and transmission at fluid / porous media interfaces. We will finalize with a seismo-electromagnetic reciprocal modeling experiment in a geometry with fluid / porous medium transitions.

4.4.3 Results

We want to focus on the validation of the global reflection algorithm that underlies the seismo-EM layer-code, adapted for typical laboratory configurations that contain fluid / porous medium / fluid transitions. To this end, we compare the electromagnetic part of our code, with the results of an already existing, purely electromagnetic layered-Earth code, referred to as ‘EMMOD’ (Hunziker *et al.*, 2015).

We model for $N_t = 2048$ amount of time samples, with a sampling step $\Delta t = 2.083333 \cdot 10^{-5}$ s. The number of radial frequencies ω is defined as $N_\omega = N_t/2 + 1$, and the radial frequency sampling rate $\Delta\omega = 2\pi/(N_t \cdot \Delta t)$ rad \cdot s $^{-1}$. The wavelet is a first derivative of a Gaussian, with a peak frequency of 3 kHz. We consider 51 receivers in both horizontal directions, with a spacing of 10 m. All results represent the shot records at zero-offset for x_2 , sliced along the x_1 direction. The positive x_3 -axis is pointing downwards, indicating depth.

Let us consider a geometry with a porous medium (represented by a porous layer) in between two fluid-halfspaces. We study a purely electromagnetic scenario. We focus on three different experiments. Firstly, a full transmission experiment where we place the electric current source (in the horizontal x_1 direction) in the upper fluid halfspace at -40 m depth (40 m above the fluid/porous medium interface), and the horizontal x_1 electric field component receivers in the lower fluid halfspace at 1200 m depth. The fluid / porous medium and porous medium / fluid interfaces are located at 0 m and 1000 m depth, respectively. As can be clearly observed

in Figure 4.41, the modeled results of ESSEMOD and EMMOD almost perfectly match in both amplitude and phase. Small differences are observable in the later arriving, weaker field, around $t=0.45$ s. Despite these small differences, the results are clearly demonstrating that the full transmission is correctly modeled in our seismo-EM layer-code. Often in seismo-electromagnetic wave propagation laboratory tests, the receivers / electrodes are placed in the solid, whereas the source is an acoustic pressure source located in the fluid. To model a similar configuration, we again consider a source at -40 m in the upper fluid halfspace, but now the receivers are being placed in the porous medium, at 600 m. The rest of the geometry remains the same. The results are presented in Figure 4.42. It can be clearly observed that the global reflection algorithm of the seismo-EM layer-code can also handle these specific geometries correctly. Thirdly, we will consider a pure reflection geometry, i.e. source and receivers both placed in the upper fluid halfspace. To investigate whether the recursive updating of the global reflection matrices works properly, we have added another porous layer to the porous medium. The interface separating these two porous layers is positioned at 700 m. We now place the source at -400 m and the receivers at -30 m. The rest of the geometry stays identical to the previous model runs. Figure 4.43 clearly shows that the results of ESSEMOD and EMMOD also perfectly match for this reflection experiment, except for small differences in amplitude for the later arriving, weaker field, around $t = 0.22$ s. Despite these small differences, the results indicate correct recursive calculation of the global reflection matrices.

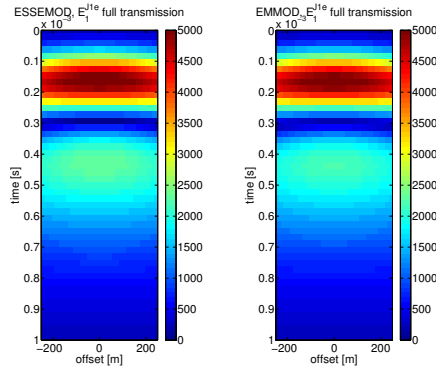


Figure 4.41: Full transmission comparison between ESSEMOD (left panel) and EMMOD (right panel) for $E_1^{J_1^e}$.

As a final experiment, we simulate seismo-electromagnetic wave propagation in a fluid / porous medium configuration, with the interface located at $x_3 = 0$ m. We have removed the lower fluid halfspace, to avoid complex shot records due to multiple seismic reverberations in the porous layer. We will test the algorithm by carrying out a reciprocity test. We first model a horizontal particle velocity field in the x_1 direction, registered in the porous halfspace at $x_3 = 800$ m, due to a horizontal x_1 oriented electric current source placed in the fluid halfspace at $x_3 = -100$ m. For

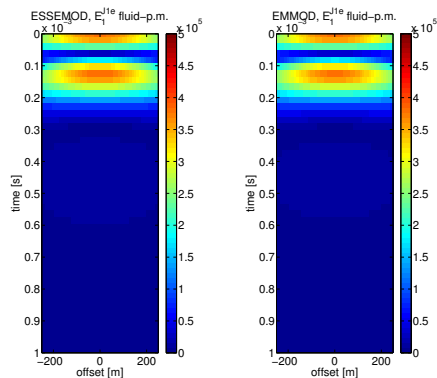


Figure 4.42: Source in the fluid, receivers in the porous medium comparison between ESSEMOD (left panel) and EMMOD (right panel) for E_1^{J1e} .

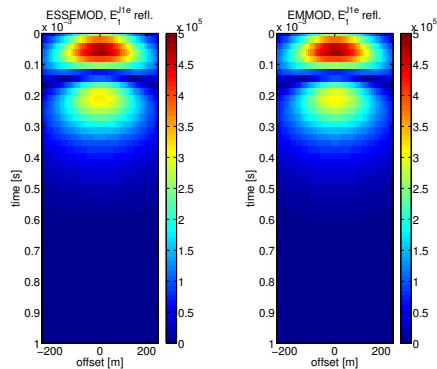


Figure 4.43: Reflection comparison between ESSEMOD (left panel) and EMMOD (right panel) for E_1^{J1e} .

the reciprocal test, we turn every receiver at $x_3 = 800$ m into a source and place only one receiver at $x_3 = -100$ m. The seismo-electromagnetic reciprocal field of v_1^{J1e} is E_1^{J1b} , the horizontal component electric field in the x_1 direction due to a seismic dipole bulk force source in the same direction. Now, the first derivative of a Gaussian wavelet has a peak frequency of 30 Hz. The results in Figure 4.44 show that also the reciprocal test for seismo-electromagnetic wave propagation in fluid / porous medium configurations matches in both phase and amplitude. We expect two interface response fields, related to the seismic P- and S-wave propagation in the porous medium. The fields arrive at traveltimes corresponding to the one-way path of the mechanical waves in the porous medium.

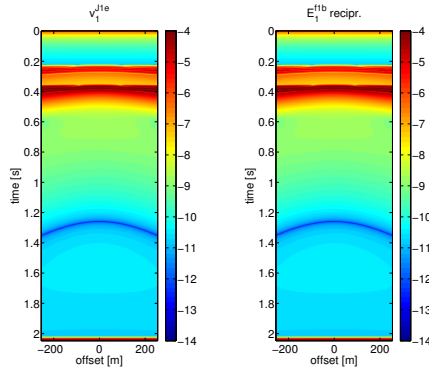


Figure 4.44: Reciprocity tests for seismo-electromagnetic wave propagation in a fluid/porous medium configuration. Note that the event at the bottom of the time window (around $t = 2$ s), represents the acausal part of the direct source-converted EM response arriving around $t = 0$ s. (left) $v_1^{J_1^e}$. (right) The reciprocal $E_1^{I_1^b}$

4.4.4 Discussion

The above results show that the global reflection algorithm underlying our seismo-EM layer-code seems to be working correctly for typical laboratory geometries with fluid/porous medium/fluid transitions. However, not all aspects of the modeling code have been validated here. Previously, the amplitudes and phases have been successfully validated for the full seismo-electromagnetic theory in homogeneous space geometries (e.g. Section 4.2, Grobde & Slob (2013)). This gives us some control on the modeling results, but it does not validate the underlying reflection mechanism of the layer-code. In an attempt to validate this reflection scheme for typical seismo-electromagnetic laboratory configurations with fluid / porous medium transitions, we have here compared the electromagnetic part of the theory with an existing layered-Earth code for electromagnetic fields. The poroelasticity part of the seismo-electromagnetic theory has not yet been compared with any other existing layered-Earth codes. Nevertheless, the reflection scheme is identical for the electromagnetic part and the full seismo-electromagnetic theory. In addition, the seismo-electromagnetic reciprocity test shows consistent modeling of seismo-electromagnetic wave phenomena in configurations with fluid / porous medium transitions. Further comparison with other seismo-EM layer-codes is desirable to compare for example the absolute amplitudes.

In order to be able to really validate the algorithm and its underlying theory, we need to compare the seismo-EM layer-code with physical laboratory experiments. The algorithm was proven to be working correctly for typical laboratory geometries, thereby clearing the way to comparisons of this type.

4.4.5 Conclusions

As we have shown in the previous section, the results of the validation tests indicate that our seismo-EM layer-code is correctly modeling the electromagnetic parts of the seismo-electromagnetic wave propagation in horizontally layered media with fluid/porous medium/fluid transitions. The results show a perfect match in both phase and amplitude for full transmission and pure reflection experiments as well as for a combination of both. By focusing on the electromagnetic parts only (by choosing the seismo-electromagnetic coupling coefficient equal to zero), we were able to effectively test the recursive global reflection algorithm of our seismo-EM layer-code in configurations that resemble typical seismo-electromagnetic laboratory configurations. In addition, the seismo-electromagnetic reciprocity test in a configuration of a fluid halfspace overlying a porous medium halfspace, shows that also the coupled poroelastic and electromagnetic fields are modeled consistently and yield the expected results.

4.5 Validation with seismo-electromagnetic modeling code of Garambois and Dietrich

4.5.1 Introduction

Thusfar, we have validated our seismo-EM layer-code ESSEMOD by

1. Comparing runs of ESSEMOD with different eigenvector sets
2. Comparing ESSEMOD with explicit homogeneous space Green's function solutions
3. Numerical Reciprocity Tests
4. Comparison of the EM-part of ESSEMOD with an independently developed EM-code.

All of these tests provide confidence that the algorithm of our seismo-EM layer-code works correctly. Nevertheless, not all aspects of the layer-code have been validated. For example, the poroelastic part has not been compared with an independently developed modeling code. Furthermore, we can check visually whether the events arrive at the expected travel times, but in terms of amplitude we have only obtained certainty for homogeneous space models and for the purely EM-scenario. There exists another seismo-EM layered-Earth modeling code, developed by [Garambois & Dietrich \(2002\)](#). The same deficiency in amplitude validation holds for their code. Therefore, in this section we try to validate the two independently developed seismo-electromagnetic layered-Earth modeling codes (ESSEMOD and the code of [Garambois & Dietrich \(2002\)](#)), not only in terms of phase, but also focusing on absolute amplitudes. It is crucial to get certainty with respect to the amplitudes that come out of the modeling codes, since the amplitudes are the bottleneck for the application of seismo-electromagnetic techniques in the field.

4.5.2 Results

We compare the results of ESSEMOD with the code of [Garambois & Dietrich \(2002\)](#) by looking at the electric field in the x_1 -direction due to a seismic bulk force source in the same direction. We consider the same model as described in Table 4.1, where we locate the source at 100 m depth in medium A, the receivers at 300 m depth in medium A, and the interface separating medium A and medium B located at 1000 m. As a source, we use a Ricker wavelet with a peak frequency of 30 Hz and an amplification factor of $1 \cdot 10^8$. We apply a time shift of 0.1 s to the wavelet such that the direct EM event arriving at $t=0$ also has a nice waveform. We use $N_t = 2048$, $\Delta t = 0.001$ s, $N_\omega = N_t/2 + 1$ and $\Delta\omega = \frac{2\pi}{N_t \cdot \Delta t}$ rad·s⁻¹. Figure 4.45 displays a shot record comparison on a logarithmic scale. We can see that the arrival times and relative amplitudes of most of the events are matching perfectly. The only events that are generated stronger by ESSEMOD are the direct S-wave and the reflected S-S wave related coseismic fields. Figure 4.46 displays a zero-offset trace comparison between

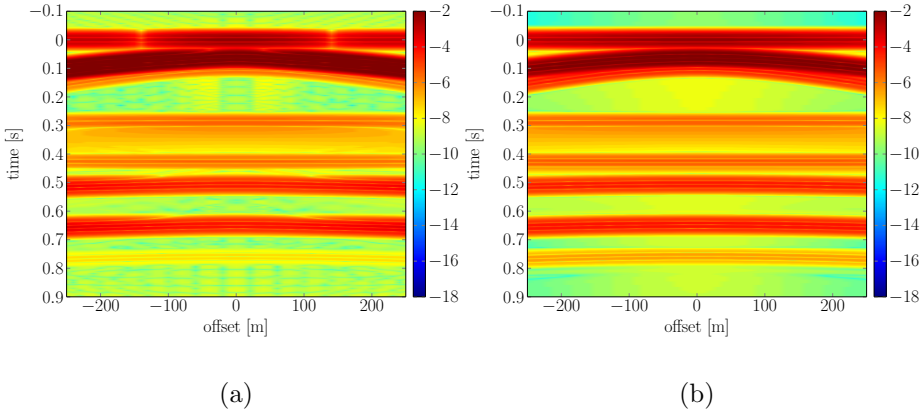


Figure 4.45: (a) Shot record comparison ESSEMOD with the code of [Garambois & Dietrich \(2002\)](#), for E_1^{fb} , plotted on a logarithmic scale. (a) Results code Garambois and Dietrich (b) Results ESSEMOD.

the result of ESSEMOD in red-dashed, and the result of Garambois and Dietrichs modeling code in blue. The results of ESSEMOD have been amplified by a factor of 4 to match the absolute amplitudes of Garambois and Dietrich. All events match perfectly, except for the direct shear wave and reflected S-S wave related coseismic fields, where the amplitudes of ESSEMOD are (after amplification with the factor of 4) stronger than the amplitudes generated by Garambois and Dietrich. Another difference is the polarity switch for the direct source converted EM fields. Since, we have validated this source-receiver combination already by homogeneous space solutions and reciprocity tests, we are quite sure that the polarity of ESSEMOD is correct.

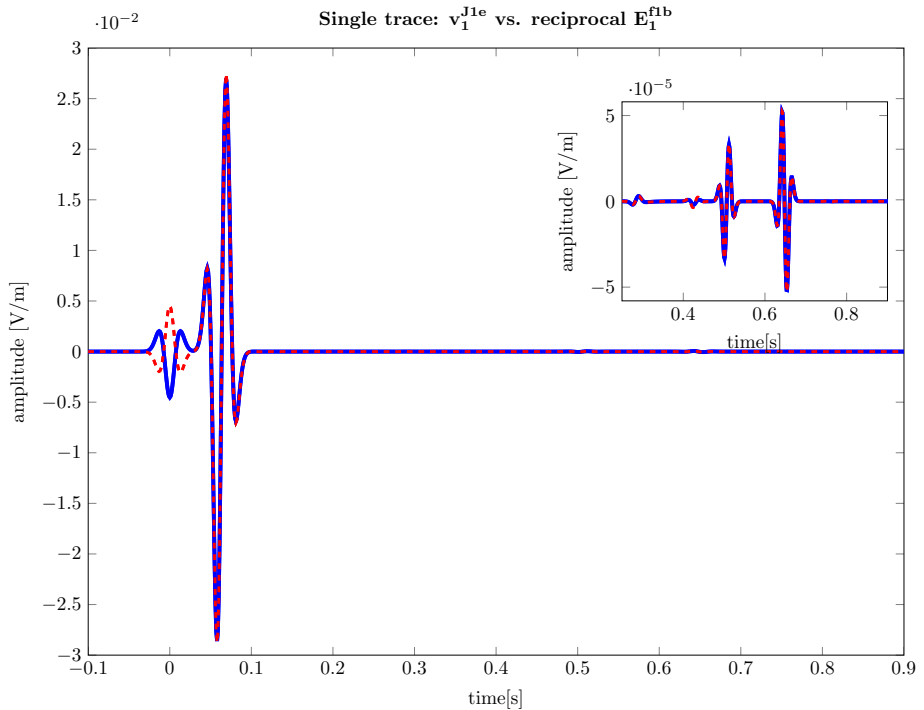


Figure 4.46: (a) Zero-offset trace comparison of ESSEMOD in red-dashed, with the code of Garambois & Dietrich (2002) in blue, for E_1^{flb} , where the results of ESSEMOD have been amplified by a factor of 4.

4.5.3 Discussion and Conclusions

For the model and source-receiver combination under consideration, we have obtained an almost perfect match in both phase and relative amplitudes between ESSEMOD and the code of Garambois & Dietrich (2002). The only anomalous events are the direct S wave and the reflected S-S related coseismic fields. In terms of absolute amplitudes, there is only a difference of a factor of about 4: the code of Garambois & Dietrich (2002) yields amplitudes that are about 4 times higher than ESSEMOD. The cause of this difference is yet unknown and currently under investigation. There is a polarity switch between the codes for the direct, source converted EM field. Based on homogeneous space validations and reciprocity tests, we are quite sure that ESSEMOD generates the correct polarity. Despite the small differences, the almost perfect match in terms of phase and relative amplitudes provides an acceptable validation of the algorithm of our seismo-EM layer-code. Further numerical validation tests and comparisons for different models and source-receiver combinations should be carried out in the future.

4.6 Seismo-electromagnetic feasibility study

4.6.1 Introduction

The major current challenge for the seismo-electromagnetic method is its measurability in the field. The technique has a lot of potential benefits compared to conventional geophysical methods. However, if the converted signals are not (or hardly) measurable by the physical devices (geophones, electrodes) or obscured by noise or other signals, the method remains mainly a theoretical exercise. There are some successful field examples of seismo-electromagnetic signals for groundwater applications (e.g. [Butler *et al.* \(2002\)](#); [Rosid & Kepic \(2005\)](#)), but even for aquifers, that are typically located at tens of meters of depth, the studies show significant challenges in signal measurability.

For oil and gas exploration, the targets are typically located at a few kilometers depth ([Thompson *et al.*, 2007](#)). To investigate the potential of the seismo-electromagnetic effect for exploration purposes, we here carry out a small numerical feasibility study. We investigate for the same model different source-receiver combinations and focus on the signal strength recorded at different distances from the target depth level, which is located at 1000 m depth. At this depth level, an interface is located separating the upper medium B from the lower medium A (which are the same media as used for our reciprocity tests in [Section 4.3](#)). There is no free surface in the model, to be able to focus better on a few major events. Currently, seismic commercial vibrators can apply a maximum pressure of about 0.5 MPa to an area of about 1 m². Geophones can generally detect surface displacements larger than the order of 10⁻⁹ m at frequencies above 1 Hz. We place our source at 1 m depth, and use a Ricker wavelet with a peak frequency of 30 Hz and an amplification factor of 5·10⁵. We focus mainly on the interface response fields, since those are the fields that can provide us with information at depth.

4.6.2 Results

For the model under consideration, we can expect P-wave related interface response fields around 0.32 s, and S-wave related interface response fields around 0.51 s (for the seismic-to-electromagnetic conversions). For the electric-to-seismic conversions, the interface response fields arrivals vary with the receiver depth, and arrive at times equal to the one-way seismic time from the interface upwards to the receiver level. We focus on 6 acquisition geometries, where the receivers are located at 10 m, 15 m, 20 m, 50 m, 500 m, 700 m and 900 m depth. We look at six different source-receiver combinations: four seismic-to-electromagnetic combinations ($E_1^{f_1^b}$, $E_1^{f_3^b}$, $E_1^{q_i}$ and $H_2^{f_1^b}$), one electromagnetic-to-seismic combination ($v_1^{f_1^e}$) and one seismic-to-seismic combination ($v_1^{f_1^b}$). Note that the logarithmic scale of the figures displaying $E_1^{q_i}$ is adjusted to higher amplitudes. Let us assume that signals equal to or larger than the order 10⁻⁸ are measurable. We start by looking at [Figure 4.47](#). In this scenario, the source is located at 1 m depth and the receivers at 10 m depth. Since the source and receivers are located at depth levels quite close to each other, the

numerical results show higher numerical noise levels than we have seen before. This can be explained due to the fact that the Fourier-Bessel transformations need to be evaluated for higher arguments in these scenarios in order to make them damp properly. This numerical noise issue can probably be tackled by increasing the number of radial wavenumber samples. Especially Figure 4.47c shows high noise levels, the rest of the figures are quite clean already for this sampling. We observe that for this

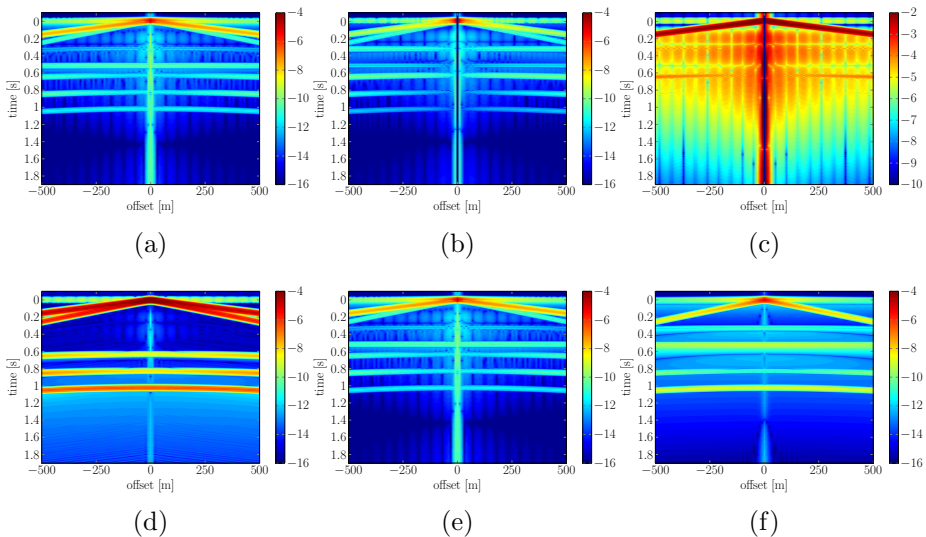


Figure 4.47: Shot records for the source at 1 m depth and the receivers at 10 m depth, with a target interface at 1000 m depth. The shot records are plotted on a logarithmic scale. (a) $E_1^{f_1}$ (b) $E_1^{f_3}$ (c) $E_1^{q_1}$ (d) $v_1^{f_1}$ (e) $v_1^{f_3}$ (v) $H_2^{f_1}$.

scenario, almost all coseismic and interface response fields are below the measurable signal strength, except for the direct P- and S-waves. Only the seismic-seismic source-receiver combination (Figure 4.47d) displays higher amplitudes for the later events. Note that it seems that there is one type of event missing (P-to-S conversion or S-to-P conversion). This is not the case: these two events arrive more or less at the same time due to the fact that the downward and upward pathlengths are more or less similar for this modeling scenario. In addition, the $E_1^{q_1}$ combination (Figure 4.47c), an electric field in the x_1 -direction due to a monopole pressure source, has higher amplitudes than the other converted field combinations. It only displays P-wave related interface response fields, due to the source type under consideration. At zero-offset, no P-SV conversion occurs, and no electric field is generated. We observe relatively high amounts of numerical noise for this specific source-receiver combination for the model configuration under consideration. This most likely has to do with the fact that the receivers (10 m depth) are located very close to the source (1 m depth). We will see that by increasing this vertical distance, the noise levels decrease rapidly. Apparently, the Fourier-Bessel transformation is not suffi-

ciently damped yet for this specific source-receiver combination with the number of radial wavenumbers κ or radial distance r (the arguments of the Fourier-Bessel transformation) under consideration. For the other source-receiver combinations, these parameters are sufficiently sampled and large enough to yield clean numerical results, also for this specific acquisition scenario.

We can observe that the coseismic magnetic field strengths (Figure 4.47f), which are purely associated with S-waves, are also slightly higher.

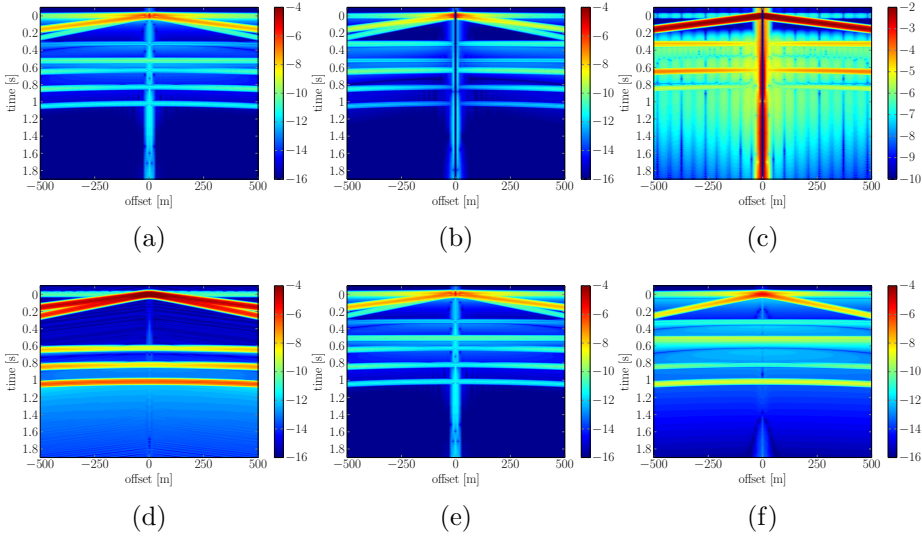


Figure 4.48: Shot records for the source at 1 m depth and the receivers at 15 m depth, with a target interface at 1000 m depth. The shot records are plotted on a logarithmic scale. (a) $E_1^{f_b}$ (b) $E_1^{f_b}$ (c) $E_1^{q_i}$ (d) $v_1^{f_b}$ (e) $v_1^{f_c}$ (v) $H_2^{f_b}$.

Figure 4.48 displays for the same radial sampling already cleaner figures, due to 5 meter depth difference in the receiver level. We can now observe that the $E_1^{q_i}$ combination shows measurable coseismic responses as well as a measurable P-wave related interface response field. The other converted field components do not display measurable converted responses yet. Moving the receiver level 5 meters downwards, we observe in Figure 4.49 still only measurable converted fields for the $E_1^{q_i}$ combination (Figure 4.49c). The amplitudes of all events have been slightly increased.

Moving the receivers to 50 m depth (Figure 4.50), we start noticing that the coseismic arrivals for the $H_2^{f_b}$ combination start to approach the measurable range as well. The interface response fields are still too weak to be measured in the field. We now move the receivers to 500 m depth (Figure 4.51). We can observe that the P-wave related interface response field at 0.3 s in Figure 4.51c, for $E_1^{q_i}$ is clearly measurable. However, we can see that the coseismic fields slowly approach the

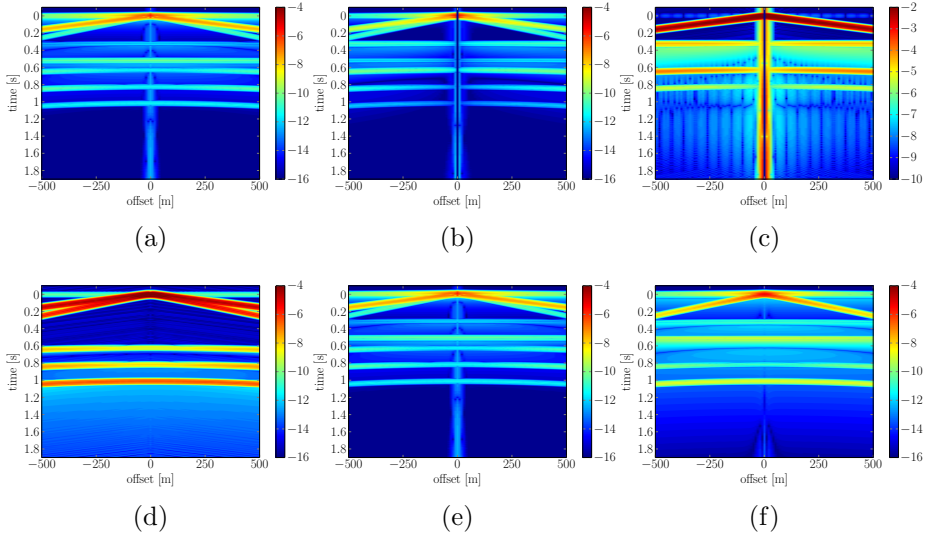


Figure 4.49: Shot records for the source at 1 m depth and the receivers at 20 m depth, with a target interface at 1000 m depth. The shot records are plotted on a logarithmic scale. (a) $E_1^{f_b}$ (b) $E_1^{f_b}$ (c) $E_1^{q_i}$ (d) $v_1^{f_b}$ (e) $v_1^{f_c}$ (v) $H_2^{f_b}$.

arrival times of the interface response field. We see an overall signal strengthening for all other source-receiver combinations, but still only the direct coseismic fields are measurable. The coseismic reflected fields and interface response fields have amplitudes of the order 10^{-10} . For the $H_2^{f_b}$ (Figure 4.51f), we can observe that the S-wave related interface response field starts to become measurable. The results for the receivers at 700 m depth, displayed in Figure 4.52, clearly show that for the $H_2^{f_b}$ combination, the interface response field is clearly measurable. For $E_1^{q_i}$, the P-wave related interface response field is still strongly visible, but starts interfering with the coseismic arrivals. The $E_1^{f_b}$ fields (Figure 4.52a) seem to show a recordable S-wave related interface response field for the near-offsets. However, this stronger amplitude in the near-offsets is probably caused by signal interference with the coseismic reflected fields.

Our final acquisition geometry has the receivers located at 900 m depth, so 100 m from the target interface (about 1 P-wavelength). We can clearly observe that this is not an optimal configuration for the $E_1^{q_i}$ combination, since all events arrive more or less at the same time. Similar behaviour is visible for the other seismic-to-electromagnetic combinations. The S-wave related interface response field for the $H_2^{f_b}$ combination is also not clearly distinguishable anymore. This can be explained by the fact that the upgoing seismic paths are not so long anymore, yielding small phase shifts on the arrival times. Therefore, the interface response fields that arrive more or less at one-way seismic downgoing time, start overlapping with the

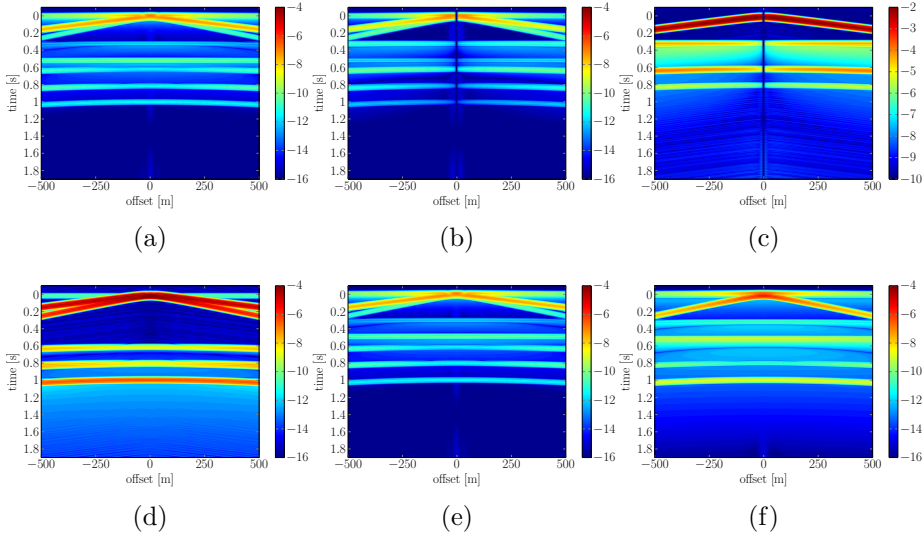


Figure 4.50: Shot records for the source at 1 m depth and the receivers at 50 m depth, with a target interface at 1000 m depth. The shot records are plotted on a logarithmic scale. (a) $E_1^{f^b}$ (b) $E_1^{f^b}$ (c) $E_1^{q^i}$ (d) $v_1^{f^b}$ (e) $v_1^{f^c}$ (f) $H_2^{f^b}$.

coseismic reflected fields and the direct fields. For the electromagnetic-to-seismic configuration of Figure 4.53e, we see that the interface response fields (that arrive at 1-way upgoing time) do not suffer from being masked by coseismic arrivals. These interface responses arrive all around zero time now. Nevertheless, the amplitudes are still in the order of 10^{-10} , just slightly weaker than required for signal measurability.

4.6.3 Discussion

We can observe that, when using source wavelets with an amplitude similar to the maximum amplitude of present-day commercial vibroseis trucks, most converted fields for most seismo-electromagnetic source-receiver combinations have amplitudes that are just outside the dynamic range of present-day geophones. The source-receiver combinations that yield the strongest converted signals are $E_1^{q^i}$ and $H_2^{f^b}$. Especially the $E_1^{q^i}$ combination seems to generate measurable responses even with acquisition geometries that approach surface-to-surface acquisition. Moving the receivers deeper, closer to the target, increases the signal strength of especially the interface response fields. This is explainable, due to the fact that the electromagnetic interface response fields are diffusive fields that decay rapidly with distance. Therefore, smaller propagation distance leads to less losses and stronger recorded signals. Nevertheless, when moving too close to the target depth, direct and reflected coseismic fields start interfering with the interface response fields, masking the desired fields. Specific filtering aimed at separating coseismic fields from interface

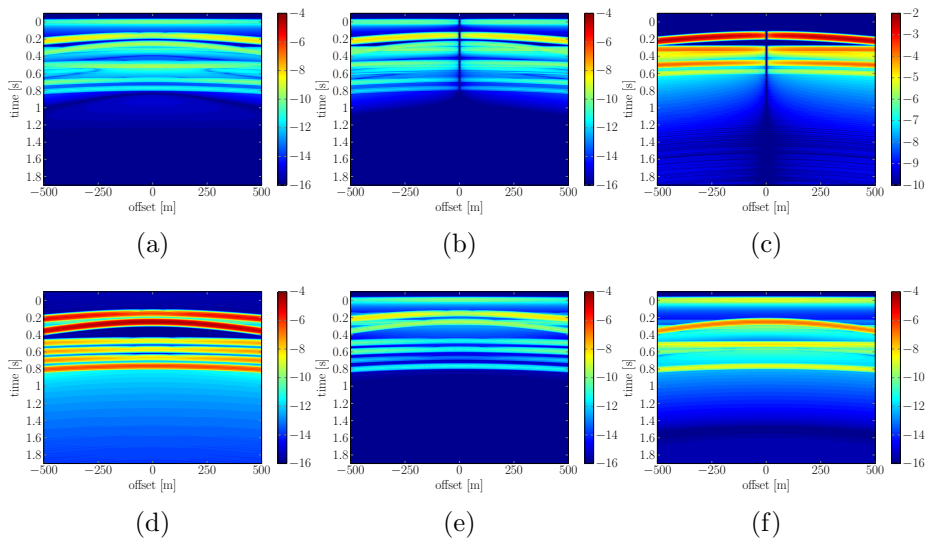


Figure 4.51: Shot records for the source at 1 m depth and the receivers at 500 m depth, with a target interface at 1000 m depth. The shot records are plotted on a logarithmic scale. (a) $E_1^{f^b}$ (b) $E_1^{f^b}$ (c) $E_1^{q^i}$ (d) $v_1^{f^b}$ (e) $v_1^{J^c}$ (v) $H_2^{f^b}$.

response fields is required for these scenarios. For the electromagnetic-to-seismic configurations, the interface response fields do not suffer from being masked by coseismic arrivals, for the acquisition geometry under consideration. Nevertheless, the amplitudes are still in the order of 10^{-10} , just slightly weaker than required for signal measurability. Vice versa, seismic-to-electromagnetic configurations would not suffer from interface response fields that are masked by coseismic fields, for acquisition geometries where the source is located close to the target, and the receivers located close to the surface. In recent years, an acquisition design appears to emerge in the industry that makes use of horizontal downhole sensor arrays or a high-density of vertical boreholes in a certain area (e.g. Bakulin *et al.* (2012b), Bakulin *et al.* (2012a) Berron *et al.* (2012), Cotton & Fergues (2012)). The results of this small feasibility study show that these types of acquisition geometries are useful, and maybe even crucial, for potential application of the seismo-electromagnetic method for exploration purposes. Being able to separate downgoing from upgoing fields and field types, could help distinguishing coseismic fields from interface response fields. However, for successful field decomposition, often many different fields need to be recorded. For seismo-electromagnetics, this number of fields is enormous and practically not feasible. Being able to decompose fields into their field types and up- and downgoing constituents using less recorded fields is beneficial. In Section 6.1, we introduce a multi-depth-level decomposition scheme that enables successful field decomposition using less different field type recordings. As a next step for feasibility studies, more realistic source signals should be used in these studies,

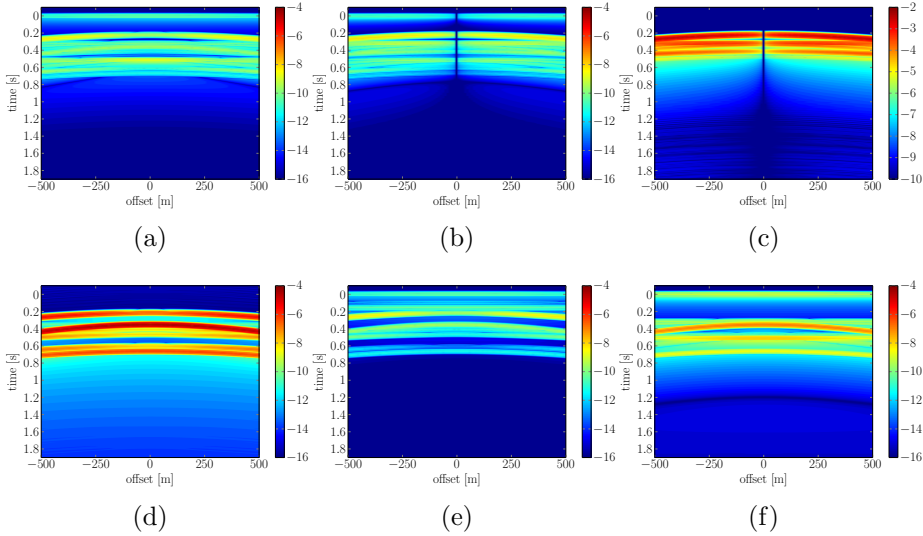


Figure 4.52: Shot records for the source at 1 m depth and the receivers at 700 m depth, with a target interface at 1000 m depth. The shot records are plotted on a logarithmic scale. (a) $E_1^{f^b}$ (b) $E_1^{f^b}$ (c) $E_1^{q^i}$ (d) $v_1^{f^b}$ (e) $v_1^{f^c}$ (v) $H_2^{f^b}$.

for example loading a vibroseis sweep signal in the seismo-EM layer-code. In this way, the responses due to realistic source signals can be investigated. The seismo-electromagnetic method is sensitive to many different parameters. Certain contrasts can yield higher converted signals than other contrasts. Therefore, as a next step, more different geological models should be tested, thereby focusing on the signal strength variability with different geological contrasts.

4.6.4 Conclusions

The source-receiver combinations that yield the strongest converted signals are $E_1^{q^i}$ and $H_2^{f^b}$. Especially the $E_1^{q^i}$ combination seems to generate measurable responses even with acquisition geometries that approach surface-to-surface acquisition. The depth of the receivers plays an important role in the signal measurability of the seismo-electromagnetic fields. The closer the receivers are located to the target, the higher the signal strengths, especially of the seismo-electromagnetic converted fields (interface responses). However, when located too close to the target depth, the coseismic reflected fields arrive at more or less the same time as the one-way seismic traveltimes interface responses, thereby masking the weaker interface response fields. The electromagnetic-to-seismic conversions do not suffer from these interferences, for the acquisition scenario under consideration (i.e. source close to the surface, receivers at depth).

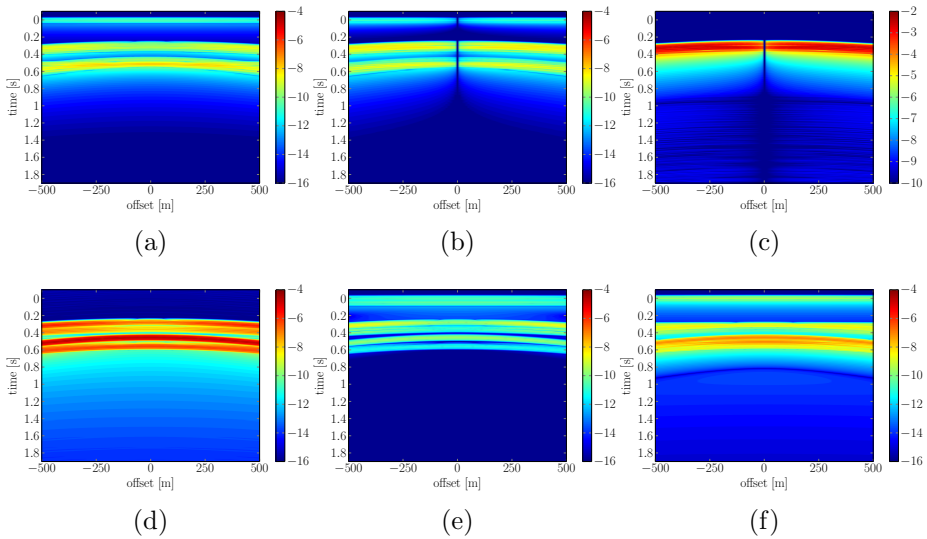


Figure 4.53: Shot records for the source at 1 m depth and the receivers at 900 m depth, with a target interface at 1000 m depth. The shot records are plotted on a logarithmic scale. (a) E_1^{fb} (b) E_1^{fb} (c) E_1^{qi} (d) v_1^{fb} (e) v_1^{jc} (v) H_2^{fb} .

4.7 Seismo-electromagnetic thin-bed responses: natural signal enhancements?ⁱⁱ

4.7.1 Abstract

We study if nature can help us to overcome the very low signal-to-noise ratio of seismo-electromagnetic converted fields by investigating the effects of thin-bed geological structures on the seismo-electromagnetic signal. To investigate the effects of bed-thinning on the seismo-electromagnetic interference patterns, we numerically simulate seismo-electromagnetic wave propagation through horizontally layered media with different amounts and thicknesses of thin-beds. We distinguish two limits of bed thickness. Below the upper limit, the package of thin-beds starts acting like an ‘effective’ medium. Below the lower limit, further thinning does not affect the seismo-electromagnetic interface response signal strength anymore. We demonstrate seismo-electromagnetic sensitivity to changes in medium parameters on a spatial scale much smaller than the seismic resolution. Increasing amounts of thin-beds can cause the interface response signal strength to increase or decrease. Whether constructive or destructive interference occurs seems to be dependent on the seismo-electromagnetic coupling coefficient contrasts. When the combined result of the

ⁱⁱThis section has been published as an open-access journal paper in *Journal of Geophysical Research* doi: 10.1002/2015JB012381 (Grobbe & Slob, 2016). Note that minor changes have been introduced to make the text consistent with the other chapters of this thesis.

contrast, between upper halfspace and package of thin-beds, and the internal thin-bed contrast, is positive, constructive interference occurs. Destructive interference occurs when the combined contrast is negative. Maximum amplitude tuning occurs for thicknesses of thin-bed packages similar to the dominant pressure- and shear wavelengths. Artefacts due to model periodicity are excluded by comparing periodic media with random models. By simulating moving oil/water contacts during production, where the oil layer is gradually being thinned, seismo-electromagnetic signals are proven very sensitive to oil/water contacts. An oil layer with a thickness of about $\frac{1}{350}$ of the dominant shear wavelength is still recognized.

4.7.2 Introduction

Despite several attempts to boost the signal strength of the seismo-electromagnetic converted fields (e.g. [Dean & Dupuis \(2011a\)](#); [Dean *et al.* \(2012\)](#); [Sava & Revil \(2012\)](#); [Sava *et al.* \(2014\)](#)) the desired amplification of the signal for guaranteed successful measurements in the field has not yet been achieved.

But what if nature itself can already help us? From seismics, it is well-known that a seismic wave travelling through a package of thin-beds can experience amplitude-tuning effects that result in anomalously high amplitudes for the seismic signal (e.g. [Widess \(1973\)](#); [Robertson & Nogami \(1984\)](#)). Can similar enhancing signal effects occur for seismo-electromagnetic phenomena? We start with a brief recapitulation of seismic amplitude tuning effects in thin-bed geological settings, including an extension towards the seismo-electromagnetic scenario. We will then numerically investigate what effects thin-beds can have on the seismo-electromagnetic signal, thereby focusing especially on the seismo-electromagnetic conversion. To this end, we use our analytically based, seismo-electromagnetic layer-code ([Grobbe & Slob, 2013](#); [Grobbe *et al.*, 2014, 2016a](#)). We observe that certain thin-bed geological settings can yield constructive interference of the seismo-electromagnetic responses, amplifying the signal strength with a factor of 3. We will highlight the factors that play a role in this possible enhancement of the seismo-electromagnetic signal strength by thin-beds. We study the effects of the seismo-electromagnetic coupling coefficient contrasts by varying the electrolyte concentrations of the pore-fluid. The seismo-electromagnetic coupling coefficient is a very important seismo-electromagnetic parameter, since this parameter controls the amount of coupling between the mechanical waves and the electromagnetic fields. At low frequencies, this coefficient is fundamentally the same as the coefficient measured in classical streaming potential laboratory experiments (e.g. [Morgan *et al.* \(1989\)](#); [Jouniaux *et al.* \(2000\)](#); [Schoemaker *et al.* \(2012\)](#)). We finalize by focusing on an oil/water contact in a reservoir, and by simulating production we will see the effects a varying ratio of oil/water thickness has on the seismo-electromagnetic signals.

4.7.3 Theory: Brief introduction to thin-beds and the relation with seismo-electromagnetics

In the field of seismic exploration, it is well-known that when a seismic wave travels through a package of thin-layers (with appropriate amplifying thickness) amplitude-tuning effects can occur resulting in anomalously high amplitudes (Robertson & Nougami, 1984). The big question is, can similar naturally signal enhancing effects occur for seismo-electromagnetic phenomena? Since the seismo-electromagnetic effect is a complex physical phenomenon of which very little is still understood, the exact effect of a seismo-electromagnetic wave propagating through a package of thin-beds is unpredictable. However, one can intuitively understand that constructive interference might take place. Let us consider the following thought-experiment: since the interface response fields arrive almost instantaneously at one-way seismic traveltime, an incremental increase in seismic traveltime (due to for example downward wave propagation through a thin-bed) followed by a seismo-electromagnetic conversion at the bottom interface of the thin-bed (that arrives instantaneously on seismic time scales), might result in constructive interference of the recorded IR fields. In other words, when the one-way seismic traveltime is not increasing too much, the generated IR field of the bottom interface of a certain thin-bed might map constructively on the generated IR field of the top interface of the thin-bed. The possibility of IR field enhancing effects due to the presence of a thin-bed has been discussed in Pride & Garambois (2005), where they show that the amplitude of the converted electric field can be drastically increased (by a factor of 10 in their example of a thin shale layer), if there is a thin layer of a third-type of material present close to the interface that generates the IR field. Furthermore, Dietrich & Garambois (2013) discuss a possible super-resolution of very thin layers using the seismo-electromagnetic conversions. When studying seismo-electromagnetic thin-bed responses, important questions to ask are of course: what is the sub-seismic resolution limit for seismo-electromagnetic sensitivity? Does an increase in the amount of thin-beds necessarily lead to an increase of the IR field signal strength? What parameters play a role in determining whether constructive or destructive interference occurs? Do different pore-fluid contrasts and relative thicknesses have an effect on the interference pattern? As Widess (1973) already acknowledges: How thin is a thin-bed? Seismically speaking, based on reflective properties, a thin-bed may be defined as a bed with a thickness that is less than $\lambda_{peak}/8$. In this case, the reflections of the top and bottom edges of the thin-bed interfere constructively (Zhou, 2014). Here, λ_{peak} is the dominant wavelength for the seismic velocity of the bed (Widess, 1973), determined by the relation between peak frequency of the source wavelet and the seismic wave velocity of the layer under consideration. In addition, Widess (1973) observed that for bed thicknesses smaller than the tuning thickness, the composite wavelet approaches the derivative of the basic wavelet (Zhou, 2014). It is important to realize, that when geologists speak of thin-beds, they often refer to beds of a few centimeters until meters thick, whereas the seismic definition of a thin-bed can result in much thicker beds. As an example, consider a peak frequency of a wavelet of 30 Hz and a medium with a P-wave velocity of 3000 m/s, which results in a peak wavelength

of 100 m. According to [Widess \(1973\)](#), every bed with a thickness of 12.5 m or less is considered a thin-bed. Geologically speaking, according to the seismic definition, most beds in nature are then a thin-bed. For seismo-electromagnetics, it is yet unknown what should be considered as a thin-bed, if tuning effects or wavelet shape changes occur, and for which bed thicknesses the seismo-electromagnetic signals are not sensitive anymore.

4.7.4 Method: Numerical modeling

To investigate the effects of thin-beds on seismo-electromagnetic signals, we make use of our seismo-EM layer-code ([Grobbe & Slob, 2013](#); [Grobbe *et al.*, 2016a](#)). Our layer-code ESSEMOD is capable of modeling all existing electroseismic and seismo-electromagnetic source-receiver combinations. In this study, we focus on the effect of thin-beds on one of the most common seismo-electromagnetic source-receiver combinations, a horizontal electric field component E_1 in the x_1 -direction due to a horizontal seismic dipole bulk force source f_1^b (for example a seismic shear wave vibrator) in the same x_1 -direction. Of course, a similar numerical study can be carried out focusing on other source-receiver combinations.

We simulate seismo-electromagnetic wave propagation through layered-Earth configurations with different amounts and thicknesses of thin-beds to study the effect of bed-thinning on the amplification or weakening of the IR fields. To fully focus on the effect of the thin-beds we use two very simple reference configurations consisting of two homogeneous halfspaces (hs), either medium A and medium B or medium A and medium C . In [Table 4.3](#), we present the effective seismo-electromagnetic velocities of the different field types, the input medium parameters and the relevant petrophysical parameters determining the static coupling coefficient, for each of the different media. We can observe that the dominant factor is the change in porosity of the medium. The shear waves are more affected by a porosity change than pressures waves (the pores are saturated with fluid, so higher porosity means more fluid), which explains why the P-wave velocity does not vary as much as the shear wave velocity does.

For convenience, we only present the effective seismo-electromagnetic wave velocities resulting from the chosen medium properties and the corresponding seismo-electromagnetic coupling coefficients. These are presented in [Table 4.3](#). We use $N_t = 2048$ time-samples with a time-sampling step of $\Delta t = 0.001$ s. The amount of radial frequencies is $N_\omega = N_t/2 + 1$ and the radial frequency sampling step $\Delta\omega = 2\pi/(N_t \cdot \Delta t)$ rad \cdot s $^{-1}$. The wavelet is a causal, first-derivative of a Gaussian with peak frequency of 30 Hz and an amplification factor of $1 \cdot 10^9$. Let us start with the reference configuration of halfspace A above halfspace B . We now define a package of certain package thickness PT , that we insert in between halfspace A and halfspace B (see [Figure 6.3](#)). We consider configurations with $PT = 20, 40, 80, 160$ m. In addition, we consider $PT = 70$ and 105 m, which correspond to the dominant wavelength of the shear (S)-wave and the Biot fast pressure (P)-wave, respectively. According to [Widess \(1973\)](#), the minimum seismic thin-bed thickness then reads by definition $\lambda_{peak}/8 = 105/8 = 13.125$ m for P-waves and $\lambda_{peak}/8 = 70/8 = 8.75$ m

Table 4.3: Overview of the velocities of the different field types, input medium parameters and relevant petrophysical parameters determining the static coupling coefficient, for each of the different media. To illustrate the frequency-dependency of certain wave/field-types, velocity ranges (the real parts of the complex velocities) are displayed for the bandwidth under consideration. Note that the EM-velocities are proportional to the square-root of frequency.

Physical quantity	Medium A (top hs)	Medium B (layer or hs)	Medium C (layer or hs)
P_f -velocity [m/s]	3159.81-3159.84	3153.67-3153.68	3348.94-3349.00
P_s -velocity [m/s]	2.89-92.96	3.98-131.09	5.46-189.62
S -velocity [m/s]	2110.79-2110.87	1952.83-1953.03	1886.09-1886.70
EM -velocity [m/s]	31796.34-1005899.70	4496.68-142233.40	20109.77-636104.47
\mathcal{L}_0 [$\text{m}^2 \cdot \text{s} \cdot \text{V}^{-1}$]	$9.07 \cdot 10^{-9}$	$2.08 \cdot 10^{-9}$	$1.65 \cdot 10^{-9}$
ζ^p [V]	$-9.6 \cdot 10^{-2}$	$-4.4 \cdot 10^{-2}$	$-7 \cdot 10^{-2}$
σ^f [S m^{-1}]	$9.27 \cdot 10^{-3}$	0.93	$9.27 \cdot 10^{-2}$
$\hat{\sigma}^e$ [S m^{-1}]	$1.24 \cdot 10^{-3}$	$6.18 \cdot 10^{-2}$	$3.09 \cdot 10^{-3}$

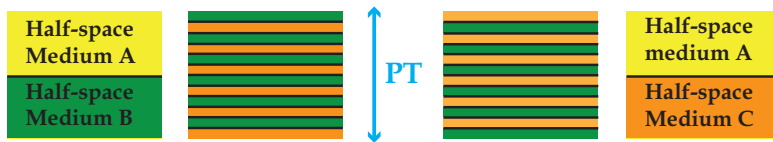


Figure 4.54: Schematic overview of the two reference configurations and the inserted packages of thin-beds, with a total package thickness PT .

for S -waves.

We divide the package PT into an even amount of thin-beds Nl . The layers alternate between medium B and medium C or vice versa. We consider the following amounts of sublayers: $Nl = 2, 4, 8, 16, 32$ and for $PT > 40$ m also $Nl = 64$. By fixing the package thickness and dividing it consistently into different amounts of thin-beds, the bed thickness changes accordingly. In this way both the effects of bed-thickness and amount of beds can be investigated.

4.7.5 Results

In this section, we present the results of the various numerical thin-bed experiments. We first present the results of the model $A - B - C - B$, which yields constructive interference. We look at both the effects of varying package thicknesses, varying bed thickness and varying amounts of sublayers. Then, we present the results of model $A - C - B - C$, which leads to destructive interference. To exclude possible artefacts due to the periodicity of the models used, we compare these results with a model with arbitrary bed thicknesses and a model with random bed thicknesses. Here, arbitrary means manually chosen by the user in an arbitrary fashion, and random means mathematically random. We slowly increase the amount of sub-layers with varying bed thicknesses for a total package thickness PT of 80 m. To study the effect of coupling coefficients on the interference patterns, we focus on varying electrolyte

concentrations in the pore fluid. We finalize by investigating the sensitivity of the model to different saturating fluids, namely an oil/water contact in a porous rock. We simulate oil production where the thickness of the oil layer compared to the water layer thickness starts varying.

Constructive Interference

Let us start with the configurations $A-B-C-B$, $A-B-C-B-C-B$ and so on. We model the reference response as halfspace A above halfspace B . A right-handed Cartesian spatial coordinate system is considered, where x_3 is pointing downwards representing depth. The source is located at $x_3 = 100$ m and the receivers are placed at $x_3 = 700$ m. The interface that separates the bottom of halfspace A from the top of the inserted thin-bed package is located at $x_3 = 1000$ m depth (or in other words, this is the interface separating halfspace A from halfspace B in the reference response). Considering the seismic wave velocities of medium A (see Table 4.3), we expect the generated IR fields to arrive at one-way seismic time $t = 0.285$ s for the P-wave associated IR field (from now on referred to as PIR), and at $t = 0.427$ s for the IR field generated by an S-wave (referred to as SIR). The rest of the visible events represent coseismic wavefields. Note that, for this specific medium configuration and acquisition scenario, the event marked as PIR is actually a combination of the P-wave associated IR field, and the coseismic field associated with the direct shear wave from the source to the receiver level. Both events arrive more or less at the same time in the seismo-electromagnetic record, especially at zero-offset. We first present the seismo-electromagnetic thin-bed responses for different package thicknesses PT with equal bed thicknesses (and hence different amounts of thin-beds Nl per package thickness). Figure 4.55a presents the results for bed thicknesses of 10 m and Figure 4.55b for bed thicknesses of 5 m. The reference response is the response when $PT = 0$ and hence $Nl = 0$. Looking at Figure 4.55, several observations can be made. We can clearly observe that the PIR signal at $t = 0.285$ s is not strengthened or weakened at all due to the presence of thin-beds. The SIR at $t = 0.427$ s on the other hand, is clearly affected by the thin-beds. Figure 4.55a shows that for bed thicknesses of 10 m, multiples are visible which are not present in the reference response. In this case, the signal can still distinguish between the individual layers. There seems to be a slight increase of the SIR amplitude with increasing Nl , but overall the beds are still too thick to yield significant constructive or destructive interference. Figure 4.55b shows that for $PT = 20$ m and $PT = 40$ m, multiples are still visible for bed thicknesses of 5 m, whereas for $PT = 80$ and $PT = 160$ m, the multiples start vanishing. Furthermore, $PT = 160$ m displays the largest SIR amplification. Hence, increasing amounts of thin-beds of the same thickness (in this case 5 m) can cause the multiples to start vanishing at a certain point (in this case for $PT = 80$ or larger) and the SIR to increase. Nevertheless, we can also observe that the SIR does not necessarily increase with increasing Nl . Figure 4.56a presents the zero-offset results for bed thicknesses of 2.5 m. Similar patterns can be observed as in Figure 4.55. Comparing the results for different PT with the reference response, we see that for $PT = 20$ and $PT = 40$, additional multiples are still visible before the SIR compared to the reference response, whereas these multiples vanish again with increasing PT

and hence increasing Nl . Overall, increasing Nl seems to yield an increase in SIR strength. Figure 4.56b shows the same results but now for 140 m offset. We can see that the shape of the PIR event changes with offset, but there is still no visible signal interference due to the presence of thin-beds. The SIR reference response is slightly diminished. In addition, the highest signal strength now occurs for $PT = 80$, instead of $PT = 160$. Furthermore, $PT = 80$ now shows an additional multiple just after the SIR response, indicating that for greater offsets, not all multiples are compressed yet for the amount of sublayers in $PT = 80$. This can be explained in terms of the apparent thicknesses of the beds, which can vary with offset.

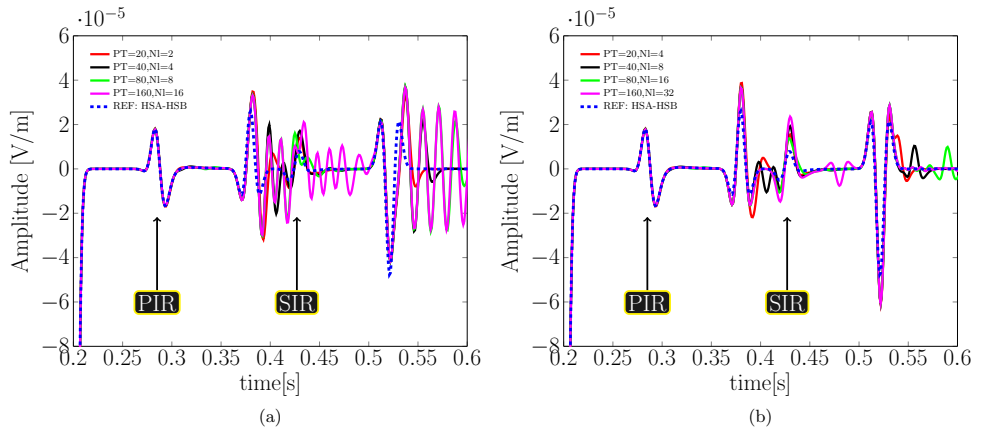


Figure 4.55: Response for thin-bed geometries of the form A-B-C-B, for different package thicknesses PT with equal individual bed thicknesses of (a) 10 m (b) 5 m.

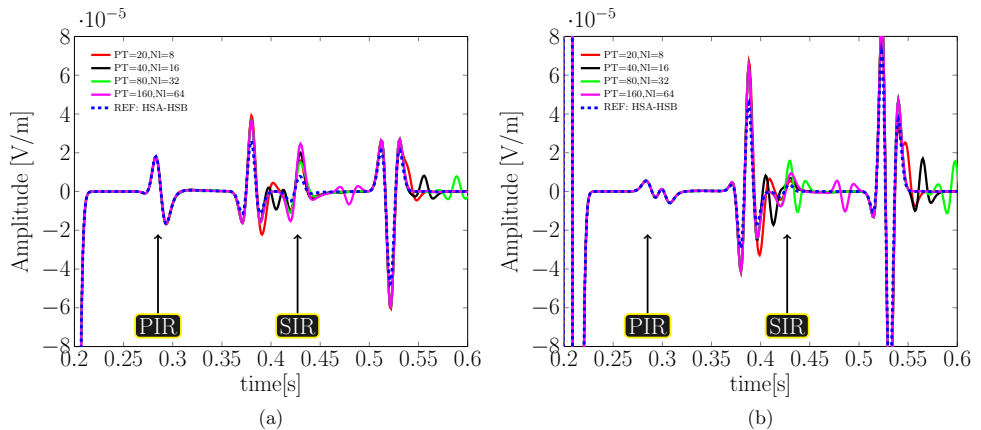


Figure 4.56: Response for thin-bed geometries of the form A-B-C-B, for different package thicknesses PT with equal individual bed thicknesses of 2.5 m (a) at zero-offset (b) at 140 m offset.

To take a closer look at the effects of increasing Nl in a certain PT , we show in Figure 4.57 the seismo-electromagnetic response for a thin-bed geometry A-B-C-B, varying with the amount of layers Nl for a fixed package thickness of either $PT = 80$ m in Figure 4.57a or $PT = 160$ m in Figure 4.57b. We can observe that the generated multiple train caused by relatively ‘thick’ beds, at low values for Nl and relatively high PT , is compressed with increasing Nl and correspondingly decreasing bed thickness. The individual beds are slowly not sensed anymore by the signal and as a result the multiples vanish and the package of thin-beds starts acting like an ‘effective’ medium. In this way the multiples start ‘mapping’ at the arrival time of the SIR. Hence, one can intuitively understand that increasing amounts of thin-beds can lead to an increased IR signal strength. This is what we also observed in Figures 4.55 and 4.56. One can argue that as soon as all multiples have been compressed, the maximum signal strengthening has been achieved. We can observe that the seismo-electromagnetic signal is still affected for a while by the amount of thin-beds even when the individual beds are already not recognized anymore (no multiples). Another way to look at this is that further thinning of the sublayers, at a certain point does not improve the signal strength of the IR fields anymore, since the thickness is below the sensitive resolution of the seismo-electromagnetic fields. Illustrative examples can be found comparing the signal of $Nl = 32$ with the signal of $Nl = 64$ for $PT = 80$ in Figure 4.57a. So, we can distinguish two limits of bed thickness: an upper and lower limit. The upper limit of bed thickness determines whether the individual layers are still recognized or not. When beds are thinner than this limit, the package of thin-beds starts acting like an ‘effective’ medium and the multiples vanish from the record. The lower limit of bed thickness determines the border from whereon further thinning does not affect the seismo-electromagnetic IR signal strength anymore, because the bed thickness is below the sensitive resolution of the seismo-electromagnetic fields.

From the results of Figures 4.55, 4.56 and 4.57, we can conclude that both the thickness of the thin-beds as well as the amount of thin-beds play a role in whether or not the multiples (created by the individual thin-beds) vanish in the record (i.e., are compressed at the SIR of the reference response). The upper limit seems to occur when the thin-bed thickness reaches a value of around 5 m thickness (and $Nl > 16$). This corresponds to thicknesses of $1/14$ and $1/21$ of the dominant S- and P-wavelengths, 70 m and 105 m, respectively. The lower limit, from whereon further thinning does not affect the signal strength anymore, seems to occur around 2.5 m thickness. This lower limit corresponds to $1/28$ and $1/42$ of the dominant S- and P-wavelengths, respectively. An important anomaly to the general pattern described above, can be observed in $PT = 160$, for $Nl = 2$. In this case the individual bed-thicknesses equal 80 m, which is around the dominant S-wavelength. This observation stimulates P- and S-wave tuning experiments, where the amount of thin-beds is increased each with a bed thickness of either the dominant P- or S-wavelength. These experiments showed that for both cases, increasing Nl did not make a difference for the amplifying effect and the results are not displayed here. In another tuning experiment, we focus on the package thickness PT . The results are displayed in Figure 4.58. We look at the interference patterns for varying

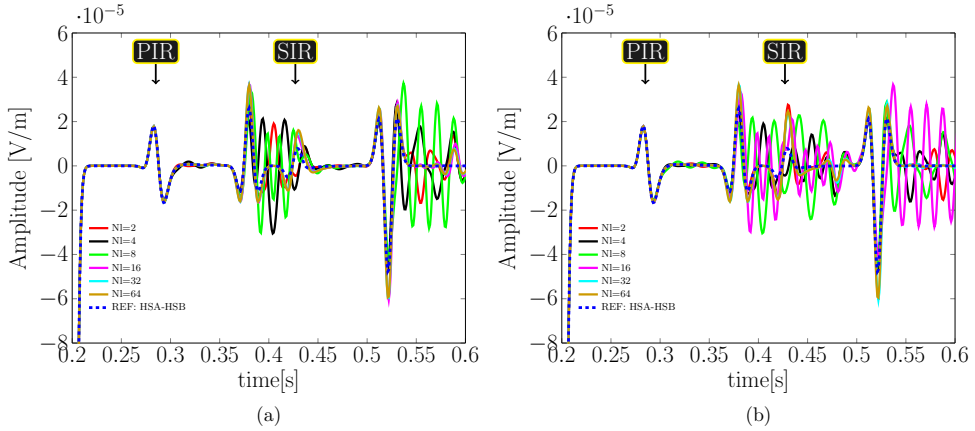


Figure 4.57: Response for thin-bed geometry A-B-C-B, varying with the amount of layers N_l , for a package thickness of (a) 80 m (b) 160 m

N_l in tuning package thicknesses of $PT = 70$ m (Figure 4.58a) or $PT = 105$ m (Figure 4.58b). We can observe that in both cases, there seems to be a maximum strengthening of the S-wave related IR signal of a factor 3, higher than we have observed in the earlier presented experiments. This is an indication that not only the amount of thin-beds N_l and the thin-bed thickness, but also the package thickness PT itself plays an important role in the amplification of the SIR due to thin-bed geological structures.

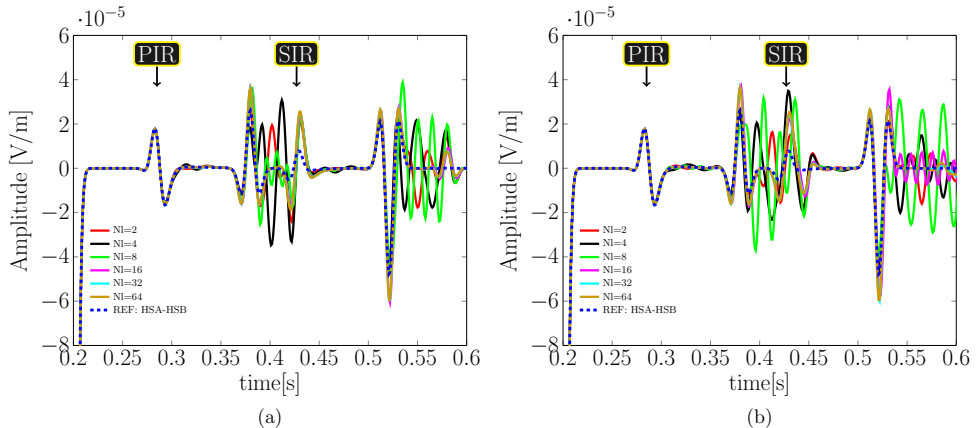


Figure 4.58: Response for thin-bed geometries of the form A-B-C-B, varying with the amount of layers N_l for packages with tuning thicknesses of (a) 70 m (dominant shear wavelength) (b) 105 m (dominant pressure wavelength)

Destructive Interference

Let us now look what happens if we change the order of the thin-beds, i.e. looking at configurations like A-C-B-C with reference response halfspace A-halfspace C. Except the change in the order of the thin-beds, the modeling experiment is identical to the experiment discussed above. In Figure 4.59, displaying the results of these experiments, similar observations can be made as before in Figures 4.55-4.58, except that now increasing Nl leads to a decreased signal strength of the S-wave related IR field. Looking at the medium properties of media B and C , two main differences can be observed. First, the contrast in electromagnetic velocity between medium B and medium A is much larger than between medium C and medium A . Second, the coupling coefficient of medium B is larger than the one of medium C and therefore forms a smaller difference with the highest coupling coefficient, that of medium A . Hence, the contrast in coupling coefficients between medium A and package of thin-beds PT is positive (i.e. the upper layer has a higher value than the lower layer of the contrast under consideration). Intuitively, one can imagine that the contrast in coupling coefficients plays an important role in the signal strengthening or weakening of the IR fields. One can observe that the reference response of halfspace A-halfspace C indeed has a higher S-wave related IR field than the reference response of halfspace A-halfspace B due to the higher contrast in coupling coefficients. However, remarkable is the fact that additional thin-bed contrasts decrease the SIR in case of a packages of thin-beds that have alternating thin-beds starting with medium C over medium B (a negative coupling coefficient contrast), but increase the SIR when the thin-bed alternations start with medium B over medium C (a positive coupling coefficient contrast).

Intuitively, the controlling factor seems to be whether the package of thin-beds starts with a positive or negative contrast in coupling coefficient. To focus on the effect of contrasts in coupling coefficients, we will now briefly investigate what happens to the thin-bed responses when we change the electrolyte concentrations in the pore fluid.

Different Electrolyte Concentrations in the Pore Fluid

The electrolyte concentration in the pore fluid directly influences the zeta-potential. For example, the empirical study by [Pride & Morgan \(1991\)](#) found

$$\zeta^p = 8 + 26 \log_{10} C, \quad (4.6)$$

to be a reasonable approximation of the zeta-potential (with the zeta-potential in millivolts). Here, C denotes the electrolyte concentration of the pore fluid in mol/L. [Revil et al. \(1999\)](#) have demonstrated this equation from first principles using electrical double layer theory. They provide a physical explanation for the two constants that appear in equation (4.6). As we have seen, the zeta-potential on its turn, directly influences the value of the static seismo-electromagnetic coupling coefficient \mathcal{L}_0 (equation (2.9)).

Several laboratory studies have shown that a higher ionic concentration leads to a lower seismo-electromagnetic coupling coefficient and a weaker observed seismo-

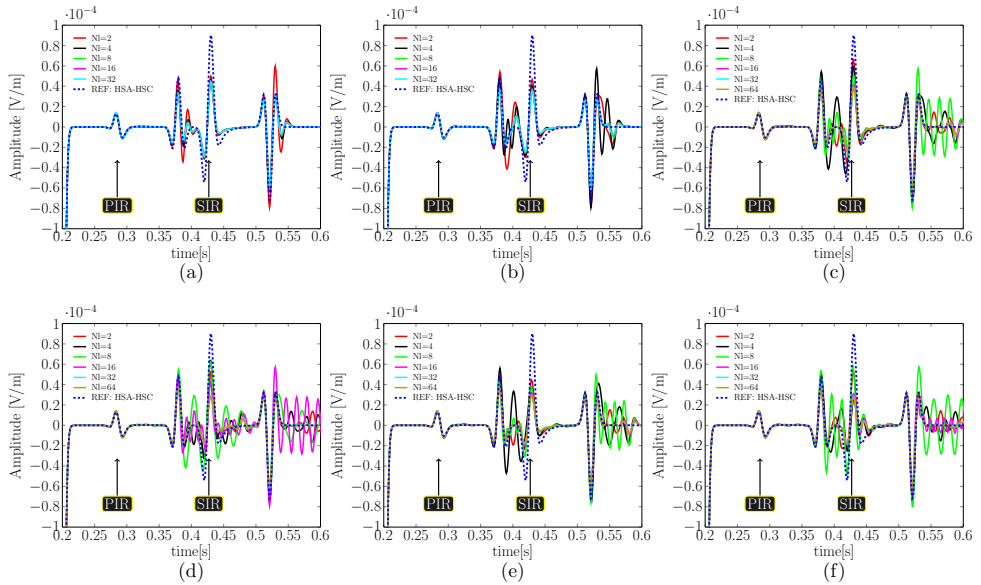


Figure 4.59: Response for thin-bed geometries of the form A-C-B-C, varying with the amount of layers Nl for package thicknesses (a) 20 m. (b) 40 m. (c) 80 m. (d) 160 m. (e) 70 m. (dominant S -wavelength) (f) 105 m. (dominant P -wavelength)

electromagnetic effect (e.g. Schoemaker (2011); Zhu & Toksöz (2013)). We here focus solely on the effect of changing electrolyte concentrations. Therefore, all other seismo-electromagnetic input model parameters are chosen equal to each other for all three media (medium A,B and C), resulting in (more or less) equal seismic velocities for all media. Since there are no seismic velocity contrasts, there are no coseismic reflection arrivals to be expected in the records. The parameters that directly or indirectly depend on the electrolyte concentration of course do change accordingly (e.g. fluid conductivity), resulting in differences in the electromagnetic velocities between the three media.

We use a package of $PT = 80$ m, with structure A-B-C-B. The electrolyte concentrations are chosen such that medium A has the highest electrolyte concentration of $1 \cdot 10^{-4}$ mol/L and hence the lowest coupling coefficient with a value of $9.07 \cdot 10^{-9}$ $\text{m}^2 \cdot \text{s} \cdot \text{V}^{-1}$. We vary the relative distribution of concentrations between medium B and C, using values of $1 \cdot 10^{-5}$ mol/L and $1 \cdot 10^{-6}$ mol/L. In this way, either medium B has a higher concentration than medium C, or vice versa. The corresponding coupling coefficients are $1.15 \cdot 10^{-8}$ $\text{m}^2 \cdot \text{s} \cdot \text{V}^{-1}$ and $1.4 \cdot 10^{-8}$ $\text{m}^2 \cdot \text{s} \cdot \text{V}^{-1}$, respectively. The contrast in coupling coefficient between medium A and the package of thin-beds PT now has a negative contrast (opposite to the results of Figure 4.57a). The results are presented in Figure 4.60. Figure 4.60a shows the results where medium C has a higher coupling coefficient than medium B, resulting in a negative thin-bed contrast within the package PT (since PT starts with medium B over medium

C). We observe, focusing on the first peak of the SIR, that with increasing Nl , the SIR response slightly increases as well. Figure 4.60b presents the results where medium B has a higher coupling coefficient than medium C , resulting in a positive thin-bed contrast within the package PT . We now observe that with increasing Nl , the SIR decreases. At first sight, this seems to be contradicting with the observations of Figure 4.57a, where a positive thin-bed contrast within package PT resulted in increasing SIR with increasing Nl , and a negative contrast resulted in decreasing SIR with increasing Nl . However, there is another difference between the experiments resulting in Figures 4.57a and 4.60. In Figure 4.57a, the contrast between medium A and package of thin-beds PT was positive, whereas for Figure 4.60, this contrast is negative. In both cases, when the combined result of the contrast between upper halfspace and package of thin-beds, and the internal thin-bed contrast is positive, constructive interference occurs, whereas destructive interference occurs when the combined contrast is negative. We can also observe in Figure 4.60b that a higher contrast between medium A and B results in a higher reference response SIR. Besides the above observations, we can observe that the PIR response in these experiments is also affected by the presence of thin-beds. In Figure 4.60a we can see that the PIR has a smaller reference response than in Figure 4.60b, but has a signal strengthening due to the presence of thin-beds. We can also observe that the PIR waveform is slightly changed (this also slightly occurs for the SIR). This impedes the interpretation of the interference patterns: it is difficult to determine whether signal strengthening or weakening occurs with increasing Nl .

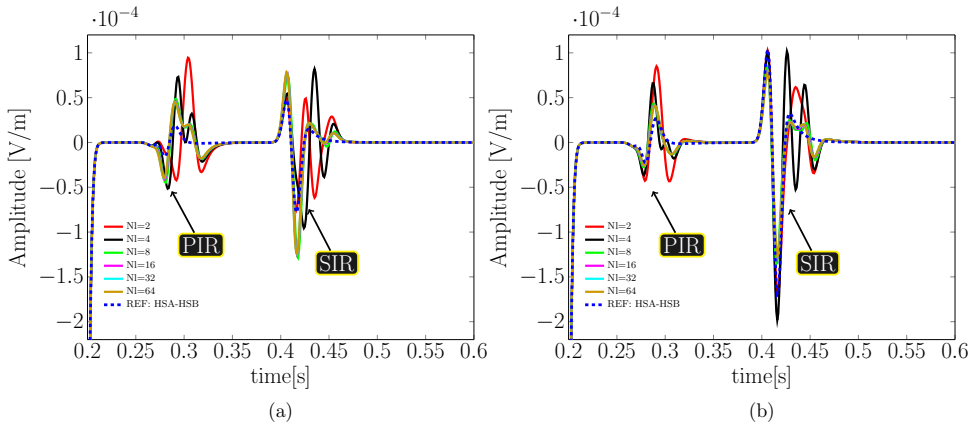


Figure 4.60: Response for thin-bed geometries of the form A-B-C-B, varying with the amount of layers Nl for package thickness $PT = 80$ and varying coupling coefficients. (a) *Relative distribution of coupling coefficients: medium $A < \text{medium } B < \text{medium } C$.* (b) *Relative distribution of coupling coefficients: medium $A > \text{medium } B > \text{medium } C$.*

Random models

To exclude the possibility of introduced artefacts due to the periodicity of the thin-bed models under consideration, we investigate the signal interference patterns for a model with package thickness $PT = 80$ m, where the added sublayers have either arbitrary arbitrarily chosen by the user or mathematically random bed thicknesses. The random bed thicknesses are determined using a single uniformly distributed random number generator in the interval $(0,1)$, that calculates the random positions (for a fixed amount) of the interfaces as a fraction of the sum of the random numbers times the fixed package thickness. In other words, each layer is a random fraction of the package thickness. We increase ‘randomisation’ going from arbitrary models to random models. We still vary the amount of sublayers Nl as we did before, with the pattern $A - B - C - B$ and so on. The results are presented in Figure 4.61a for arbitrary bed thicknesses and in Figure 4.61b for random bed thicknesses.

We compare the results of Figure 4.61 with the result of the periodic thin-bed experiments for a package thickness $PT=80$ m with equally thick thin-beds as presented earlier in Figure 4.57a. We can clearly observe similar signal-enhancing interference patterns for the shear wave related IR field. We can again observe that for increasing amounts of sublayers, the multiple arrivals from the relatively thick sublayers (low amount of sublayers) are being compressed and map at the arrival time of the shear wave-related IR field. However, where in the periodic case the line representing a total of 64 sublayers ($Nl = 64$) yields the largest signal strength for the shear wave-related IR field, in the case of arbitrary sublayer thickness of Figure 4.61a, both $Nl = 16$ and $Nl = 64$ result in the largest signal strength. Looking more closely, we can still observe that for $Nl = 64$, small multiples are being observed for example at times slightly less than $t = 0.43$ s. This might indicate that for $Nl = 64$ and $PT = 80$ m, the seismo-electromagnetic signal still did not fully reach its maximum thin-bed sensitivity in thin-bed settings with arbitrary bed thickness. When we increase the randomness of the bed-thickness, we can again observe that the multiples are being compressed with increasing Nl , but also the maximum amplification for $Nl = 64$ is less than in the case of periodic and arbitrary layering. Furthermore, there seems to be a slightly bigger phase shift on the SIR responses for different Nl in case of completely random bed thicknesses. Overall, the interference patterns between Figures 4.57a, 4.61a and 4.61b look very similar, with similar multiple convergence pattern. Therefore, we can conclude that the earlier discussed interference patterns are not artefacts due to the periodicity of the sublayer thickness, but represent seismo-electromagnetic signal-enhancing (or destructive) interference mechanisms. Nevertheless, there seems to be a higher amplification of the SIR when the thin-bed thicknesses are less random. Also, the multiples seem to converge at smaller Nl in scenarios with less randomness for the bed thicknesses (or in other words, higher periodicity).

Reservoir Monitoring: Oil-water contacts

We now focus on the sensitivity of the seismo-electromagnetic signals to different saturating fluids. We investigate what happens when the relative thickness of two

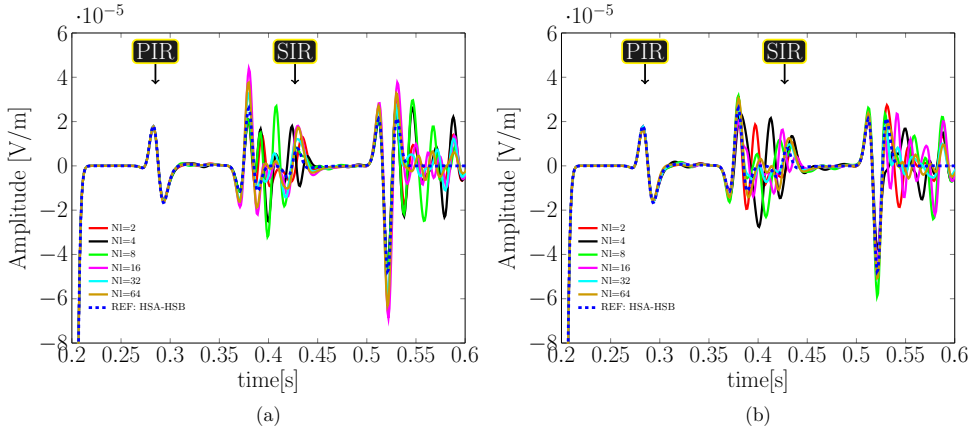


Figure 4.61: Response for thin-bed geometries of the form A-B-C-B, varying with the amount of layers Nl for a package thickness of 80 m and with (a) arbitrary bed thicknesses (b) random bed thicknesses.

different saturating fluids in a fixed package of rock of 30 m thickness (representing a reservoir) changes. To this end, we simulate a medium, where the thickness of an oil layer decreases and the thickness of a water layer increases. This situation occurs for example in an oil reservoir during production. The starting-thickness ratio is 20 m oil layer and 10 m water layer. The water layer is fully-saturated, the oil-layer has 80 % oil-saturation and 20 % water-saturation. This leads to the relevant medium parameters as presented in Table 4.4 (only the values differing from Table 4.3 are presented), where the effective values for the oil-layer are displayed (i.e. saturation has already been taken into account). We have included the effect of saturation in a linear manner, which is allowed due to the volume-averaging principles that Pride (1994) applied in deriving the seismo-electromagnetic theory. For viscosity, we have used a logarithmic version of linear addition, as presented by Warden *et al.* (2013). Figure 6.6 displays the results of the oil-water production simulation. The reference response is the seismo-electromagnetic response from halfspace *A* over halfspace *B*, where both halfspaces are fully water-saturated. Looking at the purely seismic information of the coseismic fields, we can observe a phase delay due to dispersion related to the presence of (the more viscous) oil. In addition, we can observe that the presence of oil has a signal enhancing effect on the SIR field. The highest signal strength occurs for the thickest oil-layer: 20 m oil layer, 10 m water layer, in other words the starting-thickness ratio of this model. During oil production, when the water content in the 30 m package increases and the oil layer gets thinner, the shear-wave related IR signal strength weakens. Furthermore, we can observe that the seismo-electromagnetic signal is very sensitive to the oil-water contact: an oil layer of 0.2 m thickness (the line representing p2-29p8) is still slightly recognized. Once the oil layer thickness reaches 0.02 m, the corresponding line overlaps with the reference response, indicating that the seismo-electromagnetic signal does not

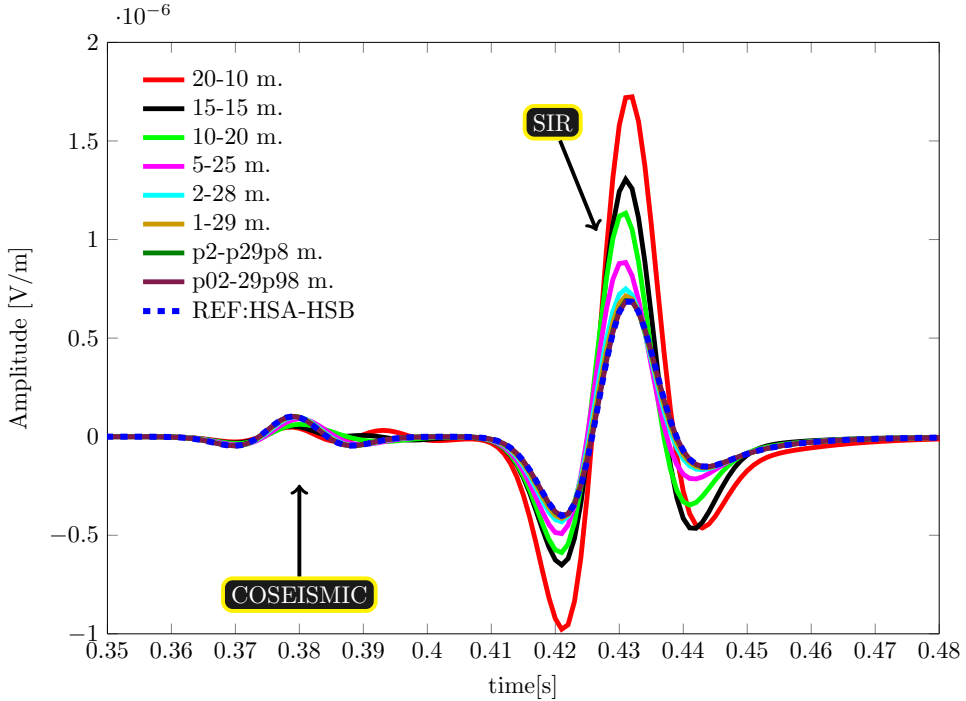


Figure 4.62: Oil-water monitoring. Different colors indicate the coupled seismo-EM response for situations with different relative thicknesses of oil-water saturation in a fixed package of rock of 30 m. The source is positioned at $x_3 = 100$ m and has an amplification factor of $1 \cdot 10^9$, the receivers are placed at $x_3 = 700$ m and the interface separating the upper halfspace from the 30 m package of rock is located at $x_3 = 1000$ m. The blue-dashed line represents the reference response from halfspace A over halfspace B , both fully water-saturated.

sense the presence of oil anymore. The thickness of 0.2 m is far below the dominant wavelength of the seismic shear wave generating this SIR, which is about 70 m. According to [Widess \(1973\)](#), beds with thicknesses less than $1/8$ of this dominant wavelength, 8.75 m, are considered thin-beds. The seismo-electromagnetic signal clearly has a very high sensitivity to the presence of oil-water contacts.

4.7.6 Discussion

We have studied the effect of changing electrolyte concentrations in the pore fluid on the seismo-electromagnetic interference patterns. Unfortunately, we cannot directly link these effects to the changing seismo-electromagnetic coupling coefficient only: for example, the fluid conductivity also changes with changing electrolyte concentration, thereby affecting the electromagnetic velocities. However, it seems reasonable to address the observed changes to changes in the seismo-electromagnetic coupling coefficients, since physically speaking these coefficients control the amount

Table 4.4: Overview of the relevant parameters and wave/field velocities for each of the different media colorcor (only the deviations from Table 4.3 are presented). Media A and B are water-saturated. To illustrate the frequency-dependency of certain wave/field-types, velocity ranges (the real parts of the complex velocities) are displayed for the bandwidth under consideration. Note that the EM-velocities are proportional to the square-root of frequency.

Physical quantity	Medium A (top hs)	Medium B (layer or hs)	Eff. Param. Oil Layer
σ^f [S/m]	0.93	0.93	0.19
δ^e [S/m]	0.12	$6.18 \cdot 10^{-2}$	$1.24 \cdot 10^{-2}$
C [mol L $^{-1}$]	$1.0 \cdot 10^{-2}$	$1.0 \cdot 10^{-2}$	0.002
ϵ_r^f [-]	70	70	20.4
η [N s m $^{-2}$]	$1 \cdot 10^{-3}$	$1 \cdot 10^{-3}$	$1.4 \cdot 10^{-3}$
K^f [N m $^{-2}$]	$2.25 \cdot 10^9$	$2.25 \cdot 10^9$	$1.49 \cdot 10^9$
ρ^f [kg m $^{-3}$]	$1.0 \cdot 10^3$	$1.0 \cdot 10^3$	$9.32 \cdot 10^2$
\mathcal{L}_0 [m $^2 \cdot$ s $ \cdot$ V $^{-1}$]	$3.64 \cdot 10^{-9}$	$1.82 \cdot 10^{-9}$	$5.35 \cdot 10^{-10}$
ζ^p [V]	$-4.4 \cdot 10^{-2}$	$-4.4 \cdot 10^{-2}$	$-6.22 \cdot 10^{-2}$
P_f [m/s]	3166.73-3166.76	3163.19-3163.19	3015.65-3015.66
P_s [m/s]	2.91-93.74	4.00-131.93	2.98-96.96
S vel. [m/s]	2110.79-2110.87	1952.83-1953.03	1958.49-1958.57
EM vel. [m/s]	3179.63-1.01 $\cdot 10^5$	4496.68-142233.38	10054.89-318044.72

of coupling between mechanical waves and electromagnetic fields. For other seismo-electromagnetic parameters, it is even harder to uniquely determine the effect of that specific parameter on the thin-bed interference patterns, since most seismo-electromagnetic parameters are mutually related. We have of course considered a simple situation where we only changed the electrolyte concentration of the pore fluid. In reality, the chance that between different media other medium properties also vary is high. Nevertheless, for monitoring purposes of for example oil or gas production, this is an interesting observation, since we purely focus on changes in the saturating pore fluid, and assume that the rest of the reservoir remains the same. Despite probable changes in permeability during production, this is a reasonable first assumption.

Our simplified oil/water contact modeling experiments simulating oil production have proven that seismo-electromagnetic signals are very sensitive to oil-water contacts. This observation has previously been made in laboratory experiments (e.g. [Smeulders *et al.* \(2014\)](#)). We have modeled a situation with two immiscible fluids using an approximative theory ([Pride, 1994](#)) in which the capillary effects are neglected. This approach is unable to describe all physical mechanisms involved in the wave propagation and attenuation in porous media containing two immiscible fluids. As an alternative, the formulations of [Revil & Mahardika \(2013\)](#) could be used. However, macroscopically we believe that the observed sensitivity effects of seismo-electromagnetic signals to oil/water contrasts are still valid, and only in terms of amplitudes or exact interference patterns differences might occur when using the formulation of [Revil & Mahardika \(2013\)](#). In our oil/water experiment, we have observed that during oil production, when the water content in the 30 m package increases and the oil layer gets thinner, the SIR signal strength weakens. However, as we have also seen, effective strengthening or weakening of thin-bed re-

sponses seems to be determined by the contrasts in seismo-electromagnetic coupling coefficient. In the laboratory experiments by [Smeulders *et al.* \(2014\)](#), an increasing interface response with decreasing oil-bed thickness was observed. However, this can probably be explained due to the fact that in this laboratory experiment, a porous sample was placed in a water tank. The pressure wave generated by the source in the water, therefore experiences a contrast between pure water on both sides of the sample (where the seismo-electromagnetic coupling coefficient is zero) and a porous medium. The contrasts in coupling coefficients are then clearly different from our modeled contrast, and therefore it is expected that different effects on the interface response signal are observed, as we have also seen in our varying electrolyte modeling experiments. However, now that we schematically have simulated an oil reservoir during production, we can use our seismo-EM layer-code to try and validate, as a next step, the oil/water contact seismo-electromagnetic laboratory experiments as presented by [Smeulders *et al.* \(2014\)](#).

Since we of course only modeled a few scenarios and contrasts, we do not exclude that different interference patterns might occur in for example media with different medium parameters for the thin-beds and thin-bed contrasts, or for example when investigating different seismo-electromagnetic source-receiver combinations. Also, in our varying electrolyte simulations, the upper halfspace always had the lowest coupling coefficient. Different interference patterns are to be expected when the upper halfspace has a coupling coefficient that has a value that lies for example in between the coupling coefficients of the thin-bed layers. Besides focusing at amplitude changes, one could also try to study and exploit the fact that interference patterns can cause phase shifts and waveform changes as well.

Are thin-bed geological structures the solution for the weak signal-to-noise ratio of the seismo-electromagnetic signals that limits the use of this technique in the geophysical community? Probably not. What is more important is the awareness that thin-bed geological settings can have serious consequences for the recorded seismo-electromagnetic interface response signals, due to complex interference patterns. For example, a strong response in the record might be due to a strong reflector/contrast, but might also be the effect of signal strengthening/weakening due to the presence of thin-beds. Due to the complexity of the interference patterns and the many possible parameter combinations that can influence these patterns, it is very difficult to find effective medium expressions that properly describe the response of the package of thin-beds.

In reality, we of course cannot control the thickness of the beds that we encounter in the field and also not the order of the contrasts (determining constructive or destructive interference). However, we have seen that we can distinguish two limits of bed thickness: an upper limit of bed thickness that determines whether the individual layers are still recognized or not and a lower limit that determines the border from whereon further thinning does not affect the seismo-electromagnetic IR signal strength anymore. To have an effective medium response, the beds need to be thinner than the upper limit. The lower limit then determines the maximum signal strengthening or weakening that can occur, together with the total package thickness of the thin-beds. The maximum amplitude tuning occurs for package thicknesses

similar to the dominant wavelengths of the P- and S-waves. We can take this knowledge into account in our acquisition design. By changing the dominant frequencies of the seismic source signal, we can effectively change the optimal tuning package thickness for the generated waves. When we have a geological setting where constructive interference occurs, we can try to optimize the amplitude tuning effects by playing with the source bandwidth. Combined with for example velocity analysis, this determined dominant wavelength can assist in determining the thin-bed package thickness of the subsurface. Can we obtain the desired factor of amplitude enhancement that we need to measure the seismo-electromagnetic signals? We are not sure. However, the investigation presented in this section is carried out only for one seismo-electromagnetic source-receiver combination and certain geological models. Different models can result in different interference patterns, that might lead to even greater amplifying effects. Furthermore, there might be differences in signal enhancing for different seismo-electromagnetic source-receiver combinations. Depending on for example the geological properties as obtained from boreholes, the optimal seismo-electromagnetic source-receiver combination can be determined (i.e. the combination that is to be expected to experience maximum signal strengthening) for the specific geological setting under consideration, and hence be taken into account in the seismo-electromagnetic acquisition design e.g. which source- and receiver-types to deploy. In addition, not only amplitude changes but also phase changes and waveform changes have been observed. These phase and waveform changes could be useful as well, but require additional investigation.

In this section, we have not focused on the sensitivity of coseismic fields to thin-bed structures. It is important to realize that coseismic electromagnetic fields can only provide localized information (at the receivers), since they co-propagate within the seismic waves. Therefore, all seismo-electromagnetic information of the subsurface thin-bed structures has been lost from the signal once the coseismic fields reach the receivers at the surface. The only information of the thin-bed structures left in the signal is purely seismic information (and we have seen that seismic signals are less sensitive to thin-beds than seismo-electromagnetic fields). Nevertheless, there might still be some useful seismic information in the coseismic fields, for example the observed phase delay due to dispersion related to the presence of (the more viscous) oil.

The challenge of the weak seismo-electromagnetic signal-to-noise ratio is unfortunately not solved yet. It is important to be aware that nature can help us in the form of thin-bed geology, but can also make our lives more difficult due to complex signal interference patterns that are hard to describe in terms of an effective medium. We could try to take these geological settings into account in our acquisition designs and the way we use our seismo-electromagnetic sources. Existing seismo-electromagnetic signal enhancing techniques like seismo-electromagnetic focusing or specific filtering techniques combined with a search for optimal natural signal enhancements due to thin-bed geology could be a way forward. Combined efforts might yield the desired amplification factor that is required for industrial and global geophysical applications.

4.7.7 Conclusions

Using numerical seismo-electromagnetic wave propagation experiments through packages of thin-beds, we have shown that thin-bed geological settings can improve the signal strength of the seismo-electromagnetic interface response fields. Increasing amounts of thin-beds can cause the shear-wave related interface response strength to increase or decrease. In our experiments, the pressure-wave related interface response fields are not visibly affected by the presence of thin-beds.

Both the thickness of the thin-beds as well as the amount of thin-beds play a role in whether or not the multiples (created by the individual thin-beds) vanish in the record (i.e., are compressed at the position of the shear-wave related interface response field in the reference response (the response for which there are no thin-beds present)). We can distinguish two limits of bed thickness: an upper and lower limit. The upper limit of bed thickness determines whether the individual layers are still recognized or not. When beds are thinner than this limit, the package of thin-beds starts acting like an 'effective' medium and the multiples vanish from the record. The lower limit of bed thickness determines the border from whereon further thinning does not affect the seismo-electromagnetic IR signal strength anymore, because the bed thickness is below the sensitive resolution of the seismo-electromagnetic fields. The upper limit seems to occur when the thin-bed thickness reaches a value of around 5 m thickness. This corresponds to thicknesses of 1/14 and 1/21 of the dominant S- and P-wavelengths in our models, 70 m and 105 m, respectively. The lower limit, from whereon further thinning does not affect the signal strength anymore, seems to occur around 2.5 m thickness. This lower limit corresponds to 1/28 and 1/42 of the dominant S- and P-wavelengths, respectively. This is far below the conventional seismic definition of a thin-bed.

Tuning package thickness experiments of 70 m and 105 m show that there seems to be a maximum strengthening of the shear-wave related interface response signal of a factor 3 for these package thicknesses. This is an indication that not only the amount of thin-beds and the thin-bed thickness, but also the package thickness itself plays an important role in the amplification of the shear-wave related interface response fields due to thin-bed geological structures. The maximum amplitude tuning occurs for package thicknesses similar to the dominant wavelengths of the P- and S-waves.

Whether the thin-beds result in an effective strengthening or weakening of the signal, seems to be determined by the contrast in seismo-electromagnetic coupling coefficients between the different thin-beds. Specific experiments where the electrolyte concentration of the pore fluid was varied have shown that when the combined result of the coupling coefficient contrast between the upper halfspace and package of thin-beds, and the internal thin-bed contrast itself is positive, constructive interference occurs, whereas destructive interference occurs when the combined contrast is negative. Other interference patterns can occur for other combinations of contrasts, impeding the description of seismo-electromagnetic thin-bed responses in terms of 'effective' media.

Arbitrary (user chosen) and mathematically random bed-thickness modeling experiments resulted in responses that are very similar to the periodic bed-thickness

results. We can therefore conclude that the observed seismo-electromagnetic interference patterns are not artefacts due to the periodicity of the bed thickness, but truly seismo-electromagnetic signal-enhancing (or destructing) interference mechanisms. Nevertheless, there seems to be a higher amplification of the shear-wave related interface response fields when the thin-bed thicknesses are less random. Also, the multiples generated by the individual thin-beds seem to converge at smaller amounts of thin-beds in scenarios with less randomness for the bed thicknesses (higher bed-periodicity).

Our oil/water contact modeling experiments where the oil layer is gradually thinned prove that the seismo-electromagnetic signal has a very high sensitivity to oil-water contacts: an oil layer with 20% water saturation and of 0.2 m thickness, a thickness of about $\frac{1}{350}$ of the dominant wavelength of the shear wave generating this response, is still slightly recognized. This is a clear indicator of the high seismo-electromagnetic sensitivity for different saturating fluids.

Chapter 5

Theory and numerical results of seismo-electromagnetic correlation-based interferometry with two-way fields

5.1 Abstract

We explore the application of interferometric techniques to the seismo-electromagnetic system, which might eventually lead to an improved signal-to-noise ratio of the weak converted fields. We present an effective way of deriving explicit homogeneous space Green's function expressions for the 2D SH-TE propagation mode, using power-flux normalized eigenvectors. We derive the theory for interferometric retrieval of 2D SH-TE seismo-EM Green's functions. Using a theoretically desirable circular source configuration as well as a more realistic configuration with sources placed along a line, we show that we can correctly retrieve the dynamic seismo-EM 2D SH-TE response in a homogeneous medium, using seismic boundary sources only. We demonstrate this for two source-receiver combinations: an electric field and a magnetic field due to a seismic source, using explicit homogeneous space Green's function solutions. The volume source contributions account for the losses in the acausal part of the retrieved response as well as the instantaneous source-converted EM field. Using seismo-EM layer-code data, we then show that we can also correctly retrieve the direct shear wave-related causal coseismic field in a homogeneous medium, in both phase and amplitude. To obtain a perfect match in absolute amplitudes, we apply a single linear scaling factor. We finally carry out interferometric experiments in a model containing a single interface at 800 m depth, proving that we can correctly retrieve all 2D SH-TE causal seismic-related direct and reflected coseismic fields, as well as interface response fields, by cross-correlation interferometry, using seismic boundary sources only. These results are promising for the application of 3D seismo-electromagnetic interferometry using our seismo-EM

layer-code, and later on, in the field.

5.2 Introduction

In order to make the seismo-electromagnetic method feasible for industrial applications, we need to somehow enhance its signal-to-noise ratio. Recently, the opportunities for applying a seismo-electromagnetic beamforming technique to maximize the seismo-electromagnetic conversion have been explored (Sava & Revil, 2012; Revil *et al.*, 2015). Another brute-force approach is to use vibroseis trucks to try and boost the signal-to-noise ratio by sending large amounts of energy into the subsurface (Dean & Dupuis, 2011b; Dean *et al.*, 2012). Having strong sources is not always possible or desirable and is likely to boost the noise-levels as well.

From an imaging point of view, the principle of interferometry has been shown effective for a wide class of phenomena, including purely seismic and electromagnetic systems (Schuster *et al.*, 2004; Draganov *et al.*, 2006; Slob *et al.*, 2007; Wapenaar *et al.*, 2008a; Schuster, 2010). When applying interferometry, responses recorded at different receivers are cross-correlated in order to obtain the Green function between these receivers. It can include the responses of both passive and active sources. The cross-correlation process reorganizes measured data such that it may allow for improved imaging compared to the situations where imaging algorithms are applied to the measured data directly. When having downhole receivers, the virtual source method based on interferometric principles (Bakulin & Calvert, 2006; Mehta *et al.*, 2007a) has been proven useful.

Recently, De Ridder *et al.* (2009) have shown that for a 1D scenario for the SH-TE propagation mode, correct Green's function retrieval via cross-correlation based interferometry is possible using only seismic boundary sources. Eventually, we desire to know the applicability of interferometric principles for seismo-EM field data examples. We here make a first step towards this goal, and extend the theory and configuration to a purely 2D scenario for the SH-TE propagation mode. Using explicit homogeneous space solutions derived directly from the system matrix using power-flux normalized eigenvectors, we investigate whether we can retrieve correct seismo-electromagnetic responses via correlation-based interferometry using boundary sources only. Starting from a general interferometric Green's function expression that is derived from correlation-type reciprocity theorems (Wapenaar *et al.*, 2006; Wapenaar & Fokkema, 2004), we select a certain seismo-electromagnetic source-receiver combination to illustrate theoretically the interferometric retrieval of seismo-electromagnetic fields. We then present two numerical examples of interferometric seismo-electromagnetic Green's function retrieval in a homogeneous medium using explicit homogeneous space Green's function solutions. We numerically investigate interferometric retrieval of an electric field and a magnetic field due to a seismic source, for a theoretically desirable circular source configuration, followed by a more realistic line source configuration. We then follow-up with correlation-based interferometry using seismo-EM layer-code data modeled in a homogeneous medium, for the 2D SH-TE scenario. We finalize modeling a scenario with our seismo-EM layer-code containing a single interface at 800 m depth, and prove that we can cor-

rectly retrieve the causal coseismic and interface responses using seismic boundary sources only.

5.3 Theory

5.3.1 Seismo-EM 2D SH-TE homogeneous space solutions

In 2D, mode separation into SH-TE and P-SV-TM occurs naturally. In this section, we will focus on the 2D SH-TE propagation mode only. A similar analysis can be carried out for the P-SV-TM propagation mode. We start by expressing the SH-TE propagation mode into the following matrix differential equation

$$\partial_3 \tilde{\mathbf{F}}^t - \tilde{\mathbf{A}} \tilde{\mathbf{F}}^t = \tilde{\mathbf{S}} \delta(x_3 - x_3^s), \quad (5.1)$$

where $\tilde{\mathbf{F}}^t = (\tilde{\mathbf{F}}_1^t, \tilde{\mathbf{F}}_2^t)$ denotes the two-way field vector, $\tilde{\mathbf{A}}$ is the two-way system matrix and $\tilde{\mathbf{S}} = (\tilde{\mathbf{S}}_1^t, \tilde{\mathbf{S}}_2^t)$ contains the two-way source terms, with x_3^s denoting the x_3 -coordinate of the source position. We obtain the 2D field quantities, system matrix and source terms by setting $k_2 = 0$ and dividing the 3D SH-TE field quantities and source terms, which are presented in e.g. [Haartsen & Pride \(1997\)](#), [Grobbe *et al.* \(2016a\)](#), by $-jk_1$, where j denotes the imaginary unit and k_1 is the horizontal wavenumber in the x_1 -direction (and k_2 the horizontal wavenumber in the x_2 -direction). The 2D field vector is composed as $\tilde{\mathbf{F}}_1^t = (\tilde{v}_2^s, \tilde{E}_2)$ and $\tilde{\mathbf{F}}_2^t = (\tilde{\tau}_{23}^b, -\tilde{H}_1)$, which are the solid particle velocity, the electric field, the bulk stress component and the magnetic field, respectively. Here the subscripts indicate the orientation with respect to the right-handed Cartesian coordinate system and the superscripts provide extra information about the field (or source) type (acting on solid (s), fluid (f), bulk (b) and so on). The superscript t denotes vector or matrix transposition. The corresponding source vector is defined as $\tilde{\mathbf{S}}_1^t = (\tilde{h}_{23}^b + \tilde{h}_{32}^b, \tilde{J}_1^m)$, $\tilde{\mathbf{S}}_2^t = (-[\tilde{f}_2^b - \frac{\rho^f}{\rho^E} \tilde{f}_2^f] - \frac{jk_1 G^{fr}}{s} [\tilde{h}_{21}^b + \tilde{h}_{12}^b], -\tilde{J}_2^e - \hat{\mathcal{L}} \tilde{f}_2^f - \frac{jk_1}{s\mu_0} \tilde{J}_3^m)$, where \tilde{h}_{23}^b is the bulk external deformation rate density, \tilde{J}_1^m the external magnetic current density, \tilde{f}_2^b the bulk dipole force source, \tilde{f}_2^f the fluid dipole force source, \tilde{h}_{12}^b is the bulk external deformation rate density, \tilde{J}_3^m the external magnetic current density, \tilde{J}_2^e the external electric current density and where $\tilde{h}_{12}^b = \tilde{h}_{21}^b$ and $\tilde{h}_{23}^b = \tilde{h}_{32}^b$. Here, $s = j\omega$ (where ω is the radial frequency) and the hat indicates the space-frequency domain (or frequency-dependency). The SH-TE two-way system matrix reads

$$\tilde{\mathbf{A}} = \begin{pmatrix} \mathbf{O} & \tilde{\mathbf{A}}_{12} \\ \tilde{\mathbf{A}}_{21} & \mathbf{O} \end{pmatrix}, \quad (5.2)$$

where the SH-TE two-way system submatrices are defined as

$$\tilde{\mathbf{A}}_{12} = \begin{pmatrix} \hat{\beta} & 0 \\ 0 & -\hat{\zeta} \end{pmatrix}; \tilde{\mathbf{A}}_{21} = \begin{pmatrix} \hat{\alpha} + \frac{k_1^2}{\hat{\beta}} & \hat{\chi} \\ \hat{\chi} & -(\hat{\eta}^E + \frac{k_1^2}{\hat{\zeta}}) \end{pmatrix}. \quad (5.3)$$

Furthermore, $\hat{\beta} = \frac{s}{G^{fr}}$, $\hat{\zeta} = \hat{\sigma}^m + s\mu$, $\hat{\chi} = s\rho^f \hat{\mathcal{L}}$, $\hat{\alpha} = s\hat{\rho}^c$ and $\hat{\eta}^E = \hat{\sigma}^e + s\epsilon$. In addition, $\hat{\sigma}^m$ is the frequency-dependent magnetic conductivity (chosen zero since we

ignore magnetic relaxation losses), $\mu = \mu_0\mu_r$, the product of the magnetic permeability in vacuum and the relative magnetic permeability, ρ^f being the density of the fluid, $\hat{\mathcal{L}}$ representing the seismo-electromagnetic coupling coefficient, $\hat{\rho}^c = \rho^b - \frac{(\rho^f)^2}{\hat{\rho}^E}$ where ρ^b is the bulk density and $\hat{\rho}^E = \frac{\eta}{sk}$ (with η being the viscosity of the fluid and \hat{k} the permeability of the medium). Furthermore, $\hat{\sigma}^e = \frac{\phi\sigma^f}{\alpha_\infty}$ is the frequency-dependent electrical conductivity with ϕ denoting the porosity of the medium, σ^f the conductivity of the fluid and α_∞ the tortuosity of the medium. Finally, $\epsilon = \epsilon_0\epsilon_r$, the product of the dielectric permittivity in vacuum and the relative dielectric permittivity. The 2D system matrix $\tilde{\mathbf{A}}$ can again be decomposed into matrices consisting of its eigenvectors and eigenvalues via $\tilde{\mathbf{A}} = \tilde{\mathbf{L}}\tilde{\mathbf{\Lambda}}_1\tilde{\mathbf{L}}^{-1}$, where $\tilde{\mathbf{L}}$ and $\tilde{\mathbf{L}}^{-1}$ represent the composition and decomposition matrices, respectively, that consist of the eigenvectors of the SH-TE system matrix. $\tilde{\mathbf{\Lambda}}_1 = \text{diag}(-\Gamma_{SH}, -\Gamma_{TE}, \Gamma_{SH}, \Gamma_{TE})$, a diagonal matrix consisting of the eigenvalues of the system, where $\Gamma_{SH,TE}^2 = \gamma_{SH,TE}^2 + k_1^2$. Similar to Section 2.4, we use the following expressions for the Green matrices

$$\check{\mathbf{G}}_{11} = -2jk_3\check{\mathbf{L}}_1^H\check{\mathbf{G}}\check{\mathbf{L}}_2^t, \quad (5.4)$$

$$\check{\mathbf{G}}_{12} = 2\check{\mathbf{A}}_{12}\check{\mathbf{L}}_2\check{\mathbf{G}}\check{\mathbf{L}}_1^t, \quad (5.5)$$

$$\check{\mathbf{G}}_{21} = 2\check{\mathbf{A}}_{21}\check{\mathbf{L}}_1\check{\mathbf{G}}\check{\mathbf{L}}_2^t, \quad (5.6)$$

$$\check{\mathbf{G}}_{22} = -2jk_3\check{\mathbf{L}}_2\check{\mathbf{G}}\check{\mathbf{L}}_1^t. \quad (5.7)$$

Here, $\check{\mathbf{G}}$ is a diagonal matrix consisting of the 2D scalar Green's functions for the two field types (horizontally polarized shear waves and transverse electric fields). The space-frequency solution of this matrix looks like $\check{\mathbf{G}} = \text{diag}\left(\frac{1}{2\pi}K_0(\gamma_{SH}R^{rs}), \frac{1}{2\pi}K_0(\gamma_{SH}R^{rs})\right)$. Here, $K_0(\gamma_{SH,TE}R^{rs})$ is the modified Bessel function of the second kind and order zero. Its argument contains the spherical wavenumber $\gamma_{SH,TE} = \frac{s}{\hat{c}_{SH,TE}}$ with $\hat{c}_{SH,TE}$ representing the SH wave or TE field velocities. Furthermore, R^{rs} denotes the distance between the source position (superscript s) and the receiver position (superscript r) $R^{rs} = \sqrt{(x_1^r - x_1^s)^2 + (x_3^r - x_3^s)^2}$. We now have all ingredients to derive the desired explicit 2D homogeneous Green's functions expressions for the SH-TE propagation mode for each source-receiver combination. This enables us to model all 2D SH-TE seismo-electromagnetic responses in a homogeneous domain that are required for the application of interferometry.

5.3.2 2D SH-TE interferometry

Following the description of the 3D seismo-electromagnetic system in [Wapenaar & Fokkema \(2004\)](#), we start by capturing the 2D SH-TE system also in the general diffusion, flow and wave equation format: $j\omega\mathbf{A}\hat{\mathbf{u}} + \mathbf{B}\hat{\mathbf{u}} + \mathbf{D}_x\hat{\mathbf{u}} = \hat{\mathbf{s}}$. Here $\hat{\mathbf{u}}$ and $\hat{\mathbf{s}}$ contain the field and source quantities, respectively, whereas \mathbf{A} and \mathbf{B} are matrices containing space-dependent material parameters and \mathbf{D}_x is a matrix containing the spatial differential operators $\frac{\partial}{\partial x_1}$ and $\frac{\partial}{\partial x_3}$. Note that this \mathbf{A} is different than before.

Here, $\hat{\mathbf{u}}^t = \left(\hat{E}_2, \hat{H}_1, \hat{H}_3, \hat{v}_2^s, -\hat{\tau}_{23}^b, -\hat{\tau}_{21}^b\right)$ and $\hat{\mathbf{s}}^t = (\hat{s}_1, \hat{s}_2, \hat{s}_3, \hat{s}_4, \hat{s}_5, \hat{s}_6)$, where $\hat{s}_1 = -\hat{J}_2^e - \hat{\mathcal{L}}\hat{f}_2^f$, $\hat{s}_2 = -\hat{J}_1^m$, $\hat{s}_3 = -\hat{J}_3^m$, $\hat{s}_4 = \hat{f}_2^b - \frac{\rho^f}{\hat{\rho}^E}\hat{f}_2^f$, $\hat{s}_5 = \hat{h}_{32}^b + \hat{h}_{23}^b$ and $\hat{s}_6 = \hat{h}_{12}^b + \hat{h}_{21}^b$. For the details of \mathbf{A} , \mathbf{B} and \mathbf{D}_x , the reader is referred to [Wapenaar & Fokkema](#)

(2004). By replacing the source vector $\hat{\mathbf{s}}$ by a point source matrix $\mathbf{I}\delta(\mathbf{x} - \mathbf{x}_A)$, the field quantities in $\hat{\mathbf{u}}$ can be replaced by a Green's matrix, resulting in

$$\hat{\mathbf{G}}(\mathbf{x}_B, \mathbf{x}_A, \omega) = \begin{pmatrix} \hat{G}^{E_2,s_1} & \hat{G}^{E_2,s_2} & \hat{G}^{E_2,s_3} & \hat{G}^{E_2,s_4} & \hat{G}^{E_2,s_5} & \hat{G}^{E_2,s_6} \\ \hat{G}^{H_1,s_1} & \hat{G}^{H_1,s_2} & \hat{G}^{H_1,s_3} & \hat{G}^{H_1,s_4} & \hat{G}^{H_1,s_5} & \hat{G}^{H_1,s_6} \\ \hat{G}^{H_3,s_1} & \hat{G}^{H_3,s_2} & \hat{G}^{H_3,s_3} & \hat{G}^{H_3,s_4} & \hat{G}^{H_3,s_5} & \hat{G}^{H_3,s_6} \\ \hat{G}^{v_2,s_1} & \hat{G}^{v_2,s_2} & \hat{G}^{v_2,s_3} & \hat{G}^{v_2,s_4} & \hat{G}^{v_2,s_5} & \hat{G}^{v_2,s_6} \\ \hat{G}^{\tau_{23},s_1} & \hat{G}^{\tau_{23},s_2} & \hat{G}^{\tau_{23},s_3} & \hat{G}^{\tau_{23},s_4} & \hat{G}^{\tau_{23},s_5} & \hat{G}^{\tau_{23},s_6} \\ \hat{G}^{\tau_{21},s_1} & \hat{G}^{\tau_{21},s_2} & \hat{G}^{\tau_{21},s_3} & \hat{G}^{\tau_{21},s_4} & \hat{G}^{\tau_{21},s_5} & \hat{G}^{\tau_{21},s_6} \end{pmatrix}, \quad (5.8)$$

where \mathbf{x}_A corresponds to the source location and \mathbf{x}_B to the receiver location and the superscripts denote (receiver-type, source-type), according to their position in $\hat{\mathbf{u}}$ and $\hat{\mathbf{s}}$, respectively. Each of the elements corresponds to a Green's function which we can model using the homogeneous space Green's function expressions as derived in the previous section. We can now select the Green function for a certain seismo-electromagnetic source-receiver combination and evaluate the interferometric Green's function retrieval expression as presented in [Wapenaar *et al.* \(2006\)](#):

$$\begin{aligned} & \hat{\mathbf{G}}(\mathbf{x}_B, \mathbf{x}_A, \omega) + \hat{\mathbf{G}}^\dagger(\mathbf{x}_A, \mathbf{x}_B, \omega) = \\ & - \oint_{\partial S} \hat{\mathbf{G}}(\mathbf{x}_B, \mathbf{x}, \omega) \mathbf{N}_x \hat{\mathbf{G}}^\dagger(\mathbf{x}_A, \mathbf{x}, \omega) d\mathbf{x} + \\ & \int_S \hat{\mathbf{G}}(\mathbf{x}_B, \mathbf{x}, \omega) \left(-2\omega \Im(\hat{\mathbf{A}}) + \hat{\mathbf{B}} + \hat{\mathbf{B}}^\dagger \right) \hat{\mathbf{G}}^\dagger(\mathbf{x}_A, \mathbf{x}, \omega), \end{aligned} \quad (5.9)$$

where the first term on the left-hand side represents the causal retrieved Green's function with the virtual source at receiver location \mathbf{x}_A and the receiver at \mathbf{x}_B and where the second term represents the acausal retrieved Green's function with the virtual source at receiver location \mathbf{x}_B and the receiver at \mathbf{x}_A . The dagger sign denotes the complex conjugate transpose. Furthermore, the first integral on the right-hand side is the boundary source integral, summing the contributions from different source locations \mathbf{x} to receivers \mathbf{x}_A and \mathbf{x}_B and the second integral represents the volume source integral. \mathbf{N}_x is the matrix consisting of normal vector elements n_1 and n_3 with positions and signs equal to the organization of partial derivative matrix \mathbf{D}_x . We will here focus on element (1,4) of equation (5.8), and evaluate expression (5.9)

for this element considering only boundary source contributions, which results in

$$\begin{aligned}
& \left[\hat{G}^{E_2, s_4}(\mathbf{x}_B, \mathbf{x}_A, \omega) + \left\{ \hat{G}^{v_2, s_1}(\mathbf{x}_A, \mathbf{x}_B, \omega) \right\}^* \right] \hat{S} = \\
& - \oint_{\partial S} \left[\hat{G}_B^{E_2, s_1}(-n_3)(\hat{G}_A^{v_2, s_2})^* + \hat{G}_B^{E_2, s_1} n_1(\hat{G}_A^{v_2, s_3})^* \right. \\
& + \hat{G}_B^{E_2, s_2}(-n_3)(\hat{G}_A^{v_2, s_1})^* + \hat{G}_B^{E_2, s_3} n_1(\hat{G}_A^{v_2, s_1})^* \\
& + \hat{G}_B^{E_2, s_4} n_3(\hat{G}_A^{v_2, s_5})^* + \hat{G}_B^{E_2, s_4} n_1(\hat{G}_A^{v_2, s_6})^* \\
& \left. + \hat{G}_B^{E_2, s_5} n_3(\hat{G}_A^{v_2, s_4})^* + \hat{G}_B^{E_2, s_6} n_1(\hat{G}_A^{v_2, s_4})^* \right] \hat{S} d\mathbf{x}, \tag{5.10}
\end{aligned}$$

where the subscript B replaces the spatial and frequency terms in the Green function argument $(\mathbf{x}_B, \mathbf{x}, \omega)$ and where the subscript A replaces $(\mathbf{x}_A, \mathbf{x}, \omega)$. We model all Green's functions using a Ricker wavelet with a peak frequency of 30 Hz. In the above equation, \hat{S} denotes the power spectrum of this Ricker wavelet and the asterisk denotes complex conjugation. We will model the left-hand side of equation (5.10) as the reference response (that will be displayed in blue), whereas the right-hand side will result in the interferometrically retrieved response (displayed in red-dashed). Similar integral representations can be derived and modeled for all other seismo-electromagnetic source-receiver combinations (including the combination of our second numerical example).

5.4 Numerical Results

5.4.1 2D SH-TE interferometry using homogeneous-space solutions

Circular source acquisition

Our aim is to investigate whether we can retrieve the correct seismo-electromagnetic response that we are after using correlation-based interferometry with boundary sources only, preferably of a certain type. We first consider a 2D circular source geometry in the (x_1, x_3) -plane with two receivers located at $\mathbf{x}_A = (0, -200)$ and $\mathbf{x}_B = (0, 200)$ and 500 sources located at the boundary of the circle with centerpoint $= (0, 0)$ and radius $R=1200$ m (see Figure 5.1). This will yield perfect illumination from all sides.

Having illumination from all sides, we should theoretically be able to retrieve the response matching in both phase and amplitude. However, the volume source terms in equation (5.9) account for the losses. When losses occur, using only boundary sources might not yield the desired retrieved responses. We consider a porous, fluid-saturated medium with properties such that in the frequency bandwidth under consideration (0-500 Hz), the shear wave velocity ranges from about $\hat{c}_{SH} = 2110.8 - 2110.9$ m/s and the transverse electric field diffusive velocity ranges from about $\hat{c}_{TE} = 31421.5 - 1005811.5$ m/s. Since we model a homogeneous medium, only coseismic fields and source-converted fields are to be expected, and no

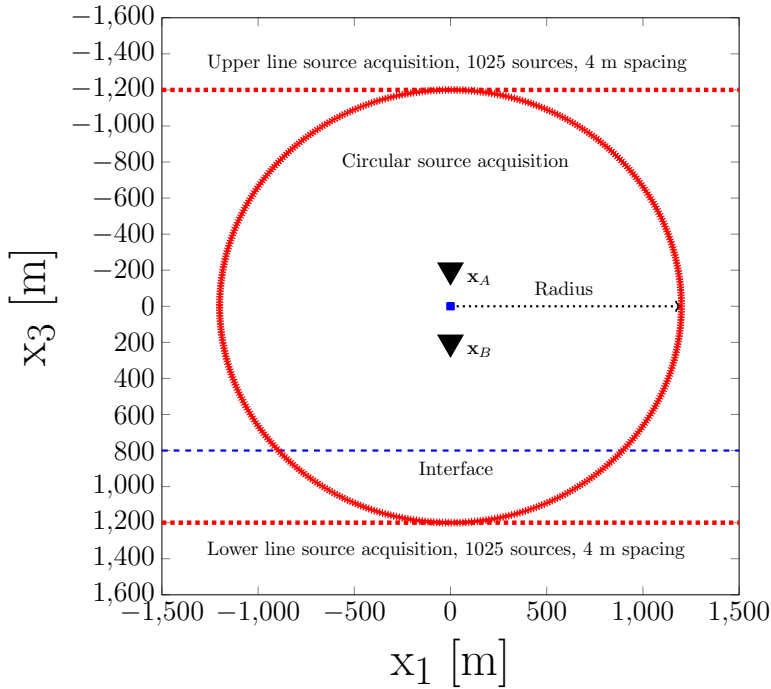


Figure 5.1: Schematic overview of the interferometric experiments. Red indicates the source positions, either circular or two line source configurations. The blue-dashed line indicates an interface, the blue square is the center point of the circle, and the black triangles are the receivers \mathbf{x}_A and \mathbf{x}_B .

interface response fields. We use the explicit homogeneous space Green's function expressions to model the responses. We investigate the retrieval of two source-receiver combinations:

1. $G^{E_2, s_4}(\mathbf{x}_B, \mathbf{x}_A, t) + G^{v_2, s_1}(\mathbf{x}_A, \mathbf{x}_B, -t)$,
2. $G^{H_1, s_4}(\mathbf{x}_B, \mathbf{x}_A, t) + G^{v_2, s_2}(\mathbf{x}_A, \mathbf{x}_B, -t)$,

where the positive times represent the causal responses and the time-reversals the acausal responses. The distance between receivers \mathbf{x}_A and \mathbf{x}_B is 400 m, resulting in a direct coseismic or coelectric event at a shear wave arrival time of around $t=0.19$ s. Furthermore, we expect a source-converted field with EM velocity, arriving more or less instantaneously at $t=0$. The results of these two interferometric numerical experiments are displayed in Figures 5.2, 5.3, and 5.4, subfigures (a) and (b), respectively. Starting by looking at Figure 5.2, we can observe that by using all boundary sources, we correctly retrieve the desired direct shear wave coseismic event in the causal part in both phase and amplitude, for both source-receiver combinations.

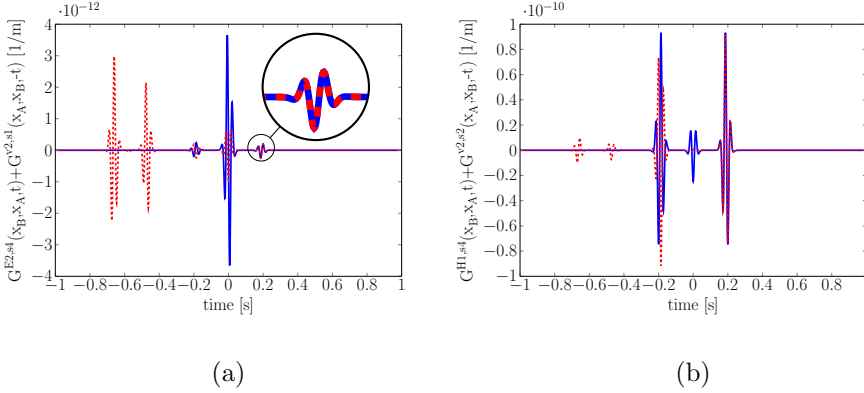


Figure 5.2: Interferometric retrieval of 2D SH-TE source-receiver combinations using all boundary sources for a circular acquisition geometry. Blue: reference, red-dashed: retrieved. **(a)** Interferometric retrieval of $G^{E2,s4}(\mathbf{x}_B, \mathbf{x}_A, t) + G^{v2,s1}(\mathbf{x}_A, \mathbf{x}_B, -t)$ **(b)** Interferometric retrieval of $G^{H1,s4}(\mathbf{x}_B, \mathbf{x}_A, t) + G^{v2,s2}(\mathbf{x}_A, \mathbf{x}_B, -t)$.

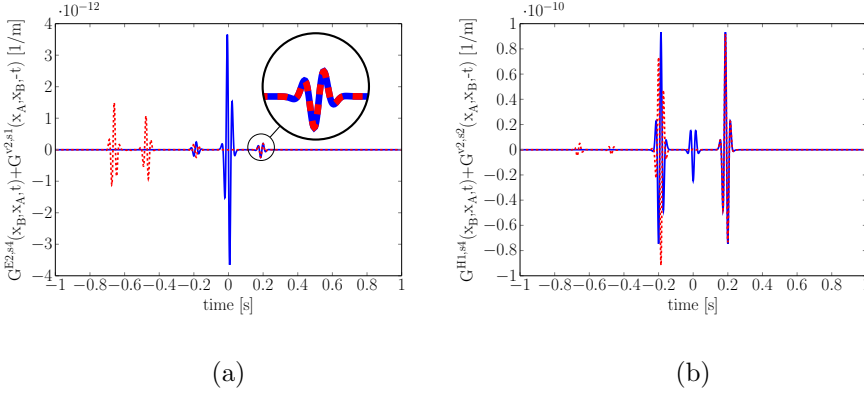


Figure 5.3: Interferometric retrieval of 2D SH-TE source-receiver combinations using seismic boundary sources only for a circular acquisition geometry. Blue: reference, red-dashed: retrieved. **(a)** Interferometric retrieval of $G^{E2,s4}(\mathbf{x}_B, \mathbf{x}_A, t) + G^{v2,s1}(\mathbf{x}_A, \mathbf{x}_B, -t)$ **(b)** Interferometric retrieval of $G^{H1,s4}(\mathbf{x}_B, \mathbf{x}_A, t) + G^{v2,s2}(\mathbf{x}_A, \mathbf{x}_B, -t)$.

The acausal part of Figure 5.2a displays a polarity reversed direct arrival and two additional spurious events. This also holds for the response of Figure 5.2b. We also observe that the instantaneously converted EM arrival at $t=0$ s is not correctly retrieved using boundary sources only. The boundary sources only slightly contribute to this source-converted EM field in Figure 5.2a, and hardly in Figure 5.2b. Based on our knowledge from 1D results (De Ridder *et al.*, 2009), we expect that by adding the volume source contributions, the spurious events will vanish, the polarity of the acausal direct shear wave arrival will be reversed, and that the instantaneous converted EM arrival will be retrieved correctly as well. In other words, the volume sources which account for the losses in the medium are necessary to correctly retrieve the events in the acausal part as well as the direct source-converted EM field. These volume sources are not required to retrieve the events in the causal part. Since we

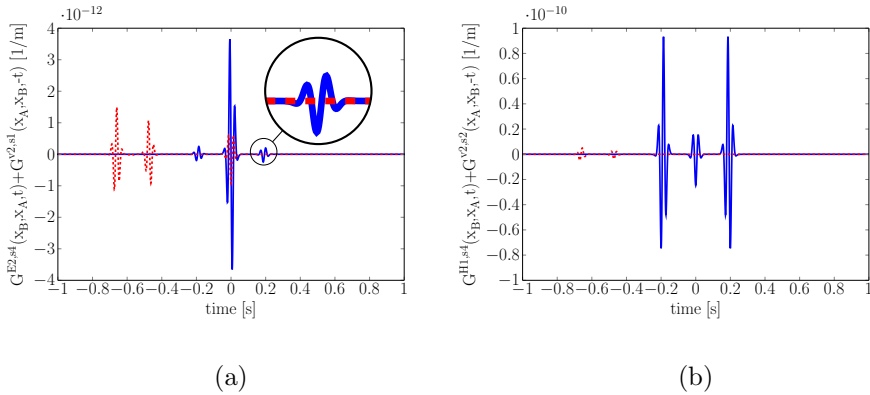


Figure 5.4: Interferometric retrieval of 2D SH-TE source-receiver combinations using EM boundary sources only for a circular acquisition geometry. Blue: reference, red-dashed: retrieved. (a) Interferometric retrieval of $G^{E2,s4}(\mathbf{x}_B, \mathbf{x}_A, t) + G^{v2,s1}(\mathbf{x}_A, \mathbf{x}_B, -t)$ (b) Interferometric retrieval of $G^{H1,s4}(\mathbf{x}_B, \mathbf{x}_A, t) + G^{v2,s2}(\mathbf{x}_A, \mathbf{x}_B, -t)$.

are interested in the causal part of the response, the losses in the medium and lack of volume sources do not matter. Figure 5.3 shows the retrieved response using only seismic boundary sources (a more realistic acquisition scenario). For both source-receiver scenarios (Figures 5.3a and 5.3b), we can still observe a correct retrieval of the event in the causal part without visible amplitude losses. We see a very small contribution of the seismic boundary sources to the source-converted EM field. Figure 5.4 shows the retrieved events using only EM boundary sources. In Figure 5.4a, we can indeed observe that these sources do not contribute to the retrieval of the shear wave velocity related direct coseismic fields, but they do contribute to the instantaneously source-converted electric field at $t = 0$ and to the spurious events at negative times greater than $t = -0.25$ s. Figure 5.4b emphasizes that the EM boundary sources do not really contribute to the source-converted magnetic field, and that this field should be almost completely recovered by the volume sources accounting for the losses in the medium.

Line source acquisition

We now move on to a slightly more realistic acquisition scenario, where sources are located at two horizontal lines above and below the receiver levels. We use two source arrays located at -1200 m and 1200 m depth (see Figure 5.1). We apply a far-field approximation, meaning that only the terms in equation (5.10) related to the n_3 normal components are contributing. Based on stationary phase analysis of the correlation gathers of $G^{E2,s4}(\mathbf{x}_B, \mathbf{x}_A, t) + G^{v2,s1}(\mathbf{x}_A, \mathbf{x}_B, -t)$, presented in Figure 5.5, we determine the maximum offset that we need for our source coverage. Based on this stationary phase analysis, we determine we need about 1025 sources with a source spacing of 4 meters to obtain enough illumination for the interferometric Green's function recovery. A Hanning taper with a taper length of 500 is applied, tapering the non-stationary zones to avoid artefacts. We have already applied this Hanning taper in Figure 5.5. We can clearly observe in Figure 5.5 that the Hanning taper

nically tapers most of the non-stationary zones in the correlation gathers, avoiding artefacts in the interferometric retrieved result. The receivers are located at the same positions as before, and we investigate the same Green's function retrieval.

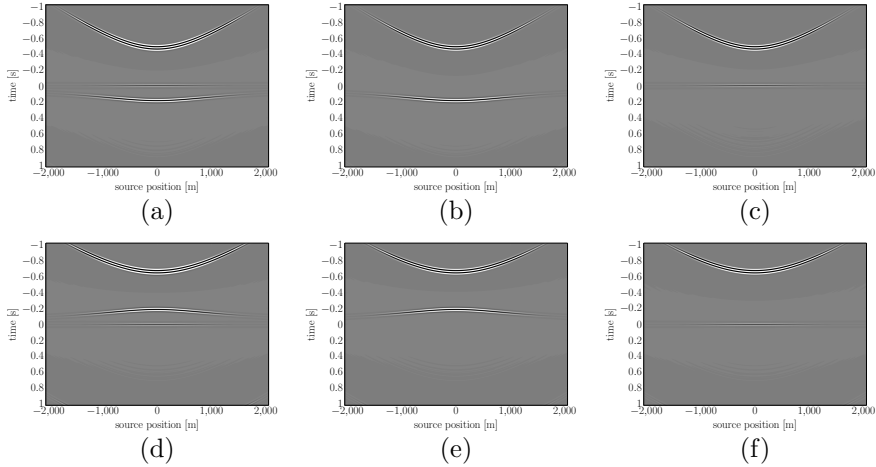


Figure 5.5: Cross-correlograms for both source acquisition lines, where a Hanning source taper with a taper length of 500 has been applied; **(a)** all source types, upper source line at -1200 m **(b)** seismic source types only, upper source line at -1200 m **(c)** EM source types only, upper source line at -1200 m **(d)** all source types, lower source line at 1200 m **(e)** seismic source types only, lower source line at 1200 m **(f)** EM source types only, lower source line at 1200 m.

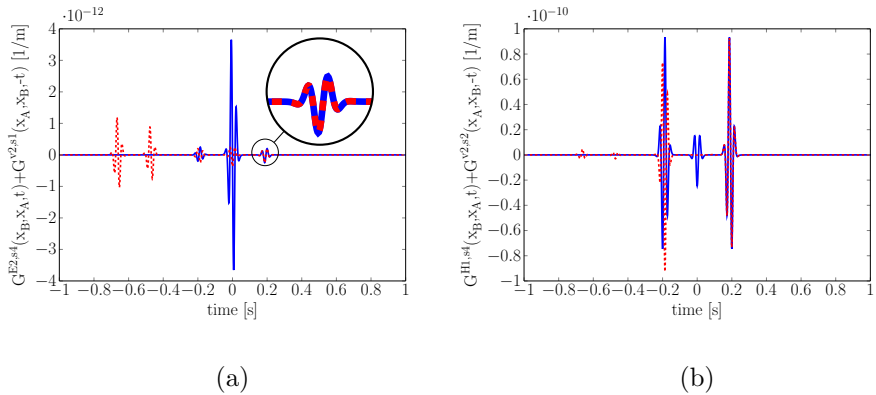


Figure 5.6: Interferometric retrieval of 2D SH-TE source-receiver combinations using all boundary sources for a line source acquisition geometry. Blue: reference, red-dashed: retrieved. **(a)** Interferometric retrieval of $G^{E2,s4}(x_B, x_A, t) + G^{v2,s1}(x_A, x_B, -t)$ **(b)** Interferometric retrieval of $G^{H1,s4}(x_B, x_A, t) + G^{v2,s2}(x_A, x_B, -t)$.

Figures 5.6a and 5.6b show again a perfect dynamic retrieval of the causal direct shear-wave related coseismic field. Comparing the red-dashed retrieved signal of Figure 5.6a, with the circular source configuration of Figure 5.2a, the amplitudes of the acausal spurious events are now slightly less, and also the source-converted response contribution has a smaller amplitude. Figures 5.7a and b show the retrieved response

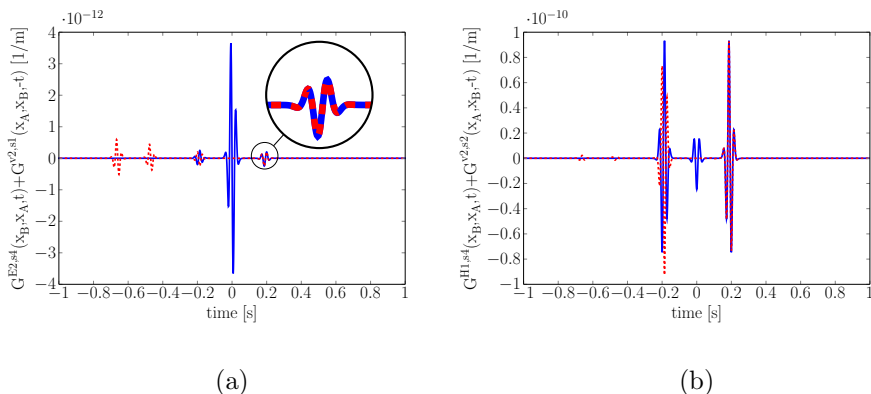


Figure 5.7: Interferometric retrieval of 2D SH-TE source-receiver combinations using seismic boundary sources only for a line source acquisition geometry. Blue: reference, red-dashed: retrieved. **(a)** Interferometric retrieval of $G^{E2,s4}(\mathbf{x}_B, \mathbf{x}_A, t) + G^{v2,s1}(\mathbf{x}_A, \mathbf{x}_B, -t)$ **(b)** Interferometric retrieval of $G^{H1,s4}(\mathbf{x}_B, \mathbf{x}_A, t) + G^{v2,s2}(\mathbf{x}_A, \mathbf{x}_B, -t)$.

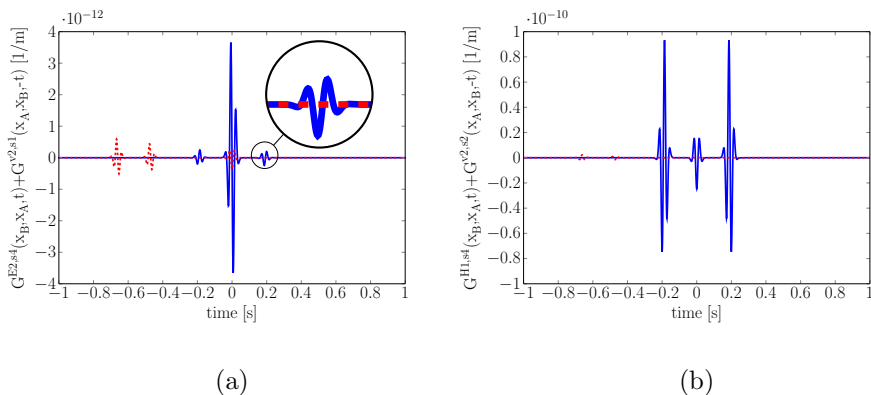


Figure 5.8: Interferometric retrieval of 2D SH-TE source-receiver combinations using EM boundary sources only for a line source acquisition geometry. Blue: reference, red-dashed: retrieved. **(a)** Interferometric retrieval of $G^{E2,s4}(\mathbf{x}_B, \mathbf{x}_A, t) + G^{v2,s1}(\mathbf{x}_A, \mathbf{x}_B, -t)$ **(b)** Interferometric retrieval of $G^{H1,s4}(\mathbf{x}_B, \mathbf{x}_A, t) + G^{v2,s2}(\mathbf{x}_A, \mathbf{x}_B, -t)$.

using only seismic boundary sources. For both scenarios, we still observe perfect retrieval of the direct shear wave coseismic event in the causal part without visible amplitude losses. There is no visible contribution of the seismic boundary sources to the source-converted EM field. Figures 5.8a and b present the retrieved events using only EM boundary sources. In Figure 5.8a, we can indeed observe that these sources do not contribute to the retrieval of the S-wave velocity related direct coseismic fields, but they do contribute to the instantaneously source-converted electric field at $t=0$ and to the spurious events at negative times greater than $t=-0.25$ s. Figure 5.8b emphasizes again that the EM boundary sources do not visibly contribute to the source-converted EM field for the magnetic field recovery, and that this field should be almost completely recovered by the volume sources accounting for the losses in the medium.

5.4.2 2D SH-TE interferometry using layer-code data

The interferometric examples thus far, have been obtained with an independent numerical script, using the explicit analytical homogeneous space Green's function expressions. From these experiments, we can conclude that also for line source configurations (i.e. having no perfect illumination from all sides), using the far-field approximation, we can still correctly retrieve dynamic seismo-EM 2D SH-TE responses, using seismic boundary sources only. This paves the way to carry out interferometric experiments with our layer-code ESSEMOD, where line source configurations can be easily modeled, exploiting the lateral invariance of the layered-Earth medium. We can model the required 2D SH-TE data using one source and an array of receivers with the length of the required line source arrays, for example 1025 receivers with 4 m receiver-spacing, corresponding to the 1025 sources with 4 m source-spacing of the homogeneous space line source experiments presented earlier. We apply the same Hanning source taper as determined previously. We will focus on interferometric retrieval of $G^{E_2, s_4}(\mathbf{x}_B, \mathbf{x}_A, t) + G^{v_2, s_1}(\mathbf{x}_A, \mathbf{x}_B, -t)$.

Homogeneous Scenario

First, we will model a homogeneous scenario, where we choose all layers to be the same medium, with identical medium parameters as used for the earlier described interferometric experiments. The results are presented in Figures 5.9 and 5.10. We can observe a perfect match for the direct shear wave-related coseismic causal event in both phase and amplitude. To obtain a correct match in absolute amplitudes, between the reference response in blue and the interferometrically retrieved result in red-dashed, we have multiplied the reference response with a single scaling factor of $6.2 \cdot 10^3$. We have determined this scaling factor by dividing the amplitude of the retrieved response at $t = 0.185$ s with the amplitude of the reference response at that time. This time corresponds more or less with the direct shear wave-related causal coseismic field arrival time. Comparing these homogeneous results with the results earlier obtained using the explicit homogeneous space Green's functions (Figure 5.6, 5.7, and 5.8), we can observe some differences. First of all, the absolute amplitudes of the results using the homogeneous space Green's function solutions are in the order of 10^{-12} , whereas the results using the seismo-EM layer-code data are in the order of 10^{-6} . In other words, the layer-code data yields larger amplitudes. Furthermore, the amplitude of the source-converted retrieved EM field using the layer-code data (red-dashed line around $t = 0$ s), is much larger compared to the result using the homogeneous space solutions. The relative amplitude of the direct shear wave with respect to the source converted field seems a bit weaker for the layer-code data than for the homogeneous space solutions. Nevertheless, despite these differences, there are also a lot of similarities. The two spurious events in the acausal part are located at the same time in both experiments, the direct shear wave related causal coseismic field is perfectly retrieved in both amplitude and phase, and the acausal direct coseismic field has a polarity reversed retrieved field. The retrieved response using the layer-code data has a larger amplitude than the reference response. This is remarkable, and indicates, together with the fact that the absolute amplitudes of

the results using the layer-code data are about 6 orders of magnitude larger than the results using the homogeneous space solutions, that probably either some of the 2D cross-correlated source-receiver combinations are modeled not perfectly correctly in terms of amplitude in our seismo-EM layer-code, or that there is a simple constant scaling factor lacking somewhere else in the 2D part of our layer-code program (e.g. a factor in the spatial Fourier transformation). Nevertheless, the dynamic match of the interferometric result, and the great similarities between the results of both experiments, provide confidence that we can trust the interferometric results obtained using our seismo-EM layer-code (except for a single scaling factor), allowing to carry out interferometric experiments in layered-Earth scenarios.

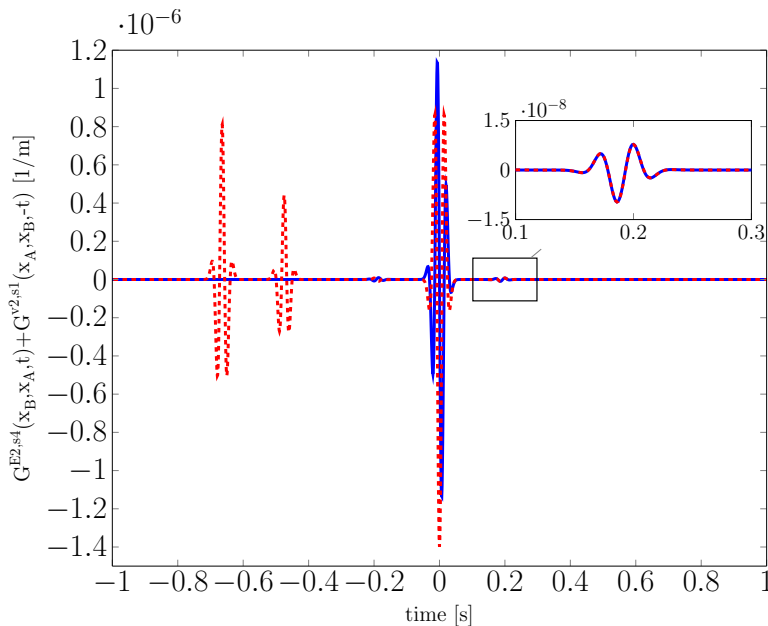


Figure 5.9: Interferometric retrieval of the 2D SH-TE $G^{E2,s4}(\mathbf{x}_B, \mathbf{x}_A, t) + G^{v2,s1}(\mathbf{x}_A, \mathbf{x}_B, -t)$ source-receiver Green's function combination in a homogeneous medium, using all boundary sources, for a line source acquisition geometry. The data being cross-correlated are modeled with our seismo-EM layer-code. Blue: reference, red-dashed: retrieved.

Looking at Figures 5.10a and 5.10b, we can again observe that the seismic sources are sufficient to retrieve the direct shear wave-related causal coseismic field, and that the EM sources contribute to the retrieval of the source-converted EM field. Furthermore, for the retrieval of the acausal direct coseismic field and the source converted EM field, we require the volume sources.

Scenario with an interface at 800 m

We now explore interferometric seismo-electromagnetic Green's function retrieval in the same model as used for the homogeneous experiment, but we add an interface at 800 m (so 600 m below receiver \mathbf{x}_B , ssee Figure 5.1). There is a contrast in porosity (0.4 above and 0.2 below), static permeability ($1.3 \cdot 10^{-12} \text{ m}^2$ above and $1.6 \cdot 10^{-12}$

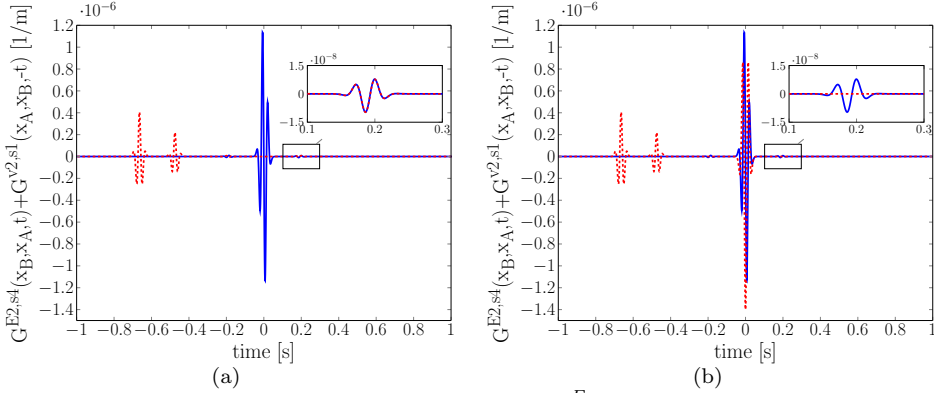


Figure 5.10: Interferometric retrieval of the 2D SH-TE $G^{E2,s4}(\mathbf{x}_B, \mathbf{x}_A, t) + G^{v2,s1}(\mathbf{x}_A, \mathbf{x}_B, -t)$ source-receiver Green's function combination in a homogeneous medium, for a line source acquisition geometry. The data being cross-correlated are modeled with our seismo-EM layer-code. Blue: reference, red-dashed: retrieved. (a) Retrieved Green's function using seismic boundary sources only. (b) Retrieved Green's function using EM boundary sources only.

m^2 below), and electrolyte concentration ($1 \cdot 10^{-4}$ mol/L above and $1 \cdot 10^{-2}$ mol/L below). We have zero-padded our data in the time domain, to avoid periodicity effects. The expected arrivals are a source converted EM field, a direct shear wave-related coseismic field around $t = 0.1896$ s, a reflected shear-wave coseismic field around $t = 0.76$ s, and a shear wave-related interface response field, arriving at one-way seismic time from the source level to the interface, $t = 0.47$ s.

The results are presented in Figures 5.11 and 5.12. We can observe a perfect match for all causal events (except the source-converted EM field) in both phase and amplitude. To obtain a correct match in absolute amplitudes, between the reference response in blue and the interferometrically retrieved result in red-dashed, we have again multiplied the reference response with a single scaling factor of $6.2 \cdot 10^3$. We have determined this scaling factor again by dividing the amplitude of the retrieved direct shear wave-related causal coseismic field with the amplitude of the reference response for that event, around $t = 0.185$ s. We can observe that this single scaling factor is sufficient to let the amplitudes of all causal events (except for the source-converted EM field) match perfectly. In other words, it only requires a constant, time-independent scaling factor. We can observe a spurious event in the acausal times, at the location of the acausal interface response field. In Figure 5.12a, we observe that all causal events (except for the source-converted EM field) can be correctly retrieved without visible amplitude losses, using seismic boundary sources only. Also the polarity reversed direct coseismic acausal field is generated solely by seismic boundary sources. Figure 5.12b emphasizes that the EM sources do not contribute to the retrieval of these events. The seismic sources contribute to half of the amplitude of the acausal spurious event (Figure 5.12a). The EM sources contribute to the other half of the amplitude of this acausal spurious event, as well as to the large amplitude of the source-converted retrieved field (Figure

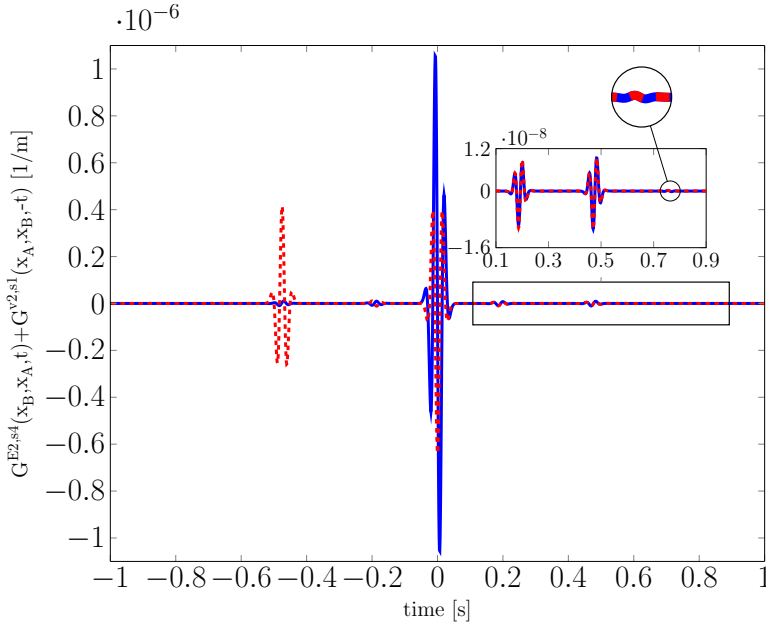


Figure 5.11: Interferometric retrieval of the 2D SH-TE $G^{E2,s4}(\mathbf{x}_B, \mathbf{x}_A, t) + G^{v2,s1}(\mathbf{x}_A, \mathbf{x}_B, -t)$ source-receiver Green's function combination in a medium with a single interface at 800 m, using all boundary sources, for a line source acquisition geometry in a homogeneous medium. The data being cross-correlated are modeled with our seismo-EM layer-code. Blue: reference, red-dashed: retrieved.

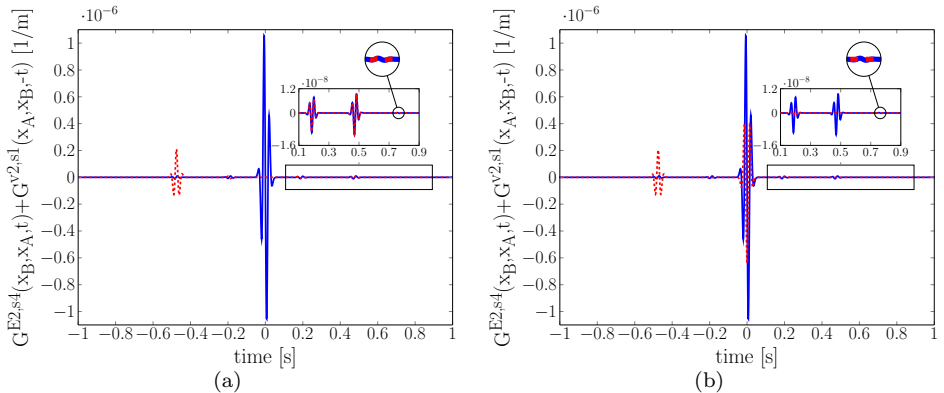


Figure 5.12: Interferometric retrieval of the 2D SH-TE $G^{E2,s4}(\mathbf{x}_B, \mathbf{x}_A, t) + G^{v2,s1}(\mathbf{x}_A, \mathbf{x}_B, -t)$ source-receiver Green's function combination in a medium with a single interface at 800 m, for a line source acquisition geometry. The data that is being cross-correlated is modeled with our seismo-EM layer-code. Blue: reference, red-dashed: retrieved. **(a)** Retrieved Green's function using seismic boundary sources only. **(b)** Retrieved Green's function using EM boundary sources only.

5.12b). The observations are again very similar to the observations made for the homogeneous model. We can conclude that we can correctly retrieve all 2D SH-

TE causal seismic-related direct and reflected coseismic fields, as well as interface response fields, by cross-correlation interferometry, using seismic boundary sources only. For the retrieval of the acausal responses, as well as the source-converted EM field, we require volume sources that account for the losses in the medium.

5.5 Discussion

We have carried out correlation-based interferometric experiments for the 2D SH-TE propagation mode. Experiments for the 2D P-SV-TM propagation mode, as well as for the full 3D system where both modes are combined, will most likely lead to similar conclusions. The observed differences in absolute amplitudes are probably related to the integration constants of the Fourier transform. Besides interferometry by cross-correlation, we can apply interferometry by multi-dimensional deconvolution (MDD), using one-way decomposed fields (Wapenaar *et al.*, 2011; Van der Neut *et al.*, 2011). The multi-component approach to decomposition requires recordings of different field quantities (e.g. White (1965)). The seismo-EM scenario is described by many different field quantities. It is practically unfavorable, or maybe even impossible, that recordings of a wide-variety of these field quantities are required to decompose seismo-EM field data into one-way fields. Therefore, in Section 6.1, we will present an effective way of decomposing seismo-EM fields using recordings at multiple depth levels, thereby reducing the amount of field quantities necessary for the decomposition. The decomposed fields can then be used for e.g. interferometry by MDD.

5.6 Conclusions

We have presented an effective way of deriving explicit homogeneous space Green's function expressions for the 2D SH-TE propagation mode, using power-flux normalized eigenvectors. The theory for interferometric retrieval of 2D SH-TE seismo-EM Green's functions was also presented. Using both a circular source configuration and a line source configuration, we have shown that we can correctly retrieve the dynamic seismo-EM 2D SH-TE response in a homogeneous medium, using seismic boundary sources only. This was demonstrated for two source-receiver combinations: an electric field and a magnetic field due to a seismic source, using explicit homogeneous space Green's function solutions. The volume source contributions account for the losses in the acausal part of the retrieved response as well as the instantaneous source-converted EM field. Using seismo-EM layer-code data, we have shown that we can also correctly retrieve the direct shear wave-related causal coseismic field in a homogeneous medium, in both phase and amplitude. To obtain a perfect match in absolute amplitudes, a single linear scaling factor was required. Finally, the interferometric experiments in a model containing a single interface at 800 m depth prove that we can correctly retrieve all 2D SH-TE causal seismic-related direct and reflected coseismic fields, as well as interface response fields, by cross-correlation interferometry, using seismic boundary sources only.

Chapter 6

Methods and applications of seismo-electromagnetic phenomena

6.1 Unified Multi-Depth-Level field decompositionⁱ

6.1.1 Abstract

Wavefield decomposition forms an important ingredient of various geophysical methods. An example of wavefield decomposition is the decomposition into up- and down-going wavefields and simultaneous decomposition into different wave-/field-types. The multi-component field decomposition scheme makes use of the recordings of different field quantities (such as particle velocity and pressure). In practice, different recordings can be obscured by different sensor characteristics, requiring calibration with an unknown calibration factor. Not all field quantities required for multi-component field decomposition might be available, or they can suffer from different noise levels. The multi-depth-level decomposition approach makes use of field quantities recorded at multiple depth levels, e.g. two horizontal boreholes closely separated from each other, a combination of a single receiver array combined with free-surface boundary conditions or acquisition geometries with a high-density of vertical boreholes. We theoretically describe the multi-depth-level decomposition approach in a unified form, showing that it can be applied to different kinds of fields in dissipative, inhomogeneous, anisotropic media: e.g. acoustic, electromagnetic, elastodynamic, poroelastic and seismo-electromagnetic fields. We express the one-way fields at one depth level in terms of the observed fields at multiple depth levels, using extrapolation operators that are dependent on the medium parameters between the two depth levels. Lateral invariance at the depth level of decomposition allows us to carry out the multi-depth-level decomposition in the horizontal wavenumber-frequency domain. We illustrate the multi-depth-level decomposition scheme using two synthetic elastodynamic examples. The first example uses particle velocity recordings at two

ⁱThis section has been published as a journal paper in *Geophysical Prospecting* doi:10.1111/1365-2478.12290 (Grobbe *et al.*, 2016b). Note that minor changes have been introduced to make the text consistent with the other chapters of this thesis.

depth levels, the second example combines recordings at one depth level with the Dirichlet free-surface boundary condition of zero-traction. Comparison with multi-component decomposed fields shows a perfect match in both amplitude and phase for both cases. The multi-depth-level decomposition scheme is fully customizable to the desired acquisition geometry. The decomposition problem is in principle an inverse problem. Notches may occur at certain frequencies, causing the multi-depth-level composition matrix to become uninvertible, requiring additional notch filters. We can add multi-depth-level free-surface boundary conditions as extra equations to the multi-component composition matrix, thereby overdetermining this inverse problem. The combined multi-component-multi-depth-level decomposition on a land data set clearly shows improvements in the decomposition results, compared to the performance of the multi-component decomposition scheme.

6.1.2 Introduction

Separation of recorded fields into downgoing and upgoing constituents is a technique that is used in many geophysical methods. Decomposed fields form the basis for various surface-related multiple elimination and deghosting procedures (e.g. [Frijlink *et al.* \(2011\)](#), [Majdanski *et al.* \(2011\)](#)) and for depth imaging using primary and multiple reflections (e.g. [Muijs *et al.* \(2007\)](#)). Novel methodologies that make use of horizontal downhole sensors, such as the virtual source method (e.g. [Bakulin & Calvert \(2006\)](#), [Mehta *et al.* \(2007b\)](#), [Alexandrov *et al.* \(2012\)](#)) and multidimensional deconvolution ([Wapenaar *et al.*, 2011](#)), rely on decomposing the seismic field at depth.

The principle of decomposition can be applied to all kinds of fields. However, applying field decomposition to a real data set is often quite challenging. The multi-component (MC) field decomposition scheme makes use of differently recorded field components, for example both pressure (p) and vertical component particle velocity (v_3) data for a purely acoustic case (e.g. [White \(1965\)](#), [Day *et al.* \(2013\)](#)).

In practice, recordings can be obscured by different sensor characteristics, requiring calibration with an unknown calibration factor e.g. [Schalkwijk *et al.* \(2003\)](#), [Day *et al.* \(2013\)](#). A way to find the calibration factor for land data with buried receivers is described by [Alexandrov *et al.* \(2014\)](#). They make use of auto- and cross-correlations between the geophone and hydrophone data (with muted direct arrivals) and find the calibration factor by minimizing the auto-correlation energy in a time window placed around an estimated two-way travel time. In addition to the problem of an unknown calibration factor, the noise levels might be different for different sensor types, resulting in different data quality for different fields ([Burnstad *et al.*, 2012](#)). This can lead to unsatisfactory decomposed data. Furthermore, not all field quantities required for MC field decomposition might be available. Especially, when dealing with more complex field phenomena (e.g. elastodynamic or seismo-electromagnetic fields), the MC field decomposition requires measuring many different field quantities. Let us focus for example on the elastodynamic fields. Theory tells us that for decomposing non-normal incidence elastodynamic fields into upgoing and downgoing compressional waves (P-waves) and shear waves (S-waves),

it is required to record, at a certain desired decomposition receiver level, all three components of the particle velocity fields and all three components of the traction tensor (Wapenaar *et al.*, 1990). Depending on the setting and respective boundary conditions, certain components might vanish. For example, considering a typical land acquisition geometry with receivers placed at the Earth's surface, it is well known that the traction tensor is zero due to the Dirichlet boundary condition. As a result, MC decomposition can be carried out with 3-component geophones only (e.g. Dankbaar (1985), Nakata *et al.* (2014)). At the seafloor (for example in marine Ocean-Bottom-Cable or Ocean-Bottom-Node acquisition), only the shear tractions vanish, such that 4-component sensors are required (e.g. Schalkwijk *et al.* (2003), Amundsen & Reitan (1995)). When considering an acquisitional setting with receivers placed in a horizontal or vertical borehole in the subsurface, all traction and particle velocity components are non-zero. For this case, to carry out successful elastodynamic MC field decomposition, registration of all six components is required. However, shear tractions are in general not recorded, leading to an underdetermined problem (Van der Neut *et al.*, 2010).

In recent years, an acquisition design appears to emerge in the industry that makes use of horizontal downhole sensor arrays (e.g. Bakulin *et al.* (2012b), Bakulin *et al.* (2012a) Berron *et al.* (2012), Cotton & Forgues (2012)). Inspired by marine acquisition designs that utilize recordings at multiple depth levels for successful field decomposition (e.g. Moldoveanu *et al.* (2007), Van Borselen *et al.* (2013)), we develop a multi-depth-level (MDL) field decomposition scheme for land acquisition. This MDL approach uses configurations with field quantity information on multiple depth levels, for example two horizontal boreholes that are closely separated from each other. Alternatively, a combination of a single receiver array just below a free surface combined with the natural (Dirichlet) free-surface boundary conditions could be considered as well.

The MDL decomposition scheme might provide solutions to practical issues of the MC decomposition scheme, since the MDL decomposition scheme requires only specific field quantities to be recorded, and fields with different receiver signatures or noise levels can be treated separately. In modern seismic acquisition, it can be highly relevant to have a configuration of two horizontal boreholes that are closely separated from each other. Effectively, a similar acquisition geometry, with recordings at multiple depth levels, can be obtained by having a high density of vertical boreholes in a certain area (e.g. Bakulin *et al.* (2012b), Bakulin *et al.* (2012a)). In the fields of microseismic monitoring and passive interferometry, downhole sensors are often being deployed to reduce the noise level (e.g. Maxwell *et al.* (2010), Almagro Vidal *et al.* (2011) and Xu *et al.* (2012)). Applying the MDL decomposition scheme using a single horizontal sensor array in combination with the free-surface Dirichlet boundary condition, might be useful for these scenarios.

Since the principle of decomposition is not limited to acoustic fields only, we will present a unified MDL decomposition scheme that can be applied to all kinds of fields. In the appendices, we explicitly show how to apply the MDL theory to acoustic, elastodynamic, poroelastic, electromagnetic and seismo-electromagnetic phenomena. Special attention is paid to possible issues concerning the measurability

of certain fields in 2D borehole configurations.

We will illustrate the MDL decomposition first with two synthetic examples for a flux-normalized elastodynamic case. However, the MDL decomposition problem cannot always be solved. Depending on the acquisition design and the wave velocities, the problem can be ill-posed at certain (notch) frequencies. In practice, these problems can be circumvented by designing appropriate notch filters (see e.g. Appendix A for the acoustic case). An alternative route is to integrate MC and MDL decomposition, leading to a joint inverse problem that can be solved in the least-squares sense, thereby combining the best of both worlds. We refer to this approach as MC-MDL decomposition. We demonstrate with a field data example that MC-MDL decomposition can lead to better decomposition results than pure MC decomposition, since additional data are utilized.

6.1.3 Unified theory of multi-depth-level field decomposition

Our starting point is the following matrix-vector representation of the two-way wave equation in the space-frequency domain (denoted by the hat), for a right-handed Cartesian coordinate system where the positive x_3 -direction is pointing downwards (depth),

$$\frac{\partial \hat{\mathbf{q}}(\mathbf{x}, \omega)}{\partial x_3} = \hat{\mathbf{A}}(\mathbf{x}, \omega) \hat{\mathbf{q}}(\mathbf{x}, \omega). \quad (6.1)$$

Equation (6.1) expresses the vertical variations of the field quantities in $\hat{\mathbf{q}}(\mathbf{x}, \omega)$, in terms of the medium parameters and the horizontal partial differentiation operators in matrix $\hat{\mathbf{A}}(\mathbf{x}, \omega)$ acting on these field quantities (e.g. Woodhouse (1974), Kennett (1983), Ursin (1983), Wapenaar & Grimbergen (1996)). The field quantities in $\hat{\mathbf{q}}$ are continuous across horizontal interfaces. Considering the fact that in the Earth the major variations occur in the depth direction, it makes sense to take the vertical axis as the direction of preference and separate the vertical variations of the field from the horizontal variations of the same field. However, the coordinate system can also be rotated and alternative expressions can be derived in for example curvilinear coordinates (Frijlink & Wapenaar, 2010). In equation (6.1), \mathbf{x} is the space-coordinate vector (x_1, x_2, x_3) and ω represents radial frequency (we will omit these terms now for notational convenience). Throughout this section, boldface symbols indicate vector or tensor quantities. We use $\hat{f}(x_i, \omega) = \int_{-\infty}^{\infty} f(x_i, t) e^{-j\omega t} dt$ as the definition for the forward temporal Fourier transform. Throughout this section we consider positive ω only.

The general two-way wave equation holds for different kinds of fields in dissipative, inhomogeneous, anisotropic media, e.g. acoustic fields, electromagnetic wave and/or diffusive fields, elastodynamic fields, poroelastic fields and seismo-electromagnetic fields (Wapenaar *et al.*, 2008b). We can carry out the MDL decomposition in the space-frequency domain, making use of pseudo-differential operators as illustrated for an acoustic case in e.g. Grimbergen *et al.* (1998). However, already for the elastodynamic system this process is both mathematically and numerically quite tedious. In this section, we will assume that the medium is laterally invariant at the depth level of decomposition. This assumption allows us to carry out

the decomposition in the horizontal wavenumber-frequency domain (denoted by the tilde sign). We use the following definition for the forward spatial Fourier transform: $\tilde{f}(k_1, k_2, x_3, \omega) = \int_{-\infty}^{\infty} \int_{-\infty}^{\infty} \hat{f}(x_i, \omega) e^{jk_1 x_1} e^{jk_2 x_2} dx_1 dx_2$. The following general relation then holds between the recorded two-way fields and the decomposed one-way fields

$$\begin{pmatrix} \tilde{\mathbf{q}}_1 \\ \tilde{\mathbf{q}}_2 \end{pmatrix} = \begin{pmatrix} \tilde{\mathbf{L}}_1^+ & \tilde{\mathbf{L}}_1^- \\ \tilde{\mathbf{L}}_2^+ & \tilde{\mathbf{L}}_2^- \end{pmatrix} \begin{pmatrix} \tilde{\mathbf{p}}^+ \\ \tilde{\mathbf{p}}^- \end{pmatrix}, \quad (6.2)$$

where the + sign indicates downgoing fields (in the positive x_3 -direction) and the - sign indicates upgoing fields. For wavefields, $\tilde{\mathbf{p}}^+$ represents the one-way, decomposed downgoing field and $\tilde{\mathbf{p}}^-$ the one-way, decomposed upgoing field at a certain level of decomposition. For diffusive fields, $\tilde{\mathbf{p}}^+$ is the field that decays in the positive x_3 -direction and $\tilde{\mathbf{p}}^-$ is the field that decays in the negative x_3 -direction. Furthermore, $\tilde{\mathbf{L}}_1^\pm$ and $\tilde{\mathbf{L}}_2^\pm$ represent submatrices of the composition matrix $\tilde{\mathbf{L}}$ that depend on the horizontal wavenumber and the medium properties at the receiver level (e.g. Ursin (1983), Wapenaar *et al.* (2008b)). Decomposed fields are not uniquely defined. The fields can be normalized with respect to different quantities. Depending on our wishes, we can retrieve the up- and downgoing constituents of a particular field component (e.g. pressure or particle velocity normalization). Most of the marine wavefield separation/deghosting schemes make use of either pressure or vertical component particle velocity normalization (e.g. Beasley *et al.* (2013b), Day *et al.* (2013)). However, in principle any normalization of the composition matrix will work. Throughout this section, we will consider a normalization based on power, referred to as power flux-normalized composition matrices. One of the advantages of using power flux-normalization is that favourable reciprocity relations hold for the flux-normalized one-way fields (Frasier (1970), Wapenaar (1998)). In equation (6.2), $\tilde{\mathbf{q}}_1$ represents a subvector of the two-way field quantity vector $\tilde{\mathbf{q}}$, being composed from one-way fields by applying the $\tilde{\mathbf{L}}_1^\pm$ submatrices to the one-way fields $\tilde{\mathbf{p}}^\pm$. Similarly, $\tilde{\mathbf{q}}_2$ is the subvector being composed from one-way fields by applying the $\tilde{\mathbf{L}}_2^\pm$ submatrices to the one-way fields $\tilde{\mathbf{p}}^\pm$. Note that for both $\tilde{\mathbf{L}}$ and $\tilde{\mathbf{q}}$ the subscripts 1 and 2 do not represent spatial directions.

In the multi-component (MC) field decomposition schemes, the downgoing and upgoing one-way fields can be obtained by left-multiplying the two-way field vector with the inverse of the composition matrix,

$$\begin{pmatrix} \tilde{\mathbf{p}}^+ \\ \tilde{\mathbf{p}}^- \end{pmatrix} = \begin{pmatrix} \tilde{\mathbf{L}}_1^+ & \tilde{\mathbf{L}}_1^- \\ \tilde{\mathbf{L}}_2^+ & \tilde{\mathbf{L}}_2^- \end{pmatrix}^{-1} \begin{pmatrix} \tilde{\mathbf{q}}_1 \\ \tilde{\mathbf{q}}_2 \end{pmatrix}. \quad (6.3)$$

Here, additional regularization can be applied or, alternatively, equation (6.3) can be solved for by a sparsity promoting algorithm (Van der Neut & Herrmann, 2012). When dealing with an power flux-normalized composition matrix, we can express the inverse of the composition matrix in terms of the transposes of the composition submatrices as follows

$$\tilde{\mathbf{L}}^{-1}(\mathbf{k}_H) = \begin{pmatrix} -\tilde{\mathbf{L}}_2^-(-\mathbf{k}_H)^t & \tilde{\mathbf{L}}_1^-(-\mathbf{k}_H)^t \\ \tilde{\mathbf{L}}_2^+(-\mathbf{k}_H)^t & -\tilde{\mathbf{L}}_1^+(-\mathbf{k}_H)^t \end{pmatrix}. \quad (6.4)$$

Here, $\mathbf{k}_H = (k_1, k_2)$ is the horizontal wavenumber vector. For notational convenience, the x_3 and ω arguments are omitted here. Equation (6.4) generally holds, i.e. for both anisotropic and isotropic media. In case of an isotropic medium, we can organize the field quantities in $\tilde{\mathbf{q}}$ in such a way that we obtain an anti-blockdiagonal symmetry in the system matrix $\tilde{\mathbf{A}}$. In this case, the following properties hold for the composition submatrices $\tilde{\mathbf{L}}_1^- = \tilde{\mathbf{L}}_1^+$ and $\tilde{\mathbf{L}}_2^- = -\tilde{\mathbf{L}}_2^+$. As can be observed in equation (6.3), in order to be able to perform the up/down decomposition correctly, all two-way field components of $\tilde{\mathbf{q}}$ must have been recorded.

In the multi-depth-level (MDL) decomposition scheme, we express the one-way fields at one level in terms of the observed fields at multiple levels. In this way, we require only a certain selection of field quantities to be measured on multiple depth levels for carrying out successful up/down decomposition. With closely we here mean a distance over which it is reasonable to assume a homogeneous domain between the two depth levels, or where smooth velocity variations can occur and the propagators need to be correctly estimated from the data. It is important that no reflectors are present between the two depth levels. Let us first illustrate the principle of MDL decomposition in terms of the governing matrix-vector equations. We start by defining equation (6.2) in terms of multiple depth levels. In this section, we will develop MDL decomposition for the minimum requirement of two different depth levels, $x_{3,A}$ and $x_{3,B}$, where $x_{3,A} < x_{3,B}$. However, when information at more depth levels is available, this can help stabilizing the decomposition procedure (Van der Neut *et al.*, 2013). We start expressing the decomposed downgoing and upgoing power flux-normalized fields at one depth level in terms of the observed fields at multiple levels. We do so by extrapolating one-way fields from one depth level to another,

$$\tilde{\mathbf{p}}_B^+ = \tilde{\mathbf{W}}^+(x_{3,B}, x_{3,A})\tilde{\mathbf{p}}_A^+ \quad (6.5)$$

$$\tilde{\mathbf{p}}_B^- = \tilde{\mathbf{F}}^-(x_{3,B}, x_{3,A})\tilde{\mathbf{p}}_A^- \quad (6.6)$$

When using these extrapolation operators, it is implicitly assumed that the medium between the two depth levels is source-free and homogeneous. For all kinds of fields, the inverse extrapolation operator $\tilde{\mathbf{F}}^-(x_{3,B}, x_{3,A})$ in equation (6.6) is closely related to the forward propagator $\tilde{\mathbf{W}}^+(x_{3,B}, x_{3,A})$ as:

$$\tilde{\mathbf{F}}^-(x_{3,B}, x_{3,A}) = (\tilde{\mathbf{W}}^+(x_{3,B}, x_{3,A}))^{-1}. \quad (6.7)$$

When we are dealing with purely propagating waves in a lossless medium, the following relation holds

$$\tilde{\mathbf{F}}^-(x_{3,B}, x_{3,A}) = (\tilde{\mathbf{W}}^+(x_{3,B}, x_{3,A}))^*. \quad (6.8)$$

Here, the asterisk (*) denotes complex conjugation. The forward extrapolation operator $\tilde{\mathbf{W}}^+(x_{3,B}, x_{3,A})$, extrapolates the downgoing (+) fields downwards, from depth level $x_{3,A}$ to depth level $x_{3,B}$. The inverse extrapolation operator $\tilde{\mathbf{F}}^-(x_{3,B}, x_{3,A})$, extrapolates the upgoing fields (-) downwards from depth level $x_{3,A}$ to depth level $x_{3,B}$. The downgoing and upgoing forward extrapolation operators $\tilde{\mathbf{W}}^+(x_{3,B}, x_{3,A})$

and $\tilde{\mathbf{W}}^-(x_{3;A}, x_{3;B})$ are defined as

$$\tilde{\mathbf{W}}^+(x_{3;B}, x_{3;A}) = \tilde{\mathbf{W}}^-(x_{3;A}, x_{3;B}) = \exp(-j\tilde{\mathbf{H}}|x_{3;B} - x_{3;A}|), \quad (6.9)$$

where $-j\tilde{\mathbf{H}}$ represents an n -by- n diagonal matrix containing the eigenvalues for each of the n -wavetypes present in the system under consideration (for example $n = 3$ for the elastodynamic case, where the P -wave and S -wave are the wavetypes under consideration). Note that the above equation (6.9) is a symbolic notation (due to the use of a matrix in the argument of the exponent). Effectively, the exponent of each of the individual elements in diagonal matrix $\tilde{\mathbf{H}}$ is taken. Since we are dealing with laterally invariant media, $\tilde{\mathbf{H}}$ is a purely diagonal matrix with elements that correspond to the vertical wavenumbers $k_{3;w}$ and that can be defined for each wavetype w as

$$k_{3;w} = \sqrt{\frac{\omega^2}{\hat{c}_w^2} - \kappa^2}. \quad (6.10)$$

Here, the radial wavenumber is defined as $\kappa = \sqrt{k_1^2 + k_2^2}$, ω denotes the radial frequency and \hat{c}_w represents the complex, frequency-dependent velocity for each field type (Wapenaar & Berkhout, 1989) (i.e. in its general form it includes attenuation). Note that it is crucial to define the sign of the field extrapolation operators in such a way that evanescent and diffusive fields decay. The sign of the square root in equation (6.10) should be therefore chosen accordingly.

Let us look for example at electromagnetic fields. Similar to Amundsen *et al.* (2006), we can express the complex electromagnetic velocity as

$$\hat{c} = \frac{1}{\sqrt{\mu\bar{\varepsilon}}}, \quad (6.11)$$

where

$$\bar{\varepsilon} = \varepsilon + \frac{\sigma}{j\omega}, \quad (6.12)$$

is the complex electric permittivity, consisting of the electric permittivity ε , the electric conductivity σ and the magnetic permeability μ , which is often taken equal to the magnetic permeability in free space, $\mu_0 = 4\pi \cdot 10^{-7}$. Examining equations (6.11) and (6.12) more closely, we can distinguish three different scenarios depending on the medium parameters and the frequencies under consideration. When the term $\frac{\sigma}{j\omega} \gg \varepsilon$, which is effectively the case for very low frequencies (and/or high conductivity values), we can neglect the first (electric permittivity) term and the expression for the complex velocity becomes purely imaginary. We refer to this case as purely diffusive fields (Figure 6.1(a)). We can observe that the k_3 -values in this case start at a -45 degree angle in the complex plane (opposite real and imaginary parts) for $\kappa = 0$ and that both the real and imaginary parts of k_3 decrease with increasing κ -values. Going towards higher frequencies (and/or lower conductivity values), the first term becomes more important and we are dealing with a ‘mixed’

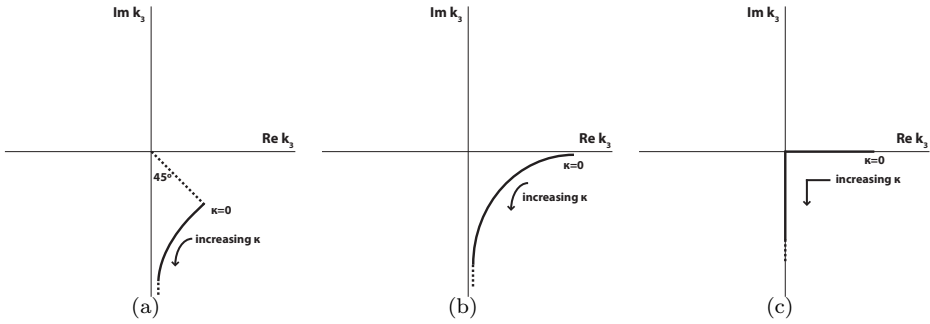


Figure 6.1: Real and imaginary parts of k_3 in the complex plane. (a) Purely diffusive fields. Only the sign of the imaginary part of k_3 needs to be constrained. (b) Wave propagation with losses. Only the sign of the imaginary part of k_3 needs to be constrained. (c) Wave propagation without losses. In this case the sign of both the real and imaginary parts of k_3 need to be constrained.

scenario; this scenario occurs for wave propagation in a medium with losses (Figure 6.1(b)). In this case the k_3 -value for $\kappa = 0$ is almost purely real, and moves with increasing values for κ via combinations of non-zero real and imaginary parts of k_3 towards an almost purely imaginary k_3 -value. Finally, when we reach a frequency bandwidth that results in $\frac{\sigma}{j\omega} \ll \varepsilon$, we can neglect the second term and the expression for the complex velocity becomes purely real in the limit. This scenario occurs for wave propagation in lossless media (Figure 6.1(c)). Here, k_3 is in the limiting case purely real for $\kappa = 0$ and remains purely real with increasing values for κ until $\kappa^2 = \frac{\omega^2}{\hat{c}_w^2}$, which can be described as

$$k_{3;w} = \sqrt{\frac{\omega^2}{\hat{c}_w^2} - \kappa^2}, \quad \text{for } \kappa^2 \leq \frac{\omega^2}{\hat{c}_w^2}. \quad (6.13)$$

When κ then further increases,

$$k_{3;w} = -j\sqrt{\kappa^2 - \frac{\omega^2}{\hat{c}_w^2}}, \quad \text{for } \kappa^2 > \frac{\omega^2}{\hat{c}_w^2}, \quad (6.14)$$

holds, resulting in purely imaginary k_3 -values in the limiting case. So in this scenario we can basically distinguish these two separate cases (for our definition of the Fourier transform).

What can be clearly observed in Figure 6.1 is that for the first and second case (purely diffusive fields and wave propagation with losses) it is sufficient to constrain the sign of the square root such that the imaginary part of $k_3 < 0$. For the third case, since we have obtained equations (6.13) and (6.14) by taking $\lim_{\sigma \downarrow 0} k_3$ actually still has a very small imaginary part for propagating waves. Hence, by constraining the sign of the imaginary part (equation (6.14)), the sign of the real part (equation (6.13)) is still automatically determined as well.

If σ is exactly equal to zero (and ω exactly real-valued), an ambiguous situation is created for the third case of wave propagation in lossless media. To overcome this ambiguity, we then need to constrain the signs of both the real and imaginary parts of k_3 . Note that in this case equation (6.13) results in a purely real-valued k_3 , and that equation (6.14) yields a purely imaginary k_3 . Since we want the real part of the arguments of the exponents in equation (6.9) to be negative (in order to avoid that the exponents blow up), we take the negative sign of the square root in equation (6.14). We choose the correct sign for the real part (equation (6.13)) based on the fact that we desire that the phase decreases with increasing distance, whereas the amplitude stays constant. One can physically link these choices to the fact that for propagating waves in lossless media, the amplitude remains constant (no losses), whereas the phase is decreasing with increasing distance. On the contrary, for evanescent fields in lossless media, the phase remains constant whereas the amplitude is decreasing with increasing distance. Please note that the first case of purely diffusive fields as described above, is in principle also a limiting case, where the $\lim_{\varepsilon \downarrow 0}$ is taken, resulting in an almost purely imaginary complex velocity. However, for this case, regardless of whether we consider the limiting case or whether we take ε exactly equal to zero, constraining the sign of the imaginary part is always sufficient to constrain the problem, as can be observed in figure 6.1(a).

Imagine now a field situation where we have obtained only $\tilde{\mathbf{q}}_2$ field quantity recordings, at different depth levels. According to equation (6.2) we can express the two-way field quantities of $\tilde{\mathbf{q}}_2$ recorded at depth level $x_{3;A}$ in terms of the one-way up- and downgoing fields as

$$\begin{pmatrix} \tilde{\mathbf{L}}_2^+ & \tilde{\mathbf{L}}_2^- \end{pmatrix} \begin{pmatrix} \tilde{\mathbf{p}}_A^+ \\ \tilde{\mathbf{p}}_A^- \end{pmatrix} = \tilde{\mathbf{q}}_{2;A}, \quad (6.15)$$

and for the recordings at depth level $x_{3;B}$

$$\begin{pmatrix} \tilde{\mathbf{L}}_2^+ & \tilde{\mathbf{L}}_2^- \end{pmatrix} \begin{pmatrix} \tilde{\mathbf{p}}_B^+ \\ \tilde{\mathbf{p}}_B^- \end{pmatrix} = \tilde{\mathbf{q}}_{2;B}. \quad (6.16)$$

Note that the subscripts A and B have been omitted in the composition submatrices, since we have already assumed that the medium is homogeneous between those two depth levels. If recordings at more than two depth levels are available, this procedure can be extended for all possible depth levels. By using equations (6.5) and (6.6), we can express the one-way fields for depth level $x_{3;B}$ also in terms of the one-way fields for level $x_{3;A}$,

$$\begin{pmatrix} \tilde{\mathbf{L}}_2^+ \tilde{\mathbf{W}}^+ & \tilde{\mathbf{L}}_2^- \tilde{\mathbf{F}}^- \end{pmatrix} \begin{pmatrix} \tilde{\mathbf{p}}_A^+ \\ \tilde{\mathbf{p}}_A^- \end{pmatrix} = \tilde{\mathbf{q}}_{2;B}. \quad (6.17)$$

Combining equations (6.15) and (6.17) in terms of the one-way fields at depth level $x_{3;A}$, we obtain

$$\begin{pmatrix} \tilde{\mathbf{L}}_2^+ & \tilde{\mathbf{L}}_2^- \\ \tilde{\mathbf{L}}_2^+ \tilde{\mathbf{W}}^+ & \tilde{\mathbf{L}}_2^- \tilde{\mathbf{F}}^- \end{pmatrix} \begin{pmatrix} \tilde{\mathbf{p}}_A^+ \\ \tilde{\mathbf{p}}_A^- \end{pmatrix} = \begin{pmatrix} \tilde{\mathbf{q}}_{2;A} \\ \tilde{\mathbf{q}}_{2;B} \end{pmatrix}, \quad (6.18)$$

or more general

$$\tilde{\mathbf{S}} \begin{pmatrix} \tilde{\mathbf{p}}_A^+ \\ \tilde{\mathbf{p}}_A^- \end{pmatrix} = \begin{pmatrix} \tilde{\mathbf{q}}_{2;A} \\ \tilde{\mathbf{q}}_{2;B} \end{pmatrix}. \quad (6.19)$$

Here, $\tilde{\mathbf{S}}$ represents the MDL composition matrix. When we assume that the medium properties between the levels are known (for example from borehole data), the extrapolators can be computed. Alternatively, one might be interested to estimate the extrapolation operators directly from the data. One way of doing this is via direct-field interferometry. For a discussion on interferometric propagator estimation, the reader is referred to [Van der Neut *et al.* \(2013\)](#). We have now obtained an expression relating the one-way fields at depth level $x_{3;A}$ via the MDL composition matrix $\tilde{\mathbf{S}}$ to the recorded two-way field quantities of the subvector $\tilde{\mathbf{q}}_2$ at both depth levels $x_{3;A}$ and $x_{3;B}$. By multiplying both the left- and right-hand sides of equation (6.19) with the inverse of the MDL composition matrix $\tilde{\mathbf{S}}^{-1}$, the one-way up- and downgoing flux-normalized fields (for each wavetype (e.g. P-waves and S-waves in the elastodynamic case)) at depth level $x_{3;A}$ can be obtained

$$\begin{aligned} \begin{pmatrix} \tilde{\mathbf{p}}_A^+ \\ \tilde{\mathbf{p}}_A^- \end{pmatrix} &= \begin{pmatrix} \tilde{\mathbf{L}}_2^+ & \tilde{\mathbf{L}}_2^- \\ \tilde{\mathbf{L}}_2^+ \tilde{\mathbf{W}}^+ & \tilde{\mathbf{L}}_2^- \tilde{\mathbf{F}}^- \end{pmatrix}^{-1} \begin{pmatrix} \tilde{\mathbf{q}}_{2;A} \\ \tilde{\mathbf{q}}_{2;B} \end{pmatrix} \\ &= \tilde{\mathbf{S}}^{-1} \begin{pmatrix} \tilde{\mathbf{q}}_{2;A} \\ \tilde{\mathbf{q}}_{2;B} \end{pmatrix}. \end{aligned} \quad (6.20)$$

In other words, the two-way field system under consideration has now been decomposed (for depth level $x_{3;A}$), using only $\tilde{\mathbf{q}}_2$ field recordings at two depth levels. We can invert the modified composition matrix $\tilde{\mathbf{S}}$ numerically at each frequency and horizontal wavenumber individually. Additional regularization can be applied to solve the inverse problem. Note that in this decomposition procedure we treat the different vertical arrays simultaneously. The benefit of this procedure is that instead of decomposing only for the plane wave, normal incidence (wavenumber $k_1 = 0$) events, we decompose for all the angles of incidence. A drawback of this procedure is that since we treat everything in the horizontal wavenumber-frequency domain, our horizontal spatial sampling must fulfill the Nyquist sampling criterion. Be aware that the inversion of the composition matrix in equation (6.20) might not always be stable, due to the occurrence of notches at certain frequencies. The matrix inversion is unstable, when the determinant of the composition matrix is equal to zero. In other words, for certain frequency-wavenumber combinations and certain velocities and depths, the field extrapolation operators can obtain a value that makes the rows of matrix $\tilde{\mathbf{S}}$ no longer linearly independent ([Van der Neut *et al.*, 2013](#)). Looking at the definitions of the field extrapolation operators (equations (6.9) and (6.10)), it can be seen that the notch frequencies are highly dependent on the vertical distance between the receiver arrays ([Day *et al.*, 2013](#)). The notch problem is further addressed in Appendix A, using the acoustic representation of the field data example of this section. Bear in mind that similar notch problems can occur for all wave and diffusion phenomena captured in this unified MDL scheme.

In addition to the notch problems, alternative instabilities can occur for example at the critical angles in the wavenumber-frequency spectrum. This is because at the critical angle, $k_3 = 0$ and elements of the composition matrix $\tilde{\mathbf{L}}$ can contain divisions by k_3 . The MDL decomposition of equation (6.20) will be illustrated by Synthetic Elastodynamic Example 1.

Depending on the data acquisition geometry under consideration, one might prefer to express the one-way fields at depth level $x_{3;A}$ in terms of the one-way fields at depth level $x_{3;B}$. This can be beneficial for example in passive geometries with the earthquake or microseismic sources below the lowest receiver level $x_{3;B}$. Slightly different to the basic case described above in equations (6.5) and (6.6), we then express the up- and downgoing fields at $x_{3;A}$ in terms of the up- and downgoing fields at $x_{3;B}$ as

$$\tilde{\mathbf{p}}_A^+ = \tilde{\mathbf{F}}^+(x_{3;A}, x_{3;B})\tilde{\mathbf{p}}_B^+, \quad (6.21)$$

$$\tilde{\mathbf{p}}_A^- = \tilde{\mathbf{W}}^-(x_{3;A}, x_{3;B})\tilde{\mathbf{p}}_B^-, \quad (6.22)$$

where

$$\tilde{\mathbf{F}}^+(x_{3;A}, x_{3;B}) = (\tilde{\mathbf{W}}^-(x_{3;A}, x_{3;B}))^{-1}. \quad (6.23)$$

Again, in the case of purely propagating waves,

$$\tilde{\mathbf{F}}^+(x_{3;A}, x_{3;B}) = (\tilde{\mathbf{W}}^-(x_{3;A}, x_{3;B}))^*, \quad (6.24)$$

holds. The MDL decomposition procedure can be further modified according to one's preferences. For example, combinations of the field subvectors $\tilde{\mathbf{q}}_1$ and $\tilde{\mathbf{q}}_2$ and the corresponding submatrices of the composition matrix $\tilde{\mathbf{L}}$, might be useful. For example, when a certain depth level, in our case $x_{3;A}$ since $x_{3;A} < x_{3;B}$, coincides with the free surface of the Earth (or for example the ocean-bottom), the boundary conditions at that level might imply that certain field quantities in either $\tilde{\mathbf{q}}_1$ or $\tilde{\mathbf{q}}_2$ are equal to zero.

Let us consider this specific case, where we move depth level $x_{3;A}$ upwards such that it coincides with the Earth's free surface and where we assume that the (passive) source is located in the subsurface. We now assume that the field quantity subvector $\tilde{\mathbf{q}}_1$ is zero at the free surface due to the Dirichlet boundary condition. Hence, we do not explicitly need physical receivers at depth level $x_{3;A}$. We combine this constraint with the physical recordings of field quantity subvector $\tilde{\mathbf{q}}_2$ at depth level $x_{3;B}$. Analogous to equation (6.20), we can then obtain the one-way up- and downgoing fields at depth level $x_{3;B}$, by solving

$$\begin{aligned} \begin{pmatrix} \tilde{\mathbf{p}}_B^+ \\ \tilde{\mathbf{p}}_B^- \end{pmatrix} &= \begin{pmatrix} \tilde{\mathbf{L}}_1^+ \tilde{\mathbf{F}}^+ & \tilde{\mathbf{L}}_1^- \tilde{\mathbf{W}}^- \\ \tilde{\mathbf{L}}_2^+ & \tilde{\mathbf{L}}_2^- \end{pmatrix}^{-1} \begin{pmatrix} \tilde{\mathbf{q}}_{1;A} = 0 \\ \tilde{\mathbf{q}}_{2;B} \end{pmatrix} \\ &= \tilde{\mathbf{S}}^{-1} \begin{pmatrix} \tilde{\mathbf{q}}_{1;A} = 0 \\ \tilde{\mathbf{q}}_{2;B} \end{pmatrix}. \end{aligned} \quad (6.25)$$

Alternatively, one could derive explicit expressions for $\tilde{\mathbf{p}}_B^+$ and $\tilde{\mathbf{p}}_B^-$ using analytical

expressions for the inverse of the composition matrix, yielding

$$\tilde{\mathbf{p}}_B^+ = \left[\tilde{\mathbf{L}}_2^+ - \tilde{\mathbf{L}}_2^- \left\{ \tilde{\mathbf{L}}_1^- \tilde{\mathbf{W}}^- \right\}^{-1} \tilde{\mathbf{L}}_1^+ \tilde{\mathbf{F}}^+ \right]^{-1} \tilde{\mathbf{q}}_{2;B}, \quad (6.26)$$

$$\tilde{\mathbf{p}}_B^- = \left[\tilde{\mathbf{L}}_2^- - \tilde{\mathbf{L}}_2^+ \left\{ \tilde{\mathbf{L}}_1^+ \tilde{\mathbf{F}}^+ \right\}^{-1} \tilde{\mathbf{L}}_1^- \tilde{\mathbf{W}}^- \right]^{-1} \tilde{\mathbf{q}}_{2;B}. \quad (6.27)$$

The system of the wave/field phenomenon under consideration has now been decomposed (for depth level $x_{3;B}$), using only the field quantity recordings of field subvector $\tilde{\mathbf{q}}_2$ measured at depth level $x_{3;B}$, combined with the fact that the field quantities of the subvector $\tilde{\mathbf{q}}_1$ at level $x_{3;A}$ are zero. Note that if $x_{3;A}=x_{3;B}$, equation (6.25) reduces to the MC decomposition scheme of equation (6.3). The application of equation (6.25) will be illustrated with Synthetic Elastodynamic Example 2. Interesting to mention is the similarity between equation (6.25) and deghosting procedures (e.g. Fokkema & Van den Berg (1993), Frijlink *et al.* (2011)). However, in equation (6.25), the deghosting procedure is expressed more generally, holding for all kinds of fields.

We can summarize the MDL decomposition theory using a general notation, distinguishing between decomposition at the upper depth level and decomposition at the lower depth level (hereby still assuming that $x_{3;A} < x_{3;B}$). For the decomposition at the upper level, we would like to express the one-way fields at level $x_{3;B}$ in terms of the one-way fields at $x_{3;A}$

$$\begin{pmatrix} \tilde{\mathbf{L}}_j^+ & \tilde{\mathbf{L}}_j^- \\ \tilde{\mathbf{L}}_k^+ \tilde{\mathbf{W}}^+ & \tilde{\mathbf{L}}_k^- \tilde{\mathbf{F}}^- \end{pmatrix} \begin{pmatrix} \tilde{\mathbf{p}}_A^+ \\ \tilde{\mathbf{p}}_A^- \end{pmatrix} = \begin{pmatrix} \tilde{\mathbf{q}}_{j;A} \\ \tilde{\mathbf{q}}_{k;B} \end{pmatrix}, \quad (6.28)$$

where j and k can take up the values 1 or 2 and j is not necessarily equal to k . Similarly, for the decomposition at the lower level, we express the one-way fields at level $x_{3;A}$ in terms of the one-way fields at $x_{3;B}$

$$\begin{pmatrix} \tilde{\mathbf{L}}_j^+ \tilde{\mathbf{F}}^+ & \tilde{\mathbf{L}}_j^- \tilde{\mathbf{W}}^- \\ \tilde{\mathbf{L}}_k^+ & \tilde{\mathbf{L}}_k^- \end{pmatrix} \begin{pmatrix} \tilde{\mathbf{p}}_B^+ \\ \tilde{\mathbf{p}}_B^- \end{pmatrix} = \begin{pmatrix} \tilde{\mathbf{q}}_{j;A} \\ \tilde{\mathbf{q}}_{k;B} \end{pmatrix}. \quad (6.29)$$

Equations (6.28) and (6.29) form the basis of the MDL field decomposition scheme. Theoretically, one can even set-up the decomposition problem in a similar way as equations (6.28) and (6.29), but then trying to obtain one-way fields at both depth levels, e.g. $\tilde{\mathbf{p}}_B^+$ and $\tilde{\mathbf{p}}_A^-$.

When looking at equations (6.28) and (6.29), we can observe that in order to successfully carry out MDL up/down field decomposition, we either need field quantity recordings at at least two depth levels $x_{3;A}$ and $x_{3;B}$, or recordings at one depth level $x_{3;B}$ combined with boundary conditions at depth level $x_{3;A}$. One can imagine that instead of measuring the full field quantity subvectors $\tilde{\mathbf{q}}_1$ or $\tilde{\mathbf{q}}_2$ and their corresponding submatrices $\tilde{\mathbf{L}}_{1,2}$, one wishes to select only a few, easily measurable or well-constrained field quantities of $\tilde{\mathbf{q}}_1$ and $\tilde{\mathbf{q}}_2$ to solve the decomposition problem. By selecting the desired rows of the composition submatrices corresponding with the selected field quantities, the MDL decomposition can be carried out. Be aware that

this can only be done if the selected rows that compose the matrix $\tilde{\mathbf{S}}$ have sufficient rank. In other words, the matrix to be inverted should not be rank-deficient. If the matrix is full-rank, the custom character of the adapted composition matrix $\tilde{\mathbf{S}}$ will not cause any additional problems since the decomposition matrix is obtained via numerical inversion. The customly defined combinations of measured or boundary condition-defined field quantities and selected composition submatrix rows are not explicitly defined in the general scheme of equations (6.28) and (6.29). Here, we only want to point out the possibility of these kinds of combinations.

Please remain aware that the equations above are defined in the horizontal wavenumber-frequency domain, implicitly assuming lateral invariance at the depth level of decomposition. A similar scheme can be developed in the space-frequency domain for inhomogeneous media, using pseudo-differential operators (e.g. Fishman *et al.* (1987), Grimbergen *et al.* (1998), Wapenaar *et al.* (2001), Wapenaar *et al.* (2008b)). However, already for the elastodynamic case, the space-frequency derivations become quite a tedious exercise, both analytically and numerically.

Now that we have obtained a unified MDL decomposition scheme, we can apply the scheme to different wave phenomena. The Appendices A-E show in more detail how to apply the scheme when dealing with acoustic, elastodynamic, poroelastic, electromagnetic and seismo-electromagnetic fields. Throughout this section, we will consider geometries where horizontal boreholes are located in the subsurface. The MDL decomposition scheme is then applied to obtain up/down field separation. Besides up/down decomposition, the scheme also decomposes the field quantities into its different wave modes. One can theoretically imagine that when considering surface measurements at several horizontal spatial locations and rotating the geometry of the MDL scheme, one might also apply the MDL decomposition principles to field left/right decomposition.

We will start illustrating the principle of the MDL decomposition scheme further with two synthetic flux-normalized elastodynamic examples. In this case, $\tilde{\mathbf{q}}_1 = -\tilde{\boldsymbol{\tau}}_3$ and $\tilde{\mathbf{q}}_2 = \tilde{\mathbf{v}}$ and the flux-normalized composition matrix $\tilde{\mathbf{L}}$ is chosen according to Wapenaar *et al.* (2008b). Here, $\tilde{\boldsymbol{\tau}}_3$ represents the traction vector acting at a horizontal plane and $\tilde{\mathbf{v}}$ denotes the particle velocity vector. Note that for these two synthetic examples no approximations regarding amplitudes have been made. After the synthetic elastodynamic examples, we will present an acoustic representation of a field land data example where the MC and MDL decomposition schemes are combined.

Before we look in closer detail to the examples, let us make some final, but crucial remarks regarding borehole measurements. First of all, one can imagine that if the receivers are placed in a horizontal borehole, this results in a ‘line’ measurement. Let us for example consider a horizontal borehole in the x_1 -direction. When we then consider propagation/diffusion in a 3D medium, out-of-plane waves/fields are still taken into account, and hence variations of a certain field quantity in the x_2 -direction are still considered (e.g. Bleistein *et al.* (1987), Bleistein (1987)). This is called the 2.5D situation. In contrast, we can consider a purely 2D situation where effectively line-sources in e.g. the x_2 -direction are considered. In this situation, the field quantity components have no variations with respect to the x_2 -direction. The

resulting data are referred to as 2D (e.g. [Bleistein *et al.* \(1987\)](#), [Bleistein \(1987\)](#)). In the 2D scenario, natural mode separation can occur for e.g. elastodynamic (P-SV and SH mode), electromagnetic (TE and TM mode) or seismo-electromagnetic (SH-TE and P-SV-TM mode) phenomena.

In addition, the type of borehole also plays a crucial role. For example, if the borehole has a concrete casing and is filled with a fluid, this has consequences for the receivers and types of fields that can be recorded. For example, theoretically no shear waves will be measurable inside the borehole if it is fluid-filled. Certain field quantities might then be zero at for example depth level $x_{3,B}$, whereas the field quantity is theoretically non-zero and measurable (in absence of the borehole). However, in practice, shear waves are routinely measured in for example VSP and logging using sensors in a fluid-filled borehole (e.g. [Cheng & Toksöz \(1981\)](#)). In this section, we will develop everything from an ideal theoretical point-of-view. Keep in mind that in reality, the situation is far more complex. Fluid-filled boreholes modify the responses as for example formulated by [Peng *et al.* \(2003\)](#). This does not necessarily mean that the MDL decomposition scheme does not work. On the contrary, having for example shear wave measurements available in fluid-filled boreholes might help the MDL decomposition scheme (it does need additional calibration).

In case of electromagnetic fields, metallic borehole casings can cause problems as well. In the following synthetic examples, we assume that the receivers are buried on a horizontal line in the subsurface, but not placed in a fluid-filled borehole. In the field data example presented afterwards, the receivers are similarly placed in the subsurface. We will use an acoustic scheme for decomposing this data set.

6.1.4 Synthetic Elastodynamic Example 1: Configuration with Two Receiver Depth Levels

To illustrate the MDL decomposition approach, we will apply the method to a synthetic elastodynamic example, using equation (6.20). We make use of a 2D elastodynamic finite-difference model ([Thorbecke & Draganov, 2011](#)), where receivers are being placed at two depth levels $x_{3,A} = 1000$ m and $x_{3,B} = 1010$ m, below a strongly reflecting salt body (see [Figure 6.2](#)). We consider the plane spanned by x_1 and x_3 . Hence, the fields in the x_2 -direction in the field vector of [Appendix C](#) decouple. The P-wave and S-wave velocities for the layer in which the receivers are located are 2500 m/s and 1800 m/s, respectively. The density of the layer is 1500 kg/m³. The source is a monopole pressure source with a peak frequency of 20 Hz. We use the more stable, alternative 2D versions of the power flux-normalized composition matrix $\tilde{\mathbf{L}}$, as presented in [Wapenaar *et al.* \(2008b\)](#). [Figure 6.3](#) represents the original shot records as recorded at depth level $x_{3,A}$, with the two-way physical field quantities τ_{13} , τ_{33} , v_1 and v_3 . Due to the complexity of the model, up- and downgoing events are interfering. Furthermore, the presence of the strongly reflecting salt body results in strong differences in amplitudes between down- and upgoing events.

We now carry out both MC and MDL field decomposition, resulting in the decomposed fields of [Figure 6.4](#), where the MC decomposed one-way fields are shown in black and the MDL decomposed fields in red (dashed). There is an excellent match

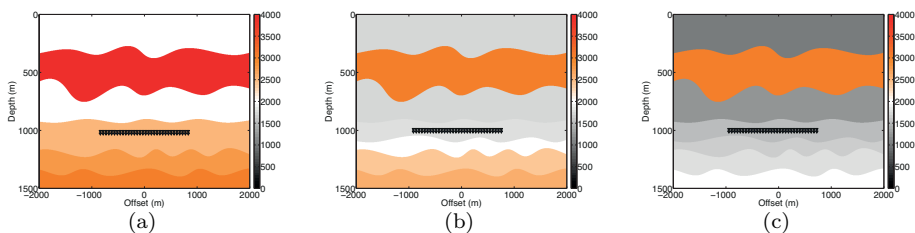


Figure 6.2: Geometry of Synthetic Elastodynamic Example 1. (a) The colors represent P-wave velocities in m/s. (b) The colors represent S-wave velocities in m/s. (c) The colors represent density values in kg/m^3 .

in both amplitude and phase. In other words, the MDL decomposition scheme manages to retrieve the correct one-way fields at $x_{3;A}$ using only particle velocities at $x_{3;A}$ and $x_{3;B}$. There is a difference for the first upgoing P-wave event (Figure 6.4(c)). The MC decomposition scheme shows a (black) event where this event is absent for the MDL decomposition scheme. It turns out that this is leakage from the strong downgoing P-wave energy. This is most likely caused by small numerical errors in the computed pressure fields (in combination with the large relative strength of this downgoing event), which had to be interpolated in time and space to align with the particle velocity fields, because a staggered grid has been used in the finite difference code (Virieux, 1986). The MDL decomposition scheme does not suffer from this problem, since it only uses particle velocity data.

For the MDL decomposition, we have carried out a damped least-squares inversion of the customized composition matrix $\tilde{\mathbf{S}}$, using a Tikhonov regularization with damping factor of $1 \cdot 10^{-4}$ of the maximum amplitude of $\tilde{\mathbf{S}}\tilde{\mathbf{S}}^\dagger$. Here the dagger-sign denotes the complex conjugate transpose.

It is very nice to see the effect of the strongly reflecting salt body. One can observe in the downgoing fields (for both P- and S-waves) three pronounced downgoing events, corresponding to the direct downgoing field and the internal multiples within the salt layer. Also when looking at the two-way input data, one can clearly see that the upgoing fields are obscured due to the presence of the salt body. However, after decomposition, the upgoing fields are clearly distinguishable and similar results are obtained for the MC decomposition and the MDL decomposition methods. In addition, the MC and MDL decomposition schemes are handling the interference between up- and downgoing fields equally well.

Note that for a 2.5D scenario, also $\tilde{\tau}_{23}$ and \tilde{v}_2 should be measured for MC decomposition, and only \tilde{v}_2 should be measured additionally for MDL decomposition. Similar results are then to be expected.

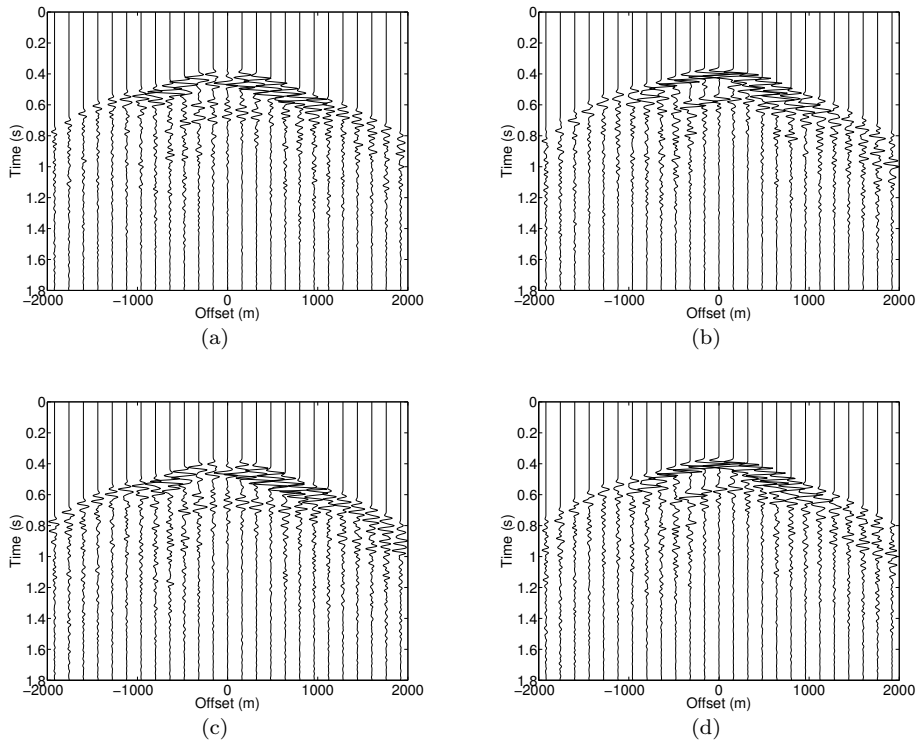


Figure 6.3: Original shot records registered at depth level $x_{3;A} = 1000$ m. (a) Two-way data $-\tau_{13}$ (b) Two-way data $-\tau_{33}$ (c) Two-way data v_1 (d) Two-way data v_3

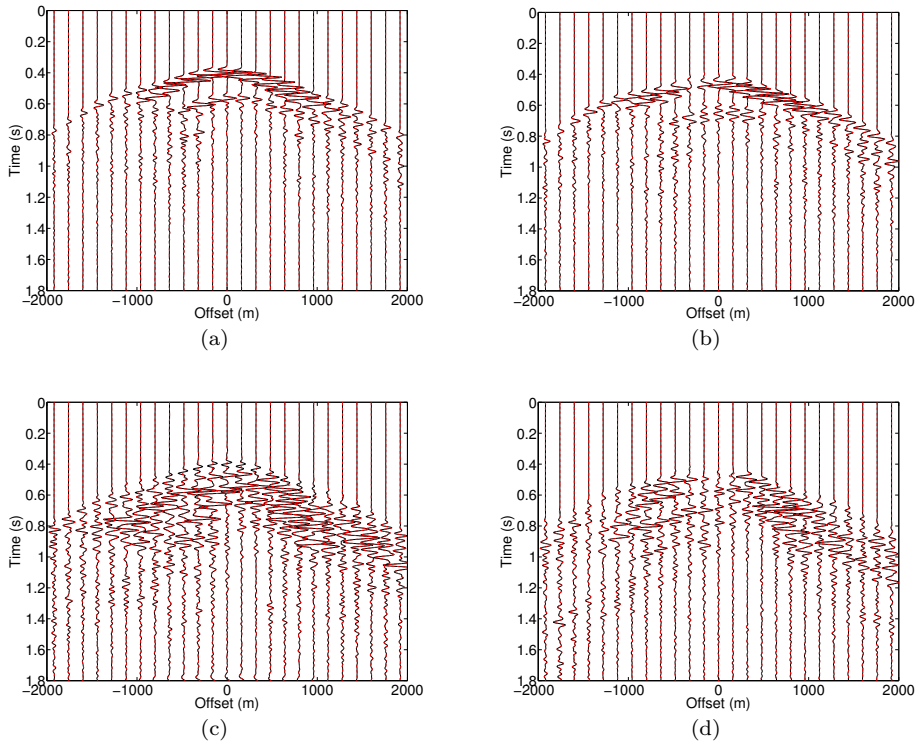


Figure 6.4: Comparison between the MC decomposition results in black and the MDL decomposition results in red (dashed). (a) Downgoing P-waves (b) Downgoing S-waves (c) Upgoing P-waves (d) Upgoing S-waves

6.1.5 Synthetic Elastodynamic Example 2: Configuration with a Single Horizontal Sensor Array below a Free Surface

As mentioned above, the MDL decomposition procedure is fully customizable according to one's preferences. Here we will consider a special case, moving depth level $x_{3;A}$ upwards such that it coincides with the Earth's free surface. Effectively we have an acquisition geometry consisting of a single horizontal sensor array combined with a free-surface constraint. We will use equation (6.25) as the governing equation of the MDL decomposition scheme matching the acquisition geometry under consideration. Again, a 2D finite-difference elastodynamic model will be used, with receivers placed only at $x_{3;B}$, at 5 m depth. We first consider a homogeneous medium. The P-wave velocity of the medium is 2000 m/s, the S-wave velocity 1400 m/s and the density is 1000 kg/m³. A 45 degrees (anti-clockwise) oriented dipole force source with a peak frequency of 20 Hz, buried at 2000 m depth, is considered as the (passive) source. The only upgoing fields to be expected, are one upgoing P-wave and one upgoing SV-wave. At the free surface, P-SV field conversion can occur (Aki & Richards, 1980). Therefore, we expect two downgoing P-wave events (P-P and SV-P) and two downgoing SV-wave events (P-SV and SV-SV).

The originally recorded two-way fields are presented in Figure 6.5. Due to the 45 degrees anti-clockwise diagonally oriented force source, the recorded fields reveal asymmetric amplitudes along the hyperbolas. We again compare the results of the MC decomposition and the MDL decomposition approach in Figure 6.6. The black lines represent the one-way fields at depth level $x_{3;B}$ obtained via MC decomposition. In this case, both stress and particle velocity measurements were required. The MDL decomposition results are displayed in red (dashed). These up/down and wave mode decomposed fields were obtained using only particle velocity recordings at $x_{3;B}$ combined with the free-surface Dirichlet boundary condition of zero traction. One can clearly observe that the MDL approach, using now only particle velocity data at one depth level, again retrieves the correct one-way fields. There is a perfect match in both phase and amplitude. In addition, the decomposition results show indeed only the expected one-way fields, i.e. one upgoing P-wave and one upgoing SV-wave, two downgoing P-wave events and two downgoing SV-wave events. Again, by measuring additionally $\tilde{\tau}_{23}$ and \tilde{v}_2 for MC decomposition and only \tilde{v}_2 as extra quantity for MDL decomposition, similar results are to be expected for the 2.5D scenario.

The downgoing field can be interpreted as the elastodynamic free-surface ghost of the upgoing field. The proposed algorithm can therefore be used for elastodynamic deghosting. This can be very useful for passive data processing, for instance for passive seismic interferometry (Draganov *et al.*, 2006; Xu *et al.*, 2012). In addition, decomposition has been used in combination with multi-dimensional deconvolution of passive recordings at the surface (Nakata *et al.*, 2014). Using MDL decomposition, similar multi-dimensional deconvolution procedures can be carried out on passive data with receivers located in the subsurface (which might lead to a better signal-to-noise ratio of the recordings) (Almagro Vidal *et al.*, 2014; Almagro Vidal & Wapenaar, 2014).

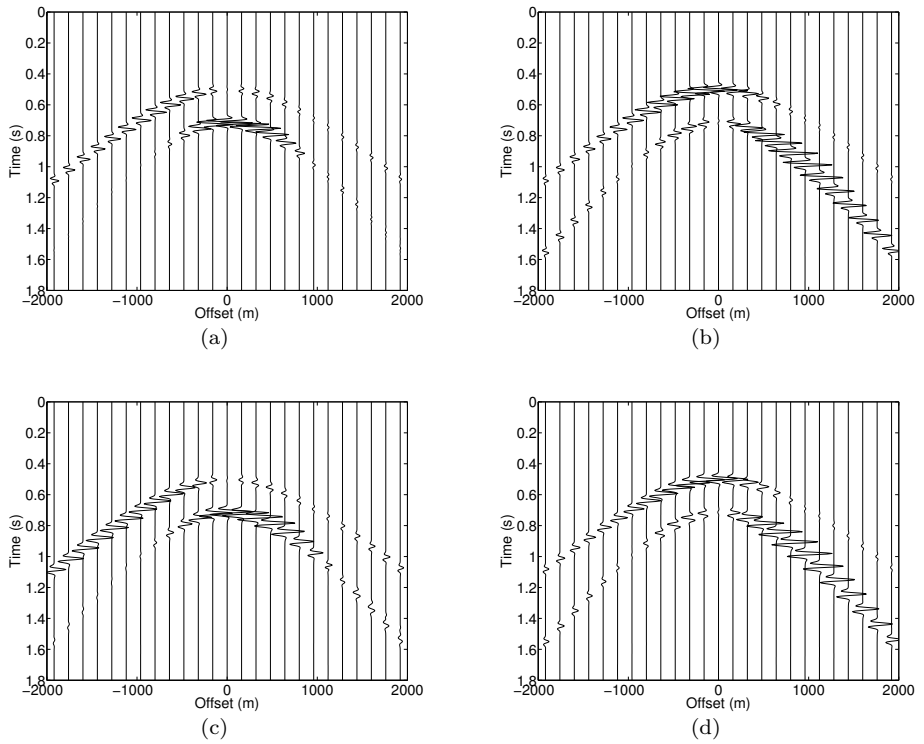


Figure 6.5: Original shot records for a homogeneous model registered at depth level $x_{3;B} = 5$ m.
 (a) Two-way data $-\tau_{13}$ (b) Two-way data $-\tau_{33}$ (c) Two-way data v_1 (d) Two-way data v_3

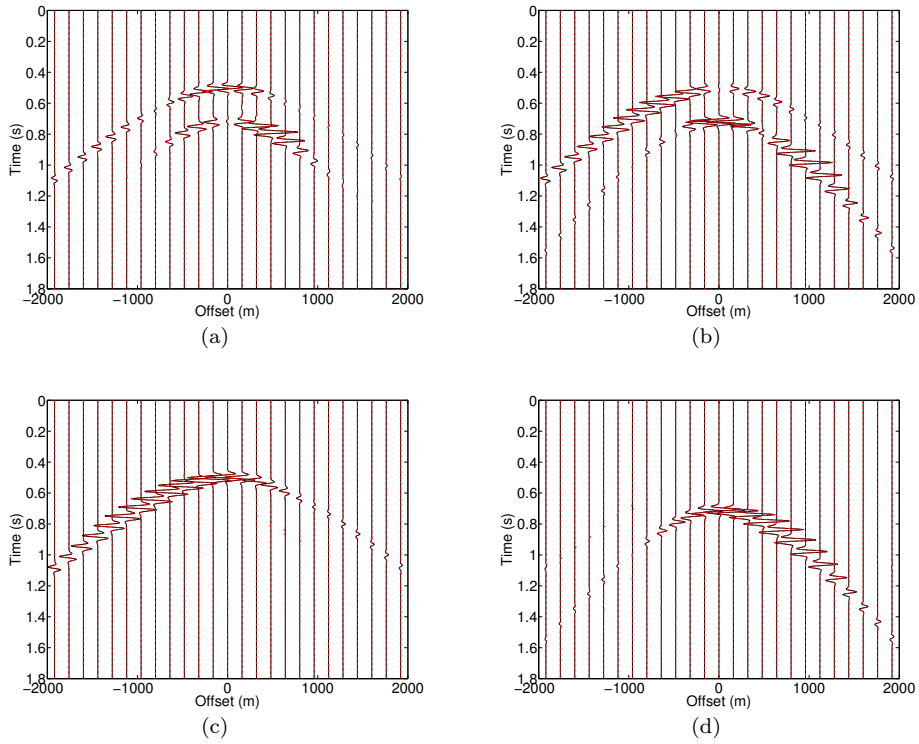


Figure 6.6: Comparison between the MC decomposition results in black and the MDL decomposition results in red (dashed) for the homogeneous model. (a) Downgoing P-waves (b) Downgoing S-waves (c) Upgoing P-waves (d) Upgoing S-waves

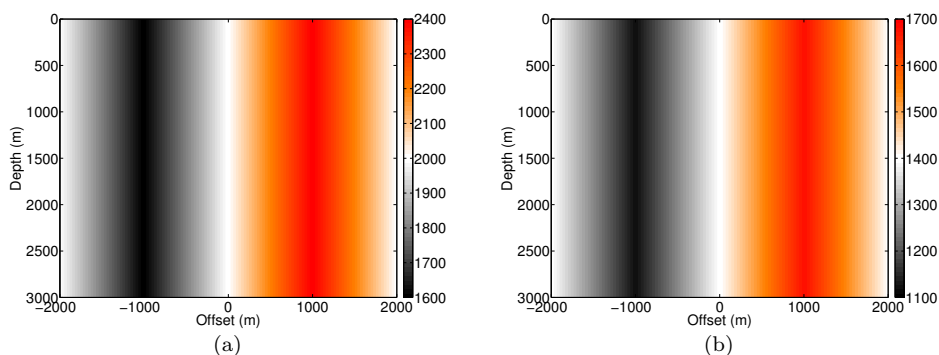


Figure 6.7: Geometry of Synthetic Elastodynamic Example 2 with velocity variations of -20% to $+20\%$ with respect to the homogeneous velocities. (a) The colors represent P-wave velocities in m/s. (b) The colors represent S-wave velocities in m/s.

So far, we have only considered scenarios where the correct velocity has been used at the decomposition level as well as for extrapolating the fields between the different depth levels. We will now investigate the sensitivity of the MDL decomposition scheme to errors in the velocity model. We therefore consider the same acquisition geometry as described for the homogeneous example above, but now with a velocity model that experiences a horizontal gradient from -20% velocity error to $+20\%$ velocity error with respect to the homogeneous P- and S-wave velocities (see Figure 6.7). The resulting two-way data is presented in Figure 6.8. We apply MC and MDL decomposition using the homogeneous velocities. In this way, the effects of using erroneous velocities on both the MC and MDL decomposition scheme are investigated.

The results of both decomposition schemes are displayed in Figure 6.9. In black, the results of MC decomposition using an erroneous velocity at the depth level of decomposition are displayed. In red, dashed, the results are displayed of applying MDL decomposition with erroneous velocities at the depth level of decomposition as well as for the extrapolation operators. We can observe that the downgoing P- and S- fields are correctly resolved and equally-well in terms of both phase and amplitude. The upgoing P- and S- fields show leakage of downgoing energy (indicated by the arrows), but again the amount of leakage is comparable for the MC and MDL decomposition schemes. However, please note that it is crucial to have properly dealt with the notch problems (due to e.g. notch filters), or that the distance over which extrapolation takes place is small enough to avoid notches that overlap with the data bandwidth. If this is namely not the case, the undesired notch effects on the decomposition results will become more pronounced when using incorrect velocity models.

Since we are here effectively considering a laterally varying medium, which is a realistic scenario for (near-surface) land data, we know that theoretically the applied

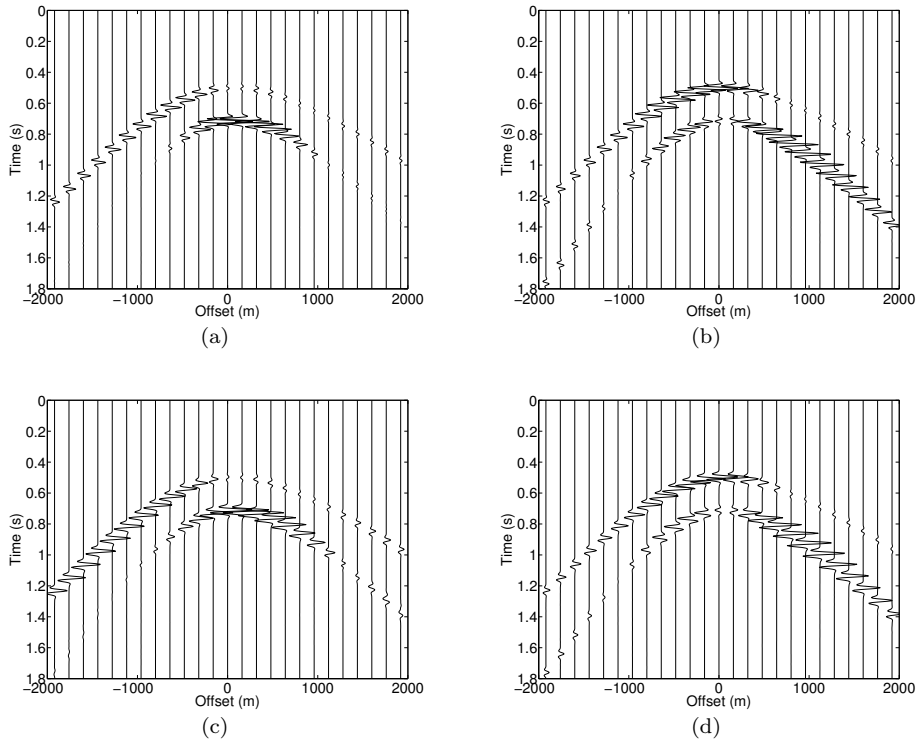


Figure 6.8: Original shot records registered at depth level $x_{3;B} = 5$ m, for the velocity model with velocity variations of -20% to $+20\%$ with respect to the homogeneous velocities. (a) Two-way data $-\tau_{13}$ (b) Two-way data $-\tau_{33}$ (c) Two-way data v_1 (d) Two-way data v_3

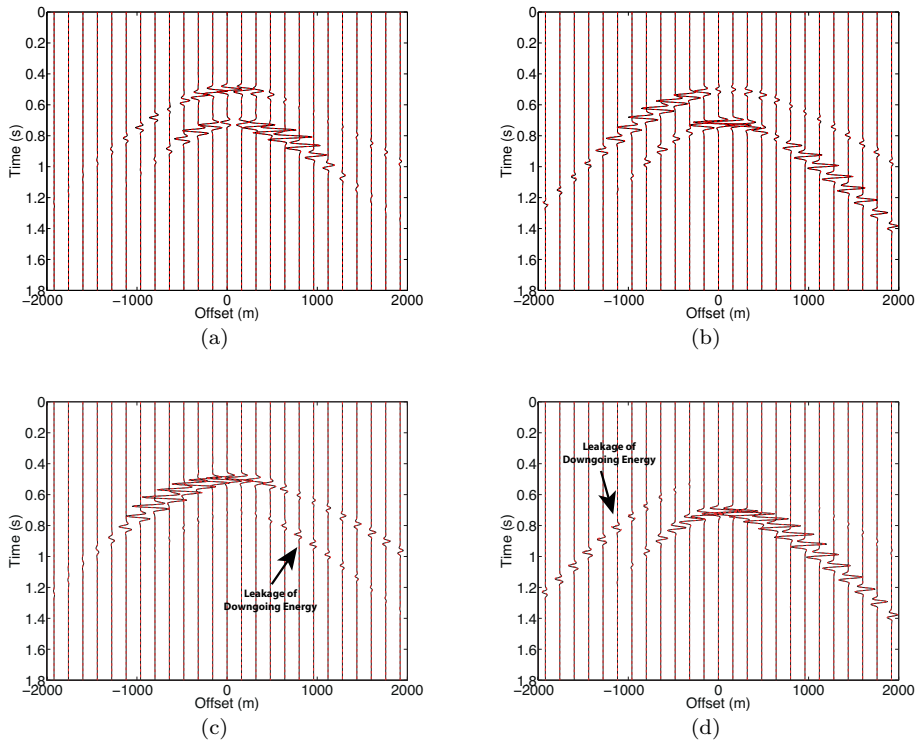


Figure 6.9: Comparison between the MC decomposition results in black and the MDL decomposition results in red (dashed) for the velocity model with velocity variations of -20% to $+20\%$ with respect to the homogeneous velocities. (a) Downgoing P-waves (b) Downgoing S-waves (c) Upgoing P-waves (d) Upgoing S-waves

horizontal wavenumber-frequency decomposition approach is not valid. We predict that the leakage (for both decomposition schemes) can be avoided when carrying out the field decomposition in the space-frequency domain (e.g. [Grimbergen *et al.* \(1998\)](#)).

For the MDL decomposition, we have carried out a damped least-squares inversion of the customized composition matrix $\tilde{\mathbf{S}}$, using a Tikhonov regularization with damping factor of $1 \cdot 10^{-4}$ of the maximum amplitude of $\tilde{\mathbf{S}}\tilde{\mathbf{S}}^\dagger$.

6.1.6 MC-MDL Acoustic Decomposition applied to a Field Land Data Set

Theory of the MC-MDL Decomposition

Following the MC decomposition procedure, up- and downgoing one-way fields can be obtained by inverting the forward problem of equation (6.2). In the MDL decomposition scheme, the decomposition problem is treated slightly different. We have seen that using field extrapolation operators, we can express the one-way fields at one depth level in terms of the observed fields at multiple levels. The synthetic elastodynamic examples have shown that the MDL up/down decomposition obtains correct one-way fields in both amplitude and phase. However, as discussed in Appendix A for acoustic fields, the MDL inversion can suffer from notches at certain frequencies. The MC decomposition scheme does not suffer from these notches, but might suffer from different sensor characteristics ([Schalkwijk *et al.*, 2003](#)) or the fact that differently recorded field quantities might not be of similar quality due to different noise levels ([Burnstad *et al.*, 2012](#)). The success of the MDL decomposition scheme on synthetic data combined with the discussion of the notch problems, has led to the idea of combining the MC decomposition scheme with the MDL decomposition schemes (MC-MDL), thereby combining the best of both worlds. We will investigate this idea by applying it to an acoustic representation of a real land data set recorded in Annerveen, the Netherlands. Here, the aim is to perform up/down field separation at depth level $x_{3;B}$.

We start by looking at the decomposition problem as an inverse problem. Using equation (6.2) as the basic equation, we try to improve the decomposition with an additional inversion constraint: the free-surface condition from the MDL decomposition scheme, where depth level $x_{3;A}$ coincides with the free surface. This corresponds to the Annerveen acquisition geometry, where $x_{3;A} = 0$ m and $x_{3;B} = 50$ m. This leads to the following overdetermined inverse problem:

$$\begin{pmatrix} \tilde{\mathbf{q}}_{1;B} \\ \tilde{\mathbf{q}}_{2;B} \\ \mathbf{0} \end{pmatrix} = \begin{pmatrix} \tilde{\mathbf{L}}_{1;B}^+ & \tilde{\mathbf{L}}_{1;B}^- \\ \tilde{\mathbf{L}}_{2;B}^+ & \tilde{\mathbf{L}}_{2;B}^- \\ \tilde{\mathbf{L}}_{1;A}^+ \tilde{\mathbf{F}}^+ & \tilde{\mathbf{L}}_{1;A}^- \tilde{\mathbf{W}}^- \end{pmatrix} \begin{pmatrix} \tilde{\mathbf{P}}_B^+ \\ \tilde{\mathbf{P}}_B^- \end{pmatrix}. \quad (6.30)$$

For our field data example, we will consider scalar versions of equation (6.2), referred to as the MC decomposition problem, and equation (6.30), referred to as the MC-MDL decomposition problem. Here, $\tilde{q}_1 = \tilde{p}$, the acoustic pressure field, and $\tilde{q}_2 = \tilde{v}_3$, the vertical component of the particle velocity (see also Appendix A for an extensive

discussion on acoustic MDL field decomposition). The flux-normalized scalars \tilde{L}_1^\pm and \tilde{L}_2^\pm , as well as the scalar field extrapolation operators \tilde{W}^- and \tilde{F}^+ , are taken as defined in Wapenaar (1998). For clarity, the subscripts A and B have been added in equation (6.30). However, as discussed earlier, we assume that the medium between depth levels $x_{3;A}$ and $x_{3;B}$ is homogeneous. Although the distance between $x_{3;A}$ and $x_{3;B}$ is only 50 m, and taking into account the near-surface geology of this specific part of the Netherlands, this seems a valid assumption. Due to this assumption we can omit the subscripts of the composition submatrices. As can be observed, the added row in equation (6.30) overdetermines the inverse problem, but does not require additionally recorded fields. The added equation makes use of the Dirichlet free-surface boundary condition, that is, the pressure at the free surface equals zero. We will now investigate whether this overdetermined inverse problem improves the decomposition results of the Annerveen data set. The inverse problem will be solved in the least-squares sense. Again, other approaches, like sparsity promotion (Van der Neut & Herrmann, 2012), could also be considered. For both the MC and MC-MDL decomposition, we have carried out a damped least-squares inversion of the (customized) composition matrix $\tilde{\mathbf{S}}$, using a Tikhonov regularization with damping factor of $1e^{-4}$ of the maximum amplitude of $\tilde{\mathbf{S}}\tilde{\mathbf{S}}^\dagger$.

Up/Down Decomposition Results of the Annerveen data set

The data have been acquired on land in Annerveen, located in the North of the Netherlands. One receiver array consisting of 96 receivers with a spacing of 11.75 m was buried at 50 m depth. In addition, 144 shots were fired at 4 m depth with a source spacing of 11.75 m, alternating positions with respect to the receiver positions. The receivers have registered both the pressure and vertical component particle velocity fields.

Several initial data processing steps need to be performed, before we carry out the field decomposition. We use standard filtering techniques to filter out the surface-waves. In addition, all dead traces are removed. Since we are dealing with a pseudo-2D data set, we correct the amplitudes by multiplying with the square root of time. In addition, the data show quite a variety in amplitudes for different shots. Therefore, we carry out a shot normalization, where we normalize the shotgathers with the power of each shot. Since the MC-MDL decomposition scheme assumes depth level $x_{3;A}$ to be coinciding with the free surface of the Earth, and depth level $x_{3;B}$ corresponding to the receiver level at 50 m depth, one can directly notice that our source in this configuration is located between the two depth levels. The theory does not account for this configuration. This has to do with the fact that in the derivation of the field extrapolation operators (Wapenaar, 1998), it is assumed that no sources are located between the depth levels. However, by removing the incident fields from the data set (i.e. direct field and direct source ghost), the MC-MDL decomposition can still be applied to the remaining reflected data set. We remove these direct fields by applying a time gate, which has been selected by visual inspection (Figure 6.10).

We carry out the visual inspection looking at an average over 10 adjacent common-source gathers. The underlying assumption of this approach is that the Earth is laterally invariant over the distance of these 10 shots, which is a reasonable assumption

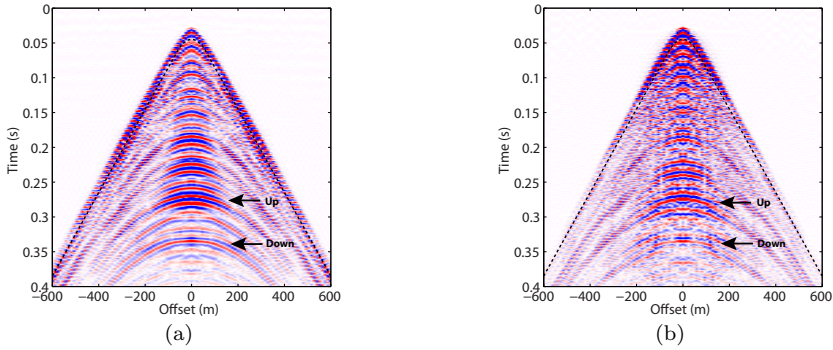


Figure 6.10: Average over 10 common-source gathers. The black line represents the start of the Hanning taper, separating incident fields from reflected fields, and has a taper length of 10 samples downwards. The black arrows indicate a strong upgoing reflection and its receiver side ghost. We make use of our knowledge of polarity reversal between the two data sets to estimate the P-wave velocity. (a) Pressure data p (b) Vertical component particle velocity data v_3

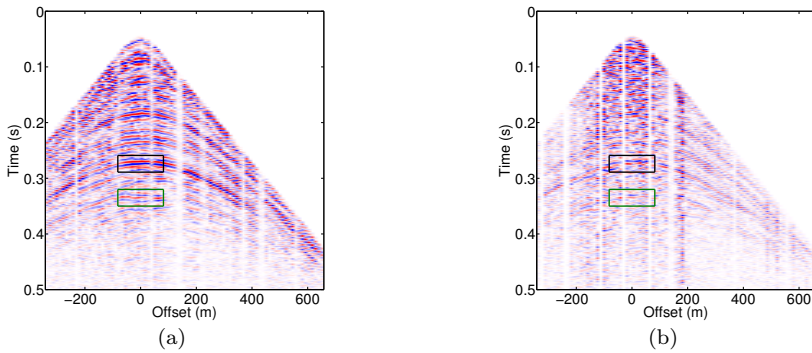


Figure 6.11: Two-way reflected data. The boxes represent selected windows for data calibration. The black box is used for calibrating \bar{p} and \bar{v}_3 in MC decomposition. The black and the dark green box are used for up/down calibration in the MDL decomposition scheme. (a) Pressure data p (b) Vertical component particle velocity data v_3

considering the area of interest.

The crucial parameter for our acoustic MC-MDL decomposition that needs to be determined, is the P-wave velocity in the layer between depth levels $x_{3,A}$ and $x_{3,B}$. The P-wave velocity determines, via the vertical wavenumber k_3 , the forward and inverse extrapolation operators \tilde{W}^- and \tilde{F}^+ , respectively. Furthermore, the P-wave velocity is an important constituent in the composition matrix $\tilde{\mathbf{L}}$ (Wapenaar, 1998). Here, we determine the P-wave velocity by looking at the arrival time difference between a strong upgoing reflection and its receiver side ghost. To identify these two events, we make use of the two individual pressure and particle velocity data sets, and exploit our knowledge about polarity reversal of registered events. Effectively, this means that p and v_3 have opposite polarity for the first upgoing reflection, but identical polarities for the later arriving receiver side ghost. This can be clearly observed in Figure 6.10, indicated by the two arrows. Based on the zero-offset time difference between those two events and knowing the propagation pathlength ($2 \times 50 = 100$ m), the P-wave velocity can be estimated. Our best estimate of the P-wave velocity is $c_P = 1639$ m/s. Exact knowledge of the density is not required, since it appears as a scalar that occurs in each element of the composition matrix. To precondition the inversion, we scale composition matrix element \tilde{L}_2 from Wapenaar (1998) with the impedance (with the density taken as 1 kg/m^3), resulting in a better-posed inverse problem.

We start with the MC field decomposition, according to equation (6.2). Since both the pressure and particle velocity data are involved simultaneously in the MC decomposition schemes, we want to make sure that the sensors are correctly calibrated. Therefore, we focus on a clear event in the two-way recorded data set and select a data window around this event. We select the top, black box, as indicated in Figure 6.11. The event in this data window is a purely upgoing event. We therefore want to minimize the downgoing energy in this data window. We use a least-squares minimization subtraction algorithm to find the correct scaling factor between the pressure and particle velocity data that minimizes the downgoing energy and scale the data accordingly. We now carry out the MC decomposition, resulting in the decomposed flux-normalized one-way fields shown in Figures 6.12(a) and 6.12(b).

Next, we focus on the MC-MDL decomposition. Looking at row 3 of equation (6.30), we observe that the following relation must hold at the free surface

$$\tilde{L}_1^+ \tilde{F}^+ \tilde{p}_B^+ = -\tilde{L}_1^- \tilde{W}^- \tilde{p}_B^-. \quad (6.31)$$

This equation also holds for an individual event. We enforce equation (6.31) to hold by selecting a certain upgoing event and its corresponding downgoing event, indicated with the two boxes in Figure 6.11. The term $\tilde{L}_1^+ \tilde{p}_B^+$ then corresponds to the selected downgoing event in the two-way pressure data set, illustrated by the dark green boxes in Figure 6.11, and $\tilde{L}_1^- \tilde{p}_B^-$ to the selected upgoing event in the two-way pressure data set, indicated by the black boxes in Figure 6.11. We will propagate the two-way data set, including the selected upgoing event, forwards (in the propagation direction) to the free surface using \tilde{W}^- . Secondly, we will propagate the two-way data set, including the selected downgoing event, backwards (against the propagation direction) to the free surface. Here, equation (6.31) must

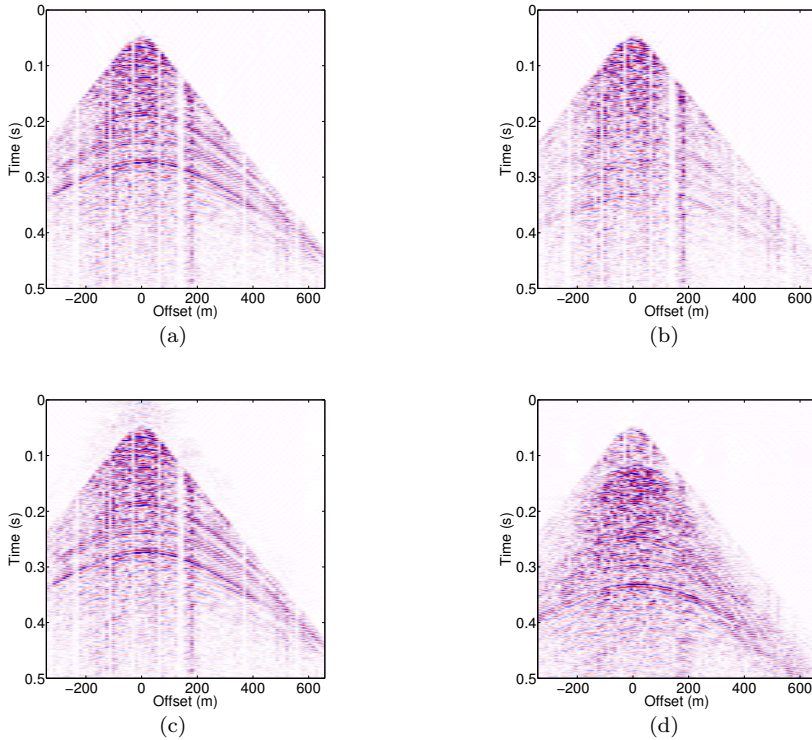


Figure 6.12: Comparison of the decomposition results of the Annerveen land data set (a) MC decomposed upgoing fields (b) MC decomposed downgoing fields (c) MC-MDL decomposed upgoing fields (d) MC-MDL decomposed downgoing fields.

hold. We now calibrate the two shifted two-way events at the free surface with each other, using a least-squares minimization subtraction algorithm on the selected event. A similar minimization problem has been defined for the vertical component particle velocity field. Both minimization problems are solved for simultaneously. We then apply this calibration factor to the composition matrix element containing \tilde{F}^+ , corresponding to the downgoing fields (see equation (6.30)). The overall weight of the extra equation in the inversion can be further tuned according to preference.

We are now all set to carry out the MC-MDL field decomposition. The decomposition is carried out by least-squares in version of equation (6.30).

Figures 6.12(a) and 6.12(b) display the up- and downgoing MC decomposed fields. The results of the overdetermined MC-MDL decomposition problem are shown in Figures 6.12(c) and 6.12(d). What can be clearly observed is that by adding the extra constraint to the inversion (the third row in the composition matrix of equation (6.30)), we have improved the decomposition results, especially for the downgoing fields (compare Figures 6.12(b) and 6.12(d)). In addition, it can be

observed that the MC decomposition result has vertical ‘white’ bands at certain offsets, corresponding to dead or noisy traces in the two-way recorded data. Our MC-MDL decomposition result does not show these ‘white’ bands so strongly. This is explainable due to the applied field extrapolation operators in the wavenumber-frequency domain, implicitly yielding an interpolation between the traces.

6.1.7 Discussion

We have shown that the MDL decomposition scheme correctly decomposes different kinds of fields. However, the MDL scheme might suffer from invertibility issues due to the presence of notches. The notch problems have been investigated more closely for an acoustic example (Appendix A). We have shown that notch filters can be designed such that the MDL field decomposition for the acoustic case can still be carried out using only pressure or particle velocity recordings. Similar notch filters might be required for the other field phenomena treated in the appendices. The notch filters remove certain (notch) frequencies from the data. Which frequencies are missing depends on which data set is used for the decomposition. Since, for the acoustic case, the pressure and vertical component particle velocity data are complementary to each other, combining the two data sets will result again in full-bandwidth decomposed fields.

A way to avoid suffering from notches in the frequency spectrum of the data is to carry out deghosting in the space-time domain. Using single-component measurements only (e.g. only pressure data), [Beasley *et al.* \(2013b,a\)](#) show that by using the wave equation to simulate up- and down-going wavefield propagation between the receiver level and the water surface, wavefield separation can be achieved. In addition, [Robertsson & Amundsen \(2014\)](#) show that by using finite-difference modeling to predict ghosts from upgoing waves (after removal of the direct wave) and by instantaneously injecting these predicted ghosts, destructive interference takes place with the recorded ghosts. In this way, successful deghosting in the space-time domain is achieved, without suffering from notches. Furthermore, [Amundsen & Robertsson \(2014\)](#) present a similar method for deghosting in the space-time domain that relies on multi-component recordings. An important challenge of these space-time domain decomposition approaches based on wave propagation is the fact that they require unaliased data and hence fine receiver sampling ([Beasley *et al.*, 2013b](#)). For 3D deghosting this fine sampling is also required in the cross-line direction. In order for the method to work, the water velocity, receiver depth and receiver positions must be known. However, these are mainly challenges that also hold for most other deghosting procedures (including our MDL decomposition scheme). If one would like to apply a similar space-time domain approach to land data, the fact that the velocities are required to be known might be problematic, and one should carefully investigate the sensitivity of this method to the use of incorrect velocity models. The same holds for the MDL decomposition scheme, for which we investigated the velocity sensitivity in Synthetic Elastodynamic Example 2.

As we discussed in Appendix A, we can straightforwardly add the pressure and vertical component particle velocity data (with some calibration factor) to obtain

the full-frequency spectrum decomposed fields. Alternatively, one might for example prefer to combine the two data sets in a very late stage. One possible way would be via multidimensional deconvolution (Wapenaar *et al.*, 2008b). The multidimensional deconvolution method can be useful for e.g. surface- and sea bottom-related multiple elimination (Wapenaar & Verschuur, 1996; Amundsen, 1999). Via multidimensional deconvolution, that makes use of upgoing and downgoing (flux-normalized) fields, the reflection response of the medium below a certain depth level can be obtained, as if the medium above this depth level was homogeneous. The multidimensional deconvolution procedure can be applied to different types of fields (Amundsen & Holvik, 2004; Holvik & Amundsen, 2005; Van der Neut *et al.*, 2010; Wapenaar *et al.*, 2008b). Instead of adding the pressure and vertical component particle velocity data to obtain full-frequency spectrum decomposed fields, we can alternatively combine these two data sets smoothly at the stage of multidimensional deconvolution, thereby exploiting the benefit of treating the two data sets separately until a very late stage of the imaging workflow. Despite the problem of the notches, one of the benefits of applying MDL decomposition based on either pressure or vertical component particle velocity data independently (for the acoustic case), is that sensor calibration (as is needed for MC decomposition) is not required. Combining these two data sets in the stage of multidimensional deconvolution also avoids the need of sensor calibration, since the same sensor calibration functions act on both the up- and downgoing fields. Therefore, they will occur at both the left- and right-hand side of the multidimensional deconvolution equations to be solved and will drop out of the equations automatically.

The MDL decomposition scheme makes use of recordings at multiple depth levels. So far, we have shown land data examples, where recordings in a horizontal borehole (or recordings using a high-density of vertical boreholes) on land were used. More generally speaking, the MDL scheme needs recordings at multiple depth levels, applicable to any medium. One can think of combining for example marine (dual) streamer data with Ocean-Bottom Node (OBN) data.

6.1.8 Conclusions

Applying field decomposition to a real data set is often quite challenging. The multi-component (MC) field decomposition scheme makes use of differently recorded field components, for example both pressure (p) and vertical component particle velocity (v_3) data in a purely acoustic case. In practice, recordings can be obscured by different sensor characteristics, requiring calibration with an unknown calibration factor. In addition, not all field quantities required for MC field decomposition might be available and they may not always be of similar quality due to different noise levels. Especially, when dealing with more complex field phenomena (e.g. elastodynamic or seismo-electromagnetic fields), the MC field up/down decomposition requires measuring many different field quantities.

We have presented a multi-depth-level (MDL) field decomposition scheme for land acquisition that is inspired by marine acquisition designs that make use of recordings at multiple depth levels for successful field decomposition. Our MDL

decomposition approach makes use of configurations with field quantity information on multiple depth levels, for example two horizontal boreholes that are closely separated from each other, or a combination of a single receiver array just below a free surface, thereby exploiting the natural (Dirichlet) free-surface boundary conditions.

We have theoretically described the MDL decomposition approach in a unified form, showing that in principle it can be applied to different kinds of fields in dissipative, inhomogeneous, anisotropic media, like for example acoustic fields, electromagnetic fields, elastodynamic systems, poroelastic fields and seismo-electromagnetic fields. The theoretical details of decomposing each of these types of fields, for laterally invariant media at the depth level of decomposition, are given in the Appendices A-E.

Assuming that the medium is laterally invariant at the depth level of decomposition allows us to carry out the MDL decomposition in the horizontal wavenumber-frequency domain. We have illustrated the MDL decomposition scheme using two synthetic elastodynamic modeling examples. We have first demonstrated that the MDL decomposition scheme leads to correctly retrieved power flux-normalized one-way fields, for both P- and S-waves, using only particle velocity recordings at two depth levels. Secondly, we showed that when we have particle velocity recordings at one depth level, in combination with the free-surface Dirichlet boundary condition of zero-traction, we can correctly decompose the data into one-way fields as well. Comparison with MC obtained decomposed fields shows a perfect match in both amplitude and phase for both cases.

We have additionally tested the effects of using erroneous velocities on both the MC and MDL decomposition schemes. For the considered example, we observed that the downgoing P- and S- fields are correctly and equally-well resolved in terms of both phase and amplitude. The upgoing P- and S- fields show leakage of downgoing energy, but the amount of leakage is comparable for the MC and MDL decomposition schemes. Please note that it is crucial to have properly dealt with possible notch problems. Otherwise, the undesired notch effects on the decomposition results will become more pronounced when using incorrect velocity models.

We have shown that the MDL decomposition scheme is fully customizable to the acquisition geometry and measured field quantities under consideration. Care must be taken that the customized composition matrix to be inverted is always of sufficient rank. However, depending on the acquisition design and wave velocities under consideration, notches may occur at certain frequencies, causing the customizable MDL composition matrix to become uninvertible. Additional notch filters are then required.

The success of the MDL decomposition scheme on the synthetic elastodynamic data, combined with the problem of the notches, has led to the idea of combining the MC and MDL decomposition schemes. The decomposition problem is in principle an inverse problem. By adding an extra equation of the MDL decomposition scheme to the MC composition matrix, we can overdetermine the inverse problem and hereby better constrain the inversion. Since this equation makes use of the Dirichlet free-surface boundary condition, where for the acoustic case the pressure at the free surface equals zero, we do not require additionally recorded fields for

this extra inversion constraint. Comparison of the results of this overdetermined MC-MDL decomposition scheme with the results of the conventional MC field decomposition, clearly showed improvements in the obtained one-way flux-normalized fields, especially for the downgoing fields.

Appendix

6.1.A Acoustic Field Decomposition, Notches and Filters

In this appendix we closely investigate the notch patterns for an acoustic case and show that acoustic MDL decomposition can also be carried out using only pressure or vertical component particle velocity data, in combination with notch filters. We use a scalar version of equation (6.2) as the basic starting equation for field decomposition, where we take $\tilde{q}_1 = \tilde{p}$ and $\tilde{q}_2 = \tilde{v}_3$. Here, \tilde{p} corresponds to the acoustic pressure field and \tilde{v}_3 denotes the vertical component particle velocity field. We will focus on single horizontal downhole sensor arrays combined with a free-surface constraint, which corresponds to the acquisition geometry of our present field data example. Let us consider two scalar versions of equation (6.29), where level $x_{3;A}$ coincides with the free surface and level $x_{3;B}$ is located at some arbitrary shallow depth level, measuring either pressure or vertical component particle velocity fields. We locate the source for example at the free surface. This leads to

$$\begin{aligned} \begin{pmatrix} \tilde{p}_B^+ \\ \tilde{p}_B^- \end{pmatrix} &= \begin{pmatrix} \tilde{L}_1^+ \tilde{F}^+ & \tilde{L}_1^- \tilde{W}^- \\ \tilde{L}_1^+ & \tilde{L}_1^- \end{pmatrix}^{-1} \begin{pmatrix} \tilde{q}_{1,A} \\ \tilde{q}_{1,B} \end{pmatrix} \\ &= \tilde{\mathbf{S}}_p^{-1} \begin{pmatrix} \tilde{q}_{1,A} \\ \tilde{q}_{1,B} \end{pmatrix}, \end{aligned} \quad (6.32)$$

where, as defined above, $\tilde{q}_1 = \tilde{p}$ and to

$$\begin{aligned} \begin{pmatrix} \tilde{p}_B^+ \\ \tilde{p}_B^- \end{pmatrix} &= \begin{pmatrix} \tilde{L}_1^+ \tilde{F}^+ & \tilde{L}_1^- \tilde{W}^- \\ \tilde{L}_2^+ & \tilde{L}_2^- \end{pmatrix}^{-1} \begin{pmatrix} \tilde{q}_{1,A} \\ \tilde{q}_{2,B} \end{pmatrix} \\ &= \tilde{\mathbf{S}}_{v_3}^{-1} \begin{pmatrix} \tilde{q}_{1,A} \\ \tilde{q}_{2,B} \end{pmatrix}, \end{aligned} \quad (6.33)$$

where $\tilde{q}_2 = \tilde{v}_3$. As can be seen, the same downgoing and upgoing decomposed fields at depth level $x_{3;B}$ can be obtained in two independent ways. We can either apply the inverse of the MDL composition matrix, $\tilde{\mathbf{S}}_p^{-1}$, to a zero value of the pressure field at level $x_{3;A}$ combined with a measured pressure field at $x_{3;B}$ (equation (6.32)), or apply the inverse $\tilde{\mathbf{S}}_{v_3}^{-1}$ to a zero pressure field at level $x_{3;A}$ combined with a measured vertical particle velocity at level $x_{3;B}$ (equation (6.33)). Here, \tilde{L}_1^\pm and \tilde{L}_2^\pm are again taken as defined in [Wapenaar \(1998\)](#). However, notches occurring at certain notch frequencies, can cause the $\tilde{\mathbf{S}}$ matrix to become uninvertible. In both our elastodynamic synthetic examples, the distance was small enough, to avoid suffering from notches when solving the inverse problem. However, for certain distances, notches will occur at certain frequencies overlapping with the data band. In these cases, additional notch filters are required in order to be able to invert the MDL composition matrices correctly. In our field data example we combined MC with MDL decomposition, such that we did not suffer from the notches. Alternatively, the following approach could be taken.

From a mathematical point of view, we expect the notches to occur in those situations where the determinant of the composition matrix to be inverted, $\tilde{\mathbf{S}}_{p;v_3}$,

becomes zero (or close to zero). By evaluating when the determinant becomes zero (or close to zero), we can analytically obtain information about the specific notch frequency patterns at which the matrix becomes uninvertible (or poorly invertible). Starting from equation (6.32) we can determine the notch patterns for the pressure data. We can see that in case of a zero-determinant, the following equation holds

$$\tilde{L}_1^+ \tilde{L}_1^- \left[\tilde{F}^+ - \tilde{W}^- \right] = 0. \quad (6.34)$$

Besides the zero-solutions for \tilde{L}_1^\pm (or for \tilde{L}_2^\pm in case of equation (6.33)), the term in between the square brackets can be zero. Considering propagating waves, we can apply equation (6.24) leading to

$$\tilde{L}_1^+ \tilde{L}_1^- \left[\left(\tilde{W}^- \right)^* - \tilde{W}^- \right] = 0. \quad (6.35)$$

Rewriting the term in the square brackets using Euler's formula, yields the following relation describing the notch patterns

$$\begin{aligned} \left(\tilde{W}^- \right)^* - \tilde{W}^- &= -2j\Im\{\tilde{W}^-\} \\ &= -2j \sin(-k_3|x_{3;B} - x_{3;A}|) = 0. \end{aligned} \quad (6.36)$$

When we start from equation (6.33), we can obtain the notch patterns for the vertical component particle velocity data in a similar way. We can use the following properties $\tilde{L}_1^- = \tilde{L}_1^+$ and $\tilde{L}_2^- = -\tilde{L}_2^+$. This leads to the following zero-determinant condition

$$\tilde{L}_1^\pm \tilde{L}_2^\pm \left[-\tilde{F}^+ - \tilde{W}^- \right] = 0. \quad (6.37)$$

Considering propagating waves, we can again apply equation (6.24) leading to

$$\tilde{L}_1^{+,-} \tilde{L}_2^+ \left[-\left(\tilde{W}^- \right)^* - \tilde{W}^- \right] = 0. \quad (6.38)$$

Rewriting the term in the square brackets using Euler's formula, yields the following relation describing the notch patterns

$$\begin{aligned} -\left(\tilde{W}^- \right)^* - \tilde{W}^- &= -2\Re\{\tilde{W}^-\} \\ &= -2 \cos(-k_3|x_{3;B} - x_{3;A}|) = 0. \end{aligned} \quad (6.39)$$

We can clearly observe that the notch patterns for the pressure and vertical component particle velocity data follow a complementary trigonometric pattern (sine or cosine) with identical argument. This complementary pattern has been widely exploited for marine/OBC deghosting procedures (e.g. Day *et al.* (2013)).

As an alternative approach, as known from inverse theory, the condition numbers can provide us with information about the invertibility of a certain matrix. The condition number represents the ratio between the largest and smallest singular value of the matrix. High condition numbers indicate that the matrix is poorly

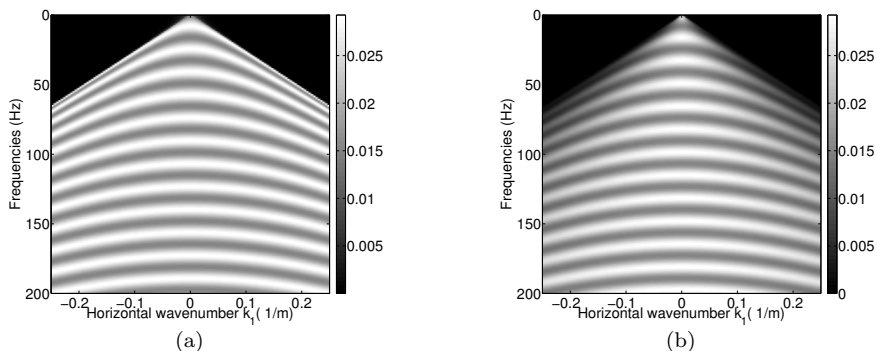


Figure 6.13: Wavenumber-frequency domain plots indicating the invertibility of the matrices $\tilde{\mathbf{S}}_p$ and $\tilde{\mathbf{S}}_{v_3}$. The plots show the inverse of the condition numbers for (a) the pressure field data (b) the vertical component particle velocity data.

conditioned and therefore difficult to invert (Van der Neut *et al.* (2013)). Investigating the invertibility of $\tilde{\mathbf{S}}_{p,v_3}$ by looking at $1/(\text{Condition Number})$, clearly shows us the locations of the notches for both the pressure and vertical component particle velocity data (see Figures 6.13(a) and 6.13(b), respectively). Since we here display the inverse of the condition numbers, low values correspond to the notch frequencies for that specific type of data. One can see that the two types of data are indeed complementary to each other. In other words, where a notch occurs for the pressure data at a certain frequency-wavenumber combination, the particle velocity field can provide the data and vice versa.

We have designed two filters that follow these notch patterns and are also complementary to each other. To exploit the fact that the filters should be complementary to each other, we have used $\sin^2(a) + \cos^2(a) = 1$. In this way we try to find a certain a that matches the notch patterns, such that a maximum contribution is given to the maximum amplitudes in the inverse condition number plots (corresponding to low condition numbers and good matrix invertibility) and a minimum contribution is given to the minimum amplitudes in the inverse condition number plots. Using the analytical solutions of equations (6.36) and (6.39), we have found that $a = k_3(x_{3;B} - x_{3;A})$ exactly follows the moveout patterns in the wavenumber-frequency plots. The notch filters are therefore taken as $w_p = \sin^2(k_3(x_{3;B} - x_{3;A}))$ and $w_{v_3} = 1 - w_p$, for the pressure field and vertical component particle velocity field data, respectively (see Figure 6.14).

Applying these filters to the MDL decomposition matrices $\tilde{\mathbf{S}}_{p,v_3}^{-1}$, avoids suffering from the notches in the MDL decomposition. In this way, the acoustic field up/down decomposition can be carried out using either solely pressure recordings at $x_{3;B}$ combined with a free-surface, zero-pressure constraint or solely vertical component particle velocity recordings at $x_{3;B}$ combined with a free-surface, zero-pressure constraint (equations (6.32) and (6.33), respectively). The MDL decomposition res-

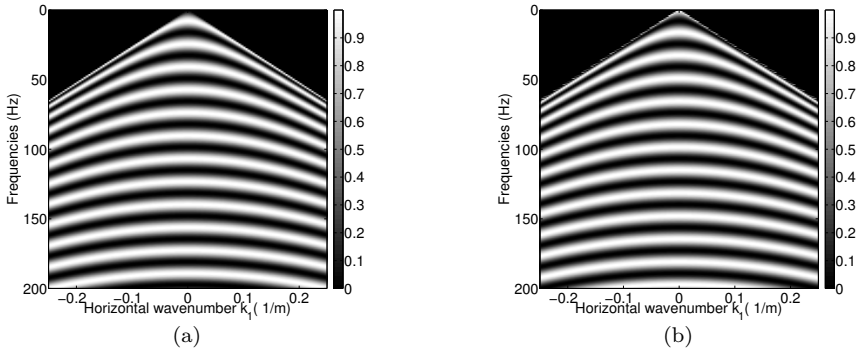


Figure 6.14: Designed notch filters to deal with the notch frequencies and hence overcoming the invertibility issues of $\tilde{\mathbf{S}}_p$ and $\tilde{\mathbf{S}}_{v_3}$. (a) Notch filter for the pressure field data. (b) Notch filter for the vertical component particle velocity data.

ults obtained by using either solely pressure field data or solely vertical component particle velocity data are presented in Figures 6.15 and 6.16, respectively.

Since we have applied specific notch filters to each of the two data sets, certain frequencies are missing in the resulting decomposed data. Which frequencies are missing depends on which data set is used for the decomposition. However, since the pressure field data and particle velocity field data are complementary to each other, combining them will result again in full-frequency spectrum decomposed fields.

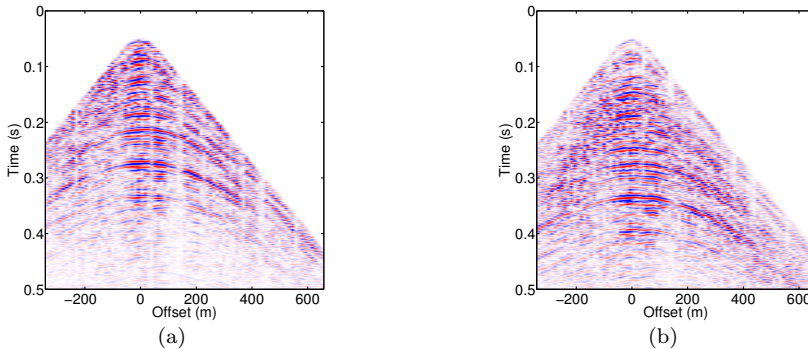


Figure 6.15: MDL decomposition results of the Annerveen data set using only pressure recordings at $x_{3;B}$ combined with a free-surface, zero-pressure constraint and after applying the designed notch filter. (a) MDL upgoing fields using only pressure field data and a free-surface zero-pressure constraint. (b) MDL downgoing fields using only pressure field data and a free-surface zero-pressure constraint.

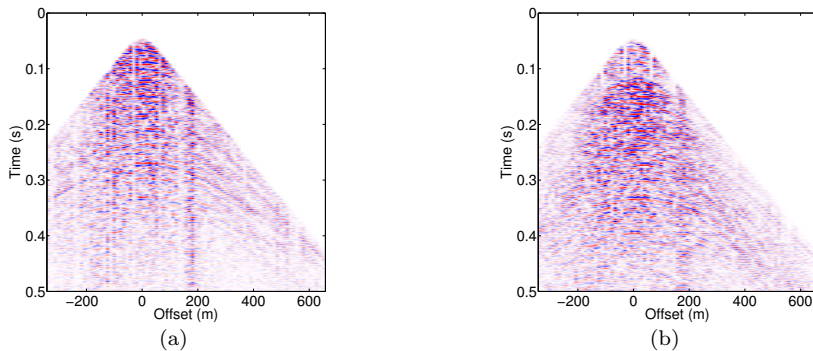


Figure 6.16: MDL decomposition results of the Annerveen data set using only vertical component particle velocity data at $x_{3;B}$ combined with a free-surface, zero-pressure constraint and after applying the designed notch filter. **(a)** MDL upgoing fields using only vertical component particle velocity field data and a free-surface zero-pressure constraint. **(b)** MDL downgoing fields using only vertical component particle velocity data and a free-surface zero-pressure constraint.

Combining these two data sets can be performed at various stages.

A straightforward way of combining pressure and particle velocity data is to add them. This addition can be designed in any desired way. One can for example normalize the two data sets by the norm of the energy of each data set, before adding them up. The underlying assumption is then that the total energy in the two data sets should be identical. The result of this addition is shown in Figure 6.17. Comparing Figures 6.15, 6.16 and 6.17 with the MC or MC-MDL results of Figure 6.12, again shows that similar results can be obtained by using only pressure or vertical component particle velocity data.

Despite the drawback of the notches, the introduced independency between the pressure and vertical component particle velocity recordings has an additional benefit. As is well-known for field data, differently recorded field quantities can have different receiver signatures superimposed. Each receiver modifies the recorded field via a specific transfer function when converting it to a voltage (El Allouche (2011)). Since we can treat certain field quantities separately in the MDL decomposition scheme (\tilde{p} and \tilde{v}_z for the acoustic case), a compensation for these sensor characteristics is not required. The same transfer functions act on both the up- and downgoing fields.

6.1.B Electromagnetic Field Decomposition

We start by capturing the electromagnetic problem in the format of equation (6.1). When considering a medium that is invariant in two directions, it can be useful to decouple the total 3D system into two independent electromagnetic propagation modes: the transverse electric (TE) mode and the transverse magnetic (TM) mode, resulting in mode field vectors (Nabighian, 1987). In 2D (when defining line sources

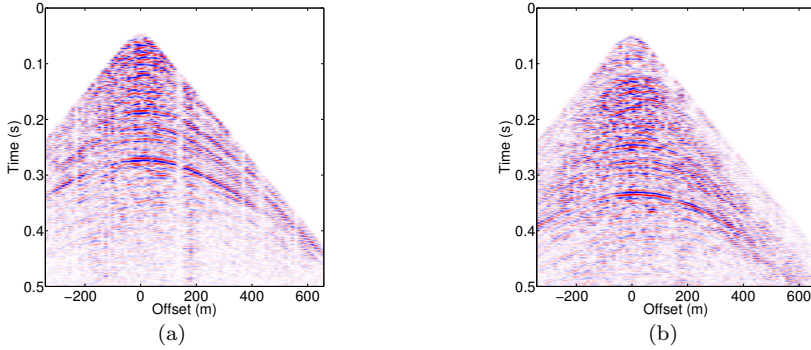


Figure 6.17: Summed MDL decomposition results of the Annerveen data set using only pressure recordings at $x_{3;B}$ or vertical component particle velocity recordings at $x_{3;B}$ (a) Upgoing fields, by summing Figures 6.15(a) and 6.16(a). (b) Downgoing fields, by summing Figures 6.15(b) and 6.16(b).

in the crossline (x_2 -) direction), the mode separation occurs naturally. Since the eigenvectors of the full electromagnetic system in laterally invariant media are well-known (Slob, 2009), we here skip the theory of mode separation and directly describe how to apply the MDL field decomposition scheme to arbitrary subsurface geometries, just like the acoustic and elastodynamic systems treated in this section.

Following Slob (2009), we might define the electromagnetic field vector $\tilde{\mathbf{q}}$ in this case as:

$$\tilde{\mathbf{q}} = \begin{pmatrix} \tilde{\mathbf{q}}_1 \\ \tilde{\mathbf{q}}_2 \end{pmatrix} = \begin{pmatrix} \tilde{E}_1 \\ \tilde{E}_2 \\ \tilde{H}_2 \\ -\tilde{H}_1 \end{pmatrix}. \quad (6.40)$$

The whole electromagnetic system is described if we know four out of the six existing electromagnetic field quantities (\tilde{E}_i and \tilde{H}_i). Recordings in a horizontal borehole result in recordings on a ‘line’. Let us take the x_1 -direction as the direction of our borehole, and refer to this direction as the inline direction. Not all components of the electric field can be measured in a borehole. In the above described case, only the inline electric field (\tilde{E}_1) can be measured in the borehole. Using coils, we can additionally measure

$$j\omega\tilde{B}_3 = -\tilde{E}^H = j\omega\mu_0\mu_R\tilde{H}_3, \quad (6.41)$$

$$j\omega\tilde{B}_\alpha = j\omega\mu_0\mu_R\tilde{H}_\alpha, \quad (6.42)$$

where the subscript α can take the values 1 and 2. Here, \tilde{B}_k (with $k=1,2$ or 3) denotes the different field components of the averaged magnetic flux density. The coils can directly measure the time derivative of these magnetic flux densities. In addition, for Earth materials the relative magnetic permeability $\mu_R \approx 1$ and the

magnetic permeability for vacuum μ_0 is a known constant. The quantity \tilde{E}^H denotes the TE mode gradient of the electric field, which can be composed from the rotation of the horizontal component electric field quantities \tilde{E}_1 and \tilde{E}_2 via,

$$\tilde{E}^H = -jk_1\tilde{E}_2 + jk_2\tilde{E}_1. \quad (6.43)$$

At depth, the TE mode gradient of the electric field is proportional to the vertical component magnetic field \tilde{H}_3 . We see that we can measure at least four components in an x_1 -oriented borehole, where the magnetic fields are directly measured with coils and the electric fields (\tilde{E}_1) with electrodes. In the space-frequency domain, a few electrodes in the x_2 -direction might be sufficient to measure the spatial derivative in the x_2 -direction of the inline electric field in the x_1 -direction (space-frequency version of equation (6.43)). Since we also know $j\omega\tilde{B}_3$ (space-frequency version of equation (6.41)), we can calculate the derivative of \tilde{E}_2 in the x_1 -direction using the space-frequency versions of equations (6.41) and (6.43). Together with the space-frequency version of equation (6.42), we have access to the required four electromagnetic components of our field vector. However, in the horizontal wavenumber-frequency domain, we encounter some practical issues. Suppose we can measure the spatial derivative of \tilde{E}_1 in the x_2 -direction. Transforming this field to the horizontal wavenumber-frequency domain to determine $jk_2\tilde{E}_1$ requires much more spatial measurements in the x_2 -direction. This is practically impossible since we typically only have one borehole with limited borehole size in the x_2 -direction. Hence, for an x_1 -oriented borehole, we can only transform to the k_1 -domain. Equation (6.43) shows that we then need to measure \tilde{E}_2 , which is practically also impossible due to limited borehole size in this direction.

The system can still be solved in the horizontal wavenumber-frequency domain, in case of a purely 2D situation. In this case mode separation occurs naturally. The TE-mode field vector then reads

$$\tilde{\mathbf{q}}^H = \begin{pmatrix} \tilde{q}_1^H \\ \tilde{q}_2^H \end{pmatrix} = \begin{pmatrix} \tilde{E}_2 \\ -\tilde{H}_1 \end{pmatrix}, \quad (6.44)$$

the TM-mode field vector consists of

$$\tilde{\mathbf{q}}^V = \begin{pmatrix} \tilde{q}_1^V \\ \tilde{q}_2^V \end{pmatrix} = \begin{pmatrix} \tilde{E}_1 \\ \tilde{H}_2 \end{pmatrix}, \quad (6.45)$$

Now, no gradients are required to obtain the necessary fields. When we have an acquisition geometry where the sources are located directly above an x_1 -oriented borehole, \tilde{E}_2 and \tilde{H}_1 are zero in the (x_1, x_3) plane, leaving us with only a *TM*-mode electromagnetic system, which is the desired mode in electromagnetic acquisition for hydrocarbon exploration.

When using these 2D field vectors for the MDL decomposition, it can be easily seen that sufficient field quantities are measurable to carry out field decomposition. The composition matrix $\tilde{\mathbf{L}}$ belonging to these 2D field vectors can be easily derived from the 3D version as presented in Slob (2009). The MDL theory in this section was presented in the horizontal wavenumber-frequency domain. When rewriting the

system in terms of operators, the same MDL scheme can be applied in the space-frequency domain for laterally varying media at the level of decomposition. An example of how to apply these spatial operators for the electromagnetic case can be found in [Van Stralen \(1997\)](#).

From the presented MDL decomposition scheme we know that we either need to measure $\tilde{\mathbf{q}}_1$ or $\tilde{\mathbf{q}}_2$. Depending on the acquisition geometry, we either look at multiple depth level recordings or a single level recording combined with free-surface constraints. None of the presented field quantities in either $\tilde{\mathbf{q}}_1^{H,V}$ or $\tilde{\mathbf{q}}_2^{H,V}$ have a zero-value free-surface boundary constraint. Hence, in order to apply the MDL decomposition scheme to electromagnetic phenomena, we need recordings at at least two depth levels. Whether the borehole is fluid filled or whether the receivers are buried in the subsurface does not make a difference for the electromagnetic case, since all tangential field components are continuous at a horizontal fluid-solid interface ([Nabighian, 1987](#)). However, the borehole wall should be non-metallic.

6.1.C Elastodynamic Field Decomposition

In the elastodynamic case, we organize the two-way field vector as follows

$$\tilde{\mathbf{q}} = \begin{pmatrix} \tilde{\mathbf{q}}_1 \\ \tilde{\mathbf{q}}_2 \end{pmatrix} = \begin{pmatrix} -\tilde{\tau}_{13} \\ -\tilde{\tau}_{23} \\ -\tilde{\tau}_{33} \\ \tilde{v}_1 \\ \tilde{v}_2 \\ \tilde{v}_3 \end{pmatrix}. \quad (6.46)$$

Hence, $\tilde{\mathbf{q}}_1 = -\tilde{\tau}_3$ and $\tilde{\mathbf{q}}_2 = \tilde{\mathbf{v}}$. Since the eigenvectors for arbitrary, laterally invariant subsurface geometries are well-known for the elastodynamic system, we will here not consider the mode separation in independent SH and P-SV propagation modes. Our synthetic elastodynamic examples were based on 2D modeling. In this case, all x_2 -directed field quantities in $\tilde{\mathbf{q}}$ and corresponding eigenvector elements in $\tilde{\mathbf{L}}$ decouple (and do not exist in our 2D example). In equation (6.46), we have organized the field quantities in such a way that the field quantities that are likely to be measured (the particle velocity in $\tilde{\mathbf{q}}_2$) are separated from the ones that are unlikely to be measured (traction components acting on a horizontal plane in $\tilde{\mathbf{q}}_1$). Alternatively, we can organize the field quantities in such a way that the system matrix $\tilde{\mathbf{A}}$ obtains an anti-blockdiagonal symmetry for isotropic media ([Ursin, 1983](#)):

$$\tilde{\mathbf{q}} = \begin{pmatrix} \tilde{\mathbf{q}}_1 \\ \tilde{\mathbf{q}}_2 \end{pmatrix} = \begin{pmatrix} \tilde{v}_3 \\ -\tilde{\tau}_{13} \\ -\tilde{\tau}_{23} \\ -\tilde{\tau}_{33} \\ \tilde{v}_1 \\ \tilde{v}_2 \end{pmatrix}. \quad (6.47)$$

Once the eigenvectors are known for a certain arrangement of the field vector (for example the arrangement of equation (6.46)), one can easily reorganize the field

quantities and eigenvector matrix elements using permutation matrices (Wapenaar & Berkhout, 1989).

For laterally varying media at the level of decomposition, all expressions need to be evaluated in the space-frequency domain, and the use of pseudo-differential operators is required. An example of how to properly use these operators is given in e.g. Grimbergen *et al.* (1998) or Wapenaar *et al.* (2008b), for a 3D acoustic and electromagnetic case, with 2D numerical examples. Elastodynamically, the derivation becomes already much more tedious (Wapenaar & Grimbergen, 1996). In addition, coding everything numerically correct in the space-frequency domain might introduce new challenges. In the space-frequency domain we need to be able to determine the derivative in the x_2 -direction (when considering a borehole in the x_1 -direction), just like for the electromagnetic case discussed previously. Also for pseudo-differential operators, a two-point measurement might not be sufficient to determine these derivatives. Therefore, multiple parallel boreholes (x_1 -oriented boreholes parallel in the x_2 -direction) might be required. A high-density of vertical boreholes (e.g. Bakulin *et al.* (2012b), Bakulin *et al.* (2012a)) might be of use here as well. A practical solution might be to assume the medium is purely 2D and hence has no variations in the x_2 -direction.

6.1.D Seismo-electromagnetic and Poroelastic Field Decomposition

Seismoelectric phenomena deal with the coupling that occurs between seismic and electromagnetic fields, when those fields propagate through a fluid-filled porous medium. The governing equations as derived by Pride (1994), show that this complex physical phenomenon can be described by Biot's poroelasticity equations coupled to Maxwell's electromagnetic equations via a coupling coefficient $\hat{\mathcal{L}}$. The theory as derived by Pride (1994) holds for fluid-saturated porous media, which we will focus on in this appendix. Recently, the theory has been extended to partially saturated porous media (Warden *et al.*, 2013). Since the necessary changes for this extension do not directly affect the eigenvectors of the seismo-electromagnetic system, the theory as presented in this appendix can still be applied.

One can capture the seismo-electromagnetic phenomenon in the form of equation (6.1) (Haartsen & Pride, 1997). When considering a medium that is invariant in two directions, the total system can be separated into two independent propagation modes SH-TE and P-SV-TM. In 2D, this mode separation occurs naturally. The full, mode-coupled eigenvector sets of the seismo-electromagnetic system for any arbitrary subsurface geometry are not known yet. We here focus on the known eigenvectors for the mode separated seismo-electromagnetic system (Pride & Haartsen, 1996; Haartsen & Pride, 1997; Grobbe & Slob, 2013). In the SH-TE mode, the horizontally polarized shear waves are coupled to the transverse electric fields, whereas in the P-SV-TM propagation mode the pressure waves (fast and slow) are coupled to the transverse magnetic fields via the vertically polarized shear waves. Here, P_{fast} describes the fast compressional wave (the P-wave in the elastodynamic system) and P_{slow} describes the diffusive Biot slow compressional field (associated with an

out-of-phase pore-fluid movement compared to the porous material (Kelder, 1998)).

Starting with equation (6.2), the field vector $\tilde{\mathbf{q}}$ can be organized in different ways. We can follow the order of the field quantities as presented by Haartsen & Pride (1997). Alternatively, we here follow the system as used by Grobbe & Slob (2013). The two main differences with the scheme of Haartsen & Pride (1997) are that Grobbe & Slob (2013) have power flux-normalized their derived eigenvectors and in addition have adjusted the system to correctly model situations where the seismo-electromagnetic coupling coefficient is set to zero (i.e. when the poroelastic system decouples from the electromagnetic system). In addition, Grobbe & Slob (2013) make use of an opposite definition of the Fourier Transform (the same one as is used in this section) compared to Haartsen & Pride (1997) and they use particle velocity field vectors instead of displacement vectors.

We can treat the two modes separately in equations (6.1) and (6.2). The field vectors for both the SH-TE (superscript H) and P-SV-TM (superscript V) modes then read

$$\tilde{\mathbf{q}}^H = \begin{pmatrix} \tilde{\mathbf{q}}_1^H \\ \tilde{\mathbf{q}}_2^H \end{pmatrix} = \begin{pmatrix} \tilde{v}_{norm}^{s,H} \\ \tilde{E}_{norm}^H \\ \tilde{\tau}_{norm}^{b,H} \\ -\tilde{H}_{norm}^H \end{pmatrix} \quad (6.48)$$

and

$$\tilde{\mathbf{q}}^V = \begin{pmatrix} \tilde{\mathbf{q}}_1^V \\ \tilde{\mathbf{q}}_2^V \end{pmatrix} = \begin{pmatrix} \tilde{v}_3^s \\ \tilde{w}_3 \\ \tilde{\tau}_{norm}^{b,V} \\ \tilde{H}_{norm}^V \\ \tilde{\tau}_{33}^b \\ -\tilde{p}^f \\ \tilde{v}_{norm}^{s,V} \\ \tilde{E}_{norm}^V \end{pmatrix}. \quad (6.49)$$

The superscript (H or V) indicates that certain field quantities are mode-quantities. This means that the two modes need to be combined in 3D to obtain the true physical field quantities. We have normalized the field quantities of the SH-TE and P-SV-TM mode with a factor $-j\kappa$, such that at the left-hand side and right-hand side of the equation the same physical quantities are written. The different mode-quantities are then defined as follows

$$\tilde{v}_{norm}^{s,H} = \frac{k_1}{\kappa} \tilde{v}_2^s - \frac{k_2}{\kappa} \tilde{v}_1^s, \quad (6.50)$$

$$\tilde{\tau}_{norm}^{b,H} = \frac{k_1}{\kappa} \tilde{\tau}_{23}^b - \frac{k_2}{\kappa} \tilde{\tau}_{13}^b, \quad (6.51)$$

$$\tilde{E}_{norm}^H = \frac{k_1}{\kappa} \tilde{E}_2 - \frac{k_2}{\kappa} \tilde{E}_1, \quad (6.52)$$

$$\tilde{H}_{norm}^H = \frac{k_1}{\kappa} \tilde{H}_1 + \frac{k_2}{\kappa} \tilde{H}_2, \quad (6.53)$$

$$\tilde{v}_{norm}^{s,V} = \frac{k_1}{\kappa} \tilde{v}_1^s + \frac{k_2}{\kappa} \tilde{v}_2^s, \quad (6.54)$$

$$\tilde{\tau}_{norm}^{b,V} = \frac{k_1}{\kappa} \tilde{\tau}_{13}^b + \frac{k_2}{\kappa} \tilde{\tau}_{23}^b, \quad (6.55)$$

$$\tilde{E}_{norm}^V = \frac{k_1}{\kappa} \tilde{E}_1 + \frac{k_2}{\kappa} \tilde{E}_2, \quad (6.56)$$

$$\tilde{H}_{norm}^V = \frac{k_1}{\kappa} \tilde{H}_2 - \frac{k_2}{\kappa} \tilde{H}_1. \quad (6.57)$$

This normalization additionally aims to obtain a certain symmetry in the P-SV-TM system matrix $\tilde{\mathbf{A}}^V$ that helps to determine the power flux-normalized eigenvectors of the composition matrix $\tilde{\mathbf{L}}^V$. In the above, \tilde{v}_i^s (with $i = 1, 2$ or 3) denote the phase-averaged solid particle velocity field components, \tilde{w}_3 the vertical component of the Biot filtration velocity, \tilde{p}^f the phase-averaged fluid pressure, $\tilde{\tau}_{i3}^b$ the bulk-averaged stress components in the x_3 -direction, and \tilde{E}_α and \tilde{H}_α the horizontal components of the electric field and magnetic field, respectively (with $\alpha = 1$ or 2).

We know that for MC field decomposition all field quantities in $\tilde{\mathbf{q}}$ must be measured. For seismo-electromagnetics, a large number of field quantities needs to be measured. In reality, not all field quantities can be measured (e.g. certain stress field components or the filtration velocity are not measurable). They also might be obscured by different sensor characteristics or noise levels. Finally, requiring to measure many different quantities in the field makes the operation financially and practically unfavourable.

From equations (6.28) and (6.29), we know that the MDL scheme is customizable. We can select those field quantities that are easily measurable in reality, or that are well-defined by certain boundary conditions. We thereby need to take care that the customized composition matrix is of sufficient rank and notch problems are properly taken care of.

We focus on a single horizontal sensor array at depth level $x_{3;B}$ and $x_{3;A}$ coinciding with the free surface. If we make use of the dynamic boundary conditions (Aki & Richards, 1980), this implies that all stress components go to zero at the free surface: $\tilde{\tau}^{b,H,V} = 0$ and $\tilde{p}^f = 0$. Constraining the stress implies that the particle velocity fields (kinematic boundary conditions) are then ‘free’ variables. In addition, at the free surface, continuity of the horizontal components of the electromagnetic field quantities holds. We can carry out MDL decomposition by having measurements of either $\tilde{\mathbf{q}}_1$ or $\tilde{\mathbf{q}}_2$ at $x_{3;B}$, with the field quantity subvector at $x_{3;A}$ being equal to zero. In the case of the SH-TE system, this means that we need at least two field quantities equal to zero and have two measured quantities. For the P-SV-TM system, we need four field quantities equal to zero and four measured quantities.

For Controlled Source Electromagnetics (CSEM), the TM-mode magnetic field \tilde{H}^V can be taken zero at the Earth’s surface under the diffusive field approximation (Nabighian, 1987). Looking at the P-SV-TM system, we can now see that we have four quantities that are zero at the free surface (the stress quantities, pore-fluid pressure and the P-SV-TM mode magnetic field). At the measurement level $x_{3;B}$,

we then need to select 4 quantities that we can measure, for example \tilde{v}_3^s , \tilde{E}_{norm}^V , \tilde{p}^f , \tilde{H}_{norm}^V or $\tilde{v}_{norm}^{s,V}$. Two of those quantities are directly measurable in the borehole \tilde{v}_3^s and \tilde{p}^f . From the electromagnetic scenario we concluded that due to limited borehole dimensions, we can only transform to the k_1 -domain (for an x_1 -oriented borehole). So all combined mode quantities in the horizontal wavenumber-frequency domain are hard to obtain since they all require an additional transformation to the k_2 -domain. A difference between the mode electric fields and for example the mode particle velocity fields is that the \tilde{E}_2 component is additionally not measurable in an x_1 -directed borehole due to the limited borehole size, whereas both the \tilde{v}_1^s and \tilde{v}_2^s particle velocity components are measurable.

When we carry out the field decomposition in the space-frequency domain, we can determine the spatial derivatives with respect to the x_1 - and possibly also with respect to the x_2 -directions. We can then obtain the four required field quantities to carry out the MDL decomposition: \tilde{v}_3^s and \tilde{p}^f , $\tilde{v}_{norm}^{s,V}$ and \tilde{H}_{norm}^V . However, for this we need to be able to derive correct pseudo-differential operators, which will be extremely tedious for this complex physical phenomenon.

It is good to be aware that certain seismo-electromagnetic source-receiver combinations (for example looking at a horizontal electric field in the x_1 -direction \tilde{E}_1 due to a vertical seismic bulk force source \tilde{f}_3^b), are purely described by the P-SV-TM propagation mode (Grobbe & Slob, 2013). Hence, for these recorded source-receiver combinations, MDL decomposition according to the P-SV-TM mode only is sufficient.

For the SH-TE case, we see that only the stress field $\tilde{\tau}^{b,H}$ is zero at the free surface. The second required quantity at $x_{3,A}$ should then be measured. So, we can place for example a vertical magnetic coil at the free surface and measure \tilde{E}^H . Combining surface and buried measurements is for practical purposes not so attractive, since surface measurements suffer too much from low fidelity, significant noise (e.g. surface waves or power line noise) and low repeatability. However, when $x_{3,A}$ coincides with the Earth's surface, we are for our measurements not limited in any horizontal spatial direction. At depth level $x_{3,B}$ we can then select two field quantities we would like to measure to solve the MDL decomposition problem for the SH-TE mode. Since \tilde{E}^H is directly measurable (equation (6.41)) this is a logical choice. However, when trying to obtain the mode quantities \tilde{H}^H and \tilde{v}^H , the same issues are encountered as discussed above for the P-SV-TM case. Luckily, as discussed in the other appendices, we can still solve the seismo-electromagnetic MDL decomposition problem in the horizontal wavenumber-frequency domain in case of a purely 2D situation.

When we look at the dual depth horizontal sensor arrays, we can select the desired measurable field quantities for each mode at both depth levels $x_{3,A}$ and $x_{3,B}$ and adjust the composition matrix $\tilde{\mathbf{S}}$ accordingly. The issues in obtaining certain field quantities due to limited borehole size now play a role at both depth levels.

Sometimes the mode splitting into SH-TE and P-SV-TM propagation modes might not be useful or even not applicable, for example when we are considering anisotropic media or in non-layered Earth systems. Alternatively, we can take the field vector as defined in Wapenaar & Fokkema (2004), where all physical field

quantities are directly present. However, this system is probably redundant and the decomposition problem might be solvable with less field quantities (comparable to the electromagnetic case of Appendix B). Theoretically, we can describe the field decomposition starting from equation (6.2). However, the composition matrix $\tilde{\mathbf{L}}$ consisting of the eigenvectors of the full non-mode separated system of seismo-electromagnetic equations is not yet derived. Furthermore, the equations should be explicitly extended for anisotropic media. Nevertheless, if we assume that we know the corresponding eigenvectors of the system of equations, we can select desired measured field quantities and carry out MDL decomposition according to the presented scheme. In this case we do not suffer from separate modes and mode quantities that need to be combined via spatial derivatives and hence also not from issues when transforming to the horizontal wavenumber-frequency domain.

The poroelastic system can be considered as a special case of the seismo-electromagnetic system. If the seismo-electromagnetic coupling coefficient $\hat{\mathcal{L}}$ is equal to zero, there is no coupling between the poroelastic system and the electromagnetic system. In this case, we can treat the electromagnetic system and the poroelastic system separately (Grobbe *et al.*, 2014).

We can obtain the mode-separated poroelastic field vectors directly from the seismo-electromagnetic field vectors by omitting the electromagnetic field quantities from equations (6.48) and (6.49) and keeping the order of the mechanical field quantities the same.

So, starting from the seismo-electromagnetic eigenvectors used by Grobbe & Slob (2013), removing the columns belonging to the TE and TM mode electromagnetic fields and putting the coupling coefficient to zero, results in the poroelastic eigenvectors corresponding to this poroelastic field vector ordering. Alternatively, Jocker *et al.* (2004) derive and present the poroelastic eigenvectors for a 2D scenario. As discussed earlier, when we have line recordings in a borehole, this results effectively in a 2.5D or 2D scenario. For the 2.5D scenario, we again encounter the same issues in obtaining the mode quantities due to the limited size of a borehole. In 2D, the mode separation in SH and P-SV modes occurs naturally, assuming line sources in the x_2 -direction. In 2D the MDL decomposition problem is straightforwardly solvable, similar to the scenarios discussed for seismo-electromagnetic fields.

Alternatively to mode separation, the full poroelastic system and corresponding eigenvectors for arbitrary subsurface geometries can be used. However, to our knowledge, the eigenvector system forming the composition matrix for 3D poroelastic fields is not yet published. If these eigenvectors are known, we can select desired measured field quantities. Measurements of four field quantities, e.g. three component particle velocity recordings in combination with pore fluid pressure measurements, would be sufficient to solve the MDL decomposition problem for poroelastic fields.

6.2 Towards Inversion: Electromagnetic and seismo-electromagnetic sensitivity analysis using resolution functionsⁱⁱ

6.2.1 Abstract

We explore the use of resolution functions for the sensitivity analysis of the coupled seismo-electromagnetic system, which is a multi-parameter problem. Using this resolution function analysis, we aim to provide a fast method to determine whether seismo-electromagnetic signals are sensitive to certain subsurface parameters of interest. We here present a first step in this direction. We start by explaining the theory of resolution functions using a seismo-electromagnetic example. We define the seismo-electromagnetic resolution function for inversion for a bulk density perturbation. We compute this resolution function as the least-squares solution to the normal equation. The synthetic data and Green's functions required to construct the resolution function are computed with our seismo-EM layer-code. We demonstrate the effectiveness of this method by first carrying out a purely electromagnetic sensitivity analysis for a point perturbation in conductivity, located in an isotropic homogeneous half-space. These results are compared with literature results based on analytical homogeneous space Green's function expressions. The result using the seismo-EM layer-code modeling is nearly identical to the literature result. The position of the scatterer is correctly resolved. We continue by investigating the electromagnetic sensitivity to point scatterers in a layered background medium, located above and below highly conductive layers. Again, the resolution function is capable of correctly mapping the scatterer when it is above as well as below a layer of increased conductivity. Having a scatterer below this highly conductive layer leads to a lower resolution. We finalize by presenting the results of the fully-coupled seismo-electromagnetic sensitivity analysis for a bulk density contrast for a specific source-receiver combination, using single-frequency multi-component line data. We show that the coupled seismo-electromagnetic system is sensitive to a perturbation in bulk density and that the position of the perturbation can be correctly recovered. This paves the way for studying the seismo-electromagnetic sensitivity for other medium parameters, such as the seismo-electromagnetic coupling coefficient, as well as for other source-receiver combinations.

6.2.2 Introduction

Several studies have already shown that the seismo-electromagnetic method can provide supplemental information about porosity, permeability, and pore-fluid properties such as viscosity (Haines & Pride, 2006; Revil *et al.*, 2007). This offers potential to use seismo-electromagnetic signals for detecting and monitoring e.g. gas-water

ⁱⁱThis section has been published as an extended abstract paper at the *EAGE Conference & Exhibition* (Maas *et al.*, 2015), and as a conference paper at the *Japan Geoscience Union Meeting* (Grobbe *et al.*, 2015). Note that additions have been made, and changes have been introduced to make the text consistent with the other chapters of this thesis.

and oil-water contacts (Smeulders *et al.*, 2014). It can also offer useful applications in the field of hydrology/hydrogeophysics, e.g. for characterizing and monitoring aquifers (Dupuis *et al.*, 2007). Furthermore, seismo-electromagnetic signals might provide information on the near-borehole flow properties by the use of well-logging techniques (Zhu & Toksöz, 2005). We can observe that these medium parameters (e.g. porosity, permeability, and viscosity) are explicitly present in the governing equations describing the seismo-electromagnetic phenomenon (Section 2.1). The big question is, how sensitive is the seismo-electromagnetic system actually to these parameters?

Since the seismo-electromagnetic effect is determined by a combination of many subsurface parameters which are often mutually related, inversion of seismo-electromagnetic data for each of these parameters individually is costly. Therefore, performing a sensitivity analysis prior to inversion is crucial. It can, for example, focus on acquisition design or investigate time-lapse perturbations and more importantly, show whether the measured fields are actually sensitive to the parameter of interest. Applying a quasi-static electromagnetic approach helps to simplify the system, which can be beneficial to further develop the seismo-electromagnetic method towards imaging and inversion (Jardani *et al.*, 2010; Mahardika *et al.*, 2012; Sava & Revil, 2012; Revil *et al.*, 2015). We here present a first step towards resolution function analysis, aiming to provide a low-cost, fast method for determining the sensitivity of seismo-electromagnetic signals to certain subsurface parameters.

We start by presenting the theory of resolution functions using a specific seismo-electromagnetic example: we derive the resolution function for inversion for a bulk density contrast, for a specific seismo-electromagnetic source-receiver combination. Afterwards, we illustrate the sensitivity analysis by comparing an EM parameter sensitivity analysis for a point perturbation in conductivity using seismo-EM layer-code data, with literature results based on analytical homogeneous space Green's function expressions. We follow-up by investigating the EM sensitivity to point scatterers above and below highly conductive layers. We then present the results of the fully-coupled seismo-electromagnetic sensitivity analysis for a bulk density contrast, using single-frequency multi-component line data.

6.2.3 Theory: seismo-electromagnetic resolution function for bulk density contrast

Let us start by defining a large background (or incident) domain \mathbb{D} , in which the smaller scattering domain \mathbb{D}^s is embedded ($\mathbb{D}^s \subset \mathbb{D}$). The background model is known throughout \mathbb{D} (including \mathbb{D}^s), whereas the actual scattering parameters in the scattering domain are unknown (see Figure 6.18). The scattering domain is in most cases inconvenient or inaccessible for direct measurements, and is often an area of interest such as a hydrocarbon reservoir. The objective of inverse scattering problems is to gather information about the scattering domain from observations outside of that domain (Oristaglio & Blok, 1995). The incident domain is associated with the incident field: the field that is present in the entire domain if the scattering domain has no contrast with the background domain. The scattered field is the field

resulting from the interaction between the incident field, the contrast in medium parameters between the incident and scattered domain and the total wavefield inside the scattering domain. The incident field and the scattered field together form the total field (Fokkema & Van den Berg, 1993):

$$\hat{u}(\mathbf{x}, \omega) = \hat{u}^i(\mathbf{x}, \omega) + \hat{u}^s(\mathbf{x}, \omega), \quad (6.58)$$

where $\hat{u}(\mathbf{x}, \omega)$ is the total field, $\hat{u}^i(\mathbf{x}, \omega)$ denotes the incident field, and $\hat{u}^s(\mathbf{x}, \omega)$ represents the scattered field. The sources of the total wavefield are located outside the scattering domain, but inside the background domain. In a situation where the scattering has the same parameters as the background domain, the sources remain present and therefore form the sources of the incident field (Fokkema & Van den Berg, 1993). We assume that we know the medium parameters of the background domain, and hence we know the incident wavefield, which can be expressed as a background Green's function. We extend the boundary $\partial\mathbb{D}$ of the background domain to infinity, for which, in the case that both reciprocity states A and B are causal in time (applying to physical wavefields), the far-field solutions for the wave equations apply, resulting in a vanishing surface integral contribution in the reciprocity expression (based on Gauss' theorem) (Fokkema & Van den Berg, 1993; De Hoop, 1995).

Expressing the scattered wavefield in terms of an integral equation, we can write equation (6.58) in general terms as

$$\hat{u}(\mathbf{x}, \omega) = \hat{u}^i(\mathbf{x}, \omega) + \int_{\mathbb{D}^s} \hat{G}_0(\mathbf{x}, \mathbf{x}', \omega) \chi(\mathbf{x}', \omega) \hat{u}(\mathbf{x}', \omega) d^3\mathbf{x}', \quad \mathbf{x} \notin \mathbb{D}^s, \quad (6.59)$$

where $\hat{G}_0(\mathbf{x}, \mathbf{x}', \omega)$ is the incident field expressed as a background Green's function, $\chi(\mathbf{x}', \omega)$ represents the scattering contrast, and $\hat{u}(\mathbf{x}', \omega)$ is the total field in the scattering domain. Since the scattering contrast as well as the total field in the scattering domain are both unknowns, we have an underdetermined problem. We need an additional constraint on the total field in the scattering domain. We can define the same equation as (6.59), but now for the condition that $\mathbf{x} \in \mathbb{D}^s$. We can substitute this equation in equation (6.59) and solve it iteratively, using a Neumann series expansion (Born, 1926). If we consider first order scattering only (single scattering from each point in the scattering domain), we select the first two terms of this expansion: the incident field and first order scattering term, to approximate the total field $\hat{u}(\mathbf{x}, \omega)$. Using this so-called Born approximation, the total field may be defined in the space-frequency domain as the following integral equation (Oristaglio & Blok, 1995; Maas, 2014)

$$\hat{u}^{(1)}(\mathbf{x}, \omega) = \hat{u}^i(\mathbf{x}, \omega) + \int_{\mathbb{D}^s} \hat{G}_0(\mathbf{x}, \mathbf{x}', \omega) \chi(\mathbf{x}', \omega) \hat{u}^i(\mathbf{x}', \omega) d^3\mathbf{x}', \quad (6.60)$$

where, $\hat{u}^{(1)}$ denotes that it is the first order approximation of \hat{u} , and where we can observe that the total field in the scattering domain is approximated by the incident field (see also Figure 6.18).

Let us now consider a specific seismo-electromagnetic case, for the total particle velocity field due to an electric current source $\hat{G}_{js}^{ve}(\mathbf{x}^r, \mathbf{x}^s, \omega)$, with a scattering

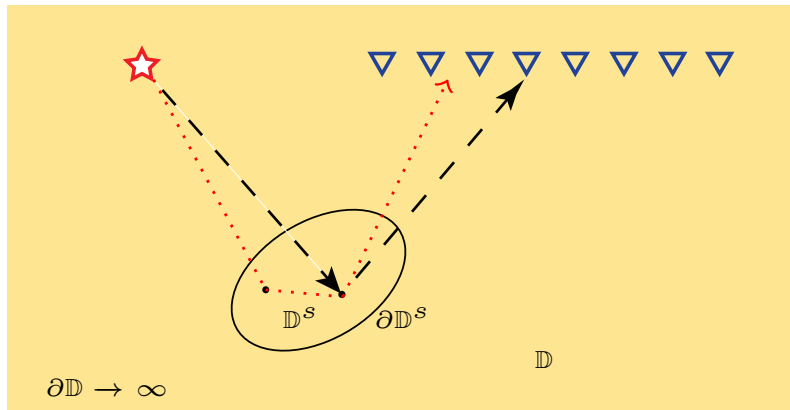


Figure 6.18: Schematic illustration of the incident (background) domain and the scattering domain and their boundaries. The black-dashed scattering path corresponds to the Born approximation, where the incident field is scattered once by each point in the object. The red-dotted scattering path corresponds to second-order scattering in the Neumann series. Figure is adapted from (Oristaglio & Blok, 1995; Maas, 2014).

domain containing a spatially-dependent bulk density contrast function $\chi^\rho(\mathbf{x}) = (\hat{\rho}_A^b - \hat{\rho}_B^b)$, where A represents the incident reciprocity state and B represents the true state. Using the Born approximation, we can express the total field as the following integral equation:

$$\hat{G}_{js}^{ve}(\mathbf{x}^r, \mathbf{x}^s, \omega) = \hat{G}_{js}^{ve;i}(\mathbf{x}^r, \mathbf{x}^s, \omega) + \int_{\mathbb{D}^s} [\chi^\rho(\mathbf{x}) \hat{D}_{js}(\mathbf{x}^r, \mathbf{x}^s, \mathbf{x}, \omega)] d^3\mathbf{x}. \quad (6.61)$$

Equation (6.61) holds for a fixed pair of source- and receiver-locations \mathbf{x}^s and \mathbf{x}^r , respectively. It shows that the total field is the sum of the incident field and scattered field, which consists of the contribution of all scatterers \mathbf{x} within the scattering domain \mathbb{D}^s . When we would express the equations in terms of the underlying defined reciprocity states A (incident state) and B (true state), then $\mathbf{x}^s = \mathbf{x}_B$ and $\mathbf{x}^r = \mathbf{x}_A$ (Maas, 2014). In equation (6.61), \hat{G}_{js}^{ve} denotes the first order Green's field for the j -component of the particle velocity field generated by the s -component of an electric current source. The additional superscript i indicates the Green function describes an incident field. All Green's functions together form a three-by-three Green's function matrix. Furthermore, the two-way wavefield operator is defined as

$$\hat{D}_{js}(\mathbf{x}^r, \mathbf{x}^s, \mathbf{x}, \omega) = j\omega \hat{G}_{jm}^{vf;i}(\mathbf{x}^r, \mathbf{x}, \omega) \hat{G}_{ms}^{ve;i}(\mathbf{x}, \mathbf{x}^s, \omega), \quad (6.62)$$

where $\hat{G}_{jm}^{vf;i}$ is the incident Green's particle velocity field generated by a bulk-force source. Resolving for the contrast function is our goal, the resulting expression is the resolution function for a bulk density contrast. Since we are dealing with a linearized

inverse problem, the contrast cannot be too large with respect to the background model, since otherwise the higher order scattering terms cannot be neglected (Born & Wolf, 1980; Habashy *et al.*, 1993; Wapenaar *et al.*, 2010).

To obtain the desired expression for the resolution function, it is assumed that the inverse two-way wavefield operator $\hat{\mathcal{D}}_{kr}(\mathbf{x}^r, \mathbf{x}^s, \mathbf{x}, \omega)$ (note the different use of \mathcal{D}) satisfies Fourier orthogonality and is defined as follows

$$\int_{\omega=-\infty}^{\infty} \int_{\mathbf{x}^r \in \mathbb{R}^2} \int_{\mathbf{x}^s \in \mathbb{R}^2} \hat{\mathcal{D}}_{rk}(\mathbf{x}^r, \mathbf{x}^s, \mathbf{x}^I, \omega) \hat{\mathcal{D}}_{rp}(\mathbf{x}^r, \mathbf{x}^s, \mathbf{x}, \omega) d^2\mathbf{x}^s d^2\mathbf{x}^r d\omega = \delta_{kp} \delta(\mathbf{x} - \mathbf{x}^I). \quad (6.63)$$

If a possible image location \mathbf{x}^I coincides with a true scattering location \mathbf{x} then the resolution function will show an image in that location only, when considering a perfect solution with infinite bandwidth. However, in case of limited bandwidth, smearing around that scattering location will occur, and instead, the resolution function will highlight a volume in which the scatterer is likely to be located.

Alternative definitions of the inverse two-way wavefield operator are also possible:

$$\int_{\omega=-\infty}^{\infty} \int_{\mathbf{x}^r \in \mathbb{R}^2} \int_{\mathbf{x}^s \in \mathbb{R}^2} \hat{\mathcal{D}}_{rp}(\mathbf{x}^r, \mathbf{x}^s, \mathbf{x}^I, \omega) \hat{\mathcal{D}}_{rp}(\mathbf{x}^r, \mathbf{x}^s, \mathbf{x}, \omega) d^2\mathbf{x}^s d^2\mathbf{x}^r d\omega = \delta(\mathbf{x} - \mathbf{x}^I), \quad (6.64)$$

or

$$\int_{\omega=-\infty}^{\infty} \int_{\mathbf{x}^r \in \mathbb{R}^2} \int_{\mathbf{x}^s \in \mathbb{R}^2} \hat{\mathcal{D}}_{RP}(\mathbf{x}^r, \mathbf{x}^s, \mathbf{x}^I, \omega) \hat{\mathcal{D}}_{RP}(\mathbf{x}^r, \mathbf{x}^s, \mathbf{x}, \omega) d^2\mathbf{x}^s d^2\mathbf{x}^r d\omega = \delta(\mathbf{x} - \mathbf{x}^I), \quad (6.65)$$

where for equation (6.65) the Einstein summation convention does not hold, indicated by the capitalized subscripts.

In this study, we choose (6.63) as the definition for the inverse two-way wavefield operator. This choice allows for studying the separate sensitivities of different source-receiver components, whereas equation (6.64) implicitly sums over all source-receiver components, which might lead to enhanced resolution. Equation (6.65) can be used to study the sensitivity using single component data, for example in situations where not all source-receiver components are available. Applying the inverse operator of equation (6.63) to both the left- and right-hand side of the expression for the scattered field (equation (6.61) without the incident field), we obtain a *resolution function for inversion* for a bulk density point perturbation:

$$\chi^{\rho;Inv}(\mathbf{x}^I) \delta_{kp} = \int_{\omega=-\infty}^{\infty} \int_{\mathbf{x}^r \in \mathbb{R}^2} \int_{\mathbf{x}^s \in \mathbb{R}^2} \hat{\mathcal{D}}_{rk}(\mathbf{x}^r, \mathbf{x}^s, \mathbf{x}^I, \omega) \hat{G}_{rp}^{ve;s}(\mathbf{x}^r, \mathbf{x}^s, \omega) d^2\mathbf{x}^s d^2\mathbf{x}^r d\omega. \quad (6.66)$$

Note that $\hat{G}_{rp}^{ve;s}(\mathbf{x}^r, \mathbf{x}^s, \omega)$ is the scattered particle velocity field due to an electric current source, under the Born approximation. Let us now briefly discuss how

we properly deal with the amount of data involved. More details can be found in [Maas \(2014\)](#). To calculate the seismo-electromagnetic resolution function, we are dealing with modeled results of two seismo-electromagnetic source-receiver type combinations. This already increases the size of the problem significantly, compared to for example the purely electromagnetic scenario ([Slob & Mulder, 2011](#)). We use a data matrix to describe the two-way field operator, which consists of data submatrices. These data submatrices consist of the amount of sources (actual shots) times receivers (actual recording devices) as the number of rows, and the amount of possible image locations (amount of x_1 times x_3) as the number of columns. For the seismo-electromagnetic system under consideration, the two-way field operator, $\hat{\mathbf{D}}$ in matrix notation, contains all source-side and receiver-side multicomponent field data for all possible image locations \mathbf{x}^I , and consists of nine data submatrices, arranged as

$$\hat{\mathbf{D}} = \begin{bmatrix} \hat{\mathbf{D}}_{11} & \hat{\mathbf{D}}_{12} & \hat{\mathbf{D}}_{13} \\ \hat{\mathbf{D}}_{21} & \hat{\mathbf{D}}_{22} & \hat{\mathbf{D}}_{23} \\ \hat{\mathbf{D}}_{31} & \hat{\mathbf{D}}_{32} & \hat{\mathbf{D}}_{33} \end{bmatrix}, \quad (6.67)$$

Each data submatrix is computed according to equation (6.62). For example, the data submatrix $\hat{\mathbf{D}}_{11}$ is filled with

$$\hat{D}_{11}(\mathbf{x}^r, \mathbf{x}^s, \mathbf{x}, \omega) = j\omega \left(\hat{G}_{11}^{vf;i} \hat{G}_{11}^{ve;i} + \hat{G}_{12}^{vf;i} \hat{G}_{21}^{ve;i} + \hat{G}_{13}^{vf;i} \hat{G}_{31}^{ve;i} \right), \quad (6.68)$$

for all sources and receivers and all possible image locations. Here, we have applied the Einstein summation convention. This single data submatrix has exactly the same size as the data matrix for the EM problem ([Slob & Mulder, 2011](#)). However, the EM problem consists of single component data, whereas this specific seismo-electromagnetic sub-data matrix consists of several field components. Note that if we would have chosen the definition of equation (6.64) as the definition for our inverse two-way wavefield operator, we would arrange the data submatrices (still having the amount of sources (actual shots) times receivers as the number of rows, and the amount of possible image locations (amount of x_1 times x_3) as the number of columns) in equation (6.67) in one column below each other, resulting in a 9 times 1 data vector consisting of data submatrices. Choosing the definition of equation (6.65) would result in a data matrix $\hat{\mathbf{D}}$ consisting of one data submatrix.

We can define $\hat{\mathbf{D}}^\dagger$ as the complex conjugate transpose of $\hat{\mathbf{D}}$, where the superscript dagger denotes complex conjugation and transposition. Note that in this way, the transposition and complex conjugation applies to the matrix as a whole. The scattered data matrix $\hat{\mathbf{S}}$ contains the *true* scattered data, computed for a known bulk density point perturbation at the *true* scattering location \mathbf{x} . We define this scattered data matrix in a similar way as the two-way field operator, where now each data submatrix is a vector of size (number of sources times number of receivers) times 1. As a result, the resolution function data matrix consists of data submatrices (therefore the bold face symbol) having size (amount of image locations x_1 times amount

of image locations x_3) times 1, arranged as:

$$\chi^{\rho;Inv} = \begin{bmatrix} \chi_{11} & \chi_{12} & \chi_{13} \\ \chi_{21} & \chi_{22} & \chi_{23} \\ \chi_{31} & \chi_{32} & \chi_{33} \end{bmatrix}. \quad (6.69)$$

Each data submatrix of the resolution function data matrix $\chi^{\rho;Inv}$ that we solve for, represents one seismo-electromagnetic sensitivity function for the entire investigated area. The diagonal elements represent three estimates of the resolution function. The off-diagonal elements should theoretically be equal to zero. Note that if we would have chosen the definition of equation (6.64) as the definition for our inverse two-way wavefield operator, the resulting resolution function data matrix $\chi^{\rho;Inv}$ would consist of a single data submatrix, representing the resolution function that we are after, which would be based upon all source-receiver component data. This could possibly offer a better resolution than the three resolution estimates of equation (6.69). Alternatively, if we would have chosen equation (6.65) as the definition for our inverse two-way wavefield operator, the resulting resolution function data matrix $\chi^{\rho;Inv}$ would also consist of a single data submatrix, but now based upon single-component data.

Following Slob & Mulder (2011), we compute the formal resolution function by expressing the scattering problem as the *normal equation* for a linear inverse problem for subsurface scatterers. as (Maas, 2014):

$$\underline{\hat{\mathbf{D}}}^\dagger \underline{\hat{\mathbf{D}}} \chi^{\rho;Inv} = \underline{\hat{\mathbf{D}}}^\dagger \hat{\mathbf{S}}. \quad (6.70)$$

Note that the matrix multiplications yield implicit summation over all sources and receivers. Additionally, we could choose to apply a summation over different frequencies as well (Slob & Mulder, 2011). In our seismo-electromagnetic examples, we only consider single-frequency data.

The regularized least-squares solution of 6.70 then reads

$$\chi^{\rho;Inv} = \left(\underline{\hat{\mathbf{D}}}^\dagger \underline{\hat{\mathbf{D}}} + \varepsilon \mathbf{I} \right)^{-1} \underline{\hat{\mathbf{D}}}^\dagger \hat{\mathbf{S}}, \quad (6.71)$$

where \mathbf{I} is the identity matrix and ε the regularization parameter.

6.2.4 Numerical Results

We now present the results of three sensitivity analysis scenarios: a purely EM scenario with a single conductivity scatterer in an isotropic homogeneous background medium, a purely EM scenario with a single conductivity scatterer in a layered background medium containing a highly conductive layer, and a coupled seismo-electromagnetic scenario for a single bulk density contrast function in an isotropic homogeneous background medium. The line acquisition geometry used for these experiments consists of 201 sources located at the surface with a horizontal source spacing of 25 m, combined with a line of 41 receivers, located 50 m below the surface with a horizontal receiver spacing of 250 m. For the EM scenarios, these sources

and receivers are x_1 -directed electric current sources and electrodes, whereas for the seismo-electromagnetic scenario we use three-component electric current sources, three-component bulk-force sources, and three-component particle velocity receivers. The investigated area is centrally located in the (x_1, x_3) -plane directly below the acquisition line and has a total offset of 3000 m and a depth coverage of up to 1600 m (see Figure 6.20 for the geometry). We use our seismo-EM layer-code to generate the synthetic data used to resolve for the contrast functions. We model an isotropic homogeneous half-space, or a layered-Earth model, computing the multi-component response to a unit-impulse source for all source-side and receiver-side fields. For the purely EM scenario, the seismo-electromagnetic coupling coefficient is chosen equal to zero. Our seismo-EM layer-code generates 3D data cubes. From these data cubes, we select the vertical cross-section through our line-acquisition geometry, corresponding with the sensitivity analysis study-area. This might result in amplitude differences, for example when comparing with purely 2D homogeneous space solutions. The EM resolution functions are calculated for a single frequency of 0.5 Hz, the seismo-electromagnetic resolution functions for a single frequency of 30 Hz.

To test our sensitivity analysis resolution function-approach, we first investigate the scalar resolution function for a conductivity point perturbation for a purely EM scenario, as derived by Slob & Mulder (2011). Figure 6.19-a shows the EM resolution

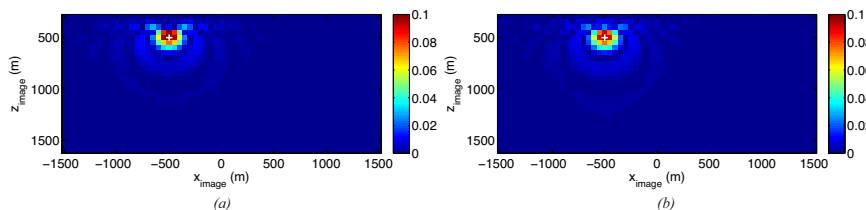


Figure 6.19: EM resolution functions for inversion, (a) from Green's function solutions, and (b) obtained using seismo-EM layer-code data for a single frequency of 0.5 Hz. The white 'plus'- sign indicates the true location of the conductivity point perturbation $(-500, 500)$ m.

function for inversion where both the two-way field operator as well as the data were computed through the use of explicit analytical homogeneous-space Green's function solutions (Slob & Mulder, 2011). Figure 6.19-b presents the resolution function for the case where both the two-way field operator as well as the data have been computed using our seismo-EM forward modelling layer-code, assuming that there is no coupling between mechanical waves and electromagnetic fields. We observe that in both cases the resolution function is capable of correctly mapping the conductivity perturbation, where the horizontal location and depth location are equally well resolved. We also observe that both approaches deliver nearly identical results. This provides a solid basis for extending the sensitivity analysis to the fully coupled seismo-electromagnetic system. In addition, it allows us to explore more complex cases for which deriving explicit analytical solutions is more challenging, like a layered-Earth scenario.

Figure 6.20 presents the geometry used for the EM sensitivity analysis in a layered

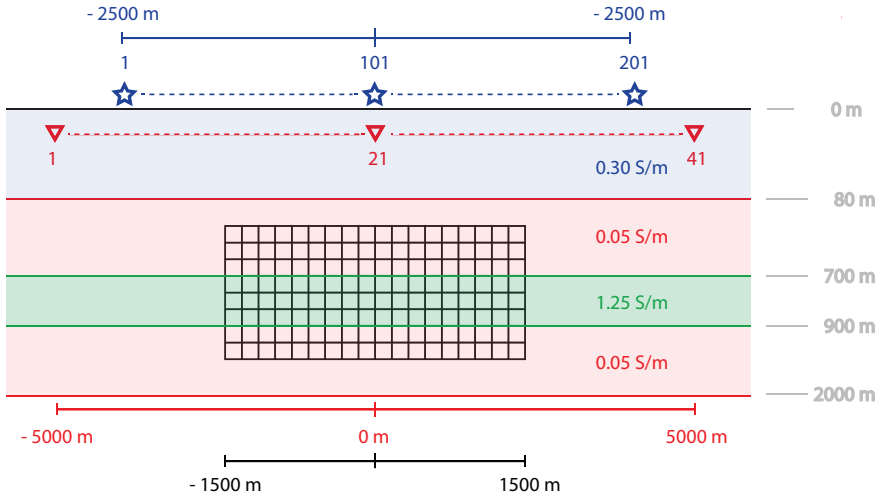


Figure 6.20: Geometry of the layered-Earth model containing a highly conductive layer. We try to resolve the EM resolution functions for a conductivity point perturbation in this model.

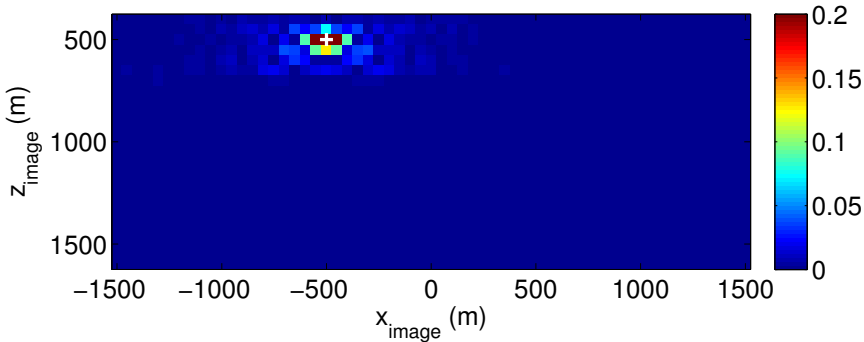


Figure 6.21: EM resolution function for a conductivity point perturbation at $(-500, 500)$ m, located above the highly conductive layer in the layered background medium, for a single frequency of 0.5 Hz.

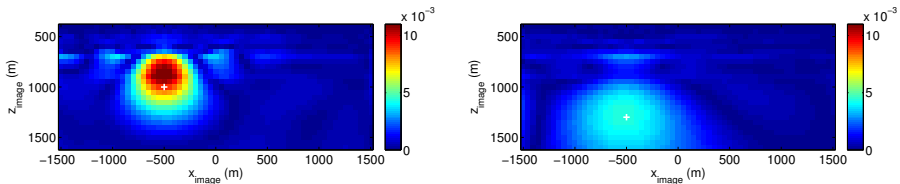


Figure 6.22: EM resolution function for a conductivity point perturbation at (a) $(-500, 1000)$ m, and (b) $(-500, 1300)$ m, both located below the highly conductive layer in the layered background medium, for a single frequency of 0.5 Hz.

background medium. Figure 6.21 shows the EM sensitivity analysis for a conduct-

ivity perturbation above a layer of increased conductivity. We observe that the resolution function maps the position of the scatterer correctly. Figures 6.23a and 6.23b present the results of the sensitivity analysis for scatterers located at two depth levels below the layer of increased conductivity. We now observe that, although the EM resolution function more or less correctly maps the perturbations, the resolution has clearly deteriorated, especially for the deepest located scatterer. This is probably related to the fact that the highly conductive layer above the scatterers strongly reflects the incident field back towards the surface, decreasing the amount of transmitted energy that is available to illuminate the scatterers below.

Let us now look at the results of the coupled seismo-electromagnetic sensitivity analysis for a bulk density perturbation located at $(-500, 500)$ m in a homogeneous background medium. Figures 6.23-a and 6.23-c show the diagonal element χ_{22}^{ρ} , whereas figures 6.23-b and 6.23-d present the off-diagonal element χ_{31}^{ρ} of the seismo-electromagnetic contrast function matrix. This result was computed according to equation (6.71) where the regularization parameter ε was chosen by using the maximum of the approximate Hessian ($\hat{\mathbf{D}}^{\dagger} \hat{\mathbf{D}}$) and multiplying it with an arbitrary small number (10^{-5}), resulting in $\varepsilon = 9.3 \cdot 10^{-33}$. We can observe that the diagonal element χ_{22}^{ρ} clearly resolves the density perturbation at the correct location. At the same time, it can be seen that the off-diagonal elements show resolution patterns with amplitudes that are generally one order smaller than the diagonal elements of the contrast function matrix. Based on equation (6.66) this is to be expected: in an ideal case, the diagonal terms show a clear point-response whereas the off-diagonal terms should be zero.

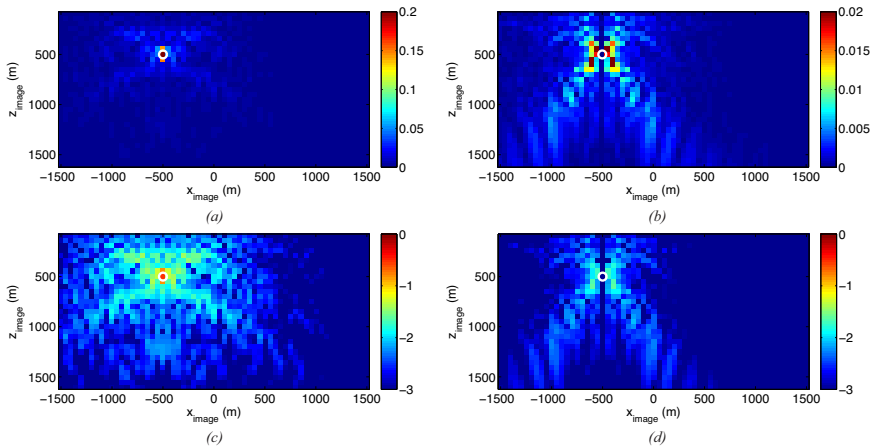


Figure 6.23: Seismo-electromagnetic resolution function for a density perturbation at $(-500, 500)$ m as indicated by the white circle. (a) and (c) diagonal element χ_{22}^{ρ} , (b) and (d) off-diagonal element χ_{31}^{ρ} . (a) and (b) are displayed according to true amplitude, whereas (c) and (d) are displayed on a logarithmic scale.

6.2.5 Conclusions

We have carried out two electromagnetic and one seismo-electromagnetic sensitivity analysis, using three examples. To model the data, we have used our seismo-EM layer-code, either without seismo-electromagnetic coupling, for the purely EM scenario, or with seismo-electromagnetic coupling. We have tested our approach on an example using single-component, single-frequency electromagnetic line-data for a conductivity point perturbation in a homogeneous isotropic half-space background medium. We successfully validated this result by comparing it with the literature results based on explicit analytical homogeneous-space Green's function solutions. We then used the seismo-EM layer-code to study the EM resolution functions in a layered background medium containing a highly conductive layer. We have shown that the single-component electromagnetic data still provide the necessary resolution to resolve a point conductivity scatterer, located either above or below a highly conductive layer. However, when the scatterers are located below the highly conductive layer, the resolution severely decreases. Finally, for the case of multi-component coupled seismo-electromagnetic data in a homogeneous isotropic half-space background model, we have successfully computed a resolution function for a single point perturbation in bulk density. We can conclude that the coupled seismo-electromagnetic system is sensitive to this perturbation and that its position can be correctly recovered. This paves the way to study the seismo-electromagnetic sensitivity to contrasts in for example the seismo-electromagnetic coupling coefficient, the medium permeability, or the pore-fluid viscosity.

6.3 Discussion on potential seismo-electromagnetic applications

In the previous chapter, I have presented a field decomposition scheme exploiting recordings at multiple depth levels, which can provide us with an effective way to carry-out seismo-electromagnetic field decomposition (into up- and downgoing waves and field types), using a limited amount of measured field quantities. I have also presented an effective way of studying the seismo-electromagnetic sensitivity to certain medium parameters, using resolution functions, which can provide us with crucial information when making the step towards coupled seismo-electromagnetic inversion. Here, I briefly discuss some potential applications of seismo-electromagnetic phenomena, not yet discussed in the introduction of this thesis. It is well-known that the main limitation of seismo-electromagnetic applications in the field, is the weak signal strength of the fields. It is also known, that the further away we record from the target, the weaker the recorded signals are, due to attenuation and geometrical spreading effects. It therefore makes sense, not only to investigate seismo-electromagnetic applications for surface acquisition scenarios, but to also focus on borehole applications. Nice borehole laboratory experiments have been carried out by [Zhu *et al.* \(2000\)](#); [Zhu & Toksöz \(2005\)](#). In the study of [Dupuis & Butler \(2006\)](#), the results suggest that coseismic effects have potential as a porosity/permeability logging tool in borehole environments. Due to the seismo-electromagnetic sensitivity

to permeability, a useful borehole application could be to map the permeability close around the well, with the purpose of determining where to optimally perforate the well-casings for optimal flow conditions, instead of more or less randomly perforate the casings.

Recently, studies showing the existence of seismo-electromagnetic evanescent fields at solid-porous interfaces have been reported (Ren *et al.*, 2012a). I have carried out preliminary experiments, modeling fluid/porous medium transitions, where similar evanescent fields can be observed. Considering the fact that most boreholes are containing a borehole fluid, it is possible to visualize the transition from inside the borehole to the surrounding rock formations as a fluid/porous medium transition. One application could be to deploy for example acoustic sources and electrode-receivers in the borehole, and exploit the evanescent field recordings from the fluid/porous medium transition, using these signals to infer medium property information from the formations surrounding the borehole. With every application, we need to remember that theoretical aspects and the physical practice in the field often differ from each other. For example, theoretically unexpected shear waves are routinely measured in fluid-filled boreholes (Cheng & Toksöz, 1981). In addition, fluid-filled boreholes can modify the responses as for example formulated by Peng *et al.* (2003). We always need to keep in mind that in reality, the situation is far more complex.

The fundamental interferometric principles, as illustrated in Chapter 5, have of course a wide-variety of useful applications. One only needs to think of the successes of interferometric principles applied to purely seismic and purely electromagnetic signals (Curtis *et al.*, 2006; Vasconcelos *et al.*, 2008; Hunziker *et al.*, 2012). As an example, we can try to apply correlation-based interferometry to (passive) recordings, trying to stack over long periods of time, in an attempt to improve the signal-to-noise ratio of the seismo-electromagnetic fields. Another application is related to recordings in boreholes, either configurations of (high-density) vertical boreholes or horizontal borehole configurations. The virtual source method (Bakulin & Calvert, 2006; Mehta *et al.*, 2007c; Van der Neut *et al.*, 2010), exploits downhole recordings, allowing imaging below a complex overburden due to redatuming. The virtual source method also enables sensitive reservoir monitoring below a complex, time-variant near-surface that is not achievable with surface 4D seismic or conventional 4D vertical seismic profiling VSP (Bakulin & Calvert, 2006). This repeatability is very interesting for seismo-electromagnetic signals as well, due to the high sensitivity of the seismo-electromagnetic converted fields to for example oil/water contacts. Also, changes in for example permeability during production could be monitored. An additional advantage is that we redatum the surface sources to the receiver locations in the boreholes, resulting in source-receiver paths that are closer to the target zone of interest. I schematically illustrate this interferometric redatuming for the seismo-electromagnetic method in Figure 6.24.

Seismo-electromagnetic signals are not only useful for borehole applications. In situations with complex near-surface geology, unresolved velocity anomalies in the near-surface sections of the velocity models degrade deeper imaging (Jones, 2012). Full-waveform inversion is nowadays a useful, but computationally expensive, tech-

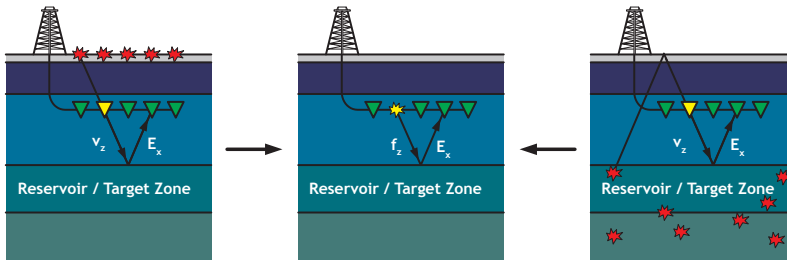


Figure 6.24: Schematic configuration for applying the virtual source method to the seismo-electromagnetic system. Cross-correlation of electric (E_x) and acoustic signals (v_z) from active sources located at the surface (a) or passive sources located in the bulk (c) results in the electromagnetic response of an acoustic source (f_z) generating a seismo-electromagnetic field (b).

nique to resolve small-scale near-surface velocity anomalies. As is known, the seismo-electromagnetic signals suffer from weak signal strength. However, for near-surface applications, the sources and receivers are close to the target zone of interest, enhancing the probability of clearly recording the coupled signals. Since the seismo-electromagnetic signals are sensitive to a wide-variety of medium parameters, and deal with different wave and field types at the same time, they have a great potential to assist in high-definition near-surface velocity model building and characterization. I have shown already that seismo-electromagnetic signals have a high sensitivity to thin-bed geological settings, being able to sense the presence of beds that are thinner than the conventional seismic definition of a thin-bed predicts (Section 4.7). In addition, the direct sensitivity to permeability can assist in characterizing fracture networks in for example complex near-surface settings. A recent study by [Zhu *et al.* \(2015\)](#) on samples with anisotropic permeability proves that the seismo-electromagnetic conversion is related to permeability in the frequency range of their measurements. They show that the seismo-electromagnetic amplitudes are correlated with permeability, where larger seismo-electromagnetic amplitudes are occurring for larger permeability values. These are encouraging results since it opens the possibility of determining the permeability of a formation from seismo-electromagnetic measurements. Having this sensitivity to permeability, the seismo-electromagnetic signals could also be used for detection of microcracks, for example as a method for developing Earthquake early-warning systems, or when studying induced seismicity ([Fujinawa & Noda, 2016](#)).

Thusfar, I have looked into borehole applications, near-surface applications, and the earlier discussed hydrogeophysical applications such as mapping of aquifers, monitoring of groundwater contamination, or monitoring salt water-fresh water contacts at (drinking) water pumping wells in coastal areas (see [Cooper \(1959\)](#) for an illustration of this problem).

However, coupled seismo-electromagnetic signals also have potential applications in other fields of science, where an interaction between a porous framework and moving pore-fluids occurs. I can think of interesting applications in for example the

field of medical imaging. For seismo-electromagnetic phenomena to occur, we need a system of a porous solid, and a pore-fluid. A great example of such a system is bone tissue. Bone represents a porous tissue containing a fluid phase, a solid matrix, and cells (Knothe Tate, 2003; Steck *et al.*, 2003). Seismo-electromagnetic (imaging) techniques could be applied to the fluid flow that occurs in the bone, providing sensitivity to a wide-variety of medium and pore-fluid properties. Additionally, it might be applicable for studying bone marrow as well, which plays a role in many physiological processes, such as leukemia, or sickle cell anemia (Vogler III & Murphy, 1988).

Chapter 7

Conclusions and Outlook

7.1 Conclusions

The key aim of this thesis was two-fold:

1. Increase our theoretical and physical understanding of the seismo-electromagnetic phenomenon by analytically-based numerical modeling.
2. Investigate the potential of seismo-electromagnetic interferometry.

In light of these research targets, I can conclude the following from my work. I have carefully derived and presented the governing system of seismo-electromagnetic equations, and captured this system in a compact matrix-vector notation of the two-way wave equation. I have incorporated all possible source-types in the starting equations, providing a complete theoretical framework based on the underlying assumptions of Pride's theory. I have discussed an alternative description based on the assumptions of Revil as well. I have focused mainly on the implications that different assumptions have for the formulations of the dynamic coupling coefficient, the dynamic permeability, and the complex conductivity. These different formulations can both be incorporated in my theoretical description. I have successfully developed an analytically-based, layered-Earth electromagneto-seismic and seismo-electromagnetic modeling code in a combined Fortran/C programming language, referred to as ESSEMOD, which is capable of modeling all possible source-receiver combinations.

Eigenvector sets form the basis of this layered-Earth modeling code. I have successfully normalized the eigenvector sets known from the literature with respect to power-flux. Due to observed numerical instabilities and inaccuracies, I have effectively derived an alternative power-flux normalized eigenvector set (referred to as the GST set), straight from the seismo-electromagnetic system matrices. The procedure used can in principle be applied to derive any desired eigenvector set, starting from the system matrices and the eigenvalue matrices. Numerical stability tests have proven that flux-normalizing the eigenvector sets stabilizes the numerical results and improves numerical accuracy. My newly derived GST eigenvector set overall results

in the best numerical performance. Using a two-halfspace model, I have validated my modeling results when using three different eigenvector sets (literature set, flux-normalized literature set, and the GST set). I conclude that each eigenvector set generates identical results for all the major events in the model under consideration. I also prove that the numerical differences between the different eigenvector sets have obvious implications on finding small amplitude signals when there are also strong signals in the data. Especially, later arriving, weak events are masked by numerical noise using the literature sets, whereas these events are correctly modeled with the GST set. When there is no seismo-electromagnetic coupling, the literature eigenvector sets model the purely poroelastic and purely electromagnetic systems incorrectly, whereas the GST set correctly models the decoupled scenarios. Furthermore, I can conclude that as soon as there is little coupling between the mechanical and electromagnetic fields, for example at low porosity values or high electrolyte concentrations, the modeling results of the GST set compared to the literature sets behave differently. The GST set remains stable at all times and models all events correctly and clean, whereas the literature sets show clearly numerical noise levels that are of similar amplitude as the weak events in the data, making a distinction between noise and physical weak events impossible.

I have presented an effective way of deriving explicit homogeneous space Green's function solutions for the seismo-electromagnetic system, which have been used to successfully validate the results of ESSEMOD in a homogeneous medium. I conclude that ESSEMOD correctly models the fields in a homogeneous space.

To model the propagation/diffusion of the waves/fields through a layered-Earth model, I have developed a Global Reflection Scheme. I also incorporated different boundary conditions, enabling modeling of porous medium configurations, porous medium configurations in combination with a free-surface, and fluid/porous medium/fluid configurations to resemble typical seismo-electromagnetic laboratory experiments. Several reciprocity tests have proven that the Global Reflection Scheme consistently models configurations where sources are located either above or below the receiver level. I can also conclude from comparisons with a purely electromagnetic modeling code, that ESSEMOD correctly models configurations with fluid/porous medium/fluid transitions. My comparison with an independently developed coupled seismo-electromagnetic modeling code shows that the results of ESSEMOD match almost perfectly in terms of both phase and relative amplitude with the results of this independently developed code. The absolute amplitudes of the two codes differ by a constant factor of four, which should be further investigated. I theoretically show how to effectively combine the two propagation modes of the seismo-electromagnetic system (SH-TE and P-SV-TM) in the final stage of the algorithm of ESSEMOD. To transform the modeling results in a computationally effective manner from the horizontal wavenumber-frequency domain to the space-frequency domain, I have derived for all source-receiver combinations explicit Fourier-Bessel transformations.

My seismo-electromagnetic feasibility studies have provided a better insight in what amplitudes to expect for different modeling scenarios and for different source-receiver combinations. The source-receiver combinations that yield the strongest

converted signals are $E_1^{q_i}$ and $H_2^{f_b}$. Especially the $E_1^{q_i}$ combination seems to generate measurable responses even with acquisition geometries that approach surface-to-surface acquisition. The depth of the receivers plays an important role in the signal measurability of the seismo-electromagnetic fields. The closer the receivers are located to the target, the higher the signal strengths, especially of the seismo-electromagnetic converted fields (interface responses). However, when located too close to the target depth, the coseismic reflected fields arrive at more or less the same time as the one-way seismic traveltime interface responses, thereby masking the weaker interface response fields. The electromagnetic-to-seismic conversions do not suffer from these interferences, for these acquisition scenarios.

I have studied the potential of natural signal enhancements in thin-bed geological settings. Using numerical seismo-electromagnetic wave propagation experiments through packages of thin-beds, I have shown that thin-bed geological settings can improve the signal strength of the seismo-electromagnetic interface response fields. Increasing amounts of thin-beds can cause the shear-wave related interface response strength to increase or decrease. Both the thickness of the thin-beds as well as the amount of thin-beds play a role in whether or not the multiples vanish in the record. I can distinguish two limits of bed thickness: an upper and lower limit. The upper limit of bed thickness determines whether the individual layers are still recognized or not. When beds are thinner than this limit, the package of thin-beds starts acting like an 'effective' medium and the multiples vanish from the record. The lower limit of bed thickness determines the border from whereon further thinning does not affect the seismo-electromagnetic IR signal strength anymore, because the bed thickness is below the sensitive resolution of the seismo-electromagnetic fields. Whether the thin-beds result in an effective strengthening or weakening of the signal, seems to be determined by the contrast in seismo-electromagnetic coupling coefficients between the different thin-beds. My oil/water contact modeling experiments where the oil layer is gradually thinned prove that the seismo-electromagnetic signal has a very high sensitivity to oil-water contacts: an oil layer with 20% water saturation and of 0.2 m thickness, a thickness of about $\frac{1}{350}$ of the dominant wavelength of the shear wave generating this response, is still slightly recognized. This is a clear indicator of the high seismo-electromagnetic sensitivity for different saturating fluids.

To study the potential of seismo-electromagnetic interferometry, I have first presented an effective way of deriving explicit homogeneous space Green's function expressions for the 2D SH-TE propagation mode, using power-flux normalized eigenvectors. The theory for interferometric retrieval of 2D SH-TE seismo-EM Green's functions was also presented. Using both a circular source configuration and a line source configuration, I have shown that it is possible to correctly retrieve the dynamic seismo-EM 2D SH-TE response in a homogeneous medium, using seismic boundary sources only. This was demonstrated for two source-receiver combinations: an electric field and a magnetic field due to a seismic source, using explicit homogeneous space Green's function solutions. The volume source contributions account for the losses in the acausal part of the retrieved response as well as the instantaneous source-converted EM field. Using ESSEMOD data, I have shown that

we can also correctly retrieve the direct shear wave-related causal coseismic field in a homogeneous medium, in both phase and amplitude. To obtain a perfect match in absolute amplitudes, a single linear scaling factor was required. Finally, the interferometric experiments in a model containing a single interface at 800 m depth prove that it is possible to correctly retrieve all 2D SH-TE causal seismic-related direct and reflected coseismic fields, as well as interface response fields, by cross-correlation interferometry, using seismic boundary sources only.

I have presented a multi-depth-level (MDL) field decomposition scheme for land acquisition that is inspired by marine acquisition designs that makes use of recordings at multiple depth levels for successful field decomposition. My MDL decomposition approach makes use of configurations with field quantity information on multiple depth levels, for example two horizontal boreholes that are closely separated from each other, or a combination of a single receiver array just below a free surface, thereby exploiting the natural (Dirichlet) free-surface boundary conditions. In this way, field decomposition can be carried out using a smaller amount of different field quantities than in the case of the classical multi-component (MC) decomposition. This is especially useful for decomposition of seismo-electromagnetic signals, where theoretically many different field quantities should be measured. My tests on a synthetic elastodynamic data set, have shown that the MDL decomposition scheme leads to correctly retrieved power flux-normalized one-way fields, for both P- and S-waves, using only particle velocity recordings at two depth levels. Secondly, I showed that when having particle velocity recordings at one depth level, in combination with the free-surface Dirichlet boundary condition of zero-traction, it is possible to correctly decompose the data into one-way fields as well. I have additionally tested the effects of using erroneous velocities on both the MC and MDL decomposition schemes. For the considered example, I observed that the downgoing P- and S- fields are correctly and equally-well resolved in terms of both phase and amplitude. The upgoing P- and S- fields show leakage of downgoing energy, but the amount of leakage is comparable for the MC and MDL decomposition schemes. The MDL decomposition scheme is fully customizable to the acquisition geometry and measured field quantities under consideration. Depending on the acquisition design and wave velocities under consideration, notches may occur at certain frequencies, causing the customizable MDL composition matrix to become uninvertible. Additional notch filters are then required. I also presented a way of combining the MC and MDL decomposition schemes: by adding an extra equation of the MDL decomposition scheme to the MC composition matrix, it is possible to overdetermine the inverse problem and hereby better constrain the inversion. I have tested this approach on a field data set, clearly showing improvements in the obtained one-way flux-normalized fields, compared to the results obtained using an MC decomposition scheme.

Finally, moving towards inversion, I have carried out two electromagnetic and one seismo-electromagnetic sensitivity analysis, using three examples modeled with ES-SEMOD. I have tested the approach on an example using single-component, single-frequency electromagnetic line-data for a conductivity point perturbation in a homogeneous isotropic half-space background medium. I successfully validated this result by comparing it with the literature results based on explicit analytical homogeneous-

space Green's function solutions. I then used ESSEMOD to study the EM resolution functions in a layered background medium containing a highly conductive layer. I have shown that the single-component electromagnetic data still provide the necessary resolution to resolve a point conductivity scatterer, located either above or below a highly conductive layer. However, when the scatterers are located below the highly conductive layer, the resolution severely decreases. Finally, for the case of multi-component coupled seismo-electromagnetic data in a homogeneous isotropic half-space background model, I have successfully computed a resolution function for a single point perturbation in bulk density. I can conclude that the coupled seismo-electromagnetic system is sensitive to this perturbation and that its position can be correctly recovered.

7.2 Outlook

The coupled seismo-electromagnetic phenomenon is an extremely interesting physical phenomenon, with a lot of proven and potential applications. However, more than 20-years have passed since [Pride \(1994\)](#) formulated the theoretical framework to describe the seismo-electromagnetic phenomenon, which forms one of the important pillars on which many present-day seismo-electromagnetic research leans. The research has focused on understanding the method, its potential applications, and trying to apply the method as a geophysical technique in the field. The major challenge of the method is the very weak signal strength of the converted fields that we are after. In my opinion, if you cannot measure the fields, or the fields are masked by noise levels, the method is practically useless.

So it should be our top-priority to find a solution for the challenge of non-measurability of seismo-electromagnetic signals that are too weak. I believe that in order to make the method a true success for a wide variety of applications, it is required to first come up with an idea to really boost the seismo-electromagnetic conversion, such that more of the converted signals lie in the dynamic range of the geophones ([Ongkiehong & Huizer, 1987](#); [Barzilai *et al.*, 1998](#); [Mougenot, 2004](#)). In addition, successful laboratory and mainly also field experiments need to be carried out to test the method and bring seismo-electromagnetics to the next level. In [Section 6.3](#), I have highlighted a few promising applications of seismo-electromagnetic phenomena. Especially borehole applications are offering a great potential, and part of the research should focus in that direction.

Once the signals are measurable by the physical devices, studies to improve the signal-to-noise ratio of the signals, as well as additional data processing and filtering techniques, can come into play. As an example, stacking active and passive sources via the principle of interferometry over long periods of time could potentially enhance the signal-to-noise ratio of the converted fields.

Additionally, it is still unclear how sensitive the seismo-electromagnetic conversion is to high-value parameters like permeability and porosity, and also for which parameters we can actually invert. I believe that in the future, due to better measuring devices, as well as more control on the source-side of the acquisition scenarios, we will be increasingly capable of obtaining clear seismo-electromagnetic signals in

our records. The big question is then, what is the optimal information that we can retrieve from these signals, and what are the optimal scientific areas to apply this method effectively? For exploration, monitoring, Earthquake early-warning systems, hydrogeophysics, or perhaps medical imaging? In my view, future research on the seismo-electromagnetic phenomenon should mainly focus on the above mentioned aspects.

Bibliography

- Abramowitz, M., & Stegun, I.A. 1965. *Handbook of Mathematical Functions*. Dover Publications, New York.
- Airy, G. B. 1833. On the Phenomena of Newton's Rings when formed between two transparent Substances of different refractive Powers. *The London and Edinburgh Philosophical Magazine and Journal of Science*, **2**, 20–30.
- Aki, K., & Richards, P. G. 1980. Quantitative seismology. *Freeman and Co., New York*.
- Alexandrov, D., Bakulin, A., & Burnstad, R. 2012. Redatuming of synthetic land data with shallow buried receivers using the virtual source method. *SEG Expanded Abstracts Las Vegas*, 1–5.
- Alexandrov, D., Bakulin, A., Leger, P., & Kashtan, B. 2014. Dual-sensor summation with buried land sensors. *SEG Expanded Abstracts Denver, 1929–1933*.
- Allègre, V., Jouniaux, L., Lehmann, F., & Sailhac, P. 2010. Streaming potential dependence on water-content in Fontainebleau sand. *Geophysical Journal International*, **182**, 1248–1266.
- Almagro Vidal, C., & Wapenaar, K. 2014. Passive Seismic Interferometry by Multi-Dimensional Deconvolution-Decorrelation. *SEG Expanded Abstracts Denver, 2224–2228*.
- Almagro Vidal, C., van der Neut, J., Draganov, D., Drijkoningen, G., & Wapenaar, K. 2011. Retrieval of reflections from ambient-noise field data using illumination diagnostics. *SEG Expanded Abstracts San Antonio*, 1613–1617.
- Almagro Vidal, C., Draganov, D., Van der Neut, J., Drijkoningen, G., & Wapenaar, K. 2014. Retrieval of reflections from ambient noise using illumination diagnosis. *Geophysical Journal International*, **198**, 1572–1584.
- Amundsen, L. 1999. Elimination of free surface-related multiples without need of the source wavelet. *SEG Expanded Abstracts Houston*, 1064–1067.
- Amundsen, L., & Holvik, E. 2004. Processing electromagnetic data. *Patent GB2415511*.

- Amundsen, L., & Reitan, A. 1995. Decomposition of multicomponent sea-floor data into upgoing and downgoing P- and S-waves. *Geophysics*, **60**, 563–572.
- Amundsen, L., & Robertsson, J.O.A. 2014. Wave equation processing using finite-difference propagators, Part 1: Wavefield dissection and imaging of marine multicomponent seismic data. *Geophysics*, **79**, T287–T300.
- Amundsen, L., Løseth, L., Mittet, R., Ellingsrud, S., & Ursin, B. 2006. Decomposition of electromagnetic fields into upgoing and downgoing components. *Geophysics*, **71**, G211–G223.
- Archie, G.E. 1942. The electrical resistivity log as an aid in determining some reservoir characteristics. *Transactions of the AIME*, **146**, 54–62.
- Bakulin, A., & Calvert, R. 2006. The virtual source method: theory and case study. *Geophysics*, **71**, SI139–SI150.
- Bakulin, A., Burnstad, R., Jervis, M., & Kelamis, P. 2012a. Evaluating permanent seismic monitoring with shallow buried sensors in a desert environment. *SEG Expanded Abstracts Las Vegas*, **2012**, 1–5.
- Bakulin, A., Burnstad, R., Jervis, M., & Kelamis, P. 2012b. The feasibility of permanent land seismic monitoring with buried geophones and hydrophones in a desert environment. *74th EAGE Conference & Exhibition Copenhagen*, 1–4.
- Barzilai, A., VanZandt, T., & Kenny, T. 1998. Improving the performance of a geophone through capacitive position sensing and feedback. *Proceeding of 1998 ASME International Mechanical Engineering Congress and Exposition*, 15–20.
- Beasley, C.J., Coates, R., & Lapilli, C. 2013a. Wave equation receiver dehosting. *IEEE 5th International Workshop on Computational Advances in Multi-Sensor Adaptive Processing*, 280–283.
- Beasley, C.J., Coates, R., Ji, Y., & Perdomo, J. 2013b. Wave equation receiver dehosting: a provocative example. *SEG Expanded Abstracts Houston*, 4226–4230.
- Berron, C., Forgues, E., Jervis, M., Bakulin, A., & Burnstad, R. 2012. Buried sources and receivers in a Karstedt desert environment. *74th EAGE Conference & Exhibition Copenhagen*, **X040**, 1–4.
- Biot, M. A. 1962. Mechanics of deformation and acoustic propagation in porous media. *Journal of Applied Physics*, **33**, 1482–1498.
- Bleistein, N. 1987. On the imaging of reflectors in the earth. *Geophysics*, **52**, 931–942.
- Bleistein, N., Cohen, J. K., & Hagin, F. G. 1987. Two and one-half dimensional Born inversion with an arbitrary reference. *Geophysics*, **52**, 26–36.

- Bordes, C., Jouniaux, L., Garambois, S., Dietrich, M., Pozzi, J., & Gaffet, S. 2008. Evidence of the theoretically predicted seismo-magnetic conversion. *Geophysical Journal International*, **174**, 489–504.
- Bordes, C., Sénéchal, P., Barrière, J., Brito, D., Normandin, E., & Jougnot, D. 2015. Impact of water saturation on seismoelectric transfer functions: a laboratory study of coseismic phenomenon. *Geophysical Journal International*, **200(3)**, 1317–1335.
- Born, M., & Wolf, E. 1980. *Principles of Optics*. Pergamon, New York.
- Born, Max. 1926. Quantenmechanik der Stossvorgänge. *Zeitschrift für Physik*, **38**, 803–827.
- Bourbié, T., Coussy, O., & Zinszner, B. 1987. *Acoustics of porous media*. Gulf Publ. Co.
- Bracewell, R.N. 2000. *The Fourier Transform and its applications*. McGraw-Hill, New York.
- Brooks, R.H., & Corey, A.T. 1964. Hydraulic Properties of Porous Media. *Hydrology papers Colorado State University*, **3**, 1–37.
- Burnstad, R., Bakulin, A., Jervis, M., & Alexandrov, D. 2012. Successful imaging of land hydrophone and dual sensor data in a dry desert environment. *SEG Expanded Abstracts Las Vegas*, **2012**, 1–5.
- Butler, K. E., Don Russell, R., Kepic, A. W., & Maxwell, M. 1996. Measurement of the seismoelectric response from a shallow boundary. *Geophysics*, **61**, 1769–1778.
- Butler, K.E., & Russell, R.D. 1993. Subtraction of powerline harmonics from geophysical records. *Geophysics*, **58(6)**, 898–903.
- Butler, K.E., Kepic, A.W., & Rosid, M.S. 2002. An experimental seismoelectric survey for groundwater exploration in the Australian Outback. *SEG Expanded Abstracts*, 1484–1487.
- Cagniard, L. 1953. Basic Theory of the Magneto-Telluric Method of Geophysical Prospecting. *Geophysics*, **18**, 605–635.
- Carbajal, M.R., Linde, N., & Kalscheuer, T. 2012. Focused time-lapse inversion of radio and audio magnetotelluric data. *Journal of Applied Geophysics*, **84**, 29–38.
- Carcione, J.M., Morency, C., & Santos, J.E. 2010. Computational Poroelasticity - A Review. *Geophysics*, **75**, 75A229–75A243.
- Chave, A.D., & Cox, C.S. 1982. Controlled Electromagnetic Sources for Measuring Electrical Conductivity Beneath the Oceans. *Journal of Geophysical Research*, **87(B7)**, 5327–5338.
- Chen, J., & De Hoop, M. 2014. Inverse problem of electroseismic conversion. I: Inversion of Maxwell's equations with internal data. *ArXiv e-prints*.

- Cheng, C.H., & Toksöz, M.N. 1981. Elastic wave propagation in a fluid-filled borehole and synthetic acoustic logs. *Geophysics*, **46**, 1042–1053.
- Colombo, D., & De Stefano, M. 2007. Geophysical modeling via simultaneous joint inversion of seismic, gravity, and electromagnetic data: Application to prestack depth imaging. *The Leading Edge*, **26**, 326–331.
- Colombo, D., McNeice, G., Curiel, E.S., & Fox, A. 2013. Full tensor CSEM and MT for subsalt structural imaging in the Red Sea: Implications for seismic and electromagnetic integration. *The Leading Edge*, **32**, 436–449.
- Constable, S. 2010. Ten Years of Marine CSEM for Hydrocarbon Exploration. *Geophysics*, **75**, 75A67–75A81.
- Cooper, Jr., H.H. 1959. A hypothesis concerning the dynamic balance of fresh water and salt water in a coastal aquifer. *Journal of Geophysical Research*, **64**, 461–467.
- Cotton, J., & Forgues, E. 2012. Dual-depth hydrophones for ghost reduction in 4D land monitoring. *SEG Expanded Abstracts Las Vegas*, 1–5.
- Curtis, A., Gerstoft, P., Sato, H., Snieder, R., & Wapenaar, K. 2006. Seismic Interferometry - turning noise into signal. *The Leading Edge*, **25(9)**, 1082–1092.
- Dankbaar, J. W. M. 1985. Separation of P- and S-waves. *Geophysical Prospecting*, **33**, 970–986.
- Day, A., Klüver, T., Söllner, W., Hocine, T., & Carlson, D. 2013. Wavefield-separation methods for dual-sensor towed-streamer data. *Geophysics*, **78**, WA55–WA70.
- De Hoop, A.T. 1995. *Handbook of Radiation and Scattering of Waves*. Academic Press.
- De Ridder, S.A.L. 2007. *Simulation of Interferometric Seismoelectric Green's Function Recovery - For the SH-TE Propagation Mode*. MSc Thesis Delft University of Technology.
- De Ridder, S.A.L., Slob, E., & Wapenaar, K. 2009. Interferometric seismoelectric Green's function representations. *Geophysical Journal International*, **178**, 1289–1304.
- Dean, T., & Dupuis, J. C. 2011a. The Vibroelectric Method - A New Tool for Near-surface Characterisation and Improved Seismic Data Quality. *73rd EAGE Conference & Exhibition Vienna*, **I040**, 1–4.
- Dean, T., & Dupuis, J.C. 2011b. The Vibroelectric Method - A New Tool for Near-Surface Characterisation and Improved Seismic Data Quality. *73rd EAGE Conference & Exhibition Vienna*, **I040**, 1–5.

- Dean, T., Dupuis, C., Herrmann, R., & Valuri, J. 2012. A brute-strength approach to improving the quality of Seismoelectric data. *SEG Expanded Abstracts Las Vegas*, 1–5.
- Debye, P. von, & Hückel, E. 1923. Zur Theorie der Elektrolyte. *Physikalische Zeitschrift*, **9(24)**, 185–206.
- Deresiewicz, H., & Skalak, R. 1963. On Uniqueness in Dynamic Poroelasticity. *Bulletin of the Seismological Society of America*, **53**, 783–788.
- Dietrich, M., & Garambois, S. 2013. Some Theoretical and Practical Questions in Transient Electrokinetic Coupling in Fluid-Saturated Porous Media. *Poromechanics*, **V**, 299–305.
- Draganov, D., Wapenaar, K., & Thorbecke, J. 2006. Seismic interferometry: reconstructing the earth's reflection response. *Geophysics*, **71**, SI61–SI70.
- Dupuis, J. C., Butler, K. E., & Kepic, A. W. 2007. Seismoelectric imaging of the vadose zone of a sand aquifer. *Geophysics*, **72**, A81–A85.
- Dupuis, J.C., & Butler, K.E. 2006. Vertical seismoelectric profiling in a borehole penetrating glaciofluvial sediments.
- Eidesmo, T., Ellingsrud, S., MacGregor, L.M., Constable, S., Sinha, M.C., Johansen, S., Kong, F.N., & Westerdahl, H. 2002. Sea Bed Logging (SBL), a new method for remote and direct identification of hydrocarbon filled layers in deepwater areas. *First Break*, **20(3)**, 144–152.
- El Allouche, N. 2011. Converted waves in shallow marine environments: modelling and field experiments. *dissertation*.
- Feld, R., & Slob, E. 2014. GPR Without a Source by use of Interferometry by Multi-Dimensional Deconvolution. *SEG Expanded Abstracts Denver*, 844–849.
- Fishman, L., McCoy, J. J., & Wales, S. C. 1987. Factorization and path integration of the Helmholtz equation: Numerical algorithms. *Journal of the Acoustical Society of America*, **81**, 1355–1376.
- Fokkema, J. T., & Van den Berg, P. M. 1993. *Seismic Applications of Acoustic Reciprocity*. Elsevier Science Publishers B.V.
- Fokkema, J.T., & Ziolkowski, A. 1987. The critical reflection theorem. *Geophysics*, **52**, 965–972.
- Frasier, C. W. 1970. Discrete time solution of plane P-SV waves in a plane layered medium. *Geophysics*, **35**, 197–219.
- Frenkel, J. 1944. On the theory of seismic and seismoelectric phenomena in moist soil. *Journal of Physics*, **8**, 230–241.

- Frijlink, M., & Wapenaar, K. 2010. Reciprocity Theorems for One-Way Wave Fields in Curvilinear Coordinate Systems. *Society for Industrial and Applied Mathematics - Journal on Imaging Sciences*, **3**, 390–415.
- Frijlink, M., Van Borselen, R., & Soellner, W. 2011. The free surface assumption for marine data-driven demultiple methods. *Geophysical Prospecting*, **59**, 269–278.
- Fujinawa, Y., & Noda, Y. 2016. Characteristics of seismoelectric wave fields associated with natural microcracks. *Pure and Applied Geophysics*, **173**, 255–268.
- Fujinawa, Y., Takahashi, K., Noda, Y., Iitaka, H., & Y., Shinobu. 2011. Remote Detection of the Electric Field Change Induced at the Seismic Wave Front from the Start of Fault Rupturing. *International Journal of Geophysics*, **0033-4553**, 1–11.
- Garambois, S., & Dietrich, M. 2001. Seismoelectric wave conversions in porous media: Field measurements and transfer function analysis. *Geophysics*, **66-5**, 1417–1430.
- Garambois, S., & Dietrich, M. 2002. Full waveform numerical simulations of seismoelectromagnetic wave conversions in fluid-saturated stratified porous media. *Journal of Geophysical Research*, **107**.
- Grimbergen, J. L. T., Dessing, F. J., & Wapenaar, K. 1998. Modal expansion of one-way operators in laterally varying media. *Geophysics*, **63**, 995–1005.
- Grobbe, N., & Slob, E. 2013. Validation of an electroseismic and seismoelectric modeling code, for layered earth models, by the explicit homogeneous space solutions. *SEG Expanded Abstracts Houston*, 1847–1851.
- Grobbe, N., & Slob, E.C. 2016. Seismo-Electromagnetic Thin-Bed Responses: Natural Signal Enhancements? *Journal of Geophysical Research*, doi: 10.1002/2015JB012381.
- Grobbe, N., Hunziker, J., & Slob, E. 2014. Seismoelectric wave propagation modeling for typical laboratory configurations: A numerical validation. *SEG Expanded Abstracts Denver*, **2014**.
- Grobbe, N., Maas, P., Slob, E., & Mulder, W. 2015. Towards Seismoelectric Inversion: Sensitivity Analysis using Resolution Functions. *Japan Geoscience Union Meeting 2015*, **SCG15-P01**, 1.
- Grobbe, N., Slob, E. C., & Thorbecke, J. W. 2016a. Comparison of Eigenvectors for Coupled Seismo-Electromagnetic Layered-Earth Modeling. *Geophysical Journal International*, doi:10.1093/gji/ggw128.
- Grobbe, N., Van der Neut, J., Slob, E., Wapenaar, K., Almagro Vidal, C., & Drijkoningen, G. 2016b. Unified Multi-Depth-Level Field Decomposition. *Geophysical Prospecting*, **64**, 361–391.

- Guha, S., Kruse, S.E., Wright, E.E., & Kruse, U.E. 2005. Spectral analysis of ground penetrating radar response to thin sedimentary layers. *Geophysical Research Letters*, **32**, L23304: 1–4.
- Haartsen, M.W., & Pride, S.R. 1997. Electro seismic waves from point sources in layered media. *Journal of Geophysical Research*, **102-B11**, 24745–24769.
- Haas, A.K., Revil, A., Karaoulis, M., Frash, L., Hampton, J., Gutierrez, M., & Mooney, M. 2013. Electric potential source localization reveals a borehole leak during hydraulic fracturing. *Geophysics*, **78(2)**, D93–D113.
- Habashy, T.M., Groom, R.W., & Spies, B.R. 1993. Beyond the Born and Rytov Approximations: A Nonlinear Approach to Electromagnetic Scattering. *Journal of Geophysical Research*, **98**, 1759–1775.
- Haines, S. S. 2004. *Seismoelectric imaging of shallow targets*. Ph.D. thesis, Stanford University.
- Haines, S. S., & Pride, S. R. 2006. Seismoelectric numerical modeling on a grid. *Geophysics*, **71-6**, N57–N65.
- Holvik, E., & Amundsen, L. 2005. Elimination of the overburden response from multicomponent source and receiver seismic data, with source designation and decomposition into PP-, PS-, SP-, and SS-wave responses. *Geophysics*, **70**, S43–S59.
- Hu, H., & Gao, Y. 2011. Electromagnetic field generated by a finite fault due to electrokinetic effect. *Journal of Geophysical Research*, **116-B08302**, 1–14.
- Hunziker, J., Slob, E., & Wapenaar, K. 2011. Time-lapse controlled-source electromagnetics using interferometry. *The Leading Edge*, **30**, 564–567.
- Hunziker, J., Slob, E., Fan, Y., Snieder, R., & Wapenaar, K. 2012. Two-dimensional controlled-source electromagnetic interferometry by multidimensional deconvolution: spatial sampling aspects. *Geophysical Prospecting*, **60**, 974–994.
- Hunziker, J., Thorbecke, J., & Slob, E. 2014. Probing the solution space of an EM inversion problem with a genetic algorithm. *SEG Expanded Abstracts Denver*, 833–837.
- Hunziker, J., Thorbecke, J., & Slob, E. 2015. The electromagnetic response in a layered vertical transverse isotropic medium: A new look at an old problem. *Geophysics*, **80(1)**, F1–F18.
- Ivanov, A.G. 1940. Seismoelectric effect of the second kind (in Russian). *Bulletin Academy of Sciences USSR, série géographique et géophysique*, **5**, 699–727.
- Jardani, A., & Revil, A. 2015. Seismoelectric couplings in a poroelastic material containing two immiscible fluid phases. *Geophysical Journal International*, **202**, 850–870.

- Jardani, A., Revil, A., Slob, E., & Söllner, W. 2010. Stochastic joint inversion of 2D seismic and seismoelectric signals in linear poroelastic materials. *Geophysics*, **75**, N19–N31.
- Jocker, J., Smeulders, D., Drijkoningen, G., Van der Lee, C., & Kalfsbeek, A. 2004. Matrix propagator method for layered porous media: Analytical expressions and stability criteria. *Geophysics*, **69**, 1071–1081.
- Johnson, D.L., Koplik, J., & Dashen, R. 1987. Theory of dynamic permeability and tortuosity in fluid-saturated porous media. *Journal of Fluid Mechanics*, **176**, 379–402.
- Jones, I.F. 2012. Tutorial: Incorporating near-surface velocity anomalies in pre-stack depth migration models. *First Break*, **30**, 47–58.
- Jouniaux, L., & Pozzi, J. 1995. Permeability dependence of streaming potential in rocks for various fluid conductivities. *Geophysical Research Letters*, **22**, 485–488.
- Jouniaux, L., Bernard, M.L., Zamora, M., & Pozzi, J.P. 2000. Streaming potential in volcanic rocks from Mount Pelée. *Journal of Geophysical Research*, **105(B4)**, 8391–8401.
- Kelder, O. 1998. Frequency-dependent wave propagation in water-saturated porous media. *PhD Thesis*.
- Kennett, B. L. N. 1983. *Seismic wave propagation in stratified media*. Cambridge University Press.
- Knothe Tate, M.L. 2003. "Whither flows the fluid in bone?" An osteocyte's perspective. *Journal of Biomechanics*, **36**, 1409–1424.
- Kröger, B., Yaramanci, U., & Kemna, A. 2014. Numerical analysis of seismoelectric wave propagation in spatially confined geological units. *Geophysical Prospecting*, **2014**, 133–147.
- Kruse, S., Grasmueck, M., Weiss, M., & Viggiano, D. 2006. Sinkhole Structure Imaging in Covered Karst Terrain. *Geophysical Research Letters*, **33**, L16405: 1–6.
- Kullessa, B., Murray, T., & Rippin, D. 2006. Active seismoelectric exploration of glaciers. *Geophysical Research Letters*, **33**, 1–4.
- Maas, P. J., Grobde, N., Slob, E. C., & Mulder, W. A. 2015. Electromagnetic & Seismoelectric sensitivity analysis using resolution functions. *77th EAGE Conference & Exhibition Madrid*, 1–4.
- Maas, P.J. 2014. *Electromagnetic & Seismoelectric sensitivity analysis using resolution functions*. Ph.D. thesis, Delft University of Technology.

- Mahardika, H., Revil, A., & Jardani, A. 2012. Waveform joint inversion of seismograms and electrograms for moment tensor characterization of fracking events. *Geophysics*, **77**(5), ID23–ID39.
- Majdanski, M., Kostov, C., Kragh, E., Moore, I., Thompson, M., & Mispel, J. 2011. Attenuation of free-surface multiples by up/down deconvolution for marine towed-streamer data. *Geophysics*, **76**, V129–V138.
- Marshall, D.J., & Madden, T.R. 1959. Induced Polarization, A Study of Its Causes. *Geophysics*, **24**, 790–816.
- Martner, S.T., & Sparks, N.R. 1959. The electroseismic effect. *Geophysics*, **24**, 297–308.
- Maxwell, S. C., Rutledge, J., Jones, R., & Fehler, M. 2010. Petroleum reservoir characterization using downhole microseismic monitoring. *Geophysics*, **75**, 75A129–75A137.
- Mehta, K., Bakulin, A., Snieder, R., Sheiman, J., & Calvert, R. 2007a. Improving the virtual source method by wavefield separation. *Geophysics*, **72**, V79–V86.
- Mehta, K., Bakulin, A., Sheiman, J., Calvert, R., & Snieder, R. 2007b. Improving the virtual source method by wavefield separation. *Geophysics*, **72**(4), V79–V86.
- Mehta, K., Bakulin, A., Snieder, R., Sheiman, J., & Calvert, R. 2007c. Improving the virtual source method by wavefield separation. *Geophysics*, **72**, V79–V86.
- Moldoveanu, N., Combee, L., Egan, M., Hampson, G., Sydora, L., & Abriel, W. 2007. Over/under towed-streamer acquisition: A method to extend seismic bandwidth to both higher and lower frequencies. *The Leading Edge*, **26**, 41–58.
- Morgan, F.D., Williams, E.R., & Madden, T.R. 1989. Streaming potential properties of Westerly Granite with applications. *Journal of Geophysical Research*, **94**(B9), 12449–12461.
- Mougenot, D. 2004. How digital sensors compare to geophones. *SEG Expanded Abstracts Denver*, 1–4.
- Muijs, R., Robertsson, J. O., & Holliger, K. 2007. Prestack depth migration of primary and surface-related multiple reflections: part i imaging. *Geophysics*, **72**, S59–S69.
- Mulder, W.A., Wirianto, M., & Slob, E.C. 2008. Time-domain modeling of electromagnetic diffusion with a frequency-domain code. *Geophysics*, **73**(1), F1–F8.
- Nabighian, M. N. 1987, reprint 2008. *Electromagnetic methods in applied geophysics*. Society of Exploration Geophysicists.
- Nakata, N., Snieder, R., & Behm, M. 2014. Body-wave interferometry using regional earthquakes with multidimensional deconvolution after wavefield decomposition at free surface. *Geophysical Journal International*, **199**, 1125–1137.

- Neev, J., & Yeats, F.R. 1989. Electrokinetic effects in fluid-saturated poroelastic media. *Physical Review B*, **40**, 9135–9141.
- Oldenburg, D.W., & Li, Y. 1994. Inversion of induced polarization data. *Geophysics*, **59**, 1327–1341.
- Ongkiehong, L., & Huizer, W. 1987. Dynamic range of the seismic system. *First Break*, **5(12)**, 435–439.
- Oristaglio, M., & Blok, H. 1995. *Wavefield Imaging and Inversion in Electromagnetics and Acoustics*. Lecture Notes Delft University of Technology.
- Peng, C., Cheng, C.H., & Toksöz, M.N. 2003. Borehole effects on downhole seismic measurements. *Geophysical Prospecting*, **41**, 883–912.
- Press, W.H., Teukolsky, S.A., Vetterling, W.T., & Flannery, B.P. 1988. *Numerical Recipes in C - The Art of Scientific Computing (second edition)*. Cambridge University Press.
- Pride, S. 1994. Governing equations for the coupled electromagnetics and acoustics of porous media. *Physical Review B*, **50-21**, 15678–15696.
- Pride, S. R., & Garambois, S. 2005. Electrostatic Wave Theory of Frenkel and More Recent Developments. *Journal of Engineering Mechanics*, **131**, 898–907.
- Pride, S. R., & Haartsen, M. W. 1996. Electrostatic wave properties. *Journal of the Acoustical Society of America*, **100**, 1301–1315.
- Pride, S.R., & Morgan, F.D. 1991. Electrokinetic dissipation induced by seismic waves. *Geophysics*, **56**, 914–925.
- Redheffer, R. 1961. *Difference equations and functional equations in transmission-line theory*. McGraw-Hill.
- Ren, H., Huang, Q., & Chen, X. 2010. A new numerical technique for simulating the coupled seismic and electromagnetic waves in layered porous media. *Earthquake Science*, **23**, 167–176.
- Ren, H., Huang, Q., & Chen, X. 2012a. Existence of evanescent electromagnetic waves resulting from seismoelectric conversion at a solid?porous interface. *Geophysical Journal International*, **204**, 147–166.
- Ren, H., Chen, X., & Huang, Q. 2012b. Numerical simulation of coseismic electromagnetic fields associated with seismic waves due to finite faulting in porous media. *Geophysical Journal International*, **188**, 925–944.
- Revil, A. 2012. Spectral induced polarization of shaly sands: Influence of the electrical double layer. *Water Resources Research*, **48**, W02517.
- Revil, A. 2013. Effective conductivity and permittivity of unsaturated porous materials in the frequency range 1 mHz-1GHz. *Water Resources Research*, **49**, 306–327.

- Revil, A., & Florsch, N. 2010. Determination of permeability from spectral induced polarization in granular media. *Geophysical Journal International*, **181**, 1480–1498.
- Revil, A., & Mahardika, H. 2013. Coupled hydromechanical and electromagnetic disturbances in unsaturated porous materials. *Water Resources Research*, **49**, 744–766.
- Revil, A., Pezard, P.A., & Glover, P.W.J. 1999. Streaming potential in porous media 1. Theory of the zeta potential. *Journal of Geophysical Research*, **104(B9)**, 20021–20031.
- Revil, A., Naudet, V., Nouzaret, J., & Pessel, M. 2003. Principles of electrography applied to self-potential electrokinetic sources and hydrogeological applications. *Water Resources Research*, **39**, SBH3–1–SBH3–15.
- Revil, A., Linde, N., Cerepi, A., Jougnot, D., Matthäi, S., & Finsterle, S. 2007. Electrokinetic coupling in unsaturated porous media. *Journal of Colloid and Interface Science*, **313**, 315–327.
- Revil, A., Barnier, G., Karaoulis, M., Sava, P., Jardani, A., & Kulesa, B. 2013. Seismoelectric coupling in unsaturated porous media: theory, petrophysics, and saturation front localization using an electroacoustic approach. *Geophysical Journal International*, **196**, 867–884.
- Revil, A., Jardani, A., Sava, P., & Haas, A. 2015. *The Seismoelectric Method: Theory and Application*. John Wiley & Sons, Ltd.
- Robertson, J. D., & Nogami, H. H. 1984. Complex seismic trace analysis of thin beds. *Geophysics*, **49**, 344–352.
- Robertsson, J.O.A., & Amundsen, L. 2014. Wave equation processing using finite-difference propagators, Part 2: Deghosting of marine hydrophone seismic data. *Geophysics*, **79**, T301–T312.
- Rosid, M.S., & Kopic, A.W. 2005. Hydrogeological mapping using the Seismoelectric Method. *Geophysics*, **36(2)**, 245–249.
- Rubino, J.G., Castromán, G.A., Müller, T.M., Monachesi, L.B., Zyserman, F.I., & Holliger, K. 2015. Including Poroelastic Effects in the Linear Slip Theory. *Geophysics*, **80**, A51–A56.
- Sambuelli, L., Socco, L.V., & Brecciaroli, L. 1999. Acquisition and processing of electric, magnetic and GPR data on a Roman site (Victimulae, Salussola, Biella). *Journal of Applied Geophysics*, **41**, 189–204.
- Sava, P., & Revil, A. 2012. Virtual electrode current injection using seismic focusing and seismoelectric conversion. *Geophysical Journal International*, **191**, 1205–1209.

- Sava, P., Revil, A., & Karaoulis, M. 2014. High definition cross-well electrical resistivity imaging using seismoelectric focusing and image-guided inversion. *Geophysical Journal International*, **198**, 880–894.
- Schakel, M., & Smeulders, D. 2010. Seismoelectric reflection and transmission at a fluid/porous medium interface. *Journal of the Acoustical Society of America*, **127**, 13–21.
- Schakel, M. D., Smeulders, D. M. J., Slob, E. C., & Heller, H. K. J. 2011. Laboratory measurements and theoretical modeling of seismoelectric interface response and coseismic wave fields. *Journal of Applied Physics*, **109**, 074903–1 – 074903–5.
- Schalkwijk, K. M., Wapenaar, C. P. A., & Verschuur, D. J. 2003. Adaptive decomposition of multicomponent ocean-bottom seismic data into downgoing and upgoing P- and S-waves. *Geophysics*, **68**, 1091–1102.
- Schoemaker, F. C., Grobbe, N., Schakel, M. D., de Ridder, S. A. L., Slob, E. C., & Smeulders, D. M. J. 2012. Experimental Validation of the Electrokinetic Theory and Development of Seismoelectric Interferometry by Cross-Correlation. *International Journal of Geophysics*, **2012**.
- Schoemaker, F.C. 2011. *Electrokinetic conversion*. PhD Thesis, Delft University of Technology.
- Schuster, G.T. 2010. *Seismic Interferometry*. Cambridge University Press.
- Schuster, G.T., Yu, J., Sheng, J., & Rickett, J. 2004. Interferometric/daylight seismic imaging. *Geophysical Journal International*, **157**, 838–852.
- Slob, E. 2009. Interferometry by Deconvolution of Multicomponent Multioffset GPR Data. *IEEE Transactions on Geoscience and Remote Sensing*, **47**, 828–838.
- Slob, E.C., & Mulder, W.A. 2011. CSEM Sensitivity Analysis Through Resolution Functions for Migration and Inversion. *73rd EAGE Conference & Exhibition*, **P161**, 1–5.
- Slob, E.C., Draganov, D., & Wapenaar, K. 2007. Interferometric electromagnetic Green's functions representations using propagation invariants. *Geophysical Journal International*, **169**(1), 60–80.
- Smeulders, D. M. J., Grobbe, N., Heller, H. K. J., & Schakel, M. D. 2014. 'Seismoelectric conversion for the detection of porous medium interfaces between wetting and nonwetting fluids. *Vadose Zone Journal*, **13**(5), 1–7.
- Steck, R., Niederer, P., & Knothe Tate, M.L. 2003. A Finite Element Analysis for the Prediction of Load-induced Fluid Flow and Mechanochemical Transduction in Bone. *Journal of Theoretical Biology*, **220**, 249–259.

- Thompson, A. H., Hornbostel, S., Burns, J., Murray, T., Raschke, R., Wride, J., McCammon, P., Sumner, J., Haake, G., Bixby, M., Ross, W., White, B. S., Zhou, M., & Peczak, P. 2007. Field tests of electroseismic hydrocarbon detection. *Geophysics*, **72**, N1–N9.
- Thompson, R.R. 1936. The Seismic Electric Effect. *Geophysics*, **1**, 327–335.
- Thorbecke, J. W., & Draganov, D. 2011. Finite-difference modeling experiments for seismic interferometry. *Geophysics*, **76**, H1–H18.
- Ursin, B. 1983. Review of elastic and electromagnetic wave propagation in horizontally layered media. *Geophysics*, **48**, 1063–1081.
- Valuri, J., Dean, T., & Dupuis, J.C. 2012. Seismoelectric acquisition in an arid environment. *22nd International Geophysical Conference and Exhibition, Australia*, 1–4.
- Van Borselen, R. G., Fokkema, J., & Van den Berg, P. 2013. Wavefield decomposition based on acoustic reciprocity: Theory and applications to marine acquisition. *Geophysics*, **78**, WA41–WA54.
- Van Dalen, K. 2011. *Multi-component acoustic characterization of porous media*. Ph.D. thesis, Delft University of Technology.
- Van der Neut, J., & Herrmann, F. J. 2012. Up / down wavefield decomposition by sparse inversion. *74th EAGE Conference & Exhibition Copenhagen*, **A029**, 4693–4698.
- Van der Neut, J., El Allouche, N., & Wapenaar, K. 2010. Elastic decomposition with downhole geophones and hydrophones. *SEG Expanded Abstracts Denver*, 1708–1713.
- Van der Neut, J., Thorbecke, J., Mehta, K., Slob, E., & Wapenaar, K. 2011. Controlled-source interferometric redatuming by crosscorrelation and multidimensional deconvolution in elastic media. *Geophysics*, **76**, SA63–SA76.
- Van der Neut, J., Bakulin, A., & Alexandrov, D. 2013. Acoustic wavefield separation using horizontal receiver arrays deployed at multiple depth on land. *SEG Expanded Abstracts Houston*, 4601–4607.
- Van Stralen, M. J. N. 1997. *Directional Decomposition of Electromagnetic and Acoustic Wave-Fields-Applications in integrated optics, exploration seismics and underwater acoustics*. PhD Thesis, Delft University of Technology.
- Vasconcelos, I., Snieder, R., & Hornby, B. 2008. Imaging internal multiples from subsalt VSP data ? Examples of target-oriented interferometry. *Geophysics*, **73(4)**, S157–S168.
- Virieux, J. 1986. PSV-wave propagation in heterogeneous media: velocity-stress finite difference method. *Geophysics*, **51**, 889–901.

- Vogler III, J.B., & Murphy, W.A. 1988. Bone Marrow Imaging. *Radiology*, **168**, 679–693.
- Vozoff, K. 1972. The Magnetotelluric Method in the Exploration of Sedimentary Basins. *Geophysics*, **37**, 98–141.
- Wapenaar, C. P. A., & Berkhout, A. J. 1989. *Elastic Wavefield Extrapolation - Redatuning of Single and Multi-Component Seismic Data*. Elsevier.
- Wapenaar, C. P. A., & Grimbergen, J. L. T. 1996. Reciprocity theorems for one-way wavefields. *Geophysical Journal International*, **127**, 169–177.
- Wapenaar, C. P. A., & Verschuur, D. J. 1996. Processing of ocean bottom data. *The Dolphin Project*, **Volume I**, 6.1–6.26.
- Wapenaar, C. P. A., Herrmann, P., Verschuur, D. J., & Berkhout, A. J. 1990. Decomposition of multi-component seismic data into primary P- and S-wave responses. *Geophysical Prospecting*, **38**, 633–661.
- Wapenaar, C. P. A., Dillen, M. W. P., & Fokkema, J. T. 2001. Reciprocity theorems for electromagnetic or acoustic one-way wave fields in dissipative inhomogeneous media. *Radio Science*, **36**, 851–863.
- Wapenaar, K. 1998. Reciprocity properties of one-way propagators. *Geophysics*, **63**, 1795–1798.
- Wapenaar, K., & Fokkema, J. 2004. Reciprocity theorems for diffusion, flow and waves. *Journal of Applied Mechanics*, **71**(revised 2010), 145–150.
- Wapenaar, K., Slob, E., & Snieder, R. 2006. Unified Green's Function Retrieval by Cross Correlation. *Physical Review Letters*, **97**, 234301–1 – 234301–4.
- Wapenaar, K., Slob, E., & Snieder, R. 2008a. Seismic and electromagnetic controlled-source interferometry in dissipative media. *Geophysical Prospecting*, **56**, 419–434.
- Wapenaar, K., Slob, E., & Snieder, R. 2008b. Seismic and electromagnetic controlled-source interferometry in dissipative media. *Geophysical Prospecting*, **56**, 419–434.
- Wapenaar, K., Slob, E., & Snieder, R. 2010. On seismic interferometry, the generalized optical theorem, and the scattering matrix of a point scatterer. *Geophysics*, **75**(3), SA27–SA35.
- Wapenaar, K., Van der Neut, J., Ruigrok, E., Draganov, D., Hunziker, J., E., Slob., Thorbecke, J., & Snieder, R. 2011. Seismic interferometry by crosscorrelation and by multidimensional deconvolution: a systematic comparison. *Geophysical Journal International*, **185**, 1335–1364.
- Warden, S., Garambois, S., Sailhac, P., Jouniaux, L., & Bano, M. 2012. Curvelet-based seismoelectric data processing. *Geophysical Journal International*, **190**, 1533–1550.

- Warden, S., Garambois, S., Jouniaux, L., Brito, D., Sailhac, P., & Bordes, C. 2013. Seismoelectric wave propagation numerical modelling in partially saturated materials. *Geophysical Journal International*, **194**, 1498–1513.
- White, J. E. 1965. *Seismic waves; Radiation, transmission, and attenuation*. McGraw-Hill, New York.
- Widess, M. B. 1973. How thin is a thin bed? *Geophysics*, **38**, 1176–1180.
- Woodhouse, J. H. 1974. Surface waves in a laterally varying layered structure. *Geophysical Journal of the Royal Astronomical Society*, **37**, 461–490.
- Xu, Z., Juhlin, C., Gudmundsson, O., Zhang, F., Yang, C., Kashubin, A., & Luth, S. 2012. Reconstruction of subsurface structure from ambient seismic noise: an example from Ketzin, Germany. *Geophysical Journal International*, **189**, 1085–1102.
- Zhou, H. 2014. *Practical Seismic Data Analysis*. Cambridge University Press.
- Zhu, Z., & Toksöz, M. N. 2005. Seismoelectric and seismomagnetic measurements in fractured borehole models. *Geophysics*, **70**, F45–F51.
- Zhu, Z., & Toksöz, M. N. 2013. Experimental measurements of the streaming potential and seismoelectric conversion in Berea sandstone. *Geophysical Prospecting*, **61**, 688–700.
- Zhu, Z., Haartsen, M. W., & Toksöz, M. N. 2000. Experimental studies of seismoelectric conversions in fluid-saturated porous media. *Journal of Geophysical Research*, **105**, 28055–28064.
- Zhu, Z., Toksöz, M. N., & Zhan, X. 2015. Seismoelectric measurements in a porous quartz-sand sample with anisotropic permeability. *Geophysical Prospecting*, doi: 10.1111/1365-2478.12304.
- Zyserman, F. I., Gauzellino, & P. M., Santos, J. E. 2010. Finite element modeling of SHTE and PSVTM electroseismics. *Journal of Applied Geophysics*, **72**, 79–91.

Summary

Coupled Poroelastic Waves and Electromagnetic Fields in Layered Media

Theory, Modeling, and Interferometric Synthesis

In this thesis, I study coupled poroelastic waves and electromagnetic fields in layered media. The focus is two-fold:

1. Increase the theoretical and physical understanding of the seismo-electromagnetic phenomenon by analytically-based numerical modeling.
2. Investigate the potential of seismo-electromagnetic interferometry.

After presenting the governing equations that form the basis of the theoretical framework, I capture this system into a matrix-vector representation of the wave equation. I first use literature eigenvector sets, which I normalize with respect to power-flux. I then derive new, alternative power-flux normalized eigenvector sets that I prove to be numerically more stable and accurate. The eigenvector sets form the basis of the analytically-based numerical modeling code ‘ESSEMOD’ that I developed to model seismo-electromagnetic wave/field propagation/diffusion in layered-Earth media. The alternative eigenvector set models scenarios with no seismo-electromagnetic coupling correctly, where the literature eigenvector sets fail. In addition, the alternative set properly deals with scenarios where both small amplitude signals and large amplitude signals occur in the record, whereas the literature eigenvector sets result in noise levels masking the small events. The same holds for scenarios with a small seismo-electromagnetic coupling coefficient. I design an effective global reflection scheme that properly describes the primary and multiple reflections in the models. I implement the correct boundary conditions to account for scenarios with a free-surface, and also for scenarios containing fluid/porous medium/fluid transitions. To transform all the seismo-electromagnetic source-receiver combinations in a numerically effective way back from the horizontal wavenumber-frequency domain to the space-frequency domain, I derive and implement explicit Fourier-Bessel transformations.

I then validate the developed modeling code in numerous ways. First of all, I compare the results of seismo-EM layer-code modeling in a homogeneous medium with explicit homogeneous space Green’s function expressions. This comparison provides

a clear validation that the layer-code models the dynamic responses in homogeneous scenarios correctly. Next, I check numerical consistency by carrying out reciprocity checks. I study homogeneous space models, models containing a free-surface and models with interfaces. As a next step, I validate the modeling results of seismo-EM layer-code modeling for typical seismo-electromagnetic laboratory configurations, i.e. models containing fluid/porous medium/fluid transitions. I first compare the purely electromagnetic part of the seismo-EM layer-code with an independently developed purely electromagnetic layered-Earth code. The results match perfectly in both phase and amplitude for full transmission and pure reflection experiments, as well as for a combination of both. I then carry out a seismo-electromagnetic reciprocity test for a fluid halfspace overlying a porous medium halfspace, proving that the coupled poroelastic and electromagnetic fields are modeled consistently and yield the expected results. As a final validation step, I compare ESSEMOD with an independently developed seismo-electromagnetic layered-Earth modeling code. The results display an almost perfect match in both phase and relative amplitudes, and a constant amplitude correction factor of 4 needs to be applied to let the absolute amplitudes match.

I then carry out a small feasibility test to study the potential of the seismo-electromagnetic effect for exploration purposes. I investigate different source-receiver combinations for the same model, and focus on the signal strength recorded at different distances from the target depth level. I conclude that for the source-receiver combinations studied, the electric field due to a volume injection monopole source, as well as the magnetic field due to a seismic bulk force source, yield the strongest converted signals. The receiver-distance from the target of interest plays an important role in the signal measurability. The closer the receivers to the target, the higher the signal strengths. However, when the receivers are located too close to the target, the coseismic reflected fields can mask the interface response fields that we are mainly interested in.

Next, I study if nature itself can help us to overcome the very low signal-to-noise ratio of seismo-electromagnetic converted fields, by investigating the effects of thin-bed geological structures on the seismo-electromagnetic signal. To investigate the effects of bed-thinning on the seismo-electromagnetic interference patterns, I numerically simulate seismo-electromagnetic wave propagation through horizontally layered media with different amounts and thicknesses of thin-beds. I demonstrate seismo-electromagnetic sensitivity to changes in medium parameters on a spatial scale much smaller than the seismic resolution. By simulating moving oil/water contacts during production, where the oil layer is gradually being thinned, seismo-electromagnetic signals are proven very sensitive to oil/water contacts.

I now explore the application of interferometric techniques to the seismo-electromagnetic system, which might eventually lead to an improved signal-to-noise ratio of the weak converted fields. I derive the theory for interferometric retrieval of 2D SH-TE seismo-electromagnetic Green's functions. Using both a circular source configuration and a line source configuration, I show that it is possible to correctly retrieve the dynamic seismo-electromagnetic 2D SH-TE response in a homogeneous medium, using seismic boundary sources only. Using seismo-EM layer-code data, I

then show that it is also possible to correctly retrieve the direct shear wave-related causal coseismic field in a homogeneous medium, in both phase and amplitude. To obtain a perfect match in absolute amplitudes, I apply a single linear scaling factor. I finally carry out interferometric experiments in a model containing a single interface at 800 m depth, proving that it is possible to correctly retrieve all 2D SH-TE causal seismic-related direct and reflected coseismic fields, as well as interface response fields, by cross-correlation interferometry, using seismic boundary sources only. These results are promising for the application of 3D seismo-electromagnetic interferometry using seismo-EM layer-code modeling, and later on, in the field.

Next, I present an alternative way to effectively decompose fields into their up- and downgoing components and different field types, using recordings at multiple depth levels. I present the theory of this MDL decomposition scheme, followed by successful decomposition of synthetic elastodynamic data sets. I additionally study the implications of laterally-varying media on the horizontal wavenumber-frequency domain MDL decomposition scheme. I demonstrate successful decomposition, using an acoustic approximation and applying a combined multi-component / MDL decomposition approach, of a field data set recorded in Annerveen, in the North of the Netherlands. I address how to effectively use the MDL decomposition scheme in a unified fashion, applied to all wave phenomena including seismo-electromagnetic phenomena.

I then make a step towards seismo-electromagnetic inversion, presenting an effective way to carry out a seismo-electromagnetic sensitivity analysis using resolution functions. I start by explaining the theory of resolution functions using a seismo-electromagnetic example. I define the seismo-electromagnetic resolution function for inversion for a bulk density perturbation. I demonstrate the effectiveness of this method by first carrying out a purely electromagnetic sensitivity analysis for a point perturbation in conductivity, located in an isotropic homogeneous half-space. These results are compared with literature results based on analytical homogeneous space Green's function expressions. The result using the seismo-EM layer-code is nearly identical to the literature result. The position of the scatterer is correctly resolved. At the end of this section, I present the results of the fully-coupled seismo-electromagnetic sensitivity analysis for a bulk density contrast for a specific source-receiver combination, using single-frequency multi-component line data. I show that the coupled seismo-electromagnetic system is sensitive to a perturbation in bulk density and that the position of the perturbation can be correctly recovered.

I finalize this thesis by discussing potential seismo-electromagnetic applications, as well as by providing a brief outlook for future research.

Samenvatting

Gekoppelde Poroelastische Golven en Elektromagnetische Velden in Gelaagde Media

Theorie, Modelling, en Interferometrische Synthese

In dit proefschrift onderzoek ik gekoppelde poroelastische golven en elektromagnetische velden in gelaagde media. Het doel van het onderzoek is twee-ledig:

1. Het vergroten van het theoretische en fysische begrip van het seismo-elektromagnetische fenomeen door gebruik te maken van analytisch-gebaseerde numerieke modellering.
2. Het onderzoeken van de potentie van seismo-elektromagnetische interferometrie.

Nadat ik de systeem vergelijkingen heb gepresenteerd die de basis vormen voor het theoretische raamwerk, beschrijf ik dit systeem door middel van een matrix-vector representatie van de golfvergelijking. Ik maak eerst gebruik van eigenvector sets uit de literatuur, op welke ik een power-flux normalisatie toepas. Daarna leid ik nieuwe, alternatieve power-flux genormaliseerde eigenvector sets af, waarvan ik bewijs dat ze numeriek stabiel en preciezer zijn. De eigenvector sets vormen de basis voor de analytisch-gebaseerde numerieke modelleringscode 'ESSEMOD', welke ik ontwikkeld heb om seismo-elektromagnetische golf propagatie / veld diffusie te modelleren in gelaagde-Aarde modellen. Scenario's waar geen seismo-elektromagnetische koppeling optreedt, worden correct gemodelleerd door de alternatieve eigenvector sets, daar waar de eigenvector sets uit de literatuur te kort schieten.

Situaties waar in de opnames zowel signalen van kleine amplitude als signalen van grote amplitude voorkomen, worden op een correcte manier gemodelleerd door de alternatieve eigenvector set, terwijl de literatuur eigenvector sets resultaten opleveren waar de kleine amplitude signalen worden bedekt door de ruis niveaus. Hetzelfde geldt voor scenario's met een kleine seismo-elektromagnetische koppelingscoëfficiënt. Ik ontwikkel een effectief globaal reflectie schema, dat zowel de primaire reflecties als de meervoudige reflecties in de modellen op een correcte manier beschrijft. Om scenario's met een vrij-oppervlak te beschrijven, alsmede scenario's die overgangen bevatten in de vorm vloeistof / poreus medium / vloeistof, heb ik de juiste randvoorwaarden geïmplementeerd. Ik leid expliciete Fourier-Bessel transformaties af en im-

plementeer deze in de gelaagde-Aarde code, om alle seismo-elektromagnetische bron-ontvanger combinaties op een numeriek gezien effectieve manier te transformeren van het horizontale golfgetal-frequentie domein naar het ruimte-frequentie domein.

Vervolgens valideer ik de ontwikkelde modelleringscode op verscheidene manieren. Allereerst vergelijk ik de resultaten van ESSEMOD voor een homogeen medium met expliciete homogene-ruimte Greense functie uitdrukkingen. Deze vergelijking toont aan dat de gelaagde-Aarde modelleringscode de dynamische velden in homogene situaties correct modelleert. Vervolgens controleer ik de numerieke consistentie door het uitvoeren van reciprociteitstesten. Ik bestudeer homogene modellen, modellen met een vrij-oppervlak en modellen met lagen. Daarna valideer ik de modelleringsresultaten van de gelaagde-Aarde code voor typische seismo-elektromagnetische laboratorium configuraties, dat wil zeggen, voor modellen die overgangen bevatten in de vorm vloeistof / poreus medium / vloeistof. Ik vergelijk allereerst het pure elektromagnetische deel van de seismo-EM gelaagde-Aarde code met een onafhankelijk ontwikkelde, pure elektromagnetische gelaagde-Aarde code. De resultaten komen perfect overeen in zowel fase als amplitude, voor volledige transmissie en pure reflectie experimenten, alsmede voor een combinatie van die twee experimenten. Vervolgens voer ik een seismo-elektromagnetische reciprociteitstest uit voor een vloeistof halfruimte boven een halfruimte bestaande uit een poreus medium, waarmee ik bewijs dat de gekoppelde poroelastische en elektromagnetische velden consistent gemodelleerd worden en de verwachte resultaten opleveren. Als laatste validatie stap, vergelijk ik ESSEMOD met een onafhankelijk ontwikkelde seismo-elektromagnetische gelaagde-Aarde modelleringscode. De resultaten laten een bijna perfecte overeenstemming in zowel fase als relatieve amplitude zien, en tonen ook aan dat een constante amplitude correctie factor van 4 nodig is om de absolute amplitudes met elkaar te laten overeenstemmen.

Hierna voer ik een kleine test uit om de potentie van het seismo-elektromagnetische effect voor exploratie doeleinden te bestuderen. Ik onderzoek verschillende bron-ontvanger combinaties voor hetzelfde model, en richt mijn aandacht op de signaalsterkte zoals die wordt gemeten op verschillende afstanden van de diepte van het gebied van interesse. Ik concludeer dat, van de bron-ontvanger combinaties die ik bestudeerd heb, het elektrische veld ten gevolge van een volume-injectie monopool bron, alsmede het magnetische veld ten gevolge van een seismische bulk krachtbron, de sterkste geconverteerde signalen opleveren. De ontvanger afstand tot het gebied van interesse speelt een belangrijke rol bij de signaal meetbaarheid. Echter, als de ontvangers te dicht bij het gebied van interesse geplaatst worden, worden de velden die gegenereerd worden door de laag-contrasten, en die onze prioriteit hebben, bedekt door de coseismische gereflecteerde velden.

Daarna bestudeer ik of de natuur zelf kan helpen om het probleem van de zwakke signaal-ruis verhouding van de seismo-elektromagnetisch geconverteerde velden op te lossen. Ik doe dit door de effecten van geologische structuren, die bestaan uit pakketten van dunne-lagen, op de seismo-elektromagnetische signalen te onderzoeken. Om de effecten van dunner-wordende lagen op de seismo-elektromagnetische interferentie patronen te bestuderen, simuleer ik seismo-elektromagnetische golf propagatie door horizontaal-gelaagde media die verschil-

lende aantallen en diktes aan dunne lagen bevatten. Ik demonstreer dat de seismo-elektromagnetische signalen een gevoeligheid voor veranderingen in de medium eigenschappen hebben op een spatiële schaal die veel kleiner is dan de seismische resolutie. Ik bewijs dat seismo-elektromagnetische signalen erg gevoelig zijn voor olie/water contacten, door bewegende olie/water contacten ten gevolge van productie te simuleren, waarbij de olie laag langzaam dunner wordt.

Vervolgens bestudeer ik de toepassing van interferometrische technieken op het seismo-elektromagnetische systeem, wat uiteindelijk mogelijkerwijs kan leiden tot een verbeterde signaal-ruis verhouding van de zwakke, geconverteerde velden. Ik leid de theorie af voor het verkrijgen van 2D SH-TE seismo-elektromagnetische Green's functies via interferometrie. Door gebruik te maken van zowel een bron configuratie op een cirkel, alsmede een bron configuratie op een lijn, laat ik zien dat de dynamische seismo-elektromagnetische 2D SH-TE signalen correct kunnen worden verkregen in een homogeen medium, door slechts gebruik te maken van seismische bronnen. Vervolgens, door gebruik te maken van data gegenereerd met de seismo-EM gelaagde-Aarde code, laat ik zien dat wederom het directe schuifgolf-gerelateerde causale coseismische veld in een homogeen medium correct kan worden verkregen, in termen van zowel fase als amplitude. Om een perfecte overeenstemming te verkrijgen in termen van absolute amplitude, wordt een enkele lineaire schalingsfactor toegepast. Hierna, voer ik interferometrische experimenten uit in een model dat een enkel contrast bevat op 800 m diepte, waarmee ik bewijs dat alle 2D SH-TE causale seismisch-gerelateerde directe en gereflecteerde coseismische velden door middel van interferometrie door kruiscorrelatie kunnen worden verkregen, alsmede de geconverteerde velden die gerelateerd zijn aan het contrast. Hiervoor hoeft slechts gebruik gemaakt te worden van seismische bronnen. Deze resultaten zijn veelbelovend voor de toepassing van 3D seismo-elektromagnetische interferometrie op data gegenereerd door de seismo-EM gelaagde-Aarde code, en later, op veld data.

Ik presenteer vervolgens een alternatieve manier om velden op een effectieve manier te scheiden in hun op- en neergaande componenten en in de verschillende veld-types, waarbij ik gebruik maak van opnames op verschillende diepte niveaus. Ik beschrijf de theorie van dit MDL decompositie schema, gevolgd door een demonstratie van een succesvolle decompositie van synthetische, elastodynamische data sets. Ik bestudeer ook de effecten van lateraal-variërende media op ons MDL decompositie schema welke geformuleerd is in het horizontale golfgetal-frequentie domein. Ik laat een succesvolle decompositie zien van een veld data set die is verkregen in Annerveen, in het noorden van Nederland. Hierbij maak ik gebruik van een akoestische benadering en een gecombineerd multi-componenten / MDL decompositie schema. Ik beschrijf ook hoe het MDL decompositie schema op een effectieve en uniforme manier te gebruiken, dat wil zeggen dat het schema toepasbaar is op alle golf fenomenen, inclusief het seismo-elektromagnetische fenomeen.

Hierna maak ik een stap in de richting van seismo-elektromagnetische inversie, waar ik een effectieve manier demonstreer om een seismo-elektromagnetische gevoeligheidsstudie uit te voeren, gebruikmakend van resolutiefuncties. Ik begin met een uitleg van de resolutiefunctie theorie, gebruikmakend van een seismo-elektromagnetisch voorbeeld. Ik definieer een seismo-elektromagnetische resolutie-

functie voor inversie voor een perturbatie in de bulk-dichtheid van het medium. Ik demonstreer de effectiviteit van deze methode door allereerst een pure elektromagnetische gevoeligheidsanalyse uit te voeren voor een puntperturbatie in conductiviteit, die zich in een isotrope, homogene halfruimte bevindt. Deze resultaten vergelijk ik met resultaten uit de literatuur die gebaseerd zijn op analytische homogene-ruimte Greense functie uitdrukkingen. De resultaten die zijn gebaseerd op de seismo-EM gelaagde-Aarde code zijn vrijwel identiek aan de resultaten uit de literatuur. De positie van de verstrooiër wordt correct bepaald. Aan het einde van dit hoofdstuk, presenteer ik de resultaten voor de volledig gekoppelde seismo-elektromagnetische gevoeligheidsanalyse voor een contrast in de bulk dichtheid. Ik laat dit zien voor een specifieke bron-ontvanger combinatie, gebruikmakend van multi-componenten lijn data voor een enkele frequentie. Ik toon aan dat het gekoppelde seismo-elektromagnetische systeem gevoelig is voor een verstoring in de bulk dichtheid, en dat de positie van de perturbatie correct bepaald kan worden.

Ik eindig dit proefschrift met een beschrijving van mogelijke seismo-elektromagnetische toepassingen, alsmede met een korte vooruitblik op toekomstig onderzoek.

Acknowledgements

Writing these thesis acknowledgements means that I have reached the final stage of my PhD research. A wonderful moment to reflect on the PhD process, and remember all the people that have contributed in one way or another for me to make this great achievement. I apologize in advance if I, at this moment, forget to mention anybody that has contributed. I hope you always know how grateful I am for your support.

I would like to start by expressing my deepest gratitude to my promotors, Prof.dr.ir. Evert Slob and Prof.dr.ir. Kees Wapenaar. I still remember the great joy I experienced when you confirmed that you would offer me the PhD position on the project ‘Correlation Imaging with Seismo-Electromagnetic Waves’. At that time, I could have never imagined the extend of how wonderful it is to work with you, and how privileged I am to have had both of you as my supervisors and promotors. I am very grateful for the strong physical, mathematical, and computational background that you helped me obtain during my PhD research. Evert, your high-quality supervision demonstrates a broad and detailed scientific knowledge in physics and mathematics, as well as great management skills. On the one hand, you displayed a long-term vision for the project, providing me with perfect guidelines and milestones to achieve, on the other hand, you always actively and enthusiastically supported and assessed all creative ideas from my side, allowing a lot of freedom and flexibility in the project, as well as my personal development as a geophysicist. In addition, you actively stimulated scientific independence, in the broadest sense of the word. Kees, your scientific integrity, mathematical and physical precision in all your research, your very strong theoretical knowledge, and endless creativity are of exceptional quality and a true inspiration. You always have, or create time whenever needed, to discuss science into its greatest details, providing me with strong foundations at each step of the research, and allowing me to continue building onwards to create something amazing. Above all this, both of you have wonderful, friendly, and very approachable personalities, with a lot of humor, which are in my opinion invaluable qualities every supervisor should possess. I am looking forward to our continued collaborations in the future. I would also like to warmly thank Boris Kuvshinov from Shell Global Solutions International B.V., for always being a very supportive, sharp and critical, constructive, positive and knowledgeable Shell mirror-supervisor in this project. Especially interesting discussions regarding the challenge of (too) weak seismo-electromagnetic signal strengths are greatly appreciated. This provides me with the perfect moment to thank the sponsors of this project: Shell Global Solutions International B.V. and FOM, the Dutch Foundation for Fundamental Research

on Matter. This research was funded as a Shell-FOM project within the research program 'Innovative physics for oil and gas'.

Besides supervisors, the people that define your everyday scientific life are your colleagues, not only in Delft, but world-wide. Thanks to all of you for being wonderful colleagues, creating a great work environment, joining and organizing social activities, discussing science, and being always willing to help with scientific problems. I will now address some of you in greater detail. Let me start by addressing Jan Thorbecke. Jan, your support in the development of ESSEMOD has been invaluable. I actually see you as one of my supervisors. You were always ready to help, always excited to find out how to solve another bug in the program, always creative in ways to deal numerically efficient with the many, many source and receiver fields of the seismo-electromagnetic system. Besides all this, you have a great, unselfish, and very friendly personality. I greatly appreciate everything you have done for me in the last couple of years. Joost van der Neut. Joost, your wonderful personality I will never forget. Scientifically, you are always ready to help, you are extremely creative and absolutely not selfish. You always try to connect people, research and ideas. It is inspiring. Besides scientifically, I want to thank you also for many social moments. I never forget our amazing USA road trips. You guided me in my quest to discover the United States of America. You did not only show me the touristy aspects and sites, no, you tried to let me experience the true America. From small pubs in even smaller towns, to our Greyhound bus experience from Las Vegas to Los Angeles. Each moment was precious, each moment I will never forget. Thank you for being a great colleague and an even greater friend. I hope we will have many more road trips in the future. Carlos Almagro Vidal. I want to thank you for many scientific discussions, support with Matlab, social discussions that go beyond the field of geophysics, and of course our wonderful conference visit and holiday in Russia. Especially the train experience from St. Petersburg to Moscow, as well as our St. Petersburg Hostel I will never forget. Thank you Carlos! Asiya Kudarova, thank you for arranging the wonderful visit to Russia. It has been a very impressive visit, and made me fall in love with Russia and Russian food. I hope to visit Russia again in the future, I have only seen the tip of the iceberg yet. I also thank you for being a great 'office-island' colleague. We have laughed a lot, studied Russian and Dutch language together, and teamed-up to develop the DOGS (Delft Organization of Geophysics Students) to what it is today. I truly enjoyed our company visit trips to France, but I especially enjoyed the trip to the United Arab Emirates and Oman which was together with Russia really one of the highlights of my travelling career. I also would like to thank Maria Tatanova, for arranging a wonderful invitation for me and Carlos to have a dinner at your parent's place in St. Petersburg, without actually being there yourself. It was an experience that I will never forget. Jürg Hunziker, you have been a great friend and colleague throughout my PhD career. Your Swiss preciseness and thorough scientific knowledge are a very strong combination. I thank you for all your help and a great collaboration on comparing EMMOD with ESSEMOD. Socially, you were the glue that kept our lunch breaks and apple-breaks together. Unfortunately, things changed after you left. I never forget the wonderful ski-trip you organized to Engelberg. Thank you so much for inviting me

and letting me experience a wonderful ski resort. I hope we can go skiing together again in the future. Christiaan Schoemaker, I want to thank you for many reasons. First of all, for the great enthusiasm you showed about my project from the first moment I arrived in the department. I remember how in the first week you gave me a slingshot into the world of seismo-electromagnetics, by providing a USB-drive full of journal papers, as well as by having many conversations regarding the research already carried out on the topic in Delft, including many nice anecdotes. From day one, you have always been very supportive to and interested in my research. Besides that, you have a great personality, you are always there to help, you are very social (just think of the Christmas cards each year), and full of energy. I remember the workshop we gave on the Children's Science Day in Zaandam, where all the heavy equipment needed to be loaded into your small, blue Volkswagen. You were full of excitement to make the day a true success. Christiaan, thanks for everything! Claudio Patriarca. You made me experience the 'world of the Italians'. With delicious food, warm hospitality, good coffees (and I mean really good), humor, and a family feeling. I want to thank you and Federica for inviting me to all the Italian dinners at your place, where me and Carlos were the only non-Italians. I still remember our language-lessons: you trying to learn Dutch, me learning the basics of Italian. I should not forget to mention Fabio Tosti here, for his energetic and persistent approach of teaching Italian, and of course convincing me about what is the best Italian football team. Claudio, Federica and Fabio, thanks for making me part of the Italian community. I hope we will have another dinner all together soon. Andreas Schaller. I want to thank you, not only for interesting scientific discussions, but moreover for the many social aspects of life we experienced together. I will never forget our weekend morning coffees and afternoon drinks, enjoying the few sun hours the Netherlands have to offer, while sitting at many beach clubs in Scheveningen. You were never too tired to come all the way from Delft, preferably in an active fashion by bike or by roller skates (which then got stuck in the sand), to enjoy the sun together with me and have interesting conversations. These conversations inevitably led to the great plan of going wave surfing together. Yes, wave surfing in the Netherlands. That means, surfing in autumn, winter and early spring, since that's when the waves are at their best. We bought our fancy equipment, were very excited and went... not so often, unfortunately. Travelling from Delft to Scheveningen with a 2 m longboard is apparently less easy than rollerskating that distance. Nevertheless, I hope we will enjoy the waves together soon. Boris Boullenger. After Claudio left as my office neighbour, it was waiting for a new neighbour. Who could possibly substitute Claudio in a good way? Well, it was certainly you! I enjoyed a lot our discussions on research, the future of research, and all other aspects of life. You introduced the after lunch coffee and muffin-breaks, which have become a daily moment in our office routine. You were actively pursuing me to join the Tuesday night colleague-football event, which I truly enjoyed the moments I could join. A true highlight for me was our shared hotel experience in Denver, at the SEG, which was both socially and scientifically a lot of fun. I am still convinced that our evening practice dry-rounds of our presentations have played a key role in my achievement of that year, to win the SEG Award of Merit best student paper

presented. Thanks for being a great colleague Boris. Yohei Nishitsuji, thank you very much for many coffee conversations, and also for being a great personal travel agent during my trip to Japan. Especially when a volcano decided to erupt a few miles from my holiday destination hotel on Yakushima Island, you truly made sure that I would arrive safely and checked what are the alternatives. The idea to visit Yakushima was amazing, and I should also give my warm thanks to Shohei Minato for recommending this beautiful island to me, especially the hike to the old Yomon Sugi tree. I hope I get the opportunity to visit Japan again, and maybe we can then travel all together. Rik Noorlandt, I am grateful for our endless discussions on the Fourier Transform, and the minor but crucial differences between the routines used by Matlab and alternative FFT routines. I will also not forget our creative brainstorm sessions on seismic vibrators, and other geophysical aspects. Thank you also for many social coffee breaks. Alex Kirichek, thank you very much for being such a social and involved colleague. Our joint efforts in the DOGS board were always fruitful and constructive. We had lots of fun and a great educational experience during our DOGS visit to the Emirates and Oman. I wish you all the best pursuing your dreams. Pawan Bharadwaj, Siddarth Sharma, and Amarjeet Kumar, besides for scientific interactions, I wish to thank you all for introducing delicious Indian food to me, and for joining for many beach visits to Scheveningen, where you were all showing off your swimming skills. I hope you will keep practicing this crucial skill in life. Elmer Ruigrok, thank you for inspiring me to organize a seismo-electromagnetic session at AGU, this event was a great success! Nihed El Allouche, thanks for being a wonderful and involved friend in our community. Ralph Feld, thanks for arranging a nice colleagues-trip to Apeldoorn, to enjoy the Dutch forests and good food. I would like to specifically thank Ranjani Shamasundar and Sixue Wu for bringing delicious, real tea for me to enjoy, all the way from India and China! I am still treasuring these leaves, enjoying good quality tea at the moments that it is truly required. Cees Willems, thank you for sharing a great hobby: wave surfing. Your enthusiastic stories were actually part of the inspiration to start surfing. I hope one day we can ride the waves together. I thank Koen van Dongen for a short but inspiring discussion on medical applications of seismo-electromagnetic phenomena. Furthermore, I am very grateful to Karel van Dalen and David Smeulders for useful discussions on eigenvectors and possible ways to derive them. I would like to thank David specifically for involving me in the development of the wonderful Vadose Zone Journal paper we wrote together. I thank Karel for providing me with a very well-designed and user-friendly LaTeX PhD thesis template, that forms the basis for this thesis. The final colleague I want to specifically address is Max Holicki. Max, I still remember how me and Asiya tried to convince you that you would be a perfect president of the DOGS. After some initial doubts, you were mainly very enthusiastic about it and developed yourself in no time into a very responsible and active leader. You had a vision for continuous development of the DOGS, and worked hard to achieve that. I also want to thank you for being a very social and friendly colleague, and for introducing me to the LaTeX graphical system TikZ. Without TikZ, I would have had a way more difficult time to incorporate all the figures of this thesis so nicely into this final work, as well as with displaying very small amplitude

seismo-electromagnetic signals. I am very grateful for all the TikZ support that you have given me, whenever I had another difficult demand on how I desired to display my results. Thanks for always being willing to create some free time to help me out. I furthermore would like to thank the three IDEA-league MSc students that I had the honour to supervise during my PhD research: Gavin Menzel-Jones, Iris Hartstra, and Peter Maas. Many thanks to all of you for the unlimited faith and trust you always had in me, for choosing my research topics for your final thesis work, for working so hard and enthusiastically on the research topics I was so passionate about, for your persistence, and for expressing your sincere gratitude for my supervision. These supervising experiences are invaluable for my future career. I am very grateful that you could be part of that. I will now do an effort to list all other colleagues I have met in Delft over the last couple of years: Panos, Araz, Wieske, Adriaan, Geertje, Ilya, Tomohide, Kasaki, Navid, Helena, Koen, Kevin, Rémi, Andrea, Mattia, Marwan, Michel, Menne, Deyan, Alimzhan, Daria, Silvian, Xander, Xiaoxi, Huajun, Jiaguang, Mohsen, Rahul, Matteo, Lisanne, Myrna, Runhai, Chris, Lele, Gil, Kees, Pieter, Jesper, Reuben, Guy, Ranajit, Láslo, Auke, Wim, Rik, Gert-Jan, and Jan-Kees. I want to thank all of you, and any colleagues that I may have accidentally forgotten, for your direct or indirect contributions to this major achievement in my life. I also thank Karel Heller for introducing me to the endless possibilities of our laboratory. In addition, I now want to take a moment to thank all the people involved in supporting the department as a whole: our beloved secretaries Marlijn Ammerlaan, Lydia Broekhuijsen-Bentvelzen, Margot Bosselaar-Perk, Asha Doergaram, Marja Roep-Van der Klis, Marijke Schillemans-Van Tuijl, and Hannie Zwiers, for providing us with clear communication and support on practically any issue, Ralf Haak for always managing to arrange free working spaces, good computer equipment, and creating a great work atmosphere as a whole, and Anke Dählmann for organizing wonderful science days and great coordination of outreach activities. Furthermore, I want to thank Joost van Meel and Guus Lohlefink for continuous and effective computational hardware support. Guus, I still remember how you tried to help me out remotely, late in the evening, while I was sitting in my hotelroom in Vienna, and you were persistently trying to add the hotel IP-address to the safe list of our cluster, in order for me to be able to still run some modeling experiments. Your support was indispensable for this work.

Besides my colleagues at Delft University of Technology, colleagues from all over the world have contributed to this thesis. I want to highlight a few of these precious people here. First of all, my sincerest gratitude goes out to André Revil. André, I was amazed and extremely grateful when you and Paul Sava asked me to write the preface of your seismoelectric book. It was a true honour for me, and a great acknowledgement for my research. I greatly appreciate the ways you try to involve me in projects, and how you always support me in my scientific career. One of the highlights was the AGU session we organized together, which resulted in the current book development contract we have with Wiley. Another highlight was how we enjoyed delicious food together in Japan, both not really familiar with the language. I am looking forward to our continued collaborations André! Thank you.

Secondly, I would like to thank the researchers of the Earth Resources Laborat-

ory at MIT in general, and more specifically Nafi Toksöz, Zhenya Zhu, and Laurent Demanet. Nafi, thank you for allowing me to visit MIT for several weeks, and for many warm and positive discussions we had. You always created time for me to drop by your office. I really felt at home, and your research suggestions after my presentation at MIT have really helped to improve my thin-bed journal paper. Zhenya, thank you so much for your inexhaustible enthusiasm for seismo-electromagnetics, and for being a wonderful host at MIT. Your laboratory experiments are in my opinion displaying great creativity and show that you have an eye for important research questions and where the potential of the seismo-electromagnetic method lies. The lunch you arranged at MIT was very delicious, and once again displayed what a friendly and social person you are. Thank you Zhenya! Laurent, meeting you at MIT was a truly inspiring experience. Your creativity and energy levels are of exceptional quality! I greatly appreciate our wonderful scientific discussion, that lasted for almost 2 hours. The speed with which you grasp new topics is remarkable, and shows you are a very skilled scientist with a broad vision. Besides all that, you possess a very friendly personality. Unfortunately, I did not grab the amazing opportunity to work with you as a postdoctoral researcher at that time, but hopefully we can work together in the future. I additionally would like to thank Anna Shaughnessy, for her warm hospitality at ERL as well as her continued efforts and involvement in my career development.

My PhD project was a collaboration between the University of Amsterdam UvA (laboratory experiments) and Delft University of Technology (theory and numerical modeling). I would like to thank my colleagues Sareh Nakhaee, Thanh Luong, and Rudolph Sprik from the UvA for stimulating discussions and useful feedback from their laboratory experiments, that helped designing my modeling code and gaining additional insight into the seismo-electromagnetic phenomenon. I would also like to warmly thank Stéphane Garambois and Michel Dietrich of Université Joseph Fourier in Grenoble for the fruitful and very effective collaboration on the comparison of both our numerical modeling codes. Unfortunately, I did not find a moment to visit you in Grenoble, to intensify the collaboration, but hopefully this will happen in the near-future. Nevertheless, Stéphane, you did a wonderful job modeling my benchmark models leading to the numerical comparison section in this thesis. We stay in touch! Yukio Fujinawa, my Japanese colleague and friend. It was you who invited me to be a chairman of and invited speaker in your session ‘Detection of microcracks prior to rupture and layered interfaces by the seismoelectrical method’ at the JpGU meeting in Chiba-city, Japan. Our meeting and your publications have inspired me to study the seismo-electromagnetic phenomenon in relation to Earthquake-related electromagnetic signals and for developing the method as a possible early-warning system. I greatly appreciate your kindness, hospitality, and the honour to be a chairman of your session. I hope we will keep working together to use seismo-electromagnetics for natural hazard-research. I also thank my colleagues from Aramco Overseas Company B.V., at the Global Research Center Delft. Hannes Kutscha, Yimin Sun, Mikhail Belonosov, and Jewoo Yoo, I have spent only a few months with you guys, but those months were a unique experience. You made me part of the Aramco-family in no-time, and creatively supported me in my first

research project. Aramco is a unique place to work, having a great diversity and a lot of scientific knowledge, and offering a very friendly and supportive atmosphere. It truly gives you a family-feeling. I have decided to choose the academic career path, but I sincerely hope we will stay in touch and keep our collaborations alive. Besides the people already mentioned, I additionally thank Sjoerd de Ridder for being a great friend and colleague in the scientific community. I also thank the editors and (anonymous) reviewers of my papers for their time and their useful and constructive comments. Each review report helped improving my manuscripts, and the task of reviewing should never be under-valued.

Not only people in the scientific community have contributed to this work. One should never underestimate the importance of people with different backgrounds, different sets of knowledge, different qualities, and different views. They help to keep you sharp, complement you, make you think critically, support you unconditionally, stimulate and vitalize you, and make you a more complete and balanced person. I would therefore like to address some of you in greater detail, simply because you deserve it.

First of all, my great and wise friend Frans Snel. Frans, you have guided me on my path of life already since I was a small boy. You are always there for me, to listen, to advice, to support, to share our thoughts on life in all its aspects, and to offer me and introduce me to invaluable knowledge and the sources of this knowledge. There are not enough words to express my gratitude. Thank you Frans!

Markwin Seur, another person that I am blessed with to have in my life. Your clear vision, knowledge, and support always help me to keep growing. I greatly appreciate it Markwin.

Paulien Heideman, my beloved mother, thanks for your continuous interest and support in what I am doing, and endless attempts to understand what I am exactly doing. You and dad have provided me with the fundamentals on which I am building my life. I will always be grateful for that, to both of you.

Tom Grobbe, thank you for being a great brother! Whenever I needed to move to a new home, you were always at the forefront to help me voluntarily, energetically developing detailed moving plans to effectively carry out the complete movement in one or two days. We have had some very nice holidays together as well, and I hope we will continue doing so in the future.

Ben Mol, thank you for your help with all kinds of technical issues in my house, for your warm personality and your sharp humor.

Carmelita Poeran, my mother in law, you always make me happy. The delicious food you prepare every time we visit, and the large amounts of it, are a true delight. I hope we will celebrate my PhD degree with one of your famous dishes.

Finally, last but definitely not least: Patricia Mangal. My love, you are truly amazing! I greatly appreciate all your love, care, and patience. You always support me unconditionally, stimulating me to follow my dreams, and seize the opportunities whenever they arise. Your vision on life, and the way you live your life, are truly inspiring. I enjoy every single moment with you. I cannot wait to discover together what beautiful things the future will bring us.

Niels Grobbe

Curriculum Vitae

Personal information

Niels Grobbe *Email:* ngrobbe@gmail.com
Rotterdam *Date of Birth:* March 23, 1987
The Netherlands *Nationality:* Dutch

Job History

December 2015-May 2016 Postdoctoral Researcher in Applied Geophysics at Delft University of Technology

September 2015-November 2015 Research Geophysicist at Aramco Overseas Company B.V., GRC Delft

Education

2010-August 2015 Ph.D. student Applied Geophysics
Delft University of Technology, The Netherlands
2008-2010 M.Sc. Geophysics
Utrecht University, The Netherlands
2005-2008 B.Sc. Earth Sciences (Major Geophysics)
Utrecht University, The Netherlands
1999-2005 High School-Gymnasium
CSG Het Streek, Ede, The Netherlands

Grants and Awards

2015 SEG Award of Merit, Best Student Paper Presented at 2014 SEG Annual Meeting, Denver (Paper title: 'Seismoelectric interface response signal behaviour in thin-bed geological settings').

2012 SEG (Society of Exploration Geophysicists)/Chevron Student Leadership Symposium (SLS) Travel Grant, Las Vegas, USA

Professional Responsibilities

2015 Convener of JpGU session ‘Detection of microcracks prior to rupture and layered interfaces by the seismoelectrical method’, JpGU Annual Meeting, Japan
2014 Primary convener and chairman of AGU session NS ‘The Seismoelectric Method: Going Together to the Next Level’, AGU Fall Meeting, San Francisco, USA
Several Years Reviewer of various GJI (Geophysical Journal International), GEOPHYSICS, and JGR (Journal of Geophysical Research) journal papers, as well as SEG and EAGE conference abstracts.

Councils / Committees / Boards

2013-2015 Member of the Central Works Council of FOM
2011-2013 Secretary of the Central Works Council of FOM
 Additional Committees within this Central Works Council (selection): *Chairman* of ‘Science and Structure’, *FOM Representative* in ‘KORRI’ (Council of National Research Institutes), *Negotiation-committee member* for the secondary labour conditions, *Member* of the ARCNL-Institute (founded 2014) Committee
2011-2012 PhD representative Department Meetings, Delft University of Technology
2010-2013 President (2012-2013) and Treasurer (2010-2012) of the SEG student chapter D.O.G.S. (Delft Organization of Geophysics Students)
2005-2009 Member of several U.G.V. (Utrecht Geological Society) committees

Teaching and Outreach

2014-2015 Started developing MOOC (Massive Open-Online Course) on ‘Mathematical Methods for Geophysicists’
2014 Workshop for the IDEA-league M.Sc. Program in Applied Geophysics: ‘Mathematical Methods for Geophysicists’
2013 Filmed for the Dutch Children’s Educational Television Program ‘Het Klokhuis’ session on the Earth-Geophysics. Later, also asked to give a Children’s Science Day Workshop on Geophysics and contributed to Children’s Science Book.
2011-2013 In charge of the Promotional Days for the Earth Science - Geophysics Program at Delft University of Technology
2011-2013 Assistant in B.Sc. Course ‘Introduction to Reflection Seismology’ at Delft University of Technology

Supervision M.Sc. Research IDEA-league Program in Applied Geophysics

2014 Graduation Committee Member of *Ali Alfaraj*, Thesis title: ‘Elastic Wavefield Decomposition at the Ocean Bottom’

2014 Principle Supervisor of *Petrus Johannes Maas*, Thesis title: ‘Electromagnetic & Seismoelectric sensitivity analysis using resolution functions’

2012 Principle Supervisor of *Iris Hartstra*, Thesis title: ‘Analysis of 2D homogeneous space solutions of the seismoelectric P-SV-TM mode for interferometric purposes’

2011 Principle Supervisor of *Gavin Menzel-Jones*, Thesis title: ‘Seismoelectric Modelling of the Flux-Normalized P-SV-TM Propagation Mode’

Research Collaborations

2014 Massachusetts Institute of Technology (MIT), Boston, USA, 5 weeks visiting researcher.

Training / Courses

- Various CTG Graduate School Courses of Delft University of Technology.
- Several Central Working Council-related training days, including: negotiation-, general working council-, communication- and management team specific-training
- Other FOM Courses: ‘Art of Scientific Writing’, ‘Research Validation / IP / Patents’, ‘Taking Charge of Your PhD’
- IKON Science Americas 3-day Course: Essentials of Rock Physics for Seismic Amplitude Interpretation (by Cristian Malaver, June 2014, Houston, USA)
- PRACE Advanced Training Centre (PATC)-course: Fortran for Scientific Computing (2013, HLRS Stuttgart, Germany)
- SEG/Chevron Student Leadership Symposium (2012, Las Vegas, USA)

Publications and presentations

Peer reviewed articles

Grobbe, N., Thorbecke, J.W. and Slob, E.C. (2016). ‘ESSEMOD- Electromagneto-Seismic and Seismo-Electromagnetic Layered-Earth Modeling’. *Geophysics Algorithms, to be submitted*.

Grobbe, N., Slob, E.C. and Thorbecke, J.W. (2016). ‘Comparison of Eigenvectors for Coupled Seismo-Electromagnetic Layered-Earth Modeling’. *Geophysical Journal International*, doi: 10.1093/gji/ggw128.

Grobbe, N. and Slob, E.C. (2016). ‘Seismo-Electromagnetic Thin-Bed Responses: Natural Signal Enhancements?’. *Journal of Geophysical Research*, doi: 10.1002/2015JB012381.

Grobbe, N., Van der Neut, J., Slob, E., Wapenaar, K., Almagro Vidal, C. and

- Drijkoningen, G. (2015). 'Unified Multi-Depth-Level Field Decomposition'. *Geophysical Prospecting*, doi:10.1111/1365-2478.12290.
- Smeulders, D.M.J., **Grobbe, N.**, Heller, H.K.J. and Schakel, M.D. (2014). 'Seismoelectric conversion for the detection of porous medium interfaces between wetting and nonwetting fluids'. *Vadose Zone Journal*, 13(5), 1-7.
- Schoemaker, F.C., **Grobbe, N.**, Schakel, M.D., Ridder, S.A.L. de, Slob, E.C. and Smeulders, D.M.J. (2012). 'Experimental validation of the electrokinetic theory and development of seismoelectric interferometry by cross-correlation'. *International Journal of Geophysics*, 2012(ID 514242), 1-23.

Conference Oral Presentations

- Grobbe, N.**, Slob, E.C., and Wapenaar, C.P.A. (2016). 'Coupled Seismo-Electromagnetic Interferometry for 2D Homogeneous SH-TE Scenarios'. *78th EAGE Conference & Exhibition incorporating SPE EUROPEC 2016 pp. 1-5.*
- Grobbe, N.** and Slob, E.C. (2015). 'Seismoelectric Interferometry' (*invited*). *JpGU Annual Meeting 2015, Chiba-city, Japan.*
- Smeulders, D., **Grobbe, N.**, Heller, K. and Schakel, M. (2014). 'Saturation-dependent Coupled Seismic and Electromagnetic Wave Propagation in Porous Media'. *AGU Fall Meeting 2014, San Francisco, USA.*
- Grobbe, N.** and Slob, E.C. (2014). 'Seismoelectric interface response signal behaviour in thin-bed geological settings'. *SEG Technical Program Expanded Abstracts pp. 3428-3432.*
- Grobbe, N.**, Hunziker, J.W. and Slob, E.C. (2014). 'Seismoelectric wave propagation modeling for typical laboratory configurations: A numerical validation'. *SEG Technical Program Expanded Abstracts, pp. 2072-2077.*
- Grobbe, N.**, Van der Neut, J., Almagro Vidal, C., Drijkoningen, G. and Wapenaar, K. (2014). 'Wavefield Decomposition of Field Data, Using a Shallow Horizontal Downhole Sensor Array and a Free-surface Constraint'. *76th EAGE Conference & Exhibition incorporating SPE EUROPEC 2014 pp. 1-5.*
- Grobbe, N.** and Slob, E.C. (2013). 'Validation of an electroseismic and seismoelectric modeling code, for layered earth models, by the explicit homogeneous space solutions'. *SEG Technical Program Expanded Abstracts pp. 1847-1851.*
- Van der Neut, J.R., Almagro Vidal, C., **Grobbe, N.** and Wapenaar, C.P.A. (2013). 'Turning one-sided illumination into two-sided illumination by target-enclosing interferometric redatuming'. *75th EAGE Conference & Exhibition incorporating SPE EUROPEC 2013 pp. 1-5.*
- Grobbe, N.**, Thorbecke, J.W. and Slob, E.C. (2012). 'ESSEMOD - electroseismic and seismoelectric flux-normalized modeling for horizontally layered, radially symmetric configurations'. *Proceedings of the EGU General Assembly 2012 Vol. 14, Geophysical Research Abstracts pp. 10011-10011.*

Conference Poster Presentations

Grobbe, N., Maas, P.J., Slob, E.C. and Mulder, W.A. (2015). ‘Towards Seismoelectric Inversion: Sensitivity Analysis using Resolution Functions’. *JpGU Annual Meeting 2015, Chiba-City, Japan*.

Maas, P.J., **Grobbe, N.**, Slob, E.C. and Mulder, W.A. (2015). ‘Electromagnetic & Seismoelectric Sensitivity Analysis using Resolution Functions’. *77th EAGE Conference & Exhibition incorporating SPE EUROPEC 2013 pp. 1-5*.

Grobbe, N. and Slob, E. (2014). ‘Numerical Modeling of Seismoelectric Fields through Thin-Beds’. *AGU Fall Meeting 2014, San Francisco, USA*.

Slob, E. and **Grobbe, N.** (2014). ‘Determining Green’s Functions for Coupled Elastic Waves and Electromagnetic Fields in a Homogeneous Porous Medium’. *AGU Fall Meeting 2014, San Francisco, USA*.

Grobbe, N., Van der Neut, J.R. and Almagro Vidal, C. (2013). ‘Flux-normalized elastodynamic wavefield decomposition using only particle velocity recordings’. *SEG Technical Program Expanded Abstracts pp. 4693-4698*.

Grobbe, N., Thorbecke, J.W. and Slob, E.C. (2012). ‘Seismoelectric numerical modeling of the SH-TE propagation mode in 3D’. *Dutch inter pore meeting: Rijswijk, the Netherlands*.

Grobbe, N., Schoemaker, F.C., Schakel, M.D., Ridder, S.A.L. de, Slob, E.C. and Smeulders, D.M.J. (2012). ‘Electrokinetic fields and waves: Theory, experiments and numerical modeling’. *Proceedings of the EGU General Assembly 2012 Vol. 14, Geophysical Research Abstracts pp. 1-1*.

Grobbe, N., Slob, E.C. and Wapenaar, C.P.A. (2011). ‘Correlation imaging with seismo-electromagnetic waves’. *Seismoelectric Workshop pp. 1-1, Hannover, Germany: Leibniz Institute for Applied Geophysics*.

Books and Others

2015 Started to develop an AGU/Wiley Book on ‘Seismoelectric exploration: Theory, Experiments and Applications’, as Chief-editor.

2015 Poster ‘Seismoelectric Thin-Bed Responses: Can Geology Help Us?’ at Annual Research Meeting Delft University of Technology.

2014 Wrote the ‘Preface’ of the book: ‘The Seismoelectric Method — Theory and Applications’, by A. Revil, A. Jardani, P. Sava and A. Haas.

2014 Oral presentation ‘Seismoelectric Phenomena: Modeling Typical Laboratory Configurations and Thin-bed Responses’, during visit at ERL Massachusetts Institute of Technology, USA.

2013 Oral presentation ‘The Seismoelectric Phenomena: Wave Propagation Modeling and Trying to Meet the Industrial Challenges’ at Annual Research Meeting Delft University of Technology.

2012 Oral presentation ‘Correlation Imaging with Seismo-Electromagnetic Waves’, during visit at SEP Stanford, USA.